Physics of the Solid State, Vol. 45, No. 7, 2003, pp. 1207–1212. Translated from Fizika Tverdogo Tela, Vol. 45, No. 7, 2003, pp. 1153–1158.

METALS AND SUPERCONDUCTORS

Low-Temperature Anomalies in the Specific Heat and Thermal Conductivity of MgB_2

N. V. Anshukova*, B. M. Bulychev, A. I. Golovashkin*, L. I. Ivanova***, A. A. Minakov****, and A. P. Rusakov*****

**Lebedev Physical Institute, Russian Academy of Sciences, Leninskiĭ pr. 53, Moscow, 119991 Russia*
***Moscow State University, Vorob'evy gory, Moscow, 119899 Russia*
****Moscow Institute of Steel and Alloys, Leninskiĭ pr. 4, Moscow, 119991 Russia*
*****General Physics Institute, Russian Academy of Sciences, ul. Vavilova 38, Moscow, 119991 Russia*

Received October 11, 2002

Abstract—The temperature dependences of the specific heat $C(T)$ and thermal conductivity $K(T)$ of MgB_2 were measured at low temperatures and in the neighborhood of T_c. In addition to the well-known superconducting transition at $T_c \approx 40$ K, this compound was found to exhibit anomalous behavior of both the specific heat and thermal conductivity at lower temperatures, $T \approx 10$–12 K. Note that the anomalous behavior of $C(T)$ and $K(T)$ is observed in the same temperature region where MgB_2 was found to undergo negative thermal expansion. All the observed low-temperature anomalies are assigned to the existence in MgB_2 of a second group of carriers and its transition to the superconducting state at $T_{c2} \approx 10$–12 K. © *2003 MAIK "Nauka/Interperiodica".*

1. INTRODUCTION

The unexpected discovery [1] of high-temperature superconductivity in MgB_2 has spurred intense interest in the properties of this compound. A wealth of studies dealing with MgB_2 have been published thus far [2]. The interest in this compound stems, besides from its high critical temperature $T_c \approx 40$ K, from its comparatively simple structure, high conductivity, and relatively high critical fields and currents, including the case of strong magnetic fields. Critical current densities in excess of 10^7 A/cm^2 and critical fields of 40 T have already been reached in MgB_2 [2]. Unlike the cuprate high-temperature superconductors (HTSCs), the properties of the new material are less anisotropic. It features a large coherence length, which makes this material very attractive for application in superconductor-based electronics.

At this stage of research, it is essential to understand whether the critical temperature of this class of superconductors can be increased. First of all, one has to learn whether the MgB_2 compound belongs to traditional superconductors, whose characteristics are described by the Bardeen–Cooper–Schrieffer theory (BCS), or if it is close in properties to the cuprate HTSCs. The available data do not offer an unambiguous answer to the question of the nature of superconductivity in this compound. Its critical temperature is close to the theoretical limit predicted by BCS theory and can even be in excess of it. This may be considered an argument supporting the mechanism of superconductivity in MgB_2 being unusual. On the other hand, the high carrier concentration $N \approx 1.5 \times 10^{23}$ cm^{-3} suggests the standard mechanism of superconductivity in MgB_2 [3]. The carrier concentration in cuprate HTSCs is typically $N \approx (3–5) \times 10^{21}$ cm^{-3}. As follows, however, from band structure calculations made for MgB_2, the concentration indicated above relates to carriers of two types [4] deriving from different parts of the Fermi surface (originating from different boron states). If the quasi-two-dimensional boron p_{xy} states with the carrier concentration $N_{xy} \approx 10^{22}$ cm^{-3} play the same role as the quasi-two-dimensional states of oxygen in the cuprate HTSC CuO_2 sheets, the high-temperature superconductivity of MgB_2 at $T \approx 40$ K may be due to only one of these two carrier groups. The available theoretical calculations [5, 6] and experimental data on the specific heat [7–13] and thermal conductivity [12–15] reveal the possible existence of two superconducting transitions, at $T \approx 40$ and ≈10 K. Additional experiments are needed, however, before a final conclusion can be reached.

The cuprate HTSCs are known to exhibit a number of characteristic anomalies in their properties. In particular, thermal expansion of high-quality samples of cuprate HTSCs at low temperatures reveals an anomaly, namely, a negative thermal expansion coefficient α [16]. In addition, a magnetic field has been found to strongly affect the temperature dependence $\alpha(T)$ in the region of this anomaly [17]. These features are not observed in conventional superconductors. Preliminary data reported recently in [18] show, however, the same anomalies to exist in MgB_2 at low temperatures. Thus, there are no grounds to maintain that MgB_2 is similar to conventional superconductors.

This communication reports on measurements of the temperature dependences of the specific heat $C(T)$

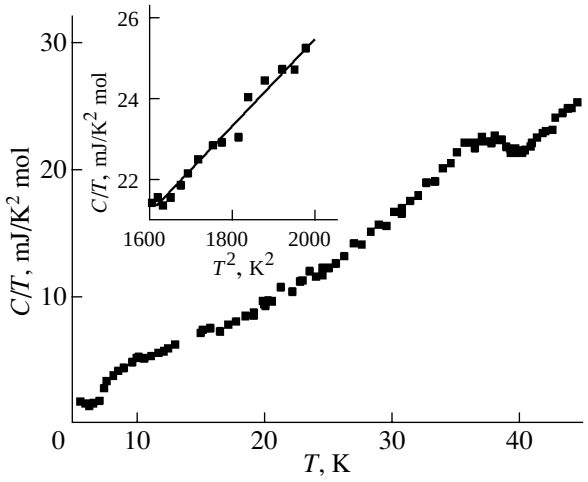

Fig. 1. Temperature dependence of the specific heat for the MgB_2 sample 1 plotted in the C/T vs. T coordinates. Inset compares the interpolation relation $C/T = 4.394 + 1.065 \times 10^{-2}T^2$ for the MgB_2 specific heat (solid line) with the experimental data obtained for $40 < T < 45$ K on the same sample (symbols).

and thermal conductivity $K(T)$ of MgB_2 in the neighborhood of T_c and at lower temperatures.

2. EXPERIMENTAL TECHNIQUES

The temperature dependences of the specific heat and thermal conductivity of samples were measured using modulation calorimetry [19, 20] (temperature modulation frequency 20 Hz) under continuous temperature scanning at a rate of about 1 K/min, as well as in quasi-isothermal conditions at different frequencies in the range 0.05–160 Hz to monitor the measurements. The amplitude of the modulating heat flux was 0.1, 0.45, and 0.7 mW at temperatures of 5–10, 10–20, and 20–50 K, respectively. The sample temperature oscillation amplitude was varied in the 0.002 to 0.07-K interval. A variable heat flux $P(T) = P_0\cos\omega t$ was supplied to one side of the disk. In this way, decaying temperature waves $T(t) = \mathrm{Re}[T_0\exp(i\omega t \pm kz)]$ were excited in the sample. The specific heat and thermal conductivity of the sample were derived from the measured T_{01} and T_{02} amplitudes, as well as from the phases φ_1 and φ_2 of the temperature oscillations $T_{01}\sin(\omega t + \varphi_1)$ and $T_{02}\sin(\omega t + \varphi_2)$ on opposite sides of the sample. The dependence of the specific heat and thermal conductivity on temperature could be obtained with a resolution of 0.01 K. The relative measurement errors of the specific heat was 0.3% and of the thermal conductivity, 1%. The method of two-channel modulation calorimetry is described in detail in [19, 20].

3. SAMPLES

The MgB_2 samples were obtained by hot pressing of MgB_2 powders. The starting magnesium diboride powder was synthesized by reacting metallic magnesium with elemental boron. Standard conditions were used, with the temperature 950–1000°C maintained for four hours at atmospheric pressure. The material thus prepared was single phase. MgB_2 pellets were prepared at a high pressure, 50 kbar, and temperatures of 950–1000°C. The sintering pressure was varied only slightly. The sample density varied within a 3% interval. The density of the MgB_2 samples synthesized at a higher pressure was 97–98% of the ideal density determined from the x-ray diffraction data. The x-ray diffraction patterns of the MgB_2 samples were obtained on a DRON-4 diffractometer and agree with the standard values quoted in review [2]. The quality of the samples was characterized by measuring their electrical and magnetic properties, which were found to match the reference data [2]. The Meissner effect was over 44%. To study the specific heat and thermal conductivity, samples 2.8–3.2 mm in diameter and 1–5 mm high were prepared.

4. EXPERIMENTAL DATA

Figure 1 presents the temperature dependence of specific heat drawn in C/T vs. T coordinates for MgB_2 (sample 1) obtained in this study in the range 5–45 K. The curve exhibits two clearly pronounced features, namely, at $T \approx 38$–40 and ≈10 K. The feature at $T \approx 38$–40 K reflects the sample transition to the superconducting state. A similar curve was obtained in the region of T = 5–50 K for sample 2. A slight difference was observed only in the magnitude of the jumps of the specific heat; this could be assigned to the samples differing insignificantly in density (3%).

One usually estimates the jump in the specific heat ΔC by applying a strong magnetic field which destroys the superconducting state. In this case, one can determine not only ΔC but also the entropy, free energy, and the superconducting-transition parameters in terms of, for instance, BCS theory [7]. If one intends, however, to estimate the magnitude of ΔC only, one can use the difference between the experimental $C(T)$ curve and an interpolation relation $C(T)$, provided the maximum in the specific-heat jump ΔC for $T < T_c$ lies near T_c and an interpolation relation for $T > T_c$ is fitted to the experiment in the immediate vicinity of T_c. In our case, the interpolation relation obtained in an extended version of the Debye model $C/T = \gamma + \beta_2T^2 + \beta_4T^4$ was found to agree well with experimental data for MgB_2 for $40 < T < 50$ K. In the region of the specific-heat jump, however, the difference between this interpolation expression and the simpler relation $C/T = \gamma + \beta_2T^2$ was only 1–1.5%, to become negligible at higher temperatures. The inset to Fig. 1 illustrates the agreement of the interpolation relation $C/T = 4.394 + 1.065 \times 10^{-2}T^2$ obtained by least squares fitting with the experimental data for MgB_2 sample 1 in the temperature interval $40 < T < 45$ K. The applicability of such simple expressions to interpolation is due to the temperature of the interpolation

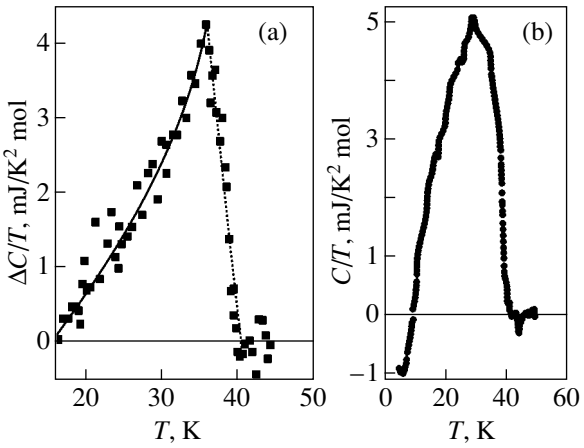

Fig. 2. Specific-heat jump in the neighborhood of T_c plotted as $\Delta C/T$. (a) Sample 1 (the dotted and solid lines are interpolations for the corresponding parts of the $\Delta C/T$ vs. T relation) and (b) sample 2.

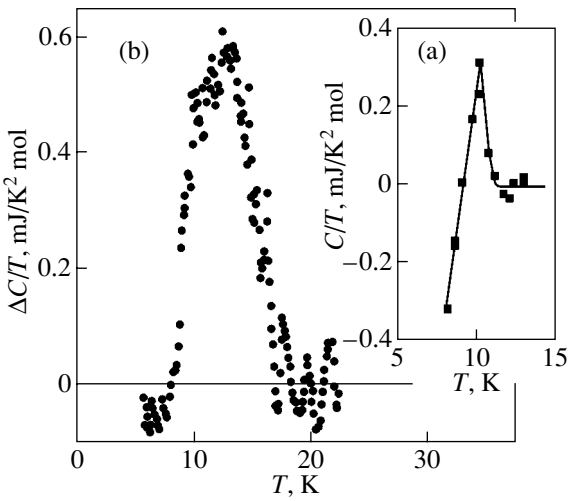

Fig. 3. Difference between the specific heats of MgB_2 in the low-temperature domain obtained by subtracting the interpolation relation from the experimental curve. (a) Sample 1 (solid lines are drawn to aid the eye) and (b) sample 2.

region ($T \approx 40$ K) being substantially lower than the Debye temperature for MgB_2 ($\Theta \approx 900$–1000 K [7–11]).Therefore, this interpolation can be safely employed, with due account of the fact, however, that it is valid for the narrow temperature interval $\Delta T \approx 15$–20 K only [7–11].

Figure 2 shows specific-heat jumps $\Delta C/T$ in the vicinity of T_c for both MgB_2 samples, which were obtained by subtracting the interpolation relations from the experimental curves. The superconducting transitions in both samples are seen to start at $T \approx 40$ K. Thus, the critical temperature derived from the start of the specific-heat jump is $T_c \approx 40$ K. The maxima in the specific-heat jumps lie close enough to the boundary of the interpolation region, $T \approx 40$ K, which validates the applicability of the simple Debye interpolation relation to estimation of the specific-heat jump ΔC near T_c. As follows from Fig. 2, for the MgB_2 samples studied, $\Delta C \approx 145$–152 mJ/K mol. These figures are generally in accord with literature data [7–12] but are slightly larger.

The second feature in the $C(T)/T$ is observed in both samples in the region $T \approx 10$–15 K. At higher temperatures, the $C(T)/T$ relation near this feature is fitted well by the Debye expressions. The differences obtained by subtracting the interpolation relations from the experimental curves for the low-temperature specific heats of the MgB_2 samples studied are displayed in Fig. 3. Both samples are seen to exhibit an additional sharp jump ΔC_2 in the specific heat. The maxima of these features are located at $T \approx 10$–12 K. This behavior of the specific heat attests to a phase transition occurring in MgB_2 at $T = T_{c2} \approx 10$–12 K. There are theoretical grounds to believe [4–6] that this is the temperature at which the second group of carriers becomes superconducting. Below the temperatures corresponding to the maxima in the features, one observes a strong decrease in the measured specific heat, as is the case with conventional superconductors at their transition to the superconducting state. Estimation yields $\Delta C_2 = 3.2$ mJ/K mol for sample 1 and $\Delta C_2 \approx 7.6$ mJ/K mol for sample 2. Note that the number of experimental points obtained for sample 1 in this temperature interval is fairly small and, therefore, the value of ΔC_2 derived for it should be considered a lower bound.

The thermal conductivity $K(T)$ of the MgB_2 samples studied depended considerably on the conditions in which they were fabricated, i.e., on the temperature and pressure. The thermal conductivity of MgB_2 at low temperatures is fairly small and coincides, for instance, with that of Nb_3Sn. Figure 4 presents the $K(T)$ dependence obtained for sample 1 in the interval $T = 5$–45 K. The $K(T)$ curve of MgB_2 is seen to have both anomalies observed in $C(T)$. The $K(T)$ anomaly in the region of the critical temperature at $T \approx 38$–40 K (shown in the inset to Fig. 4 in expanded scale) is less pronounced and seen as a hump above the dotted line drawn to aid the eye. Note that the higher the sample thermal conductivity, the weaker this anomaly. The anomaly in the low-temperature domain, $T \approx 10$–12 K, is more distinct. This anomaly is displayed in Fig. 5 in expanded scale for both samples. The dashed lines plot the interpolation relations obtained at low temperatures near the corresponding anomaly. In all cases (both at T_c and at $T \approx 10$–12 K), the falloff of $K(T)$ with decreasing temperature slows down as one approaches the phase transition. One clearly sees that the three anomalies observed in MgB_2 at $T \approx 10$–12 K coincide, namely, the anomalies in the specific heat $C(T)$ and thermal conductivity $K(T)$ revealed in the present study and the anomaly in thermal expansion $\alpha(T)$ discovered by us earlier [18].

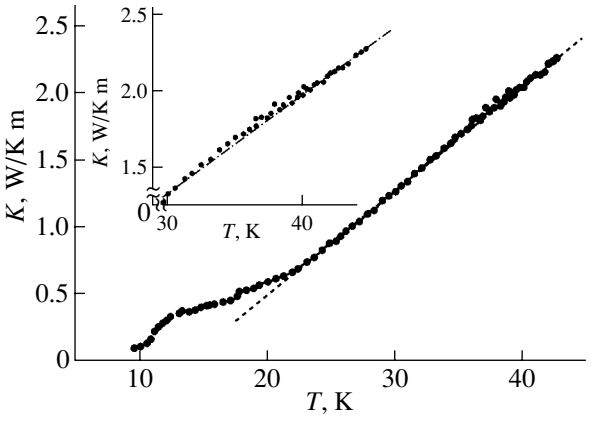

Fig. 4. Temperature dependence of the thermal conductivity of MgB_2 measured in the interval 5–45 K (sample 1). The dotted line was drawn to make the feature in the temperature interval corresponding to the superconducting transition at T_c more revealing. Inset shows the feature near T_c in expanded scale.

5. DISCUSSION

(1) As follows from the results obtained for MgB_2 in this study and in [18], the temperature dependences of the specific heat $C(T)$, thermal conductivity $K(T)$, and thermal expansion coefficient $\alpha(T)$ exhibit anomalies in the temperature region $T \approx 10$–12 K. This coincidence can hardly be considered accidental. However, there should be a common reason accounting for the anomalous behavior of the three different quantities in the given temperature interval. We believe that, at $T \approx 10$–12 K, MgB_2 undergoes a transition to the superconducting state (the Bose condensate) of the second group of carriers. In this case, the $C(T)$ anomaly has a natural explanation. An increase in the thermal conductivity $K(T)$ near the superconducting transition has been frequently observed to occur in various alloys and compounds [21] and was assigned to a decrease in the phonon scattering from electrons or holes caused by their pairing. As is evident from Fig. 4, a slight increase in $K(T)$ of MgB_2 is also seen to exist against the background of the overall falloff of the thermal conductivity in the interval $T \approx 38$–40-K, i.e., in the neighborhood of the main critical temperature T_c. Because the concentration of the freezing-out carriers responsible for this transition, $N \approx 10^{22}$ cm^{-3}, is substantially lower than the total carrier concentration $N \approx 1.5 \times 10^{23}$ cm^{-3} [3], one should expect a considerably stronger effect at the second transition in the region $T \approx 10$–12 K where most of the carriers undergo pairing.

(2) It is more difficult to interpret the coincidence of the $K(T)$ and $C(T)$ anomalies with the anomaly in $\alpha(T)$. The presently accepted model [17, 18] relates the appearance of negative values of $\alpha(T)$ at low temperatures in MgB_2 and the cuprate HTSCs to the structural instability of these compounds. Note that the anomalous (negative) thermal expansion can be accounted for

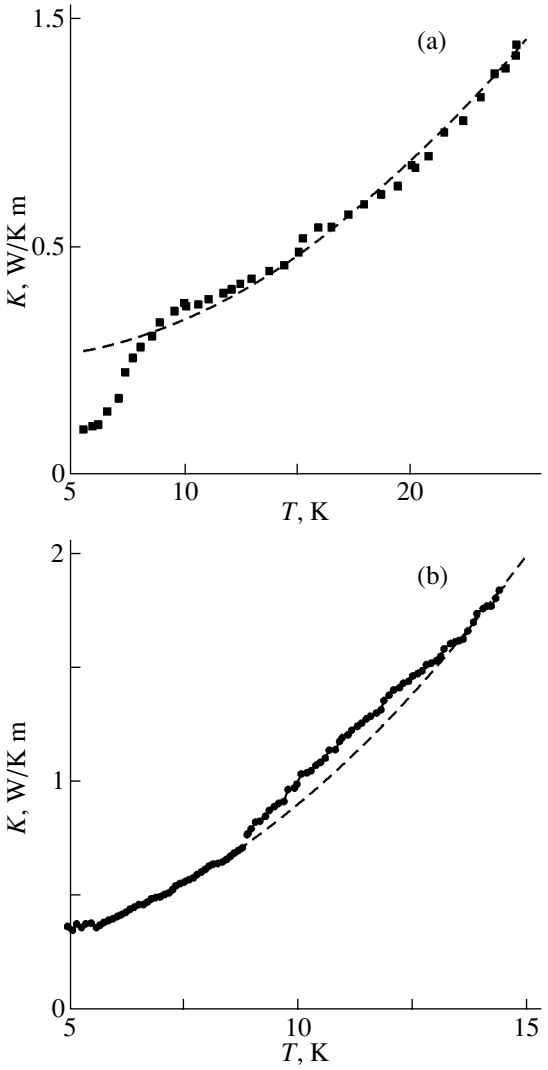

Fig. 5. Low-temperature anomalies in the thermal conductivity of MgB_2 at $T \approx 10$–12 K. (a) Sample 1 and (b) sample 2. Dashed lines are the interpolation relations for the thermal conductivity obtained in the vicinity of the anomalies.

by the influence of charge density waves (CDWs) on the lattice stability [22]. If the additional Coulomb interaction of CDWs with the ionic lattice is disregarded, the structure of these compounds is unstable; i.e., the transverse acoustic phonon frequency ω_{TA} at the Brillouin zone edge tends to zero. As a result of CDW interaction with the lattice ions in these compounds, the frequency ω_{TA} at the zone edge becomes positive ($\omega_{TA} > 0$). Heating (starting from $T = 0$) excites first only the low-frequency modes of the phonon spectrum with $\omega \approx kT/\hbar$ (here, k is the Boltzmann constant, $\hbar$ is Planck's constant). The lowest frequency ω_{TA} branch near the Brillouin zone edge has a large phonon density of states (the low-frequency peak). The major contribution to the ω_{TA} frequency near the zone edge in such compounds comes from CDWs. A charge density wave appears on the oxygen sublattice in an HTSC due to the

existence of large congruent parts of the Fermi surface [22, 23]. In MgB_2, the planes formed by boron atoms play the role of CuO_2 sheets. Electron–phonon coupling in the presence of such congruent Fermi surface regions gives rise to divergence of the dielectric susceptibility and to a negative dielectric permittivity $\varepsilon(\omega, Q)$ for the wave vectors Q connecting these regions. Therefore, excitation of phonons with such values of Q and ω should cause the crystal to contract because $\varepsilon(\omega, Q) < 0$. The temperature corresponding to this region of frequencies ω is $T \approx \hbar\omega/k$, and it is near this temperature that a negative value of α should be observed. Further heating excites phonons of other spectral modes with higher frequencies. For those modes, $\varepsilon(\omega, Q) > 0$, which brings about normal behavior of $\alpha(T)$ (i.e., $\alpha > 0$). Thus, the anomaly $\alpha < 0$ may appear without any phase transition at all. Such an anomalous $\alpha(T)$ relation, accounted for by an electronic contribution to thermal expansion at low temperatures, is observed to occur, for instance, in tetrahedral semiconductors (Ge, Si, GaAs, ZnS, etc.), where the role of CDWs in our situation is played by the so-called electronic charges on covalent tetrahedral bonds [24, 25].

We believe that, in the case of MgB_2, the freezing out of high-frequency phonons under sample cooling and the formation of $\varepsilon(\omega, Q) < 0$ provides an additional possibility of carrier pairing and transition of the second group of carriers to the superconducting state. Anomalies in the properties of MgB_2 at temperatures $T \approx 10$–12 K have also been detected using other methods and can also be related to the existence of a second superconducting gap [2].

(3) The above interpretation of the experimental data (the existence of two carrier transitions to the superconducting state) offers the possibility of estimating the value of γ (the coefficient of the linear term in the temperature dependence of the specific heat that is proportional to the density of states at the Fermi level) for each carrier group. The value of γ derived from the temperature dependence of specific heat for $T > T_c$ is actually a sum of the corresponding values for each group of carriers, i.e., $\gamma = \gamma_1 + \gamma_2$. The coefficient γ_1 relates to the first carrier group, which is responsible for $T_c \approx 40$ K in MgB_2, and γ_2 is associated with the second carrier group, which accounts for the anomalies at $T_{c2} \approx$ 10–12 K. The figures obtained are $\gamma = 4.39$ mJ/K^2 mol (sample 1) and $\gamma = 3.99$ mJ/K^2 mol (sample 2). Assuming the contribution due to the electronic specific heat of the second carrier group to be negligible for temperatures below 15 K (this is suggested by the nearly linear C/T vs. T^2 plot in this temperature region above the anomaly), one can determine the values of γ_1 and γ_2 independently: $\gamma_1 = 1.48$ and 1.44 mJ/K^2 mol and $\gamma_2 =$ 2.91 and 2.55 mJ/K^2 mol for samples 1 and 2, respectively. Thus, our measurements yield for MgB_2 $\gamma_1 =$ 1.4–1.5 mJ/K^2 mol and $\gamma_2 = 2.55$–2.9 mJ/K^2 mol.

Since the magnitude of γ is proportional to the electronic density of states at the Fermi level, the ratio $\gamma_2/\gamma_1 \approx 2$ is a characteristic of the ratio of these densities for the two groups of carriers in MgB_2. A more precise estimate of the ratio of the densities of states can be obtained by taking into account the difference in bond strength between these two groups. To estimate the concentration ratio of these groups of carriers, one also has to take into account the difference between their effective masses. Unfortunately, we are not aware of any reliable experimental data on these quantities for MgB_2.

(4) One can estimate the ratio of the specific-heat jump at T_c to the product of T_c multiplied by the coefficient of the linear term in the temperature dependence of the specific heat γ. According to the BCS theory, $\Delta C/\gamma T_c = 1.43$. Taking for $\Delta C/T_c$ its value at the maximum (Fig. 2), we find that $\Delta C/\gamma_1 T_c \approx 2.89$ for sample 1 and ≈2.57 for sample 2. These values of the ratio suggest the first group of carriers present at a lower concentration to be strongly bound in MgB_2. The ratio $\Delta C_2/\gamma_2 T_{c2}$ for the second (low-temperature) transition as determined directly from the curves in Fig. 2 does not exceed 0.2. Such a small value may indicate the formation of a superconducting gap only in certain regions of the Fermi surface corresponding to the second carrier group. Determination of these regions requires additional study.

6. CONCLUSION

To sum up, we have found MgB_2 to exhibit an anomalous behavior of the specific heat and thermal conductivity at low temperatures. The temperature region where these anomalies are observed coincides with the region of an anomalous (negative) coefficient of thermal expansion. These anomalies are assigned to the existence in MgB_2 of a second group of carriers and to its transition to the superconducting state at $T \approx 10$–12 K. Studies of other properties of MgB_2 [2] lend support to this conclusion.

ACKNOWLEDGMENTS

The authors are indebted to Ya.G. Ponomarev for assistance in this study.

This study was supported by the Russian Foundation for Basic Research (project no. 01-02-16395) and the Scientific Council for Research and Development Programs ("Topical Problems in the Physics of Condensed Media," subprogram "Superconductivity").

REFERENCES

1. J. Nagamatsu, N. Nakagawa, T. Nuranaka, *et al.*, Nature **410**, 63 (2001).
2. C. Buzea and T. Yamashita, Supercond. Sci. Technol. **14**, R115 (2001).
3. S. L. Bud'ko, C. Petrovic, G. Lapertot, *et al.*, cond-mat/0102413 (2001).

4. J. Kortus, I. I. Mazin, K. D. Belashchenko, *et al.*, Phys. Rev. Lett. **86**, 4656 (2001).
5. A. Y. Liu, I. I. Mazin, and J. Kortus, Phys. Rev. Lett. **87**, 087005 (2001).
6. A. A. Golubov, J. Kortus, O. V. Dolgov, *et al.*, J. Phys.: Condens. Matter **14**, 1353 (2002).
7. Y. Wang, T. Plackowski, and A. Junod, Physica C (Amsterdam) **355**, 179 (2001).
8. F. Bouquet, R. A. Fisher, N. E. Phillips, *et al.*, Phys. Rev. Lett. **87**, 047001 (2001).
9. S. L. Bud'ko, G. Laperton, C. Petrovic, *et al.*, Phys. Rev. Lett. **86**, 1877 (2001).
10. H. D. Yang, J.-Y. Lin, H. H. Li, *et al.*, Phys. Rev. Lett. **87**, 167003 (2001).
11. Ch. Wälti, E. Felder, C. Degen, *et al.*, Phys. Rev. B **64**, 172515 (2001).
12. E. Bauer, Ch. Paul, St. Berger, *et al.*, J. Phys.: Condens. Matter **13**, L487 (2001).
13. N. V. Anshukova, B. M. Bulychev, A. I. Golovashkin, *et al.*, Kratk. Soobshch. Fiz. (2002) (in press).
14. A. V. Sologubenko, J. Jun, S. M. Kazakov, *et al.*, cond-mat/0111273 (2001); cond-mat/0112191 (2001); cond-mat/0201517 (2002).
15. M. Schneider, D. Lipp, A. Gladun, *et al.*, Physica C (Amsterdam) **363**, 6 (2001).
16. N. V. Anshukova, A. I. Golovashkin, L. I. Ivanova, and A. P. Rusakov, Usp. Fiz. Nauk **167**, 887 (1997) [Phys. Usp. **40**, 843 (1997)].
17. N. V. Anshukova, A. I. Golovashkin, L. I. Ivanova, *et al.*, Pis'ma Zh. Éksp. Teor. Fiz. **71**, 550 (2000) [JETP Lett. **71**, 377 (2000)].
18. N. V. Anshukova, B. M. Bulychev, A. I. Golovashkin, *et al.*, Kratk. Soobshch. Fiz., No. 7, 16 (2001); Fiz. Tverd. Tela (St. Petersburg) **45** (1), 8 (2003) [Phys. Solid State **45**, 6 (2003)].
19. A. A. Minakov, Yu. V. Bugoslavsky, and C. Schick, Thermochim. Acta **317**, 117 (1998).
20. A. A. Minakov, S. A. Adamovsky, and C. Schick, Thermochim. Acta **377**, 173 (2001).
21. R. Berman, *Thermal Conduction in Solids* (Clarendon, Oxford, 1976; Mir, Moscow, 1979).
22. L. N. Bulaevskiĭ, V. L. Ginzburg, G. F. Zharkov, D. A. Kirzhnits, Yu. V. Kopaev, E. G. Maksimov, and D. I. Khomskiĭ, *Problems in High-Temperature Superconductivity*, Ed. by V. L. Ginzburg and D. A. Kirzhnits (Nauka, Moscow, 1977).
23. A. I. Golovashkin and A. P. Rusakov, Usp. Fiz. Nauk **170**, 192 (2000) [Phys. Usp. **40**, 184 (2000)].
24. H. Wendel and R. M. Martin, Phys. Rev. B **19**, 5251 (1979).
25. O. E. Kvyatkovskiĭ and E. G. Maksimov, Usp. Fiz. Nauk **154**, 3 (1988) [Sov. Phys. Usp. **31**, 1 (1988)].

Translated by G. Skrebtsov

Physics of the Solid State, Vol. 45, No. 7, 2003, pp. 1213–1218. Translated from Fizika Tverdogo Tela, Vol. 45, No. 7, 2003, pp. 1159–1163.

METALS AND SUPERCONDUCTORS

On the Superconducting Transition Temperature for Metallic Nanocrystals

M. N. Magomedov

Institute of Geothermal Problems, Dagestan Scientific Center, Russian Academy of Sciences, pr. Kalinina 39a, Makhachkala, 367030 Russia

e-mail: musa@dinet.ru

Received October 28, 2002

Abstract—A new approach is proposed for calculating the Debye temperature of a nanocrystal in the form of an n-dimensional rectangular parallelepiped with an arbitrary microstructure and the number of atoms N ranging from 2^n to infinity. The geometric shape of the system is determined by the lateral-to-basal edge ratio of the parallelepiped. The size dependences of the Debye and melting temperatures for a number of materials are calculated using the derived relationship. The theoretical curves thus obtained agree well with the experimental data. The calculated dependences of the superconducting transition temperature T_c on the size d of aluminum, indium, and lead nanocrystals are also in reasonable agreement with the experimental estimates of $T_c(d)$. It is demonstrated that, as the nanocrystal size d decreases, the greater the deviation of the nanocrystal shape from an equilibrium shape (in our case, a cube), the higher the temperature of the superconducting transition $T_c(d)$. The superconducting transition temperature is calculated as a function of the thickness (diameter) of a plate (rod) with an arbitrary length. It is found that a decrease in the thickness (diameter) of the plate (rod) leads to an increase in the temperature $T_c(z)$: the looser the microstructure of the metallic nanocrystal, the higher the temperature $T_c(z)$. *© 2003 MAIK "Nauka/Interperiodica".*

1. INTRODUCTION

There are many works concerned with the analysis of the size dependences of the physical properties of nanocrystals. However, the majority of the theoretical studies are based on the assumption that a nanocrystal has a fixed (as a rule, spherical or cubic) shape. To the best of my knowledge, the problem regarding the dependence of a particular physical property not only on the size but also on the shape of a nanocrystal has never been considered before. The first attempts to solve this problem were made in my recent works [1, 2]. In the present paper, I propose a new, more correct approach to the solution of the formulated problem.

2. THEORETICAL BACKGROUND

We consider a one-dimensional chain consisting of N atoms in which the distance between the centers of the nearest neighbor atoms is equal to c. Let B be some (linear) property of an atom located inside the chain and having two nearest neighbors and A be an analogous property for a terminal atom with only one neighbor. In this case, the averaged (over all N atoms of the chain) property $\langle B_1\rangle$ can be represented as

$$\langle B_1\rangle = B - (2/N)(B - A). \quad (1)$$

Next, we consider a two-dimensional rectangular system formed by N atoms, of which N_{po} atoms are located in the base and $N_{ps} = fN_{po}$ atoms occupy the lateral edge of the rectangle. The total number of atoms in this system can be defined as $N = fN_{po}^2/\alpha_2$, where $f = N_{ps}/N_{po}$ is the shape parameter and α_2 is the microstructure parameter, which depends on the packing type of the regular two-dimensional atomic lattice. Hence, for the property $\langle B_2\rangle$, we obtain $2N\langle B_2\rangle = [N - 2(N_{fo} + N_{fs}) - 4]2B + 2(N_{fo} + N_{fs})(B + A) + 8A$, where $N_{fo} = N_{po} - 2$ and $N_{fs} = N_{ps} - 2$ are the numbers of atoms located in the base and along the lateral edge (without regard for the terminal atoms) of the rectangle, respectively. Then, it is a simple matter to derive the following relationship for the two-dimensional rectangle:

$$\langle B_2\rangle = B - (\alpha_2/f)^{1/2}[(1 + f)/N^{1/2}](B - A). \quad (2)$$

Similarly, in the case of a three-dimensional rectangular parallelepiped with a square base [$N = (f/\alpha_3)N_{po}^3$], we obtain the expression $3N\langle B_3\rangle = (N - 4N_{ss} - 2N_{so} - 8N_{fo} - 4N_{fs} - 8)3B + (4N_{ss} + 2N_{so})(2B + A) + (8N_{fo} + 4N_{fs})(B + 2A) + 24A$. Here, $N_{ss} = N_{fo}N_{fs}$ and $N_{so} = N_{fo}^2$ are the numbers of atoms arranged on the lateral face and the basal face (without regard for the atoms located along the edges and at vertices) of the parallelepiped, respectively, and $N_{fs} = N_{ps} - 2$ and $N_{fo} = N_{po} - 2$ are the numbers of atoms occupying the lateral edge and the basal edge (without regard for the atoms located at vertices) of the parallelepiped, respectively. As a result, the

property $\langle B_3 \rangle$ for the three-dimensional rectangular parallelepiped can be represented in the form

$$\langle B_3 \rangle = B - (\alpha_3/f)^{2/3}[(2f+1)/3N^{1/3}]2(B-A). \quad (3)$$

From a comparison of relationships (1)–(3), we can assume that, in the n-dimensional case,

$$\langle B_n \rangle = B - (\alpha_n/f)^{(n-1)/n}\{[(n-1)f+1]/nN^{1/n}\}2(B-A). \quad (4)$$

For the microstructure parameters α_n in expression (4), we easily found that $\alpha_1 \equiv 1$, $\alpha_2 = \pi/4k_y(2)$, and $\alpha_3 = \pi/6k_y(3)$. Here, $k_y(n)$ is the packing coefficient of the atomic lattice: $0 < k_y(n) < 1$.

With the use of expression (4), we determine the mean coordination number for an n-dimensional nanocrystal. An atom has B nearest neighbors in the bulk of the nanocrystal (on average, $B = k_n/n$ in a linear direction) and A nearest neighbors at the boundary ($A = k_n/2n$). Consequently, the expression for the relative value of the mean coordination number k_n^* takes the form

$$k_n^* = \langle k_n \rangle/k_n = 1 - [F_n(f)\alpha_n^{n-1}/N]^{1/n}, \quad F_n(f) = [(n-1)f+1]^n/n^n f^{n-1}. \quad (5)$$

The shape function $F_n(f)$ reaches a minimum when the system has an n-dimensional cubic form: $F_n(f=1) = 1$. For platelike ($f < 1$) or rodlike ($f > 1$) nanocrystals, the shape function is universally larger than unity; i.e., $F_n(f \neq 1) > 1$.

A comparison of the results obtained from relationship (5) with direct calculations of the mean coordination numbers $\langle k_n \rangle$ for nanocrystals with square ($n = 2$) and cubic ($n = 3$) lattices demonstrates exact coincidence for all possible shapes of nanocrystals, provided the number of atoms N varies from 2 to 512. Relationship (5) is more accurate than the expression used in my previous works [1, 2] and, furthermore, involves the parameter α_n accounting for the microstructure type of the nanocrystal. This gives grounds to assert that relationship (5) holds true for arbitrary values $N \geq 1$. However, it should be remembered that the dimensionality of the structure under investigation takes values $n \leq 2$ when the number of atoms falls in the range $N \leq 3$ and $n = 1$ when $1 \leq N \leq 2$. This restriction stems from the fact that the system composed of three atoms has either a one-dimensional structure or a two-dimensional structure, whereas the structure of the system consisting of two atoms is universally linear. As a consequence, from relationship (5), we obtain the trivial results $\langle k_{n=1} \rangle(N=2) = 1$ and $\langle k_{n=1} \rangle(N=1) = 0$. By virtue of the model restrictions, the number of atoms in an n-dimensional system cannot be less than $N_{\min} = 2^n$ and the shape parameter f must satisfy the following conditions [2]: $2/N_{po} \leq f \leq N_{ps}/2$, where the quantity on the left side determines the shape parameter for an n-dimensional biatomic plate and the quantity on the right side specifies the shape parameter for an n-dimensional rod with a biatomic diameter. From the expressions $N_{ps} = \mathrm{INT}[N\alpha_n/2^{n-1}]$ for an n-dimensional rod with a biatomic diameter and $N_{po} = \mathrm{INT}[N\alpha_n/2]^{1/(n-1)}$ for an n-dimensional biatomic plate, we obtain the following relationships for the minimum and maximum shape parameters at a given number of atoms N (hereafter, INT[x] is the integer part of the number x):

$$f_{\min} = 2/N_{po} = 2/\mathrm{INT}[N\alpha_n/2]^{1/(n-1)}, \quad f_{\max} = N_{ps}/2 = (1/2)\mathrm{INT}[N\alpha_n/2^{n-1}]. \quad (6)$$

For a two-dimensional structure ($n = 2$), the shape parameter satisfies the condition $f_{\max} = 1/f_{\min}$.

It can easily be verified that, at arbitrary constant values of N, k_n, and α_n, the mean coordination number $\langle k_n \rangle$ [see relationship (5)] as a function of the shape parameter f reaches a maximum at $f = 1$. This indicates that the cubic (square) shape of a three-dimensional (two-dimensional) system corresponds to a maximum value of $\langle k_n \rangle$. Therefore, a nanocrystal of cubic (square) shape should possess maximum thermodynamic stability (for at least zero values of the temperature and external pressure).

As follows from relationship (5), three-dimensional crystals are characterized by a U-shaped dependence of the function $F_3(f)$ on the shape parameter with a minimum at $f = 1$ and, consequently, can exhibit a dimorphism. This phenomenon is observed under the condition $\langle k_3 \rangle(N)_{\mathrm{plate}} = \langle k_3 \rangle(N)_{\mathrm{rod}}$ at $a_3 = \mathrm{const}$. A nanocrystal has the form of a cube only in the case when the number of atoms satisfies the relationship $N_{\mathrm{cube}} = \mathrm{INT}[N_{po}^3/\alpha_3]$, where $N_{po} = 2, 3, \ldots$. Hence, at a given number of atoms $N \neq N_{\mathrm{cube}}$, nanocrystals of different (for example, oblate and prolate) shapes are characterized by the same binding energy. This is responsible for the dimorphism of nanocrystals: under identical external conditions, platelike and rodlike nanocrystals containing the same number of atoms can be formed with an equal probability.

The thickness of an n-dimensional parallelepiped can be represented as

$$d^* = d/c = N_{\mathrm{po}}(n-1+f^2)^{1/2}, \quad N_{po} = (N\alpha_n/f)^{1/n}, \quad (7)$$

where c is the distance between the centers of the nearest neighbor atoms. Form relationship (5), we obtain the expression relating the mean coordination number k_n^* to the thickness d of the n-dimensional parallelepiped:

$$k_n^*(d) = 1 - \alpha_n n^{1/2} L_n(f)/d^*, \quad L_n(f) = \{[(n-1)f+1]/nf\}\{[(n-1)+f^2]/n\}^{1/2}. \quad (8)$$

It follows from expressions (7) and (8) that, at $f = 1$, the function $d^*(f)$ reaches a minimum whereas the function $k_n^*(d)$ reaches a maximum. These results confirm the validity of the above expressions.

Now, we use formula (8) and the results presented in [1] to calculate the size dependences of the physical properties determined by the coordination number $k_n^*(d)$. If the energy of zero-point vibrations is considerably less than the energy of interatomic bonds (this conditions is satisfied for all substances, except crystalline helium, hydrogen, and neon), the size dependence of the Debye temperature Θ can be described by the expression [1–3]

$$\Theta^*(d) = \Theta(d)/\Theta(\infty) \cong [k_n^*(d)]^{1/2}. \quad (9)$$

According to the Lindemann criterion [4], the melting temperature T_m as a function of the size d can be estimated from the relationship

$$T_m^*(d) = T_m(d)/T_m(\infty) \cong [\Theta^*(d)]^2 \cong k_n^*(d). \quad (10)$$

The size dependence of the superconducting transition temperature T_c for metallic nanocrystals can be calculated using the Garland formula (which is more correct than the McMillan formula) [5–7]:

$$\begin{aligned} T_c^*(d) &= T_c(d)/T_c(\infty) \\ &\cong \Theta^*(d)\exp[F_g(\infty) - F_g(d)], \end{aligned} \quad (11)$$

where the function $F_g(d)$ is defined by the expression

$$F_g(d) = [1 + \lambda(d)]/[(1 - 0.5\mu)A(d)\lambda(d) - \mu]. \quad (12)$$

Here, μ is the Coulomb pseudopotential and the electron–phonon coupling constant $\lambda(d)$ and the parameter $A(d)$ as functions of the size d are given by

$$\lambda(d) \cong \lambda/[\Theta^*(d)]^2, \quad A(d) \cong A[\Theta^*(d)]^\beta. \quad (13)$$

In expressions (12) and (13), the parameters A, λ, β, and μ, which are constant for each metal, fall in the following ranges: $A \cong 0.9$–0.76, $\lambda \cong 1.54$(Hg)–0.41(Al), $\beta \cong 0.52$, and $\mu \cong 0.08$–0.12 [5, 6].

3. RESULTS AND DISCUSSION

From formulas (8), we can easily determine the critical size of nanocrystals as follows [1, 4, 8, 9]:

$$\begin{aligned} d_{cr}^*(n) &= \lim_{d^* \to \infty} [dk_n^*/d(1/d^*)] \\ &= \begin{cases} 1 & n = 1 \\ (\alpha_2/2f)(f+1)(1+f^2)^{1/2}, & n = 2 \\ (\alpha_3/3f)(2f+1)(2+f^2)^{1/2}, & n = 3. \end{cases} \end{aligned} \quad (14)$$

As a result, for three-dimensional nanocrystals of cubic shape (i.e., at $n = 3$ and $f = 1$), we obtain

$$\begin{aligned} d_{cr}^*(3) &= 3^{1/2}\alpha_3 \\ &= \begin{cases} 1.225 \quad \text{for a face-centered cubic structure} \\ (k_3 = 12, \alpha_3 = 0.7071); \\ 1.299 \quad \text{for a tetragonal structure} \\ (k_3 = 10, \alpha_3 = 0.75); \\ 1.333 \quad \text{for a body-centered cubic structure} \\ (k_3 = 8, \alpha_3 = 0.7698); \\ 1.732 \quad \text{for a cubic structure} \\ (k_3 = 6, \alpha_3 = 1); \\ 2.667 \quad \text{for a diamond-like structure} \\ (k_3 = 4, \alpha_3 = 1.5396). \end{cases} \end{aligned} \quad (15)$$

For the majority of metals studied in [4, 8, 9], the distance c between the centers of the nearest neighbor atoms lies in the range 0.3–0.4 nm. Hence, for close-packed (fcc and bcc) nanocrystals of cubic shape, we obtain the critical size $d_{cr} = 0.37$–0.52 nm. These results are in good agreement with the experimental estimates made from the size dependences of the Debye temperature and the melting point [see relationship (10)] for metallic nanocrystals: $d_{cr} = 0.6$ nm [8] and 1 ± 0.25 nm [9]. It should be noted that the metallic nanocrystals deposited on a substrate during experiments could undergo a Jahn–Teller distortion [10]. Upon distortion, the critical size d_{cr} of a cubic nanocrystal increases drastically. According to expression (14), the critical size of a nanocrystal at $f = 0.5$ is estimated as $d_{cr} = 0.43$–0.62 nm.

The size dependences of the superconducting transition temperature of aluminum, indium, and lead nanocrystals were calculated from formulas (11)–(13). For aluminum nanocrystals with a face-centered cubic structure [$k_y(n = 3) = 0.7405$], the calculation was performed with the following parameters: the distance between the centers of the nearest neighbor atoms $c = 0.286$ nm [11], $T_c(\infty) = 1.18$ K [11], $\beta = 0.52$ [5], $\lambda = 0.41$ [5], $\mu = 0.1$ [5], $A = 0.9$ [5], and $F_g(\infty) = 5.6276$. For indium nanocrystals with a tetragonal structure [$k_y(n = 3) = 0.6981$], the parameters used in the calculation are as follows: $c = 0.325$ nm [11], $T_c(\infty) = 3.4$ K [11], $\beta = 0.48$ [6], $\lambda = 0.84$ [6], $\mu = 0.09$ [6], $A = 0.85$ [6], and $F_g(\infty) = 3.1088$. For lead nanocrystals with a body-centered cubic structure, we used the following parameters: $c = 0.35$ nm [11], $T_c(\infty) = 7.193$ K [11], $\beta = 0.52$ [5], $\lambda = 1.22$ [5], $\mu = 0.09$ [5], $A = 0.9$ [5], and $F_g(\infty) = 2.316$. The calculated dependences $T_c(d)$ for aluminum and indium nanocrystals of different shapes are shown in Figs. 1 and 2, respectively. The experimental data taken from [6, 12, 13] are also presented in these figures. As is clearly seen from Figs. 1 and 2, the calculated and experimental dependences $T_c(d)$ are in good agreement. For lead nanocrystals, the supercon-

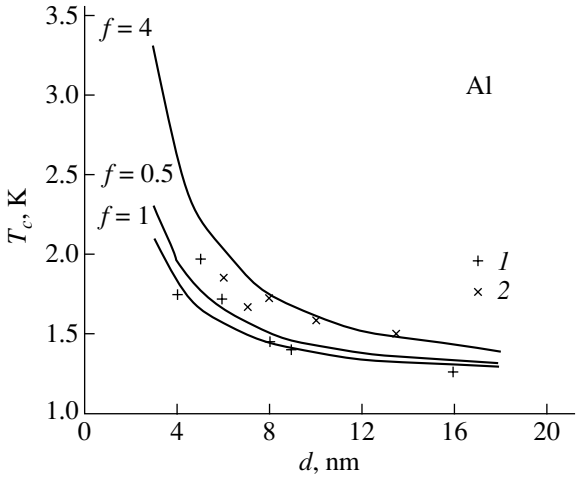

Fig. 1. Calculated dependences of the superconducting transition temperature on the size of cubic (lower line, $f = 1$), platelike (intermediate line, $f = 0.5$), and rodlike (upper line, $f = 4$) aluminum nanocrystals. Points are the experimental data taken from (*1*) [12] and (*2*) [13].

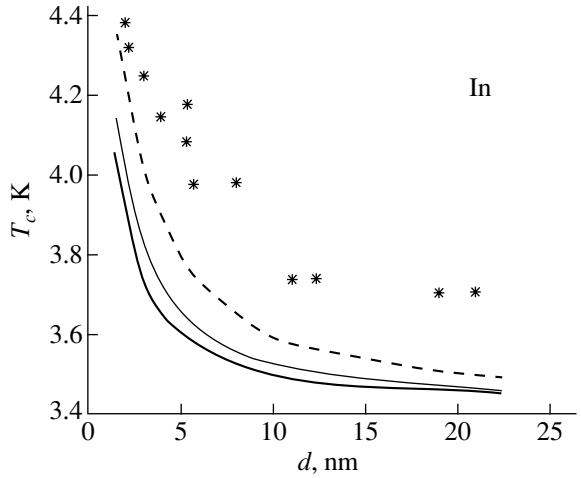

Fig. 2. Calculated dependences of the superconducting transition temperature on the size of cubic (thick line, $f = 1$), platelike (thin line, $f = 0.5$), and rodlike (dashed line, $f = 4$) indium nanocrystals. Points are the experimental data taken from [6].

ducting transition temperature $T_c(d)$ depends on the nanocrystal size only slightly, which also agrees with the experimental results reported in [7].

As the nanocrystal size decreases, the superconducting transition temperature $T_c(d)$ first increases, passes through a maximum, and then decreases. The calculated size dependences of the superconducting transition temperature in the vicinity of the maximum of the function $T_c(d)$ for aluminum nanocrystals of different shapes are depicted in Fig. 3. The table lists the parameters corresponding to the maxima of the function $T_c(d)$ for aluminum and indium nanocrystals of different shapes. It can be seen from the table that, at large parameters λ, the dependence $T_c^*(d)$ exhibits a maximum for a large size d, even though the value of $T_c^*(d)$ at the maximum is relatively small. For example, the electron–phonon coupling constant for bulk lead is comparatively large: $\lambda(\mathrm{Pb}) = 1.22$ [5]. This is the reason why the calculations performed with the use of formulas (11)–(13) for lead nanocrystals resulted in a very weak dependence $T_c^*(d)$. The function $T_c^*(d)$ even at the maximum observed for the nanocrystal size $d = 0.366$ nm proved to be $T_c^*(\max) = 1.0063$. According to the experimental data obtained in [7], the size dependence of the superconducting transition temperature T_c^* is not observed. It can be assumed that, for mercury nanocrystals characterized by the electron–phonon coupling constant $\lambda(\mathrm{Hg}) \cong 1.54$ [5], the size dependence of the superconducting transition temperature is considerably less pronounced. The weaker the electron–phonon coupling λ in the metal, the higher the temperature of the superconducting transition $T_c^*(d)$ with a decrease in the nanocrystal size.

For an n-dimensional rod whose diameter accommodates z_R atoms, the shape parameter is defined as $f_R = \alpha_n N z_R^n$. In this case, relationship (5) can be transformed into the expression

$$k_n^*(N, z_R)_{\mathrm{rod}} = 1 - [(n-1)/n](\alpha_n/z_R) - (z_R^{n-1}/nN). \quad (16)$$

For an n-dimensional plate of thickness z_p, the shape parameter is given by the formula $f_p = z_p^{n/(n-1)}/(N\alpha_n)^{1/(n-1)}$. Hence, from expression (8), we derive the relationship

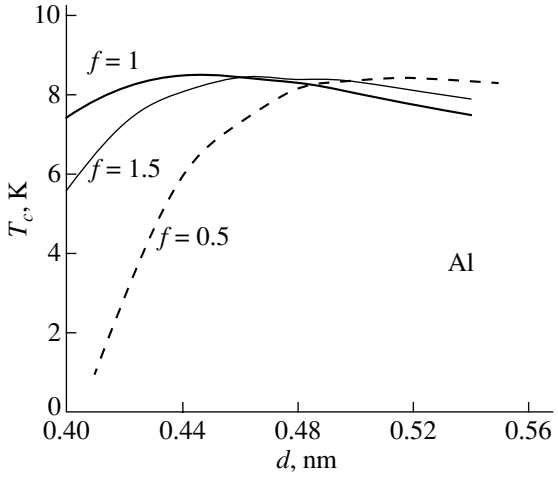

Fig. 3. Calculated dependences of the superconducting transition temperature in the vicinity of the maximum of the function $T_c(d)$ on the size of cubic (thick line, $f = 1$), rodlike (thin line, $f = 1.5$), and platelike (dashed line, $f = 0.5$) aluminum nanocrystals.

Parameters corresponding to the maxima of the function $T_c(d)$ for face-centered cubic aluminum and tetragonal indium nanocrystals of different shapes according to the calculation from formulas (11)–(13)

Metal	f	d^*	d, nm	N	k_3^*	k_3	Θ, K	T_c^*	T_c, K
Al	0.5	1.82	0.52	1	0.223	2.67	201.7	7.254	8.560
c = 0.286 nm [11]	1	1.57	0.45	1	0.222	2.66	201.5	7.254	8.560
$\Theta(\infty)$ = 428 K [11]	1.5	1.64	0.47	1	0.212	2.54	196.9	7.252	8.557
$T_c(\infty)$ = 1.18 K [11]	4	2.90	0.83	2	0.224	2.70	202.9	6.912	8.156
In	0.5	3.08	1.00	6	0.512	5.12	77.31	1.278	4.345
c = 0.325 nm [11]	1	2.62	0.85	5	0.503	5.03	76.62	1.278	4.344
$\Theta(\infty)$ = 108 K [11]	1.5	2.77	0.90	5	0.504	5.04	76.65	1.278	4.345
$T_c(\infty)$ = 3.4 K [11]	4	4.77	1.55	8	0.500	5.00	76.34	1.278	4.345

$$k_n^*(N, z_p)_{\text{plate}} = 1 - (\alpha_n/nz_p) - \alpha_n^{(n-2)/(n-1)}[(n-1)/n](z_p/N)^{1/(n-1)}. \quad (17)$$

It is easy to verify that functions (16) and (17) exhibit a maximum at $f = 1$. As can readily be seen, expressions (16) and (17) at $n = 2$ coincide with each other, which also confirms the validity of the calculation technique proposed in this work. Consequently, we can write the following relationship for a two-dimensional strip whose width accommodates z_s atoms:

$$k_2^*(N, z_s)_{\text{strip}} = 1 - (\alpha_2/2z_s) - (z_s/2N). \quad (18)$$

From expressions (16) and (17) for a rod and a plate at $n = 3$, we obtain

$$k_3^*(N, z_R)_{\text{rod}} = 1 - (2\alpha_3/3z_R) - (z_R^2/3N), \quad (19)$$

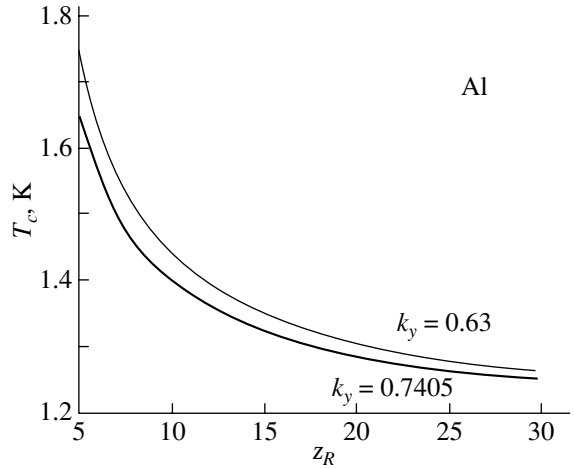

Fig. 4. Calculated dependences of the superconducting transition temperature on the diameter (expressed in atomic diameters) of aluminum rods with face-centered cubic (thick line, k_y = 0.7405, k_3 = 12, α_3 = 0.7071) and amorphous (thin line, k_y = 0.63 [14], $k_3 \approx 7$, α_3 = 0.831) microstructures.

$$k_3^*(N, z_p)_{\text{plate}} = 1 - (\alpha_3/3z_p) - (2/3)(\alpha_3 z_p/N)^{1/2}. \quad (20)$$

It is evident from analyzing the above relationships that the looser the microstructure of the metallic nanocrystal, the stronger the thickness (diameter) dependence of k_n^* (plate) [k_n^* (rod)]. Note that, in the case of a rod, this dependence is more pronounced. For a macrorod, expression (19) can be transformed as follows: $k_3^*(N \longrightarrow \infty, z_R)_{\text{rod}} = 1 - (2\alpha_3/3z_R)$.

Figure 4 depicts the calculated dependences of the superconducting transition temperature on the diameter of aluminum macrorods with face-centered cubic (thick line) and amorphous (thin line) microstructures. It can be seen that, at the same diameter z_R, the looser the microstructure of the aluminum nanocrystal, the higher the temperature $T_c(z_R)$.

4. CONCLUSIONS

Thus, the main results obtained in the above analysis of the temperatures of superconducting transitions in metallic nanocrystals of different shapes can be summarized as follows.

(i) A deviation of the nanocrystal shape from an equilibrium shape (in our case, a cube) leads to a decrease in the Debye temperature $\Theta(d)$ and an increase in the temperature of the superconducting transition $T_c(d)$. Therefore, the temperatures $\Theta(d)$ and $T_c(d)$ for a particular metal can be controlled by varying the shape of the metallic nanocrystal.

(ii) The weaker the electron–phonon coupling in the metal, the higher the temperature of the superconducting transition $T_c^*(d)$ with a decrease in the nanocrystal size.

(iii) As the thickness (diameter) of the plate (rod) decreases, the looser the microstructure of the metal, the higher the temperature of the superconducting transition.

When designing high-temperature superconductor compounds, it is possible to use the currently available techniques of preparing platelike, needle-shaped, and

more complex-shaped nonequilibrium modifications of existing superconducting metals, as well as metal nanocrystalline materials with an amorphous loose microstructure.

ACKNOWLEDGMENTS

The author would like to thank K.N. Magomedov and Z.M. Surkhaeva for their assistance in performing this work.

This work was supported by the Russian Foundation for Basic Research, project no. 02-03-33301.

REFERENCES

1. M. N. Magomedov, Zh. Fiz. Khim. **73** (12), 2211 (1999).
2. M. N. Magomedov, Zh. Fiz. Khim. **76** (4), 752 (2002).
3. M. N. Magomedov, Zh. Fiz. Khim. **61** (4), 1003 (1987).
4. V. P. Skripov and V. P. Koverda, *Spontaneous Crystallization of Supercooled Liquids* (Nauka, Moscow, 1984).
5. J. W. Garland, K. H. Bennemann, and F. M. Mueller, Phys. Rev. Lett. **21** (18), 1315 (1968).
6. J. H. P. Watson, Phys. Rev. B **2** (5), 1282 (1970).
7. Yu. I. Petrov, *Physics of Small Particles* (Nauka, Moscow, 1982).
8. V. P. Koverda, Fiz. Met. Metalloved. **51** (3), 569 (1981).
9. M. Wautelet, J. Phys. D: Appl. Phys. **24** (3), 343 (1991).
10. É. L. Nagaev, Usp. Fiz. Nauk **162** (9), 49 (1992) [Sov. Phys. Usp. **35**, 747 (1992)].
11. C. Kittel, *Introduction to Solid State Physics*, 5th ed. (Wiley, New York, 1976; Nauka, Moscow, 1978).
12. R. B. Pettit and J. Silcox, Phys. Rev. B **13** (7), 2865 (1976).
13. K. Ohshima, T. Kuroishi, and T. Fujita, J. Phys. Soc. Jpn. **41** (4), 1234 (1976).
14. A. P. Mozhaev, Dokl. Akad. Nauk **384** (2), 185 (2002) [Dokl. Phys. **47**, 370 (2002)].

Translated by O. Borovik-Romanova

Physics of the Solid State, Vol. 45, No. 7, 2003, pp. 1219–1222. Translated from Fizika Tverdogo Tela, Vol. 45, No. 7, 2003, pp. 1164–1167.

METALS AND SUPERCONDUCTORS

Andreev Reflection in Natural Grain Boundaries of Polycrystalline High-T_c Superconductor $La_{1.85}Sr_{0.15}CuO_4$

M. I. Petrov[1], D. A. Balaev[1], D. M. Gokhfel'd[1, 2], and K. A. Shaikhutdinov[1]

[1] *Kirensky Institute of Physics, Siberian Division, Russian Academy of Sciences, Akademgorodok, Krasnoyarsk, 660036 Russia*

e-mail: smp@iph.krasn.ru

[2] *Reshetnev Siberian State Aerospace University, Krasnoyarsk, 660014 Russia*

Received December 2, 2002

Abstract—The temperature evolution of the current–voltage characteristic (CVC) of a "break junction" with metal-type conductivity on the polycrystalline $La_{1.85}Sr_{0.15}CuO_4$ high-temperature superconductor is investigated. The CVC exhibits gap peculiarities and hysteresis, which is observed in the region of negative differential resistance. The experimental results are described well in terms of the Kümmel–Gunsenheimer–Nicolsky theory for an S–N–S junction (S is a superconductor, N is a normal metal) this theory takes into account multiple Andreev reflection of quasiparticles. It is shown that the shape of the CVC and the existence and the shape of hysteresis are determined by the ratio of "long" and "short" grain boundaries in the polycrystal under investigation. © *2003 MAIK "Nauka/Interperiodica".*

1. INTRODUCTION

The investigation of the current–voltage characteristic (CVC) of a Josephson junction makes it possible to obtain information on the physical properties of superconductors. The peculiarities of a CVC contain information about the energy gap [1, 2] and may depend on the symmetry of the superconductor order parameter [3]. Since the discovery of high-temperature superconductivity (HTSC), different Josephson structures [4] and polycrystalline high-T_c materials [5–7] in which Josephson medium is realized [8] have been actively studied. Technically, it is very difficult to prepare a single Josephson junction with high-quality superconducting "banks" because of the high chemical activity of high-T_c compounds, and on polycrystalline samples inevitable heating makes it difficult to measure the temperature evolution of a CVC in a wide range of currents, including the range where the CVC becomes linear. Many experimental investigations of the transport properties of polycrystalline superconductors with different compositions have been carried out with the use of break junctions [9–12]. Break-junction technology allows one to decrease the self-heating of a sample significantly. Break junctions prepared on bulk samples require small measuring currents, like films, but they are free from a number of drawbacks inherent to the latter (lower critical temperature, smaller energy gap). While a microcrack develops, the cross section of the sample decreases until only a narrow conducting channel is left and a tunneling junction is formed in the limit. In the first case, the current density flowing through the crystallites in the break region significantly exceeds the current density in the sample volume. Thus, the break region determines the critical current in the whole sample. This fact allows one to use relatively small measuring currents to obtain CVC sections reflecting the gap peculiarities of the superconductor. In the present work, break junction CVCs of a exhibiting a hysteretic behavior are measured on $La_{1.85}Sr_{0.15}CuO_4$ at different temperatures. The first measurements on a polycrystalline sample of this system [13], which represents a network of weak links, were carried out soon after the discovery of HTSC. In the experiment in [13], the CVC of a sample had a number of peculiarities, which probably resulted from the presence of foreign phases and self-heating of the sample. This makes comparison with the theoretical characteristics of weak links junctions extremely difficult. From the presence of excess voltage on the CVC in [13], it follows that the boundaries between superconducting granules in ceramics were probably insulating and, thus, a chaotic network of Josephson junctions was formed in the material. The synthesis technology for high-T_c superconductors of lanthanum and yttrium systems has been significantly improved since the pioneering work performed in [13] and make it possible to provide natural boundaries of metal character between high-T_c superconductor crystallites.

2. EXPERIMENTAL

$La_{1.85}Sr_{0.15}CuO_4$ is prepared using the solid-state reaction technique. Samples with a typical size of $2 \times 2 \times 10$ mm^3 were sawed out from synthesized tablets. The samples were glued onto a sapphire substrate. The central part of a sample was ground down to a cross section $S \sim 0.2 \times 1$ mm^2. A further decrease in S is

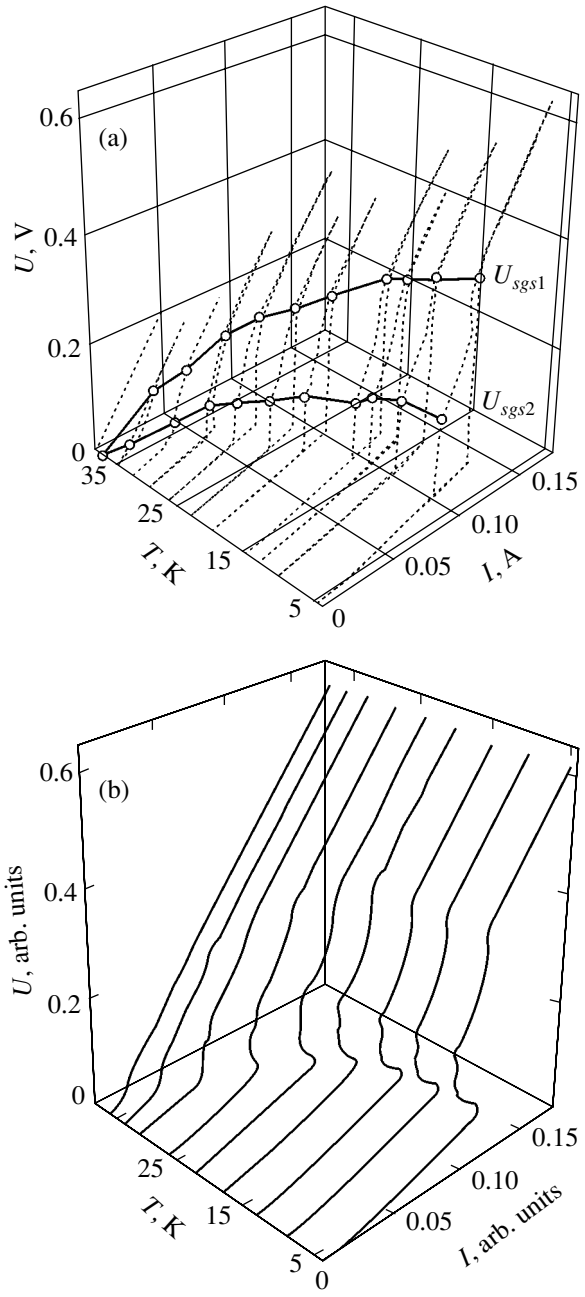

Fig. 1. Temperature evolution of the CVC of a break junction: (a) experiment and (b) theory.

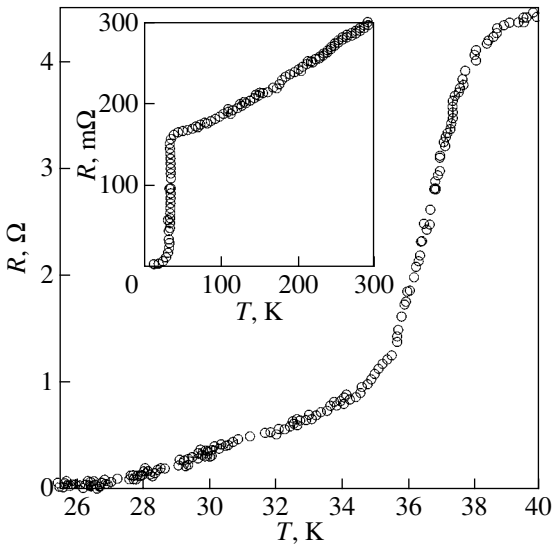

Fig. 2. Temperature dependence of the break-junction resistance. Inset: temperature dependence of the resistance of a bulk sample.

extremely difficult to control because of the inevitable mechanical stresses at current- and potential-lead terminals. To obtain a break junction, a sample with the cross-sectional area S mentioned above, together with the substrate, was bent by means of screws on pressed current-lead terminals, which caused a microcrack to appear in the part of the sample between the potential-lead terminals. In this case, either a tunneling junction (resistance $R > 100\ \Omega$) or a junction with metal-type conductivity ($R < 10\ \Omega$) appeared. For the measurements carried out in this work, the samples with the lowest resistance were chosen. During the measurements, samples were held in a heat-exchange helium atmosphere. CVC measurements were carried out under isothermal conditions by slowly scanning a bias current.

3. RESULTS AND DISCUSSION

The temperature evolution of the CVC of a break junction on $La_{1.85}Sr_{0.15}CuO_4$ is shown in Fig. 1a. All CVCs are characterized by the presence of a critical current and a region with a small differential resistance; at low temperatures, this region is followed by a hysteretic jumplike increase in voltage U. In the region of high values of current I and U, the $U(I)$ dependence is close to linear; its extrapolation to the value $U = 0$ gives the value of excess current I_{ex}, the existence of which confirms the metallic character of the conductivity of the junction under investigation [14]. The hysteretic peculiarity of a CVC obtained in the current-scanning mode is often observed on S–N–S junctions [5, 7, 14]. Such a peculiarity was shown in [15] to appear if there is a region of negative differential resistance (NDR) on a CVC; this region can be observed only in the bias voltage regime on an S–N–S junction.

Figure 2 presents the temperature dependence of the resistance $R(T)$ of the break junction. The inset to Fig. 2 shows the $R(T)$ dependence measured up to 300 K before the break formation. The linear character of the $R(T)$ dependence above T_c confirms the metal type of conductivity of the sample. A comparison of the resistance R of the sample just above, superconducting the transition temperature before (0.15 Ω) and after the microcrack appearance (4 Ω) indicates that the contact area decreased by approximately 27 times. After the break junction was created, the temperature at which

the resistance disappears became 2.5 K lower than that in a bulk sample. It is known that thermal fluctuations in weakly coupled superconductors (thermally activated phase slip [16]) decrease the transition temperature from a resistive state into the state with zero resistance. The dispersion of the parameters of individual weak-link junctions leads to dispersion of the temperatures at which the resistances of separate weak-link junctions disappear. In a bulk sample, current flows through the "best" weak links and the influence of the dispersion of these parameters is insignificant. In a break junction, the majority of percolation paths are broken up; therefore, "poorer" weak links (with smaller critical currents and lower temperatures at which the resistance disappears) begin to influence the transport characteristics, in particular, to decrease the temperature at which the resistance of the whole sample disappears. Thus, when a microcrack is formed, the current flows not through a three-dimensional network but rather through a network of a smaller dimensionality.

Consider a chain of weak links connected in series which have different thickness of normal-metal region between the superconductive banks. The current–voltage relation for this chain is

$$U(I, T) = \sum_i V_i U_i(I, T, S_i, d_i), \quad (1)$$

where $U_i(I, T, S_i, d_i)$ is the CVC of an individual S–N–S junction whose N layer has a thickness d_i and cross section S_i and V_i is a weighting coefficient showing the degree of influence of this junction on the resulting CVC of the chain ($\sum_i V_i = 1$). In the model under investigation, the dispersion of cross sections is ignored and $S_i = S$ (the dispersion of cross sections, as well as the presence of parallel-connected junctions, smears the of the CVC).

There are several theories which could be applied to calculate $U_i(I, T, d_i)$ of a single S–N–S junction. The RSJ model and its modifications [17–19], in our opinion, cannot adequately describe the physical processes operating in S–N–S junctions. The current flowing through an S–N–S junction and the CVC peculiarities accompanying it are determined by the Andreev reflection [20]. Currently, a number of theories [1, 2, 21–23] are used for the description of CVCs of weak-link junctions. Kümmel–Gunsenheimer–Nicolsky theory (KGN) [2], unlike the other theories, describes the appearance of an NDR region in the CVC of an S–N–S junction observations; the other theories do not take into account the contribution from bound states in the S–N–S junction to the current [24]. The KGN theory deals with weak-link in which the Fermi velocities in the superconductor and the normal metal are equal. We assume that high-T_c ceramics meet this requirement and, thus, the KGN theory can be used to calculate $U_i(I, T, d_i)$ in Eq. (1). The KGN theory is also convenient because in this theory the ratio d_i/l (where l is the mean free path of electrons in the N metal) is used as the weak-link parameter determining the CVC shape. The current flowing through a weak link in the KGN theory [2] is given by

$$I = \frac{1}{d}\frac{e}{m}\sum_k \sum_{n=1}^{\infty} P_N(E_k) \times \{[f(E_k)k_e - (1 - f(E_k))k_h]e^{-nd/l}(|A_n^-|^2 - |A_n^+|^2)\}, \quad (2)$$

where $f_0(E_k)$ is the Fermi function describing the energy distribution of quasiparticles, P_N is the probability of the presence of quasiparticles in the N region, e is the electronic charge, m is the electronic mass, n is the number of Andreev reflections undergone by a quasiparticle before it escapes from the quantum well (the normal metal between the superconductors), $A_n^-(E)$ and $A_n^+(E)$ are the probabilities of the nth Andreev reflection of quasiparticles with directions of hole propagation parallel or antiparallel to the electric field, and k_e and k_h depend on the energy and direction of motion of electrons and holes and are determined in [2].

The experimental CVC obtained can be qualitatively described using only one term in sum (1). However, the inclusion of longer junctions (with larger values of d) significantly improves the agreement between the experimental data and the theoretic dependence. With two terms in sum (1), the calculated curve well describes the experimental CVC (Fig. 1). In this case, the best-fit curve corresponds to the values $d_1/l = 0.2$, $V_1 = 0.93$, $d_2/l = 0.6$, and $V_2 = 0.07$. By using our results and the data from review [25], we obtained $l \sim 10$ Å for $La_{1.85}Sr_{0.15}CuO_4$; therefore, $d_1 = 2$ and $d_2 = 6$ Å.

This model allowed us to describe the unusual shape of experimental CVCs. The arch-shaped peculiarity of an experimental CVC corresponds to the last arch-shaped peculiarity on the calculated curve. This peculiarity is due to multiple Andreev reflection in the S–N–S junction. According to the theories mentioned above, multiple Andreev reflection of quasiparticles leads to the appearance of a subharmonic gap structure on the CVC of the S–N–S with minima at $U = 2\Delta(T)/en$, where Δ is the energy gap of the superconductor. The last arch-shaped peculiarity corresponds to $n = 1$ and 2.

In [3], the authors come to the conclusion that, in the case of d-wave symmetry of electron pairs in the superconductor, the peculiarities of the CVC of a weak-link junction that correspond to subharmonics of the energy gap are heavily suppressed. The arch-shaped peculiarities distinctly visible on our CVCs probably confirm that the symmetry of the superconducting order parameter is different from the d-wave symmetry.

The literature data on the symmetry and temperature dependence of the energy gap in a high-T_c superconductor are contradictory (see, e.g., reviews [26–30]). Special points $U_{sgs1}(T)$ and $U_{sgs2}(T)$, marking the arch-

shaped peculiarity, are shown on the experimental CVCs in Fig. 1. The relations $U_{sgs1}(T) = 2\Delta(T)/e$ and $U_{sgs2}(T) = \Delta(T)/e$ are not strictly satisfied because the current flows through several weak-link junctions. However, the proportionality to $\Delta(T)$ should remain for these special points. The observed $U_{sgs1}(T)$ and $U_{sgs2}(T)$ dependencies are slightly different from the temperature dependence of the energy gap in the BCS theory.

In polycrystalline high-T_c superconductors, crystallites are also distributed in orientation [8] and, due to a strong anisotropy of these crystallites, there is a dispersion of energy gap values on a current-flow path. One can simply, but not sufficiently correctly, take this dispersion into account by substituting different energy gap values into the KGN equation for different terms in Eq. (1). This operation improves the agreement of the theoretical curves with the experimental CVCs only insignificantly, but the number of fitting parameters increases in this case. It should be noted that the thickness distribution function of grain boundaries and the energy-gap distribution function of crystallites on a current-flow path may be related because of the peculiarities of ceramic synthesis. Our further investigations will be devoted to this issue.

4. CONCLUSIONS

Thus, we have successfully described both the CVC shape with a hysteretic peculiarity and its temperature evolution by means of the KGN theory [2], which takes into account multiple Andreev reflection. This allows us to conclude that, for natural grain boundaries of a metallic type in the polycrystalline high-T_c superconductor $La_{1.85}Sr_{0.15}CuO_4$, Andreev reflection determines the characteristic features of the current-voltage curve.

ACKNOWLEDGMENTS

This work was supported by the joint program "Eniseĭ" of the Krasnoyarsk Region Science Foundation and the Russian Foundation for Basic Research (grant no. 02-02-97711).

REFERENCES

1. T. M. Klapwijk, G. E. Blonder, and M. Tinkham, Physica B (Amsterdam) **109–110**, 1657 (1982).
2. R. Kümmel, U. Gunsenheimer, and R. Nicolsky, Phys. Rev. B **42** (7), 3992 (1990).
3. T. P. Devereaux and P. Fulde, Phys. Rev. B **47** (21), 14638 (1993).
4. M. Yu. Kupriyanov and K. K. Likharev, Usp. Fiz. Nauk **160** (5), 49 (1990) [Sov. Phys. Usp. **33**, 340 (1990)].
5. M. I. Petrov, S. N. Krivomazov, B. P. Khrustalev, and K. S. Aleksandrov, Solid State Commun. **82** (6), 453 (1992).
6. M. I. Petrov, D. A. Balaev, S. V. Ospishchev, *et al.*, Phys. Lett. A **237**, 85 (1997).
7. M. I. Petrov, D. A. Balaev, D. M. Gohfeld, *et al.*, Physica C (Amsterdam) **314**, 51 (1999).
8. E. Z. Meĭlikhov, Usp. Fiz. Nauk **163** (3), 27 (1993) [Phys. Usp. **36**, 129 (1993)].
9. U. Zimmermann, S. Abens, D. Dikin, *et al.*, Physica B (Amsterdam) **218**, 205 (1996).
10. V. M. Svistunov, V. Yu. Tarenkov, A. I. D'yachenko, and E. Hatta, Pis'ma Zh. Éksp. Teor. Fiz. **71** (7), 418 (2000) [JETP Lett. **71**, 289 (2000)].
11. R. S. Gonnelli, A. Calzolari, D. Daghero, *et al.*, Phys. Rev. Lett. **87** (9), 097001 (2001).
12. M. I. Petrov, D. A. Balaev, D. M. Gokhfel'd, *et al.*, Fiz. Tverd. Tela (St. Petersburg) **44** (7), 1179 (2002) [Phys. Solid State **44**, 1229 (2002)].
13. C. W. Chu, P. H. Hor, R. L. Meng, *et al.*, Phys. Rev. Lett. **58** (4), 405 (1987).
14. K. K. Likharev, Rev. Mod. Phys. **51** (1), 101 (1979).
15. R. Kümmel, B. Huckestein, and R. Nicolsky, Solid State Commun. **65** (12), 1567 (1988).
16. V. Ambegaokar and B. J. Galperin, Phys. Lett. **22** (25), 1364 (1969).
17. D. E. McCumber, J. Appl. Phys. **39** (7), 3113 (1968).
18. R. G. Seed, C. Vittoria, and A. Widom, J. Appl. Phys. **75** (12), 8195 (1994).
19. K. Saitoh, I. Ishimaru, H. Fuke, and Y. Enomoto, Jpn. J. Appl. Phys. **36** (3A), L272 (1997).
20. A. F. Andreev, Zh. Éksp. Teor. Fiz. **46** (5), 1823 (1964) [Sov. Phys. JETP **19**, 1228 (1964)].
21. U. Gunsenheimer and A. D. Zaikin, Phys. Rev. B **50** (9), 6317 (1994).
22. D. Averin and A. Bardas, Phys. Rev. Lett. **75** (9), 1831 (1995).
23. E. N. Bratus', V. S. Shumeiko, E. V. Bazuglyi, and G. Wendin, Phys. Rev. B **55** (18), 12666 (1997).
24. A. Jacobs, R. Kümmel, and H. Plehn, Superlattices Microstruct. **25** (5/6), 669 (1999).
25. L. P. Gor'kov and N. B. Kopnin, Usp. Fiz. Nauk **156** (1), 117 (1988) [Sov. Phys. Usp. **31**, 850 (1988)].
26. Yu. A. Izyumov, Usp. Fiz. Nauk **169** (3), 225 (1999) [Phys. Usp. **42**, 215 (1999)].
27. V. A. Gavrichkov, E. V. Kuz'min, and S. G. Ovchinnikov, Usp. Fiz. Nauk **170** (2), 189 (2000) [Phys. Usp. **43**, 181 (2000)].
28. V. L. Ginzburg, Usp. Fiz. Nauk **170** (6), 619 (2000) [Phys. Usp. **43**, 573 (2000)].
29. E. G. Maksimov, Usp. Fiz. Nauk **170** (10), 1033 (2000) [Phys. Usp. **43**, 965 (2000)].
30. Yu. V. Kopaev, Usp. Fiz. Nauk **172** (6), 712 (2002).

Translated by A. Titov

Physics of the Solid State, Vol. 45, No. 7, 2003, pp. 1223–1232. Translated from Fizika Tverdogo Tela, Vol. 45, No. 7, 2003, pp. 1168–1176.

METALS AND SUPERCONDUCTORS

Pseudogap and Its Temperature Dependence in YBCO from the Data of Resistance Measurements

D. D. Prokof'ev, M. P. Volkov, and Yu. A. Boĭkov

Ioffe Physicotechnical Institute, Russian Academy of Sciences, Politekhnicheskaya ul. 26, St. Petersburg, 194021 Russia

Received August 16, 2002; in final form, December 3, 2002

Abstract—The temperature dependence of the excess conductivity $\Delta\sigma$ for $\Delta\sigma = A(1 - T/T^*)\exp(\Delta^*/T)$ (YBCO) epitaxial films is analyzed. The excess conductivity is determined from the difference between the normal resistance extrapolated to the low-temperature range and the measured resistance. It is demonstrated that the temperature dependence of the excess conductivity is adequately described by the relationship $\Delta\sigma = A(1 - T/T^*)\exp(\Delta^*/T)$. The pseudogap width and its temperature dependence are calculated under the assumption that the temperature behavior of the excess conductivity is associated with the formation of the pseudogap at temperatures well above the critical temperature T_c of superconductivity. The results obtained are compared with the available experimental and theoretical data. The crossover to fluctuation conductivity near the critical temperature T_c is discussed. *© 2003 MAIK "Nauka/Interperiodica".*

1. INTRODUCTION

Experimental investigations of high-temperature superconducting single crystals with a carrier concentration corresponding to the maximum critical temperature T_c (optimally doped crystals) and of crystals with a lower carrier concentration (underdoped crystals) have revealed that specific features in the electrical, magnetic, and optical properties are observed below the temperature T^* ($T^* > T_c$), which increases with a decrease in the carrier concentration [1]. A possible explanation for these features is based on the assumption that a pseudogap is formed in the excitation spectrum of high-temperature superconducting single crystals at temperatures considerably above the critical temperature T_c. This implies that the density of states near the Fermi level in an energy range of several tens of millielectron-volts decreases to a finite value rather than to zero (as would be the case with a superconducting gap at $T < T_c$). At present, there exist two basic approaches to the problem of the origin of the pseudogap. Within the first approach, the formation of the pseudogap is associated with fluctuations of the dielectric type (such as antiferromagnetic, charge density wave, and phase separation fluctuations). According to the second approach, the pseudogap has superconducting nature. This problem is under continuing discussion [2, 3]. In our consideration, we will adhere to the latter approach, which, in essence, is as follows: superconducting pairs are formed at the temperature T^*, whereas the coherence (of the phase of the order parameter) in the sample bulk and, hence, superconductivity arise at the critical temperature T_c [4–7]. Consequently, the existence of superconducting pairs at $T_c < T < T^*$ should manifest themselves in the temperature dependence of the resistance in this temperature range.

2. SAMPLE PREPARATION AND EXPERIMENTAL TECHNIQUE

Epitaxial films of the composition $YBa_2Cu_3O_{7-\delta}$ (YBCO) were grown through laser-induced evaporation on $SrTiO_3$ substrates [8]. The x-ray diffraction investigations demonstrated that the **c** axis of the films was perpendicular to the substrate plane. Bridges 3 μm wide and 40 μm long were prepared from 260-nm-thick films. Electrodes were produced through evaporation of silver films. Wires were cemented to the electrodes with a conducting adhesive prepared from a silver powder. The high degree of structural perfection of the films was judged from the low resistivity at room temperature ($\rho_{300} \sim 160$ μΩ cm), the large ratio $\rho_{300}/\rho_{100} \sim 2.1$, and the narrow transition range $\Delta T_c = T(0.9R_n) - T(0.1R_n) = 2.7$ K. The oxygen content in the films was slightly less than the optimum content, because the films were prepared *in situ* without additional annealing in an oxygen atmosphere. The oxygen content was estimated at $(7 - \delta) \sim 6.85$ from the critical temperature $T_c(0.5R_{100}) = 89.5$ K and the lattice parameter. The temperature dependences of the resistance of the studied films were measured by the four-point probe method at a dc density from $J_a = 10^3$ A/cm^2 at room temperature to $J_a = 10$ A/cm^2 at low temperatures. The temperature was changed in steps of 1.5–2.0 K at high temperatures and 0.2 K in the superconducting transition range. The temperature was measured with the use of copper–constantan thermocouples and maintained accurate to within ~0.02 K. In order to decrease the systematic error in measuring the temperature of the sample, the temperature gradient in the vicinity of the sample at each temperature was minimized using an additional heater. The measuring technique and storage of the sample between experimental cycles at the liquid-nitrogen temperature provided reproducibility of the measurements to within experimental accuracy ~0.005 Ω.

1063-7834/03/4507-1223$24.00

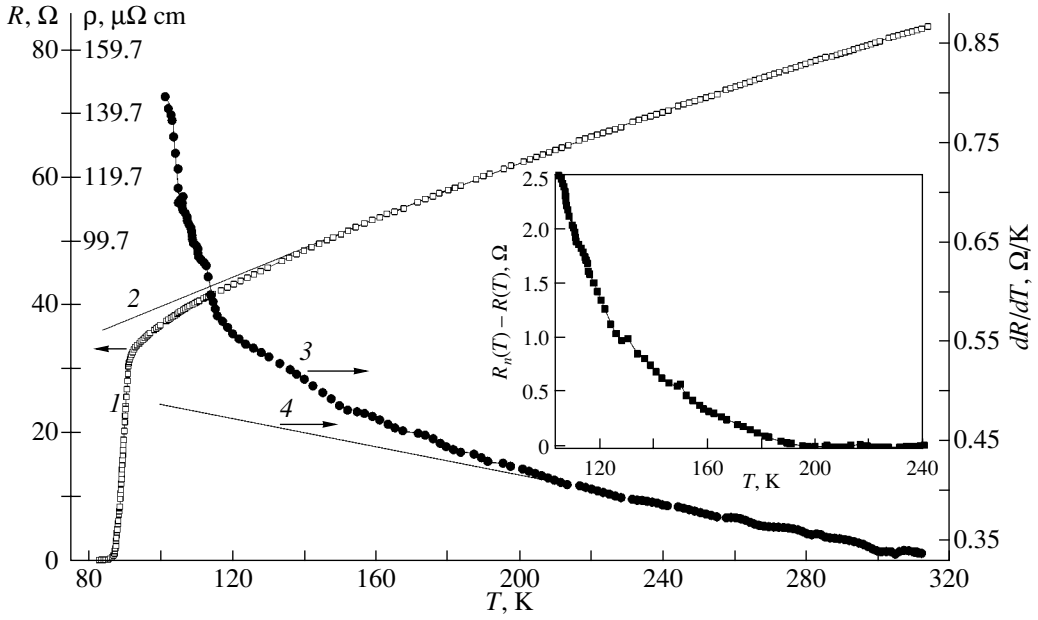

Fig. 1. Temperature dependences of the resistance R, the derivative dR/dT, and the function R_n approximating the dependence $R(T)$ in the range 200–300 K [the root-mean-square deviation of $R_n(T)$ at these temperatures is equal to 0.01 Ω]: (*1*) the experimental dependence $R(T)$, (*2*) the extrapolated dependence $R_n(T) = -1.749 \times 10^{-4}T^2 + 0.2774T + 13.98$, (*3*) the derivative $d[R(T)]/dT$, and (*4*) the extrapolation of the high-temperature portion of the dependence $d[R(T)]/dT$. The inset shows the dependence of $R_n(T) - R(T)$.

3. EXPERIMENTAL RESULTS AND THEIR PROCESSING

Figure 1 shows the temperature dependence of the resistance for one of the bridges (curve *1*). At high temperatures (from 300 to ≈ 200 K), the dependence $R(T)$ is adequately described by the relationship $R_n(T) = AT^2 + BT + C$, where the coefficient A is small in magnitude. The extrapolation of this dependence to the low-temperature range is depicted by solid curve *2* in Fig. 1. The dependence of the difference between the extrapolated and measured resistances $R_n(T) - R(T)$ is shown in the inset to Fig. 1. It can be seen that, as the temperature decreases, a decrease in the resistance beginning with the temperature $T^* \approx 203$ K becomes more pronounced than that at high temperatures. A similar behavior of the resistance has been observed for many optimally doped and underdoped YBCO single crystals and other cuprates [1, 9–11]. The temperature dependence of dR/dT (curve *3*) is also plotted in Fig. 1. As can be seen, the dependence $dR(T)/dT$ exhibits a linear behavior (curve *4*) in the temperature range $T = 300$–200 K and noticeably deviates from linearity at $T \sim T^*$. Curves *3* and *4* clearly illustrate a change in the behavior of the dependence $R(T)$ when passing through the temperature T^*.

By assuming that a sharper decrease in the resistance below the temperature T^* is caused by the formation of superconducting pairs at this temperature, we analyzed the experimental data in terms of the excess conductivity $\Delta\sigma$, which was calculated from the measured and extrapolated resistivities $\Delta\sigma = 1/\rho(T) - 1/\rho_n(T)$. This approach is similar to that used in analyzing the fluctuation component of the conductivity in superconductors at temperatures slightly higher than the critical temperature. Figure 2 depicts the dependences of the excess conductivity $\Delta\sigma$ (curve *1*) and $\ln\Delta\sigma$ (curve *2*) on the reciprocal of the temperature. It can be seen that, over a wide range of temperatures, the curve $\ln\Delta\sigma(T)$ is well approximated by the linear relationship $\ln(\Delta\sigma) = a + b/T$ (curve *3*). Consequently, we can write the expression

$$\Delta\sigma = D\exp(b/T), \tag{1}$$

where a, b, and D are constants. The inclusion of the factor $(1 - T/T^*)$ allows us to improve substantially the approximation of the experimental curve at high temperatures; that is,

$$\Delta\sigma = A(1 - T/T^*)\exp(\Delta^*/T), \tag{2}$$

where Δ^* and A are the constants determined by fitting the experimental data to the theoretical curve described by this formula. The temperature dependence of the function $\ln\Delta\sigma$ calculated as the logarithm of relationship (2) is represented by curve *4* in Fig. 2.

A comparison of curves *2* (experiment) and *4* shows that formula (2) adequately describes the experimental data in the temperature range from 95 to 165 K. At higher temperatures ($165 < T < T^* = 203$ K), as the temperature T^* is approached, the excess conductivity decreases faster than follows from formula (2). The behavior of the function $\ln\Delta\sigma$ at these temperatures can be analyzed in more detail in inset (a) to Fig. 2. Inset (a)

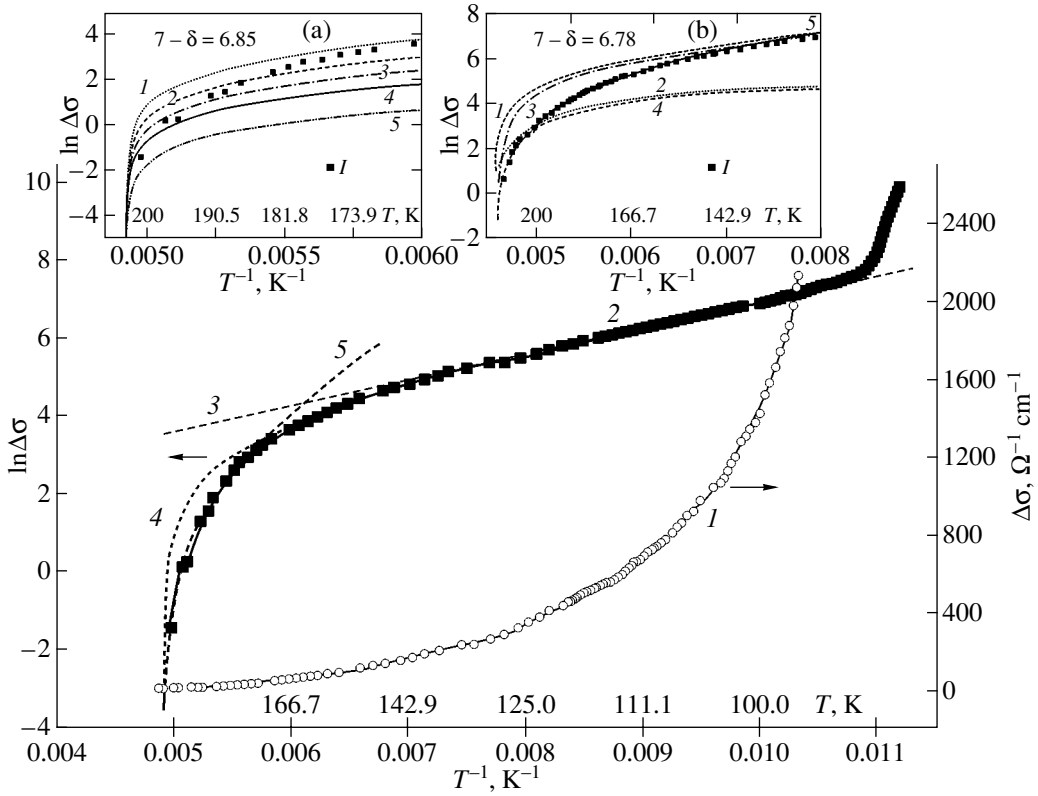

Fig. 2. Dependences of the excess conductivity, logarithm of the excess conductivity, and approximating functions [calculated from formulas (1) and (2)] on the reciprocal of the temperature: (*1*) the dependence $\Delta\sigma(T^{-1})$; (*2*) the dependence $\ln\Delta\sigma(T^{-1})$; (*3*, *4*) the dependences $\ln\Delta\sigma(T^{-1})$ calculated from formulas (1) and (2), respectively ($T^* = 203.3 \pm 0.5$ K, $D = 1.244\ \Omega^{-1}\ \text{cm}^{-1}$, $b = 676$ K, $A = 10.9 \pm 0.3\ \Omega^{-1}\ \text{cm}^{-1}$, and $\Delta^* = 524 \pm 3$ K); and (*5*) the dependences $\ln\Delta\sigma(T^{-1})$ for $\Delta\sigma$ calculated with formula (2) in which $\Delta^* = \Delta^*(T)$ satisfies relationship (3). Inset (a) illustrates (*I*) the experimental data and the dependences $\ln\Delta\sigma(T^{-1})$ calculated according to formula (2) at $\Delta^* =$ (*1*) 524, (*2*) 400, (*3*) 300, (*4*) 200, and (*5*) 0 K. Inset (b) presents the results of the processing of the data taken from [9] for the $YBa_2Cu_3O_{6.78}$ single crystal: (*I*) the experimental data, (*1*, *2*) the curves $\ln\Delta\sigma(T^{-1})$ calculated from formula (2), and (*3*, *4*) the curves $\ln\Delta\sigma(T^{-1})$ obtained from formula (A2). Parameters T^*, Δ^*, A, and M are given in the text and the table. The value of M was determined from the experimental data in the immediate vicinity of T^* with a small ratio $\Delta^*(T)/T$ (the contribution to $\ln\Delta\sigma$ is less than 0.5%). (*5*) Dependence $\ln\Delta\sigma(T^{-1})$ in which the excess conductivity is calculated from formula (A2) for $\Delta^* = \Delta^*(T) = 37.5\sqrt{198 - T}$.

shows the curves plotted with formula (2) at parameters Δ^* varying from 524 to 0 K (the constant A remains unchanged for all the curves). Curves *2*, *3*, and *4* intersect experimental curve *I* at points corresponding to the parameters $\Delta^*(T) = 400$, 300, and 200 K, respectively. It is evident that the deviation of the experimental dependence from curve *1* in inset (a) (see Fig. 2) at temperatures $T \geq 165$ K (or, what is the same, the deviation of curve *2* from curve *4* in Fig. 2) can be described by the temperature-dependent function $\Delta^*(T)$. Consequently, the temperature dependence of the function Δ^* up to the temperature T^* can be constructed from the experimental temperature dependence of $\ln\Delta\sigma$. The dependence $\Delta^*(T)$ obtained in this way is depicted by curve *3* in Fig. 3. The parameter Δ^* is nearly independent of the temperature over a wide temperature range. At temperatures close to T^*, the function $\Delta^*(T)$ is well approximated by the square-root relationship

$$\Delta^*(T) = 95.5\sqrt{203.2 - T}, \qquad (3)$$

which is represented by curve *5* in Fig. 2.

In this processing of the experimental data, we introduced the quantity Δ^*, which possesses the following properties.

(1) As follows from the form of relationship (1), the quantity Δ^* determines a thermal activation process through the energy gap.

(2) The inequality $\Delta^* \neq 0$ holds in the same temperature range in which cuprates exhibit deviations from a Fermi-liquid behavior due to the presence of a pseudogap in the excitation spectrum [1, 9–11].

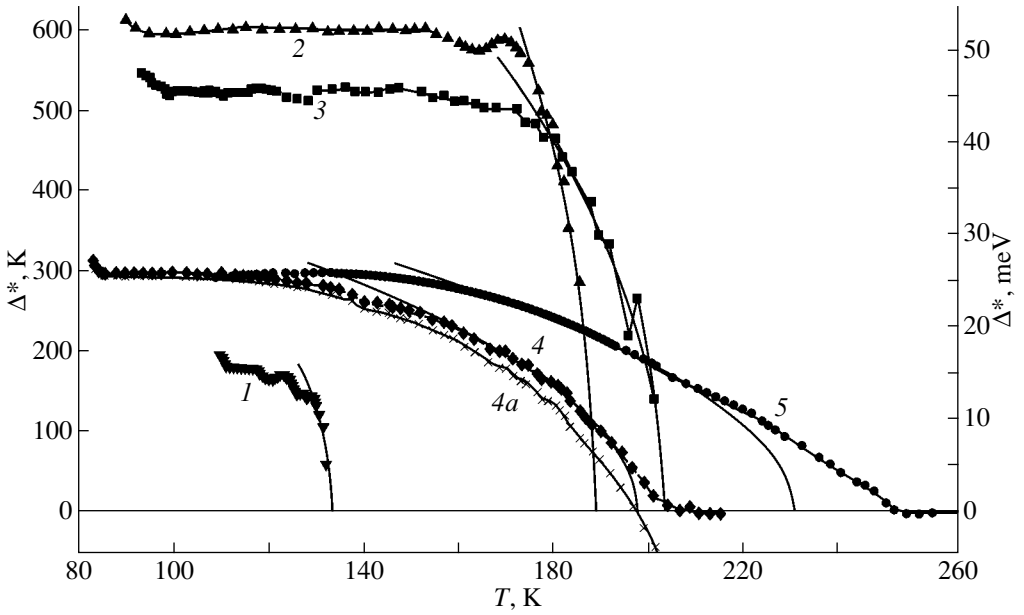

Fig. 3. Temperature dependences of the pseudogap width Δ* for $YBa_2Cu_3O_{7-\delta}$ single crystals at oxygen contents $(7-\delta)$ = (*1*) 6.93, (*2*) 6.88, (*3*) 6.85, (*4*) 6.78, and (*5*) 6.68. Solid lines indicate the results of the fitting with the square-root relationships whose parameters are listed in the table. The temperature dependence of the pseudogap width Δ* calculated from formula (2) (curve *4a*) is shown for comparison with the dependence Δ*(*T*) calculated from formula (A2) (curve *4*).

(3) The quantity $\Delta_m^* \approx 520$ K (45 meV) corresponding to the low-temperature plateau is close to the pseudogap width Δ* ≈ 500 K, which was obtained by Kabanov *et al.* [12] for YBaCuO thin films with the same oxygen content from an analysis of the relaxation of a photoinduced decrease in the light transmission measured by picosecond time-resolved optical spectroscopy.

(4) The behavior of Δ* at temperatures close to *T** is characteristic of the temperature dependence of the order parameter in the vicinity of the second-order phase transition point [this is admitted by the theory proposed in [13], even though a smooth transition (crossover) from the normal state to the state with a nonzero pseudogap is assumed to be more probable].

In our opinion, the dependence $\Delta\sigma(T)$ satisfying relationship (2) can be interpreted as follows: the excess conductivity is proportional to the density of superconducting carriers, which, to a first approximation, can be estimated as $n_s \sim (1 - T/T^*)$ at temperatures not far from *T**, and inversely proportional to the number of pairs broken by thermal motion [$\sim\exp(-\Delta^*/kT)$]. It is assumed that the formulas appropriate in the Bardeen–Cooper–Schrieffer (BCS) theory are applicable, as a first approximation, in the temperature range $T \le T^*$. This assumption is based on the inferences made by Emery *et al.* [4]. According to [4], the temperature *T** is treated as the mean-field temperature of the superconducting transition and the temperature range $T_c < T < T^*$, in which the pseudogap state occurs, is determined by the order-parameter phase stiffness decreasing with a decrease in the doping level (i.e., the carrier concentration). Oda *et al.* [14] analyzed the experimental data for different cuprates and drew a similar conclusion that $T^* \sim T^{MF}$, where T^{MF} is the superconducting transition temperature in the mean-field approximation.

The above properties give grounds to believe that the quantity Δ* determined from analyzing the temperature dependence of the excess conductivity can be identified with the pseudogap revealed in high-temperature superconductors by a number of experimental techniques [1]. Since the pseudogap is observed in materials with a carrier concentration variable over a wide range below the optimum concentration (with $T_c < T_{c\max}$), it is of interest to investigate more thoroughly the excess conductivity with the use of the available data on *R*(*T*) at different oxygen contents in YBCO. For this purpose, we processed the experimental data obtained by Takenaka *et al.* [9] for the temperature dependence of the resistance of $YBa_2Cu_3O_{7-\delta}$ twin-free single crystals with different oxygen contents (δ = 0.07, 0.12, 0.22, and 0.32). The dependences $f(T) \equiv [\rho(T) - \rho_0]/\alpha T$ [9] (where ρ is the resistivity of the single crystal along the **a** axis and α is the coefficient in the linear dependence $\rho_n(T) = \rho_0 + \alpha T$) permitted us to calculate the excess conductivity $\Delta\sigma = \rho^{-1} - \rho_n^{-1} = [1 - f(T)]/[(1 + \rho_0/\alpha T)\rho(T)]$ and to determine the dependence Δ*(*T*) from relationship (2). Figure 3 depicts the dependences Δ*(*T*) for single crystals with δ = 0.07 (curve *1*) and 0.12 (curve *2*). The excess conductivity in strongly underdoped single crystals (δ = 0.22 and 0.32)

Parameters determined from analyzing the temperature dependence of the resistance of $YBa_2Cu_3O_{7-\delta}$ high-temperature superconductors with different oxygen contents

$(7-\delta)$	T_c, K	T^*, K	T_{sqr}, K	Δ_m^*		Q, $K^{1/2}$	k
				K	meV		
6.93	91.2	133	133	180	15.5	72.2	4.62
6.88	90.8	189	189	602	52	148	3.38
6.85	89.5	203.3	203.2	524	45	95.5	2.6
6.78	80.5	220	198	298	25.7	37.4	1.86
6.68	58.7	268	231	299	25.7	33.8	1.72

Note: T_c is the critical temperature, T^* is the temperature of pseudogap opening in the excitation spectrum, Δ_m^* is the pseudogap width in the plateau at temperatures considerably below the temperature T^*, and T_{sqr} is the fitting parameter in the formula approximating the dependence $\Delta^*(T \longrightarrow T^*)$ by the square-root relationship $\Delta^*(T) = Q\sqrt{T_{sqr} - T}$ or $\Delta^*(t)/\Delta_m^* = k\sqrt{1 - T/T_{sqr}}$.

can also be described by relationship (2), except in the temperature range in the immediate vicinity of T^*, in which the preexponential factor decreases faster than $1 - T/T^*$. This situation for the single crystal with $\delta = 0.22$ is illustrated in inset (b) to Fig. 2. The experimental dependence $\ln\sigma(T)$ (curve *1*) at ≈ 200 K $< T$ lies below curve *2* calculated from relationship (2) at $\Delta^* = 0$. Therefore, in order to describe the excess conductivity $\Delta\sigma$ up to the temperature T^* (by eliminating the values of $\Delta^* < 0$ from our consideration), it is necessary to introduce a stronger dependence of the decrease in the preexponential factor on the temperature as compared to that used in relationship (2). The possibility of modifying relationship (2) for describing the excess conductivity in strongly underdoped single crystals is considered in Item 1 of the Appendix.

Figure 3 shows the dependences $\Delta^*(T)$ for single crystals at different doping levels $(7-\delta)$ and the curves approximating the high-temperature portions of $\Delta^*(T)$ by the square-root relationship $\Delta^* \sim \sqrt{(T_{sqr} - T)}$. As can be seen, the descending portion of the curves $\Delta^*(T)$ can be described by the square-root relationship over almost the entire range (up to T^*) for materials at doping levels $(7-\delta) = 6.93$–6.85 or over a sufficiently wide range of temperatures for materials at lower doping levels (in the latter case, the parameter of the square-root approximation must satisfy the inequality $T_{sqr} < T^*$). The possibility of constructing the square-root approximation will be discussed in Item 2 of the Appendix. The parameters derived in the above processing for materials with different δ are given in the table.

Figure 4 depicts the dependences $\Delta^*(t)/\Delta_m^*$ on the reduced temperature $t = T/T^*$, where Δ_m^* is the value of Δ^* in the plateau at temperatures considerably below T^*. This figure also shows the dependences $\Delta^*(t)/\Delta(0)$ calculated by Babaev and Kleinert [6] in the framework of the theory of the crossover from the Bardeen–Cooper–Schrieffer mechanism to the Bose–Einstein condensation (BEC) mechanism at different parameters $\mu/\Delta(0)$ of the theory, where μ is the chemical potential of charge carriers and $\Delta(0)$ is the energy gap at $T = 0$. Theoretical curves *6*–*9* lie between experimental curves *1*–*3* [$(7-\delta) = 6.93$, 6.88, and 6.85] and experimental curves *4* and *5* [$(7-\delta) = 6.78$ and 6.68].

The inset in Fig. 4 shows the dependences Δ^*/Δ_m^* on the reduced temperature $t = T/T_{sqr}$; i.e., the temperature in the inset is normalized to T_{sqr} rather than to T^* as in Fig. 4. Curves *1* and *2* in the inset correspond to $(7-\delta) = 6.78$ and 6.68, respectively. Note that the experimental curves in the inset to Fig. 4, especially curve *1*, are very similar to theoretical curve *3* at $\mu/\Delta(0) = -2$.

4. DISCUSSION

An exponential temperature dependence of the excess conductivity has been observed for a number of high-temperature superconductors. In particular, Prekul *et al.* [15] demonstrated that the excess conductivity in YBaCuO and LaSrCuO ceramic materials can be described by relationship (1) at $b \approx 800$ and ≈ 400 K, respectively. Vyas *et al.* [16] also revealed an exponential dependence of the excess conductivity of $YBa_2(Cu_{1-x}Mg_x)_3O_{7-\delta}$ samples. In this case, a linear portion in the dependence of $\ln(\rho^{-1} - \rho_n^{-1})$ on T^{-1} was observed approximately in the same temperature range as in our work (curve *3* in Fig. 2) and [15]. In [16], the authors assumed that the parameter b in the numerator of the exponent in expression (1) is equal to the pseudogap width, which decreases from 1000 K for compounds at a doping level close to the optimum value $x = 0.002$ to 170–200 K with an increase in the Mg content to $x \approx 0.02$. The parameters b determined in [15, 16] agree well with our results obtained by processing the experimental data with the use of formula (1): $b \approx 900$ K at $(7-\delta) = 6.88$ and $b \approx 680$ K at $(7-\delta) = 6.85$ (especially when taken into account that the carrier concentration is known only approximately).

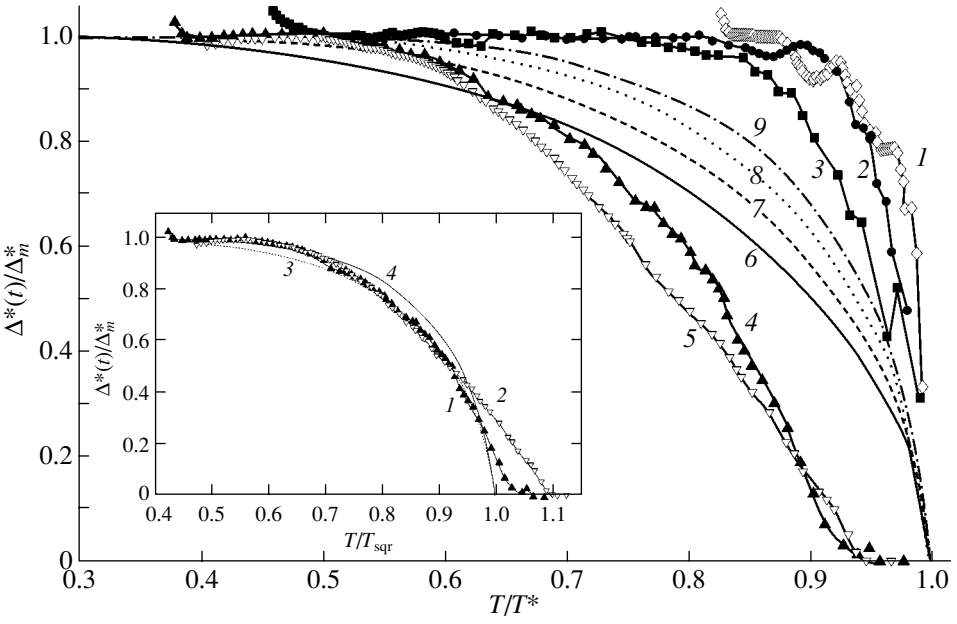

Fig. 4. Experimental and theoretical temperature dependences of the pseudogap width in reduced coordinates. (*1*–*5*) Dependences of $\Delta^*(t)/\Delta_m^*$ (normalized to the maximum pseudogap width) on the reduced temperature $t = T/T^*$ at oxygen contents $(7 - \delta)$ = (*1*) 6.93, (*2*) 6.88, (*3*) 6.85, (*4*) 6.78, and (*5*) 6.68. (*6*–*9*) Graphs of the reduced pseudogap width $\Delta^*(t)/\Delta(0)$ calculated as a function of the reduced temperature $t = T/T^*$ in terms of the BCS–BEC crossover theory [6] in the mean-field approximation at the crossover parameters $\mu/\Delta(0)$ = (*6*) 10 (BCS limit), (*7*) –2, (*8*) –5, and (*9*) –10 (BEC limit). μ is the chemical potential of charge carriers, and $\Delta(0) \equiv \Delta(T = 0)$. The inset shows the dependences $\Delta^*(t)/\Delta_m^*$ on the reduced temperature $t = T/T_{sqr}$ at oxygen contents $(7 - \delta)$ = (*1*) 6.78 and (*2*) 6.68 (corresponding to curves *4* and *5* in the main part of Fig. 4) and the theoretical dependences of the reduced pseudogap width $\Delta^*(t)/\Delta(0)$ [6] at crossover parameters of (*3*) –2 and (*4*) –5. T_{sqr} is the parameter of the square-root approximation of $\Delta^*(T \longrightarrow T^*)$.

However, relationship (1) enables one to describe only a portion of the experimental curve $\Delta\sigma(T)$ in the temperature range 100–140 K. At the same time, the excess conductivity is adequately described by relationship (2) over the entire temperature range of existence of the pseudogap in $YBa_2Cu_3O_{7-\delta}$ single crystals at doping levels $(7 - \delta) = 6.93$–6.85 (close to the optimum level) and, after an appropriate modification [see formula (A2)], at doping levels $(7 - \delta) = 6.78$ and 6.68.

The dependences $\Delta^*(T)$ shown in Fig. 3 are characterized by the following features.

(i) The dependences $\Delta^*(T)$ for compounds at doping levels $(7 - \delta) = 6.88$ and 6.85 exhibit a plateau with $\Delta^*(T) \sim$ const over a wide temperature range.

(ii) The quantity $\Delta^*(T)$ for the compounds doped at levels close to the optimum value increases drastically with a decrease in the temperature from T^*, and the dependence $\Delta^*(T)$ becomes progressively smoother with an increase in δ.

(iii) As the oxygen content δ increases, the quantity Δ_m^* corresponding to the plateau in the dependence $\Delta^*(T)$ varies in a nonmonotonic way; i.e., it passes through a rather sharp and asymmetric maximum at doping levels δ slightly below the optimum value.

(iv) The temperature T^* monotonically increases with an increase in δ.

(v) The properties of the materials at doping levels $(7 - \delta) = 6.93$, 6.88, and 6.85 differ significantly from those of the lightly doped materials at levels $(7 - \delta) = 6.78$ and 6.68. For the former materials, the excess conductivity is adequately described by formula (2), the obtained dependence $\Delta^*(T)$ exhibits a wide plateau at low temperatures and obeys the square-root relationship at temperatures close to T^*, and the temperatures T_{sqr} and T^* coincide with each other. For the latter compounds, the excess conductivity should be described by the more complex expression (A2) (see Appendix) and the dependence $\Delta^*(T)$ calculated according to this formula deviates from the square-root behavior in the immediate vicinity of the temperature T^*, which results in $T_{sqr} < T^*$.

These properties of the pseudogap revealed from analyzing the temperature dependence of the resistance of $YBa_2Cu_3O_{7-\delta}$ compounds can be compared with the data available in the literature.

It should be noted that a monotonic increase in the temperature T^* with a decrease in the doping level has been observed in all the works dealing with pseudogaps [1]. Angle-resolved photoelectron spectroscopic investigations performed by Ding *et al.* [17] revealed a gap

in the spectrum of $Bi_2Sr_2CaCu_2O_8$ at $T_c < T$, which depends on the wave vector and rather rapidly decreases with an increase in the temperature T. According to our data for the compound with the optimum doping ($\delta = 0.07$), the dependence $\Delta^*(T)$, which is characterized by a rapid decrease from $\Delta_m^* \approx 16$ meV at $T = 110$ K to 0 at $T = 133$ K, is qualitatively similar to the dependence $\Delta^*(T)$ obtained from the angle-resolved photoelectron spectroscopic and electronic heat capacity data [1]. A pseudogap Δ^* independent of temperature over a wide range was observed for YBaCuO films (according to the data on a photoinduced decrease in the light transmission) [12] and for $Bi_{2.1}Sr_{1.9}CaCu_2O_{8+\delta}$ crystals (scanning tunneling microscopy) [18], which is in agreement with our results at $\delta = 0.22$–0.25. The pseudogap width is close to that found in [12] at this concentration. A difference is observed in the temperature range close to the temperature T^*. In this range, the resolution of the method used to examine the relaxation of a photoinduced decrease in the light transmission is insufficient for observing the temperature dependence of $\Delta^* \longrightarrow 0$ at $T \longrightarrow T^*$.

The results obtained in this work demonstrated that a further increase in δ leads to a nonmonotonic change in the value of Δ_m^*. This behavior differs from the data reported in [12, 14], according to which the pseudogap width increases monotonically with a decrease in the doping level: $\Delta^* \sim 1/(0.6 - \delta)$. As in our work, Vyas *et al.* [16] investigated the temperature dependences of the excess conductivity. In [16], it was found that an increase in the Mg content in $YBa_2(Cu_{1-x}Mg_x)_3O_{7-\delta}$ compounds results in a decrease in the parameter b in formula (1). This parameter is proportional to the pseudogap width Δ_m^* derived when the experimental data are processed using relationship (2). Since an increase in the Mg content is accompanied by an increase in the resistivity of the material and a decrease in the critical temperature, it is reasonable to assume that an increase in x leads to a decrease in the carrier concentration below the optimum level, i.e., to an increase in the "degree of underdoping" of the material. Therefore, in [16], the authors most likely observed a decrease in the pseudogap width with a decrease in the carrier concentration from a concentration slightly lower than the optimum level at a lowest content equal to 0.002 at. % Mg, i.e., when going far into the underdoped region. This behavior is similar to the decrease in the value of Δ_m^* calculated in our work with a decrease in $(7 - \delta)$ from 6.88 to 6.78. However, the data obtained in a number of works are inconsistent with a simple monotonic increase in the pseudogap width with a decrease in the doping level. In particular, Blumberg *et al.* [19] noted that the suppression of low-frequency excitations in BiSrCaCuO (i.e., the manifestation of the pseudogap) becomes less pronounced with a decrease in the doping level in the range of relatively low concentrations. Moreover, these authors revealed [19] that, as the doping level decreases from a level slightly above the optimum level, the 2Δ quasiparticle Raman peak at $\lambda^{-1} = 420$ cm^{-1} (52 meV) transforms first into a peak at $\lambda^{-1} \sim 540$ cm^{-1} (67 meV) at the optimum doping level and then into a partially coherent peak at $\lambda^{-1} \sim 600$ cm^{-1} (75 meV). Consequently, in [19], it was demonstrated that a decrease in the carrier concentration can lead to a decrease in the pseudogap width at a shift of ≈10 meV (in the range of low concentrations) and to an increase in the energy of the peak (i.e., in the value of $2\Delta^* \approx 50$–75 meV) at doping levels close to the optimum level. Mihailovic *et al.* [20] measured the relaxation times of quasiparticles excited by laser pulses in $YBa_2Cu_3O_{7-\delta}$ compounds and revealed that the concentration dependence of the quasiparticle relaxation time drastically changes in character at $(7 - \delta) \approx 6.8$–6.85. At higher values, the relaxation time sharply increases with an increase in the oxygen content (to the optimum level). At the same time, at lower contents, the relaxation time virtually does not depend on δ. Hence, there are grounds to believe that a decrease in the oxygen content below 6.8 results in a considerable change in the properties of $YBa_2Cu_3O_{7-\delta}$ compounds, which accounts for the specific features observed in the behavior of the pseudogap determined from the resistance data. In our opinion, the discrepancy between our results and the data obtained in [12, 14] stems from the fact that, at relatively low contents, the excitation of the studied system in measurements of the Raman shifts and relaxation after optical pumping and also in observations with scanning tunneling microscopy is substantially higher than that in experiments on the conductivity measurement.

It should be noted that, compared to other techniques, the analysis of the excess conductivity provides a means for determining the dependence $\Delta^*(T)$ up to the temperature T^*. Consequently, it becomes possible to compare the obtained results with theoretical data. As can be seen from Fig. 4, the results of the BCS–BEC crossover theory disagree with the dependences Δ^*/Δ_m^* on T/T^*, which were calculated from the experimental data. In the case of materials with concentrations close to the optimum level, the dependences determined from the experimental data cannot be described within the theory developed in [6] due to the occurrence of a plateau over a wide temperature range with $\Delta^*(T) \approx$ const and a sharp decrease in Δ^* in the vicinity of the temperature T^*. Mathematically, the last fact is reflected in the large parameter $k = 2.5$–4.6 in the reduced square-root dependence $\Delta^*(t)/\Delta_m^* = k\sqrt{1 - T/T_{sqr}}$ for these materials (for comparison, $k \approx 1.74$ in the BCS theory). For materials at a lower doping level, the dependences $\Delta^*(t)/\Delta_m^*$ are in satisfactory agreement with the dependences $\Delta^*(t)/\Delta(0)$ obtained in [6] at the crossover parameter $\mu/\Delta(0) = -2$ after replacing $t = T/T^*$ by $t =$

T/T_{sqr}. Here, T_{sqr} is the parameter of the square-root approximation of the descending portion in the dependence $\Delta^*(T)$. The exception is provided by the range in the immediate vicinity of the T^* temperature. This agrees with the theoretical concept according to which the transition at the temperature T^* is treated as a smooth crossover (more probable than the phase transition). For this reason, in [6], it was not expected that the dependences $\Delta^*(t)/\Delta(0)$ deduced in the mean-field approximation could be applicable in the vicinity of the temperature T^*. Thus, the comparison of our results with the theoretical data, first, demonstrates that the $YBa_2Cu_3O_{7-\delta}$ compounds at concentrations slightly less than the optimum level possess specific properties, second, confirms the proposed interpretation of the data for materials at $(\delta - 7) < 6.8$ [more precisely, the introduction of the characteristic temperature T_{sqr} and the use of formula (A2) for processing the results], and, third, provides further evidence supporting the applicability of the mean-field theory to rather lightly doped $YBa_2Cu_3O_{7-\delta}$ compounds at temperatures well below T^* (the experimental results in the vicinity of this temperature should be explained in terms of other theories). The last inference directly follows from our interpretation of the excess conductivity $\Delta\sigma$ with the use of expression (2). At temperatures close to T^*, the preexponential factor in formula (2) decreases faster than $1 - T/T^*$ [as a result, it is necessary to use relationship (A2)]; i.e., the density of superconducting carriers n_s deviates from that predicted by the mean-field theory and, hence, this theory is inapplicable. This is also supported by the fact that the square-root approximation of the dependence $\Delta^*(T)$ [curve *5* in inset (b) in Fig. 2] becomes invalid approximately at the temperature (≈195 K) at which expression (2) becomes inapplicable.

Finally, we consider the crossover to fluctuation conductivity in the case when the critical temperature T_c is approached. It can be seen from Fig. 3 that, with a decrease in the temperature, the curves $\Delta^*(T)$ in the vicinity of the critical temperature T_c begin to deviate upward from the plateau. In this range (down to T_c), there arises fluctuation conductivity characterized by a more rapid increase in the excess conductivity $\Delta\sigma$ with a decrease in the temperature as compared to the excess conductivity considered above. It seems likely that superconducting pairs cease to be independent in the range of the crossover to paraconductivity. In any case, the excess conductivity $\Delta\sigma$ in the paraconductivity range cannot be described by the exponential dependence proposed above. For the sample at the doping level $(7 - \delta) = 6.85$ (for which the most exact results were obtained, we revealed that the excess conductivity $\Delta\sigma$ in the temperature range $T = 92.5$–106 K is well described in the framework of the Aslamazov–Larkin theory [21] for a two-dimensional system; that is,

$$\Delta\sigma = (e^2/16\hbar d)T_c/(T - T_c),$$

where d is the thickness of the layer in which superconducting fluctuations occur. The transformation into a three-dimensional system is observed at ≈92.3 K. In this case, the excess conductivity can be written in the form

$$\Delta\sigma = (e^2/32\hbar\xi(0))(T_c/(T - T_c))^{1/2},$$

where $\xi(0)$ is the coherence length at $T = 0$. The determined layer thickness $d \approx 91$ nm agrees with the data obtained in [22], and the calculated coherence length $\xi(0) \approx 0.23$ nm is close to that reported in [23]. In the present work, we are interested in the temperature up to which the dependence $\Delta\sigma(T)$ can be described within the concept of fluctuation conductivity, because the excess and fluctuation conductivities are calculated from the experimental data according to the same formula $\Delta\sigma = 1/\rho(T) - 1/\rho_n(T)$. Previously, Hopfengartner *et al.* [24] experimentally found that, at temperatures substantially higher than the critical temperature T_c, the fluctuation conductivity decreases more rapidly than that predicted theoretically. It was assumed that this stems from the underestimation of the contribution from short-wavelength order parameter fluctuations, whereas this contribution increases with an increase in the temperature. Reggani *et al.* [25] performed microscopic calculations of the excess conductivity $\Delta\sigma$ with allowance made for all the order parameter components. A comparison shows that our data for the sample at $(7 - \delta) = 6.85$ and the theoretical results obtained in [25] are in agreement up to a temperature of approximately 118 K. Therefore, in the temperature range 100–118 K, the excess conductivity $\Delta\sigma$ can be described to within our accuracy of measurement both by the aforementioned exponential relationship [formula (2)] and in the framework of the fluctuation conductivity theory developed in [25]. With a further increase in the temperature, the excess conductivity $\Delta\sigma$ decreases faster than follows from the theory proposed in [16]. However, the exponential description remains valid and $\Delta^* \sim$ const up to $T \approx 160$ K. In concluding, one further remark should be made. Let us assume that the crossover to the fluctuation conductivity with a decrease in the temperature occurs at the temperature T_{fl} at which the dependence $\Delta^*(T)$ deviates upward from the plateau. Then, it turns out that the relative temperature range of the paraconductivity $(T_{fl} - T_c)/T_c$ decreases from 0.217 to 0.137, 0.106, and 0.0646 with a decrease in $(7 - \delta)$ from 6.93 to 6.78. Therefore, we can draw the inference that a weakening of superconducting correlations with a decrease in the doping level with respect to the optimum level leads to a decrease in the critical temperature and the temperature range characterized by a pronounced fluctuation conductivity.

5. CONCLUSIONS

Thus, the main results obtained in this work can be summarized as follows:

(1) It was found that the temperature dependence of the excess conductivity for YBaCuO films and single crystals with carrier concentrations slightly lower than the optimum concentration exhibits an exponential behavior over a wide range of temperatures. The assumption was made and justified that the exponent in the expression describing the corresponding dependence in this concentration range can be represented in the form Δ^*/T, where Δ^* is the pseudogap width.

(2) The temperature dependence of the pseudogap width in the range from $T = T^*$ to temperatures (above the critical temperature) at which the fluctuation conductivity plays the decisive role was obtained under simple assumptions.

(3) It was shown that the temperature dependence of the excess conductivity for compounds with concentrations close to (and including) the optimum concentration $0.07 \le \delta < 0.2$ can be interpreted in terms of the mean-field theory. For compounds in this concentration range, the temperature dependence of the pseudogap width in the vicinity of the temperature T^* exhibits the behavior characteristic of second-order phase transitions described in the framework of the mean-field theory.

(4) When changing over to samples at a lower doping level ($\delta > 0.2$), the pseudogap width increases and its temperature dependence transforms such that good agreement can be achieved with the BCS–BEC crossover theory (except in the temperature range close to T^*). It was demonstrated that, at these concentrations, the low-temperature portion of the dependence $\Delta^*(T)$ can be described within the mean-field theory; however, this approximation is inapplicable at temperatures close to T^*.

APPENDIX

1. Let us modify formula (2). The dependences calculated using formula (2) for the compound with $(7 - \delta) = 6.78$ at $A = 270\ \Omega^{-1}\ \text{cm}^{-1}$ and $\Delta^* = 294$ K (curve *1*) and 0 K (curve *2*) are depicted in inset (b) in Fig. 2. At $\approx 195\ \text{K} < T$, experimental curve *1* lies below curve *2*. Therefore, as was noted above, in order to describe the excess conductivity up to the temperature T^*, it is necessary to transform formula (2) in such a way as to provide a faster decrease in the preexponential factor in this temperature range. For this purpose, the excess conductivity $\Delta\sigma$ can be written in the form

$$\Delta\sigma = A(1 - T/T^*)^{\beta(T)}\exp(\Delta^*/T), \qquad \text{(A1)}$$

where $\beta = 1$ at $T < 195$ K increases to $\beta(T^*) \sim 1.34$ at $T \longrightarrow T^*$. The factor $(1 - T/T^*)^{\beta(T)}$ can be replaced by the expression $(1 - T/T^*)\exp[-M/(T^* - T)]$ (where M is a constant), which is more convenient for comparing with the experimental data. Inset (b) in Fig. 2 shows curves *3* and *4* constructed using the relationship

$$\Delta\sigma = A\exp[-M/(T^* - T)](1 - T/T^*)\exp(\Delta^*/T) \qquad \text{(A2)}$$

with the same parameters A and $\Delta^* = 294$ K (curve *3*) and 0 K (curve *4*) as for curves *1* and *2* and $M = 5.86$ K. It can be seen that the curves calculated from relationship (A2) at $T < 200$ K are sufficiently close to the curves constructed with formula (2) and the use of relationship (A2) makes it possible to describe the temperature dependence of the conductivity up to the temperature T^*. Curves *4* and *5* in Fig. 3 depict the dependences $\Delta^*(T)$ obtained by applying relationship (A2) for processing the experimental data for single crystals at doping levels $(7 - \delta) = 6.78$ and 6.68, respectively. For comparison, the dependence $\Delta^*(T)$ calculated from formula (2) is represented by curve *4a* in Fig. 3. As could be expected, the difference between curves *4* and *4a* is insignificant at low temperatures $T < 190$ K. At the same time, we believe that curve *4* qualitatively reflects the behavior of the dependence $\Delta^*(T)$ in the immediate vicinity of the temperature T^*.

2. The possibility of describing the dependence $\Delta^*(T)$ in the vicinity of the temperature T^* with the use of the square-root relationship was determined in the following way. (1) The dependence of Δ^* on $(T^* - T)^{1/2}$ was analyzed for the occurrence of a linear portion in the range close to T^*. (2) The characteristic temperature, which is referred to as the temperature T_{sqr} (square root), was varied so that the linear dependence had the form $\Delta^* = Q(T_{sqr} - T)^{1/2}$ (the free term should be equal to zero). The dependences $\Delta^*(T)$ calculated from the obtained parameters Q and T_{sqr} are shown by the solid lines in Fig. 3.

REFERENCES

1. T. Timusk and B. Statt, Rep. Prog. Phys. **62**, 61 (1999).
2. V. M. Sadovskiĭ, Usp. Fiz. Nauk **171** (5), 539 (2001) [Phys. Usp. **44**, 515 (2001)].
3. P. Pieri, G. C. Strinati, and D. Moroni, Phys. Rev. Lett. **89** (12), 127003 (2002).
4. V. J. Emery and S. A. Kivelson, Nature **374**, 434 (1995); V. J. Emery, S. A. Kivelson, and O. Zachar, Phys. Rev. B **56** (10), 6120 (1997).
5. V. M. Loktev, R. M. Quick, and S. G. Sharapov, Physica C (Amsterdam) **314**, 233 (1999).
6. E. Babaev and H. Kleinert, cond-mat/9804206 (1998); Phys. Rev. B **59** (18), 12083 (1999).
7. V. B. Geshkenbein, L. B. Ioffe, and A. L. Larkin, Phys. Rev. B **55** (5), 3173 (1997).
8. Yu. A. Boikov and T. Claeson, J. Appl. Phys. **81** (7), 3232 (1997); Yu. A. Boikov and Z. G. Ivanov, J. Alloys Compd. **251**, 193 (1997).
9. K. Takenaka, K. Mizuhashi, H. Takagi, and S. Uchida, Phys. Rev. B **50** (9), 6534 (1994).
10. Z. Konstantinovic, Z. Z. Lee, and H. Raffy, Physica C (Amsterdam) **341–348**, 859 (2000).
11. K. Q. Ruan, Q. Cao, S. Y. Li, *et al.*, Physica C (Amsterdam) **351**, 402 (2001).
12. V. V. Kabanov, J. Demsar, B. Podobnic, and D. Mihailovic, Phys. Rev. B **59** (2), 1497 (1999).

13. V. P. Gusynin, V. M. Loktev, and S. G. Sharapov, Fiz. Nizk. Temp. **23** (8), 816 (1997) [Low Temp. Phys. **23**, 612 (1997)].
14. M. Oda, K. Hova, N. Momonj, *et al.*, J. Phys. Chem. Solids **59** (10–12), 2071 (1998).
15. A. F. Prekul, V. A. Rassokhin, A. B. Rol'shchikov, *et al.*, Sverkhprovodimost: Fiz., Khim., Tekh. **3** (3), 381 (1990).
16. A. Vyas, C. C. Lam, and L. J. Shen, Physica C (Amsterdam) **341–348**, 935 (2000).
17. H. Ding, J. C. Campuzano, M. R. Norman, *et al.*, J. Phys. Chem. Solids **59** (10–12), 1888 (1998).
18. A. Matsuda, S. Sugita, and T. Watanabe, Phys. Rev. B **60** (2), 1377 (1999).
19. G. Blumberg, M. V. Klein, K. K. Kadowaki, *et al.*, J. Phys. Chem. Solids **59** (10–12), 1932 (1998).
20. D. Mihailovic, B. Podobnic, J. Demsar, *et al.*, J. Phys. Chem. Solids **59** (10–12), 1937 (1998).
21. L. G. Aslamazov and A. I. Larkin, Fiz. Tverd. Tela (Leningrad) **10** (4), 1104 (1968) [Sov. Phys. Solid State **10**, 875 (1968)].
22. A. I. Golovashkin, K. V. Mitsen, G. P. Motulevich, and Ch. Shukurov, Sverkhprovodimost: Fiz., Khim., Tekh. **5** (12), 2205 (1992).
23. Y. Matsuda, A. Fujiama, S. Komiama, *et al.*, Phys. Rev. B **45** (9), 4901 (1992); M. Hikita and M. Suzuki, Phys. Rev. B **41** (1), 834 (1990).
24. R. Hopfengartner, B. Hensel, and G. Saemann-Ischenko, Phys. Rev. B **44** (2), 741 (1991).
25. L. Reggani, R. Vaglio, and A. A. Varlamov, Phys. Rev. B **44** (17), 9541 (1991).

Translated by O. Borovik-Romanova

Physics of the Solid State, Vol. 45, No. 7, 2003, pp. 1233–1241. Translated from Fizika Tverdogo Tela, Vol. 45, No. 7, 2003, pp. 1177–1184.

SEMICONDUCTORS AND DIELECTRICS

Excitons in Monoclinic Zinc Diphosphide: The *A*-Exciton Series and Fano Effect

A. P. Krokhmal', V. A. Gubanov, and Z. Z. Yanchuk

Shevchenko National University, Vladimirskaya ul. 64, Kiev, 01033 Ukraine

e-mail: krokhmal@mail.univ.kiev.ua

Received July 3, 2002

Abstract—The *A*-exciton series in the absorption spectra of β-ZnP_2 monoclinic zinc diphosphide samples is investigated at different directions of the wave vector and different polarization states of radiation. It is shown that the oscillator strengths determined for the observed transitions are adequately described by the relationship $F_n \propto n^{-3}$ characteristic of *S*-type exciton states. The assumption is made that the *A*-exciton series is associated with the partially allowed dipole transitions to *nS* states of the orthoexciton with $\Gamma_2^-(x)$ symmetry at $m_s = 0$. These states are mixed, to a first approximation, with *nS* states of the $\Gamma_2^-(z)$ singlet exciton due to the spin–orbit interaction and are split off by the long-range (nonanalytical) part of the exchange interaction. The Fano antiresonances arise in the absorption spectra at resonances of the *A*-exciton series when the radiation vector **E** (or the induction vector **D**) has a component along the crystallographic axis **c**. These antiresonances are induced by the configurational interaction of discrete exciton states of the *A* series with the continuum of the exciton–phonon spectrum due to indirect transitions to the 1*S* band of the singlet exciton with phonon emission. © *2003 MAIK "Nauka/Interperiodica".*

1. INTRODUCTION

Monoclinic zinc diphosphide β-ZnP_2 is a low-symmetry direct-band-gap semiconductor in which several hydrogen-like exciton series can be excited as a result of electric-dipole [1–4] and dipole-forbidden [1, 3, 5] transitions. However, unlike cubic Cu_2O and other thoroughly studied direct-band-gap semiconductors (for example, CdS), all the series for β-ZnP_2 are most likely associated with the same pair of electron energy bands, because these series converge virtually to the same limit $E_\infty = 1.6026 \pm 0.0002$ eV [3, 6]. It is significant that, since the crystal lattice has low symmetry of the class $2/m(C_{2h})$, the orbital degeneracy of exciton states (except for the degeneracy caused by the time inversion) is completely removed by the anisotropic crystal field and the series of exciton absorption lines are observed for different directions of the wave vector $\mathbf{s} = \mathbf{q}/q$ and different polarization states of radiation [6].

In the universally accepted setting of the crystallographic axes in the monoclinic system, i.e., $C_2 \parallel \mathbf{b} \parallel Y$, the well-known *C* series of the singlet exciton (with a large oscillator strength of the exciton transition) associated with the electric-dipole ($E1$) transitions is observed for the polarization $\mathbf{E} \parallel \mathbf{c}$ at $\mathbf{s} \perp (100)$ [1–4]. A mixed mode of the singlet exciton arises when the wave vector **s** is aligned with the dipole moment $\mathbf{P}_m(\mathbf{c})$ of the exciton polarizability tensor [6]. For the polarization $\mathbf{E} \parallel \mathbf{b}$, the absorption spectra observed for all orientations of the wave vector with respect to the crystallographic axes are characterized by the dipole-forbidden *B* series of the orthoexciton [1, 5, 6]. The higher energy *A* series of the absorption lines has not been adequately studied. In our earlier work [6], we uniquely established that the *A* series observed upon normal incidence of radiation on the (110) plane at the polarization $\mathbf{E} \perp \mathbf{c}$ is the exciton series of monoclinic zinc diphosphide and is not related to ZnP_2 crystals of the so-called orthorhombic modification [7]. The maximum intensity of the absorption lines of the *A* series is reached at $\mathbf{s} \perp (010)$ and $\mathbf{E} \parallel X \parallel \langle 100 \rangle$ [6]. Gorban *et al.* [8] assumed that the *A* series should be assigned to the orthoexciton.

Moreover, the considerable interest expressed by researchers in β-ZnP_2 stems from the fact that, in this compound, the biexciton gas undergoes condensation [9] into an electron–hole quantum liquid [10]. In this respect, monoclinic zinc diphosphide is a convenient model material for use in the study of Wannier–Mott excitons and related phenomena in low-symmetry crystals.

In this work, we thoroughly investigated the properties of the *A*-exciton series with the aim of elucidating its origin.

2. SAMPLES AND EXPERIMENTAL TECHNIQUE

Large-sized single crystals of β-ZnP_2 were grown for the purpose of examining the exciton absorption at different directions of the wave vector of radiation [6]. Plates oriented parallel to natural crystallographic faces with indices of the (100), (110), (210), and (102) types and plates oriented parallel to the (010) and (001)

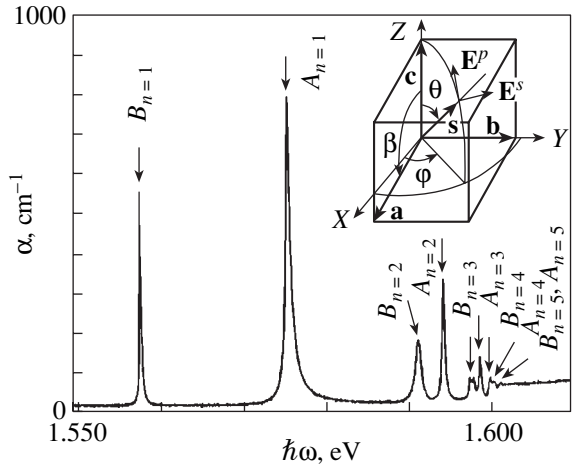

Fig. 1. Absorption spectrum of the β-ZnP_2 crystal at **s** ⊥ (010) and polarization **E** ∥ *X* ∥ [**b** × **c**]. *T* = 1.7 K. The sample thickness is 0.060 mm. The inset shows the orientation of the wave vector **s** and the parallel ($\mathbf{E}^p$) and perpendicular ($\mathbf{E}^s$) components of the radiation polarization with respect to the basis vectors of the monoclinic lattice **a**, **b**, and **c** in the general case in the spherical coordinate system. β = 102.3° is the monoclinic angle.

planes (absent in natural crystal faces) were cut from single crystals with the use of a diamond wheel. Furthermore, we also used plates cut in such a way that, upon normal incidence of radiation on the section plane, the vector **s** lying in the *XY* plane formed a specified angle φ with the *X* axis or the ⟨100⟩ direction. The misorientation of the section planes with respect to the crystallographic planes or directions was no more than 0.3°. After mechanical grinding and subsequent polishing with an ASM-1/0 diamond paste, the samples were subjected to soft chemical etching in a dilute methanol solution of bromine. The absorption spectra were determined from the transmission spectra recorded on a modified DFS-12 automated spectrometer with diffraction gratings (1200 grooves/mm) operating in a first-order spectral mode. The other experimental procedures and parameters were described in our earlier works [6, 11].

Energies of the absorption lines of the *A* series in the geometry **s** ⊥ (010) at **E** ∥ [**b** × **c**] ∥ *X*, the energies calculated in the hydrogen-like approximation, and their differences

Line no.	E_{exp}, eV	E_H, eV	$\Delta E = E_{exp} - E_H$, eV
1	1.57553	1.56703	0.00850
2	1.59410	1.59357	0.00053
3	1.59848	1.59848	0
4	1.60020	1.60020	0
5	1.60097	1.60099	–0.00002

3. RESULTS

Figure 1 depicts the absorption spectrum of the β-ZnP_2 crystal upon normal incidence of radiation with the polarization **E** ∥ [**b** × **c**] ∥ *X* on the (010) plane, i.e., in the geometry **s** ⊥ (010) or **s** ∥ **b** ∥ C_2. The spectrum contains two exciton series, namely, the known *B* series and the higher energy *A* series. The absorption coefficient α for the $A_{n=1}$ line at the maximum reaches 780 cm^{-1} for the sample thickness *d* = 0.060 mm. Note that the line is asymmetric in shape and has a short-wavelength tail. The half-width of the line is found to be *H* = 0.62 meV, and the asymmetry parameter [12] is determined to be $\delta = (H^+/2 - H^-/2)/H = 0.08$. The energies of the lines of the *A* series, the corresponding energies calculated in the hydrogen-like approximation, and their differences are listed in the table. As in [5, 6], the calculations were performed using the photon energies for the lines with *n* = 3 and 4 in order to minimize the disturbance of a hydrogen-like regularity by corrections for a central unit cell, i.e., by a change in the potential energy of an electron due to the non-Coulomb part of the potential of interaction with a hole in the vicinity of **r** = 0 and also by a change in the exciton energy owing to the anisotropic part of the Hamiltonian [13, 14]. The energies of the lines of the *A* series also obey the hydrogen-like regularity but with deviations that are noticeable for the line with *n* = 1 and insignificant for the line with *n* = 2. The deviation of the energies of these lines toward the high-energy range indicates that either there are contributions from the repulsive part of the non-Coulomb interaction potential between electrons and holes in the vicinity of **r** = 0 [15] and from the nonspherical part of the Hamiltonian [13, 14] or this deviation is predominantly caused by other interactions, for example, the exchange interaction. It should be noted that the *A* spectrum in the geometry **s** ⊥ (010) is slightly shifted toward the high-energy range with respect to the spectrum in the geometry **s** ⊥ (110). In this case, the spectral shift of the $A_{n=1}$ line is determined to be Δ*E* = 0.0002 eV and the deviation of the energy of this line from the hydrogen-like regularity increases by 0.25 meV as compared to the analogous deviation at **s** ⊥ (110) [6]. The exciton Rydberg for the *A* series in the geometry under consideration, i.e., Ry^A = 35.4 meV, is considerably less than the exciton Rydberg Ry^C = 42.4 meV for the singlet exciton [6, 8]. However, the convergence energy for the *A* series E_∞ = 1.60240 eV is very close to the band gap E_g = 1.60263 eV [6, 8].

It is important that, in the traditional geometry **s** ⊥ (100) and **E** ∥ **b**, i.e., upon normal incidence of radiation on the **bc** plane, we for the first time succeeded in recording a very weak line with α ~ 0.5 cm^{-1} at 1.57507 eV in the absorption spectra of the samples $d \gtrsim 0.5$ mm in thickness. This line is observed at a small step with the edge at 1.5728 eV against the background of continuous absorption (Fig. 2). If the sample with the (100) plane is rotated about the **c** axis through a certain angle *i* such that the refracted beam deviates from the initial

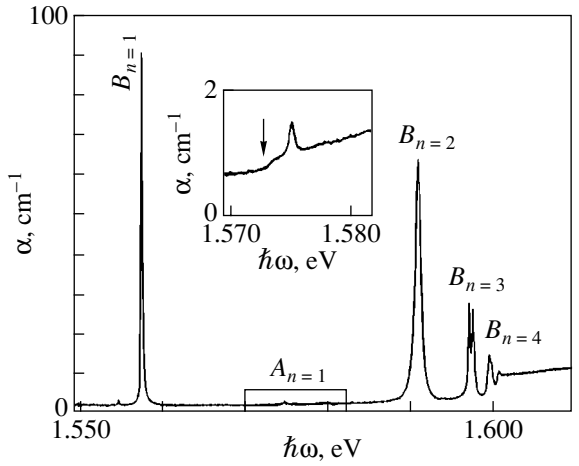

Fig. 2. Absorption spectrum of the β-ZnP_2 crystal at **s** ⊥ (100) and polarization **E** ∥ **b**. T = 1.7 K, d = 0.445 mm. The arrow in the enlarged fragment of the spectrum indicates the edge of the exciton–phonon step.

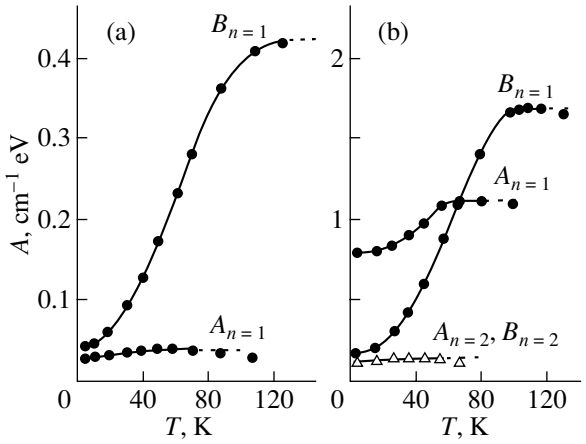

Fig. 3. Temperature dependences of the integrated absorption coefficient for the lines $A_{n=1}$, $B_{n=1}$, $A_{n=2}$, and $B_{n=2}$ in two geometries: (a) φ = 10°, **E** ⊥ **c**, and d = 0.372 mm; and (b) φ = 90°, **E** ∥ X, and d = 0.060 mm.

direction **s** ∥ ⟨100⟩ ∥ X and makes an angle φ with the X axis, the intensity of the observed line at 1.57507 eV increases noticeably. This is also accompanied by the appearance of weak lines at photon energies corresponding to the lines with $n \geq 2$ in the A spectrum. Hence, we can draw the inference that the weak line observed at 1.57507 eV in the geometry **s** ⊥ (100) and **E** ∥ **b** is the line of the A series with n = 1. Consequently, the A spectrum is considered to be "forbidden" when the wave vector **q** of radiation (or the vector **k** of the exciton) is aligned with the crystallographic direction **s** ∥ ⟨100⟩ ∥ [**b** × **c**] ∥ X at the polarization **E** ∥ **b**. On the other hand, in the geometry **s** ∥ ⟨010⟩ ∥ **b** ∥ C_2 at the polarization **E** ∥ X, the A spectrum is "allowed," because the absorption intensity is maximum in this case. If the wave vector **s** forms an angle φ with the X axis in the XY plane, the lines of the A series are characterized by intermediate intensities. It should be noted that the change in the direction of the wave vector **s** from **s** ∥ ⟨100⟩ ∥ X (φ = 0) to **s** ∥ ⟨010⟩ ∥ Y (φ = π/2) leads to a shift in the A series by ≈0.45 meV toward the high-energy range. As a result, the half-width of the line with n = 1 increases from H = 0.47 meV to H = 0.62 meV and the asymmetry parameter increases from approximately zero to δ = 0.08. The changes in the half-width H and the asymmetry parameter δ indicate that the exciton–phonon interaction in β-ZnP_2 is anisotropic, and the small asymmetry parameter suggests that this interaction is weak.

The quantitative measurements of the integrated absorption coefficient A (in terms of eV cm^{-1}) for different directions of the wave vector **s** in the XY plane demonstrate that the absorption for the lines of the A series can be adequately described by the relationship $A_n \propto n^{-3}$ characteristic of S-type exciton envelope functions [16]. Note that, when the wave vector **s** makes a small angle φ with the X axis (for example, φ = 10°) at **E** ⊥ **c**, the ratio of the integrated absorption coefficients for the first two lines of the A series $A_{n=1}/A_{n=2}$ = 8.2 ± 0.2 strictly obeys the relationship $A_n \propto n^{-3}$. With an increase in the angle φ, this ratio decreases to $A_{n=1}/A_{n=2}$ = 6.54 at φ = 49.9° [**s** ⊥ (110) and **E** ⊥ **c**] and $A_{n=1}/A_{n=2}$ = 5.75 at φ = 90° [**s** ⊥ (010) and **E** ∥ X]. A decrease in this ratio indicates that, with an increase in the absorption coefficient (i.e., when the transition becomes more allowed), the oscillator strength appears to be not proportional to the area under the absorption curve. This fact is well known for the exciton absorption at low temperatures and is explained by the polariton effects and the spatial dispersion [5, 17–20]. Note that, at low temperatures, the violation of the classical relationship between the area under the absorption curve and the oscillator strength [21] is pronounced for the exciton resonances at n = 1 and weak for the exciton resonances at n = 2 [5, 18–20].

The integrated absorption coefficient for the lines of the A series was investigated as a function of the temperature at two angles φ = 10° and 90°. As could be expected, with an increase in the temperature, the integrated absorption coefficient for the $A_{n=1}$ line remains nearly constant at the small angle (Fig. 3a) and increases by a factor of approximately 1.4 at φ = π/2 (Fig. 3b). In the latter case, the integrated absorption coefficient for the plate d = 0.060 mm in thickness reaches saturation at the critical temperature T_c = 55 K. On the other hand, the integrated absorption coefficient for the $B_{n=1}$ line increases by one order of magnitude and reaches saturation at a higher critical temperature T_c, as is the case at **s** ⊥ (100) and **E** ∥ **b** [5]. This suggests that the scattering of mechanical energy of exciton polaritons at the $A_{n=1}$-exciton resonance predominantly proceeds not through the exciton–phonon mechanism. The dominant mechanism can be, for example,

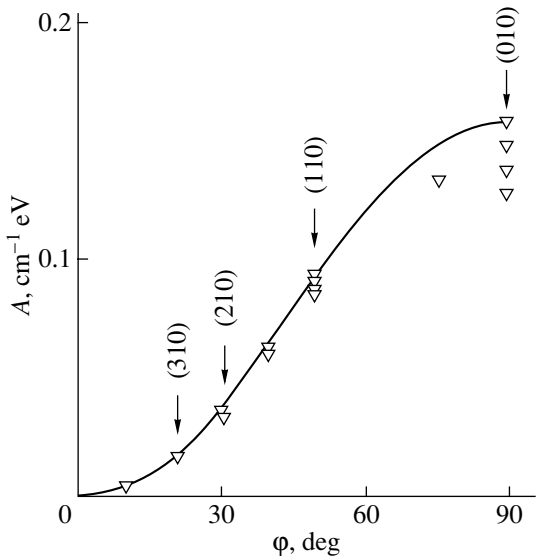

Fig. 4. Angular dependence of the integrated absorption coefficient for the $A_{n=2}$ line upon normal incidence of radiation on the sample plane. Points are the experimental data. The solid line represents the theoretical dependence $A(\varphi) = A_{n=1}^{\langle 010\rangle} \sin^2\varphi$. The scatter of experimental points is caused by the samples used in the measurements being different. Arrows indicate the angles φ for different crystallographic planes.

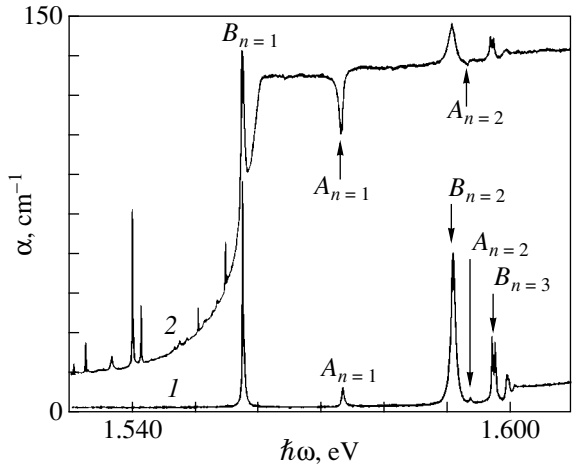

Fig. 5. Absorption spectra of the β-ZnP_2 crystal at **s** ⊥ (102) for polarizations (*1*) **E** ∥ **b** and (*2*) **E** ⊥ **b**. T = 1.7 K, d = 0.482 mm. Arrows indicates the Fano antiresonances for an orthoexciton in the $A_{n=1}$ and $A_{n=2}$ states.

a fast conversion of a higher lying *A* orthoexciton to the ground state of the singlet exciton due to the spin–lattice relaxation or the polariton–polariton scattering. The ratio of the integrated absorption coefficients for the first two lines of the *A* series at **s** ⊥ (010) and **E** ∥ *X*, which is decreased at a low temperature, increases to $A_{n=1}/A_{n=2}$ = 8.05 at T_c = 55 K. This ratio corresponds to the theoretically predicted ratio for *S*-type excitons. At the critical temperature T_c (above which the polariton effects and the spatial dispersion can be ignored), we determined the oscillator strengths for the A_n-exciton transitions according to the procedure described in [21]. The oscillator strengths per molecule (the unit cell involves eight formula units) for the transitions in the *A* series at **s** ∥ ⟨010⟩ ∥ **b** and the polarization **E** ∥ *X* are as follows: $F_{n=1}^{\langle 010\rangle} = (2.02 \pm 0.03) \times 10^{-6}$, $F_{n=2}^{\langle 010\rangle} = 2.52 \times 10^{-7}$, and $F_{n=3}^{\langle 010\rangle} = 8.1 \times 10^{-8}$. In the calculations of the oscillator strength, the refractive index, which is determined as $\sqrt{\varepsilon_{xx}}$ for the direction **s** ∥ ⟨010⟩ and the polarization **E** ∥ *X*, was taken to be ε_a = 9.1 [22]. For the forbidden direction **s** ∥ ⟨100⟩ ∥ *X* and **E** ∥ **b**, the $A_{n=1}^{\langle 100\rangle}$ transition is characterized by the oscillator strength $F_{n=1}^{\langle 100\rangle} = (6.5 \pm 1.2) \times 10^{-10}$. The superscript indicates the crystallographic direction of the unit wave vector **s** of incident radiation or the vector **k** of the exciton. The obtained oscillator strength of transitions to the state with n = 1 for the *A* series turns out to be more than three orders of magnitude larger than that of transitions to the state with n = 1 for the electric-dipole singlet *C* exciton ($F_{n=1}^{\langle 100\rangle} = 6.0 \times 10^{-3}$) [5, 6]. We experimentally measured the dependence of the integrated absorption coefficient on the angle φ upon changing the direction of radiation propagation in the *XY* plane at **E** ⊥ **c** for the line of the *A* series in the exciton state with n = 2, for which the resonance is weakly affected by the polariton effects (Fig. 3b). It was found that this dependence for the $A_{n=2}$ line is similar to that described by the relationship $A_{n=2}(\varphi) = A_{n=1}^{\langle 010\rangle} \sin^2\varphi$ (Fig. 4). It should be emphasized that, in the present work, we apparently for the first time revealed experimentally an enhancement of the polariton effect with an increase in the oscillator strength of the exciton transition.

Figure 5 shows the absorption spectra of the β-ZnP_2 crystal in the geometry **s** ⊥ (102) at the polarizations **E** ∥ **b** and **E** ⊥ **b**, which correspond to the *s* and *p* polarizations of the vector **E** in the spherical coordinates (see inset in Fig. 1). This geometry is characterized by the meridional angle φ = 0° and the azimuthal angle θ = 33.2°. At the polarization **E** ∥ **b**, the weak *A* series is clearly observed in addition to the *B* series. The *A* series is shifted by 0.0015 eV toward the low-energy range with respect to the very weak $A_{n=1}$ line observed in the forbidden geometry **s** ⊥ (100) at **E** ∥ **b** (φ = 0° and θ = 90°). The oscillator strength $F_{n=1}^{\langle 102\rangle} = (7.7 \pm 0.1) \times 10^{-9}$ for the $A_{n=1}^{\langle 102\rangle}$ transition in this geometry is one order of magnitude larger than that for the $A_{n=1}^{\langle 100\rangle}$ transition.

It can be seen from Fig. 5 that, at the polarization **E** ⊥ **b** (*p* polarization), the pronounced Fano antiresonance [23] occurs in place of the $A_{n=1}$ line. Note that

the configurational interaction of discrete *A*-exciton states should be characterized by a wider continuum of the same nature and in the same energy range. As was noted above, the $A_{n=1}^{\langle 100\rangle}$ line is always observed at a small step with the edge at 1.5728 eV against the background of continuous absorption. By assuming that this step is associated with the indirect transitions to the 1*S* band of the dipole-forbidden orthoexciton with phonon emission, the above phenomenon appears to be similar to that observed for cubic CuO_2 [24, 25]. In this situation, the energy separation between the edge of the step and the $B_{n=1}$ line of the orthoexciton (1.55775 eV) is equal to the energy of a phonon involved in the indirect exciton transition: $\hbar\Omega$ = 15.05 meV. This energy is in agreement with the phonon energy (14.76 meV) obtained from an analysis of the Raman spectra in [26]. Apparently, the transitions that are forbidden at the polarization **E** || **b** to the 1*S* band of the singlet exciton at **k** = 0 become allowed with the participation of phonons with a nonzero wave vector. However, the corresponding absorption should be small because of the weak exciton–phonon interaction. At the polarization **E** || **c**, the transitions to the 1*S* exciton band of the singlet exciton is likely also attended by indirect transitions with phonon emission, but these transitions are difficult to observe experimentally due to a large oscillator strength of the direct exciton transition and a weak exciton–phonon coupling. Consequently, it can be assumed that the interference interaction of exciton polaritons at discrete *nS* resonances of the *A* series occurs with the continuum of the exciton–phonon spectrum of the $C_{n=1}$-exciton band, because these antiresonances are observed at such a polarization at which the vector **E** (or the induction vector **D**) has a component along the **c** axis. The antiresonances of the *A* series are also observed at **s** ⊥ (010) and **E** || **c**, but they are hard to record against the background of strong absorption of the *C* series. The shape of the absorption curve in the case of the configurational interaction of a discrete state with a continuum depends on the asymmetry parameter *q* [23]. This parameter is determined as the ratio between the matrix element of the transition to the discrete state that has already interacted with the continuum and the matrix element of the transition to the undisturbed continuum with the width of the discrete level. The absorption coefficients are additive at $q \gg 1$. At $q = 1$, the absorption line modified by the interaction has a symmetric dispersion contour. The antiresonance is observed at $q \longrightarrow 0$. The oscillator strength for the transitions to the $A_{n=1}$-exciton state modified by the interaction with the continuum was estimated at $F_{n=1}^{\langle 102\rangle} = 3.7 \times 10^{-8}$. The oscillator strength for the indirect exciton–phonon transitions is approximately four orders of magnitude less than that for the direct transitions. Consequently, the approximate estimate of the asymmetry parameter gives $q \approx 0.29$. Analysis of the antiresonance shape according to the technique proposed in [27] offers the asymmetry parameter $q = 0.18$, which agrees with the above estimate. It should be noted that the interference interaction substantially depends on the sample thickness and the phase of the dispersion antiresonance contour can change by π.

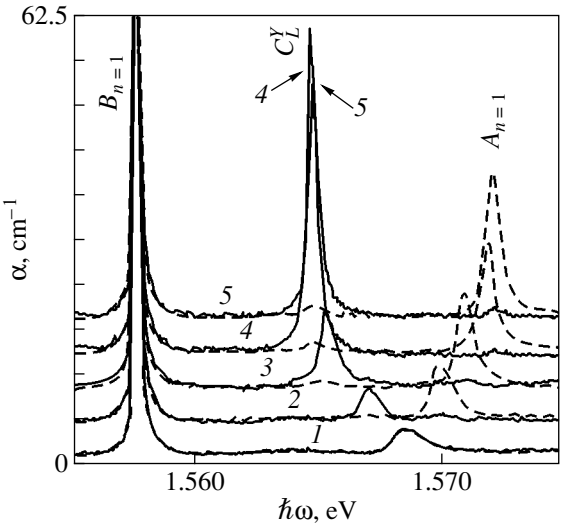

Fig. 6. Evolution of the $B_{n=1}$ and $A_{n=1}$ absorption lines upon incidence of radiation with polarization **E** || **b** at different angles *i* on the (001) plane. *i* = (*1*) 0° [**s** ⊥ (001)], (*2*) 10°, (*3*) 20°, (*4*) 32°, and (*5*) 36°. Dashed curves correspond to the absorption lines measured at the angles of incidence –*i*. *T* = 1.7 K, *d* = 0.386 mm.

A fragment of the absorption spectrum of the β-ZnP_2 crystal at **s** ⊥ (001) and **E** || **b** is displayed in Fig. 6 (curve *1*). This geometry corresponds to the meridional angle φ = 0 and the azimuthal angle θ = 12.3°, which is less than that in the case of the geometry **s** ⊥ (102) and **E** || **b**. In our earlier work [6], we demonstrated that the absorption spectrum of β-ZnP_2 crystals in the geometry **s** || (001) and **E** || **b** contains two series of lines. The first series is the well-known *B* series in which the intensities of lines at $n \geq 2$ are approximately identical to those observed in the geometry **s** ⊥ (100) and **E** || **b**. In the second series, the line intensities are substantially lower and the leading line with $n' = 1$ is located at 1.5690 eV. The line with $n' = 1$ is noticeably shifted toward the low-energy range as compared to the $A_{n=1}$ lines observed at **s** ⊥ (100) and **E** || **b** (by ~6.1 meV) and at **s** ⊥ (102) and **E** || **b** (by 4.7 meV). The line with $n' = 1$ has a relatively large half-width ($H \cong 2$ meV) and an asymmetric contour with a high-energy tail. As was noted in [6], an interesting feature of this series is an appreciable nonlinear shift of the lines (especially the leading line with $n' = 1$) upon vertical rotation of the sample with the (001) or **ab** plane around the **b** (C_2) axis through a certain angle *i* with respect to the incident radiation. When the sample is rotated such that the direction of the refracted beam approaches the direction of the **c** axis (i.e., the initial angle $\theta_0 = 12.3°$ between the vectors **s** and **c** decreases), the line with

$n' = 1$ (and the entire series) shifts toward the low-energy range and the intensities of the lines increase. With an increase in the angle of incidence to $i \approx 32°$, the line with $n' = 1$ is shifted to 1.5649 eV, which almost coincides with the energy of the mixed mode C_L^Y = 1.56491 eV at the frequency of the longitudinal exciton in the *Y* direction [6]. Moreover, the half-width of the line with $n' = 1$ decreases to 0.4 meV. Upon opposite rotation of the (001) plane (when the angle between the vector **s** of the refracted beam and the **c** axis increases; i.e., $\theta > \theta_0$), the line with $n' = 1$ (and the entire series) shifts toward the high-energy range to the position of the $A_{n=1}$ line. However, the intensities of the lines in this case increase more slowly. The parameters Ry' = 37.65 meV and E_∞ = 1.60230 eV for this series are close to those determined for the *A* series. This suggests that the high-energy series of the absorption lines observed at $\mathbf{s} \perp 001$ and $\mathbf{E} \parallel \mathbf{b}$ is also the *A* series. The specific feature of the absorption spectra with the line at $n' = 1$ shifting toward either the low- or high-energy range is that this line increases in intensity and is superimposed on the weak residual line observed upon opposite rotation of the crystal, i.e., when the angle of incidence changes from *i* to *–i*. It should be noted that the intensity and location of the lines of the *B* series upon rotation of the sample remain almost unchanged.

4. DISCUSSION

As follows from the group-theoretic analysis [6], the quadruply degenerate *nS* states of an exciton in a low-symmetry crystal with simple electron energy bands (for example, β-ZnP_2) consist of four simple odd-parity terms: $D_{ex} \rightleftharpoons 2\Gamma_1^- + 2\Gamma_2^-$. The degeneracy of the exciton state is partially removed by the exchange electron–hole interaction or, more precisely, by the exchange interaction of conduction band electrons with valence band electrons. The short-range (analytical) part of the exchange interaction leads to the formation of singlet and triplet exciton states or paraexcitons and orthoexcitons with different energies. In [6], it was experimentally shown that the singlet exciton has $\Gamma_2^-(z)$ symmetry with wave functions transformed along the *Z* coordinate. The other three states with symmetry $2\Gamma_1^- + \Gamma_2^-$ belong to the orthoexciton and should remain randomly degenerate in the absence of an external magnetic field. In the electric-dipole approximation, the optical transitions to the triplet exciton states are forbidden, because they require the flip of the spin of the bound electron, whereas the electric-dipole transition operator does not act on the spin operator. However, these transitions can be observed owing to the mixing of triplet and singlet exciton states with the same symmetry by the spin–orbit interaction or the mixing of upper valence bands [28]. One of the aforementioned states of the triplet exciton with $m_s = 0$, $\Gamma_2^-(x)$ symmetry, and wave functions likely transformed along the *X* coordinate, to a first approximation, is mixed with the $\Gamma_2^-(z)$ singlet exciton through the spin–orbit interaction. Moreover, owing to the mixing with the singlet exciton by the spin–orbit interaction, the $\Gamma_2^-(x)$ orthostate in an anisotropic crystal can be split off by the long-range (nonanalytical) part of the exchange interaction and behave like a longitudinal orthoexciton [21, 29]. In turn, this longitudinal orthoexciton can be mixed with the longitudinal paraexciton of the same symmetry $\Gamma_2^-(z)$ in a particular direction [6]. It is known that the energy of the exciton state determined by the long-range exchange interaction depends on the direction of the wave vector [29]. This agrees well with the observed dependence $E(\mathbf{k})$ for the *A* series, especially in the geometry $\mathbf{s} \perp (001)$ (when the vector **s** lies in the **ac** plane) and $\mathbf{E} \parallel \mathbf{b}$ upon rotation of the crystal around the axis $\mathbf{b} \parallel Y \parallel \langle 010 \rangle$ and also in the geometry $\mathbf{s} \parallel \mathbf{c}$ and $\mathbf{E} \parallel \mathbf{b}$ upon rotation of the *XY* plane of the sample around the direction $[\mathbf{b} \times \mathbf{c}]$ or *X* (see the evolution of the C_L^Y absorption line at an energy of 1.56491 eV in Fig. 5 in [6]). In this case, the other two states of the orthoexciton are unmixed, degenerate due to the time inversion, and split off by the short-range exchange interaction; have $2\Gamma_1^-(y)$ symmetry and $m_s = \pm 1$; and remain purely triplet states. These states are responsible for the *B* series, and their energy should not depend on the direction of the wave vector [29], which is actually observed for the *B* series [6]. An external transverse magnetic field removes the degeneracy, and the lines of the *B* series are split into two components [13, 30].

In order to confirm the validity of the proposed hypothesis, we measured the exciton absorption in the β-ZnP_2 crystals at $\mathbf{s} \perp (010)$ or $\mathbf{s} \parallel \mathbf{b} \parallel C_2$ and the polarization $\mathbf{E} \parallel X$ in magnetic fields with an induction up to 5 T in two geometries: at the transverse field $\mathbf{s} \perp \mathbf{B} \parallel X$ (the Voigt configuration) and the longitudinal field $\mathbf{s} \parallel \mathbf{B} \parallel \mathbf{b}$ (the Faraday configuration) (Fig. 7). As could be expected, the lines of the *A* series are not split either in the transverse magnetic field or in the longitudinal magnetic field and exhibit a diamagnetic shift at $n \geq 2$, which is characteristic of the *S* states. No diamagnetic shift in the used magnetic fields is observed for the states with $n = 1$ due to the small Bohr radius. By contrast, the lines of the *B* series are split into two components in the transverse magnetic field and are not split in the longitudinal magnetic field, as was previously observed in longitudinal fields at $\mathbf{s} \perp (100)$ and $\mathbf{E} \parallel \mathbf{b}$ in [13, 30]. It should be noted that an additional mixing of the *nS* orthostates at $m_s = 0$ with the *nS* states of the paraexciton by the magnetic field leads to a considerable increase in the intensity of the absorption lines of the *A* series with an increase in the field induction.

The probability of transitions to mixed triplet states depends on the degree of overlap of the corresponding wave functions. However, since the spin–orbit interac-

tion in β-ZnP_2 is hypothetically weak [6], the mixing of these states should also be insignificant. The degree of admixture of the wave functions of the orthoexciton (with $m_s = 0$) split off by the long-range interaction to the wave functions of the longitudinal exciton (or, more exactly, the mixed mode along the **c** direction [6]) is estimated at $\approx 3.8 \times 10^{-3}$ from the experimental ratio between the integrated absorption coefficients for the $A_{n=1}$ line and the line of the C_L^Y mixed mode at the polarization **E** ∥ **b** and **s** ∥ **c** (Fig. 6). At **s** ⊥ **c** and **E** ∥ *X*, the degree of admixture of the wave functions of the singlet exciton to the wave functions of the orthoexciton with $m_s = 0$ is estimated as $f^A_{n=1}/f^C_{n=1} \cong 3.33 \times 10^{-4}$.

An attempt to assign the *A* series to the *nS* states of the electric-dipole singlet exciton, which is excited with a small oscillator strength from the lower valence band and whose dipole moment $\mathbf{P}_m(\mathbf{s})$ of the exciton polarization is aligned along the *X* (or **a**) direction, involves considerable problems. First, the absorption intensity for the studied series upon radiation propagation in the geometry **s** ∥ **c** ∥ *Z* at the polarization **E** ∥ *X* is lower than that in the geometry **s** ∥ **b** ∥ *Y* at the same polarization **E** ∥ *X* [6]. Second, the absorption intensity for the *A* series is characterized by a strong anisotropy, especially when the vector *s* remains perpendicular to the **c** axis. On the other hand, the assumption that the *A* series is associated with the lower valence band possibly split off by the crystal field (by $\Delta_{cf} \approx 15$ meV) could be supported by the very small increase in the integrated absorption coefficient of the $A_{n=1}$ line with an increase in the temperature and also the Fano effect observed for this series. However, we did not reveal noticeable differences in the shift of the lines in the *A* and *B* series under the temperature deformation of the lattice in the range from 1.7 to 170 K nor in the *A*, *B*, and *C* series under uniaxial compressive deformation of the crystal along the **b** or **c** crystallographic axis up to 360 MPa [5, 31]. The data on the uniaxial deformation of crystals and the convergence of all three exciton series virtually to the same limit $E_\infty = 1.6026 \pm 0.0002$ eV with an increase in the principal quantum number *n* indicate that the same pair of electron energy bands is responsible for the formation of the *A*, *B*, and *C* series in the absorption spectra of the β-ZnP_2 crystals. This is in agreement with the inferences made in [6, 30] that, in β-ZnP_2, the splitting of the *p* valence band by the anisotropic crystal field substantially exceeds the spin–orbit splitting and the lower valence subbands are located deeply.

The concept proposed above is confirmed by the results of investigations into the exciton spectra of β-ZnP_2 crystals with a high concentration of intrinsic defects (most probably, ~10^{19} cm^{-3}) at which the disturbance of the long-range order becomes pronounced. For these crystals, the *A* spectrum appears to be strongly suppressed and its lines are distorted, whereas

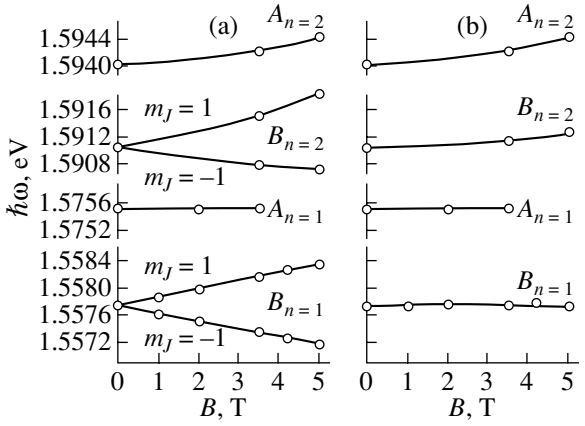

Fig. 7. Field dependences of the Zeeman effect for the $A_{n=1}$, $A_{n=2}$, $B_{n=1}$, and $B_{n=2}$ absorption lines of β-ZnP_2 crystals at **s** ⊥ (010) and **E** ∥ *X* in (a) the Voigt (**B** ⊥ **s**) and (b) Faraday (**B** ∥ **s**) geometries. *T* = 1.7 K.

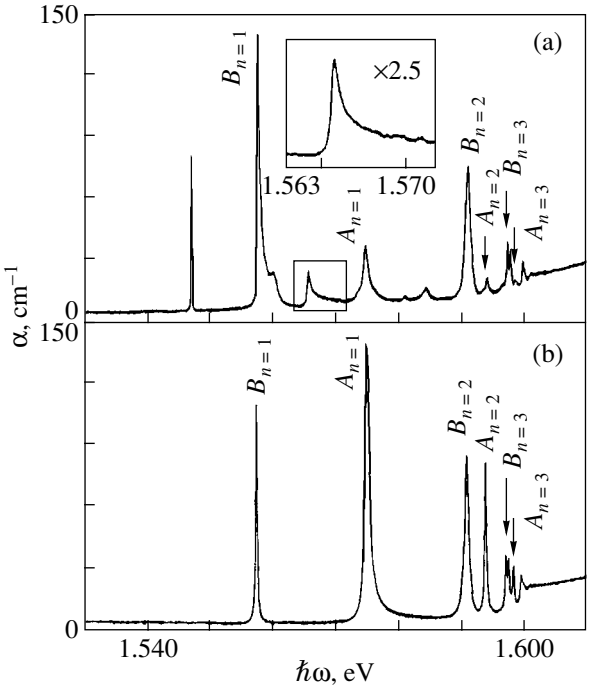

Fig. 8. Absorption spectra of β-ZnP_2 crystals at **s** ⊥ (210) and **E** ⊥ **c**: (a) impurity sample (*d* = 0.351 mm) and (b) high-quality sample (*d* = 0.416 mm). *T* = 1.7 K.

the *B* spectrum (except for the $B_{n=1}$ line [5, 6]) remains almost unchanged (Fig. 8a).[1]

For comparison, the spectrum of a high-quality sample with a thickness comparable to that of the impurity sample in the same geometry **s** ⊥ (210) and **E** ⊥ **c** is

[1] It seems likely that the presence of lattice defects also leads to a decrease in the integrated absorption coefficient for the lines in the *A* spectrum shown in Fig. 4.

shown in Fig. 8b. The specific feature of the spectra of impurity crystals is the weak absorption line at 1.56026(4) eV, which is frequently observed as a shoulder in the high-energy wing of the *B* line at $\mathbf{s} \perp \mathbf{c}$ and $\mathbf{E} \perp \mathbf{c}$. We can assume that the breaking of the translational symmetry of the lattice results in a violation of the selection rules at $\mathbf{k} = 0$; consequently, a weak line of the *C* series at $n = 1$ appears at the forbidden polarization ($\mathbf{E} \perp \mathbf{c}$) for the electric-dipole singlet exciton. Hence, the energy of this line at the maximum [1.56026(4) eV] is equal to the energy E_T of the transverse exciton, because the spatial dispersion effects in this case are of no significance [32]. This energy coincides with the energy E_T estimated in the hydrogen-like approximation from the analysis of the mixed mode made in our earlier work [6] and from the examination of the dispersion contour of the exciton reflection spectrum performed in [2]. The coincidence of the energy E_T obtained in the hydrogen-like approximation [6] with the energy $E_{n=1}$ of the *C*-exciton series suggests that, for the singlet exciton in the β-ZnP_2 crystal, the energy corrections for a central unit cell compensate for the energy associated with the anisotropic part of the Hamiltonian. It is worth noting that, in the spectra of defect crystals, the weak line of the transverse *C* exciton with $n = 1$ always manifests itself at $\mathbf{s} \perp \mathbf{c}$ and the polarization $\mathbf{E} \perp \mathbf{c}$ (i.e., when the *A* series is observed) and is not observed in the geometry $\mathbf{s} \perp (100)$ at $\mathbf{E} \parallel \mathbf{b}$, when the *A* series is forbidden. Note that, at the polarization $\mathbf{E} \perp \mathbf{c}$ (forbidden for the singlet exciton), the $C_{n=1}$ line is more pronounced in the absorption spectra of more imperfect crystals. This conclusively indicates that the admixture of the split-off state with $m_s = 0$ to the states of the transverse singlet exciton increases most probably due to strong local fields.

The presence of a large number of lattice defects in the studied samples is confirmed by the intense line attributed to the exciton-impurity complex in the absorption spectra (Fig. 8a) at an energy of 1.54732 eV ($\alpha \approx 83$ cm^{-1}). This line nearly coincides with the most intense line in the narrow-line spectrum [6] but exhibits a different nature, because it is not accompanied by a narrow-line spectrum. In addition to this line of the exciton-impurity complex, the spectrum contains a narrow asymmetric band at 1.56583 eV with a short-wavelength tail (hereafter, this band will be referred to as the α band) and also two high-energy lines, which are most probably associated with the excited states of the exciton-impurity complex. The α band can be attributed to photoneutralization of small-sized ionized centers, because this band, first, is located in the range of the intrinsic exciton spectrum and, second, has a characteristic shape with a sharp long-wavelength edge and an extended short-wavelength wing (see inset to Fig. 8a). It seems likely that the ionized centers have an acceptor nature (according to rough estimates, $E_A \approx 0.037$ eV). This can be judged from the fact that the β-ZnP_2 samples without special doping possess *p*-type conductivity [6].

5. CONCLUSION

Thus, the experimental results obtained in this work demonstrated that the *A* series observed in the absorption spectra of β-ZnP_2 crystals is associated with the partially allowed dipole transitions to *nS* states of the $\Gamma_2^-(x)$ orthoexciton with $m_s = 0$. These states are most likely split off by the long-range (nonanalytical) part of the exchange interaction due to their mixing, to a first approximation, with *nS* states of the $\Gamma_2^-(z)$ singlet exciton through the spin–orbit interaction.

ACKNOWLEDGMENTS

We would like to thank V.D. Kulakovskiĭ for the opportunity to perform magneto-optical measurements of the exciton absorption spectra.

REFERENCES

1. A. B. Pevtsov, S. A. Permogorov, A. V. Sel'kin, and N. N. Syrbu, Fiz. Tekh. Poluprovodn. (Leningrad) **16** (8), 1399 (1982) [Sov. Phys. Semicond. **16**, 897 (1982)].
2. R. S. Berg, P. Y. Yu, and Th. Mowles, Solid State Commun. **46** (2), 2101 (1983).
3. I. S. Gorban', N. M. Belyĭ, V. A. Borbat, *et al.*, Dokl. Akad. Nauk Ukr. SSR, Ser. A, No. 4, 48 (1988).
4. O. Arimoto, M. Tachiki, and K. Nakamura, J. Phys. Soc. Jpn. **60** (12), 4351 (1991).
5. I. S. Gorban', A. P. Krokhmal', and Z. Z. Yanchuk, Fiz. Tverd. Tela (St. Petersburg) **42** (9), 1582 (2000) [Phys. Solid State **42**, 1625 (2000)].
6. I. S. Gorban', A. P. Krokhmal', and Z. Z. Yanchuk, Fiz. Tverd. Tela (St. Petersburg) **41** (2), 193 (1999) [Phys. Solid State **41**, 170 (1999)].
7. N. N. Syrbu and V. M. Mamaev, Fiz. Tekh. Poluprovodn. (Leningrad) **17** (4), 694 (1983) [Sov. Phys. Semicond. **17**, 433 (1983)].
8. I. S. Gorban, M. M. Bilyi, I. M. Dmitruk, and O. A. Yeshchenko, Phys. Status Solidi B **207**, 171 (1998).
9. N. M. Belyĭ, I. S. Gorban', V. A. Gubanov, and I. N. Dmitruk, Pis'ma Zh. Éksp. Teor. Fiz. **50** (2), 75 (1989) [JETP Lett. **50**, 85 (1989)].
10. I. S. Gorban, O. A. Yeshchenko, I. M. Dmitruk, and M. M. Bilyi, Low Temp. Phys. **27** (6), 498 (2001).
11. S. I. Boĭko, I. S. Gorban', A. P. Krokhmal', *et al.*, Fiz. Tekh. Poluprovodn. (St. Petersburg) **27** (5), 822 (1993) [Semiconductors **27**, 447 (1993)].
12. Y. Toyozava, J. Phys. Chem. Solids **25** (1), 59 (1964).
13. S. Taguchi, T. Goto, H. Takeda, and G. Kido, J. Phys. Soc. Jpn. **57** (9), 3256 (1988).
14. D. Fröhlich, M. Schlierkamp, J. Schubert, *et al.*, Phys. Rev. B **49** (15), 10337 (1994).
15. J. Hermanson and J. C. Phillips, Phys. Rev. **150** (2), 652 (1966).
16. R. J. Elliott, Phys. Rev. **108** (6), 1384 (1957).
17. F. I. Kreĭngol'd and V. L. Makarov, Pis'ma Zh. Éksp. Teor. Fiz. **20** (7), 441 (1974) [JETP Lett. **20**, 201 (1974)].

18. J. Voigt, Phys. Status Solidi B **64** (2), 549 (1974).
19. N. I. Akhmadiev, G. P. Golubev, V. S. Dneprovskiĭ, and E. A. Zhukov, Fiz. Tverd. Tela (Leningrad) **25** (7), 2225 (1983) [Sov. Phys. Solid State **25**, 1284 (1983)].
20. G. N. Agiev, O. S. Koshchug, and R. P. Seĭsyan, Fiz. Tverd. Tela (St. Petersburg) **36** (2), 373 (1994) [Phys. Solid State **36**, 203 (1994)].
21. R. S. Knox, *Theory of Excitons* (Academic, New York, 1963; Mir, Moscow, 1966).
22. J. Engbring, D. Fröhlich, R. Schere, *et al.*, Phys. Status Solidi B **196** (1), 461 (1996).
23. U. Fano, Phys. Rev. **124** (6), 1866 (1961).
24. R. J. Elliott, Phys. Rev. **15** (2), 340 (1961).
25. I. S. Gorban' and V. B. Timofeev, Fiz. Tverd. Tela (Leningrad) **3** (12), 3584 (1961) [Sov. Phys. Solid State **3**, 2606 (1961)].
26. I. M. Dmytruk, M. M. Bilyi, I. S. Gorban, and Z. Z. Yanchuk, in *Proceedings of 15th International Conference on Raman Spectroscopy, Pittsburg, PA, USA* (Wiley, Chichester, 1996), p. 874.
27. Ya. O. Dovgyi and J. V. Kityk, Phys. Status Solidi B **157** (1), 473 (1990).
28. E. Mooser and M. Schlüter, Nuovo Cimento B **18**, 164 (1973).
29. G. L. Bir and G. E. Pikus, *Symmetry and Strain-Induced Effects in Semiconductors* (Nauka, Moscow, 1972; Wiley, New York, 1975).
30. T. Goto, S. Taguchi, K. Cho, *et al.*, J. Phys. Soc. Jpn. **59** (2), 773 (1990).
31. I. S. Gorban', A. P. Krokhmal', and Z. Z. Yanchuk, Funct. Mater. **7** (3), 464 (2000).
32. J. Voigt, M. Senoner, and I. Rückmann, Phys. Status Solidi B **75** (1), 213 (1976).

Translated by O. Borovik-Romanova

Physics of the Solid State, Vol. 45, No. 7, 2003, pp. 1242–1250. Translated from Fizika Tverdogo Tela, Vol. 45, No. 7, 2003, pp. 1185–1192.

SEMICONDUCTORS AND DIELECTRICS

The Influence of Imperfection of the Crystal Lattice on the Electrokinetic and Magnetic Properties of Disordered Titanium Monoxide

A. I. Gusev and A. A. Valeeva

Institute of Solid-State Chemistry, Ural Division, Russian Academy of Sciences, ul. Pervomaĭskaya 91, Yekaterinburg, 620219 Russia

e-mail: gusev@ihim.uran.ru

Received November 5, 2002

Abstract—The conductivity and magnetic susceptibility of disordered titanium monoxide TiO_y ($0.920 \le y \le 1.262$) containing vacancies in titanium and oxygen sublattices are investigated. For TiO_y monoxides with an oxygen content $y \le 1.069$, the temperature dependences of the conductivity are described by the Bloch–Grüneisen function at a Debye temperature ranging from 400 to 480 K and the temperature dependences of the magnetic susceptibility are characterized by the contribution from the Pauli paramagnetism due to conduction electrons. The behavior of the conductivity and magnetic susceptibility of TiO_y monoxides with an oxygen content $y \ge 1.087$ is characteristic of narrow-gap semiconductors with nondegenerate charge carriers governed by the Boltzmann statistics. The band gap ΔE between the valence and conduction bands of TiO_y monoxides with $y \ge 1.087$ falls in the range 0.06–0.17 eV. © *2003 MAIK "Nauka/Interperiodica".*

1. INTRODUCTION

Disordered nonstoichiometric titanium monoxide TiO_y has a *B*1-type cubic crystal structure, is homogeneous over a wide range from $TiO_{0.70}$ to $TiO_{1.25}$, and contains 10–15 at. % structural vacancies simultaneously in each of the titanium and oxygen sublattices [1]. Since the formulation of the composition of titanium monoxide as TiO_y does not carry information on the concentration of structural vacancies in the metallic and nonmetallic sublattices, it is more correct to represent the titanium monoxide composition taking into account the content of structural vacancies in each of the sublattices, i.e., as $Ti_xO_z \equiv Ti_x\blacksquare_{1-x}O_z\square_{1-z} \equiv TiO_y$ (where $y = z/x$ and ■ and □ stand for the structural vacancies in the titanium and oxygen sublattices, respectively). This formula accounts for both the real composition and the structure of the titanium monoxide. For example, titanium monoxide of formal stoichiometry $TiO_{1.00}$ contains 16.7 at. % vacancies in both titanium and oxygen sublattices and, hence, its real composition is $\sim Ti_{0.833}O_{0.833}$.

At present, the properties of TiO_y have not been adequately investigated. This can be explained as follows. Titanium monoxide TiO_y is difficult to synthesize, because its composition is unstable at temperatures in the range 700–800 K and, even at a controlled partial pressure of oxygen, this compound itself can undergo disproportionation to form Ti_2O ($TiO_{0.50}$) or Ti_3O_2 ($TiO_{0.67}$) and cubic oxide or cubic oxide and Ti_2O_3 ($TiO_{1.50}$) and other phases of the homologous series Ti_nO_{2n-1}, where n is an integer (n = 2–10). The disordered state of titanium monoxide is thermodynamically stable at temperatures $T > 1500$ K. At temperatures below 1500 K, a few ordered phases of different types and symmetries form in several concentration and temperature ranges. However, the disordered state of titanium monoxide TiO_y can easily be stabilized by quenching from $T > 1500$ K, whereupon it can exist as a metastable state at room temperature for any length of time. At temperatures of ~700, ~1000, and ~1100 K, TiO_y undergoes phase transformations associated with the formation of superstructures. The type and symmetry of the superstructures depend on the real initial composition of titanium monoxide TiO_y. The monoclinic [space group $C2/m$ ($A12m/1$)] superstructure $Ti_5\blacksquare O_5\square$ [2–6] has been firmly established and repeatedly confirmed experimentally. The structure of the ordered tetragonal phase $Ti_4\blacksquare O_5$ that corresponds to titanium monoxide of nominal composition $TiO_{1.25}$ is also satisfactorily described in [2, 4]. As regards the other ordered phases [orthorhombic $TiO_{0.7–0.9}$, $TiO_{1.19}$, and $Ti_{2.5}O_3$ ($Ti_5\blacksquare O_6$) and cubic $Ti_{22.5}O_{22.5}$ ($Ti_5\blacksquare O_5\square$)], the available information amounts to determining their symmetry from electron microscopy and diffraction data and to speculating about their possible belonging to one of three or four space groups [4, 7]. Watanabe *et al.* [4] and Hilti [7] considered these phases transient from the disordered cubic phase TiO_y to the ordered monoclinic phase Ti_5O_5. The possible existence of the ordered orthorhombic (space group *Immm*) phases $Ti_3O_2\square$ and $Ti_2\blacksquare O_3$ was predicted theoretically in [8]. It was shown that oxygen atoms and nonmetallic struc-

tural vacancies are ordered in the $Ti_3O_2\square$ phase, whereas the ordering of titanium atoms and metallic structural vacancies in the $Ti_2\blacksquare O_3$ phase occurs in the titanium sublattice with a random distribution of nonmetallic vacancies.

Almost without exception, all the titanium monoxide samples synthesized using traditional methods are in a two-phase state and contain both disordered and ordered phases simultaneously. The preparation of single-phase disordered samples of TiO_y requires a special quenching procedure. In the 1960s–1970s, the temperature measurements performed for kinetic and magnetic properties of TiO_y titanium monoxides revealed that the same samples prior to and after the measurements had different chemical and phase compositions. This circumstance inevitably led to contradictory results. For example, the temperature coefficient $d\rho/dT$ of the resistivity ρ measured for disordered monoxides TiO_y at $y \sim 1$ had positive sign in [9–11] and negative sign in [12]. At the same time, all the authors of experimental investigations drew the same conclusion that the thermopower and the Hall coefficient of TiO_y monoxides at $y > 0.85$ are negative in sign [9–12].

The unreliability and discrepancy in the available experimental data gave impetus to a large number of theoretical investigations into the electronic structure of TiO_y monoxides. However, the results of calculations, including *ab initio* calculations, also proved to be contradictory. In particular, it was shown in [13–17] that, in the energy spectrum of cubic titanium monoxide, the O 2*p* and Ti 3*d* electron energy bands are separated by a wide gap of several electron-volts. Huisman *et al.* [17] believed that structural vacancies are responsible for the appearance of local peaks in the electron density (vacancy peaks) in the *p–d* gap. This is in agreement with the results of theoretical calculations carried out by Gubanov *et al.* [18] and Ivanovsky *et al.* [19], according to which the energy spectrum of TiO_y is characterized by vacancy states in unoccupied regions below the Fermi level. The calculations performed by Barman and Sarma [20] also demonstrated that the band gap in the energy spectrum for a hypothetical defect-free titanium monoxide $TiO_{1.0}$ is approximately equal to 2.0 eV; however, in this case, the formation of vacancies is attended by the appearance of vacancy states only in the vicinity of the conduction band bottom and does not lead to the disappearance of the *p–d* gap. According to the calculations carried out by Leung *et al.* [21], the energy gap between the O 2*p* and Ti 3*d* electron energy bands is approximately equal to 1.8 eV for a defect-free titanium monoxide TiO and 1.2 eV for an ordered monoclinic titanium monoxide Ti_5O_5. The existence of the band gap in disordered titanium monoxides TiO_y has been confirmed by experimental investigations of x-ray photoemission spectra [20, 22], UV photoemission and bremsstrahlung spectra [20], and optical conductivity [23].

As follows from the results of another series of theoretical works [24–26], the electron energy spectrum of TiO_y does not contain the *p–d* gap. The theoretical inferences regarding the absence of the *p–d* gap in the energy spectrum of titanium monoxide has been supported by experimental investigations of the x-ray emission spectra of TiO_y monoxides with different oxygen contents [27] and also the x-ray photoelectron and x-ray emission spectra of the monoclinic ordered titanium monoxide Ti_5O_5 and defect-free cubic titanium monoxide $TiO_{1.0}$ prepared under high pressure [28].

Thus, the available experimental and theoretical data are rather contradictory. It remains unclear whether titanium monoxide is a metal or a semiconductor.

In this work, we experimentally investigated the electrical conductivity (resistivity) and the magnetic susceptibility of titanium monoxide TiO_y over the entire homogeneity region of the cubic phase.

2. SAMPLE PREPARATION AND EXPERIMENTAL TECHNIQUE

Samples of nonstoichiometric cubic titanium monoxide TiO_y with different oxygen contents ($0.920 \le y \le 1.262$) were synthesized through solid-phase sintering from powder mixtures of metallic titanium and titanium dioxide TiO_2 at a temperature of 1770 K for 70 h under vacuum at a residual pressure of 0.001 Pa. In the course of the synthesis, the sintering products were ground at 20-h intervals. All the diffraction experiments were performed on Siemens D-500 and STADI-P (STOE) automated diffractometers ($Cu K_{\alpha_{1,2}}$ radiation). In order to prepare titanium monoxide in a disordered state, the synthesized samples were placed in quartz ampules evacuated to a residual pressure of 0.0001 Pa and were then annealed at a temperature of 1330 K for 3 h. After annealing, the samples in the ampules were quenched in water. The quenching rate was approximately equal to 200 K s^{-1}. The x-ray diffraction patterns of the quenched samples contain either reflections of the disordered phase TiO_y with a *B*1-type structure (samples with an oxygen content $y \ge 1.112$) or reflections of the disordered TiO_y and monoclinic ordered Ti_5O_5 [5] phases (samples with an oxygen content $y \le 1.087$). The oxygen content in the TiO_y quenched samples proved to be higher than the oxygen content predicted from the starting mixture. This means that, during the synthesis and annealing, the samples were partially depleted in titanium and enriched in oxygen.

The resistivities ρ of the samples prepared were measured by the four-point probe method in the temperature range 77–300 K. The resistivities of $TiO_{1.262}$, $TiO_{1.087}$, and $TiO_{0.920}$ monoxides were also measured at 4.2 K. In order to ensure electric contact, the contact surfaces of the samples were coated with an In–Ga paste.

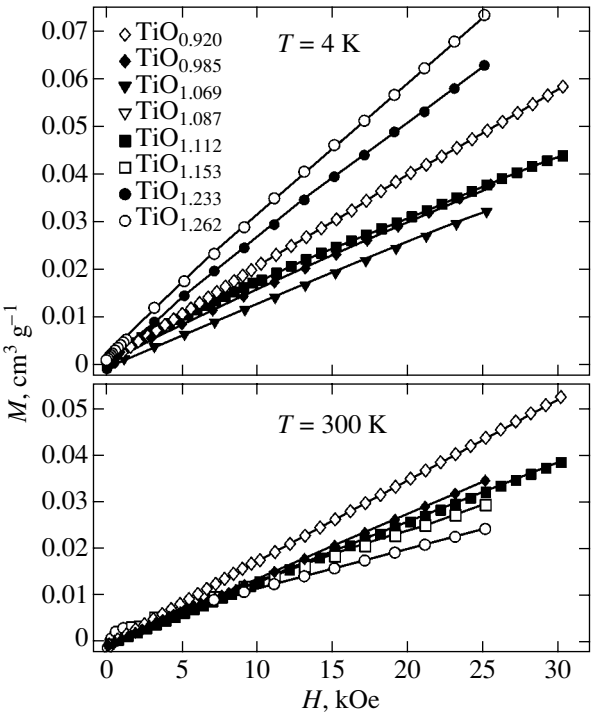

Fig. 1. Dependences of the magnetization M on the magnetic field strength H for titanium monoxides TiO_y with different oxygen contents at $T = 4$ and 300 K. The absence of remanent magnetization implies that the TiO_y samples contain no ferromagnetic impurities.

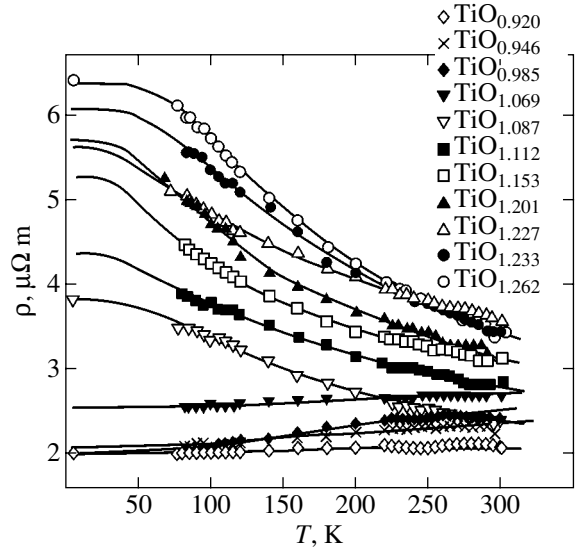

Fig. 2. Temperature dependences of the electrical resistivity $\rho(T)$ for disordered cubic titanium monoxides TiO_y with different oxygen contents. Solid lines represent the experimental results approximated by function (3) for TiO_y monoxides at $y \le 1.069$ and by function (13) for TiO_y monoxides at $y \ge 1.087$.

The magnetic susceptibility χ of TiO_y monoxides ($0.920 \le y \le 1.262$) was measured on an MPMS-XL-5 Quantum Design vibrating-coil magnetometer at temperatures ranging from 4.0 to 400 K in magnetic fields of 8.8, 25, 30, and 50 kOe. The magnetic susceptibilities of $TiO_{0.946}$, $TiO_{1.069}$, $TiO_{1.087}$, and $TiO_{1.262}$ monoxides were also measured using the Faraday method on a Domenicalli pendulum magnetic balance in the range from 300 K to the temperature of the onset of the disorder $\rightleftharpoons$ order transition (at approximately 1000 K).

The chemical and phase compositions of the samples were checked prior to and after the measurements.

3. RESULTS AND DISCUSSION

The results of measurements of the magnetization M in magnetic fields with a strength H up to 50 kOe and at temperatures of 4, 130, and 300 K demonstrate that the studied samples of TiO_y monoxides do not possess remanent magnetization, because the dependences $M(H)$ measured at different temperatures pass through the origin of the coordinates (Fig. 1). The absence of remanent magnetization implies that the TiO_y samples contain no ferromagnetic impurities.

The temperature dependences of the electrical resistivity $\rho(T)$ for TiO_y titanium monoxides of different compositions are shown in Fig. 2. In the temperature range covered, the electrical resistivity ρ increases when changing over from $TiO_{0.920}$ to $TiO_{1.262}$.

The electrical resistivity of $TiO_{1.069}$, $TiO_{0.985}$, $TiO_{0.946}$, and $TiO_{0.920}$ monoxides increases with an increase in the temperature, even though the temperature coefficient of resistivity remains small. For materials with n-type conductivity, the temperature dependence of the mean free time $\bar{\tau}$ associated with scattering by phonons at $T < 300$ K is adequately described by the Bloch–Grüneisen semiempirical function

$$\frac{1}{\bar{\tau}} = \frac{4\pi\lambda k_B \theta_D}{\hbar}\left(\frac{2T}{\theta_D}\right)^5 \int_0^{\theta_D/2T} \frac{x^5 dx}{\sinh^2 x}, \qquad (1)$$

where λ is the electron–phonon coupling constant and θ_D is the Debye characteristic temperature. In the general case, the integral $\int_0^{\theta_D/2T}(x^5/\sinh^2 x)dx$ can be calculated as follows:

$$\int_0^{\theta_D/2T} \frac{x^5 dx}{\sinh^2 x} = -x^5 \coth x\Big|_0^{\theta_D/2T} + 5\int_0^{\theta_D/2T} x^4 \coth x dx. \qquad (2)$$

Since the resistivity is defined by the formula $\rho = m/ne^2\bar{\tau}$ (where m and n are the mass and the concentration of carriers, respectively), the temperature dependence of the resistivity with allowance made for relationship (2) and the residual resistivity $\rho(0)$ can be written in the form

$$\rho(T) = \rho(0) + \frac{4\pi m\lambda k_B\theta_D}{ne^2\hbar}\left(\frac{2T}{\theta_D}\right)^5\int_0^{\theta_D/2T}\frac{x^5dx}{\sinh^2 x}$$
$$\equiv \rho(0) + \frac{4\pi m\lambda k_B\theta_D}{ne^2\hbar}\left(\frac{2T}{\theta_D}\right)^5 \quad (3)$$
$$\times\left[-\left(\frac{\theta_D}{2T}\right)^5\coth\left(\frac{\theta_D}{2T}\right) + 5\int_0^{\theta_D/2T}x^4\coth x dx\right].$$

In different temperature ranges, the integral $\int_0^{\theta_D/2T}(x^5/\sinh^2 x)dx$ takes different forms. For $T < 80$ K and $\theta_D \sim 400$–500 K, we have the ratio $\theta_D/2T > 3.14$. In this case, the integral $\int_0^{\theta_D/2T}(x^5/\sinh^2 x)dx$ can be represented in the following form:

$$\int_0^{\theta_D/2T}\frac{x^5dx}{\sinh^2 x} = x^5(1-\coth x)\Big|_0^{\theta_D/2T}$$
$$+ 10\int_0^{\theta_D/2T}x^4[\exp(-2x) + \exp(-4x) + \ldots \quad (4)$$
$$+ \exp(-2nx)]dx.$$

After the appropriate transformation with due regard for the limits of integration, expression (4) takes the form

$$\int_0^{\theta_D/2T}\frac{x^5dx}{\sinh^2 x} = x^5(1-\coth x)$$
$$+ 10\left\{\frac{3}{4} + \frac{3}{128} + \frac{1}{324} + \frac{3}{4096} + \ldots + \frac{24}{a^5}\right.$$
$$-\exp(-2x)\left[\frac{x^4}{2} + x^3 + \frac{3x^2}{2} + \frac{3x}{2} + \frac{3}{4}\right]$$
$$-\exp(-4x)\left[\frac{x^4}{4} + \frac{x^3}{4} + \frac{3x^2}{16} + \frac{3x}{32} + \frac{3}{128}\right] \quad (5)$$
$$-\exp(-6x)\left[\frac{x^4}{6} + \frac{x^3}{9} + \frac{x^2}{18} + \frac{x}{54} + \frac{1}{324}\right]$$
$$-\exp(-8x)\left[\frac{x^4}{8} + \frac{x^3}{16} + \frac{3x^2}{128} + \frac{3x}{512} + \frac{3}{4096}\right] - \ldots$$
$$\left.-\exp(-2nx)\left[\frac{x^4}{2n} + \frac{4x^3}{(2n)^2} + \frac{12x^2}{(2n)^3} + \frac{24x}{(2n)^4} + \frac{24}{(2n)^5}\right]\right\}.$$

Here, $x = \theta_D/2T$ (where $\theta_D/2T > 3.14$).

For $T > 80$ K and $\theta_D \sim 400$–500 K, we have the ratio $\theta_D/2T < 3.14$. Hence, the integral $\int_0^{\theta_D/2T}x^4\coth x dx$ can be represented as the series $\int_0^{\theta_D/2T}x^4\coth x dx = \sum_{k=0}^{\infty}2^{2k}B_{2k}x^{4+2k}/[(4+2k)(2k)!]$, where B_{2k} are the Bernoulli numbers. As a result, we obtain

$$\int_0^x x^4\coth x dx = \frac{x^4}{4} + \frac{x^6}{18} - \frac{x^8}{360} + \frac{x^{10}}{4725}$$
$$-\frac{x^{12}}{56\,700} + \frac{x^{14}}{654\,885} - \ldots. \quad (6)$$

Substitution of formula (6) into expression (2) gives

$$\int_0^x\frac{x^5dx}{\sinh^2 x} = -x^5\coth + 5\left(\frac{x^4}{4} + \frac{x^6}{18} - \frac{x^8}{360}\right.$$
$$\left.+\frac{x^{10}}{4725} - \frac{x^{12}}{56\,700} + \frac{x^{14}}{654\,885} - \ldots\right). \quad (7)$$

Here, $x = \theta_D/2T$ (where $\theta_D/2T < 3.14$). After substituting formula (7) into relationship (3) and performing simple manipulations, we obtain the expansion of the Bloch–Grüneisen formula into a series at $\theta_D/2T < 3.14$; that is,

$$\rho(T) = \rho(0)$$
$$+\frac{4\pi m\lambda k_B\theta_D}{ne^2\hbar}\left[-\coth x + 5\left(\frac{1}{4x} + \frac{x}{18} - \frac{x^3}{360}\right.\right. \quad (8)$$
$$\left.\left.+\frac{x^5}{4725} - \frac{x^7}{56\,700} + \frac{x^9}{654\,885} - \ldots\right)\right]_{x=\theta_D/2T}.$$

For $\theta_D/2T > 3.14$, the temperature dependences of the resistivity of $TiO_{1.069}$, $TiO_{0.985}$, $TiO_{0.946}$, and $TiO_{0.920}$ monoxides were approximated by formulas (3) and (5); in this case, series (5) was limited by the term with the exponential factor $\exp(-8x)$. For $\theta_D/2T < 3.14$, the temperature dependences of the resistivity of the same monoxides were approximated by function (8) taking into account only the terms with factors up to x^{13}.

The experimental dependences $\rho(T)$ for $TiO_{1.069}$, $TiO_{0.985}$, $TiO_{0.946}$, and $TiO_{0.920}$ monoxides (Fig. 2) are well approximated by function (3). The calculated parameters $\rho(0)$ and θ_D are presented in Table 1. The Debye characteristic temperature θ_D for TiO_y monoxides ($0.920 \le y \le 1.069$) falls in the range 400–480 K, which is in good agreement with the data available in the literature. According to Denker [10], the characteristic temperature θ_D for an equiatomic monoxide $TiO_{1.00}$ varies from 350 to 410 K and increases with a decrease in the annealing temperature. Leung *et al.* [21] established that the characteristic temperature θ_D for an ordered monoclinic monoxide Ti_5O_5 is equal to 500 K.

Table 1. Parameters of functions (3) and (13) for the electrical conductivity σ (resistivity ρ) of cubic titanium monoxides $TiO_y \equiv Ti_xO_z$ ($y = z/x$) in the temperature range 4.2–300 K

Chemical composition of TiO_y	Composition of Ti_xO_z with due regard for imperfection of the sublattices	Lattice constant a_{B1}, nm	Function	Parameters of the functions			
				ρ(0), μΩm	σ(0), $\mu\Omega^{-1}m^{-1}$	Δ*E*, eV	θ_D, K
$TiO_{0.920}$	$Ti_{0.887}O_{0.816}$	0.41867	3	2.01	0.4969	–	471
$TiO_{0.946}$	$Ti_{0.877}O_{0.829}$	0.41840	3	2.10	0.4773	–	470
$TiO_{0.985}$	$Ti_{0.868}O_{0.855}$	0.41834	3	2.02	0.4952	–	400
$TiO_{1.069}$	$Ti_{0.837}O_{0.895}$	0.41808	3	2.56	0.3911	–	481
$TiO_{1.087}$	$Ti_{0.833}O_{0.906}$	0.41738	13	3.81	0.2626	0.028	–
$TiO_{1.112}$	$Ti_{0.816}O_{0.907}$	0.41711	13	4.17	0.2397	0.025	–
$TiO_{1.153}$	$Ti_{0.804}O_{0.927}$	0.41704	13	6.16	0.1623	0.006	–
$TiO_{1.201}$	$Ti_{0.792}O_{0.952}$	0.41688	13	7.99	0.1251	0.006	–
$TiO_{1.227}$	$Ti_{0.787}O_{0.965}$	0.41674	13	5.47	0.1828	0.021	–
$TiO_{1.233}$	$Ti_{0.780}O_{0.961}$	0.41665	13	5.99	0.1668	0.034	–
$TiO_{1.262}$	$Ti_{0.771}O_{0.973}$	0.41662	13	6.54	0.1528	0.032	–

The resistivity of TiO_y monoxides with an oxygen content $y \geq 1.087$ decreases rapidly as the temperature increases from 4.2 to 300 K. The low resistivity (~10^{-6} Ω m) obtained for all the titanium monoxides studied is characteristic of metals. However, the negative temperature coefficient of resistivity $d\rho/dT$ for TiO_y monoxides with $y \geq 1.087$ is a basic indication of dielectric behavior. In the temperature range 4.2–300 K, the change Δρ in the resistivity due to this factor reaches 20–50%. Therefore, Δρ cannot be treated as a small correction within the relaxation time approximation.

The electrical conductivity σ is proportional to the carrier concentration *n* multiplied by the carrier mobility *u*; that is,

$$\sigma(T) = eh_{e,h}(u_e + u_h). \quad (9)$$

Under the conditions where carriers are governed by the Boltzmann statistics and the energy bands are parabolic (this virtually always holds true in the vicinity of the band edges [29]), the carrier concentration can be written in the form

$$n_e = 2(m^*)^{3/2}(k_BT/2\pi\hbar^2)^{3/2}\exp(-\Delta E/2k_BT), \quad (10)$$

where m^* is the effective mass of charge carriers and Δ*E* is the energy parameter, which has the meaning of an activation energy and, in the case of intrinsic conductivity, is equal to the energy gap E_g between the valence and conduction bands. For a Boltzmann distribution, the carrier mobility is inversely proportional to the temperature; that is,

$$u \sim AT^{-q}. \quad (11)$$

Since all the titanium monoxide samples are characterized by a nonzero residual resistivity, the conductivity of TiO_y monoxides ($y \geq 1.087$), according to formulas (10) and (11), can be represented in the form

$$\sigma(T) = \sigma(0) + 2(k_Bm^*/2\pi\hbar^2)^{3/2}T^{(3/2-q)} \times \exp(-\Delta E/2k_BT). \quad (12)$$

The constant component σ(0) has the meaning of an extrinsic conductivity of the system and implies that the conductivity at $T = 0$ K is nonzero.

The experimental dependences σ(*T*) for TiO_y monoxides ($y \geq 1.087$) were described by function (12) and the relationship $\sigma(T) = \sigma(0) + B\exp(T^{-1/4})$, which is characteristic of Mott semiconductors at low temperatures [30]. The numerical approximation demonstrated that the dependences σ(*T*) are more closely approximated by function (12); in this case, the parameter *q* falls in the range 0.9–1.1. Therefore, with due regard for the experimental error, we can assume that $q \approx 1$; hence, the conductivity can be written as

$$\sigma(T) = \sigma(0) + BT^{1/2}\exp(-\Delta E/2k_BT). \quad (13)$$

The parameter $q = 1$ is observed for many polyatomic semiconductors in which scattering occurs through acoustic and optical phonons. The numerical parameters of function (13) used to describe the dependences σ(*T*) for TiO_y monoxides ($y \geq 1.087$) are listed in Table 1.

The temperature-dependent component of the conductivity [see formula (13)] for TiO_y monoxides ($y \geq 1.087$) in the $\ln\{[\sigma(T) - \sigma(0)]/T^{1/2}\} - 1/T$ coordinates is presented in Fig. 3. It can be seen from Fig. 3 that the dependence exhibits linear behavior over the entire temperature range. The activation energy Δ*E* for titanium monoxides from $TiO_{1.087}$ to $TiO_{1.227}$ is relatively low (~ 0.01–0.03 eV). Only for the $TiO_{1.233}$ and $TiO_{1.262}$ monoxides is the activation energy slightly higher than

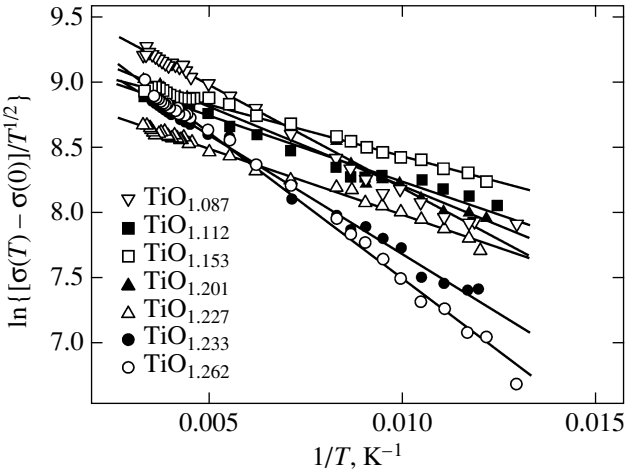

Fig. 3. Temperature dependences of the electrical conductivity $\sigma(T)$ for TiO_y titanium monoxides in the $1/T$–$\ln\{[\sigma(T) - \sigma(0)]/T^{1/2}\}$ coordinates.

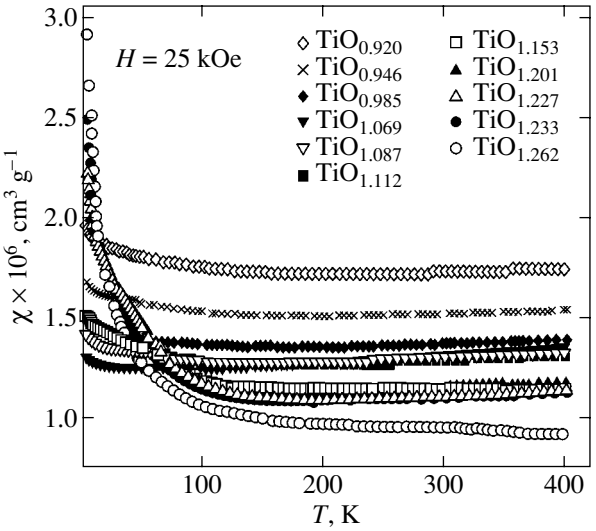

Fig. 4. Temperature dependences of the magnetic susceptibility for disordered cubic titanium monoxides TiO_y with different oxygen contents in the temperature range from 4.0 to 400 K (measurements are performed in a magnetic field with strength H = 25 kOe).

0.03 eV [calculation with the more exact formula (12) for the $TiO_{1.262}$ monoxide gives the activation energy ΔE = 0.043 eV). If the intrinsic conductivity manifests itself at temperatures of approximately 300 K and above, we cannot state with confidence that the determined quantity ΔE is the band gap of an intrinsic semiconductor or that it is the activation energy of an impurity level. The correct answer to this question can be obtained from analyzing the magnetic susceptibility.

The measured temperature dependences of the magnetic susceptibility $\chi(T)$ for TiO_y samples are depicted in Figs. 4 and 5. As can be seen from these figures, the curves $\chi(T)$ contain two portions with opposite behavior of the magnetic susceptibility χ as a function of the temperature. A decrease in the magnetic susceptibility in the low-temperature range (at T < 150–200 K) is characteristic of the paramagnetic component, which is described by the modified Curie law $\chi(T) = \chi(0) + C/(T + \Delta)$ with the temperature-independent paramagnetic contribution $\chi(0)$ and $\Delta > 0$. At temperatures above 150–200 K, the magnetic susceptibility $\chi(T)$ involves the term $\chi(0) + C/(T + \Delta)$ and a contribution described by a linear, quadratic, or more complex function of the temperature.

The Curie paramagnetic contribution to the magnetic susceptibility per unit volume of the material is defined by the formula $\chi_V = Nn_m\mu_{\text{eff}}^2/3k_BT$, where N is the number of atoms per unit volume, n_m is the relative concentration of atoms with magnetic moments, $\mu_{\text{eff}} = p\mu_B$ is the effective magnetic moment, and μ_B is the Bohr magneton. Since the number of atoms per unit volume is determined by the expression $N = N_Ad/M$ (where N_A is the Avogadro number, d is the density, and M is the molecular mass), the measured magnetic susceptibility per unit mass can be written as $\chi = \chi_V/d = (n_mN_A/M)(p\mu_B)^2/(3k_BT) \equiv C/T$. From this relationship, we have $p^2 = (CM/n_m)(3k_B/N_A\mu_B^2)$. After substitution of the quantities N_A, μ_B, and k_B, we obtain $p \approx \sqrt{8CM/n_m}$, where the Curie constant C is expressed in cm^3 K g^{-1}.

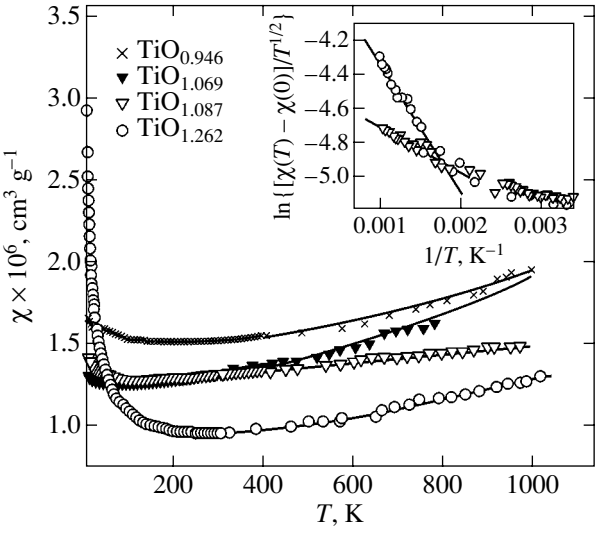

Fig. 5. Temperature dependences of the magnetic susceptibility for TiO_y monoxides in the range from 4.0 K to the temperature of the onset of the disorder $\rightleftharpoons$ order transition (at approximately 1000 K). The inset shows the high-temperature portion of the temperature dependence of the magnetic susceptibility for the $TiO_{1.087}$ and $TiO_{1.262}$ monoxides in the $1/T$–$\ln\{[\chi(T) - \chi(0)]/T^{1/2}\}$ coordinates.

Table 2. Parameters of functions (14) and (16) for the magnetic susceptibility χ and the magnetic characteristics of cubic titanium monoxides TiO_y

TiO_y	Function	Temperature range, K	Parameters of the functions						
			$\chi(0)\times10^6$, $cm^3\ g^{-1}$	$C\times10^6$, $cm^3\ K\ g^{-1}$	Δ, K	$b\times10^{12}$, $cm^3\ K^{-2}\ g^{-1}$	$a\times10^9$, $cm^3\ K\ g^{-1}$	ΔE, eV	p_{av}, μ_B
$TiO_{0.920}$	14	4.0–400	1.629	17.9	55.0	0.501	–	–	0.089
$TiO_{0.946}$	14	4.0–1000	1.410	22.9	88.6	0.493	–	–	0.100
$TiO_{0.985}$	14	4.0–400	1.290	10.7	55.4	0.469	–	–	0.069
$TiO_{1.069}$	14	4.0–1000	1.237	0.54	8.5	0.659	–	–	0.015
$TiO_{1.087}$	16	4.0–1000	1.196	14.9	71.8	–	–	0.061	0.081
$TiO_{1.112}$	17	4.0–400	1.059	44.9	96.0	–	0.889	–	0.225
$TiO_{1.153}$	17	4.0–400	0.909	56.4	89.7	–	0.898	–	0.224
$TiO_{1.201}$	17	4.0–400	0.798	58.3	39.5	–	1.243	–	0.195
$TiO_{1.227}$	17	4.0–400	0.806	51.7	34.6	–	1.025	–	0.178
$TiO_{1.233}$	17	4.0–400	0.917	28.1	14.5	–	0.578	–	0.118
$TiO_{1.262}$	16	4.0–1000	0.847	24.1	7.8	–	–	0.173	0.101

In the case when the concentration n_m of atoms with magnetic moments is unknown, the magnetic moment averaged over all atoms can be determined from the expression $p_{av} \approx \sqrt{8CM}$. It should be noted that, in order to estimate the quantities p or p_{av} correctly, it is necessary to use the molecular mass M corresponding to the real composition of the titanium monoxide with allowance made for the vacancy content in each sublattice, i.e., Ti_xO_z.

As follows from the calculations with the use of the determined constants C, the effective magnetic moment μ_{eff}, which was obtained by averaging over all atoms, amounts to 0.015–0.225 μ_B (Table 2). The low value of μ_{eff} indicates that the Curie contribution to the magnetic susceptibility can be associated with impurities. It seems likely that, in the TiO_y monoxide, the majority of Ti^{2+} ions have paired electrons or there occurs an exchange cation–cation interaction. The EPR measurements of the TiO_y monoxide failed to reveal ions with uncompensated magnetic moments because of the high concentration of delocalized electrons. Since the TiO_y samples are free of ferromagnetic impurities, the small effective magnetic moment can be due to the presence of Ti^{2+} and Ti^{3+} impurity ions in TiO_y monoxides. Judging from the values of p, the content of the above impurity ions varies from 2 to 8 at. %. The Curie paramagnetic contribution is most pronounced for TiO_y titanium monoxides with a relatively high oxygen content $y > 1.2$ (Fig. 5).

The dependence $\chi(T)$ for TiO_y titanium monoxides with an oxygen content $y \le 1.069$ (Figs. 4, 5) over the entire temperature range (4.2–400 or 4.2–1000 K) is well described by the function

$$\chi(T) = \chi(0) + C/(T + \Delta) + bT^2. \quad (14)$$

In relationship (14), the quadratic term bT^2 is characteristic of the Pauli paramagnetism due to conduction electrons. This agrees with the metallic conductivity observed in these monoxides.

The temperature dependences of the magnetic susceptibility for TiO_y monoxides with an oxygen content $y \ge 1.087$ exhibit a more complex behavior, especially in the high-temperature range (Fig. 5). Let us consider the situation where the concentration of charge carriers in TiO_y monoxides with $y \ge 1.087$ at temperatures $T > 300$ K is described by relationship (10). According to the Curie formula $\chi_p(T) = n_e(\mu_B)^2/k_BT$, the temperature-dependent component of the magnetic susceptibility involves the paramagnetic contribution

$$\chi_p(T) = 2(m^*/2\pi\hbar^2)^{3/2}(k_B)^{1/2}(\mu_B)^2T^{1/2} \times \exp(-\Delta E/2k_BT) \equiv AT^2\exp(-\Delta E/2k_BT), \quad (15)$$

where $A = 2(m_0/2\pi\hbar^2)^{3/2}(k_B)^{1/2}(\mu_B)^2(m^*/m_0)^{3/2} = 3.008\times10^{-9}(m^*/m_0)^{3/2}$ [$K^{-1/2}$] and m_0 is the electron mass. Note that expression (15) describes the dimensionless susceptibility per unit volume. Making allowance for the aforementioned features of the dependences $\chi(T)$ and introducing the designation $A_m = A/d$, the measured mass susceptibilities of TiO_y monoxides ($y \ge 1.087$) in the temperature range from 4.2 to 1000 K can be approximated by the function

$$\chi(T) = \chi(0) + A_mT^{1/2}\exp(-\Delta E/2k_BT) + C/(T + \Delta), \quad (16)$$

which includes the temperature-independent contribution $\chi(0)$, the Pauli paramagnetic contribution of the electronic system with an energy gap, and the Curie paramagnetic contribution. At $T < 400$ K, the second term in relationship (16) can be replaced by the term aT, which is linear in temperature. Hence, the susceptibility

of TiO_y monoxides ($y \geq 1.087$) in the temperature range 4.0–400 K can be described by the relationship

$$\chi(T) = \chi(0) + C/(T + \Delta) = aT. \quad (17)$$

The numerical parameters of functions (14), (16), and (17), which were used to approximate the dependences $\chi(T)$ for the TiO_y monoxides studied, are given in Table 2.

In expression (16), the coefficients A_m for the $TiO_{1.087}$ and $TiO_{1.262}$ monoxides are equal to 0.012×10^{-6} and 0.034×10^{-6} cm^3 g^{-1} K$^{-1/2}$, respectively. The densities of the $TiO_{1.087}$ and $TiO_{1.262}$ monoxides are 4.97 and 4.82 g cm^{-3}, respectively. The effective mass of charge carriers in terms of m_0 can be written in the form $m^* = 4.799 \times 10^5 (A_m d)^{2/3} m_0$. The calculations of the effective masses of charge carriers from this formula give $\sim 7m_0$ for $TiO_{1.087}$ and $\sim 14m_0$ for $TiO_{1.262}$. The sufficiently large effective mass of charge carriers confirms the validity of the Boltzmann distribution used in the description of the carrier concentration in TiO_y monoxides with $y \geq 1.087$.

The values of ΔE determined from the dependences $\chi(T)$ [formula (16)] for the $TiO_{1.087}$ and $TiO_{1.262}$ monoxides are equal to 0.061 and 0.173 eV, respectively. The values of ΔE calculated from the temperature dependences of the conductivity for the same monoxides are 0.028 and 0.032 eV, respectively. It can be assumed that the values of ΔE obtained from the low-temperature dependences of the conductivity correspond to the activation energy of impurity levels, whereas the values of ΔE derived from the dependences of the magnetic susceptibility over a wider temperature range are associated with the band gap in the case of intrinsic conductivity. The low value of the band gap makes it possible to assign the TiO_y monoxides ($y \geq 1.087$) to narrow-gap semiconductors.

Thus, the kinetic and magnetic data obtained allow us to draw the inference that an increase in the oxygen content leads to the formation of a narrow energy gap between the valence and conduction bands in the electronic structure of the disordered cubic titanium monoxide TiO_y. Consequently, the TiO_y monoxide can behave either like a *d* metal or like a semiconductor, depending on the oxygen content. Therefore, the metal–semiconductor transition is experimentally observed with an increase in the oxygen content in the disordered titanium monoxide TiO_y, i.e., with a decrease in the concentration of oxygen vacancies and a simultaneous increase in the concentration of titanium vacancies. The question now arises as to whether this concentration transition is a Mott transition. In actual fact, according to [30–32], heavily doped semiconductors (with an impurity-atom concentration of up to tenths of a percent) have disordered structures. These materials undergo a metal–insulator concentration transition at a temperature of 0 K and a metal–semiconductor transition due to correlations at $T > 0$ K. Examples of these semiconductors are provided by transition-metal oxides of the NiO type [30]. Upon the metal–insulator transition, the electrical conductivity can be measured depending on a certain external parameter whose variation leads to a change in the lattice constant. This parameter can be either the composition, the pressure, or the magnetic field strength. The material can possess *n*-type conductivity at a smaller lattice constant and can become an insulator with an increase in the lattice constant [29, 33, 34]. In the case of the TiO_y titanium monoxide, an increase in the lattice constant a_{B1} with an increase in the oxygen content is accompanied by a crossover from metallic conductivity to semiconductor conductivity. However, the temperature dependence of the conductivity for Mott semiconductors in the low-temperature range is described by the relationship $\sigma(T) \sim \exp(T^{-1/4})$ [30], whereas our numerical analysis demonstrates that the temperature dependences of the conductivity for TiO_y monoxides at $y > 1$ obey the law $\sigma(T) \sim T^{1/2}\exp(T^{-1})$. Moreover, the concentration of structural vacancies in titanium monoxide is several orders of magnitude (by a factor of thousands and even tens of thousands) higher than the concentration of randomly distributed impurity atoms in Mott semiconductors. On this basis, we can infer that the metal–semiconductor concentration transition in the disordered titanium monoxide TiO_y is not a Mott transition.

The high concentration of structural vacancies in the titanium and oxygen sublattices of the TiO_y monoxide is a prerequisite to ordering. In our recent work [35], we demonstrated experimentally and theoretically that a monoclinic superstructure of the Ti_5O_5 type involves continuous vacancy channels along particular crystallographic directions (the Ti_5O_5 structure was described and analyzed in detail in monograph [36]). In this respect, it is of considerable interest to investigate the electrokinetic and magnetic properties of an ordered nonstoichiometric titanium monoxide.

ACKNOWLEDGMENTS

We would like to thank R. Henes for his assistance in measuring the resistivity of $TiO_{1.262}$, $TiO_{1.087}$, and $TiO_{0.920}$ monoxide samples at 4.2 K.

This work was supported by the Russian Foundation for Basic Research, project no. 03-03-32033a.

REFERENCES

1. A. I. Gusev and A. A. Rempel', *Nonstoichiometry, Disorder, and Order in Solids* (Ural. Otd. Ross. Akad. Nauk, Yekaterinburg, 2001).
2. D. Watanabe, J. R. Castles, A. Jostsons, and A. S. Malin, Nature **210** (5039), 934 (1966); Acta Crystallogr. **23** (2), 307 (1967).
3. E. Hilti and F. Laves, Naturwissenschaften **55** (3), 131 (1968).
4. D. Watanabe, O. Terasaki, A. Jostsons, and J. R. Castles, in *The Chemistry of Extended Defects in Non-Metallic*

Solids, Ed. by L. Eyring and M. O. Keeffe (North-Holland, Amsterdam, 1970), p. 238.

5. A. A. Valeeva, A. A. Rempel', and A. I. Gusev, Pis'ma Zh. Éksp. Teor. Fiz. **71** (11), 675 (2000) [JETP Lett. **71**, 460 (2000)].
6. A. A. Valeeva, A. A. Rempel', and A. I. Gusev, Neorg. Mater. **37** (6), 716 (2001).
7. E. Hilti, Naturwissenschaften **55** (3), 130 (1968).
8. A. I. Gusev, Pis'ma Zh. Éksp. Teor. Fiz. **74** (2), 96 (2001) [JETP Lett. **74**, 91 (2001)].
9. A. D. Pearson, J. Phys. Chem. Solids **5** (4), 316 (1958).
10. S. P. Denker, J. Appl. Phys. **37** (1), 142 (1966).
11. M. I. Aĭvazov, I. A. Domashnev, A. G. Sarkisyan, and T. V. Rezchikova, Izv. Akad. Nauk SSSR, Neorg. Mater. **6** (4), 745 (1970).
12. M. D. Banus, T. B. Reed, and A. J. Strauss, Phys. Rev. B **5** (8), 2775 (1972).
13. M. Schoen and S. P. Denker, Phys. Rev. **184** (3), 864 (1969).
14. L. F. Mattheis, Phys. Rev. B **5** (2), 290 (1972).
15. A. Neckel, P. Rastl, R. Eibler, *et al.*, J. Phys. C: Solid State Phys. **9** (4), 579 (1976).
16. A. Neckel, Int. J. Quantum Chem. **23** (4), 1317 (1983).
17. L. M. Huisman, A. E. Carlsson, C. D. Gellat, and H. Ehrenreich, Phys. Rev. B **22** (2), 991 (1980).
18. V. A. Gubanov, A. L. Ivanovsky, G. P. Shvelkin, and D. E. Ellis, J. Phys. Chem. Solids **45** (7), 719 (1984).
19. A. L. Ivanovsky, V. I. Anisimov, D. L. Novikov, *et al.*, J. Phys. Chem. Solids **49** (5), 465 (1988).
20. S. R. Barman and D. D. Sarma, Phys. Rev. B **49** (23), 16141 (1994).
21. C. Leung, M. Weinert, P. B. Allen, and R. M. Wentzcovitch, Phys. Rev. B **54** (11), 7857 (1996).
22. G. K. Wertheim and D. N. E. Buchanan, Phys. Rev. B **17** (6), 2780 (1978).
23. S. Gokhale, S. R. Barman, and D. D. Sarma, Phys. Rev. B **52** (20), 14526 (1995).
24. D. R. Jennison and A. B. Kunz, Phys. Rev. Lett. **39** (7), 418 (1977).
25. J. K. Burdett and T. Hughbanks, J. Am. Chem. Soc. **106** (11), 3101 (1984).
26. G. Hobiger, P. Herzig, F. Schlapansky, and A. Neckel, J. Phys.: Condens. Matter **2** (20), 4595 (1990).
27. K. Tsutsumi, O. Aita, and K. Ichikawa, Phys. Rev. B **15** (10), 4638 (1977).
28. S. Bartkowski, M. Neumann, E. Z. Kurmaev, *et al.*, Phys. Rev. B **56** (16), 10656 (1977).
29. I. M. Tsidilkovski, *Gapless Semiconductors—A New Class of Materials* (Nauka, Moscow, 1986).
30. N. F. Mott and E. A. Davis, *Electronic Processes in Non-Crystalline Materials*, 1st ed. (Clarendon, Oxford, 1971; Mir, Moscow, 1974).
31. N. F. Mott, *Electrons in Disordered Structures* (Cambridge, 1967; Mir, Moscow, 1969), Adv. Phys. **16** (61), 49 (1967).
32. N. F. Mott, *Metal–Insulator Transitions* (Taylor and Fransic, London, 1974; Nauka, Moscow, 1979).
33. C. Kittel, *Introduction to Solid State Physics*, 7th ed. (Nauka, Moscow, 1978; Wiley, New York, 1996), p. 284.
34. I. M. Tsidilkovski, *Electron Spectrum of Gapless Semiconductors* (Akad. Nauk SSSR, Sverdlovsk, 1991; Springer-Verlag, Berlin, 1997), Springer Series in Solid-State Sciences, Vol. 116.
35. A. A. Valeeva, G. Tang, A. I. Gusev, and A. A. Rempel', Fiz. Tverd. Tela (St. Petersburg) **45** (1), 84 (2003) [Phys. Solid State **45**, 87 (2003)].
36. A. I. Gusev, A. A. Rempel, and A. A. Magerl, *Disorder and Order in Strongly Nonstoichiometric Compounds: Transition Metal Carbides, Nitrides, and Oxides* (Springer, Berlin, 2001).

Translated by O. Borovik-Romanova

Physics of the Solid State, Vol. 45, No. 7, 2003, pp. 1251–1253. Translated from Fizika Tverdogo Tela, Vol. 45, No. 7, 2003, pp. 1193–1195.

SEMICONDUCTORS AND DIELECTRICS

Thermal Conductivity of Bi_2Te_3 : Sn and the Effect of Codoping by Pb and I Atoms

M. K. Zhitinskaya*, S. A. Nemov*, T. E. Svechnikova, L. N. Luk'yanova***, P. P. Konstantinov***, and V. A. Kutasov*****

**St. Petersburg State Polytechnical University, Politekhnicheskaya ul. 25, St. Petersburg, 195251 Russia*

***Institute of Metallurgy and Materials Sciences, Russian Academy of Sciences, Leninskiĭ pr. 49, Moscow, 117911 Russia*

****Ioffe Physicotechnical Institute, Russian Academy of Sciences, Politekhnicheskaya ul. 26, St. Petersburg, 194021 Russia*

Received November 12, 2002

Abstract—The variation of the lattice thermal conductivity of Bi_2Te_3 induced either by alloying it with tin alone or by codoping the lattice with an acceptor or donor impurity was studied. The experimental data obtained at room and liquid nitrogen temperatures argue for the validity of the model of quasi-local impurity states associated with tin atoms. *© 2003 MAIK "Nauka/Interperiodica".*

Bismuth telluride, like lead telluride, possesses a high lattice polarizability. Therefore, neutral and charged impurities differently affect phonon scattering in these materials [1, 2]. The effective phonon scattering cross section Φ from charged impurities in these compounds exceeds that from neutral impurities by a few times. We use this observation in our study to probe the charge state of tin impurity atoms in Bi_2Te_3.

The unusual effect of tin atoms on the electrophysical properties of bismuth telluride was reported earlier in [3–5]. The observed features were attributed to the presence of resonance states in the allowed valence band spectrum. In addition, bismuth telluride is a compound with a high concentration of antisite defects, with part of the bismuth atoms (about 1 at. %) occupying the two possible tellurium positions, $Bi_{Te^{(1)}}$ and $Bi_{Te(2)}$. The atomic arrangement in a layer can be represented as $Te^{(1)}$–Bi–$Te^{(2)}$–Bi–$Te^{(1)}$.

Therefore, the tin atoms incorporated through the substitutional doping Bi ⟶ Sn may occupy three different positions, namely, the $Te^{(1)}$, $Te^{(2)}$, and Bi sites. The charge states of Sn in these positions will naturally be different.

The experiment was conducted in two stages. We first studied the effect of the concentration of the alloyed tin atoms on the lattice thermal conductivity of Bi_2Te_3. After this, we carried out experiments on codoping; more specifically, we studied the variation of the lattice thermal conductivity of Bi_2Te_3 doped both by tin and by a donor (halogen) or acceptor (lead) impurity.

Single-crystal Bi_2Te_3 samples were grown by the Czochralski and directional-crystallization methods. The composition of the samples doped by tin alone had the chemical formula $Bi_{2-x}Sn_xTe_3$, with x = 0, 0.002, 0.005, 0.007, 0.01, and 0.02 (x = 0.01 corresponds to the concentration 6×10^{19} cm^{-3}). The samples codoped by tin and iodine (or chlorine) had the formula $Bi_{2-x}Sn_xTe_3 + ySbI_3(CdCl_2)$, where x = 0.005, 0.01, and 0.02 and y = 0.05, 0.1, and 0.15 wt %. The samples alloyed with both tin and lead had the composition $Bi_{2-x-z}Sn_xPb_zTe_3$ (with the same values of x, and with z = 0.005, 0.01, 0.02, 0.03). The impurity content was verified by chemical and x-ray analysis. The uniformity of the impurity distribution in the samples was estimated at room temperature with a thermal probe. Measurements of the thermal conductivity κ_{tot} were complemented by a study of the following independent components of the kinetic tensors: Hall coefficients R_{123} and R_{321}, Seebeck coefficients S_{11} and S_{33}, and electrical conductivity σ_{11}. Thermal conductivity was measured using a steady-state technique. The heat flux and electric current were directed along the cleavage planes (indices 1, 2). The Hall coefficient was measured using two techniques, in ac and dc electric and magnetic fields.

In heavily doped semiconductors, the total thermal conductivity in the region of extrinsic conduction can be written as $\kappa_{tot} = \kappa_L + \kappa_e$, where κ_L is the lattice thermal conductivity and κ_e is the electron thermal conductivity, which was derived using the Wiedemann–Franz law $\kappa_e = L\sigma T$ (L is the Lorenz number). The Lorenz number L was calculated with inclusion of the electron gas degeneracy [2].

Consider the results obtained. As seen from Fig. 1, doping with tin alone practically does not change the magnitude of the total thermal conductivity κ_{tot}, which remains nearly constant, with the exception of the initial region. Thermal resistance of the lattice W_r doped by tin to N_{imp} = 0.2 at. % grows. As long as tin atoms are present in small amounts (below 0.2 at. %), they apparently sit primarily at the $Te^{(2)}$ sites, where they are electrically active and donate their electrons to the valence

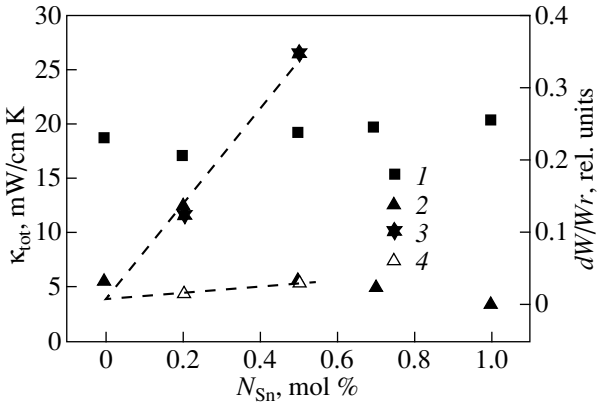

Fig. 1. Dependences (*1*) of the thermal conductivity κ_{tot} and (*2–4*) of the relative thermal lattice resistance dW/W_r of Bi_2Te_3 on dopant concentration. (*1*, *2*) tin impurity, (*3*) charged impurity, and (*4*) neutral impurity (*3*, *4*) are data from [6]).

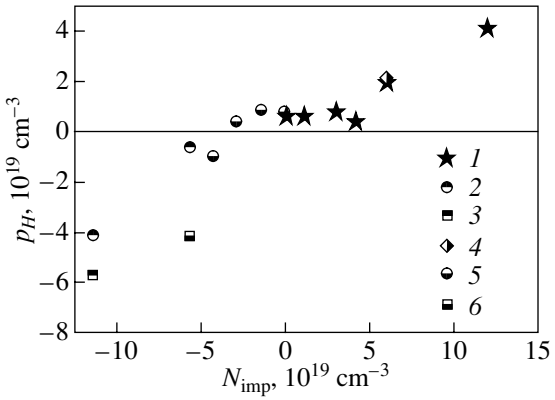

Fig. 2. Variation of the hole Hall concentration in Bi_2Te_3 (*1*) doped by tin and codoped by (*2*, *3*) Cl, (*4*) Pb, and (*5*, *6*) I.

band. This conjecture is supported by a decrease in hole concentration (points *1* in Fig. 2). The Sn atoms are charged and the lattice thermal resistance grows because of the phonons suffering additional scattering from the charged impurity.

As the tin dopant concentration was increased still more (to 1 at. %), the thermal lattice resistance decreased to the value characteristic of undoped Bi_2Te_3 and then remained at this level as the tin content was further increased. It may be conjectured that, after the Sn atoms have filled the $Bi_{Te^{(2)}}$ sites, they begin to occupy predominantly the $Bi_{Te^{(1)}}$ positions. Sn atoms sitting at the $Te^{(1)}$ sites are believed [7] to create resonance levels. In these positions, the Sn atoms are neutral with respect to the lattice. The resonance level, being located at a small depth in the valence band, accepts a very small number of electrons from higher lying valence-band states (the total hole concentration in the valence band is $p \sim 1 \times 10^{19}$ cm$^{-3} \ll N_{Sn}$). The measurements of the thermal conductivity lend support to this conjecture. The lattice thermal resistance in this range of the Sn impurity concentrations is fitted well by the law of phonon scattering from neutral impurities (Fig. 1).

Consider now the variation of the lattice thermal resistance under codoping of the material with Sn and an acceptor (Pb) or donor (I, Cl). Codoping $Bi_{2-x}Sn_xTe_3$ with acceptors (Pb atoms) also leaves the lattice thermal resistance practically unchanged (points *7–9* in Fig. 3). By contrast, additional doping $Bi_{2-x}Sn_xTe_3$ by donors, i.e., atoms of Cl (points *4–6*) or I (points *10–12*), results in an increase in the lattice thermal resistance. $W_r(N_{imp})$ was observed to behave in this way at both room and liquid nitrogen temperatures, which may be assigned to the phonon scattering from impurities being a dominant process. Assuming the difference in the pattern of W_r variation under doping with donors and acceptors to be associated with specific features of phonon scattering in Bi_2Te_3 : Sn caused by additional doping, one can use Ioffe's relation to estimate the phonon scattering cross section Φ from the data on thermal conductivity:

$$k_0/k = W_r/W_0 = 1 + (N/N_0)\Phi(l_0/a),$$

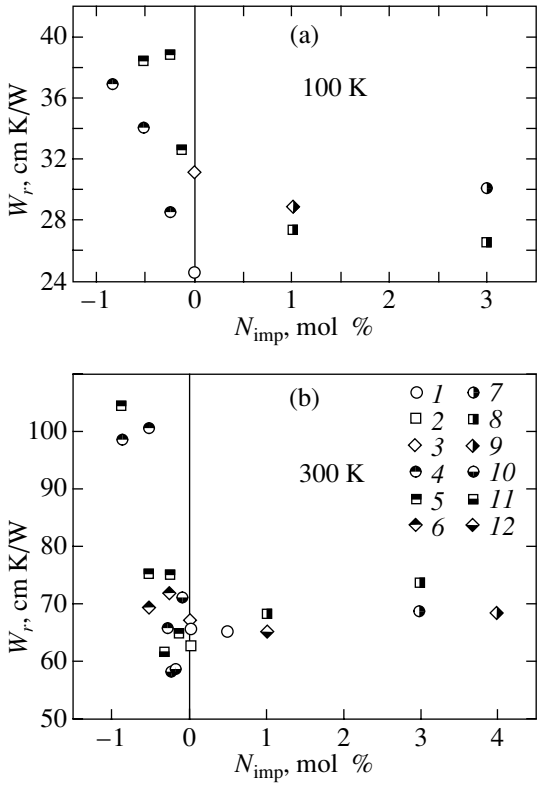

Fig. 3. Lattice thermal conductivity of Bi_2Te_3 doped by Sn atoms only (*1–3*) and codoped by (*4–6*) Cl, (*7–9*) Pb, and (*10–12*) I. N_{Sn} is equal to (*1*, *4*, *7*, *10*) 0.5, (*2*, *5*, *8*, *11*) 1.0, and (*3*, *6*, *9*, *12*) 2.0 mol %. *T* is equal to (a) 100 and (b) 300 K.

where N is the impurity concentration, N_0 is the number of atoms per 1 cm^3, a is the distance between neighboring atoms, l_0 is the phonon mean free path in an impurity-free crystal, Φ is the coefficient in the relation $S = Aa^2$ (cross section of phonon scattering from impurities), k and k_0 are the lattice thermal conductivities and W_r and W_0 are the lattice thermal resistances in a crystal with and without an impurity, respectively.

It was found that the value of Φ is practically constant, $\Phi \sim 1.3$, throughout the region of Bi_2Te_3 : Sn codoping by an acceptor impurity (Pb atoms) or a donor impurity (Cl and I atoms) to a level of 0.5 mol %. As the concentration of additional donors increases to 1 mol %, the scattering cross section grows to $\Phi \sim 8$. The values of Φ thus obtained agree well with available literature data on Bi_2Te_3 [6] for the case of phonon scattering from neutral and charged impurities.

The experimental data obtained in this study are similar to those observed earlier in PbTe : Tl codoped by Na. The Tl impurity produces a band of resonance impurity states in the valence band of PbTe, and the Na strong acceptor impurity completely depletes these states, with the Fermi level leaving the band of resonance states [8]. These data reveal a similarity with ours obtained on $Bi_{2-x}Sn_xTe_3$ in W_r being only weakly dependent on the codopant as long as the Fermi level remains within the resonance band; in Fig. 2, this case corresponds to the region of relative hole concentration stability, in which small variations of p_{300} are observed to occur. However, in contrast to PbTe : Tl doped by Na, we cannot unambiguously interpret the behavior of W_r under codoping of $Bi_{2-x}Sn_xTe_3$ by Pb atoms. The explanation of this quite ambiguous and complex character of the effect of codopants may lie not only in the variation of the filling of Sn resonance states but also in that the Pb impurity is capable of occupying different positions in the crystal lattice and, through this, differently influencing the Bi redistribution between these positions.

Thus, the experimental data obtained in this study on the effect of the Sn impurity on the lattice thermal conductivity of Bi_2Te_3 single crystals, as well as the data bearing on codoping $Bi_{2-x}Sn_xTe_3$ by an acceptor or donor impurity, argue for the existence of quasi-local tin impurity states.

REFERENCES

1. V. A. Kulbachinskii, N. B. Brandt, P. A. Cheremnykh, *et al.*, Phys. Status Solidi B **150**, 237 (1988).
2. G. T. Alekseeva, P. P. Konstantinov, V. A. Kutasov, *et al.*, Fiz. Tverd. Tela (St. Petersburg) **38**, 2998 (1996) [Phys. Solid State **38**, 1639 (1996)].
3. M. K. Zhitinskaya, S. A. Nemov, and T. E. Svechnikova, Fiz. Tverd. Tela (St. Petersburg) **40**, 1428 (1998) [Phys. Solid State **40**, 1297 (1998)].
4. V. A. Kutasov and I. A. Smirnov, Fiz. Tverd. Tela (Leningrad) **8**, 2695 (1966) [Sov. Phys. Solid State **8**, 2153 (1966)].
5. I. A. Smirnov, E. V. Shadrichev, and V. A. Kutasov, Fiz. Tverd. Tela (Leningrad) **11**, 3311 (1969) [Sov. Phys. Solid State **11**, 2681 (1969)].
6. B. M. Gol'tsman, V. A. Kudinov, and I. A. Smirnov, *Semiconducting Thermoelectric Materials Based on Bi_2Te_3* (Nauka, Moscow, 1972).
7. P. Pecheur and G. Toussaint, in *Proceedings of VIII International Conference on Thermoelectric Energy Conversion, Nancy* (1989), p. 176.
8. M. K. Zhitinskaya, S. A. Nemov, and Yu. I. Ravich, Fiz. Tverd. Tela (St. Petersburg) **40**, 1206 (1998) [Phys. Solid State **40**, 1098 (1998)].

Translated by G. Skrebtsov

Physics of the Solid State, Vol. 45, No. 7, 2003, pp. 1254–1259. Translated from Fizika Tverdogo Tela, Vol. 45, No. 7, 2003, pp. 1196–1201.

SEMICONDUCTORS AND DIELECTRICS

Description of the Thermodynamic Properties of a Nonmetallic Solid (Germanium): A Self-Consistent Thermodynamic Approach

V. Yu. Bodryakov and A. A. Povzner

Ural State Technical University, ul. Mira 19, Yekaterinburg, 620002 Russia

e-mail: povz@kf.ustu.ru

Received November 11, 2002

Abstract—An algorithm is proposed for constructing a Debye-type self-consistent model of a nonmetallic isotropic solid. Using germanium as an example, it is demonstrated that the thermodynamic quantities can be adequately described over a wide range of temperatures even under significantly simplifying assumptions about the thermodynamic parameters. © *2003 MAIK "Nauka/Interperiodica".*

1. INTRODUCTION

It is known that thermodynamic properties of real solids have defied adequate description in the framework of the Debye model, which is in essence the sole universally accepted thermodynamic model of nonmagnetic solids [1, 2]. This stems from the fact that the Debye model is extremely simplified and self-contradictory. In particular, one of the most important parameters of the theory is the Debye characteristic temperature θ, which, according to classical representations, is a material constant and does not depend on temperature. The Debye temperature is determined by the form of the phonon spectrum. In an ideal case, the phonon spectrum is assumed to be quadratic in frequency and is limited from above by the Debye frequency. The characteristic temperature θ can be expressed through the bulk and shear moduli, density, and molar volume. Simple thermodynamic calculations have demonstrated that these quantities explicitly (and substantially) depend on temperature. From the foregoing, it immediately follows that the quantity θ should also be temperature dependent. This inference contradicts the original assumptions of the Debye model in the traditional interpretation but agrees with experimental calorimetric data on the heat capacity of solids (see, for example, [3–8]). The temperature dependence of the Debye characteristic temperature is directly associated with a nonideal vibrational spectrum of a real solid (phonon anharmonicity) and accounts for the specific features observed in the thermal properties, which cannot be explained in the framework of the traditional approach [5–13]. Specifically, the deviation of the actual temperature dependence of the heat capacity of a solid from the Dulong–Petit law has defied explanation in terms of the classical Debye theory even in the absence of the electronic contribution and requires inclusion of the dependence $\theta(T)$. Similarly, the temperature dependence of the thermal expansion coefficient $\alpha(T)$ deviates from the classical Debye behavior, according to which the thermal expansion coefficient $\alpha(T)$ should approach a constant value asymptotically with an increase in the temperature [2].

It should be noted that, according to the theory of solids [2], there is a correlation between the temperature dependences of the heat capacity and the thermal expansion coefficient. However, the well-known experimental fact that the temperature dependences of the heat capacity and the elastic moduli also correlate with each other has not been interpreted theoretically (see [14]).

The above contradictions still remain unresolved. In this respect, it is important to construct a self-consistent thermodynamic model of solids that would make it possible to describe and predict the temperature dependences of the heat capacity and the elastic moduli for solid paramagnets within a unified approach.

In the present work, we developed a model concept of the Debye theory and formulated the basic principles of the construction of a model providing a self-consistent description of the most important thermodynamic properties of an isotropic nonconducting nonmagnetic solid: the heat capacity C, the bulk thermal expansion coefficient α, the bulk modulus K, etc.

For this purpose, a germanium semiconductor was chosen as the model object, because a large amount of reference experimental data on the thermal properties of this material is available in the literature [3, 4, 15–18]. In our case, the electronic conductivity of germanium can be ignored without loss of accuracy.

1063-7834/03/4507-1254$24.00

2. DEBYE TEMPERATURE AND ITS THERMODYNAMIC DERIVATIVES

One of the most important notions in the Debye theory is the Debye characteristic temperature θ. This temperature is an averaged characteristic of the phonon spectrum of thermal atomic vibrations. The phonon spectrum is considered to be quadratic in frequency and, moreover, is limited from above by the Debye frequency [1, 2]. Evidently, the true vibrational spectrum of a real solid is far from ideal. Therefore, the deviation from the ideal spectrum, as far as possible, should be taken into account properly in terms of macroscopic thermodynamics in order to describe the actual thermodynamic properties more correctly.

The characteristic temperature can be obtained by Debye averaging of the partial Debye temperatures; that is,

$$\theta = \left(\frac{3}{\frac{1}{\theta_l^3} + \frac{2}{\theta_t^3}}\right)^{1/3}. \quad (1)$$

In the framework of the classical Debye interpretation, the Debye temperature is a function of the volume V of a solid (or the pressure P) and does not depend on temperature. The longitudinal Debye temperature is associated with the longitudinal mode of acoustic vibrations and can be conveniently represented in the form

$$\theta_l = \frac{\hbar}{k_B}\left(\frac{6\pi^2 N_A}{V}\right)^{1/3}\sqrt{\frac{K + \frac{4}{3}G}{\rho}} = \frac{\hbar}{k_B}\frac{(6\pi^2 N_A)^{1/3}}{M^{1/2}}L^{1/2}V^{1/6}. \quad (2)$$

The transverse Debye temperature corresponds to the transverse mode of acoustic vibrations and can be written as

$$\theta_t = \frac{\hbar}{k_B}\left(\frac{6\pi^2 N_A}{V}\right)^{1/3}\sqrt{\frac{G}{\rho}} = \frac{\hbar}{k_B}\frac{(6\pi^2 N_A)^{1/3}}{M^{1/2}}G^{1/2}V^{1/6}. \quad (3)$$

In relationships (2) and (3), k_B is the Boltzmann constant, N_A is the Avogadro number, V is the molar volume, ρ is the mass density, M is the molar weight, K is the bulk modulus, and G is the shear modulus. It should be noted that there is no convenient thermodynamic definition of the shear modulus G. Hence, this modulus can be expressed through the bulk modulus and the Poisson ratio σ as follows [19]:

$$G = \frac{3(1-2\sigma)}{2(1+\sigma)}K. \quad (4)$$

The so-called modulus of elongation L (an analog of the Young's modulus) can also be expressed in terms of the bulk modulus K and the Poisson ratio σ; that is,

$$L = \frac{3(1-\sigma)}{(1+\sigma)}K. \quad (5)$$

For the majority of materials, the Poisson ratio is close to 1/4 and depends on the temperature only slightly. Hereafter, the Poisson ratio will be assumed to be constant (independent of the temperature). Under these conditions, the temperature dependence of the Debye characteristic temperature, when it cannot be disregarded, is determined by the temperature dependences of the bulk modulus and the molar volume, which, as will be shown below, follow directly from the Debye theory.

In further analysis, we will use the isothermal derivatives of the averaged and partial Debye temperatures with respect to the volume. These thermodynamic derivatives can be conveniently represented by introducing the following designations:

$$\gamma_i = \left(\frac{V}{i}\frac{\partial i}{\partial V}\right)_T, \quad \gamma_i^* = \left(\frac{V^2}{i}\frac{\partial^2 i}{\partial V^2}\right)_T, \quad i = \theta, \theta_t, \theta_l.$$

In the theory of solids, the parameter γ_θ and the Grüneisen parameter $\Gamma = -\left(\frac{\partial \ln\theta}{\partial \ln V}\right)_T$ coincide to the first decimal place. For the majority of solids, the Grüneisen parameter is of the order of unity.

It can easily be verified that the parameters γ_θ and γ_θ^* satisfy the relationships

$$\gamma_\theta = \frac{\gamma_{\theta l}/\theta_l^3 + 2\gamma_{\theta t}/\theta_t^3}{1/\theta_l^3 + 2/\theta_t^3}, \quad (6)$$

$$\gamma_\theta^* = \frac{\gamma_{\theta l}^*/\theta_l^3 + 2\gamma_{\theta t}^*/\theta_t^3}{1/\theta_l^3 + 2/\theta_t^3}. \quad (7)$$

In some cases, the temperature dependence of the parameters γ (the generalized Grüneisen parameters) can be ignored. In the general case, the temperature dependence of the parameters γ_θ is governed by the temperature dependences of the partial parameters γ_θ ($\gamma_{\theta l}$, $\gamma_{\theta t}$ and $\gamma_{\theta l}^*$, $\gamma_{\theta t}^*$) and the Debye temperatures (θ_l and θ_t).

3. THE FIRST AND SECOND THERMODYNAMIC DERIVATIVES

With due regard for the problems formulated in this work and the set of physical properties to be analyzed, the thermodynamics of the objects under consideration (weakly anisotropic nonmetallic solid paramagnets) will be described not only in terms of the Helmholtz thermodynamic potential (free energy) $F(T, V)$ as a

function of the temperature T and the volume V but also in terms of the Gibbs thermodynamic potential $\Phi(T, P)$ as a function of the temperature T and pressure P. It is known [2] that the molar free energy and the molar thermodynamic potential in the differential representation have the form

$$dF(T, V) = -SdT - PdV, \tag{8}$$

$$d\Phi(T, P) = -SdT + VdP, \tag{9}$$

where S is the molar entropy. Expressions (8) and (9) are similar to each other and differ only in their variables. As will be shown below, the thermal properties of materials (the heat capacity and thermal expansion) are more conveniently analyzed in terms of the thermodynamic potential $\Phi(T, P)$. This analysis allows one to derive thermodynamically exact relationships for the experimentally measured thermal expansion coefficient and heat capacity at a constant pressure. At the same time, the elastic properties can be more conveniently treated in terms of the free energy F, because this parameter permits one to obtain a thermodynamically exact relationship for the isothermal bulk modulus. It should be noted that the choice of the pressure as an independent variable is justified in the majority of cases: it is this pressure that can be arbitrarily varied in the experiments.

By ignoring the electronic contribution, the total molar free energy of an isotropic nonmetallic solid, according to thermodynamic concepts, can be written in the form

$$F = F_0 + F_p. \tag{10}$$

Here, $F_0(V)$ is the temperature-independent part of the free energy, which depends on the volume, and $F_p(T, \theta)$ is the Debye (lattice, phonon, paramagnetic) part of the free energy, which, as follows from the Grüneisen law of corresponding states [2], is a function of the ratio of the temperature T to the Debye temperature $\theta = \theta(V)$. The molar thermodynamic potential can be represented in a form similar to expression (10); that is,

$$\Phi = \Phi_0 + \Phi_p. \tag{11}$$

Here, the terms have the same meaning as for the free energy but with allowance made for the replacement of V by P.

We omit the intermediate calculations described in our previous works [11, 13] and present only final results, namely, thermodynamically exact relationships for the main physical characteristics of a nonmetallic solid.

3.1. The First Thermodynamic Derivatives

The first-order thermodynamic derivatives of the free energy and thermodynamic potential are necessary for further calculations. These are the molar entropy at a constant pressure, the isothermal molar volume, the mass density, and the isothermal pressure. Taking into account the possible temperature dependence of the Debye characteristic temperature $\theta(T)$, these quantities can be determined from the expressions

$$S = -\left(\frac{\partial\Phi}{\partial T}\right)_P = 3R\left\{\frac{4}{3}D(z) - \ln(1-e^{-z}) - \left[\frac{3}{8} + \frac{D(z)}{z}\right]\left(\frac{\partial\theta}{\partial T}\right)_P\right\}, \tag{12}$$

$$V = \left(\frac{\partial\Phi}{\partial P}\right)_T = V_0 + 3R\left[\frac{3}{8} + \frac{D(z)}{z}\right]\left(\frac{\partial\theta}{\partial P}\right)_T, \tag{13}$$

$$\rho = \frac{M}{V} = \frac{M}{V_0 + 3R\left[\frac{3}{8} + \frac{D(z)}{z}\right]\left(\frac{\partial\theta}{\partial P}\right)_T}, \tag{14}$$

$$P = -\left(\frac{\partial F}{\partial V}\right)_T = P_0 - 3R\left[\frac{3}{8} + \frac{D(z)}{z}\right]\left(\frac{\partial\theta}{\partial V}\right)_T. \tag{15}$$

In expressions (12)–(15), $S_0 = 0$; $V_0 = \left(\frac{\partial\Phi}{\partial P}\right)_T$; $P_0 = \left(\frac{\partial F}{\partial V}\right)_T$; $D(z)$ is the standard tabulated Debye function [2], which depends on the reciprocal of the reduced temperature $z = \theta/T$; and R is the universal gas constant.

Although the density or, in some cases, the volume can be measured directly, it is common practice to determine the physical quantities corresponding to second-order thermodynamic derivatives, namely, the molar heat capacity, the bulk thermal expansion coefficient, and the bulk modulus.

3.2. The Second Thermodynamic Derivatives

Making allowance for the possible temperature dependence of the Debye characteristic temperature $\theta(T)$, thermodynamically exact relationships for the molar heat capacity at a constant pressure, the bulk thermal expansion coefficient, and the bulk modulus of a nonmetallic solid have the form

$$C = T\left(\frac{\partial S}{\partial T}\right)_P = -T\left(\frac{\partial^2\Phi}{\partial T^2}\right)_P = 3R\left\{C_{VR}(z)\left[1 - \frac{T}{\theta}\left(\frac{\partial\theta}{\partial T}\right)_P\right]^2 - T\left[\frac{3}{8} + \frac{D(z)}{z}\right]\left(\frac{\partial^2\theta}{\partial T^2}\right)_P\right\}, \tag{16}$$

$$\alpha = \frac{1}{V}\left(\frac{\partial V}{\partial T}\right)_P = -\frac{1}{V}\frac{\partial^2 \Phi}{P\partial T}$$
$$= \frac{3R}{V}\left\{C_{VR}(z)\left[1 - \frac{T}{\theta}\left(\frac{\partial \theta}{\partial T}\right)_P\right]\frac{1}{\theta}\left(\frac{\partial \theta}{\partial P}\right)_T \right. \quad (17)$$
$$\left. + \left[\frac{3}{8} + \frac{D(z)}{z}\right]\frac{\partial^2 \theta}{\partial T \partial P}\right\},$$

$$K = -V\left(\frac{\partial P}{\partial V}\right)_T = \frac{1}{V}\left(V^2\frac{\partial^2 F}{\partial V^2}\right)_T$$
$$= K_0 + \frac{3R}{V}\left\{\frac{3}{8}\gamma_\theta^* \theta - T[\gamma_\theta^2 C_{VR}(z) - \gamma_\theta^* D(z)]\right\}. \quad (18)$$

We leave aside the cumbersome analysis of different limiting cases (for details, see [6–13]) and note only that, by ignoring the temperature dependence $\theta(T)$, it is possible to obtain thermodynamic results corresponding to the classical Debye theory (the Dulong–Petit law, the Grüneisen law of corresponding states, etc.). In the case when the temperature dependence of the Debye characteristic temperature is taken into account under the conditions $(\partial\theta/\partial T)_P < 0$ and $(\partial^2\theta/\partial T^2)_P < 0$, which are usually satisfied, the calculated heat capacity $C(T)$ and bulk thermal expansion coefficient $\alpha(T)$ exceed the classical limiting values even without regard for the electronic contribution. This is in agreement with the experimental results and can be taken into consideration in the experimental data processing for real solids.

Note that, here, it is also expedient to use the relationship $(\partial\theta/\partial P)_T = (-\theta/K)\gamma_\theta$.

4. ALGORITHM FOR CONSTRUCTING A SELF-CONSISTENT THERMODYNAMIC MODEL

In order to eliminate the aforementioned contradictions of the classical Debye model, it is advisable to use a self-consistent scheme of calculating the thermodynamic characteristics. For numerical calculations, this scheme is based on the method of successive approximations. Using germanium as an example, we will demonstrate below that the inclusion of the deviation of the phonon spectrum from the ideal spectrum through the allowance made for the temperature dependence $\theta(T)$ even under the simplest assumptions (the temperature independence of the parameters $\gamma_{\theta l}$, $\gamma_{\theta t}$, $\gamma^*_{\theta l}$, $\gamma^*_{\theta t}$, and σ) will make it possible to achieve reasonable agreement between the experimental and calculated data on the thermal characteristics of the studied material over a wide temperature range covering several hundreds of degrees Kelvin.

4.1. The Initial Approximation

In order to perform the approximate calculations, we specified the bare thermodynamic parameters V_0, K_0, $\gamma_{\theta l}$, $\gamma_{\theta t}$, $\gamma^*_{\theta l}$, $\gamma^*_{\theta t}$, and σ. This permits us to calculate the initial values of the averaged and partial Debye temperatures θ_0, θ_{0l}, and θ_{0t}; the density ρ_0; and the averaged generalized Grüneisen parameters $\gamma_{\theta 0}$.

4.2. The Zeroth Approximation (n = 0)

The parameters thus obtained provide a means for calculating the temperature dependences $V(T)$, $K(T)$, and $\rho(T)$ in the zeroth approximation (i.e., under the assumption that the Debye temperature is constant: $\theta = \theta_0$). Next, it becomes possible to determine the temperature dependences $\theta(T)$, $\theta_l(T)$, and $\theta_t(T)$ and the corresponding derivatives with respect to the temperature. Then, we calculate the averaged Grüneisen parameters γ_θ, which makes possible the determination of the remaining thermodynamic characteristics $C(T)$ and $\alpha(T)$ in the above approximation.

4.3. First and Subsequent Approximations (n = 1, 2, …)

In the first and subsequent approximations, the calculations are performed in the same manner as in the case of the zeroth approximation, with the only difference that the dependence $\theta(T)$ is taken into account, which leads to renormalization of the temperature dependences of the thermodynamic parameters. The iterative self-consistent process can be terminated in accordance with an arbitrarily specified condition, for example, when the difference between the Debye temperatures θ in two successive approximations becomes less than 0.01 K. As follows from the calculations, this can be achieved using the first three to five approximations.

By applying the aforementioned iterative procedure, varying the bare parameters, and minimizing the least root-mean-square difference between the available experimental data and the calculated thermodynamic parameters, it is possible to obtain the self-consistent temperature dependences of all the physical quantities determining the thermodynamic properties of the studied solid material. In the present work, these calculations were performed using germanium as an example.

5. DISCUSSION

The principal thermodynamic functions calculated for germanium according to the proposed algorithm are compared with the available reference data in Figs. 1–3. The temperature dependences of the molar heat capacity, the bulk thermal expansion coefficient, and the bulk modulus for germanium are depicted in Figs. 1, 2, and 3, respectively. The theoretical temperature dependence of the Debye characteristic temperature and the dependence $\theta(T)$ calculated using the calorimetric data taken from [3] are presented in Fig. 4.

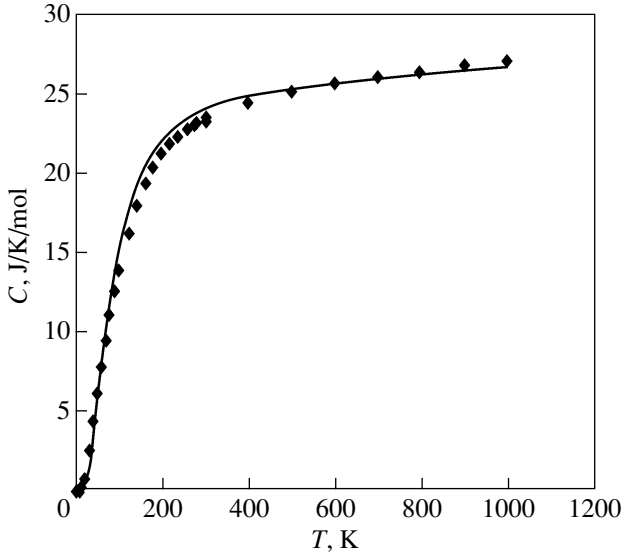

Fig. 1. Temperature dependence of the heat capacity of germanium. Points are the data taken from [17] (below 300 K) and [16] (above 300 K). The solid line corresponds to the results of calculations.

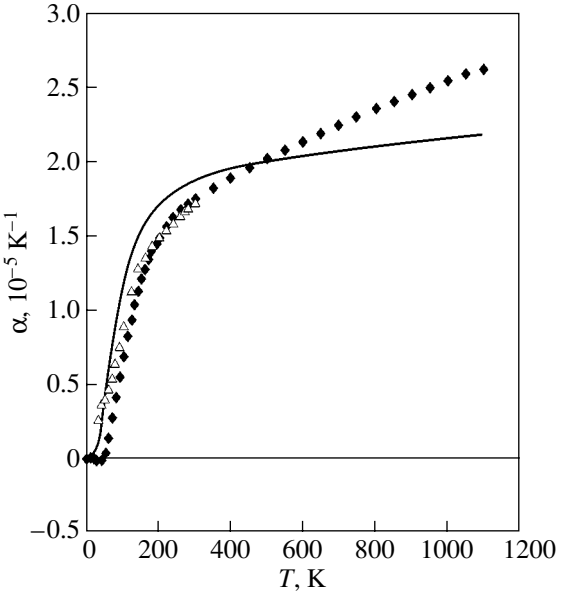

Fig. 2. Temperature dependence of the bulk thermal expansion coefficient for germanium. Squares and triangles are the data taken from [15] and [17], respectively. The solid line corresponds to the results of calculations.

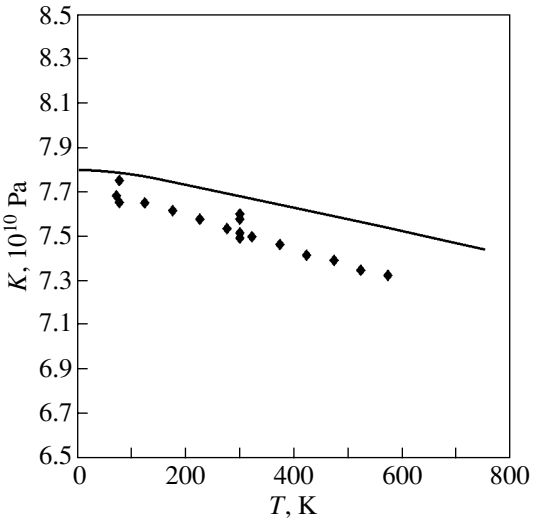

Fig. 3. Temperature dependence of the bulk modulus for germanium. Points are the data taken from [18], and the solid line corresponds to the results of calculations.

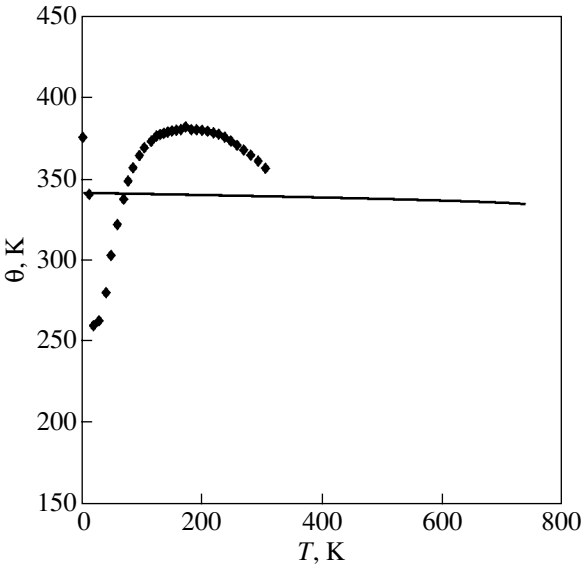

Fig. 4. Temperature dependence of the Debye temperature for germanium. Points are the data taken from [3], and the solid line corresponds to the results of calculations.

Despite the simplicity of the assumptions made in our calculations (the Grüneisen parameters $\gamma_{\theta l}$, $\gamma_{\theta t}$, $\gamma^*_{\theta l}$, and $\gamma^*_{\theta t}$ and the Poisson ratio σ were assumed to be independent of temperature), we succeeded in achieving quite reasonable agreement between the calculated and reference thermodynamic functions over a wide range of temperatures. Excellent agreement is observed for the molar heat capacity. The calculated thermodynamic parameters, which varied as free parameters in our calculations, are as follows: $V_0 = 1.43 \times 10^{-5}$ m^3 mol^{-1}, $K_0 = 78.5$ GPa, $\gamma_{\theta l} = -3.86$, $\gamma_{\theta t} = -0.588$, $\gamma^*_{\theta l} = -1.89$, $\gamma^*_{\theta t} = -2.37$, and $\sigma = 0.261$. The relative error (the relative root-mean-square difference between the calculated and reference data) is equal to ±2.4% for the heat capacity, ±11.1% for the bulk thermal expansion coefficient, ±2.2% for the bulk modulus, ±5.5% for the density, ±8.6% for the

Debye temperature, and ±0.5% for the Poisson ratio. The Poisson ratio at room temperature was taken from [18].

The calculated and reference bulk thermal expansion coefficients [15, 18] are in rather poor agreement as compared to the other thermal parameters. This can be explained by two circumstances. First, the reference books [15, 18] contain linear thermal expansion coefficients for single-crystal germanium (without indicating the crystallographic directions of measurement), whereas thermodynamic calculations hold true for the averaged bulk thermal expansion coefficient of the polycrystalline solid. Second, the thermal expansion of germanium in the low-temperature range exhibits an invar anomaly: the thermal expansion coefficient of germanium is negative in the temperature range $16 < T < 40$ K. This anomaly in the thermal expansion is accompanied by anomalous behavior of the temperature dependence of the Debye characteristic temperature (Fig. 4). The well-known anomalous behavior of the physical properties of germanium has hitherto defied satisfactory explanation. It seems likely that these anomalies cannot be described thermodynamically under the aforementioned simplifying assumptions, in particular, regarding the temperature independence of the Grüneisen parameters $\gamma_{\theta l}$ and $\gamma_{\theta t}$ (for more detail, see [15]).

6. CONCLUSIONS

Thus, the results obtained in this work demonstrated that, over a wide temperature range covering several hundreds of degrees Kelvin, the entire set of thermodynamic characteristics of a solid can be adequately described in the framework of the Debye-type self-consistent thermodynamic model even under strongly simplifying assumptions. Further refinement of the results of these calculations requires correct inclusion of the temperature dependence of the Grüneisen parameters γ_θ.

REFERENCES

1. G. Leibfried, *Gittertheorie der mechanischen und thermischen Eigenschaft der Kristalle: Handbuch der Physik* (Springer-Verlag, Berlin, 1955; GIFML, Moscow, 1963).
2. L. D. Landau and E. M. Lifshitz, *Statistical Physics*, 3rd ed. (Nauka, Moscow, 1976; Pergamon, Oxford, 1980), Part 1.
3. P. Flubacher, A. J. Leadbetter, and J. A. Morrison, Philos. Mag. **4** (39), 273 (1959).
4. D. Gerlich, B. Abeles, and R. E. Miller, J. Appl. Phys. **36** (1), 76 (1965).
5. A. J. Leadbetter, J. Phys. C **1** (2), 1481 (1968); J. Phys. C **1** (2), 1489 (1968).
6. V. Yu. Bodryakov and V. M. Zamyatin, Fiz. Met. Metallogr. **85** (4), 18 (1998).
7. V. Yu. Bodryakov and V. M. Zamyatin, Metally, No. 4, 123 (1999).
8. V. Yu. Bodryakov and V. M. Zamyatin, Teplofiz. Vys. Temp. **38** (5), 724 (2000).
9. V. Yu. Bodryakov, A. A. Povzner, and O. G. Zelyukova, Fiz. Tverd. Tela (St. Petersburg) **40** (9), 1581 (1998) [Phys. Solid State **40**, 1433 (1998)].
10. V. Yu. Bodryakov, V. V. Petrushkin, and A. A. Povzner, Fiz. Met. Metallogr. **89** (4), 5 (2000).
11. V. Yu. Bodryakov and A. A. Povzner, Fiz. Met. Metallogr. **89** (6), 21 (2000).
12. V. Yu. Bodryakov, V. V. Petrushkin, and A. A. Povzner, Fiz. Met. Metallogr. **90** (6), 45 (2000).
13. V. Yu. Bodryakov, A. A. Povzner, and O. G. Zelyukova, Metally, No. 2, 79 (2000).
14. V. Yu. Bodryakov, Solid State Commun. **83** (12), 1053 (1992).
15. S. I. Novikova, *Thermal Expansion of Solids* (Nauka, Moscow, 1974).
16. *Thermodynamic Properties of Individual Compounds*, 3rd ed., Ed. by V. P. Glushko (Nauka, Moscow, 1979), Vol. 2, Book 1.
17. L. A. Novitskiĭ and I. G. Kozhevnikov, *Thermal Properties of Materials at Low Temperatures* (Mashinostroenie, Moscow, 1975).
18. I. N. Frantsevich, F. F. Voronov, and S. A. Bakuta, *Elastic Constants and Elastic Moduli of Metals and Nonmetals* (Naukova Dumka, Kiev, 1982).
19. L. D. Landau and E. M. Lifshitz, *Course of Theoretical Physics*, Vol. 7: *Theory of Elasticity*, 4th ed. (Pergamon, New York, 1986; Nauka, Moscow, 1987).

Translated by O. Borovik-Romanova

Physics of the Solid State, Vol. 45, No. 7, 2003, pp. 1260–1266. Translated from Fizika Tverdogo Tela, Vol. 45, No. 7, 2003, pp. 1202–1208.

SEMICONDUCTORS AND DIELECTRICS

Mechanism of *F*-Center Luminescence in Anion-Defective Aluminum Oxide Single Crystals

V. S. Kortov, I. I. Mil'man, S. V. Nikiforov, and V. E. Pelenev

Ural State Technical University, ul. Mira 19, Yekaterinburg, 620002 Russia

e-mail: kortov@ustu.ru

Received November 1, 2002

Abstract—New experimental data illustrating the effect of deep traps on the luminescence properties of anion-defective α-Al_2O_3 single crystals are presented. It was established that deep traps have electronic nature and their filling occurs through photoionization of *F* centers and is accompanied by $F \longrightarrow F^+$-center conversion. Model concepts were developed that describe the luminescence mechanism in anion-defective aluminum oxide single crystals with inclusion of thermal ionization of the excited *F*-center states. The validity of the model was supported by experimental data obtained in a study of thermoluminescence, thermally stimulated exoelectron emission, and thermally stimulated electrical conductivity. *© 2003 MAIK "Nauka/Interperiodica".*

1. INTRODUCTION

The luminescence properties of anion-defective aluminum oxide single crystals grown in reductive conditions are a subject of intense study in connection with their application in the dosimetry of ionizing radiations [1–5]. Investigation of the luminescence mechanisms that are operative in the temperature range 300–600 K is of the most interest. In this region, coinciding with the main peak of thermoluminescence (TL), one observes quenching of the *F*-center luminescence and the attendant TL features, more specifically, a dependence of the TL yield in the main peak at 450 K on the heating rate and a decrease in the average activation energy when the fractional glow technique is applied [6]. Establishment of the role played by deep trapping centers in this process has highlighted progress in the understanding of the nature of quenching. It has been revealed, in particular, that the occupation of deep traps is directly connected with the above-mentioned TL features. The results obtained were interpreted within a model of an interactive trap system; according to this model, quenching sets in as a result of competing capture of the carriers, which are released during the formation of the main TL peak, by deep traps. The carrier trapping cross section by deep traps was assumed to be a temperature-dependent process, which permitted us to achieve a good enough fit of the experimental data to the model concepts [7].

At the same time, our studies of electrical properties other than the TL revealed that some of the features of the thermally stimulated electron emission (TSEE) observed in the same crystals cannot be accounted for in terms of the above model. The temperature positions of the main peaks in TSEE and TL roughly coincide. However, unlike the TL, the TSEE yield in the 450-K peak does not depend on the crystal heating rate and the average activation energy does not decrease within this peak [6]. According to the data quoted in [8], the thermally stimulated conductivity (TSC) of the crystals under study likewise does not depend on the heating rate.

The present communication reports on a further study of the part played by deep traps in the mechanism of *F*-center luminescence in aluminum oxide, as well as on a broadening of the model concepts to cover experimental results, both new and obtained earlier.

2. SAMPLES AND EXPERIMENTAL TECHNIQUES

The study was conducted on samples of nominally pure anion-defective α-Al_2O_3 single crystals grown by directional crystallization in severe reductive conditions due to the presence of graphite; this technique produces a high concentration of anion vacancies (10^{17} cm^{-3}). The method employed to fill the deep traps and measure the TL was described in [7]. In studying radioluminescence (RL), the sample was excited by a BIS-10 $^{90}Sr/^{90}Y$ beta source with an activity of 3 mCi. The dose rate at the sample was 0.05 Gy/min. To reduce the effect of TL on the RL studies, the sample was heated to 580 K at a rate of 5 K/s prior to each measurement to deplete the traps responsible for the main peak of α-Al_2O_3, followed by rapid cooling to a given temperature. Interference filters were used to isolate the spectral luminescence bands. Optical absorption (OA) spectra were taken with a Specord M-40 spectrophotometer. The spectra of photostimulated electron emis-

1063-7834/03/4507-1260$24.00

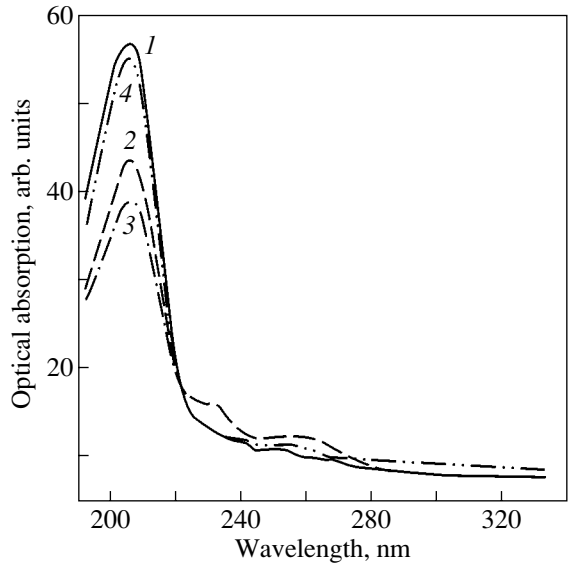

Fig. 1. Optical absorption spectra of samples of anion-defective aluminum oxide obtained in different deep-trap states: (*1*) deep traps not filled intentionally, (*2*) the deepest trap filled at 775 K, (*3*) both deep traps filled at 620 K, and (*4*) after filling, both deep traps depleted by heat treatment at 1220 K for 15 min.

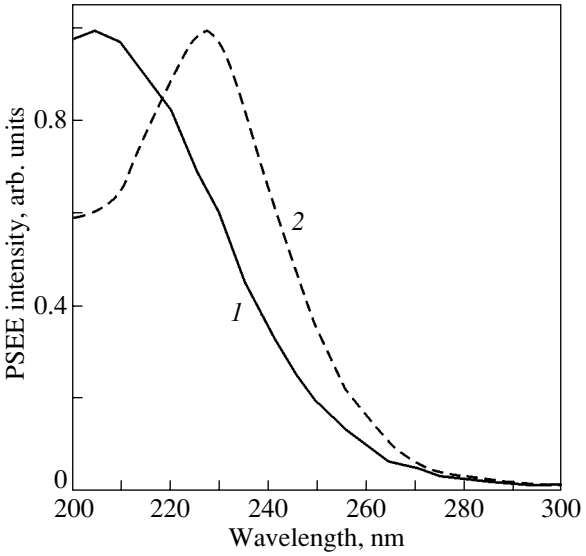

Fig. 2. PSEE spectra of anion-defective aluminum oxide: (*1*) starting sample and (*2*) after illumination by light (200 nm, 300 s).

sion (PSEE) were measured in a ~10^{-5} Pa vacuum with a secondary-emission multiplier. The photon energy range required (4.1–6.2 eV) was covered using a deuterium lamp with a monochromator.

3. RESULTS AND DISCUSSION

Deep traps in anion-defective α-Al_2O_3 crystals were identified at temperatures of 730 and 880 K [7]. Despite the reliably established effect of deep traps on the luminescence properties of the crystals under study, many aspects of their filling still remain unclear. The OA of the anion-defective aluminum oxide crystals with deep traps in different states was investigated to determine the origin of the carriers and their sign in the course of deep-trap filling. The results obtained are displayed in Fig. 1. We readily see that, as the deep traps are filling, the OA band intensity at 205 nm, which is associated with the *F* centers, decreases, while the intensities of the bands at 230 and 259 nm, originating from the F^+ centers, increase. High-temperature heat treatment restores the band intensities to their initial level. These results suggest that the deep traps are filled by electrons when the *F* centers are photoionized, with this process being accompanied by a rise in the F^+-center concentration.

The $F \longrightarrow F^+$-center conversion in the *F*-center absorption band of our crystals becomes particularly manifest in studies of PSEE spectra due to the high density of optical excitation of the thin (about 100-nm thick) surface layer serving as an electron emitter (Fig. 2). The PSEE spectrum has a maximum in the region of the *F*-center optical absorption at 205 nm (curve *1*). This suggests that the electrons we observe arise during photoionization of the *F* centers. Following exposure of the sample to light with a wavelength of 205 nm for a few minutes, the PSEE spectrum was observed to shift. The maximum of the spectrum was located now at 230 nm, which corresponds to the position of the F^+-center absorption peak (curve *2*). The data illustrated in curves *1* and *2* in Fig. 2 directly illustrate the $F \longrightarrow F^+$-center conversion.

The change in the relative concentrations of the *F* and F^+ centers caused by the deep-trap filling modifies the TL spectral response in the main peak. As shown by

Thermoluminescence intensity *I* of the main peak in the luminescence bands of F^- and F^+ centers

Sample no.	*I* (420 nm)/*I* (330 nm)	
	before deep-trap filling	after deep-trap filling
1	5.7	0.95
2	6.2	0.91
3	6.1	1.21
4	6.7	0.77
5	7.0	1.22
6	6.6	1.18

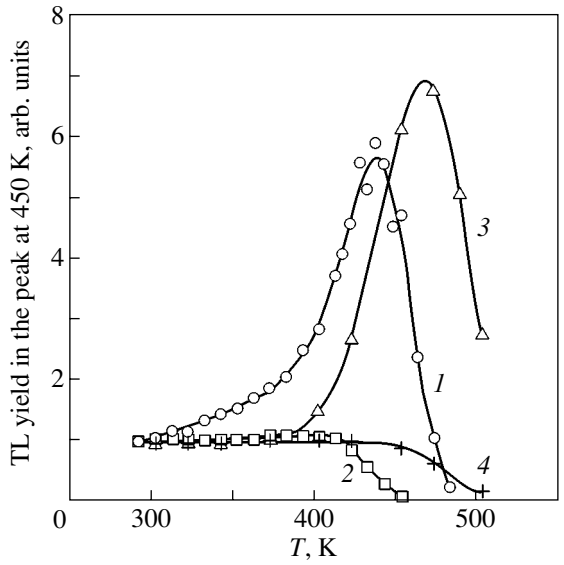

Fig. 3. TL yield in the dosimetric peak plotted vs. the temperature of excitation by (*1*, *3*) UV light and (*2*, *4*) beta radiation. (*1*, *2*) Experiment and (*3*, *4*) calculation.

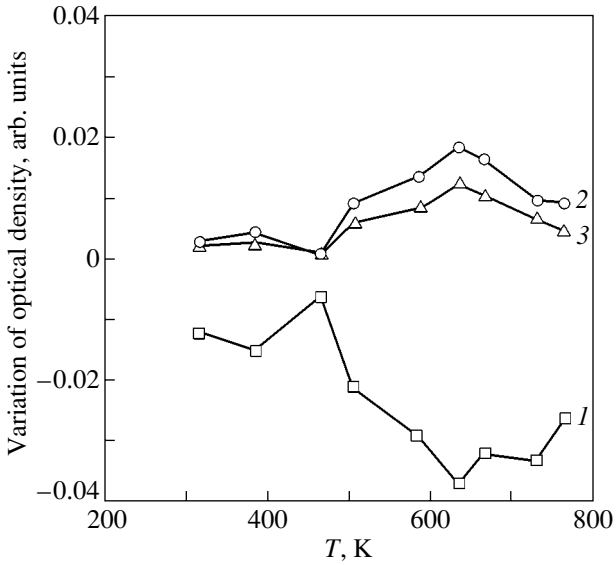

Fig. 4. Variation of optical density in the absorption bands of *F* (205 nm, curve *1*) and F^+ centers (230 nm, curve *2*; 259 nm, curve *3*) following 5-min illumination by unfiltered UV light of a deuterium lamp performed at various temperatures.

measurements of the TL intensity ratio in the *F* and F^+ luminescence bands (420 and 330 nm, respectively) conducted before and after the deep-trap filling, the 420-nm luminescence band is dominant in the starting crystals. After the deep-trap filling has come to completion, the intensities of the 420- and 330-nm bands become comparable (see table), which is in accord with the above-mentioned F^+-center concentration growth features observed to occur under deep-trap filling.

These results stress the need to modify the model describing the mechanisms of thermally stimulated processes in the crystals under study. Note the following point. In [7], the temperature dependence of the carrier trapping probability to deep levels was determined by that of the trapping cross section:

$$\delta(T) = \delta_0 \frac{C\exp(-W/kT)}{1 + C\exp(-W/kT)}, \qquad (1)$$

where *W* is the quenching activation energy, *C* is a quenching constant, *T* is the absolute temperature, *k* is the Boltzmann constant, and δ_0 is a temperature-independent factor. In this model, the function $\frac{C\exp(-W/kT)}{1 + C\exp(-W/kT)}$ is identical to the relation used to describe electron transfer from excited *F*-center levels in CaO to the conduction band as a result of thermal ionization [9]. Thermal ionization of excited states in *F*-type centers was also observed earlier in alkali halide crystals [10]. Some of the stages in this process may also be expected to occur in α-Al_2O_3. In particular, the electrons released from TL-active traps and trapped on the excited levels of *F* centers may again end up in the conduction band through thermal ionization, from where they can be captured by deep traps. If the latter are fully occupied, the probability of the electrons returning from the conduction band to the *F*-center excited levels increases, thus bringing about an increase in the TL yield in their luminescence band. Thus, the parameters of the main TL peak at 450 K turn out to be sensitive to the state of the deep traps, more specifically, to the degree of their filling by carriers, exactly what was observed by us experimentally in [7]. In such an approach, the quenching activation energy *W* can carry the meaning of the energy of thermal ionization of the *F*-center excited state.

The existence of thermal ionization of *F*-center excited states requires experimental substantiation. To do this, we carried out a comparative study of the temperature dependences of the TL yield in the 450-K peak in crystals excited by UV light in the *F*-center absorption band and by beta radiation of the $^{90}Sr/^{90}Y$ source. As seen from Fig. 3, the TL yield increases with UV excitation temperature but is independent of excitation temperature when irradiated by beta radiation. A similar growth in the TL yield of UV-excited anion-defective aluminum-oxide samples with increasing excitation temperature was reported in [11]. It thus follows that the increase in the main-trap filling probability with increasing temperature is not connected in any way with the temperature dependence of the trapping cross section but is rather due to the temperature dependence of the *F*-center ionization efficiency observed under UV excitation.

Another series of experiments was devoted to the variation of the optical absorption band intensity of the F and F^+ centers with the temperature of the sample after its excitation with unfiltered UV light. The results are presented graphically in Fig. 4. It is seen that, as the temperature at which the spectrum was measured increases, the intensity of the 205-nm band associated with the F centers decreases and the intensities of the 230- and 259-nm bands belonging to the F^+ centers increase. The relative variation of the band intensity also increases with temperature. This experiment indicates that the efficiency of the $F \longrightarrow F^+$ conversion grows with temperature as a consequence of thermal ionization of the F-center excited states. The assumption of the existence of this process underlies the model proposed here to describe the luminescence mechanisms of anion-defective aluminum oxide crystals.

According to present-day concepts, the electronic structure of the F center in aluminum oxide is believed to resemble that of the helium quasi-atom [12]. The ground state is ^1S. There are also a singlet (^1P) and a triplet (^3P) excited state. Excitation of the F center corresponds to the $^1S \longrightarrow {}^1P$ transition [the absorption band peaking at 6.1 eV (205 nm)]. Excitation by light into this band gives rise to the luminescence peaking at 3.0 eV and having a decay time of 36–40 ms (the ^3P–^1S transition). The highest excited state of the F center lies close to the conduction band bottom. Excitation into the 6.1-eV band brings about optical ionization of the F centers and electron trapping from the conduction band, which results in an increase in the F^+-center concentration.

Figure 5 presents the energy band diagram of the model of the luminescence mechanism for the crystals under study, including thermal ionization of the F centers. The modification of the well-known interactive-trap system [13] is based on the assumption that thermal ionization of the F-center excited states is a possible common cause of the probabilities of trapping into the main and deep states being temperature-dependent. The diagram corresponds to optical excitation into the F-center absorption band. In the case of RL (for instance, initiated by beta radiation), excitation (the f transition) occurs in the region of band-to-band transitions. In this diagram, N is the main trap, M_1 and M_2 are deep traps, and ^1P and ^3P are excited states of the F center. When excited by light in the absorption band, the center transfers to the ^1P excited state (the f transition). The P_F transition brings about thermal ionization of the excited state (^3P). The thermal ionization reduces the fraction of radiative intracenter transitions and is the main cause of photo- and radioluminescence quenching in the crystals under study. Optical (w_1 transition) or thermal ionization produces an F^+ center ($F^* - e = F^+$), which can trap an electron (γ transition) to become again an excited F center ($F + e = F^*$). The F-center luminescence (420 nm) corresponds to the w_3 transition. The free electrons that form during ionization of the F centers can be captured subsequently into the main or deep traps. The TL modeling in [7] did not include the process of thermal ionization of the F centers; by contrast, the model proposed here takes this process into account:

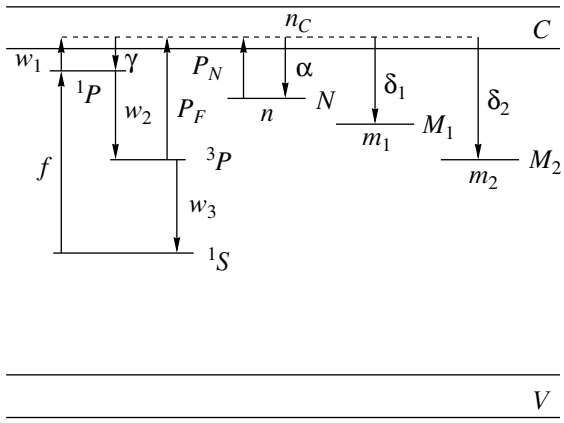

Fig. 5. Model of thermally stimulated processes in anion-defective aluminum oxide crystals.

$$\frac{dn}{dt} = -P_N n + \alpha(N-n)n_c, \tag{2}$$

$$\frac{dm_1}{dt} = \delta_1(M_1 - m_1)n_c, \tag{3}$$

$$\frac{dm_2}{dt} = \delta_2(M_2 - m_2)n_c, \tag{4}$$

$$\frac{dn_c}{dt} = P_N n - \delta_1(M_1 - m_1)n_c - \delta_2(M_2 - m_2)n_c - \gamma n_{F^+} n_c + P_F n_{3p} - \alpha(N-n)n_c + w_1 n_{1p}, \tag{5}$$

$$\frac{dn_{F^+}}{dt} = P_F n_{3p} - \gamma n_{F^+} n_c + w_1 n_{1p}, \tag{6}$$

$$\frac{dn_{3p}}{dt} = w_2 n_{1p} - P_F n_{3p} - w_3 n_{3p}, \tag{7}$$

$$\frac{dn_{1p}}{dt} = f + \gamma n_{F^+} n_c - w_1 n_{1p} - w_2 n_{1p}, \tag{8}$$

$$I_L = w_3 n_{3p}. \tag{9}$$

At any instant of time, the system under study obeys the charge neutrality condition

$$n + m_1 + m_2 + n_c = n_{F^+}. \tag{10}$$

In these equations, N, M_1, and M_2 (cm^{-3}) are the total concentrations of the dosimetric and deep traps, respectively; n, m_1, m_2, n_{1p}, and n_{3p} (cm^{-3}) are the concentra-

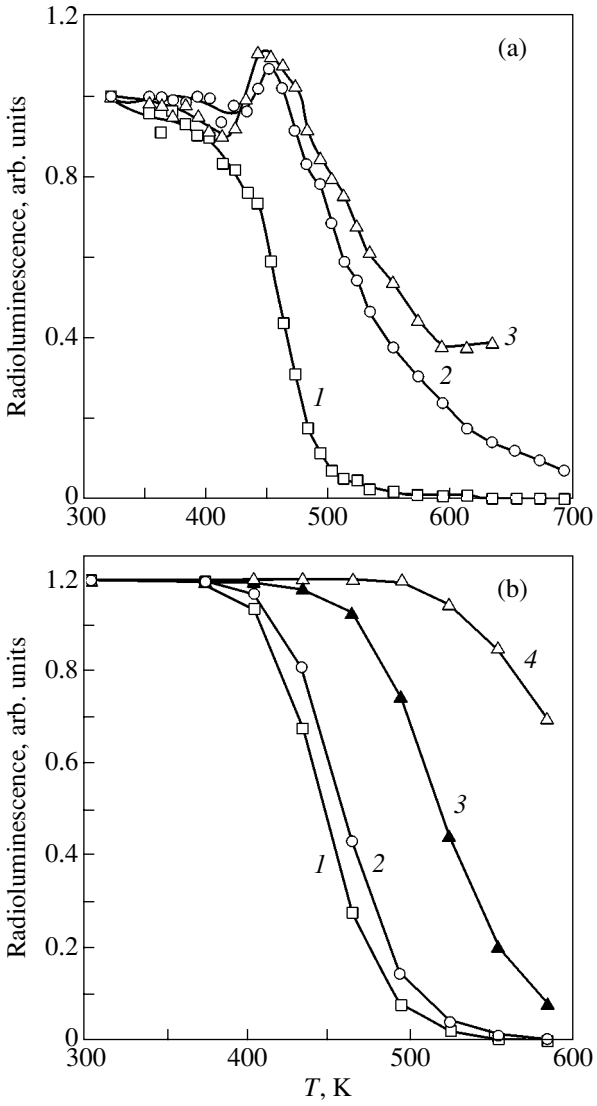

Fig. 6. Radioluminescence quenching in the *F*-center luminescence band obtained for different deep-trap states. (a) Experiment: (*1*) deep traps not filled intentionally, (*2*) the deepest trap filled at 775 K, and (*3*) both deep traps filled at 620 K. (b) Calculation: the filling of the first deep trap m_1/M_1 is (*1*) 0, (*2*) 0.1, (*3*) 0.8, and (*4*) 1.0.

tions of the filled N, M_1, M_2, ^1P, and ^3P levels, respectively; N_{F^+} (cm^{-3}) is the F^+-center concentration; n_c (cm^{-3}) is the electron concentration in the conduction band; α, δ_1, δ_2, and γ ($cm^3\ s^{-1}$) are the carrier trapping coefficients for the corresponding levels (Fig. 5); w_1, w_2, and w_3 (s^{-1}) are the transition probabilities; f ($cm^{-3}\ s^{-1}$) is the excitation intensity; and I_L is the luminescence intensity. The thermal ionization probability for the excited state of the F center (^3P) can be found from the expression $P_F = C\exp(-W/kT)$, where W is the excited-state ionization energy (quenching activation energy). The transition probability w_1 is assumed to be temperature independent, because the ^1P level is located close to the conduction band bottom. The probability of depletion of the dosimetric traps is given by the expression $P_N = S\exp(-E/kT)$, where E is the trap depth and S is a frequency factor.

This model was used to calculate the temperature dependences of the steady-state photo- and radioluminescence intensities for a range of deep-trap occupations. The coupled equations (2)–(9) were solved by the numerical method proposed by Gear, and the results were presented in the form of plots of the photo- and radioluminescence intensities vs. time. The dependences of these quantities on excitation temperature characterized the luminescence quenching process. The parameters used in the calculations were identical to those employed earlier when considering thermoluminescence within the interactive trap system model (quenching parameters, transition probabilities, trap concentrations) [7]: $E = 1.3$ eV, $S = 10^{13}\ s^{-1}$, $\alpha = 10^{-14}\ cm^3/s$, $\delta_1 = 10^{-12}\ cm^3/s$, $\delta_2 = 10^{-14}\ cm^3/s$, $\gamma = 10^{-11}\ cm^3/s$, $N = 10^{13}\ cm^{-3}$, $M_1 = 10^{14}\ cm^{-3}$, $M_2 = 10^{14}\ cm^{-3}$, $W = 1.1$ eV, and $C = 10^{11}\ s^{-1}$. The criterion for selecting the remaining parameters ($w_1 = 1\ s^{-1}$, $w_2 = 10\ s^{-1}$, $w_3 = 1\ s^{-1}$, $f = 10^{10}\ cm^{-3}/s$) was the obtainment of a stable solution providing the best fit to the experimental relations. The variable parameters were the temperature and deep-trap filling (m_1/M_1). A test of the model showed the radio- and photoluminescence quenching curves to be well approximated analytically. We readily see that, in full agreement with the observations (Fig. 6), the efficiency of thermal quenching decays with deep-trap filling.

The above model was employed to calculate the dependence of the main-trap filling on sample temperature under irradiation. It was established that the TL yield grows with increasing temperature under photoexcitation in the *F*-center absorption band and does not depend on temperature under excitation in the interband transition region, which corresponds to the case of beta excitation. The calculated curves *3* and *4* are close qualitatively to the experimentally observed curves *1* and *2* (Fig. 3).

The modeling of the TL, TSEE, and TSC features observed in anion-defective aluminum oxide crystals was done with the use of the band diagram presented in Fig. 5. Because of the absence of the ^1S–^1P transition corresponding to excitation at the instant of measurement, the quantity f in Eq. (8) was assumed to be zero. The data obtained in the modeling show that thermal ionization of the excited states of the *F* center results in the integrated intensity of the TL peak becoming dependent on the heating rate. The relative variation of the integrated intensity decreases with increasing deep-trap filling, exactly what was observed experimentally in [7].

The dependences of the TSEE yield and of TSC on the heating rate were modeled assuming the intensities of these effects to be proportional to the electron con-

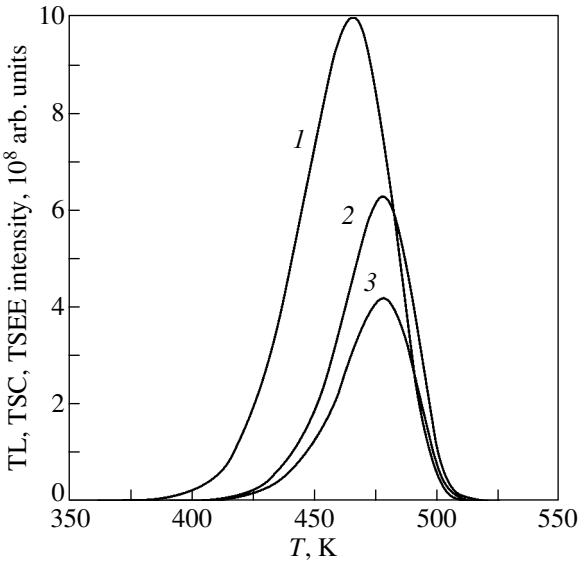

Fig. 7. (*1*) TL, (*2*) TSC, and (*3*) TSEE curves calculated in terms of the interactive model with inclusion of the *F*-center thermal ionization.

centration in the conduction band, i.e., to the quantity n_c for which Eqs. (2)–(8) were solved.

The results of the modeling showed the appearance of the main TL peak at 450 K to be accompanied by TSEE and TSC peaks shifted relative to the TL maximum by 10–15 K toward higher temperatures (Fig. 7). Unlike TL, the magnitude of TSC and the TSEE yield do not depend on the heating rate, which is in accord with the experimental data from [6, 8].

The proposed model is also capable of explaining the experimentally observed [7] effect of deep-trap occupation on the TL yield in the main peak (sensitivity) and its shape.

This model also offers an explanation for the experimentally observed leveling off of TL sensitivity (estimated from the TL yield in the main peak at 450 K) in samples of anion-defective aluminum oxide under deep-trap filling. It was established that deep-trap filling in a series of samples differing in sensitivity to within an order of magnitude reduces the scatter of this parameter by a factor 1.5–2. Calculations show that one of the reasons for the scatter in sensitivity could be the difference in the total deep-trap concentration between the samples. After the deep traps have filled to a state close to saturation, the sample sensitivity no longer depends on their presence. Another possible reason for the observed decrease in the sensitivity scatter could be the formation of an additional number of F^+ centers in the course of deep-trap filling. According to [14], the TL sensitivity of the crystals studied correlates with the F^+-center concentration. The F^+-center concentration in samples with deep traps filled to saturation is high and approximately equal. Also, in samples with an initially low sensitivity, the centers formed in photoionization of the *F* centers provide the largest contribution to the total F^+-center concentration. High-sensitivity samples have from the outset a high F^+-center concentration. This conjecture is supported by the observation that, in samples with a low TL sensitivity, the relative growth of this parameter with the filling of deep traps is substantially larger than that in the originally high-sensitivity samples. Filling of the deep traps levels off the F^+-center concentration in the samples and, as a consequence, reduces the spread in their sensitivity.

4. CONCLUSIONS

To sum up, we have presented new experimental data on the role of deep traps in the luminescence mechanism of anion-defective aluminum oxide single crystals. It was found that the deep traps are filled as a result of *F*-center photoionization and that this process is accompanied by an increase in the F^+-center concentration and a decrease in the *F*-center concentration. A model was put forward describing the mechanism of photo-, radio-, and thermoluminescence of anion-defective aluminum oxide single crystals with inclusion of thermal ionization of the *F*-center excited states. This model accounts for the following experimental observations: thermal quenching of the photo- and radioluminescence; the temperature dependence of trap filling under photoexcitation in the *F*-center absorption band and the absence of this dependence when excitation is made in the interband transition region; the effect of deep-trap filling on the thermoluminescence yield, its dependence on the heating rate, and the shape of the thermoluminescence curve; and the independence of the TSEE yield and TSC value from the heating rate.

ACKNOWLEDGMENTS

This study was supported by the Ural Scientific-Educational Center, project “Promising Materials” (CRDF award no. REC-005).

REFERENCES

1. V. S. Kortov, I. I. Milman, and S. V. Nikiforov, Radiat. Prot. Dosim. **100** (1–4), 75 (2002).
2. S. Vinceller, G. Molnar, A. Berkane-Krachai, and P. Iacconi, Radiat. Prot. Dosim. **100** (1–4), 79 (2002).
3. Y. S. Horowitz, Y. Einav, S. Biderman, and L. Oster, Radiat. Prot. Dosim. **100** (1–4), 135 (2002).
4. G. Molnar, M. Benabdesselam, J. Borossay, *et al.*, Radiat. Prot. Dosim. **100** (1–4), 139 (2002).
5. A. E. Akselrod and M. S. Akselrod, Radiat. Prot. Dosim. **100** (1–4), 217 (2002).

6. I. I. Mil'man, V. S. Kortov, and V. I. Kirpa, Fiz. Tverd. Tela (St. Petersburg) **37** (4), 1149 (1995) [Phys. Solid State **37**, 625 (1995)].
7. I. I. Mil'man, V. S. Kortov, and S. V. Nikiforov, Fiz. Tverd. Tela (St. Petersburg) **40** (2), 229 (1998) [Phys. Solid State **40**, 206 (1998)].
8. M. S. Akselrod, N. Agersnap Larsen, V. Whitley, and S. W. S. McKeever, Radiat. Prot. Dosim. **84** (1–4), 39 (1999).
9. L. S. Welch, A. E. Hughes, and G. P. Summers, J. Phys. C: Solid State Phys. **13**, 1791 (1980).
10. R. K. Swank and F. C. Brown, Phys. Rev. **130** (1), 34 (1963).
11. G. Molnar, M. Benabdesselam, J. Borossay, *et al.*, Radiat. Meas. **33** (5), 619 (2001).
12. B. D. Evans, J. Nucl. Mater. **219**, 202 (1995).
13. C. M. Sunta, E. M. Yoshimura, and E. Okuno, J. Phys. D: Appl. Phys. **27**, 852 (1994).
14. S. W. S. McKeever, M. S. Akselrod, L. E. Colyott, *et al.*, Radiat. Prot. Dosim. **84** (1–4), 163 (1999).

Translated by G. Skrebtsov

Physics of the Solid State, Vol. 45, No. 7, 2003, pp. 1267–1271. Translated from Fizika Tverdogo Tela, Vol. 45, No. 7, 2003, pp. 1209–1212.

DEFECTS, DISLOCATIONS, AND PHYSICS OF STRENGTH

Serrated Deformation of a $Pd_{40}Cu_{30}Ni_{10}P_{20}$ Bulk Amorphous Alloy during Nanoindentation

Yu. I. Golovin*, V. I. Ivolgin*, A. I. Tyurin*, and V. A. Khonik**

** Derzhavin Tambov State University, Tambov, 392622 Russia*

e-mail: golovin@tsu.tmb.ru

*** Voronezh State Pedagogical University, ul. Lenina 86, Voronezh, 394611 Russia*

Received November 1, 2002

Abstract—Depth-sensing (indentation) testing is used to study the characteristics of a serrated plastic flow in a $Pd_{40}Cu_{30}Ni_{10}P_{20}$ bulk amorphous alloy, and the boundaries between the regions of serrated and homogeneous plastic deformation are determined. © *2003 MAIK "Nauka/Interperiodica".*

1. INTRODUCTION

Although plastic deformation is always atomically inhomogeneous (contrary to elastic deformation), the physics of plasticity recognizes homogeneous and inhomogeneous flow modes [1–7]. A conventional boundary between these modes is mainly specified by the test temperature T; strain rate $\dot{\varepsilon}$; and history, size, and state of the surface of a sample [2, 5, 8–14]. The position of this boundary depends substantially on the characteristics of the testing machine, in particular, its stiffness, response time, and sensitivity to changes in the deforming force or in the sample size. Traditional equipment, such as an Instron testing machine, makes it possible to record only relatively large jumps of macroscopic deformation with low repetition frequency appearing due to the collective behavior of a huge number of elementary carriers of plastic deformation, while the other possible instabilities of a flow remain undetected. As a result, the statistics of detected jumps are scarce and not representative and the contribution from jumps to the total stored deformation is strongly underestimated.

To study the dynamics and correlation of deformation jumps on a smaller spatial scale (in particular, on the mesoscopic scale), it is necessary to substantially increase the space–time resolution of the equipment and to decrease the sample volume. A higher resolution is also required to analyze the instabilities of a plastic flow in the context of the theory of self-organization in nonequilibrium dissipative media (to which plastically deformed solids belong), since the number of recorded jumps should increase under these conditions and correlation relations between them will be more apparent.

In this work, we used depth-sensing testing to obtain the dependence of the load P on the indentation depth h (an analog of the $\sigma = f(\varepsilon)$ diagram for uniaxial deformation) and the $P(t)$ and $h(t)$ time dependences for submicron regions. The limiting resolutions of modern commercial nanoindentometers are 0.1 nm for the indentation depth, several micronewtons for the load, and 10^{-2} s for the time, which are several orders-of-magnitude higher than those of the standard testing machines. This performance allows one to study fine and rapid jumps, as well as to extend the range of strain rates toward higher values of $\dot{\varepsilon}$ (since $\dot{\varepsilon} \approx dh/hdt$ and h can be 1 μm during depth-sensing testing) and to work on one sample. Apart from these advantages, the factors mentioned above can serve to establish the boundaries of the size-strain-rate invariance for stable and unstable flow modes in nanoscale samples.

Pioneering studies [15–17] on the serrated deformation by nanoindentation were carried out several years ago and dealt with an unstable flow in fcc metals and polycrystalline aluminum–magnesium alloys that had been previously well studied using the methods of macrodeformation [18, 19]. Related information for amorphous alloys is limited, as far as we know, to papers [20, 21], in which multiple deformation nanojumps were detected during local deformation of a palladium-based bulk amorphous alloy by using nanoindentation.

Macroscopic measurements [4] show that, at moderate strain rates ($10^{-5} \le \dot{\varepsilon} \le 10^{-3}$ s^{-1}) and temperatures $T < 400$ K, a flow is localized, whereas at higher temperatures the flow becomes uniform. The transition is assumed to be due to the equalizing of the strain rates and a directed structural relaxation [4, 5, 12, 13]. It is obvious that, at room temperature, this transition is characterized by a very low critical strain rate $\dot{\varepsilon}_c'$, which cannot be achieved under the conventional conditions of active deformation. On the other hand, Kimura and Masumoto [22] showed that, at $\dot{\varepsilon}_c'' \sim 0.1$ s^{-1}, the reverse transition (from inhomogeneous to homogeneous flow) can proceed; the nature of this reverse transition was not discussed.

1063-7834/03/4507-1267$24.00

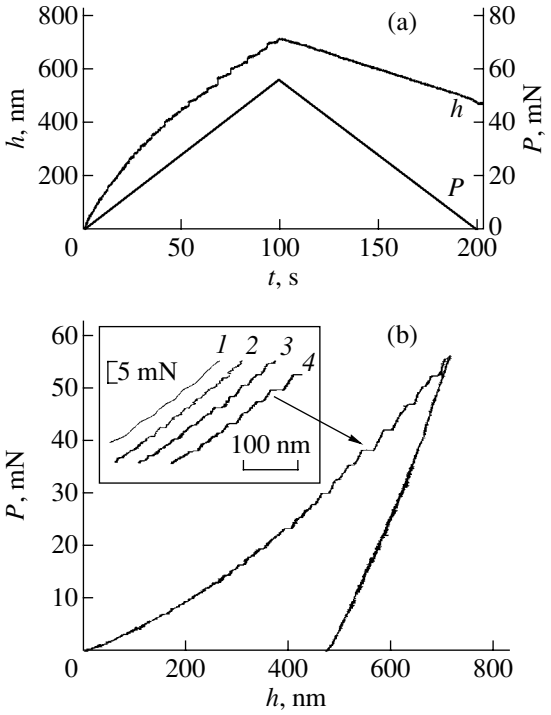

Fig. 1. (a) Typical kinetic dependences of the load $P(t)$ and depth $h(t)$ for dynamic indentation and (b) the corresponding P–h diagram. The inset shows the fragments of the P–h diagram at various values of μ: (*1*) 1120, (*2*) 56, (*3*) 1.12, and (*4*) 0.56 mN s^{-1}.

The purpose of this work is to determine the ranges of stable and unstable plastic flows in a $Pd_{40}Cu_{30}Ni_{10}P_{20}$ bulk amorphous alloy under the conditions of local deformation at various rates and depths and to measure the parameters of jumps and their contribution to the total mass transfer produced by an indenter.

2. EXPERIMENTAL

Bulk samples of a $Pd_{40}Cu_{30}Ni_{10}P_{20}$ amorphous alloy were prepared by water-cooling of the melt in a cylindrical glass ampoule with an inside diameter of 4 mm. After cooling, the glass shell was broken and the rod obtained was cut into pellets 2 mm high. Before measurements, the sample surface was polished with a diamond paste. For investigation, we used an original device developed at the Laboratory of Nanoindentation (TSU) [23, 24]; this computer-aided nanotester employs Berkovich's diamond pyramid, with a depth resolution of 1–10 nm depending on the limiting load and strain rate. The time resolution (the periodicity of discrete readings) was 50 μs, which significantly exceeds (by several orders of magnitude) the capabilities of the corresponding commercial devices and provided a resolution of the jumps with a leading-edge time longer than ~100 μs without integration.

Loading was performed by applying a triangular force pulse P, with the amplitude varied from 50 to 85 mN and the duration τ varied from 20 ms to 500 s, and we simultaneously recorded the time dependences of $P(t)$ and $h(t)$ or the $P(h)$ dependence (Fig. 1). The data obtain were stored on a computer and included more than ten different parameters characterizing the mechanical properties of the thin surface layers of the material being studied. Under the test conditions, the maximum indentation depth in the alloy under study was about 700 nm and no cracks detectable with an optical microscope were observed. We performed about 1000 individual loadings and obtained a data array sufficient for statistical processing of the jumps.

3. RESULTS AND DISCUSSION

A preliminary analysis of the data obtained showed that deformation jumps could appear both in the stage of increasing load and in the stage of unloading but not everywhere over the range of loading parameters covered. For example, the number of jumps in one indentation cycle could change from several tens at low loading rates $\mu = dP/dt$ to zero at $\mu \geq 1$ N/s. Contrary to the jumps in aluminum–magnesium polycrystalline alloys [15–17, 25], the jumps appeared irregularly, and their amplitude Δh varied from several micrometers to several tens of micrometers and was not clearly connected with h or μ. Although our apparatus had the highest resolution available, we could not measure the actual jump duration τ_j for the majority of jumps, as was the case with Al–Mg alloys, since the jumps proceeded much faster (within a time shorter than the digitization time $\tau_d = 50$ μs). With the mean jump amplitude $\Delta h_m \sim 20$ nm, this fact allows us to make a lower estimate of the average velocity of the indentation surface during a jump $\langle v \rangle = \Delta h_m/\tau_d = 10^{-1}$ cm/s. We failed to detect the case of $\tau_j > \tau_d$ for any of the several hundreds of jumps processed; therefore, the actual velocity was believed to be far above this estimate.

For the sake of convenience and comparison with data obtained by other authors, we arranged our data on ~600 jumps according to their value and plotted them as h against $\dot{\varepsilon}$ (Fig. 2), where $\dot{\varepsilon} = (dh/dt)/h$ is the strain rate averaged over the whole locally deformed volume. It is seen from Fig. 2 that, at low $\dot{\varepsilon}$ and high h, the experimental points approach the boundaries (solid lines) of the region studied in the phase space. In other words, we could not determine the minimum $\dot{\varepsilon}$ values and maximum h values at which serrated deformation disappears. Conversely, a clear boundary (marked by dashed lines) between the serrated- and homogeneous-flow modes is observed at high $\dot{\varepsilon}_c$ values. The critical rate increases from 10^{-2} to 10 s^{-1} in the range $0 < h < 100$ nm; at $h > 100$ nm, this rate is virtually independent of h and is equal to $\dot{\varepsilon}_c \approx 10$ s^{-1}. This indirectly indicates

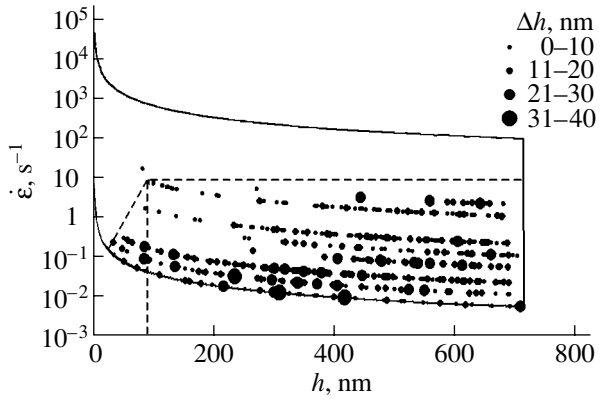

Fig. 2. Region of jumps in the *P*–*h* diagram at various rates of dynamic nanoindentation produced by a symmetrical triangular load pulse (shown by points in the diagram). The region studied is bounded by solid lines. *h* is the indentation depth, and $\dot{\varepsilon}$ is the strain rate.

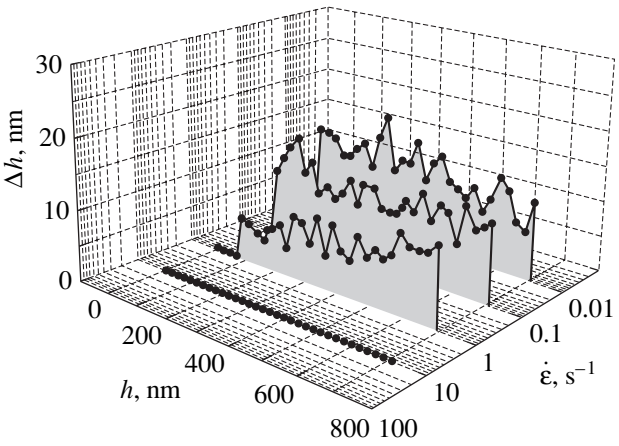

Fig. 3. Dependence of the average jump amplitude Δh_j^i on the strain rate $\dot{\varepsilon}$ and the indentation depth *h*.

that localized shear is retarded by the boundaries of the severely deformed region with a linear size of $R \sim h$ under the indenter at $h \leq 100$ nm. Since neither the number nor the amplitude of jumps changes drastically at $h \geq 100$ nm (Fig. 3), their characteristics may be assumed to be specified by inherent causes rather than by the value of *R*.

The data on the number and amplitude Δh of jumps allow us to estimate their role in the mass transfer produced by the indenter during indentation. Figure 4 shows the fraction of the volume ejected by an individual jump $\alpha = \Delta V_j^i / V_j$ as a function of *h* and $\dot{\varepsilon}$, where $\Delta V_j^i = kh^2 \Delta h_j^i$ is the volume of the material ejected by the *i*th deformation jump Δh_j^i, V_j is the volume of the indentation formed by the end of the *i*th jump, and *k* is the coefficient taking into account the indenter shape (for Berkovich's indenter, $k = 23.969$). Figure 5 illustrates the fraction of volume displaced as a result of serrated deformation $\beta = \sum_j \Delta V_j^i / V_{\max}$ and the number of jumps *N* as a function of τ, where $\sum_j \Delta V_j^i$ is the total volume of the material ejected because of serrated deformation and $V_{\max}$ is the volume of the final indentation. From Fig. 4, it follows that α varies from 0 to 40% depending on *h* and $\dot{\varepsilon}$ and that the boundary between the regions of serrated- and homogeneous-flow modes is rather diffuse.

In recent phenomenological theories, the *N*-shaped dependence of flow stresses on $\dot{\varepsilon}$ has been widely used to explain the limited $\dot{\varepsilon}$ range over which the serrated mode of plastic deformation is observed [19]. Depending on the material and the type of process analyzed, the cause of the occurrence of a segment with a negative slope can be different: local heating and strain aging during a plastic flow, nonmonotonic dependence of the critical stress intensity factor on $\dot{\varepsilon}$ upon cracking, hysteresis during pressure-induced polymorphic phase transformations, etc. In our case, all these mechanisms are unlikely or impossible. Estimates made by a number of authors (see, e.g., [26, 27]) show that the short-term heating in a localized shear band in glass at room temperature does not exceed several tens of degrees

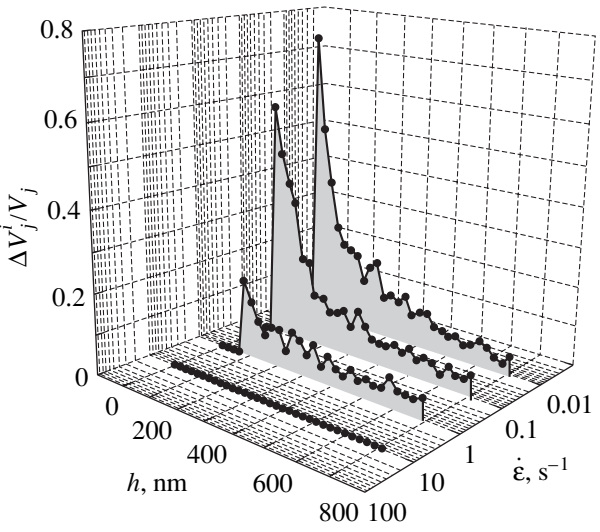

Fig. 4. Variation of the volume fraction $\alpha = \Delta V_j^i / V_j$ of the material ejected by an individual jump Δh_j^i during the formation of an indentation. ΔV_j^i is the volume of the material ejected as a result of the *i*th deformation jump Δh_j^i, and V_j is the volume of the indentation formed by the end of the *i*th jump.

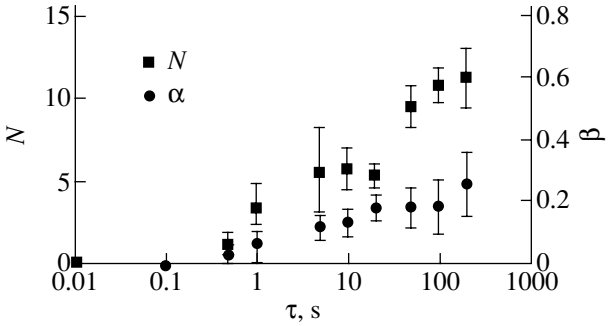

Fig. 5. Variation of the number of jumps $N = f(\tau)$ and the volume fraction $\beta = \sum_j \Delta V_j^i / V_{max} = f(\tau)$ displaced as a result of serrated deformation. $\sum_j \Delta V_j^i$ is the total volume of the material ejected because of serrated deformation, τ is the total loading time, and V_{max} is the volume of the final indentation.

Celsius even in the adiabatic mode. Moreover, this heating cannot decrease with increasing $\dot{\varepsilon}$. A thorough electron microscopic examination of the surface of an indentation and the near-indentation region shows that the deformation jumps occurring in an amorphous palladium alloy during nanoindentation are caused by localized plastic deformation rather than by fracture [21]; therefore, cracking cannot cause the transitions detected. On the other hand, the time of reaching a given indentation depth decreases with increasing $\dot{\varepsilon}$, which should lead to a decrease in the probability of initiating a jump and to a decrease in the total number of jumps in the case where jumps are thermally activated. This behavior was observed experimentally (Fig. 5).

The unstable flow during indentation can arise not only because of the formation of localized shear bands but also due to phase transformations induced by a high pressure under the indenter. For example, Kim *et al.* [26] observed the formation of nanocrystals in localized shear bands during low-rate nanoindentation of an amorphous palladium alloy at room temperature. It takes a rather long time for the nanocrystals to form at such a low temperature. The total loading time τ in [26] was 10 s. As τ decreases (with increasing $\dot{\varepsilon}$ in all stages of indentation), a new phase may have no time to nucleate and grow and this mechanism of unstable flow can be blocked. As a result, the fraction of serrated deformation in the total volume should decrease with τ. To reveal the nature of the transition from the serrated-deformation mode to the homogeneous one with increasing $\dot{\varepsilon}$ at room temperature, special investigations are required.

4. CONCLUSION

Thus, we have shown that the continuous local deformation of a $Pd_{40}Cu_{30}Ni_{10}P_{20}$ amorphous alloy is accompanied by a serrated plastic flow during both loading and unloading. The boundaries of the region where the serrated-flow mode arises in the h–$\dot{\varepsilon}$ phase space during nanoindentation were determined, and the basic characteristics of jumps (their amplitude, number, fraction in the mass transfer produced by the indenter, etc.) were found.

ACKNOWLEDGMENTS

This work was supported by the Russian Foundation for Basic Research (project no. 01-02-16573), the Ministry of Education of the Russian Federation (grant nos. E00-3.4-48, E02-3.4-263), and the U.S. Civilian Research and Development Foundation for the Independent States of the Former Soviet Union (CRDF) (grant no. RP1-2320-VO-02).

REFERENCES

1. A. S. Bakai, Mater. Sci. Forum **123–125**, 145 (1993).
2. A. M. Gleĭzer and B. V. Molotilov, *Structure and Mechanical Properties of Amorphous Alloys* (Metallurgiya, Moscow, 1992).
3. L. A. Davis and S. Kavesh, J. Mater. Sci. **10**, 435 (1975).
4. V. A. Khonik, K. Kitagawa, V. A. Mikhailov, and A. Yu. Vinogradov, J. Appl. Phys. **83** (11), 5724 (1998).
5. V. A. Khonik, Phys. Status Solidi A **177**, 173 (2000).
6. *Amorphous Metallic Alloys*, Ed. by F. E. Lyuborskiĭ (Butterworth, London, 1983; Metallurgiya, Moscow, 1987).
7. Yu. A. Osip'yan, Vestn. Akad. Nauk SSSR **9**, 3 (1987).
8. C. A. Pampillo, J. Mater. Sci. **10** (7), 1194 (1975).
9. T. Masumoto and R. Maddin, Mater. Sci. Eng. **19** (1), 1 (1975).
10. T. Masumoto and T. Murata, Mater. Sci. Eng. **25**, 71 (1976).
11. H. Kimura and T. Masumoto, Acta Metall. **28**, 1663 (1980).
12. A. Yu. Vinogradov, V. A. Mikhaĭlov, and V. A. Khonik, Fiz. Tverd. Tela (St. Petersburg) **39** (5), 885 (1997) [Phys. Solid State **39**, 787 (1997)].
13. A. Yu. Vinogradov, K. Kitagava, and V. A. Khonik, Fiz. Tverd. Tela (St. Petersburg) **41** (12), 2167 (1999) [Phys. Solid State **41**, 1989 (1999)].
14. V. Z. Bengus, E. D. Tabachnikova, V. V. Gaĭko, *et al.*, Metallofizika (Kiev) **8** (6), 3 (1986).
15. G. Berces, N. Q. Chinh, A. Juhasz, and J. Lendvai, Acta Mater. **46** (6), 2029 (1998).
16. G. Berces, N. Q. Chinh, A. Juhasz, and J. Lendvai, J. Mater. Res. **13** (6), 1411 (1998).
17. N. Q. Chinh, Gy. Horvath, Zs. Kovacs, and J. Lendvai, Mater. Sci. Eng. **324**, 219 (2002).

18. M. A. Lebedkin and L. R. Dunin-Barkovskiĭ, Zh. Éksp. Teor. Fiz. **113** (5), 1816 (1998) [JETP **86**, 993 (1998)].
19. M. Lebyodkin, Y. Brechet, Y. Estrin, and L. Kubin, Acta Mater. **44** (11), 4531 (1996).
20. Yu. I. Golovin, V. I. Ivolgin, V. A. Khonik, *et al.*, Scr. Mater. **45**, 947 (2001).
21. R. Vaidyanathan, M. Dao, G. Ravichandran, and S. Surech, Acta Mater. **49**, 3781 (2001).
22. H. Kimura and T. Masumoto, in *Amorphous Metallic Alloys*, Ed. by F. E. Lyuborskiĭ (Butterworth, London, 1983; Metallurgiya, Moscow, 1987), p. 183.
23. Yu. I. Golovin, V. I. Ivolgin, V. V. Korenkov, and A. I. Tyurin, Zh. Tekh. Fiz. **70** (5), 82 (2000) [Tech. Phys. **45**, 605 (2000)].
24. Yu. I. Golovin, V. I. Ivolgin, V. V. Korenkov, *et al.*, Kondens. Sredy Mezhfaz. Granitsy **3** (2), 122 (2001).
25. Yu. I. Golovin, V. I. Ivolgin, and M. A. Lebedkin, Fiz. Tverd. Tela (St. Petersburg) **44** (7), 1254 (2002) [Phys. Solid State **44**, 1310 (2002)].
26. J.-J. Kim, Y. Choi, S. Suresh, and A. S. Argon, Science **295**, 654 (2002).
27. W. J. Wright, R. B. Schwarz, and W. D. Nix, Mater. Sci. Eng. A **319–321**, 229 (2001).

Translated by K. Shakhlevich

Physics of the Solid State, Vol. 45, No. 7, 2003, pp. 1272–1279. Translated from Fizika Tverdogo Tela, Vol. 45, No. 7, 2003, pp. 1213–1220.

MAGNETISM AND FERROELECTRICITY

Domain Dynamics in (210)-Oriented Single-Crystal $(Bi,Y,Lu,Pr)_3(Fe,Ga)_5O_{12}$ Films

V. V. Randoshkin, V. A. Polezhaev, Yu. N. Sazhin, and R. R. Sysoev

Joint Self-Financing Laboratory Magnitooptoelektronika, Institute of General Physics (Russian Academy of Sciences) and Mordovia State University, ul. Bol'shevistskaya 68, Saransk, 430000 Russia

Received July 31, 2002; in final form, December 10, 2002

Abstract—Using high-speed photography, dynamic magnetic structures are studied in Bi-containing (210)-oriented single-crystal films of $(Bi,Y,Lu,Pr)_3(Fe,Ga)_5O_{12}$ grown through liquid-phase epitaxy from an overcooled solution in the melt on $(Gd,Ga)_3(Mg,Zr,Ga)_5O_{12}$ substrates. At various temperatures, the ranges of pulsed magnetic fields are determined in which unidirectional anisotropy of domain wall velocity and spatial distortions of moving domain walls are observed. © *2003 MAIK "Nauka/Interperiodica".*

Domain wall (DW) dynamics in Bi-containing garnet-ferrite (GF) single-crystal films with orthorhombic magnetic anisotropy, in contrast to that in magnetically uniaxial films, exhibits some specific features, such as the anisotropy of DW velocity, distortion of the shape of dynamic domains, unsteady motion of DWs, and the local rotation of magnetization near moving DWs [1–10]. These features are most pronounced in Bi-containing (210)-oriented GF films with the composition $(Bi,Y,Lu,Pr)_3(Fe,Ga)_5O_{12}$ grown through liquid-phase epitaxy from an overcooled solution in the melt on $(Gd,Ga)_3(Mg,Zr,Ga)_5O_{12}$ substrates [8].

In this paper, we report on the results of studying the effect of a pulsed magnetic field and temperature on the unidirectional anisotropy of DW velocity and distortions of the shape of dynamic domains in these films.

Data were obtained on two samples. Sample 1 had a highly pronounced unidirectional anisotropy of DW velocity. In sample 2, this anisotropy was small, but the DW shape was distorted. In the table, the following parameters of the samples are listed: the film thickness h, the equilibrium width of stripe domains w, the saturation magnetization $4\pi M_s$, the uniaxial anisotropy field H_K, the quality factor of the material Q, and the orthorhombic anisotropy field H_{K_r}.

The magnetic anisotropy parameters were determined using the phase-transition method; more specifically, we made a Fourier analysis of measured azimuthal dependences of planar H_{in}^* and normal H_b^* components of the static magnetic field corresponding to the uniform nucleation of domains [11, 12]. The azimuthal dependences of $H_{\text{in}}^*(\varphi)$ and $H_b^*(\varphi)$ are shown in Fig. 1.

Dynamic domain structures were observed with the aid of high-speed photography; the time of single-shot exposure was approximately 10 ns [13]. This method was chosen, because the details of dynamic domain structures were not reproduced in the experiments performed under the same conditions (Fig. 2). In the initial state, the films were magnetized to saturation by applying a bias field H_b normal to the film surface. A pulsed field H_p was applied in the opposite direction with the aid of two flat coils, with the film being placed halfway between them. Two kinds of domain images were taken: images of expanding stripe domains initially subjected to a field H_b close to the saturating field and images of domains of reversed magnetization nucleated on the film defects during the pulsed remagnetization. In the latter case, if a DW is located sufficiently far away from the center of nucleation, the acting magnetic field is [14]

$$H = H_p - H_b. \quad (1)$$

The field H_{K_r} for sample 1 being 4.3 times higher than that for sample 2 (see table) is probably responsible for

Parameters of Bi-containing (210)-oriented $(Bi,Y,Lu,Pr)_3(Fe, Ga)_5O_{12}$ garnet-ferrite films at room temperature

Parameter	Sample 1	Sample 2
h, μm	6.9	17.7
w, μm	14.0	20.2
$4\pi M_s$, G	70	83
H_K, Oe	3200	2700
Q	46	36
H_{Kr}, Oe	913	208

1063-7834/03/4507-1272$24.00 © 2003 MAIK "Nauka/Interperiodica"

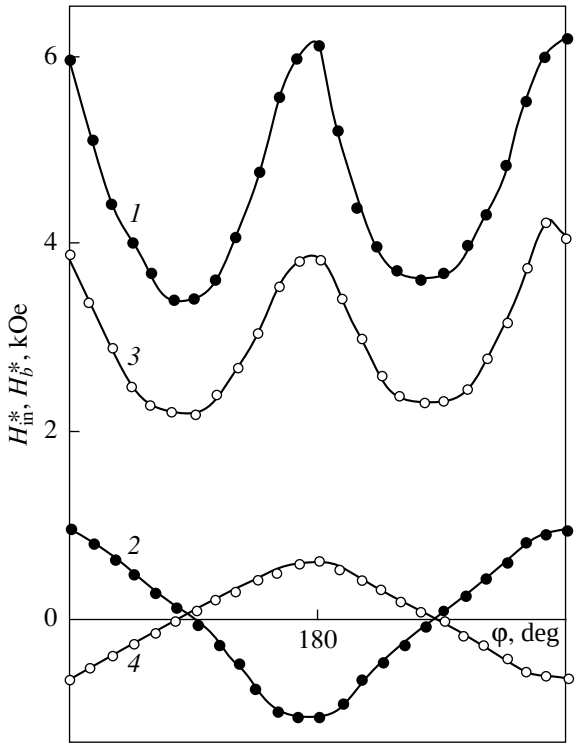

Fig. 1. Azimuthal dependences of (*1*, *3*) the in-plane H^*_{in} and (*2*, *4*) normal H^*_b components of the static magnetic field under which the uniform domain nucleation occurs in (*1*, *2*) sample 1 and (*3*, *4*) sample 2.

the absence of unidirectional anisotropy of DW velocity in sample 1, because the effective dimensionless damping parameter, which depends on the in-plane (external or effective internal) magnetic field [15–18], is larger in this sample.

Spatial distortions of the moving DW of a stripe domain in sample 1 are most clearly seen in Figs. 3h, 3i, 3k, 3l, and 3o. The moving DW of a domain of reversed magnetization nucleated on a point defect is also distorted, although the distortions are less pronounced (Fig. 4).

The dependence of DW velocity V on the acting magnetic field H for sample 1 is shown in Fig. 5a. It is seen that the initial linear part of the $V(H)$ curve intersects the abscissa axis at a negative value of H. As in [19], this can be explained by the fact that the easy magnetization axis in a (210)-oriented Bi-containing GF single-crystal film is inclined to the film surface [20, 21]; therefore, formula (1) cannot be used to calculate the acting magnetic field.

Images of the dynamic magnetic structures observed in sample 2 in various acting fields are shown in Fig. 6. The nucleation of reversed domains occurs in fields $H \geq 25$ Oe. In weak fields, these domains have a cylindrical shape, and, in the range $60 \leq H \leq 70$ Oe, the domain become elliptical without distortions of their walls. When the field attains the value $H \approx 110$ Oe, uni-

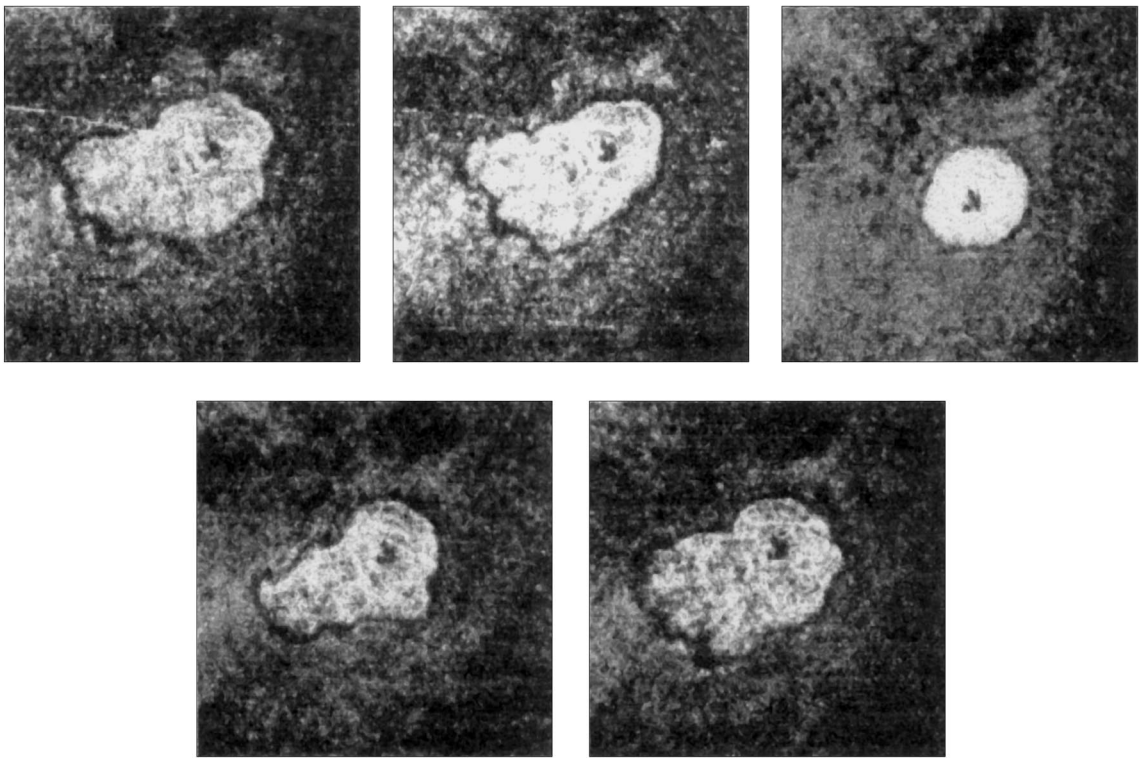

Fig. 2. Configurations of domains of reversed magnetization in sample 2 in a bias field $H_b = -127$ Oe at the same instant of time of action of a magnetic field pulse with amplitude $H_p = 284$ Oe.

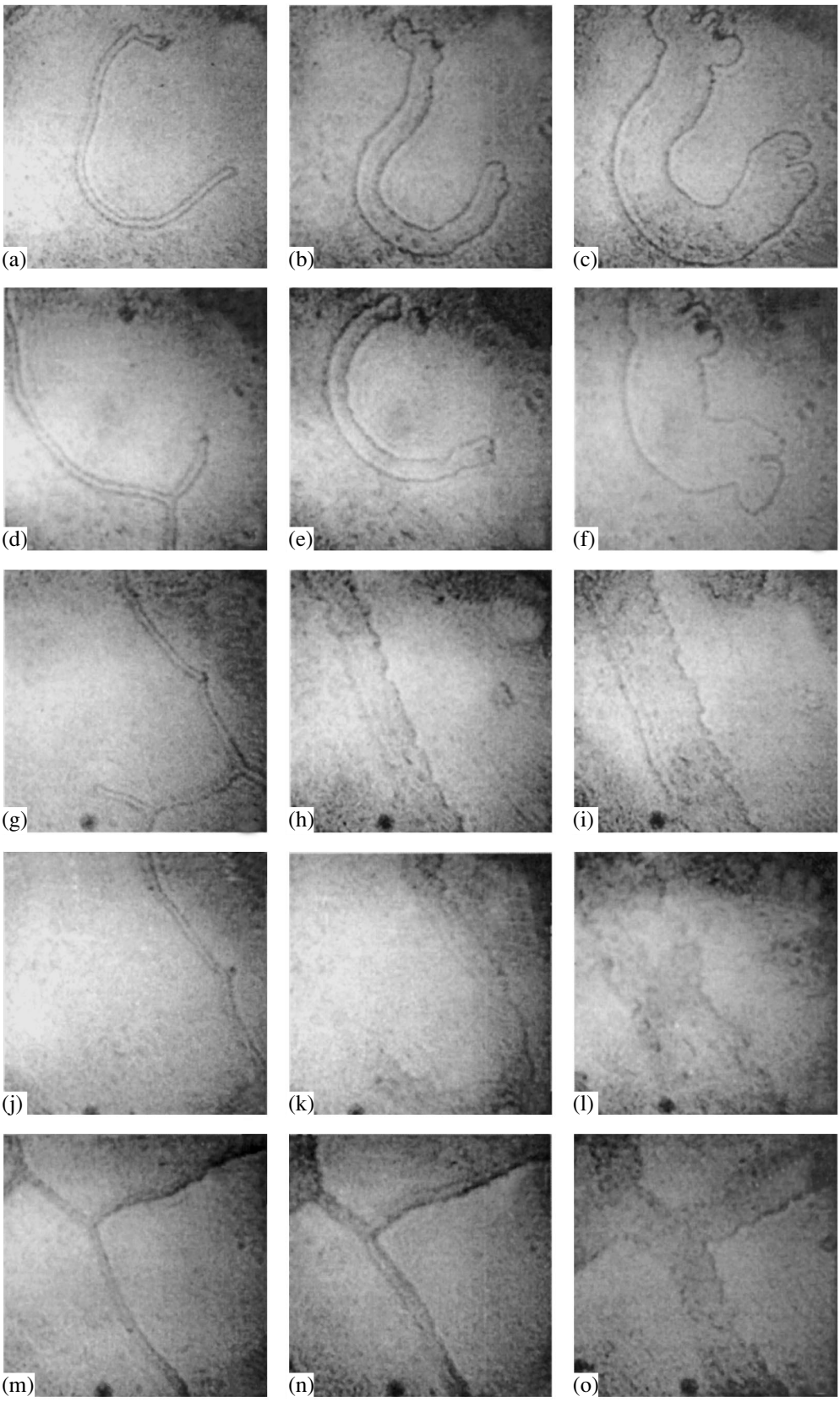

Fig. 3. Configurations of expanding stripe domains in sample 1 in a bias field H_b = –34 Oe during the action of a magnetic field pulse with amplitude H_p = (a–c) 43, (d–f) 59, (g–i) 74, (j–l) 115, and (m–o) 147 Oe at the following instants of time *t*: (a) 0, (b) 29, (c) 98; (d) 0, (e) 17, (f) 80; (g) 0, (h) 19, (i) 39; (j) 0, (k) 20, (l) 40; (m) 0, (n) 18, and (o) 34 ns.

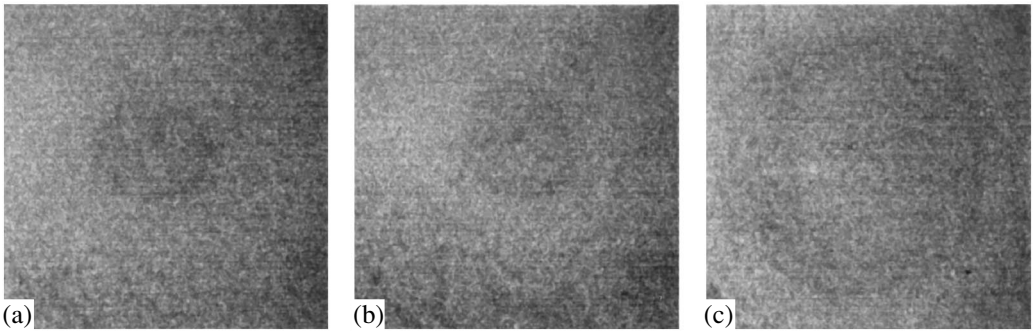

Fig. 4. Configuration of domains of reversed magnetization in sample 1 in a bias field H_b = –49 Oe during the action of a magnetic field pulse with amplitude H_p = 134 Oe at various instants of time t: (a) 20, (b) 27, and (c) 39 ns.

directional anisotropy of DW velocity arises along a certain direction. This process is accompanied by the appearance of a wedge-shaped section in a DW; the rest of the DW remains cylindrical. On a further increase in H, the parts of the DW that move with an increased velocity occupy a progressively larger area of the DW of a reversed domain (the remaining part of the DW moves without distortions) and the unidirectional anisotropy of the DW velocity attains a maximum (Figs. 6a–6f).

As the field H is increased still further, the unidirectional anisotropy of DW velocity becomes weaker; however, the DW becomes almost entirely distorted and some sections of the image of the DW become thicker (Figs. 6g–6l). In the range of $H \geq 280$ Oe, the unidirectional anisotropy of DW velocity disappears (Figs. 6m–6o), and, in the fields $H \geq 340$ Oe, the entire DW of a reversed domain becomes thicker (Figs. 6p, 6q).

From comparison of Figs. 6b, 6e, and 6i, it follows that the orientation of the axis of unidirectional anisotropy (the direction of the maximum DW velocity) varies with the acting magnetic field.

When the field H_b is smaller than the saturating field, a stripe domain structure arises, with its orientation being determined by the magnetic anisotropy in the film plane (Fig. 7a).

The threshold field for nucleation of reversed domains during pulsed remagnetization is $H \approx 45$ Oe. The shape of reversed domains depends on the magnitude of the acting magnetic field. In relatively small fields $H \leq 110$ Oe, the DWs of reverse domains have the shape of an ellipse whose axes differ by 30–40%; the DW images for these domains are rather thin and smooth. When the acting field is above this range, distortions arise in some sections of the DW and the DW image thickens in these sections (the rest of the DW image remains thin and smooth); distortions occupy a progressively larger fraction of the DW area with increasing H. The strongest distortions occur in the field $H \approx 150$ Oe, in which case the dimensions of a reversed domain in two mutually perpendicular directions differ more than two times (Fig. 7b). Note that the orientation of the axis of unidirectional DW velocity anisotropy is not related to the orientation of the axes of magnetic anisotropy in the plane of the film (compare Figs. 7a, 7b).

The $V(H)$ dependences for the parts of a DW moving with the minimum and the maximum velocity (Fig. 5b, curves *1*, *2*, respectively) also testify that the

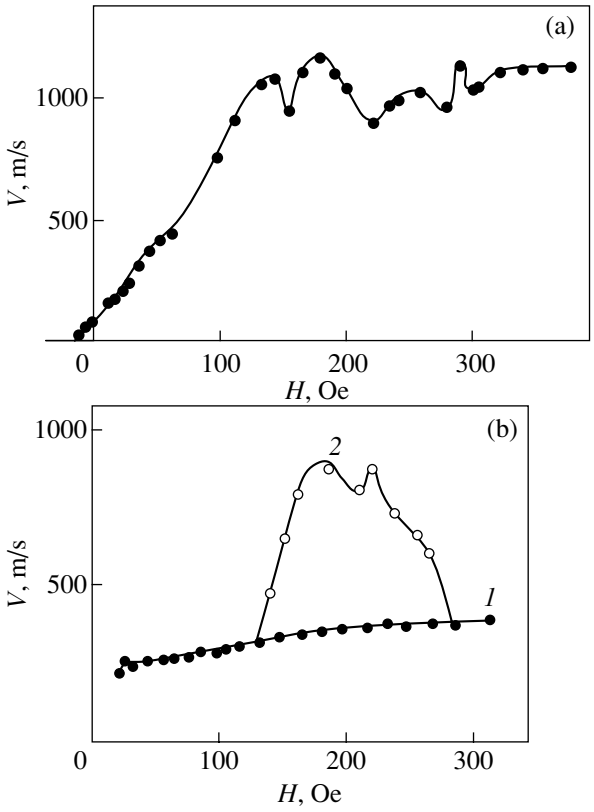

Fig. 5. DW velocity V as a function of the acting magnetic field H for (a) sample 1 and (b) sample 2.

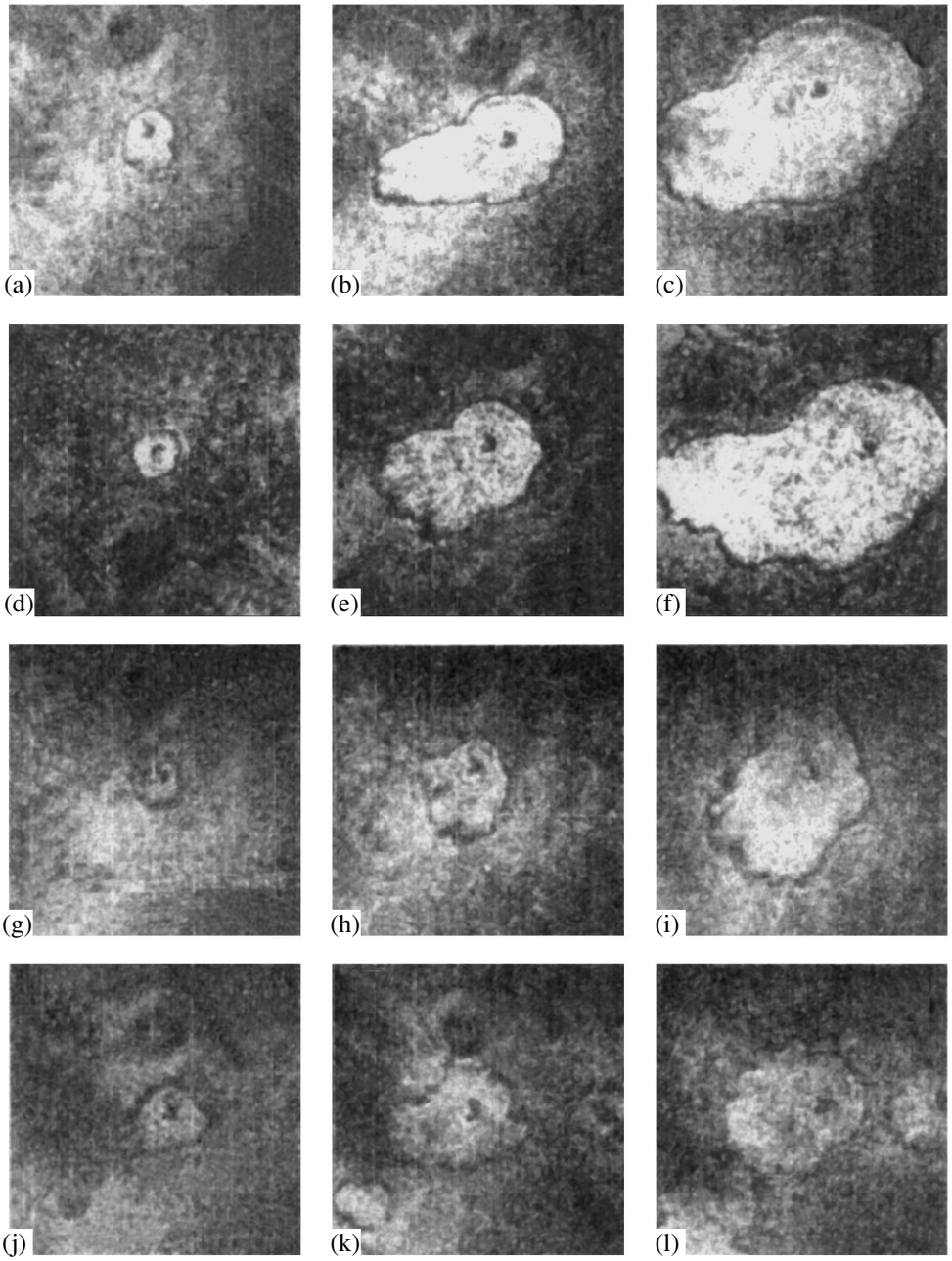

Fig. 6. Configurations of domains of reversed magnetization in sample 2 in the acting magnetic field H = (a–c) 130, (d–f) 154, (g–i) 228, (j–l) 257, (m–o) 286, (p–r) 350, (s–u) 400, and (v–x) 500 Oe at the following instants of time t: (a) 30, (b) 110, (c) 190; (d) 40, (e) 100, (f) 200; (g) 30, (h) 80, (i) 130; (j) 30, (k) 60, (l) 100; (m) 20, (n) 40, (o) 70; (p) 10, (q) 30, (r) 60; (s) 5, (t) 18, (u) 24; (v) 3, (w) 14, and (x) 20 ns.

unidirectional anisotropy of DW velocity takes place in a limited range of values of the acting magnetic field.

The results obtained show that the origin of the unidirectional anisotropy of DW velocity can be associated with the excitation of spin waves causing local rotation of the magnetization vector in the vicinity of the moving DW. Note that the spin-wave excitation by a DW takes place in the range $H^* \le H \le H^{**}$ [15, 16], where the threshold fields H^* and H^{**}, as well as the threshold field for magnetization rotation H_{rot}, in GF films with orthorhombic magnetic anisotropy are anisotropic [18]. Therefore, the directions along which a DW moves with the highest velocity in the film plane depend on the acting magnetic field.

Temperature dependences of the maximum and minimum DW velocities in sample 2 are shown in Fig. 8 (curves *1*, *2*, respectively). It can be seen that both the

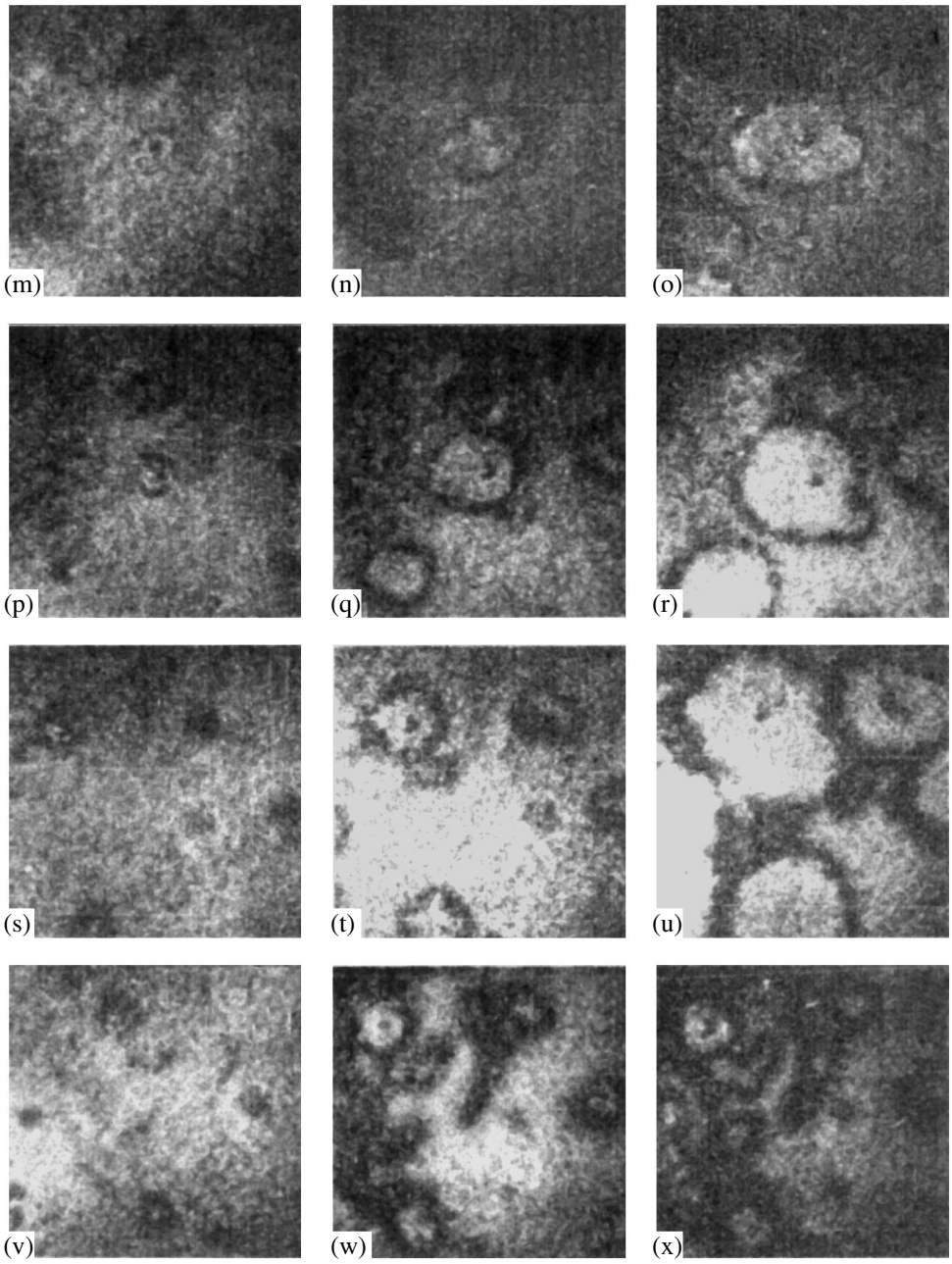

Fig. 6. (Contd.)

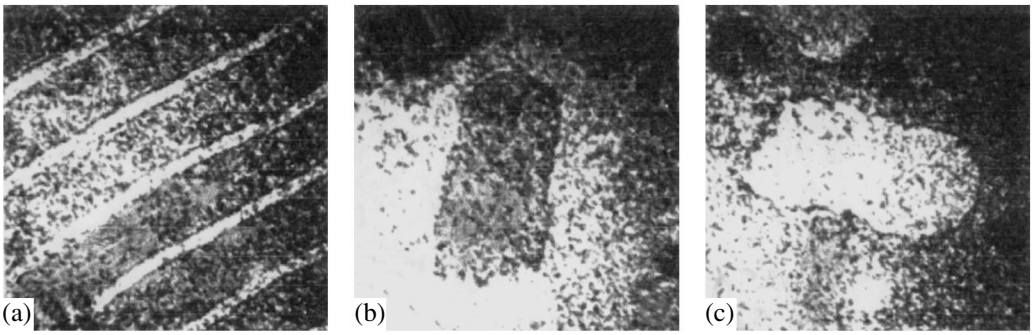

Fig. 7. Configurations of (a) stripe domains and (b, c) domains of reversed magnetization for opposite directions of the acting magnetic field $H = 150$ Oe after a time interval $t = 0.16$ μs following the instant of application of a magnetic field pulse.

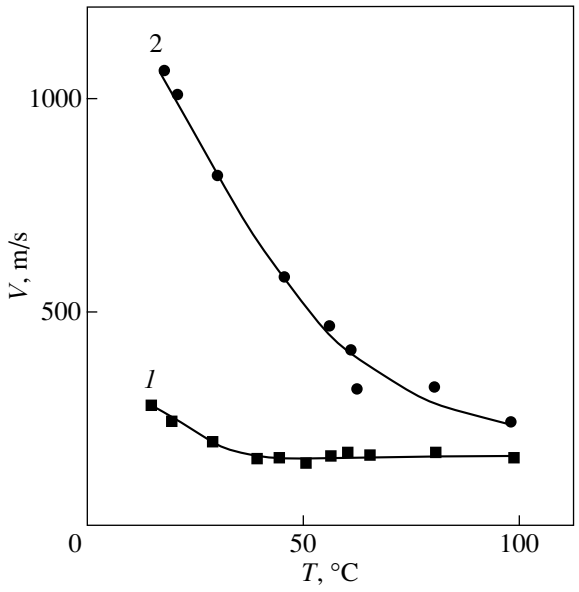

Fig. 8. Temperature dependences of (*1*) the lowest and (*2*) highest DW velocity in sample 2 in the acting field H = 180 Oe.

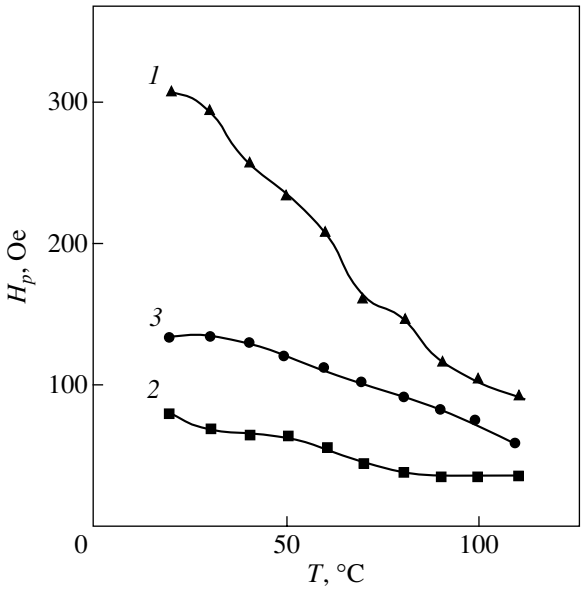

Fig. 9. Temperature dependences of (*1*) the upper $H_d^{**}(T)$ and (*2*) lower limit $H_d^{*}(T)$ of the field range within which the DWs of stripe domains in sample 2 exhibit distortions; curve *3* is the temperature dependence of the amplitude of a pulsed magnetic field $H_{pd}(T)$ corresponding to the maximum DW distortion.

values of these velocities and the difference between them decrease upon heating.

Figure 9 shows the temperature dependences of the upper $H_d^{**}(T)$ and lower limit $H_d^{*}(T)$ of the field range in which the walls of stripe domains are distorted, as well as the temperature dependence of the amplitude of a pulsed magnetic field $H_{pd}(T)$ for which the DW distortions are the strongest. Figure 10 shows the temperature dependences of the upper $H_a^{**}(T)$ and lower limit $H_a^{*}(T)$ of the field range within which the unidirectional anisotropy of DW velocity takes place in sample 2, as well as the temperature dependence of the amplitude $H_{pa}(T)$ of the pulsed magnetic field at which this anisotropy is the highest.

Notwithstanding the fact that the field ranges shown in Figs. 9 and 10 overlap, the following relations are always obeyed:

$$H_d^{*} < H_a^{*}, \tag{2}$$

$$H_d^{**} < H_a^{**}, \tag{3}$$

$$H_d^{*} < H_{pd} < H_d^{**}, \tag{4}$$

$$H_a^{*} < H_{pa} < H_a^{**}. \tag{5}$$

All these quantities decrease with increasing temperature.

Thus, the following conclusions can be drawn from the studies of Bi-containing (210)-oriented GF single-crystal films.

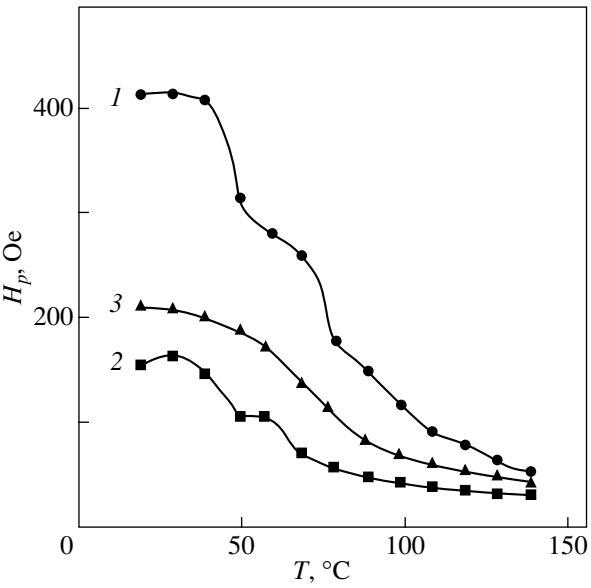

Fig. 10. Temperature dependences of (*1*) the upper $H_a^{**}(T)$ and (*2*) lower limit $H_a^{*}(T)$ of the field range within which the unidirectional anisotropy of DW velocity occurs in sample 2. Curve *3* is the temperature dependence of the amplitude of a pulsed magnetic field $H_{pa}(T)$ corresponding to the highest anisotropy.

(1) Both distortions of moving DWs and the unidirectional anisotropy of DW velocity occur within limited ranges of values of the acting magnetic field ($H_d^* \le H \le H_d^{**}$, $H_a^* \le H \le H_a^{**}$, respectively), where $H_d^* < H_a^*$ and $H_d^{**} < H_a^{**}$.

(2) The orientation of the axis of unidirectional anisotropy of DW velocity varies with the acting magnetic field.

(3) Experimentally observed features of the dynamic behavior of domain structures can be explained assuming that these features are associated with the excitation of spin waves by a moving DW and that the corresponding threshold fields H^* and H^{**} are anisotropic.

REFERENCES

1. V. V. Randoshkin, V. B. Sigachev, V. I. Chani, and A. Ya. Chervonenkis, in *Abstracts of X All-Union School–Seminar, Riga* (1986), Vol. 1, p. 21.
2. F. V. Lisovskiĭ, A. S. Logginov, G. A. Nepokoĭchitskiĭ, and T. V. Rozanova, Pis'ma Zh. Éksp. Teor. Fiz. **45** (7), 339 (1987) [JETP Lett. **45**, 430 (1987)].
3. G. Yu. Zharkov, A. S. Logginov, G. A. Nepokoĭchitskiĭ, and B. Yu. Terletskiĭ, Fiz. Tverd. Tela (Leningrad) **29** (9), 2800 (1987) [Sov. Phys. Solid State **29**, 1607 (1987)].
4. A. M. Balbashov, A. S. Logginov, G. A. Nepokoĭchitskiĭ, and E. P. Shabaeva, Pis'ma Zh. Tekh. Fiz. **13** (4), 231 (1987) [Sov. Tech. Phys. Lett. **13**, 94 (1987)].
5. V. V. Randoshkin, V. B. Sigachev, V. I. Chani, and A. Ya. Chervonenkis, Fiz. Tverd. Tela (Leningrad) **31** (7), 70 (1989) [Sov. Phys. Solid State **31**, 1138 (1989)].
6. V. V. Randoshkin, M. V. Logunov, and Yu. N. Sazhin, Fiz. Tverd. Tela (Leningrad) **32** (5), 1456 (1990) [Sov. Phys. Solid State **32**, 849 (1990)].
7. A. M. Balbashov, A. S. Logginov, and E. P. Shabaeva, Zh. Tekh. Fiz. **61** (6), 159 (1991) [Sov. Phys. Tech. Phys. **36**, 680 (1991)].
8. V. V. Randoshkin, M. V. Logunov, and Yu. N. Sazhin, Zh. Tekh. Fiz. **66** (2), 201 (1996) [Tech. Phys. **41**, 404 (1996)].
9. V. V. Randoshkin and Yu. N. Sazhin, Zh. Tekh. Fiz. **66** (8), 83 (1996) [Tech. Phys. **41**, 790 (1996)].
10. V. V. Randoshkin and Yu. N. Sazhin, Fiz. Tverd. Tela (St. Petersburg) **44** (5), 858 (2002) [Phys. Solid State **44**, 893 (2002)].
11. I. E. Dikshteĭn, F. L. Lisovskiĭ, E. G. Mansvetova, and V. V. Tarasenko, Mikroélektronika **13** (4), 337 (1984).
12. F. V. Lisovskiĭ, I. E. Dikshteĭn, E. G. Mansvetova, and V. V. Tarasenko, Mikroélektronika **19** (1), 51 (1990).
13. V. V. Randoshkin, M. V. Logunov, and V. B. Sigachev, Prib. Tekh. Éksp., No. 5, 247 (1985).
14. V. V. Randoshkin, Prib. Tekh. Éksp., No. 2, 155 (1995).
15. V. V. Randoshkin, Fiz. Tverd. Tela (St. Petersburg) **37** (10), 3056 (1995) [Phys. Solid State **37**, 1684 (1995)].
16. V. V. Randoshkin and M. V. Logunov, Fiz. Tverd. Tela (St. Petersburg) **36** (12), 3498 (1994) [Phys. Solid State **36**, 1858 (1994)].
17. V. V. Randoshkin, Pis'ma Zh. Tekh. Fiz. **21** (23), 74 (1995) [Tech. Phys. Lett. **21**, 983 (1995)].
18. V. V. Randoshkin, Fiz. Tverd. Tela (St. Petersburg) **39** (8), 1421 (1997) [Phys. Solid State **39**, 1260 (1997)].
19. V. V. Randoshkin and Yu. N. Sazhin, Fiz. Tverd. Tela (St. Petersburg) **44** (5), 858 (2002) [Phys. Solid State **44**, 893 (2002)].
20. E. N. Il'icheva, A. V. Dubova, V. K. Peterson, *et al.*, Fiz. Tverd. Tela (St. Petersburg) **35** (5), 1167 (1993) [Phys. Solid State **35**, 594 (1993)].
21. E. N. Il'icheva, Yu. N. Fedyunin, A. G. Shishkov, and A. V. Klushina, Zh. Tekh. Fiz. **63** (11), 143 (1993) [Tech. Phys. **38**, 1005 (1993)].

Translated by A. Zalesskiĭ

Physics of the Solid State, Vol. 45, No. 7, 2003, pp. 1280–1283. Translated from Fizika Tverdogo Tela, Vol. 45, No. 7, 2003, pp. 1221–1224.

MAGNETISM AND FERROELECTRICITY

The Nature of Magnetoelastic Anomalies in $Nd_{0.5}Sr_{0.5}MnO_3$ upon Suppression of Charge Ordering by a Magnetic Field

Yu. F. Popov*, A. M. Kadomtseva*, G. P. Vorob'ev*, K. I. Kamilov*, Ya. S. Shtofich*, V. Yu. Ivanov, A. A. Mukhin**, and A. M. Balbashov*****

** Moscow State University, Vorob'evy gory, Moscow, 119992 Russia*

e-mail: popov@plms.msu.su

*** Institute of General Physics, Russian Academy of Sciences, ul. Vavilova 38, Moscow, 119991 Russia*

**** Moscow Power Institute, ul. Krasnokazarmennaya 14, Moscow, 105835 Russia*

Received December 15, 2002

Abstract—This paper reports on the results of investigations into the magnetic and magnetoelastic properties of $Nd_{0.5}Sr_{0.5}MnO_3$ single crystals in pulsed magnetic fields up to 250 kOe, the magnetic and kinetic properties of these crystals in weak static magnetic fields, and their thermal expansion. It is demonstrated that the studied properties exhibit a number of anomalies due to a transition from the antiferromagnetic semiconducting state to the ferromagnetic metallic state upon suppression of charge ordering. *© 2003 MAIK "Nauka/Interperiodica".*

1. INTRODUCTION

Over the last decade, great interest has been expressed by researchers in substituted manganites of the $R_{1-x}A_xMnO_3$ system (R is a rare-earth ion and A is Sr or Ca) due primarily to the discovery of the giant magnetoresistance effect in these compounds. Recent investigations into the properties of these manganites revealed a number of new interesting phenomena which are associated, for example, with the localization of current carriers, charge ordering of Mn^{3+} and Mn^{4+} ions, orbital ordering of Mn^{3+} ions, magnetic field–induced structural phase transitions, and semiconductor–metal phase transitions.

Owing to the spin, charge, and orbital ordering, which is characteristic of rare-earth manganites, compounds in the $Nd_{1-x}Sr_xMnO_3$ system have complex phase diagrams [1].

For this system, spin, charge, and orbital ordering of the *CE*, *A*, and *C* types was observed by Kajimoto *et al.* [1].

It is of particular interest to examine the composition with $x = 0.5$, for which the Coulomb interaction of electrons results in their localization and charge ordering. The charge ordering can be suppressed by a magnetic field, because the field-stimulated spin orientation leads to an increase in the charge carrier mobility and a decrease in the tendency to carrier localization. It is upon the suppression of charge ordering that the magnetoresistance increases.

As can be seen from the phase diagram presented in [1], the *CE*-type charge-ordered antiferromagnetic state is observed only in the region close to the composition with $x = 0.5$ and coexists with the *A*-type antiferromagnetic state and the ferromagnetic state [1, 2].

According to the phase diagram, the ferromagnetic ordering is observed for the composition with $x = 0.5$ at a temperature of 250 K. A decrease in the temperature results in charge antiferromagnetic ordering at temperatures close to the charge ordering point $T_{CO} = 140$ K.

2. SAMPLE PREPARATION

Single crystals of $Nd_{0.5}Sr_{0.5}MnO_3$ were grown by zone melting with optical heating.

3. RESULTS AND DISCUSSION

The temperature dependences of the magnetization and resistivity for $Nd_{0.5}Sr_{0.5}MnO_3$ single crystals (Fig. 1) exhibit anomalies at temperatures T_C and T_{CO}. For these crystals, we also measured the thermal expansion dl/l along the direction of the magnetic moment in the absence of a magnetic field (Fig. 2). As can be seen from Fig. 2, an increase in the temperature leads to a positive jump in the thermal expansion to 2×10^{-3} at temperatures close to the charge ordering point $T_{CO} = 140°C$. This jump is associated with the transition from the antiferromagnetic state to the ferromagnetic state. The large thermal expansion of the crystal can be explained by the fact that, for this composition, according to Mahendiran *et al.* [3], there coexist three phases with different unit cell volumes. In the ferromagnetic phase, the unit cell has the largest volume ($V_{HTO} = 159.4$ Å^3). In the *A*-type antiferromagnetic phase, the unit cell has the smallest volume ($V_{LTO} = 158.65$ Å^3). It should be noted that both the ferromagnetic and *A*-type antiferromagnetic phases belong to the orthorhombic crystal system. The main phase in the low-temperature range is the *CE*-type charge-ordered

antiferromagnetic monoclinic phase with the unit cell volume $V_{LTM} = 159.1$ Å^3. The anomaly observed in the thermal expansion is apparently due to a structural phase transition from the monoclinic crystal system to the orthorhombic system. It is worth nothing that the phase transition accompanied by a sharp increase in the crystal sizes is preceded by a negative jump in the thermal expansion dl/l to 2×10^{-4} (Fig. 2). This jump can be caused by a partial change in the ratio between antiferromagnetic phases of the *A* and *CE* types. Moreover, a small anomaly in the thermal expansion is observed near the temperature of ferromagnetic ordering (T_C = 250 K).

For the $Nd_{0.5}Sr_{0.5}MnO_3$ single crystal, the magnetization and magnetostriction were also measured in strong pulsed magnetic fields up to 250 kOe in the temperature range 10–300 K.

As can be seen from Fig. 3, the magnetizations measured at temperatures below T_{CO} = 140 K in a critical magnetic field that destroys the charge ordering exhibit jumps associated apparently with the phase transition from the antiferromagnetic semiconducting state to the ferromagnetic metallic state. It is also seen that this transition is characterized by a considerable field hysteresis. We determined the threshold magnetic fields of the phase transitions and constructed the *H–T* phase diagram, in which there is an extended region of coexistence of different phases (Fig. 4). At temperatures from the charge ordering point to the Curie temperature T_C = 250 K, the magnetization jumps in the curves vanish, because the crystal becomes ferromagnetic in the absence of the magnetic field (Fig. 3).

It should be noted that, at temperatures below 50 K, a nonzero magnetic moment is observed in weak magnetic fields (Fig. 3), even though the crystal seemingly occurs in the antiferromagnetic state. Such a small moment can be associated with the existence of ferromagnetic impurities in addition to the antiferromagnetic phase at low temperatures. As the temperature increases, the impurity ferromagnetic moment persists up to a temperature of 50 K and then vanishes (see inset in Fig. 3).

The change in the magnitude of the initial magnetic moment with variations in the temperature and in the magnetic field suggests that the ratio of the phases coexisting in the $Nd_{0.5}Sr_{0.5}MnO_3$ compound can change under external actions.

Note also that, in a strong magnetic field, the magnetic moment in the ferromagnetic state does not exceed $3\mu_B$, which is smaller than the theoretically predicted value $3.5\mu_B$. This can be explained by the fact that, in the ferromagnetic state, the studied compound, most likely, contains impurities of the *A*-type antiferromagnetic phase, which leads to a decrease in the total magnetic moment.

The magnetostriction of the crystals was measured under the same conditions. The magnetic field dependences of the longitudinal magnetostriction along the

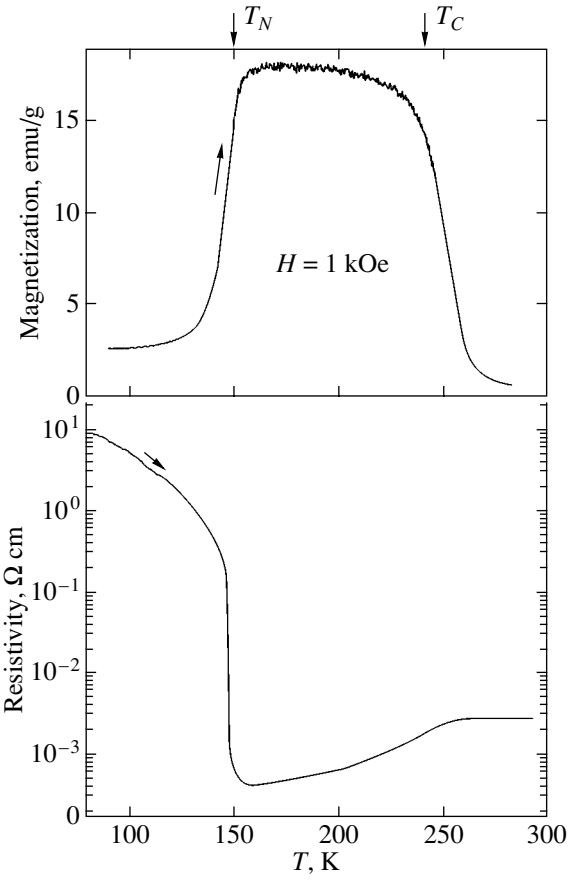

Fig. 1. Temperature dependences of the magnetization and resistivity for $Nd_{0.5}Sr_{0.5}MnO_3$ single crystals.

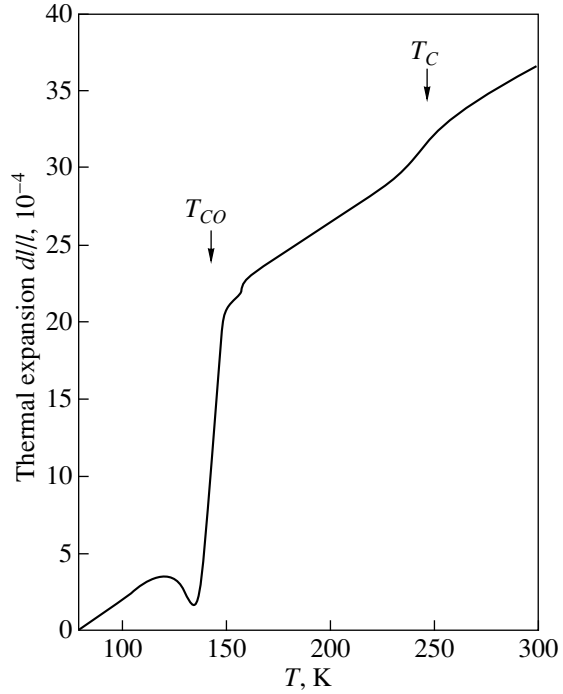

Fig. 2. Temperature dependence of the thermal expansion for the $Nd_{0.5}Sr_{0.5}MnO_3$ single crystal.

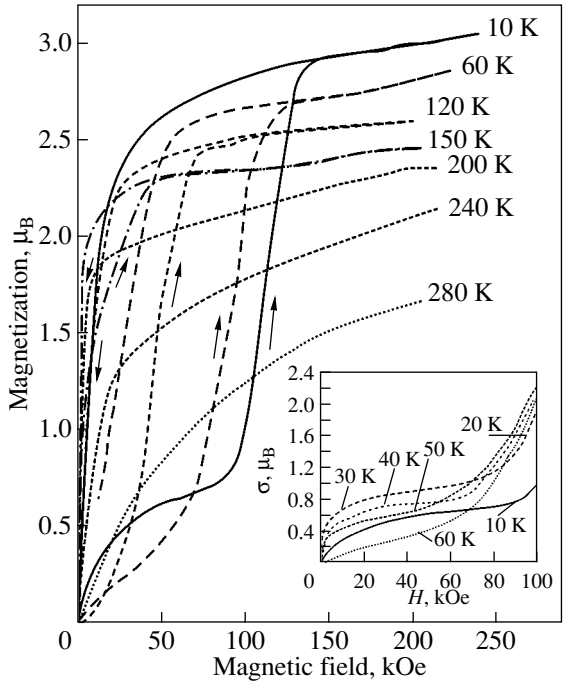

Fig. 3. Magnetization isotherms for the $Nd_{0.5}Sr_{0.5}MnO_3$ single crystal. The inset shows the initial portions of the magnetization isotherms in the temperature range 10–60 K.

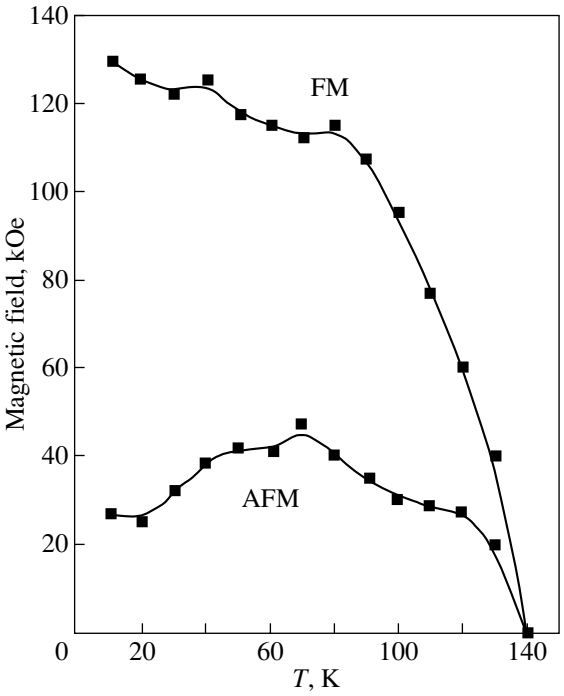

Fig. 4. *H–T* phase diagram for the $Nd_{0.5}Sr_{0.5}MnO_3$ compound.

direction of the magnetic moment at different temperatures are depicted in Fig. 5. It can be seen that, at a temperature of 10 K, the magnetostriction is small in magnetic fields $H < H_{CR} = 100$ kOe. As the magnetic field increases to H_{CR}, the magnetostriction undergoes a negative jump to -6×10^{-4}. This jump can be caused by changes in the ratio between phases with different unit cell volumes. An increase in the temperature from 50 K to T_{CO} leads to a sharp increase in the magnetostriction against the background of the negative magnetostriction. With a further increase in the temperature in the range $T_{CO} < T < T_C$, the magnetostriction first remains positive, then drastically decreases in magnitude, changes sign, and exhibits exchange nature.

Mahendiran *et al.* [3] measured the magnetostriction of the $Nd_{0.5}Sr_{0.5}MnO_3$ compound only for polycrystalline samples in the temperature range 50–250 K. In this case, the magnetostriction had positive sign and was attributed to the structural phase transition. The negative magnetostriction observed in our case precedes the appearance of positive magnetostriction and can be explained by the fact that, as was mentioned above, three phases coexist for the $Nd_{0.5}Sr_{0.5}MnO_3$ composition. Correspondingly, the ratio between the phases with different unit cell volumes can change upon the transition from the antiferromagnetic state to the ferromagnetic state. This assumption is confirmed by both the negative peak observed in the temperature dependence of the thermal expansion, which precedes the positive jump (Fig. 2), and the impurity magnetic moment at low temperatures (Fig. 3).

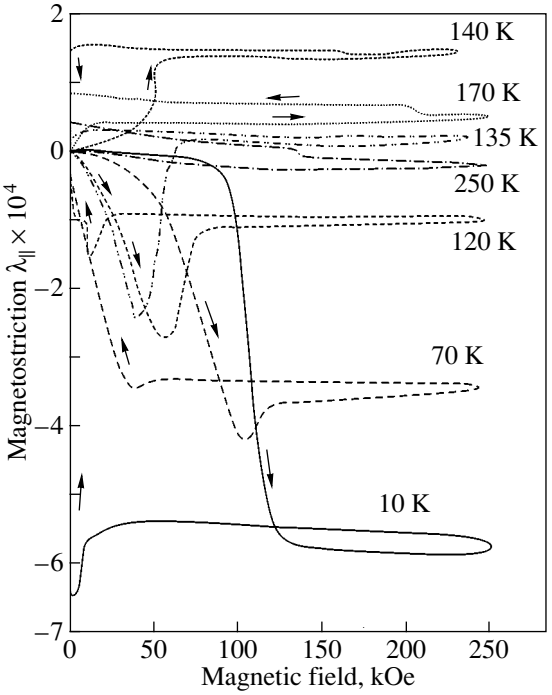

Fig. 5. Isotherms of the longitudinal magnetostriction of the $Nd_{0.5}Sr_{0.5}MnO_3$ single crystal.

4. CONCLUSIONS

Thus, all the anomalies observed can be explained if we take into account that there are two tendencies in a change in the temperature and magnetic field. The first tendency is associated with the preferable formation of the ferromagnetic state in a magnetic field upon suppression of the charge-ordered state. The second tendency apparently stems from the fact that, with allowance made for the elastic and magnetoelastic contributions to the free energy, the *A*-type orthorhombic phase is more preferable than the *CE*-type monoclinic antiferromagnetic phase. The change in the magnetostriction sign with variations in the magnetic field and the temperature, which is observed in our experiment, can be caused by the fact that the first tendency leads to positive magnetostriction, whereas the second tendency results in negative magnetostriction. The complex character of the anomalies observed in the magnetostriction is explained by the fact that the magnetic field induces a structural phase transition in addition to the metal–semiconductor phase transition.

ACKNOWLEDGMENTS

This work was supported by the Russian Foundation for Basic Research, project nos. 00-02-16500 and 00-15-96695.

REFERENCES

1. R. Kajimoto, H. Yoshizawa, H. Kawano, *et al.*, Phys. Rev. B **60** (13), 9506 (1999).
2. C. Ritter, R. Mahendiran, M. R. Ibarra, *et al.*, Phys. Rev. B **61** (14), R9229 (2000).
3. R. Mahendiran, M. R. Ibarra, A. Maignan, *et al.*, Phys. Rev. Lett. **82** (10), 2191 (1999).

Translated by N. Korovin

Physics of the Solid State, Vol. 45, No. 7, 2003, pp. 1284–1287. Translated from Fizika Tverdogo Tela, Vol. 45, No. 7, 2003, pp. 1225–1227.

MAGNETISM AND FERROELECTRICITY

Enhancement of the Magnetoelectric Effect in Thin Ferroelectric Films

I. E. Chupis

Verkin Institute of Low-Temperature Physics and Engineering, National Academy of Sciences of Ukraine, pr. Lenina 47, Kharkov, 61103 Ukraine

e-mail: chupis@ilt.kharkov.ua

Received November 6, 2002

Abstract—The enhancement of the nonlinear magnetoelectric effect in a magnetic field is predicted for a ferroelectric film in a system consisting of ferroelectric and paraelectric layers in the vicinity of the size-induced ferroelectric phase transition. This effect is assumed to be maximum in semiconductor ferroelectrics. © *2003 MAIK "Nauka/Interperiodica".*

1. INTRODUCTION

Ferroelectrics do not belong to the class of materials with a linear magnetoelectric effect in which the magnetoelectric interaction manifests itself most strongly. By contrast, ferroelectrics are characterized by nonlinear magnetoelectric effects, including an insignificant shift in the Curie temperature in an external magnetic field [1, 2]. The magnetic field primarily affects the electronic subsystem by varying the electron states (the Zeeman effect); as a result, the crystal lattice undergoes deformation and polarization due to the electron–phonon interaction and the Jahn–Teller effect [3, 4]. The ions in the crystal lattice are also directly affected by the magnetic field; however, this effect is considerably weaker than the action of the magnetic field on the electronic subsystem. As a consequence, the temperature shift of the ferroelectric transition in response to a magnetic field in semiconductor ferroelectrics [1] is one order of magnitude larger than that in dielectrics [2].

It is known that the higher the dielectric susceptibility, the greater the magnetoelectric susceptibility (see, for example, [5]). Recent studies revealed giant dielectric susceptibilities for structures consisting of thin ferroelectric ($PbTiO_3$) and paraelectric layers [6, 7]. It is found that the dielectric susceptibility of a thin ferroelectric layer is three orders of magnitude higher than the susceptibility of the bulk sample. This effect is explained by domain-wall pinning at defects and the size-induced ferroelectric phase transition [8–10]. Since the effect under investigation is observed in systems composed of alternating ferroelectric and paraelectric layers that do not interact with each other, the same effect can be observed for an individual ferroelectric film.

In this work, we demonstrated that, in a ferroelectric film without electric polarization at the boundary, the magnetoelectric effect is considerably enhanced in the vicinity of the size-induced phase transition.

2. THEORETICAL ANALYSIS

Let us consider a cubic-ferroelectric film of thickness l ($0 < z < l$) with the electric polarization **P** directed along the film plane (x, y) in an external constant magnetic field **H**, whose direction is insignificant in the further consideration. The free energy of the system can be represented in the form

$$F = \frac{1}{l}\int_0^l \left[-\frac{a}{2}P^2 + \frac{b}{4}P^4 + \frac{\lambda}{2}\left(\frac{\partial P}{\partial z}\right)^2 + \frac{1}{2}\gamma P^2 H^2\right]dz. \quad (1)$$

Here, $a = a_0(T_c - T)$ is a constant, $a_0 > 0$, and T_c is the Curie temperature for a bulk sample. The last term in functional (1) is the magnetoelectric energy of interaction of the electric polarization with the magnetic field.

The equation for equilibrium values of the polarization can be derived by varying the polarization P in functional (1). As a result, we obtain

$$aP - bP^3 + \lambda P'' - \gamma P H^2 = 0. \quad (2)$$

It is assumed that the electric polarization is absent at the boundary of the film (this corresponds to the experimental situation where the ferroelectric layers alternate with paraelectric layers); that is,

$$P(z = 0, l) = 0. \quad (3)$$

We are interested here in the magnetoelectric susceptibility $\alpha = (\partial P/\partial H)$, for which an equation can be derived by differentiating Eq. (2) with respect to the magnetic field H:

$$\lambda\alpha'' + (a - 3bP_s^2)\alpha - 2\gamma H P_s = 0. \quad (4)$$

Hereafter, the magnetic field will be considered weak. Hence, in Eq. (4), only the terms linear with respect to

the magnetic field H remain and we assume that $P = P_s$. The spontaneous polarization P_s satisfies Eq. (2) in the magnetic field $H = 0$ with boundary conditions (3) and, at temperatures $T < T_c$, can be represented in the form [10]

$$P_s(z) = P_{st}\sqrt{\frac{2m}{1+m}}\,\mathrm{sn}\left(\frac{z}{l_0\sqrt{1+m}}, m\right). \quad (5)$$

Here, $P_{st} = (a/b)^{1/2}$ is the spontaneous polarization of a thick film; $l_0 = (\lambda/a)^{1/2}$ is the correlation length; and $\mathrm{sn}(u, m)$ is the elliptic sine, for which the parameter m is determined from the equation

$$l = 2l_0\sqrt{1+m}K(m), \quad 0 \le m \le 1, \quad (6)$$

where $K(m)$ is the complete elliptic integral of the first kind.

After changing over to the variable $u = z/l_0\sqrt{1+m}$, the equation for the magnetoelectric susceptibility and the corresponding boundary conditions take the following form:

$$\begin{aligned}&\alpha'' + [1 + m - 6m\,\mathrm{sn}^2(u, m)]\alpha \\ &= -2\sqrt{2m(1+m)}\alpha_t\,\mathrm{sn}(u, m), \\ &\alpha_t = -\frac{\gamma H}{\sqrt{ab}}, \quad \alpha(u = 0, 2K) = 0.\end{aligned} \quad (7)$$

Here, α_t is the magnetoelectric susceptibility of the bulk sample, which can be easily obtained from Eq. (4) for uniform electric polarization.

The solution to Eq. (7) has the form

$$\alpha(u) = c_1\alpha_1 + c_2\alpha_2 + \alpha_3, \quad (8)$$

where α_1 and α_2 are the solutions of the homogeneous equation and α_3 is the solution of the inhomogeneous equation:

$$\alpha_1 = \mathrm{cn}(u, m)\mathrm{dn}(u, m),$$

$$\alpha_2 = \left[u - \frac{1+m}{1-m}E(amu, m)\right]\mathrm{cn}(u, m)\mathrm{dn}(u, m)$$

$$+ (1-m)^{-1}\mathrm{sn}(u, m)[\mathrm{dn}^2(u, m) + m^2\mathrm{cn}^2(u, m)], \quad (9)$$

$$\alpha_3 = -\alpha_t(1-m)^{-2}\sqrt{2m(1+m)}$$

$$\times\begin{cases}[(1-m)u - 2E(amu, m)]\mathrm{cn}(u, m)\mathrm{dn}(u, m) \\ + (1+m)\mathrm{sn}(u, m)\mathrm{cn}^2(u, m)\mathrm{dn}^2(u, m) \\ + \mathrm{sn}^3(u, m)[\mathrm{dn}^2(u, m) + m^2\mathrm{cn}^2(u, m)].\end{cases}$$

In expressions (9), $E(amu, m)$ is the elliptic integral of the second kind, $\mathrm{cn}(u, m)$ is the elliptic cosine, and $\mathrm{dn}(u, m)$ is the delta amplitudinis. We determine the constants c_1 and c_2 from boundary conditions (7); that is,

$$c_2 = \frac{\alpha_t\sqrt{2m(1+m)}}{(1-m)}\frac{[K(1-m) - 2E]}{[K(1-m) - (1+m)E]}, \quad (10)$$
$$c_1 = 0.$$

Here, E is the complete elliptic integral of the second kind.

The mean value of the magnetoelectric susceptibility $\bar{\alpha}$ in a ferroelectric film,

$$\bar{\alpha} = \frac{1}{l}\int_0^l \alpha(z)dz = \frac{1}{2K}\int_0^{2K}\alpha(u)du,$$

can be determined from expressions (8)–(10). As a result, we obtain

$$\bar{\alpha} = \frac{\alpha_t\sqrt{2m(1+m)}}{(1+m)E - (1-m)K}. \quad (11)$$

For the parameter $m \longrightarrow 1$, the magnitude of K increases logarithmically, $K(1-m) \longrightarrow 0$, and $E \longrightarrow 1$. From expression (11), we find that $\bar{\alpha} \longrightarrow \alpha_t$. The value $m = 1$ corresponds to a bulk sample. In this case, as follows from relationship (6), we have $l \gg l_0$.

The value $m \longrightarrow 0$ corresponds to a size-induced phase transition [9, 10]. In this situation, the following relationships are satisfied:

$$\begin{aligned}K(0) &= E(0) = \pi/2, \\ E(1+m) - K(1-m) &\cong 3\pi m/4.\end{aligned} \quad (12)$$

For the mean magnetoelectric susceptibility described by relationship (11), we derive the expression

$$\bar{\alpha} \cong \frac{4\sqrt{2}}{3\pi}\frac{\alpha_t}{\sqrt{m}}. \quad (13)$$

It follows from relationship (6) that, at $m \longrightarrow 0$, the film thickness l tends to the least value $l \longrightarrow \pi l_0 = l_c$, for which the spontaneous polarization becomes zero. For $l < l_c$, the spontaneous polarization is nonexistent. Therefore, the transition from the ferroelectric phase to the paraelectric phase at a constant temperature $T < T_c$ can occur with a decrease in the film thickness (the so-called size-induced phase transition). For a film thickness $l > l_c$, the temperature of the ferroelectric phase transition T_{cl} depends on the thickness [9, 10]:

$$T_{cl} = T_c\left[1 - \left(\frac{l_{c0}}{l}\right)^2\right], \quad l_{c0} = \pi\sqrt{\frac{\lambda}{a_0 T_c}}, \quad (14)$$

where l_{c0} is the critical thickness of the film at $T = 0$. For $l < l_{c0}$, we have $T_{cl} < 0$; i.e., the transition to the ferroelectric state becomes impossible. For small parameters m, from relationship (6) for films with a nearly critical thickness, we obtain

$$m \cong \frac{4}{3}\left(\frac{l}{l_c} - 1\right), \quad \bar{\alpha} \cong \frac{2\sqrt{2}}{\pi\sqrt{3}} \frac{\alpha_t}{\sqrt{\frac{l}{l_c} - 1}}, \quad l - l_c \ll l_c. \quad (15)$$

According to expressions (15), the magnetoelectric susceptibility of the film with $l > l_c$ at a constant temperature $T < T_c$ should exceed the magnetoelectric susceptibility α_t of the bulk sample at this temperature to such an extent that the film thickness l will be close to the critical thickness l_c.

On the other hand, from the expression relating the correlation length l_0 to the temperature through the parameter a and relationship (14), at temperatures close to T_{cl}, we have

$$m \cong \frac{2}{3}\frac{l^2}{l_{c0}^2}\frac{(T_{cl} - T)}{T_c}, \quad T_{cl} - T \ll T_c. \quad (16)$$

At temperatures close to T_{cl} for $l = l_c = \pi l_0$, from expressions (6), (7), (13), and (16) for the magnetoelectric susceptibility of a ferroelectric, we obtain

$$\bar{\alpha} = -\frac{4\gamma H}{\pi\sqrt{3a_0 b}} \frac{1}{\sqrt{T_{cl} - T}}. \quad (17)$$

The magnetoelectric susceptibility α_t of the bulk sample [see relationship (7)] exhibits a temperature dependence similar to that described by expression (17) in the vicinity of the Curie temperature T_c when $a \longrightarrow 0$. Note that the magnetoelectric susceptibility of the nonlinear effect at temperatures close to the temperature of the ferroelectric transition increases anomalously. By contrast, the magnetoelectric susceptibility of the linear effect in magnetoelectrics decreases and becomes zero at the magnetic transition temperature.

The parameter of the magnetoelectric interaction γ can be evaluated from the shift in the Curie temperature in a magnetic field in $BaTiO_3$ [2]. This shift implies renormalization of the parameter $a = a_0(T_c - T)$ in expression (1) for the free energy ($a \longrightarrow a - \gamma H^2$). As a result, we obtain

$$|\gamma| = \frac{a_0|\Delta T_c|}{H^2}, \quad (18)$$

where $|\Delta T_c|$ is the shift in the Curie temperature. For $BaTiO_3$, we have $\Delta T_c = 0.1$ K at $H = 10$ T [2]. The parameters a_0 and b for $BaTiO_3$ can be obtained using their values for $PbTiO_3$ [11] and the results of the comparison of the corresponding data for these compounds [12]. As a result, for $BaTiO_3$, we have $a_0 = 18.4 \times 10^{-5}$ K^{-1} and $b = 9.4 \times 10^{-13}$ CGSE. We obtain $|\gamma| = 1.8 \times 10^{-15}$ CGSE. Hence it follows that the mean magnetoelectric susceptibility of $BaTiO_3$ in the vicinity of the size-induced phase transition can be estimated as

$$\bar{\alpha} \approx \frac{10^{-7} H}{\sqrt{T_{cl} - T}}. \quad (19)$$

The same order of magnitude of the magnetoelectric susceptibility was obtained for $PbTiO_3$ at temperatures close to the size-induced phase transition ($T_{cl} \cong 533$ K [6, 7]). In this case, we used the parameters $a_0 = 7.7 \times 10^{-5}$ K^{-1} and $|b| = 4.27 \times 10^{-13}$ CGSE [11] and the magnitude of parameter γ for $BaTiO_3$.

3. RESULTS AND DISCUSSION

An analysis of expression (19) demonstrates that, in a magnetic field of approximately 10 T, the magnetoelectric susceptibility can reach values comparable to the highest susceptibility of the linear magnetoelectric effect known to date for magnetoelectrics (for example, $\alpha \approx 10^{-2}$ for $LiCoPO_4$).

For estimation, we used the parameters a_0 and b for the bulk sample. Therefore, expression (19) also gives the order of magnitude of the magnetoelectric susceptibility for the bulk sample at temperatures close to the Curie point in the case when the temperature T_{cl} is replaced by T_c in expression (19). In the model used here, the coefficients in functional (1) were considered to be independent of the sample size. In actuality, the Curie constant $C \sim a_0^{-1}$ for a $PbTiO_3$ thin film [7] is two orders of magnitude larger than the Curie constant for the bulk sample. Consequently, the magnetoelectric susceptibility in the vicinity of the size-induced phase transition should exceed the value predicted from expression (19).

The shift in the Curie temperature in a magnetic field for semiconductor ferroelectrics is one or two orders of magnitude greater than that for $BaTiO_3$ (for example, $\Delta T_c \cong 1$ K for $Pb_{1-x}Ge_xTe$ in the magnetic field $H = 3$ T). Therefore, the constant γ and, correspondingly, the magnetoelectric susceptibility, according to the estimate obtained from expression (19), should be one order of magnitude larger than those for nonconducting ferroelectrics.

For the effect considered above, the spontaneous electric polarization must go to zero at the layer boundary. In particular, this condition is satisfied in the case of contact with paraelectric layers. Therefore, the effect studied in this work can be observed in ferroelectric films and paraelectric–ferroelectric multilayer systems [6, 7].

REFERENCES

1. S. Takaoka and K. Murase, Phys. Rev. B **20**, 2823 (1979).
2. D. Wagner and H. J. M. Hanley, Phys. Lett. A **83A**, 347 (1981).
3. B. G. Vekhter, V. P. Zenchenko, and I. B. Bersuker, Fiz. Tverd. Tela (Leningrad) **18** (8), 2325 (1976) [Sov. Phys. Solid State **18**, 1356 (1976)].
4. I. B. Bersuker and V. Z. Polinger, *Vibronic Interactions in Molecules and Crystals* (Nauka, Moscow, 1983; Springer, New York, 1989).
5. G. A. Smolenskiĭ and I. E. Chupis, Usp. Fiz. Nauk **137**, 415 (1982) [Sov. Phys. Usp. **25**, 475 (1982)].
6. A. Erbil, Y. Kim, and R. A. Gerhardt, Phys. Rev. Lett. **77**, 1628 (1996).
7. Y. Kim, R. A. Gerhardt, and A. Erbil, Phys. Rev. B **55**, 8766 (1997).
8. Y. Ishibashi, H. Orihara, and D. R. Tilley, J. Phys. Soc. Jpn. **67** (9), 3292 (1998).
9. M. D. Glinchuk, E. A. Eliseev, V. A. Stephanovich, *et al.*, cond-mat/0004258.
10. M. D. Glinchuk, E. A. Eliseev, and V. A. Stefanovich, Fiz. Tverd. Tela (St. Petersburg) **44**, 912 (2002) [Phys. Solid State **44**, 953 (2002)].
11. E. G. Fesenko, N. G. Gavrilyachenko, and E. V. Zarochentsev, Izv. Akad. Nauk SSSR, Ser. Fiz. **34**, 2541 (1970).
12. B. D. Qu, W. L. Zhong, and R. H. Prince, Phys. Rev. B **55**, 11218 (1997).

Translated by N. Korovin

Physics of the Solid State, Vol. 45, No. 7, 2003, pp. 1288–1294. Translated from Fizika Tverdogo Tela, Vol. 45, No. 7, 2003, pp. 1228–1234.

MAGNETISM AND FERROELECTRICITY

Potential Relief on the Surface of Polarized Ferroelectric Electrets from an Analysis of the Anomalous Electron Emission Spectra

A. T. Kozakov, A. V. Nikol'skiĭ, and I. V. Novikov

Research Institute of Physics, Rostov State University, pr. Stachki 194, Rostov-on-Don, 344091 Russia

e-mail: kozakov@ip.rsu.ru, kozakov_a@mail.ru

Received August 8, 2002; in final form, December 2, 2002

Abstract—A technique is proposed for determining the specific features in the potential distribution over a free surface of polarized ferroelectric electrets from analyzing the anomalous electron emission spectra. This technique is applied to examine the potential distribution over the surface of a lead magnoniobate single crystal and ferroelectric ceramics. Reasoning from the results obtained for the lead magnoniobate crystal, the inference is drawn that the degree of perfection of surface layers of ferroelectric single crystals can be controlled using the anomalous electron emission spectra. *© 2003 MAIK "Nauka/Interperiodica".*

1. INTRODUCTION

In our earlier works [1–7], we revealed and investigated both experimentally and theoretically the anomalous electron emission from the surface of ferroelectrics with electret properties. The term "ferroelectric with electret properties" is used in reference to a ferroelectric that exhibits an electret effect and ferroelectric polarization generated by a field of electret charges. In [7], it was demonstrated that the shape of the anomalous electron emission spectra is determined by the potential distribution over the surface of the polarized sample under investigation. It should be noted that the potential distribution is the most important energy characteristic of the surface of ferroelectrics. In this respect, it was of interest to assess the possibility of solving the inverse problem, namely, to calculate the potential distribution over the surface of a polarized ferroelectric sample or, at least, to obtain information on the specific features of this distribution from analyzing the anomalous electron emission spectra.

The purpose of this work is to investigate analytically the anomalous electron emission spectra and to establish the relation between the potential distribution and surface characteristics of a polarized ferroelectric sample. The theoretical principles of the technique used for processing the experimental spectra will be considered below.

2. CALCULATION OF THE FUNCTION $n(\varphi)$

The potential distribution can be determined from analyzing the function $n(\varphi)$, which, in turn, can be obtained from an experimental anomalous electron emission spectrum with the use of the relationship [7]

$$I(\varepsilon) = \int j_0(\varepsilon - \varphi) n(\varphi) d\varphi, \qquad (1)$$

where ε is the kinetic energy of the electron, $I(\varepsilon)$ is the experimental spectrum, $j_0(\varepsilon)$ is the spectral density of emission from the neutral surface, $n(\varphi) = \int dl/|\nabla\varphi(\rho)|$, and $\varphi(\rho)$ is the surface potential. The summation in the integral for the function $n(\varphi)$ is performed along equipotential lines. Hence, it can be concluded that $n(\varphi)$ is proportional to the number of points with a given potential on the surface of the sample. The fine structure of the function $n(\varphi)$ indicates a potential distribution over the surface. The larger the number of specific features in the fine structure of the function $n(\varphi)$ and the larger its energy width, the more nonuniform the potential distribution. And vice versa, the smaller the energy width of the function $n(\varphi)$, the more uniform the potential distribution.

Expression (1) is a convolution-type integral equation [8], in which the sought function $n(\varphi)$ formally represents a true intensity distribution in the spectrum and $j_0(\varepsilon)$ is a distortion function. Therefore, the determination of the potential distribution on the surface of the polarized ferroelectric can be reduced to the solution of the problem frequently encountered in spectroscopy, namely, to correction of spectral distortions. In this case, the experimental anomalous electron emission spectrum is treated as a standard approximation to the function $n(\varphi)$ and the evolution of this spectrum (its shape and structure) during charge relaxation on the surface of the ferroelectric electret is associated with the change in the potential distribution over the surface in the course of relaxation. For a symmetric distortion function, the use of the available methods of solving the

1063-7834/03/4507-1288$24.00

integral equation does not lead to a change in the number of specific features in the experimental spectrum but renders them more resolved. However, in our case, the function $j_0(\varepsilon)$ is asymmetric. Therefore, the distortion of the true spectrum by this function should result not only in a smearing and smoothing of the specific features in the function $n(\varphi)$ but also in a change in their shape and, possibly, in a shift of the energy location of maxima in the experimental spectrum. At present, there exist a number of efficient methods for solving Eq. (1) [8–11]. Traditional methods that are based on the Fourier transform and the use of a symmetric distortion function turn out to be inapplicable in the case under consideration. For this reason, we used the method based on the probability Bayes theorem, which permits one to correct a spectrum by applying an asymmetric function [11]. Moreover, this method, in principle, excludes the appearance of negative intensities, is stable to insignificant statistical experimental errors, and offers equal areas of the corrected and experimental spectra, which considerably facilitates practical use of the method.

In [7], the function $j_0(\varepsilon)$ was approximated by the expression $j_0(\varepsilon) \approx \exp(\varepsilon/\gamma)\theta(\varepsilon)$, where $\theta(\varepsilon) = 0$ at $\varepsilon < 0$ and $\theta(\varepsilon) = 1$ at $\varepsilon > 0$ and γ is the half-width (~10 eV). In the present work, the form of the function $j_0(\varepsilon)$ was determined from the experimental data obtained for the surfaces of a ferroelectric ceramic sample and a lead magnoniobate single crystal. Figure 1a shows the electron emission line, which represents the distortion function in the integral equation (1).

The functions $n(\varphi)$ calculated in such a manner are displayed at the right of Figs. 1 and 2. However, the above approach does not provide a way of reliably revealing the specific features of the potential distribution. This can be done in the framework of the following approach.

3. SIMULATION OF THE SPECTRA

The proposed approach is based on the assumption that the experimental anomalous electron emission spectrum can be represented as the sum of the components, each being a theoretically calculated electron emission spectrum [7] accounting for a particular feature of the potential distribution. In [7], it was shown that the main contribution to the anomalous electron emission spectra should be made by surface regions with small gradients of the potential in the vicinity of its extrema. There are three types of extrema: maxima, minima, and inflection points. The theoretical electron emission spectra that correspond to surface regions in the vicinity of these extrema in the potential distribution were calculated in [7] within the one-dimensional approximation. The shape of the spectra for the maximum, minimum, and inflection point in the potential distribution is depicted in Figs. 1 and 2. When the experimental anomalous electron emission spectra and the theoretical electron emission spectra corresponding to the extrema are available, the problem is reduced to the decomposition of the experimental spectra into the theoretical components or, what is the same, to the simulation of the experimental spectra from the theoretical curves. In this case, the number of peaks in the function $n(\varphi)$ and their energy positions determine the number of components of the decomposition and their energy locations in the spectrum. Similar simulation techniques have been sufficiently well developed, for example, in electron and x-ray spectroscopy [12, 13]. They can be employed with due regard for the differences arising in our problem. These differences reside in the fact that the spectral components associated with maxima, minima, and inflection points in the one-dimensional potential distribution have different shapes. This substantially complicates the problem, because all components of the decomposition within traditional approaches have identical Gaussian or dispersion shapes [8, 12, 13].

The results of simulation, i.e., the quality of the simulated spectra, can be assessed using the weighted parameter χ^2 [12–14]. This criterion is relative and depends on the absolute intensity of electron emission lines. Therefore, the parameter χ^2 cannot be used for comparing the quality of the simulation of different spectra. However, when the spectra are normalized to unit area and the parameter χ^2 is treated not as a statistical parameter (as, for example, in [14]) but as a quantity proportional to the difference between the experimental and simulated spectra (as follows from its definition [12–14] and this meaning holding at a sufficiently large number of points in the spectrum), such a comparison becomes possible. These modified parameters χ^2 are given below for the anomalous electron emission spectra (Figs. 1, 2). The simulated and experimental spectra are shown at the left of Figs. 1 and 2.

4. RESULTS OF CALCULATIONS OF THE FUNCTION $n(\varphi)$ AND SIMULATION OF THE SPECTRA

The functions $n(\varphi)$ and the results of the decomposition of the experimental anomalous electron emission spectra of lead magnoniobate (PMN) single crystals and PKR-70 ceramics are presented in Figs. 1 and 2, respectively. The conditions for polarization of the samples and recording of the spectra are described in [1, 15, 16].

The spectra in Figs. 1b and 1d were measured for different polarizations of the PMN single-crystal sample. Consequently, these spectra are different in shape [1]. It can be seen that the main components of the decomposition are the theoretical spectra associated with the minima and steps in the potential distribution. The functions $n(\varphi)$ corresponding to these experimental spectra have a very complex form (indicating a considerable polarization inhomogeneity on the PMN surface) and, hence, are difficult to interpret. However, unlike single crystals, the ferroelectric ceramic sam-

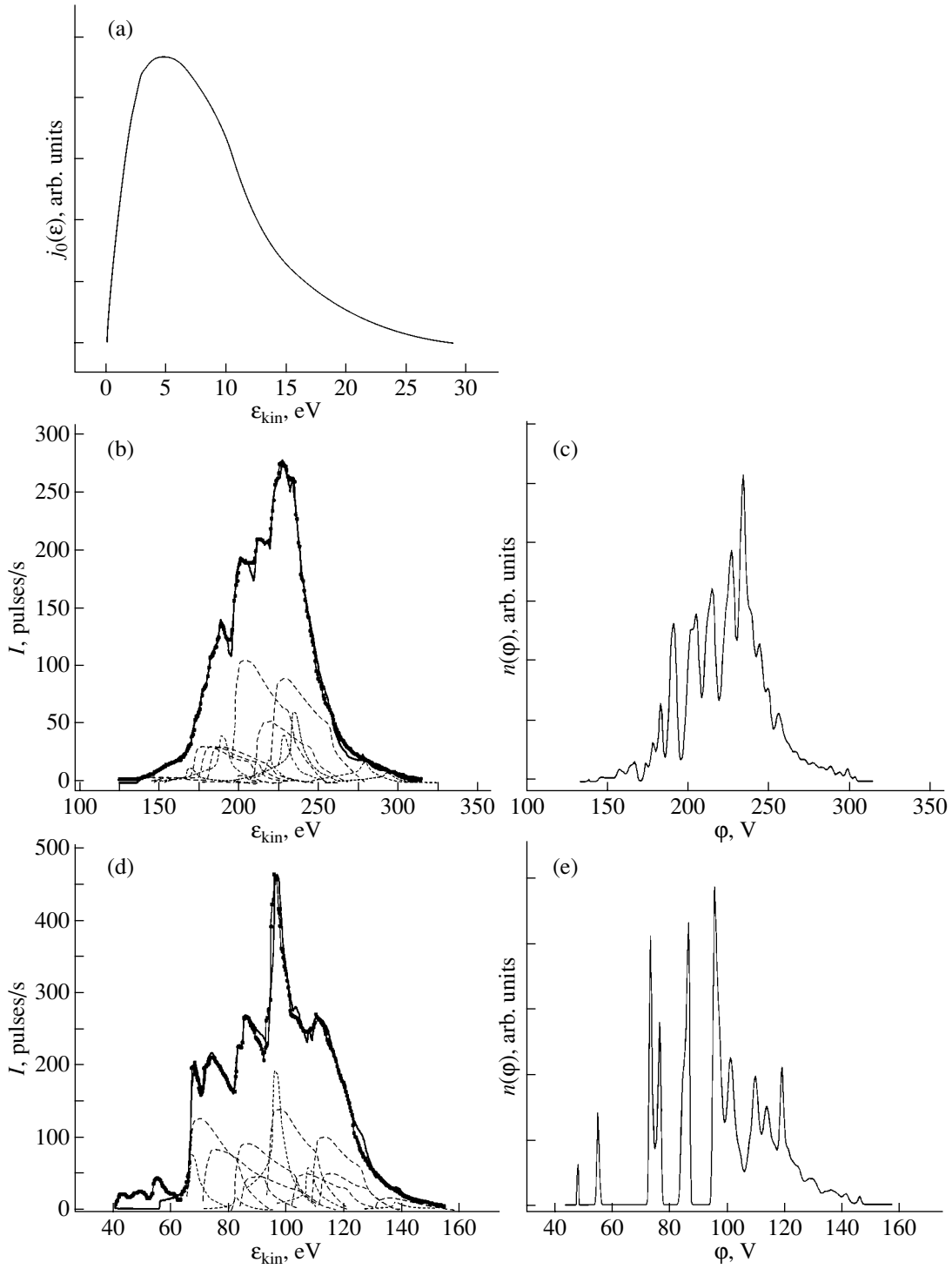

Fig. 1. (a) Distortion function $j_0(\varepsilon)$ determined from the experimental data. (b, d) Experimental anomalous electron emission spectra (points and heavy lines passing through them) of the surface of PMN single-crystal samples for different polarizations. Thin lines show the simulated anomalous electron emission spectra. Dashed lines under the experimental and simulated spectra represent the components of the spectral decomposition. (c, e) Functions $n(\varphi)$ calculated from the experimental spectra.

ples, in a number of cases, are characterized by sufficiently narrow spectra. As a result, these spectra can be decomposed into a small number of components, which simplifies their interpretation. It is this situation that is illustrated in Fig. 2.

Figures 2a, 2c, and 2e display the experimental anomalous electron emission spectra of the surface of the PKR-70 ceramic sample at the same polarization for different mean electret potentials φ = 300, 18, and 14 V. The electret potential was measured by the vibrat-

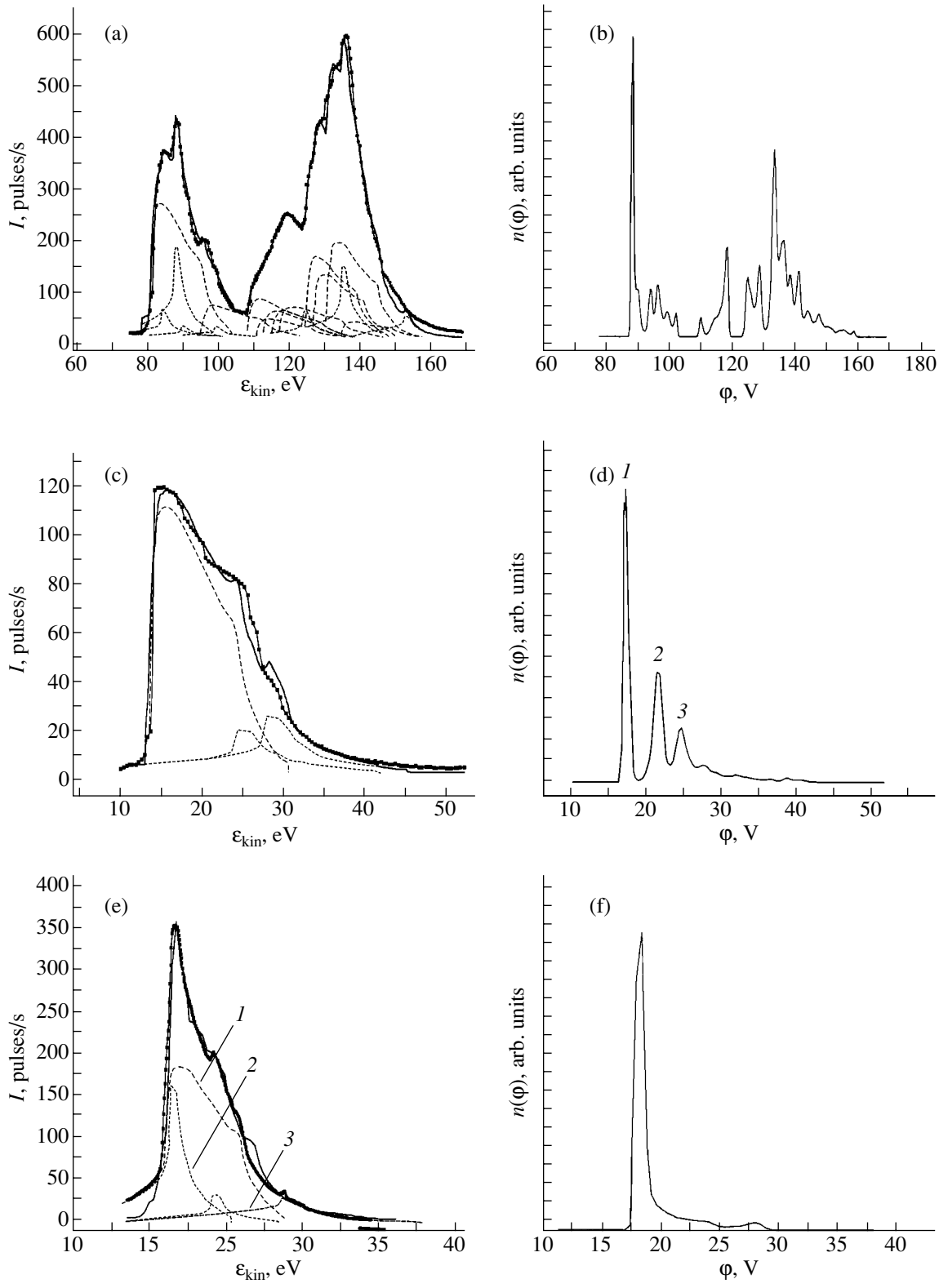

Fig. 2. (a, c, e) Experimental anomalous electron emission spectra (points and heavy lines passing through them) of the surface of PKR-70 ceramics at different mean electret potentials φ = (a) 300, (c) 18, and (e) 14 V. Thin lines show the simulated anomalous electron emission spectra. Dashed lines under the experimental and simulated spectra represent the components of the spectral decomposition. Numerals in panel (d) designate the peaks associated with the emission at (*1*) the minimum and (*2*, *3*) steps in the potential distribution. Numerals in panel (e) indicate the theoretical electron emission spectra at (*1*) the minimum, (*2*) the step, and (*3*) the maximum in the potential distribution. (b, d, f) Functions $n(\varphi)$ calculated from the experimental spectra.

ing probe technique [17]. Initially, the spectrum is recorded for the surface with a higher potential. The electret potential decreases with time. This is accompanied by a change in the potential relief on the sample surface, which results in a change in the fine structure and the energy width of the anomalous electron emission spectrum. The functions $n(\varphi)$ calculated with the use of the above technique from the corresponding experimental spectra are displayed in Figs. 2b, 2d, and 2f. The components of the spectral decomposition and the spectra simulated using these components are shown under each experimental spectrum in Figs. 2a, 2c, and 2e. It can be seen that the experimental spectra agree sufficiently well with the simulated spectra. The best agreement is observed for the spectra in Fig. 2a. This is confirmed by the modified parameters χ^2. These parameters for the simulated spectra presented in Figs. 2a, 2c, and 2e are equal to 2.36, 6.90, and 11.16%, respectively. The modified parameters χ^2 for the spectra depicted in Figs. 1b and 1d are equal to 0.49 and 0.97%, respectively. This indicates that the experimental and simulated spectra of the surface of the single crystals are in better agreement than the spectra of the ceramics. A comparison of Figs. 2c and 2d shows that, in the function $n(\varphi)$, peak *1* is associated with the emission at the minimum in the potential, whereas peaks *2* and *3* are attributed to the emission at the steps in the potential. In the function $n(\varphi)$ shown in Fig. 2f, the peak with the highest intensity is determined by the components corresponding to the minimum and the step in the potential, the second peak is associated with the step, and the third peak is attributed to the maximum in the potential. A similar analysis can also be performed for the spectra observed in a wider energy range with a larger number of components of the spectral decomposition. However, in this case, it is not always possible to identify the peaks in the spectra uniquely (for example, in the spectra displayed in Figs. 1b, 1d, and 2a).

As can be seen from the anomalous electron emission spectra and the calculated functions $n(\varphi)$ presented in Fig. 2, the potential distribution over the surface of the polarized ceramics originally exhibits two principal peaks at energies of approximately 85 and 135 eV. A large number of peaks with lower intensities in the function $n(\varphi)$ in Fig. 2b indicate that regions with other potentials also exist on the sample surface. However, the number of points with these potentials is limited as compared to points with potentials of 85 and 135 eV. An analysis of the potential distribution over the surface of the polarized sample indicates polarization inhomogeneity on the sample surface. This state is unstable and changes with a decrease in the net electret charge. These processes can be investigated in detail with the use of the anomalous electron emission spectra, the calculated functions $n(\varphi)$, and the components of the spectral decomposition.

Thus, the proposed technique makes it possible to obtain data on the specific features of the potential distribution over the surface of polarized samples, namely, the number of maxima, minima, and inflection points; the degree of polarization inhomogeneity; and the evolution of the potential during relaxation of the electret charge injected into the surface layer.

5. DISCUSSION

The theoretical electron emission spectra used in our simulation for surface regions in the vicinity of extrema in the potential distribution were calculated in [7] within the one-dimensional approximation and with the aforementioned model distortion function. Consequently, the agreement obtained in the present work between the experimental and simulated anomalous electron emission spectra is not accidental but is justified physically. This agreement indicates that, for the most part, the one-dimensional model appears to be adequate for the ferroelectric electrets under investigations. The one-dimensional approximation implies the formation of surface anisotropic stripe structures in the distributions of the electric field and polarization [7]. Moreover, the assumption that the emission occurs from the sample regions corresponding to extrema in the potential distribution over the surface should also be considered valid. This result is of interest in the study of emission from cold cathodes based on ferroelectrics. It should be noted that, for a number of ferroelectric samples, the theoretical spectra cannot be fitted well to the experimental spectra. In this case, the experimental spectra have a shape characteristic of two-dimensional polarization structures [7].

It is interesting to elucidate the physical nature of stripe charged (potential) structures on the studied surfaces. It is evident that these structures on the surfaces of both single-crystal and ceramic ferroelectrics can differ in nature. The nonuniform potential distribution over the surface of ferroelectric samples can be caused by initial structural imperfections of the crystals (dislocations, block and grain boundaries, etc.) and the specific features of the domain structure (the formation of *a* and *c* domains and their quantitative ratio, domain walls, etc.) [18, 19]. In order to identify the specific features of the anomalous electron emission spectrum with particular physical objects on the surface of the ferroelectric, we carried out the following experiment. One PMN single-crystal sample $10 \times 10 \times 1$ mm in size was subjected to different physical actions (polishing, annealing, and polarization). This resulted in the formation of a pronounced optical inhomogeneity 2×6 mm in size, which was located asymmetrically with respect to the geometric center of the sample. X-ray diffraction examination of the sample revealed a block structure with a mutual crystallographic misorientation of the order of several angular seconds.

Figure 3 shows the anomalous electron emission spectrum of the entire surface of this sample (curve *1*). It can be seen from Fig. 3 that spectrum *1* is characterized by a complex fine structure over a wide energy range (more than 120 eV). The anomalous electron

emission spectra of two different surface regions of the single-crystal sample (curves *2* and *3*) were measured by screening, in turn, these regions with a metallic shield. Spectra *1–3* are depicted in Fig. 3 on the same energy scale. Compared to the spectrum of the entire surface, the spectra of different surface regions cover a narrower energy range and exhibit a smaller number of specific features. Furthermore, spectrum *2*, which was measured for the surface region involving the inhomogeneity, has a more complex structure, covers a wider energy range, and is shifted toward high energies as compared to spectrum *3*, which was recorded for the more homogeneous surface region. The specific features in the fine structures of the spectra obtained for both surface regions agree reasonably in energy with the corresponding features in the spectrum of the entire sample surface. This spectrum is a superposition of the above two spectra of the surface regions. Note that the integrated intensity of the spectrum of the entire surface is equal to the sum of the integrated intensities of the spectra of both surface regions to an accuracy of 5%. All the foregoing demonstrates with confidence that the specific features in the potential distribution over the surface of the PMN single crystal due to crystal imperfection manifest themselves in the shape and energy location of the anomalous electron emission spectra. It should be noted that the anomalous electron emission spectra of the surface of the PMN samples without visually observed block structure also have a sufficiently complex structure. In this case, the experimental and simulated spectra agree well with each other (see, for example, Fig. 1b). Therefore, we can assume that other physical mechanisms can also be responsible for the formation of the stripe potential structures on the surface. In particular, the stripe potential distribution can be associated with the fragments of a domain structure, as can be judged from x-ray powder diffraction and scanning electron microscopic investigations of the domain structure in a number of ferroelectric materials [20]. In [18–20], the authors actually examined the potential relief, which predominantly had a stripe structure in the images. Morlon *et al.* [21] observed the stripe domain structure on the $BaTiO_3$ surface in photoelectron images obtained upon excitation with UV radiation. This type of electronic excitation is similar to that used in our experiments. In [21], it was also noted that the surface image in the form of a set of parallel stripes is associated with the potential relief that has the same shape and is hypothetically formed by positively and negatively charged stripe regions composed of *c* domains. Moreover, a number of other factors can also be responsible for the stripe potential relief in ferroelectric materials. One of the most studied factors is the formation of antiparallel domains upon polarization switching by applying a dc electric field to a material [18, 19]. The antiparallel domains are formed by charges localized in traps, which are different defects arranged near the crystal surface or along the boundaries of 180° domain walls. The exposure to radiation

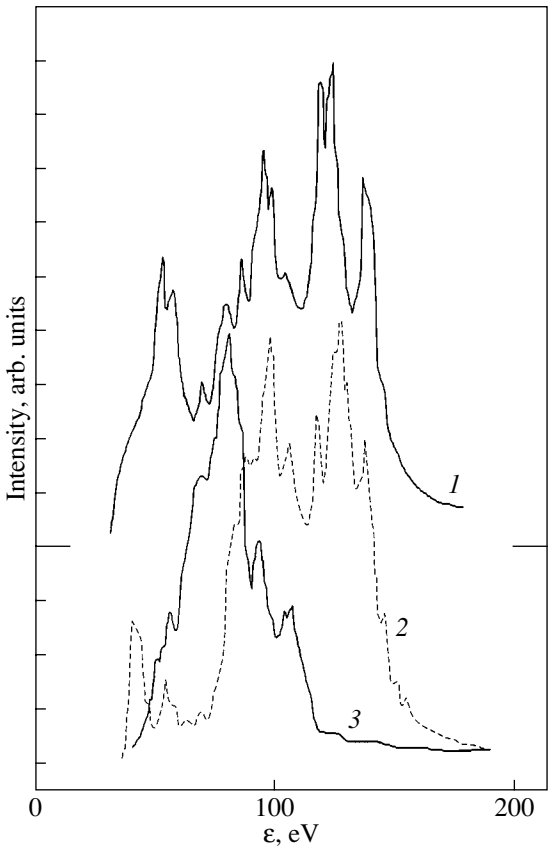

Fig. 3. Anomalous electron emission spectra of the surface of the PMN single crystal with a block structure: (*1*) spectrum of the entire surface of the sample, (*2*) spectrum of the surface region with a visually observed block structure, and (*3*) spectrum of the surface region without a visually observed block structure.

favors the growth of antiparallel domains with a positive screened charge [18]. With the use of gamma irradiation, domain boundaries can be frequently revealed from defects retained in their vicinity in the crystal prior to the polarization in a dc electric field [18]. Taking into account the method of exciting the anomalous electron emission (x-rays at $h\nu \le 3$ keV), we cannot rule out the formation of antiparallel domains on the studied surface and their manifestation in the anomalous electron emission spectra of the PKR-70 ceramic sample. Note that the anomalous electron emission spectrum shown in Fig. 1 contains components of the spectral decomposition that correspond to the minima and steps in the potential distribution. This also indicates a complex energy distribution over the surface of the polarized PMN crystal, which calls for further investigation.

Therefore, quite different structures formed on the surface of polarized ferroelectrics can give rise to a stripe potential relief, which, in turn, is responsible for the structure of the anomalous electron emission spectrum. In each specific case, it is necessary to perform

detailed investigations in order to elucidate the particular physical cause for the appearance of a fine structure in the anomalous electron emission spectrum. At the same time, such an examination leads to the refinement of the energy distribution and the parameters of energy processes on the surface of polarized ferroelectrics. This is a usual way of developing a spectroscopic method according to which the spectra are calculated within model concepts of the nature of the object under investigation. When the experimental and theoretical spectra are in agreement, these concepts are considered true. This provides information on a particular property of the studied object. In this respect, the above techniques of analyzing the potential distribution offer promise for investigation of the energy characteristics associated with the surface levels, defects, different-type traps, dislocations, and block and domain structures of the electrode-free surface of polarized ferroelectrics.

The problems associated with the surface properties of ferroelectrics were theoretically discussed in detail in the 1970s [22, 23]. Their experimental investigation becomes possible with the advent of the technique proposed in the present work for the processing of anomalous electron emission spectra.

6. CONCLUSIONS

Thus, in this work, we proposed a technique for processing anomalous electron emission spectra. It was demonstrated that this technique provides a means for obtaining information on the specific features of the potential distribution over the electrode-free surface of ferroelectric electrets.

The potential distribution over the surface of polarized PMN single crystals and PKR-70 ceramic samples was investigated using the proposed technique. It was established that the main features of the potential distribution in these materials are the minima and inflection points, whereas the high-energy tails in the anomalous electron emission spectra are formed by several maxima.

It was revealed that the anomalous electron emission spectra of the surface of the PMN single-crystal and PKR-70 ceramic samples exhibit a complex fine structure, which is associated with the stripe potential relief due to the formation of different-type charged linear structures on the surface. The inference was made that the anomalous electron emission spectra can be used to control the degree of perfection of the surface layers of PMN single crystals.

ACKNOWLEDGMENTS

This work was supported from the State Budget for the Research Institute of Physics of the Rostov State University.

REFERENCES

1. A. T. Kozakov, V. V. Kolesnikov, V. P. Sakhnenko, *et al.*, Fiz. Tverd. Tela (St. Petersburg) **38** (8), 2524 (1996) [Phys. Solid State **38**, 1385 (1996)].
2. A. T. Kozakov, V. V. Kolesnikov, A. V. Nikol'skiĭ, and V. P. Sakhnenko, Fiz. Tverd. Tela (St. Petersburg) **39** (4), 679 (1997) [Phys. Solid State **39**, 594 (1997)].
3. A. V. Nikol'skiĭ and A. T. Kozakov, Fiz. Tverd. Tela (St. Petersburg) **39** (8), 1446 (1997) [Phys. Solid State **39**, 1284 (1997)].
4. V. V. Kolesnikov, A. T. Kozakov, and A. V. Nikol'skiĭ, Fiz. Tverd. Tela (St. Petersburg) **42** (1), 141 (2000) [Phys. Solid State **42**, 146 (2000)].
5. A. T. Kozakov, A. V. Nikol'skiĭ, and I. V. Novikov, Zh. Strukt. Khim. **39** (6), 1031 (1998).
6. V. V. Kolesnikov and A. T. Kozakov, Fiz. Tverd. Tela (St. Petersburg) **42** (11), 2085 (2000) [Phys. Solid State **42**, 2148 (2000)].
7. V. V. Kolesnikov and A. T. Kozakov, Fiz. Tverd. Tela (St. Petersburg) **44** (1), 147 (2002) [Phys. Solid State **44**, 153 (2002)].
8. I. Ya. Nikiforov, Doctoral Dissertation (Rostov-on-Don, 1982).
9. A. F. Verlan' and V. S. Sizikov, *Methods of Solving Integral Equations with Computer Programs* (Naukova Dumka, Kiev, 1978).
10. W. H. Richardson, J. Opt. Soc. Am. **62** (1), 55 (1972).
11. T. J. Kennett, W. V. Prestwich, and A. Robertson, Nucl. Instr. Methods **151**, 285 (1978).
12. *Practical Surface Analysis by Auger and X-ray Photoelectron Spectroscopy*, Ed. by D. Briggs and M. Seah (Wiley, New York, 1983; Mir, Moscow, 1987).
13. R. O. Ansell, T. Dickinson, A. F. Povey, and P. M. A. Sherwood, J. Electroanal. Chem. **98**, 79 (1979).
14. D. Hudson, *Statistics: Lectures on Elementary Statistics and Probability* (Geneva, 1964; Mir, Moscow, 1970).
15. A. T. Kozakov, I. V. Novikov, V. V. Kolesnikov, and A. V. Nikol'skiĭ, Nauch. Mysl' Kavkaza, Pril. 1 (6), 90 (2000).
16. A. T. Kozakov, A. V. Nikol'skiĭ, I. V. Novikov, *et al.*, Pis'ma Zh. Tekh. Fiz. **23** (16), 55 (1997) [Tech. Phys. Lett. **23**, 640 (1997)].
17. A. N. Gubkin, *Electrets* (Nauka, Moscow, 1978).
18. V. Z. Borodin, E. N. Éknadiosyants, and A. I. Pinskaya, Kristallografiya **27** (4), 807 (1982) [Sov. Phys. Crystallogr. **27**, 486 (1982)].
19. É. Ya. Shneĭder, S. G. Gakh, V. Z. Borodin, and E. I. Éknadiosyants, Kristallografiya **28** (6), 1161 (1983) [Sov. Phys. Crystallogr. **28**, 682 (1983)].
20. I. S. Zheludev, *Principles of Ferroelectricity* (Atomizdat, Moscow, 1973), p. 171.
21. B. Morlon, E. Coquet, and A. Devin, C. R. Acad. Sci. B **270**, 283 (1970).
22. B. V. Selyuk, Kristallografiya **19** (2), 221 (1974) [Sov. Phys. Crystallogr. **19**, 133 (1974)].
23. M. E. Lines and A. M. Glass, *Principles and Applications of Ferroelectrics and Related Materials* (Oxford Univ. Press, Oxford, 1977; Mir, Moscow, 1981).

Translated by O. Borovik-Romanova

Physics of the Solid State, Vol. 45, No. 7, 2003, pp. 1295–1297. Translated from Fizika Tverdogo Tela, Vol. 45, No. 7, 2003, pp. 1235–1237.

MAGNETISM AND FERROELECTRICITY

Heterophase States in $0.10PbTiO_3$–$0.90Pb(Zn_{1/3}Nb_{2/3})O_3$ Crystals

V. Yu. Topolov

Rostov State University, ul. Zorge 5, Rostov-on-Don, 344090 Russia

e-mail: topolov@phys.rsu.ru

Received December 4, 2002

Abstract—A new model of the elastic matching of phases is proposed, and heterophase structures near the morphotropic phase boundary in $0.10PbTiO_3$–$0.90Pb(Zn_{1/3}Nb_{2/3})O_3$ crystals are studied. Unique behavior of the unit cell parameters is found to favor the elastic matching of the ferroelectric tetragonal and orthorhombic phases under the conditions of complete or partial relaxation of internal mechanical stresses at a volume concentration ratio of these phases of about 20/80% and temperatures of T = 20–300 K. Interrelations between the volume concentrations of different domain (twin) types and of the coexisting phases are analyzed. © *2003 MAIK "Nauka/Interperiodica".*

Interest in $x PbTiO_3$–$(1 - x)Pb(Zn_{1/3}Nb_{2/3})O_3$ (xPT–PZN) solid solutions with a perovskite-type structure is evoked by the following factors. First, the xPT–PZN system is characterized by unique physical properties owing to a combination of ferroelectric and relaxor components [1–3]. Second, near the morphotropic boundary ($x \approx$ 0.08–0.09), heterophase structures are observed which significantly affect the piezoelectric, dielectric, and elastic properties of xPT–PZN crystals [4–7]. Third, the low-symmetry ferroelectric phases detected recently in xPT–PZN [2, 8–10], $Pb(Zn_{1-y}Ti_y)O_3$ [11], and $z PbTiO_3$–$(1 - z)Pb(Mg_{1/3}Nb_{2/3})O_3$ [12, 13] are considered a common feature of perovskite solid solutions with high piezoactivity [9]. Fourth, the effect of a constant electric field E on xPT–PZN crystals near the morphotropic boundary is ambiguous because of the induced intermediate phases with different symmetries and of the related heterophase, domain, and twin structures [4, 8, 10]. One of the manifestations of such an ambiguity is the appearance of a new orthorhombic (O) ferroelectric phase in crystals with $x = 0.08$ and $0.09 \le x \le 0.10$ at $E \neq 0$ and $E = 0$, respectively [9].[1] The purpose of this work is to analyze the interaction between polydomain (twinned) phases in xPT–PZN crystals near the boundary of the O-phase field.

La-Orauttapong *et al*. [9] found that, as temperature T decreases, a 0.10PT–PZN crystal undergoes the first-order phase transformations: cubic paraelectric phase ⟶ tetragonal (T) ferroelectric phase ⟶ O ferroelectric phase. Below the temperature of the T–O phase transformation ($T_{t-o} \approx 320$ K), the crystal remains heterophase and the volume concentration of the metastable T phase in the range $20 \le T \le 300$ K remains virtually the same. To analytically determine the volume concentrations and optimum conditions for the elastic matching of the T and O phases in the two-phase crystal, we propose the following model. A crystalline sample is represented as a set of two types of heterophase regions with phases I and II in each of them (Fig. 1). The volume concentrations in these regions are w and $w' = 1 - w$ (we call them w- and w'-type regions, respectively). Each region is two-phase, so that the inclusion phase in a region (e.g., phase I in a w-type region; see Fig. 1) becomes the "matrix" phase in the neighboring regions (e.g., phase I in w'-type regions) and *vice versa*. To quantitatively describe the heterophase regions, we introduce the volume concentrations of "inclusions": r_t (T phase) and r_o (O phase) in the case of an xPT–PZN crystal. Assuming that the w- and w'-type regions are uniformly distributed in the crystal and that their concentrations are the same, we have $w = w' = 1/2$. Under this condition, the volume concentrations r_t and r_o describe the fractions of T and O phases, respectively, in the volume of the whole crystal and, hence, are connected by the relation

$$r_t + r_o = 1. \quad (1)$$

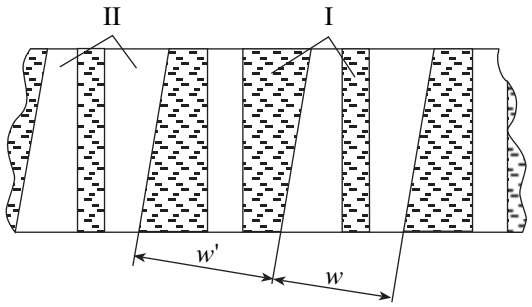

Fig. 1. Schematic of the 0.10PT–PZN crystal: (I) the O phase and (II) the T phase.

[1] This orthorhombic phase is considered as a limiting case of a monoclinic phase with symmetry P_m and a spontaneous polarization vector oriented along the [101] direction in a perovskite cell [2, 9].

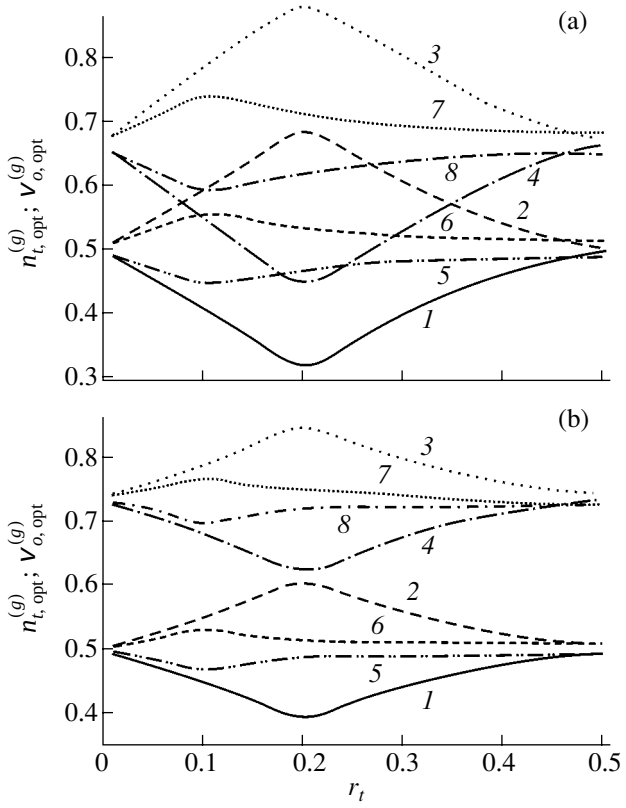

Fig. 2. Calculated concentration dependences of $n_{t,\,\mathrm{opt}}^{(g)}(r_t)$ and $\nu_{o,\,\mathrm{opt}}^{(g)}(r_t)$ characterizing the domain (twin) structure of the coexisting *T* and *O* phases in the 0.10PT–PZN crystal at (a) T = 300 and (b) 20 K: (*1*, *5*) $n_{t,\,\mathrm{opt}}^{(1)}(r_t)$, (*2*, *6*) $n_{t,\,\mathrm{opt}}^{(2)}(r_t)$, (*3*, *7*) $\nu_{o,\,\mathrm{opt}}^{(1)}(r_t)$, and (*4*, *8*) $\nu_{o,\,\mathrm{opt}}^{(2)}(r_t)$. (*1*, *4*) Calculations at f_o = 0.5 and (*5*–*8*) calculations at f_o = 0.1.

We denote the matrices of distortions in the *w*- and *w*'-type regions as $\|K\|$ and $\|K'\|$, respectively, and determine them with allowance for the electromechanical interaction between the *T* and *O* phases inside each heterophase region. Taking into account Eq. (1), we can write the matrix equations

$$\begin{aligned}\|K\| &= (1-r_t)\|K'\|\|N_o\| + r_t\|N_t\|;\\ \|K'\| &= r_t\|K\|\|N_t\| + (1-r_t)\|N_o\|.\end{aligned} \tag{2}$$

In the right-hand sides of Eqs. (2), the first terms characterize the effect of the neighboring *w*- or *w*'-type region on the inclusion phase in a given region and $\|N_o\|$ and $\|N_t\|$ are the matrices of distortions in the coexisting *O* and *T* phases, respectively.[2] The *T* phase is assumed to be divided into 90° domains [2] with the basis vectors ($\mathbf{a_t}$, $\mathbf{b_t}$, $\mathbf{c_t}$) oriented along the directions ([100], [010], [001]) and ([010], [001], [100]) of the perovskite unit cell and with the volume concentrations n_t and $1 - n_t$, respectively. According to the results in [2], the *O* phase is represented by domains of four types with the basis vectors ($\mathbf{a_o}$, $\mathbf{b_o}$, $\mathbf{c_o}$) and the volume concentrations n_{ok}, so that $\mathbf{a_o} \parallel [100]$ and $\mathbf{b_o} \parallel [0\bar{1}0]$ for k = 1, $\mathbf{a_o} \parallel [\bar{1}00]$ and $\mathbf{b_o} \parallel [010]$ for k = 2, $\mathbf{a_o} \parallel [010]$ and $\mathbf{b_o} \parallel [100]$ for k = 3, and $\mathbf{a_o} \parallel [0\bar{1}0]$ and $\mathbf{b_o} \parallel [\bar{1}00]$ for k = 4; $\mathbf{c_o} \parallel [001]$ in all domains of the *O* phase. The volume concentrations of these domains $n_{o1} = f_o\nu_o$, $n_{o2} = (1 - f_o)\nu_o$, $n_{o3} = f_o(1 - \nu_o)$, and $n_{o4} = (1 - f_o)(1 - \nu_o)$ are expressed in terms of the parameters f_o and ν_o, which are the volume concentrations of mechanical twins in the *O* phase. The domains of the *T* and *O* phases are assumed to be separated by planar boundaries (walls), according to the concepts developed in [14]. The analysis of the elastic matching of the *w*- and *w*'-type regions is based on the algorithm proposed in [15, 16] and on the matrix elements

$$D_{ij} = \sum_{i=1}^{3}(K'_{it}K'_{jt} - K_{it}K_{jt}), \tag{3}$$

expressed through the matrix elements K'_{it} and K_{it} involved in Eqs. (2). For further calculations, we use the experimental temperature dependences of the parameters of the perovskite unit cell in an *x*PT–PZN crystal [9]. Thus, we determine the dependences of the optimum concentrations for domains or twins of various types in coexisting phases (e.g., $n_{n,\,\mathrm{opt}}$, $\nu_{o,\,\mathrm{opt}}$, $f_{o,\,\mathrm{opt}}$) on the volume concentration r_t of the *T* phase. These optimum concentrations correspond to the *T*–*O* interphase boundaries, namely, zero mean strain planes (ZMSPs) [15–18], such that internal mechanical stresses are completely relaxed and the conditions $\det\|D\| = 0$ and $D_{ij}^2 - D_{ii}D_{jj} \geq 0$ are met, where ij = 12 and 13 and the matrix elements D_{ij} are specified by Eq. (3).

The most interesting case of elastic matching of the *T* and *O* phases along ZMSPs is actualized at fixed f_o and *T* values. The corresponding optimum concentrations of domains in the *T* phase $n_{t,\,\mathrm{opt}}^{(g)}$ and twins in the *O* phase $\nu_{o,\,\mathrm{opt}}^{(g)}$ (g = 1 or 2; see Fig. 2) are nonmonotonic functions of r_t. Extrema in the $n_{t,\,\mathrm{opt}}^{(g)}(r_t)$ and $\nu_{o,\,\mathrm{opt}}^{(g)}(r_t)$ curves are observed at $r_t \approx 0.1$–0.2, and their positions and values considerably vary with f_o, one of the parameters of the twin structure in the *O* phase. Changes in the temperature T at f_o = const lead to changes in the values of the extrema without changing their positions on the r_t axis. It should be noted that the correlated behavior of $n_{t,\,\mathrm{opt}}^{(g)}(r_t)$ and $\nu_{o,\,\mathrm{opt}}^{(g)}(r_t)$ leads to

[2] Distortion matrices for polydomain phases of various symmetries for *x*PT–PZN crystals can be found in [7].

the following rather original result: the differences in the volume concentrations

$$\begin{aligned}\Delta n_t(r_t) &= n^{(2)}_{t,\,\mathrm{opt}}(r_t) - n^{(1)}_{t,\,\mathrm{opt}}(r_t),\\ \Delta v_o(r_t) &= v^{(1)}_{o,\,\mathrm{opt}}(r_t) - v^{(2)}_{o,\,\mathrm{opt}}(r_t)\end{aligned} \quad (4)$$

are maximum at $f_o = 0.5$ and $r_t \approx 0.2$. A decrease in the temperature from 300 to 20 K causes the values of differences (4) near $r_t = 0.2$ to decrease (compare Figs. 2a and 2b). The orientations of the *T*–*O* interphase boundaries (ZMSPs) determined by the equations derived in [15, 16] are specified at $f_o = 0.5$ and $r_t \approx 0.2$ by a family of $\{h0l\}$ planes in terms of the perovskite axes of the crystal, where the Miller indices h and l are functions of the temperature *T*. An analysis of the invariants of the equation $\sum_{i,\,j\,=\,1}^{3} D_{ij}x_ix_j = 0$ for the surface of an interphase boundary [17], where the x_i axes of the rectangular coordinate system are parallel to the axes of the perovskite unit cell, leads to the following conclusion. Given f_o and *T*, regions with the volume concentrations $n^{(1)}_{t,\,\mathrm{opt}}(r_t) < n_t(r_t) < n^{(2)}_{t,\,\mathrm{opt}}(r_t)$ and $v^{(2)}_{o,\,\mathrm{opt}}(r_t) < v_o(r_t) < v^{(1)}_{o,\,\mathrm{opt}}(r_t)$ correspond to conic *T*–*O* interphase boundaries and to partial relaxation of internal mechanical stresses in the crystal. The fact that $\max(\Delta n_t(r_t))$ are simultaneously reached and $\max(\Delta v_o(r_t))$ near $r_t = 0.2$ allows us to characterize this volume concentration of the *T* phase as the most favorable for the stress relaxation in 0.10PT–PZN heterophase crystals and the value $f_o = 0.5$ as the concentration corresponding the most probable (uniform) distribution of mechanical twins in the *O* phase along one of the perovskite axes.

The result obtained in this work agrees well with the experimental data from [9]; namely, the volume concentration of the *T* phase coexisting with the thermodynamically stable *O* phase in 0.10PT–PZN at $T = 20$–300 K is about 20%. One of the reasons $r_t(T)$ is constant is related to the temperature dependences of the perovskite cell parameters $a_o(T)$ and $c_o(T)$ of the *O* phase and $a_t(T)$ and $c_t(T)$ of the *T* phase [9]. According to our estimation, the equality $a_o(T_1)/a_o(T_2) = c_o(T_1)/c_o(T_2)$ is satisfied with an accuracy of 2% in the temperature range $20 \le T_s \le 300$ K ($s = 1, 2$), and the changes in $a_t(T)$ and $c_t(T)$ in this range do not exceed 0.12 and 1%, respectively. Earlier, we noted in [16, 18] that the volume concentrations of domains of different types in the $Pb(Zr_{1-y}Ti_y)O_3$ monoclinic and *T* phases were virtually constant at $T = 20$–300 K and $y = 0.45$–0.46, i.e., at the morphotropic boundary [11]. However, contrary to the $Pb(Zr_{1-y}Ti_y)O_3$ system, the *T* phase in 0.10PT–PZN crystals coexists with the phase of different symmetry and the relaxation of mechanical stresses is caused by more complex heterophase structures (Fig. 1). Therefore, we believe that it is important to further consider the conditions for the formation of ZMSPs in the case of coexisting polydomain (twinned) low-symmetry phases in various ranges of *T*, *E*, and molar concentrations of the components, as well as in the case of various orientations of the developed faces in the crystal with respect to **E**.

ACKNOWLEDGMENTS

We are grateful to Dr. Z.-G. Ye (Canada) and Dr. M. Kamlah (Germany) for their continuing interest in the problem of heterophase ferroelectrics and related materials.

REFERENCES

1. S.-E. Park and T. R. Shrout, Mater. Res. Innovations **1** (1), 20 (1997).
2. B. Noheda, D. E. Cox, G. Shirane, *et al.*, Phys. Rev. Lett. **86** (17), 3891 (2001).
3. S. Wada and T. Tsurumi, Key Eng. Mater. **214–215**, 9 (2002).
4. S.-E. Park and T. R. Shrout, J. Appl. Phys. **82** (4), 1804 (1997).
5. V. Yu. Topolov and Z.-G. Ye, Ferroelectrics **253** (1–4), 71 (2001).
6. V. Yu. Topolov and A. V. Turik, Fiz. Tverd. Tela (St. Petersburg) **43** (6), 1080 (2001) [Phys. Solid State **43**, 1117 (2001)].
7. V. Yu. Topolov and A. V. Turik, Fiz. Tverd. Tela (St. Petersburg) **44** (7), 1295 (2002) [Phys. Solid State **44**, 1355 (2002)].
8. Y. Lu, D.-Y. Jeong, Z.-Y. Cheng, *et al.*, Appl. Phys. Lett. **80** (11), 1918 (2002).
9. D. La-Orauttapong, B. Noheda, Z.-G. Ye, *et al.*, Phys. Rev. B **65** (14), 144101 (2002).
10. B. Noheda, Z. Zhong, D. E. Cox, *et al.*, Phys. Rev. B **65** (22), 224101 (2002).
11. B. Noheda, D. E. Cox, G. Shirane, *et al.*, Phys. Rev. B **63** (1), 014103 (2001).
12. Z.-G. Ye, B. Noheda, M. Dong, *et al.*, Phys. Rev. B **64** (18), 184114 (2001).
13. B. Noheda, D. E. Cox, G. Shirane, *et al.*, Phys. Rev. B **66** (5), 054104 (2002).
14. J. Fousek and V. Janovec, J. Appl. Phys. **40** (1), 135 (1969).
15. G. Metrat, Ferroelectrics **26** (1–4), 801 (1980).
16. V. Yu. Topolov, Phys. Rev. B **65** (9), 094207 (2002).
17. V. Yu. Topolov, Ferroelectrics **222** (1–4), 41 (1999).
18. V. Yu. Topolov and A. V. Turik, Fiz. Tverd. Tela (St. Petersburg) **43** (8), 1525 (2001) [Phys. Solid State **43**, 1585 (2001)].

Translated by K. Shakhlevich

Physics of the Solid State, Vol. 45, No. 7, 2003, pp. 1298–1304. Translated from Fizika Tverdogo Tela, Vol. 45, No. 7, 2003, pp. 1238–1244.

MAGNETISM AND FERROELECTRICITY

On the Kinetics of Slow Polarization in the Lead Magnoniobate Ferroelectric Relaxor

V. V. Gladkiĭ, V. A. Kirikov, and E. V. Pronina

Shubnikov Institute of Crystallography, Russian Academy of Sciences, Leninskiĭ pr. 59, Moscow, 117333 Russia

e-mail: glad@ns.crys.ras.ru

Received June 4, 2002; in final form, December 24, 2002

Abstract—Polarization and repolarization of a (100)-oriented lead magnoniobate crystal in slowly varying and dc electric fields were measured in a temperature interval including the relaxor and field-induced ferroelectric states. Throughout the interval covered, the polarization was shown to exhibit features characteristic of relaxors, namely, open, nonreproducing polarization trajectories in the first few cycles of quasi-static dielectric hysteresis loops and very long relaxation times. The slow thermally activated relaxation stage follows the universal power law evolution, which permits one to determine possible simple spectra of the relaxation time distribution. Temperature dependences of some relaxation and spectral parameters were derived, and their differences in the relaxor and ferroelectric phases are discussed. © *2003 MAIK "Nauka/Interperiodica".*

1. INTRODUCTION

$PbMg_{1/3}Nb_{2/3}O_3$ (PMN) is a typical representative of the oxide solid solutions with perovskite structure, which were first synthesized by G. A. Smolenskiĭ and coworkers and termed ferroelectric relaxors [1, 2]. In contrast to conventional ferroelectrics, the relaxors have a strongly disordered structure because of compositional fluctuations and the phase transition to the polar state is diffuse over a broad temperature range (the Curie region) [2, 3].

In the Curie region, the inhomogeneous macroscopic structure of PMN can be approximated by a nonpolar matrix containing small polar regions ~100 Å in size (nanodomains) whose net polarization averaged over the crystal volume is zero, and the dielectric polarization passes through a broad maximum at $T_m \cong 270$ K and a clearly pronounced dispersion in the low-frequency region, with the dielectric hysteresis loops revealing poorly seen "saturation" and degrading slowly under heating [4]. Application of an external electric field at $T \cong 215$ K drives a phase transformation from the relaxor to ferroelectric state with the symmetry lowering from the *m*3*m* to 3*m* group, birefringence appearing, a conventional large-scale domain structure forming [5], and distinct dielectric anomalies emerging [6, 7]. A tentative electric field vs. temperature phase diagram of PMN can be found in [6–8].

Because of the unusually high values of their polarization and dielectric permittivity and many other related physical characteristics, ferroelectric relaxors are attracting interest both fundamentally and for practical application, which accounts for the intensive research being conducted in this area. More than ten publications appear annually on new materials exhibiting relaxor properties (see, e.g., [9, 10]) and new features observed in the physical properties of relaxors. The dielectric properties of PMN have been studied, as a rule, in ac low-frequency electric fields [1–17] or in ac fields with a superposed dc bias [6–8, 11–14, 18]. It has been shown that the major contribution to the high dielectric permittivity is due to domain wall motion [13]; that the electric field–induced ferroelectric transition is observed from anomalies in dielectric permittivity apparently in three crystal orientations, namely, (111), (110), and (100) [14, 18]; and that the most probable relaxation time derived from measurements of the dielectric permittivity dispersion attains giant values at low temperatures [8, 15]; the mechanism of the nonlinear-in-field polarization component was analyzed in [13, 15, 18].

This communication reports on a study of the polarization of a (100)-oriented PMN crystal measured in a slowly varying (quasi-static) electric field and on real-time measurements of the polarization relaxation and switching in dc fields [19] performed in a temperature interval including the relaxor and ferroelectric states. The results provide an idea of the longest lived metastable states of the crystal with response times to an external field in excess of 3 h, which corresponds to field frequencies $\leq 10^{-4}$ Hz.

2. EXPERIMENTAL TECHNIQUES

The dielectric permittivity ε was measured using the standard bridge technique in a weak 1-kHz field, and the polarization and depolarization were studied using electrometric compensation with an equal-arm bridge equipped with a V7-29 electrometer serving as a null indicator. The sample under study, the reference capacitance *C*, and the sources of the polarizing $U(t)$ and compensating $u(t)$ voltages made up the four arms of

1063-7834/03/4507-1298$24.00

the bridge. The voltage across the bridge diagonal was compensated using a program on an IBM PC interfaced with the peripheral devices. The compensating-voltage variation $u(t)$ was displayed visually on the monitor in real-time mode. These data were used to calculate the polarization $P = Cu(t)/S$ (S is the electrode area) and its variation with time t and voltage U. The maximum bridge sensitivity to voltage was 20 μV and to charge, 2×10^{-9} μC, for $C = 10$ pF. A detailed description of the device and of the operation of the computerized electrometric bridge in measurements of the polarization relaxation with time can be found in [20] and in measurements of the dielectric hysteresis loops in a quasi-static field, in [21]. The field variation period was ~1 h. The polarization relaxation measurement time was ~3 h, which corresponds to a lowest frequency boundary of 10^{-4} Hz. This time was chosen based on the acceptable errors in estimating the parameters of the PMN relaxation time spectra, because the error decreases with increasing measurement time [22]. The sample used for the studies was a rectangular plate $3 \times 2 \times 0.2$ mm in size, with its larger face being the PMN (100) cut. The measurement electrodes were deposited by silver paste on the larger side.

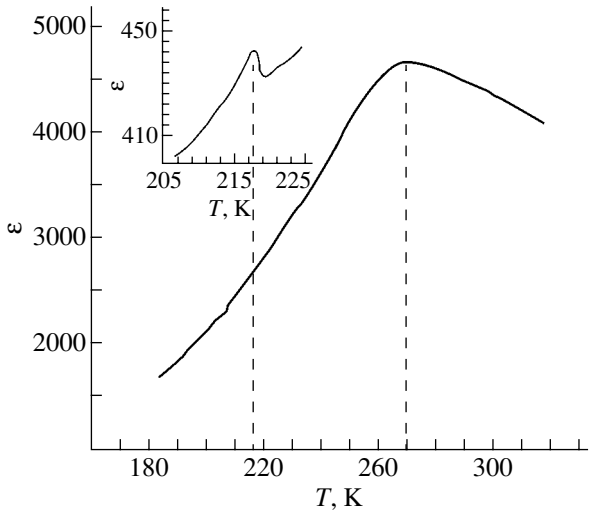

Fig. 1. Temperature dependence of the PMN dielectric permittivity ε measured at a frequency of 1 kHz. Inset shows ε in the region of the ferroelectric phase transition studied in a bias field $E = 3$ kV/cm.

3. RESULTS AND DISCUSSION

3.1. Dielectric Permittivity

The phase transformations in PMN induced by a decrease in temperature are marked by two maxima in the dielectric permittivity ε measured in a weak ac electric field with a frequency of 1 kHz (Fig. 1). The large broad maximum in ε corresponds to the sample-averaged temperature $T_m \cong 270$ K of the transition to the relaxor state. The small narrow peak is located at the temperature $T_c \cong 215$ K of the ferroelectric phase transition and is observed only under simultaneous application of a weak ac and a 3-kV/cm dc field to the sample (see inset to Fig. 1). The amplitude of this narrow peak is much smaller than that of the one reported in [6–8, 14] to occur in (111)- and (110)-oriented samples. Dielectric anomalies occurring in a (100)-oriented sample at the ferroelectric transition under an electric bias were also reported in [14, 18].

3.2. Quasi-Static Dielectric Hysteresis Loops

Each loop in the electric field dependence of the polarization was measured after a sample was heated to $T = 300$ K $> T_m$ and subsequently zero-field cooled to a given temperature; i.e., samples were not subjected to annealing, which is usually conducted at a higher temperature [15]. After the cooling, the initial sample-averaged polarization is always zero, because the PMN crystal does not exhibit the pyroelectric effect in a zero field. The hysteresis loops for different temperatures presented in Fig. 2 do not have clearly pronounced saturation, and the polarization amplitude grows rapidly with increasing amplitude of the switching field, because (100)-oriented PMN samples, as follows from the optical observation of domains [7], do not become single domain even in fields of up to 150 kV/cm. The PMN hysteresis loops have an unusual shape. Unlike homogeneous ferroelectrics, the trajectories of the first few loop cycles represent open, nonreproducing curves decreasing in amplitude. The decrease in the amplitude finally stops, and the loops take on the customary shape, i.e., become, as usual, reproducible. The difference between the first few loop cycles is particularly large in the field-induced ferroelectric phase; in the relaxor state, this difference decreases under heating, to become practically indistinguishable above T_m (Fig. 2). These features of the loops are apparently characteristic of all relaxor ferroelectrics and were first detected and studied in [23] by us and later in [24] in strontium–barium niobate (SBN) containing impurities, in contrast to the conventional loops observed in the homogeneous ferroelectric TGS in [25].

These peculiar loops probably originate from random internal local electric fields E_i, which are generated in the bulk of the relaxor in response to compositional fluctuations and a lowering of local symmetry. The field E_i distorts the pattern of the dependence of local free energy F on polarization P, which becomes an asymmetric double-minimum function of P [4]. Therefore, before a loop measurement, one part of the crystal can reside in a metastable state (with a shallow F minimum) and the other, in a stable one (with a deep minimum of F). When an ac quasi-static field E of a certain amplitude is applied, many regions of the crystal may reach the stable state with a deep F minimum, from which the reverse transition to the previous state is practically impossible because the barrier is too high. As a result, part of the crystal is not involved in the fur-

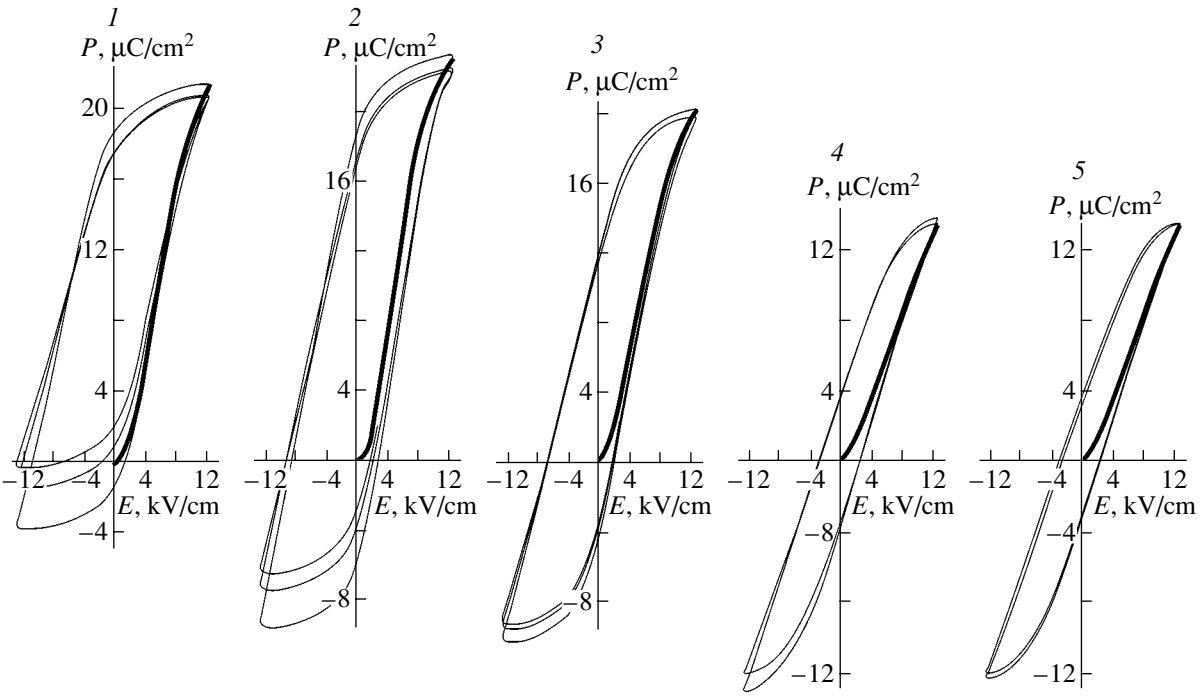

Fig. 2. Quasi-static dielectric hysteresis loops of the PMN crystal measured at different temperatures *T*: (*1*) 200, (*2*) 210, (*3*) 230, (*4*) 274, and (*5*) 283 K.

ther repolarization process and the loop trajectories are open and decrease in amplitude until transitions to stable states become no longer possible in the field of chosen strength [23]. In a high field, which should destroy all barriers under polarization switching, a dielectric hysteresis loop should apparently be always reproducible, as is the case with all homogeneous ferroelectrics.

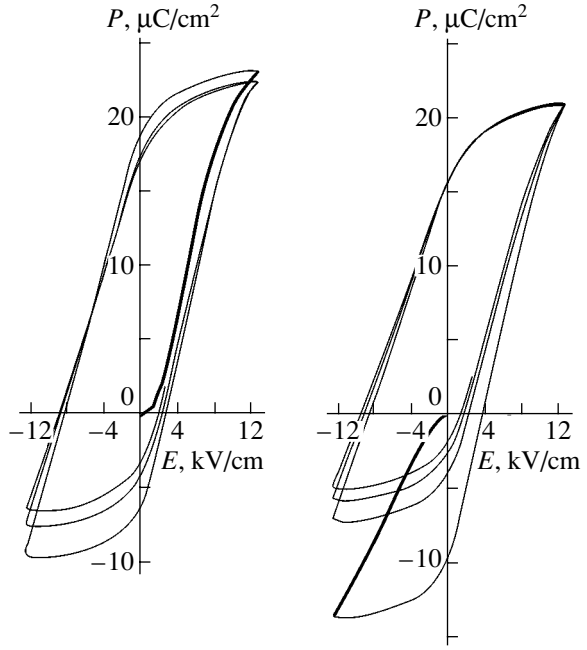

Fig. 3. Quasi-static dielectric hysteresis loops of the PMN crystal measured for different initial directions of the switching field at $T = 210$ K.

The loops in Fig. 2 are unipolar; i.e., the PMN crystal, which was initially unpolarized, becomes partially polarized in one of the two opposite directions after multiple cyclic field variation. The unipolarity is more pronounced, the closer the crystal is to the field-induced ferroelectric state with a large-scale inhomogeneous (domain) structure. We observed the SBN relaxor ferroelectric to have the same hysteresis loop feature [23]. The unipolarity of a crystal sample is not determined by the original electric field direction, because it does not change under reversal of the field (Fig. 3). The independence of the unipolarity induced by an ac field on the sign of the field in the first quarter of the field period implies that this feature of the polarization is a characteristic of the given sample having unequal polarizabilities in the two symmetry-equivalent directions. A similar situation is observed, as a rule, in all samples of conventional ferroelectrics with a large-scale domain structure, in particular, in the SBN relaxors [26], which exhibit a readily detectable pyroelectric effect in the polar phase even in the absence of an electric field; this effect is used frequently to identify the ferroelectric phase transition. A PMN crystal with a relaxor and a ferroelectric phase makes it possible to follow the variation of the field-induced unipolarity with the scale size of the inhomogeneities.

We demonstrate below, using the data obtained in polarization and depolarization measurements, that the

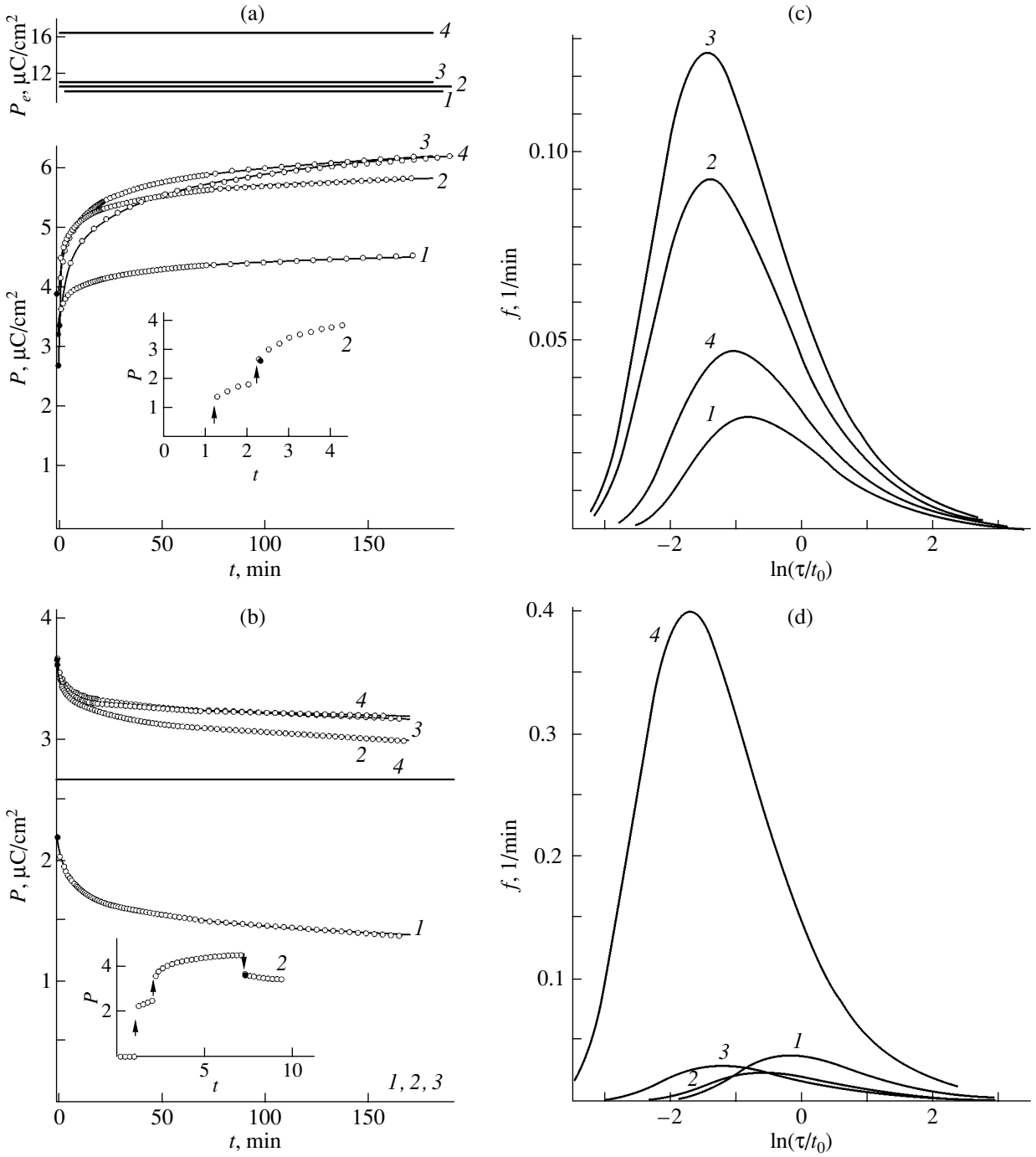

Fig. 4. Slow processes of (a) polarization and (b) depolarization of the PMN crystal and (c, d) $f(\tau)$ spectra of the relaxation time τ measured at different temperatures T: (*1*) 257, (*2*) 230, (*3*) 215, and (*4*) 205 K. Polarizing field E = 3 kV/cm. Solid curves are calculations, and circles are experimental data. Solid horizontal lines are equilibrium values of P_e, t_0 = 1 min. Insets show the beginning of the polarization and depolarization processes (the jumps in P are specified by arrows).

PMN dielectric hysteresis loops characteristic of relaxors cannot be identified with a unique coercive field and equilibrium polarization, whose magnitude in homogeneous ferroelectrics is always constant and equal to spontaneous polarization.

3.3. Polarization Relaxation

An analysis of the measurements of polarization P in dc electric fields offers data on the time variation of some parameters of a crystal with long-lived metastable

Parameters of polarization relaxation and $f(\tau)$ distribution for PMN crystals in a field E = 3 kV/cm

Process	T, K	P_0, μC/cm^2	P_e, μC/cm^2	a, min	n	τ_m, min	S
Polarization	257	3.37	9.3 ± 0.7	0.45 ± 0.02	0.037 ± 0.001	0.44 ± 0.02	0.09
	230	3.95	9.6 ± 0.1	0.252 ± 0.004	0.062 ± 0.001	0.24 ± 0.004	0.15
	215	3.28	10.38 ± 0.07	0.244 ± 0.003	0.080 ± 0.001	0.23 ± 0.003	0.18
	205	2.71	16.7 ± 0.12	0.362 ± 0.002	0.046 ± 0.005	0.346 ± 0.002	0.11
Depolarization	257	2.18	0 ± 0.2	0.89 ± 0.06	0.086 ± 0.011	0.65 ± 0.06	0.2
	230	3.64	0 ± 0.5	0.57 ± 0.03	0.034 ± 0.006	0.55 ± 0.03	0.09
	215	3.66	0 ± 0.26	0.287 ± 0.005	0.022 ± 0.002	0.281 ± 0.005	0.06
	205	3.62	2.67 ± 0.02	0.18 ± 0.005	0.09 ± 0.003	0.165 ± 0.005	0.42

states over long times. Figure 4 presents P relaxation curves for a PMN crystal obtained under application (polarization process) and removal (depolarization) of a field E = 3 kV/cm. Both processes start with a jump ΔP (see insets to Fig. 4), after which the thermal activation mechanism prevails. ΔP jumps always appear, irrespective of whether E is larger or smaller than the hysteresis loop halfwidth; the larger E, the larger ΔP. The initial fast stage in relaxation, seen in the form of the jump ΔP for any strength of field E is an argument for the absence of a unique coercive field E_c; this quantity is distributed over the crystal volume within a large range of values. In a conventional homogeneous ferroelectric, the field E_c has a well-defined magnitude and the application of $E < E_c$ immediately initiates a slow relaxation process without any preliminary jump, which appears only for $E > E_c$ [25].

The slow thermally activated stage in the $P(t)$ relaxation in PMN, as in other relaxors [25], is described with a high accuracy by a universal power law:

$$p(t) = (P_e - P(t))/(P_e - P_0) = 1/(1 + t/a)^n, \quad (1)$$

where P_0 is the initial polarization and P_e is the equilibrium polarization; P_e, a, and n are fitting parameters.

The circles in Fig. 4 indicate experimental values of $P(t)$, the solid curves are plots of Eq. (1), and the solid horizontal lines refer to the equilibrium P_e values, which are approached asymptotically by $P(t)$. The deviation of the experimental data from the calculations does not exceed 0.5%. The experimental $P(t)$ data were least squares fitted by the power-law relation (1) with three free parameters P_e, a, and n using a standard program. Note that the empirical power law (1) used for the relaxation is apparently applicable to many inhomogeneous systems, because, with certain bounds imposed on the fitting parameters, it practically does not differ from individual nonexponential functions proposed earlier for approximation of the relaxation in certain materials [26]. One can also readily verify that, unlike the well-known relaxation relation of Kohlrausch, Eq. (1) provides a more correct description of $P(t)$ relaxation on short time scales, because the derivative $dP(t)/dt$ must always be finite. Furthermore, assuming the relaxation centers to be independent, relation (1) corresponds to a simple distribution function $f(\tau)$ of the relaxation times τ. The function $f(\tau)$ and the dimensionless polarization $p(t)$ in Eq. (1) are related through

$$p(t) = \int_0^\infty f(\tau)\exp(-t/\tau)d\tau.$$

The variables $\tau^2 f(\tau)$ and $p(t)$ are an original function and its Laplace transform [27]. Therefore, if the power-law relation (1) holds with a satisfactory accuracy, the $f(\tau)$ function can be written in the form

$$f(\tau) = (1/\Gamma(n))a^n\tau^{(1-n)}\exp(-a/\tau), \quad (2)$$

where $\Gamma(n)$ is the gamma function. The $f(\tau)$ distribution passes through a maximum at $\tau = a/(1 + n)$. One may sometimes conveniently use the dimensionless function $g = \tau f(\tau)$, which is a $\ln\tau$ distribution, or the barrier height distribution in energy U for the relaxation centers, where, according to the Arrhenius law, $U = kT\ln(\tau/\tau_0)$, with τ_0 being a kinetic coefficient.

The $f(\tau)$ functions calculated using Eq. (2) and the experimental data on $P(t)$ for the polarization and depolarization processes occurring at the same temperatures are also presented in Fig. 4. The $f(\tau)$ functions are normalized; i.e.,

$$\int_0^\infty f(\tau)d\tau = 1.$$

One can readily verify that the areas S bounded in the figure by the $f(\tau)$ curves and the horizontal lines drawn at the level $f(\tau) = 0.1f_{max}$ (f_{max} is the maximum value) are much less than unity. This means that the $f(\tau)$ distribution should include very long relaxation times τ which are not plotted in the graphs. As all the times τ in the spectrum decrease, it becomes narrower and higher, its maximum shifts to the left, and the area S bounded by the $f(\tau)$ curve increases. The table lists some parameters of relaxation and of the $f(\tau)$ distribution spectra calculated from the experimental data, as well as the areas S.

The polarization $P(t)$ relaxation and the $f(\tau)$ spectra were measured over a broad temperature range. Figure 5 presents temperature dependences of the relaxation and spectral parameters for a polarizing field $E = 3$ kV/cm. We readily see, that at the ferroelectric transition at $T \cong 215$ K, the parameters P_e and S increase and that, in the transition region, the most probable relaxation time $\tau_m = a/(1 + n)$ corresponding to the maximum in the $f(\tau)$ distribution reveals a clearly pronounced minimum. Because the barrier energy U is related to $\ln\tau$ linearly, one can say that the U energies also pass through a minimum in the transition region. In other words, the crystal cooled to its field-induced transition to the ferroelectric phase becomes more receptive to an external electric field, such that the polarization and depolarization processes are accelerated. Further cooling gives rise to the formation of a large-scale domain structure [5], the barrier energy increases again, and the relaxation slows down.

Continuous polarization relaxation time spectra for PMN were constructed earlier based on measurements of the imaginary part of the dielectric permittivity in a weak ac electric field of 10^{-3}–10 Hz with no dc bias applied. Such spectra as those displayed in this publication exhibit an anomalously large width typical of inhomogeneous systems which increases with decreasing temperature; no spectra were studied, however, in dc bias fields that induce the ferroelectric phase transition [15, 17].

One of the most important results obtained in the study of relaxation is the temperature dependence of the equilibrium polarization P_e for the depolarization process. As seen from Fig. 5b, in the temperature region of existence of the PMN relaxor phase, P_e is zero everywhere except the ferroelectric region. This means that the quasi-static dielectric hysteresis loops observed under polarization switching in a field $E = 3$ kV/cm with a period of ≈1 h actually represent thermodynamically unstable characteristics, which should approach the equilibrium shape and amplitude with increasing field period. In the limit of very long field periods, the loop in the relaxor phase should transform to a nonlinear dependence of P on E with zero remanent polarization P_e and zero coercive field, while retaining their typical shape in the ferroelectric phase. This situation is possibly realized in larger amplitude switching fields. In this case, the thermodynamically equilibrium dielectric properties of the relaxor and ferroelectric states, which differ in the size scale of their inhomogeneities, should be fundamentally different. The temperature dependence of the remanent polarization, which is nonzero in the ferroelectric phase and zero in the relaxor state for (100)-oriented PMN crystals, was also reported in [14]. Those data were derived from dielectric hysteresis loops obtained in an ac electric field and are in agreement with ours.

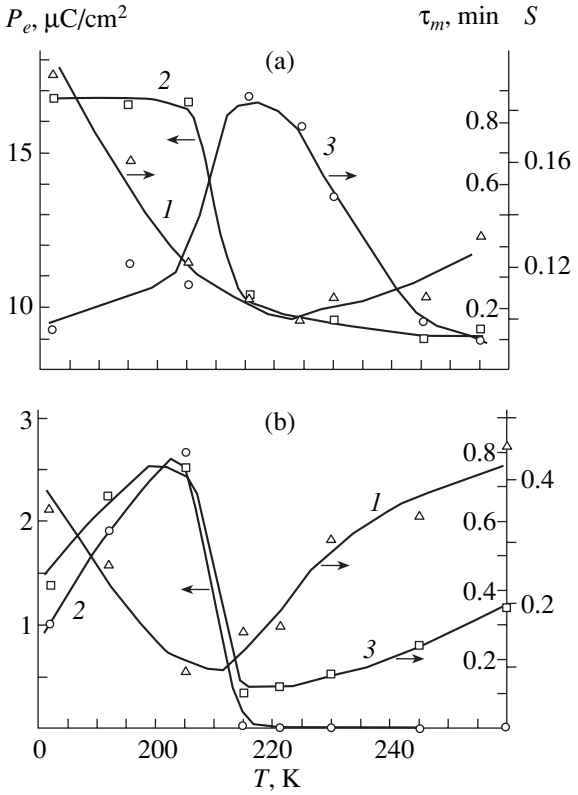

Fig. 5. Temperature dependences of the relaxation and $f(\tau)$ distribution parameters (*1*) τ_m, (*2*) P_e, and (*3*) S for (a) polarization and (b) depolarization.

4. CONCLUSIONS

To sum up, investigation of the slow polarization kinetics in the lead magnoniobate ferroelectric relaxor permits detection of its response to external action, including the contribution from the long-lived metastable states characteristic of such essentially inhomogeneous materials. Measurement of this response reveals the specific features of the PMN dielectric properties associated with random the internal electric fields, namely, the peculiar shape of the first nonreproducing cycles of dielectric hysteresis loops and the strong variation in the spectral parameters of the relaxation time distribution occurring at the electric field–induced transition from the ferroelectric to relaxor phase. Extrapolation of the results of measurements to long times also offers the possibility of estimating the crystal characteristics close to its thermodynamically equilibrium parameters.

ACKNOWLEDGMENTS

The authors are indebted to S.G. Lushnikov (PTI, RAS) for providing the crystal and T.R. Volk for her interest in the study and valuable discussions.

This study was supported by the Russian Foundation for Basic Research (project no. 02-02-16823) and INTAS (grant no. 01-0173).

REFERENCES

1. G. A. Smolenskiĭ, V. A. Isupov, and A. I. Agranovskaya, Fiz. Tverd. Tela (Leningrad) **1**, 167 (1959) [Sov. Phys. Solid State **1**, 147 (1959)].
2. G. A. Smolenskiĭ, V. A. Bokov, V. A. Isupov, N. N. Kraĭnik, R. E. Pasynkov, and M. S. Shur, *Ferroelectrics and Antiferroelectrics* (Nauka, Leningrad, 1971), p. 355.
3. M. E. Lines and A. M. Glass, *Principles and Applications of Ferroelectrics and Related Materials* (Oxford Univ. Press, Oxford, 1977; Mir, Moscow, 1981).
4. L. E. Cross, Ferroelectrics **76**, 241 (1987).
5. V. A. Bokov and I. E. Mel'nikova, Fiz. Tverd. Tela (Leningrad) **3** (3), 841 (1961) [Sov. Phys. Solid State **3**, 613 (1961)].
6. R. Sommer, N. K. Yushin, and J. J. van der Klink, Ferroelectrics **127** (1–4), 235 (1992).
7. Zuo-Guang Ye and H. Schmid, Ferroelectrics **145**, 83 (1993).
8. R. Sommer, N. K. Yushin, and J. J. Van der Klink, Phys. Rev. B **48** (18), 13230 (1993).
9. A. A. Bokov and Z.-G. Ye, J. Phys.: Condens. Matter **12**, L541 (2000).
10. A. A. Bokov and Z.-G. Ye, Appl. Phys. Lett. **77** (12), 1888 (2000).
11. A. Levstik, Z. Kutnjak, G. Filipic, and R. Pirc, Phys. Rev. B **57** (18), 11204 (1998).
12. R. Blinc, J. Dolinsek, A. Gregorovic, *et al.*, Phys. Rev. Lett. **83** (2), 424 (1999).
13. A. K. Tagantsev and A. E. Glazunov, Phase Transit. **65** (1–4), 117 (1998).
14. H. Arndt, F. Sauerbier, and G. Schmidt, Ferroelectrics **79**, 145 (1988).
15. E. V. Colla, E. Yu. Koroleva, N. M. Okuneva, and S. B. Vakhrushev, J. Phys.: Condens. Matter. **4**, 3671 (1992).
16. R. Pirc, R. Blinc, and Z. Kutnjak, Ferroelectrics **267**, 139 (2002).
17. N. K. Yushin and S. N. Dorogovtsev, Ferroelectrics **134**, 265 (1992).
18. Z. Kutnjak, A. Levstik, and R. Pirc, Ferroelectrics **270**, 283 (2002).
19. A. K. Jonscher, *Dielectric Relaxation in Solids* (Chelsea Dielectrics, London, 1983).
20. V. V. Gladkiĭ, V. A. Kirikov, S. V. Nekhlyudov, and E. S. Ivanova, Fiz. Tverd. Tela (St. Petersburg) **39** (11), 2046 (1997) [Phys. Solid State **39**, 1829 (1997)].
21. V. V. Gladkiĭ, V. A. Kirikov, S. V. Nekhlyudov, *et al.*, Fiz. Tverd. Tela (St. Petersburg) **42** (7), 1296 (2000) [Phys. Solid State **42**, 1334 (2000)].
22. V. V. Gladkiĭ, V. A. Kirikov, E. S. Ivanova, and S. V. Nekhlyudov, Fiz. Tverd. Tela (St. Petersburg) **41** (3), 499 (1999) [Phys. Solid State **41**, 447 (1999)].
23. V. V. Gladkiĭ, V. A. Kirikov, S. V. Nekhlyudov, *et al.*, Pis'ma Zh. Éksp. Teor. Fiz. **71** (1), 38 (2000) [JETP Lett. **71**, 24 (2000)].
24. T. Granzow, U. Dorfler, Th. Woike, *et al.*, Phys. Rev. B **63**, 174101 (2001).
25. V. V. Gladkiĭ, V. A. Kirikov, and T. R. Volk, Fiz. Tverd. Tela (St. Petersburg) **44** (2), 351 (2002) [Phys. Solid State **44**, 365 (2002)].
26. V. V. Gladkiĭ, V. A. Kirikov, T. R. Volk, and L. I. Ivleva, Zh. Éksp. Teor. Fiz. **120** (3), 678 (2001) [JETP **93**, 596 (2001)].
27. V. A. Ditkin and A. P. Prudnikov, *Reference Book on Operational Calculus* (Vysshaya Shkola, Moscow, 1956).

Translated by G. Skrebtsov

Physics of the Solid State, Vol. 45, No. 7, 2003, pp. 1305–1309. Translated from Fizika Tverdogo Tela, Vol. 45, No. 7, 2003, pp. 1245–1249.

MAGNETISM AND FERROELECTRICITY

Pyroelectric Effect in Lead-Magnoniobate-Based Solid Solutions

E. P. Smirnova, S. E. Aleksandrov, K. A. Sotnikov, A. A. Kapralov, and A. V. Sotnikov

Ioffe Physicotechnical Institute, Russian Academy of Sciences, Politekhnicheskaya ul. 26, St. Petersburg, 194021 Russia

Received December 27, 2002

Abstract—A coordinated study of the dielectric, electrostriction, and pyroelectric properties of the lead-magnoniobate-based ceramic solid solutions $0.9PbMg_{1/3}Nb_{2/3}O_3$–$0.1PbTiO_3$ and $0.55PbMg_{1/3}Nb_{2/3}O_3$–$0.45PbSc_{1/2}Nb_{1/2}O_3$ conducted at the relaxor transition temperatures is reported. Electromechanical coupling stimulated by the giant electrostriction effect is shown to play an essential part in the pyroelectric effect. © *2003 MAIK "Nauka/Interperiodica".*

1. INTRODUCTION

The ferroelectric relaxors, exhibiting a unique combination of physical properties (broad range of temperature anomalies, large dielectric permittivity with a strong dispersion over a frequency domain extending from a few millihertz into the gigahertz range, high sensitivity to external factors), have been attracting the interest of researchers for several decades [1–4].

Application of a dc electric field at transition temperatures brings about the appearance of a preferred direction with predominant alignment along the field of polar clusters, which, as is presently believed, can also be induced by the field. The attendant effects generated by an external electric field, such as the induced ferroelectric transition, strong dielectric nonlinearity, and giant electrostriction, have been thoroughly studied [2–8]. The processes underlying all these effects are associated with the formation and variation of macroscopic polarization. The electric-field-induced polarization is temperature-dependent, and its variation manifests itself in the form of a pyroelectric current [9, 10]. Among the factors governing this phenomenon is not only the strength of the field but also the temperature at which it was applied and removed, as well as the sample prehistory. At the same time, the induced pyroelectric effect and its relation to other phenomena occurring in an electric field under identical experimental conditions have practically not been investigated. Interest has been focused primarily on possible applications of the pyroelectric effect in relaxors [9–11].

This communication reports on a coordinated study of the dielectric, electrostriction, and pyroelectric properties of relaxors conducted under the same application regimes of the external electric field.

For the study, we chose the lead-magnoniobate-based solid solutions $0.9PbMg_{1/3}Nb_{2/3}O_3$–$0.1PbTiO_3$ (PMN–PT) and $0.55PbMg_{1/3}Nb_{2/3}O_3$–$0.45PbSc_{1/2}Nb_{1/2}O_3$ (PMN–PSN), which behave as typical relaxors (see, e.g., [12–14]).

2. EXPERIMENTAL TECHNIQUES

PMN–PT and PMN–PSN ceramic disks were fabricated using standard ceramic technology involving solid-phase reactions. The starting reactants were the lead oxide PbO, magnesium carbonate $MgCO_3$, niobium pentoxide Nb_2O_5, and scandium oxide Sc_2O_3. The solid solutions were prepared in two stages using, as intermediate compounds, the columbite $MgNb_2O_6$ (PMN–PT) and columbite and wolframite $ScNbO_4$ (PMN–PSN), an approach preventing the formation of the pyrochlore phase which has a low dielectric permittivity [15]. Preliminary firing was done at a temperature of 850°C for two hours; sintering, at 1250°C in lead oxide vapors. The completeness of formation of the columbite, wolframite, and the solid solutions was verified by x-ray diffraction measurements with CuK_α and CoK_α radiation. The ceramic thus obtained was single phase with perovskite structure and a density of 94–97% of the theoretical value. The x-ray diffraction studies did not reveal any superstructure in the compositions investigated, which argues for their being disordered [16].

Dielectric measurements were conducted in the frequency range extending from 10 Hz to 1 MHz using P 5079, E7-12, and E7-14 bridges at a measuring field amplitude of 1 V/cm. The measurements were carried out under slow cooling effected by Peltier thermoelectric elements at a rate of 1 K/min in the temperature region 273–353 K. The dependence of the dielectric permittivity on an external dc electric field was studied at a frequency of 1 kHz using the standard network with a blocking capacitor, a high voltage source, and a bridge. The samples employed in the dielectric measurements were disks 8 mm in diameter and 0.5–1.0 mm in thickness with electrodes of fired-on silver paste.

Longitudinal electrostriction strains were measured with a galvanometric dilatometer in the quasi-static mode at temperatures from 253 to 353 K. Relative strains were measured to within 10^{-6}. The samples intended for these measurements were also disks 8 mm

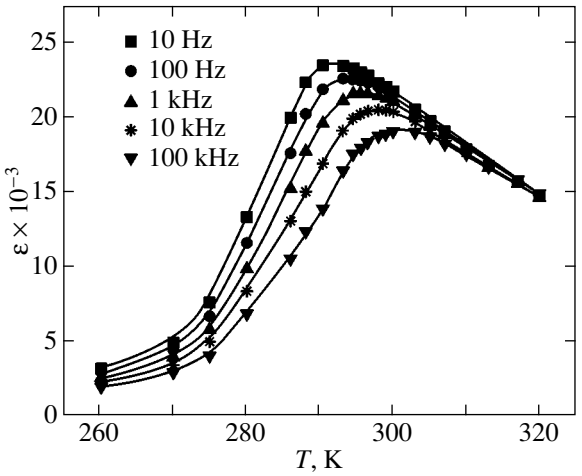

Fig. 1. Temperature dependence of dielectric permittivity for the PMN–PSN solid solution at different frequencies of the measuring field.

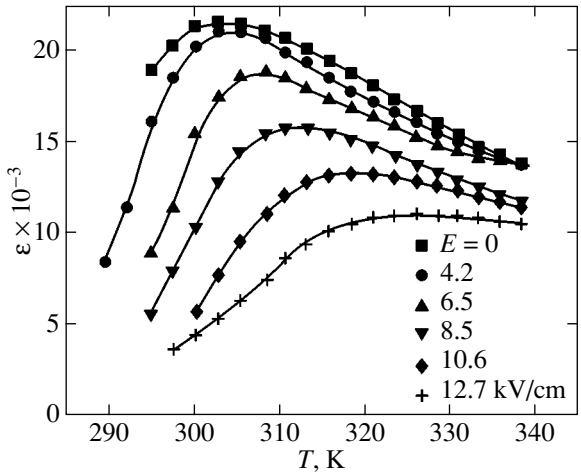

Fig. 2. Temperature dependence of dielectric permittivity measured at 1 kHz for the PMN–PSN solid solution at different bias fields.

in diameter and 0.5–3.0 mm thick with fired-on, silver-paste electrodes.

The pyroelectric response generated by a dc electric field in a sample was studied using the dynamic Laser Intensity Modulation Method (LIMM), which is a modification of the Chynoweth technique [17, 18]. In this method, the pyroelectric signal is measured at the laser modulation frequency. This permits one to avoid the shortcomings inherent in other techniques, for instance, the method of Byer–Rondy [19]. When using the latter method, the signal of interest can be masked by leakage currents arising in the presence of a bias field, by thermally stimulated currents, and by other interference signals, thus resulting quite frequently in incorrect measurements [20]. The essence of the method employed here consists in exciting a heat wave through the absorption of a modulated light flux by the top electrode of a sample. The change in the sample temperature caused by the pyroelectric effect generates a pyroelectric current that oscillates at the modulation frequency; the amplitude and phase were measured with a lock-in detector. The source of the radiation was a laser diode (wavelength 0.78 μm, power up to 20 mW), and the modulation frequency was 1–4 Hz. The pyroelectric response was studied in the temperature range 273–353 K and external fields of up to 20 kV/cm. The sample temperature could be varied and stabilized with Peltier elements. The temperature was maintained to within 0.1 K. The penetration depth d of the heat wave is given by the relation $d = (K/\pi f)^{1/2}$, where K is the thermal diffusivity coefficient and f is the light modulation frequency [21]. The thickness of the measured samples was chosen comparable to the penetration depth of the heat wave at a frequency of 1–4 Hz. The pyroelectric current, as well as the electrostriction strains, was measured under sample cooling, with the temperature stabilized at each measurement point. Following each measurement cycle in an electric field, the sample was heated to 373 K to exclude the effect of sample prehistory on the characteristics to be studied. All measurements were conducted on unclamped samples.

3. EXPERIMENTAL RESULTS AND DISCUSSION

Temperature dependences of the dielectric permittivity are exemplified through the PMN–PSN solid solution in Fig. 1. The high values of dielectric permittivity at the maximum (23 000 for PMN–PSN and 34000 for PMN–PT at 1 kHz) indicate the good quality of the ceramics. The temperature dependences of dielectric permittivity obtained at different bias electric fields (Fig. 2) are typical of relaxors and make it possible to follow the shift of the transition point toward higher temperatures with increasing applied field, as well as to estimate the temperature and field ranges most appropriate for measurement of the pyroelectric and electrostriction properties.

Figures 3 and 4 plot the temperature dependence of the pyroelectric coefficient in a bias electric field. No pyroelectric signal was observed throughout the temperature range covered with no electric field applied. In electric fields above 2 kV/cm, broadened maxima appear on the temperature dependences of the pyroelectric coefficients (PECs) for the PMN–PT and PMN–PSN solid solutions. The positions of the maxima depend on the applied field; more specifically, the maxima shift toward higher temperatures with increasing field. Figures 5 and 6 display the field dependences of the PECs measured at different fixed temperatures. These dependences are likewise seen to follow an anomalous behavior. The maximum values of the PECs for the PMN–PT and PMN–PSN ceramics are listed in the table, which also presents, for comparison, the pyroelectric coefficients for some of the relaxors measured in [22–24] using the method of Byer–Rondy on

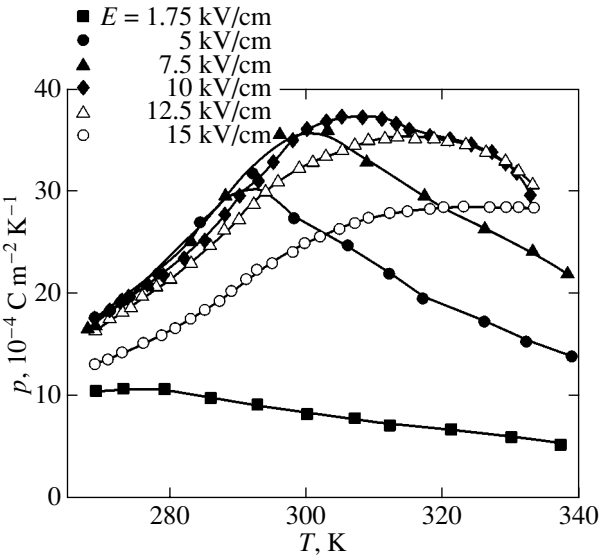

Fig. 3. Temperature dependence of the pyroelectric coefficient measured for the PMN–PT solid solution at different bias fields.

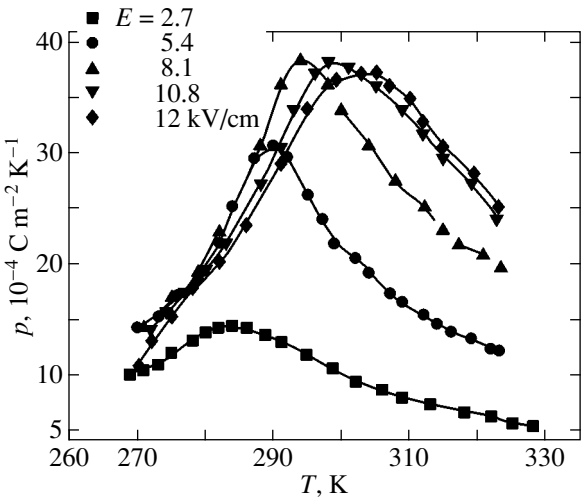

Fig. 4. Temperature dependence of the pyroelectric coefficient measured for the PMN–PSN solid solution at different bias fields.

prepolarized samples. We believe the table presents the most reliable values, because the scatter in the values of the PECs obtained using this method lies within an order of magnitude.

The modulation method and similar conditions of measurement of the pyroelectric properties directly in a bias electric field were employed in [9, 10]. The sample temperature oscillation in those studies was achieved by modulating of the black-body radiation with subsequent lock-in signal detection at the modulation frequency.

Note that the temperature and field dependences of the PECs of partially ordered lead scandotantalate (a well-known relaxor) quoted in [9, 10] coincide qualitatively with those obtained by us for the PMN–PT and PMN–PSN ceramics, with the values of these coefficients also being similar.

It is known that at the relaxor transition temperature, a ferroelectric, like any system with a center of inversion, possesses neither the piezoelectric nor pyroelectric effect. Application of an electric field induces polarization, which depends on temperature and is presently believed to account for the pyroelectric response in relaxors. At the same time, in any piezoelectrically active medium, there can exist not only the primary pyroelectric effect associated with the dependence of the polarization of a clamped sample on temperature but also a secondary pyroelectric effect, provided the sample is capable of deforming freely [25, 26]. We should stress that this condition was upheld in our measurements. When the temperature is varied, thermal expansion creates strain in the sample, which provides, through the piezoelectric effect, an additional contribution to the temperature dependence of polarization. The pyroelectric current observed in relaxors is obviously governed to a considerable extent by the electromechanical properties of the medium in a bias electric field because of the existence of such an effect as giant electrostriction [6, 7, 27]. The electric field–induced polarization accounts for the generation, in the relaxor transition region, of an electrostriction-induced strain S, which is proportional to the square of the polarization P or, in a first approximation, to the square of the field E:

$$S = QP^2 = ME^2, \quad (1)$$

where Q is the coefficient of electrostriction with respect to polarization and M is that with respect to the field.

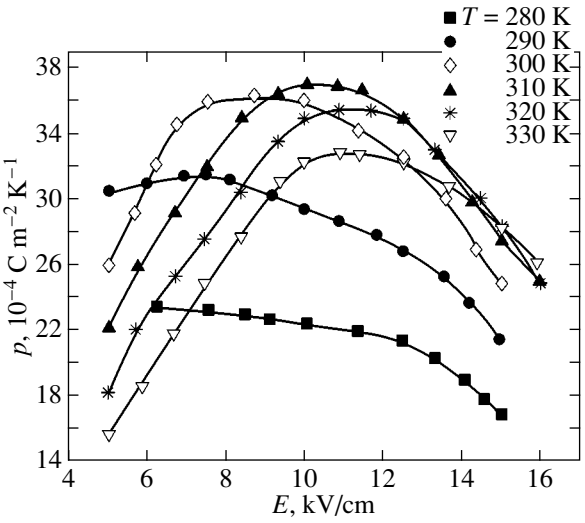

Fig. 5. Pyroelectric coefficient plotted vs. applied field for different temperatures in the region of the relaxor transition in the PMN–PT ceramic solid solution.

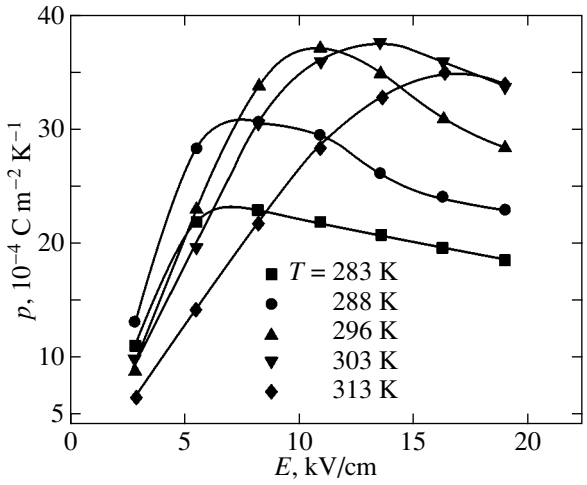

Fig. 6. Pyroelectric coefficient plotted vs. applied field for temperatures in the region of the relaxor transition in the PMN–PSN ceramics.

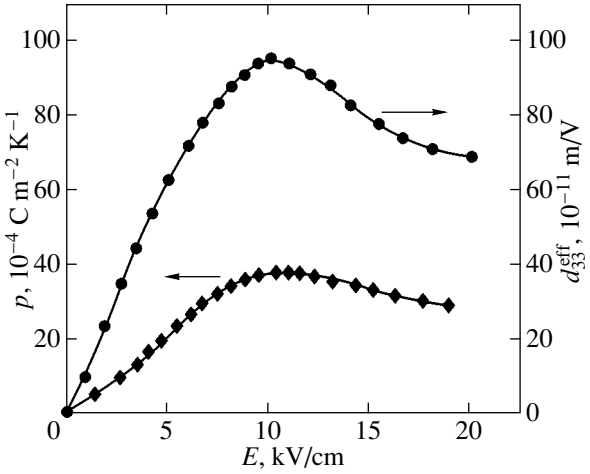

Fig. 7. Pyroelectric coefficient p_3 and effective piezoelectric modulus d_{33}^{eff} plotted vs. applied field for the PMN–PSN ceramics (T = 296 K).

Because the piezoelectric effect originates from linearization of striction in an electric field, electrostriction strain may formally be described using the effective field-dependent piezoelectric modulus d^{eff}:

$$S = M(E)E^2 \equiv d^{\text{eff}}E. \qquad (2)$$

The strain itself may be considered as resulting from the induced piezoelectric effect. The effective piezoelectric modulus d_{33}^{eff} in the best electrostriction materials may be as high as 10^{-9} m/V, which is comparable to the largest piezoelectric moduli of piezoelectric ceramics and single crystals and demonstrates the importance of including the secondary pyroelectric effect in studies of relaxors.

Figure 7 displays field dependences of the effective piezoelectric modulus d_{33}^{eff} calculated from the field dependence of longitudinal electrostriction strain and of the PEC for the PMN–PSN solid solution. Note that these relations are practically identical and pass through a maximum at the same value of the field.

Consider now the importance of electromechanical coupling in the induced pyroelectric effect in relaxors.

Maximum values of pyroelectric coefficients of the PMN–PT and PMN–PSN ceramics (the pyroelectric coefficients for other relaxors are shown for comparison)

Composition	p, 10^4 C m^{-2} K^{-1}	References
PMN–PT	38	This work
PMN–PSN	58	"
0.93PMN–0.07PT	51	[22]
0.65PMN–0.35PT	50	[23]
0.95PSN–0.05PT	53	[24]

The corresponding part of the thermodynamic potential Φ for a free sample can be written as

$$\Phi = -(\varepsilon E^2 + \eta E^4 + \ldots) - ME^2 w, \qquad (3)$$

where ε is the dielectric susceptibility, η is the nonlinear susceptibility, and the term $ME^2w = ME^2c\alpha T$ denotes the electromechanical contribution to the thermodynamic potential, because w is the component of the mechanical strain associated with the temperature variation [26]. Here, c is the elastic modulus, α is the thermal expansion coefficient, and T is the temperature. All coefficients of the thermodynamic potential are taken at a constant mechanical strain, and the tensor indices are dropped for the sake of simplicity.

In the neighborhood of a relaxor transition, not only the susceptibility but also the electrostriction coefficient M are field-dependent [7]. We include this dependence, in a first approximation, by adding an additional term to the thermodynamic potential:

$$M' = Q\varepsilon_0^2\varepsilon^2, \quad M'' = -2Q\varepsilon_0^2\varepsilon\eta, \qquad (4)$$

$$\Phi = -(\varepsilon E^2 + \eta E^4 + \ldots) - (M'E^2 + M''E^4 + \ldots)w. \qquad (5)$$

Note that, while the thermal expansion coefficient and the elastic modulus also depend on the field, their variation, as shown by our measurements, constitutes a few percent only, thus justifying their neglect at this stage of our consideration. In addition, we restrict ourselves to the first-order corrections, which take into account the dielectric nonlinearity and the field dependence of the electrostriction coefficient M. Recalling that $\partial\Phi/\partial E = -D$

and, by definition, $p = \partial D/\partial T$, we obtain the following expression for the pyroelectric coefficient:

$$p = (\partial\varepsilon/\partial T)E + (\partial\eta/\partial T)E^3 + (\partial M'/\partial T)c\alpha TE + M'c\alpha E + (\partial M''/\partial T)c\alpha TE^3 + M''c\alpha E^3. \quad (6)$$

This relation reveals that the pyroelectric response has a contribution which is directly related to the temperature dependence of both the linear and the nonlinear parts of the dielectric permittivity, as pointed out in [9, 10]. Note that neither spontaneous nor remanent polarization exists in the temperature region of the relaxor transition under study. The dielectric contribution is determined by the temperature dependence of induced polarization and, in principle, can be called the induced primary pyroelectric effect. In addition, the linearized striction (the induced piezoelectric effect) accounts for the contribution related to the electromechanical coupling, which is a manifestation of the secondary pyroelectric effect. The pyroelectric coefficient p_3 of a ceramic measured along the applied field is due primarily to the coefficients M'_{33} and M''_{333}. Because the effective piezoelectric modulus d_{33}^{eff} can be represented in the form

$$d_{33}^{\text{eff}} = M'_{33}E_3 + M''_{333}E_3^3 + \ldots, \quad (7)$$

its field dependence should become manifest in a field dependence of the PEC, which is supported experimentally. According to our preliminary evaluation, the secondary pyroelectric effect related to the induced piezoelectric effect provides a dominant contribution to the measured pyroelectric current. Final conclusion would require further comprehensive studies including the measurement of the thermal expansion and elasticity modulus.

ACKNOWLEDGMENTS

This study was supported by the Russian Foundation for Basic Research (project no. 02-02-16389a), the "Physics of Solid-State Nanostructures" program, and the program of support for leading scientific schools (project no. 00-15-96754).

REFERENCES

1. G. A. Smolenskiĭ, V. A. Isupov, A. I. Agranovskaya, and S. N. Popov, Fiz. Tverd. Tela (Leningrad) **2**, 2906 (1960) [Sov. Phys. Solid State **2**, 2584 (1960)].
2. G. A. Smolenskiĭ, V. A. Bokov, V. A. Isupov, N. N. Kraĭnik, R. E. Pasynkov, and M. S. Shur, *Ferroelectrics and Antiferroelectrics* (Nauka, Leningrad, 1971).
3. D. Vieland and Jie-Fang Li, J. Appl. Phys. **90** (6), 2995 (2001).
4. V. Bobnar, Z. Kutniak, R. Pirc, *et al.*, Phys. Rev. Lett. **84**, 5892 (2000).
5. F. Chu, N. Setter, and A. K. Tagantsev, J. Appl. Phys. **74**, 5129 (1993).
6. L. E. Cross, S. J. Jang, R. E. Newnham, *et al.*, Ferroelectrics **23**, 187 (1980).
7. V. A. Isupov and E. P. Smirnova, Ferroelectrics **90**, 141 (1989).
8. N. K. Yushin and E. P. Smirnova, Pis'ma Zh. Tekh. Fiz. **21** (10), 72 (1995) [Tech. Phys. Lett. **21**, 385 (1995)].
9. R. W. Whatmore, P. C. Osbond, and N. M. Shorrocks, Ferroelectrics **76**, 351 (1987).
10. N. M. Shorrocks, R. W. Whatmore, and P. C. Osbond, Ferroelectrics **106**, 387 (1990).
11. R. Watton and M. A. Todd, Ferroelectrics **118**, 279 (1991).
12. D. Vieland, S. J. Jang, L. E. Cross, and M. Wuttig, J. Appl. Phys. **69**, 414 (1991).
13. Z.-Y. Cheng, R. S. Katiyar, X. Xao, and A. S. Bhalla, Phys. Rev. B **57**, 8166 (1998).
14. N. K. Yushin, E. P. Smirnova, S. N. Dorogovtsev, *et al.*, Fiz. Tverd. Tela (Leningrad) **29**, 2947 (1987) [Sov. Phys. Solid State **29**, 1693 (1987)].
15. S. L. Swartz and T. R. Shrout, Mater. Res. Bull. **17**, 1245 (1982).
16. J. R. Giniewich, A. S. Bhalla, and L. E. Cross, Ferroelectrics **211**, 281 (1998).
17. S. B. Lang and D. K. Das-Gupta, Ferroelectrics **39**, 1249 (1981).
18. B. Ploss, R. Emmerich, and S. Bauer, J. Appl. Phys. **72**, 5363 (1992).
19. R. L. Byer and C. B. Rondy, Ferroelectrics **3**, 333 (1980).
20. M. Daglish, Integr. Ferroelectr. **22**, 473 (1998).
21. H. S. Carslaw and J. C. Jaeger, *Conduction of Heat in Solids*, 2nd ed. (Clarendon, Oxford, 1959; Nauka, Moscow, 1964).
22. D. J. Taylor, D. Damianovich, and A. S. Bhalla, Ferroelectrics **118**, 143 (1991).
23. Jae-Hwan Park, Byung-Kook Kim, Kug-Hyun Song, and Soon Ja Park, Mater. Res. Bull. **30**, 435 (1995).
24. J. R. Giniewicz, A. S. Bhalla, and L. E. Cross, Ferroelectrics **118**, 157 (1991).
25. J. F. Nye, *Physical Properties of Crystals: Their Representation by Tensors and Matrices*, 2nd ed. (Clarendon, Oxford, 1964; Mir, Moscow, 1967).
26. W. G. Cady, *Piezoelectricity* (McGraw-Hill, New York, 1946; Inostrannaya Literatura, Moscow, 1949).
27. V. V. Lemanov, N. K. Yushin, E. P. Smirnova, *et al.*, Ferroelectrics **134**, 139 (1992).

Translated by G. Skrebtsov

Physics of the Solid State, Vol. 45, No. 7, 2003, pp. 1310–1314. Translated from Fizika Tverdogo Tela, Vol. 45, No. 7, 2003, pp. 1250–1255.

MAGNETISM AND FERROELECTRICITY

Dielectric Properties of Betaine Phosphite–Betaine Phosphate Solid-Solution Crystals in the Improper Ferroelastic Phase

E. V. Balashova and V. V. Lemanov

Ioffe Physicotechnical Institute, Russian Academy of Sciences, Politekhnicheskaya ul. 26, St. Petersburg, 194021 Russia

Received December 27, 2002

Abstract—Temperature dependences of dielectric permittivity in the improper ferroelastic phase, including the region of the improper ferroelastic phase transition occurring at $T = T_{c1}$, were studied in the betaine phosphite–betaine phosphate solid-solution crystals. At a betaine phosphate (BP) concentration of 10%, the phase transition temperature T_{c1} was found to shift toward higher temperatures by about 5 K compared to betaine phosphite (BPI) crystals, where $T_{c1} = 355$ K. The phase transition remains in the vicinity of the tricritical point. As the BP concentration in BPI is increased, the dielectric anomaly at $T = T_{c1}$ weakens substantially compared to pure BPI. The nonlinear temperature dependence of reciprocal dielectric permittivity in the improper ferroelastic phase of BPI_xBP_{1-x} crystals is described in the concentration region $0.9 \le x \le 1$ in terms of a thermodynamic model taking into account the biquadratic relation of the nonpolar order parameter of the improper ferroelastic phase transition to polarization. The decrease in the ferroelectric phase transition temperature T_{c1} (or in the temperature of loss of improper ferroelastic phase stability) with increasing BP concentration in the above limits is due to the decreasing effect of the nonpolar mode on the polar instability, which is accompanied by a weakening of the dielectric anomaly at $T = T_{c1}$. © *2003 MAIK "Nauka/Interperiodica".*

1. INTRODUCTION

Betaine phosphite (BPI), $(CH_3)_3NCH_2COO \cdot H_3PO_3$, and betaine phosphate (BP), $(CH_3)_3NCH_2COO \cdot H_3PO_4$, are compounds of the betaine aminoacid $(CH_3)_3N^+CH_2COO^-$ with the inorganic acids H_3PO_3 and H_3PO_4, respectively [1]. Crystals of these compounds are similar in structure and undergo similar symmetry changes with decreasing temperature at the improper ferroelastic (antiferrodistorsive) phase transition $P2_1/m$ ($Z = 2$) $\longrightarrow$ $P2_1/c$ ($Z = 4$) [2–5], which occurs at $T_{c1} = 355$ K in BPI [6] and at $T_{c1} = 365$ K in BP crystals [7]. The inorganic tetrahedra HPO_3 and PO_4 in BPI and BP respectively, are connected to each other by hydrogen bonds to form zigzag-shaped chains along the monoclinic axis *b*. The betaine molecule is attached to each tetrahedron by one (in BPI) and two (in BP) hydrogen bonds and is arranged nearly perpendicular to the chains. At T_{c1}, both crystals undergo ordering of betaine molecules, which is accompanied by unitcell doubling along the *c* axis. As the temperature is lowered even further, nominally pure BPI crystals transfer to the ferroelectric state $P2_1/c$ ($Z = 4$) $\longrightarrow$ $P2_1$ ($Z = 4$) (polarization along the *b* axis) at temperatures $T_{c2} =$ 196–225 K [6, 8–10], whereas in the BP crystals, as follows from their dielectric behavior, antiferroelectric phases form with the phase transition temperatures $T_{c2} = 86$ K and $T_{c3} = 81$ K [7].

The dielectric properties of BPI_xBP_{1-x} solid-solution crystals below room temperature were studied in [11–15]. It was shown that, depending on the actual component concentration, the solid solutions can reside in an antiferroelectric (for $0 < x < 0.3$), glassy (for $0.3 < x < 0.9$), or ferroelectric state (for $0.9 < x < 1$). In particular, a glassy state was established to exist at $x = 0.85$ [14, 15] and a ferroelectric state, at $x = 0.9$ [11].

The dielectric properties of the BPI–BP solid solutions above room temperature, including the improper ferroelastic phase transition region, have not been studied previously. The temperature dependence of the dielectric permittivity of BPI and BP crystals exhibits an increase in the slope in the phase transition region at T_{c1}, at the transfer from the high-temperature symmetric to the improper ferroelastic phase [6, 7].

In [16, 17], the dielectric properties of BPI crystals in the improper ferroelastic phase were considered in terms of a thermodynamic model which relates the polar order parameter to the nonpolar order parameter through an expression of the type $\xi\eta^2\mathbf{P}^2$, where η is the order parameter of the improper ferroelastic phase transition at T_{c1}, $\mathbf{P}$ is the polarization, and $\xi < 0$ is a coupling coefficient. The model leads to an important conclusion that the ferroelectric phase transition in the crystal is driven by the nonpolar order parameter η of the structural phase transition and that the temperature of the ferroelectric phase transition T_{c2} depends on the extent to which the nonpolar order parameter affects the polar mode at the phase transition to the improper ferroelastic phase, i.e., on the magnitude of the dielectric anomaly at T_{c1}. A phenomenological model has been proposed for the BP crystals which also assumes a biquadratic relation between the order parameters of the type $\xi\eta^2\mathbf{P}^2$

($\xi < 0$) [18]. The dielectric anomaly at T_{c1} in these crystals is weaker than in BPI, and the ferroelectric transition does not occur down to low temperatures.

Adding even a small amount of BP to BPI ($0.9 \le x \le 1$) substantially reduces the temperature of the ferroelectric phase transition in the BPI_xBP_{1-x} solid solutions. The reduction of T_{c2} may be associated with a change in the influence of the order parameter of the phase transition at T_{c1} on the polar mode in the BPI–BP solid-solution crystals. This should also become manifest in the magnitude of the dielectric anomaly at T_{c1}, which has not yet been studied in the BPI–BP solid-solutions. This stimulated the present investigation of the dielectric properties in the improper ferroelastic phase (including the region of the improper ferroelastic phase transition at T_{c1}) of the BPI_xBP_{1-x} solid-solution crystals at concentrations $0.9 \le x \le 1$, at which the ferroelectric state in the low-temperature domain sets in [11–13]. We analyzed of the dielectric behavior of the crystals in terms of a model with coupled order parameters and studied the T_{c1-x} phase diagram in the above component concentration range.

2. EXPERIMENTAL RESULTS

Figure 1 displays temperature dependences of (a) the dielectric permittivity and (b) $\tan\delta$ in the neighborhood of the improper ferroelastic phase transition occurring at T_{c1} in nominally pure BPI crystals and BPI crystals with a BP content of 3% ($BPI_{0.97}BP_{0.03}$) and 10% ($BPI_{0.9}BP_{0.1}$), measured at 1 kHz. Introduction of 10% betaine phosphate into betaine phosphite is seen to shift the improper ferroelastic phase transition point up by approximately 5 K ($T_{c1} \cong 360$ K) and strongly reduce the dielectric anomaly (a decrease in the slope of the temperature dependence of dielectric permittivity at the transition to the improper ferroelastic phase at $T < T_{c1}$). Note that approximately the same increase in the temperature T_{c1} was observed to occur in solid solutions of deuterated crystals DBPI–DBP for the same component concentration, with the phase transition temperature T_{c1} in BP–DBP and BPI–DBPI being practically independent of the degree of deuteration [19].

Dielectric losses are fairly small in all samples, practically throughout the region of existence of the improper ferroelastic phase (at 1 kHz, $\tan\delta$ = 0.003–0.006), begin to increase noticeably with temperature at a few kelvins below the phase transition point, and grow strongly in the high-temperature symmetric phase, with no pronounced features seen in the temperature dependences of $\tan\delta$ at the phase transition point. The region of growth of the dielectric losses shifts towards higher temperatures with increasing concentration of BP in BPI.

Figure 2 plots the reciprocal dielectric permittivities of BPI and $BPI_{0.9}BP_{0.1}$ as a function of temperature

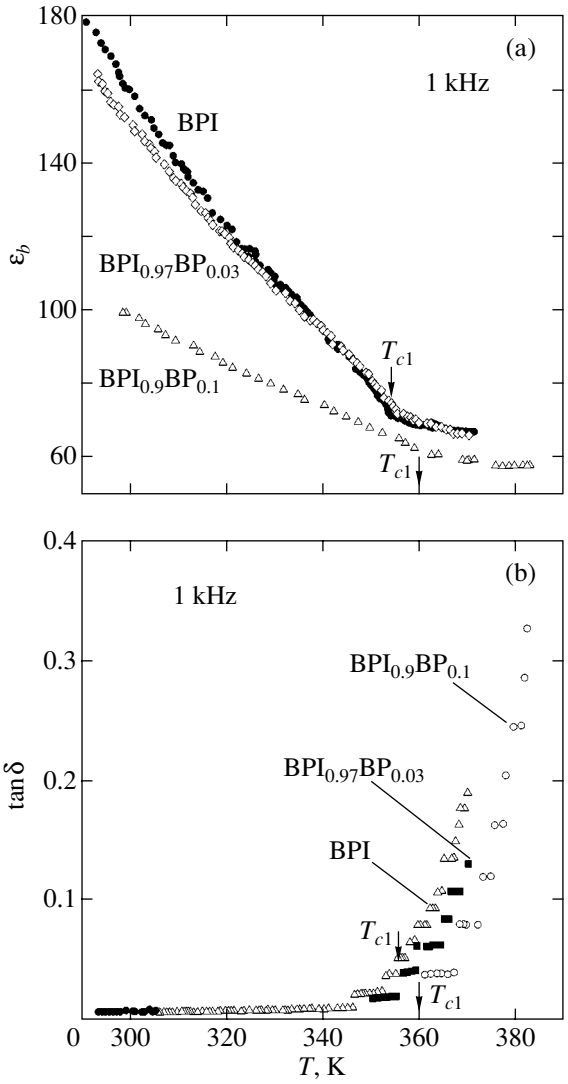

Fig. 1. Temperature dependences of (a) the dielectric permittivity ε_b and (b) $\tan\delta$ measured at 1 kHz in the region of the improper ferroelastic phase transition in the BPI, $BPI_{0.97}BP_{0.03}$, and $BPI_{0.9}BP_{0.1}$ crystals.

within the range 150–383 K. The phase transition to the ferroelectric state in the BPI crystals used in this study is observed to occur at T_{c2} = 204 K; thus, the region of the improper ferroelastic phase lies between the phase transition points T_{c1} = 355 K and T_{c2} = 204 K. $BPI_{0.9}BP_{0.1}$ crystals do not transfer to the ferroelectric state in the temperature region covered; only the improper ferroelastic phase transition is observed at T_{c1} = 360 K. As seen from Fig. 2, the reciprocal dielectric permittivity of the improper ferroelastic phase of both crystals exhibits a nonlinear temperature dependence.

Note that the dielectric permittivity of all the studied samples with different impurity concentrations does not reveal, as follows from experiments, a noticeable dispersion in the frequency range of 100 Hz to 1 MHz within the temperature region where the improper fer-

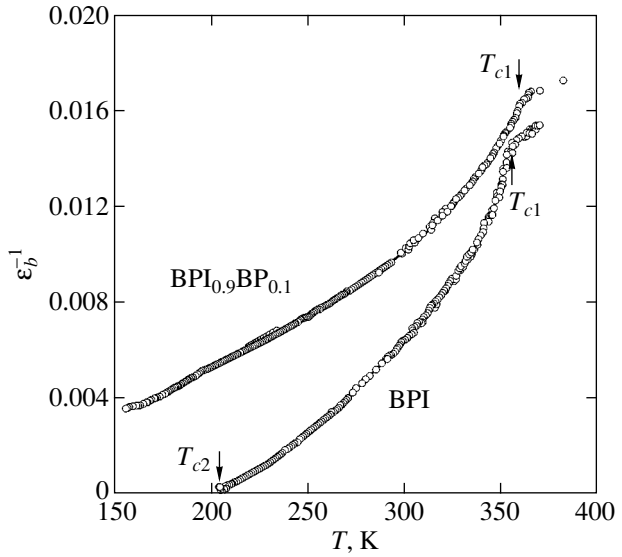

Fig. 2. Temperature dependences of the reciprocal dielectric permittivity ε_b^{-1} in the region of the improper ferroelastic phase in the BPI and $BPI_{0.9}BP_{0.1}$ crystals. Solid curves (practically coinciding with experimental points) refer to calculations made with Eq. (4).

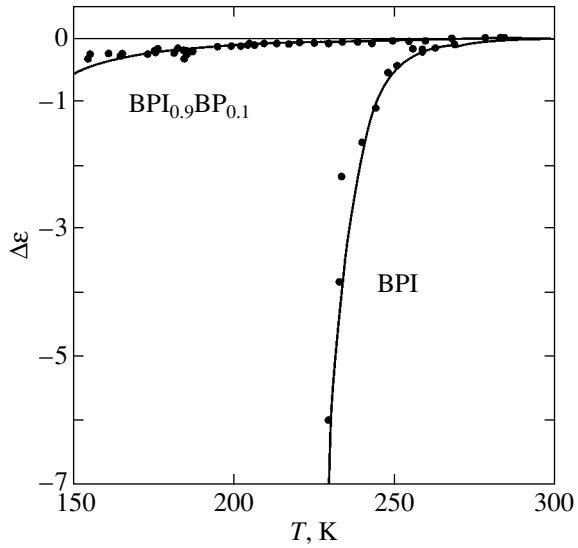

Fig. 3. Temperature dependences of the variation of dielectric permittivity $\Delta\varepsilon = \varepsilon(E) - \varepsilon(0)$ induced by an electric bias field $E = 10^5$ V/m in the improper ferroelastic phase of the BPI and $BPI_{0.9}BP_{0.1}$ crystals. Solid curves are drawn to aid the eye.

roelastic phase exists. This implies that there are no additional low-frequency contributions (not related to phase transitions to dielectric permittivity in the improper ferroelastic phase.

Figure 3 displays the temperature behavior of the dielectric permittivity $\Delta\varepsilon = \varepsilon(E) - \varepsilon(0)$ of BPI and $BPI_{0.9}BP_{0.1}$ crystals measured under an electric bias $E = 10^5$ V/m within a temperature interval 150–280 K. The dielectric permittivity of the BPI crystal is seen to decrease noticeably under the bias ($\Delta\varepsilon$) is negative as one approaches the ferroelectric phase transition point $T_{c2} = 204$ K. By contrast, in the $BPI_{0.9}BP_{0.1}$ crystal, the decrease in the dielectric permittivity under the bias remains small throughout the temperature interval covered.

3. ANALYSIS OF THE EXPERIMENTAL DATA

It was shown in [16, 17] that the nonlinear temperature dependence of reciprocal dielectric permittivity in the improper ferroelastic phase of BPI crystals can be described in terms of a thermodynamic model taking into account the biquadratic relation between the nonpolar order parameter for the high-temperature phase transition at $T_{c1} = 355$ K and polarization with a negative coupling coefficient. The negative coupling coefficient means that the ferroelectric phase transition occurring at T_{c2} is driven by the nonpolar order parameter for the phase transition at T_{c1}. The existence of coupling between the polar and nonpolar order parameters is indicated by the dielectric anomaly, which becomes manifest in the change of the slope of the temperature dependence of the dielectric permittivity at the nonpolar phase transition. The negative coupling coefficient correlates with the increase in the slope of the temperature dependence of dielectric permittivity at the transition to the nonpolar ordered state, as is the case with the crystals studied. In this model, the nonlinear temperature behavior of reciprocal dielectric permittivity is accounted for by the high-temperature phase transition occurring practically at the tricritical point [16, 20]. In all three BPI–BP solid solutions, the reciprocal dielectric permittivity in the improper ferroelastic phase likewise behaves nonlinearly with temperature. This means that the high-temperature improper ferroelastic phase transition in these crystals remains close to the tricritical point.

Thus, we approximate the temperature behavior of dielectric permittivity in the BPI–BP solid solutions studied using the following thermodynamic potential, which includes the coupling between the polar and nonpolar order parameters and the existence of the high-temperature phase transition at the tricritical point:

$$F = \frac{1}{2}\alpha_1\eta^2 + \frac{1}{6}\gamma_1\eta^6 + \frac{1}{2\chi_0}\mathbf{P}^2 + \frac{1}{4}\beta_2\mathbf{P}^4 + \frac{1}{2}\xi\eta^2\mathbf{P}^2 - \mathbf{PE}, \quad (1)$$

where $\alpha_1 = \lambda_1(T - T_{c1})$, $\beta_2 > 0$, $\xi < 0$, $\mathbf{E}$ is the macroscopic electric field, and χ_0 is the background dielectric susceptibility.

The thermodynamic potential (1) can be recast to a dimensionless form,

$$f = \frac{1}{2}ta^2q^2 + \frac{1}{6}q^6 - ap^2 + \frac{1}{2}p^4 - q^2p^2 + 2ape, \quad (2)$$

where $t = (T - T_{c1})/\Delta T$ is reduced temperature,

$$f = F\frac{8\beta_2^3\gamma_1^2}{\xi^6}, \quad q^2 = \frac{2\beta_2\gamma_1}{\xi^2}\eta^2,$$

$$p^2 = -\frac{2\beta_2^2\gamma_1}{\xi^3}P^2, \quad e = \frac{\sqrt{2\gamma_1}\beta_2\chi_0}{(-\xi)^{3/2}}E.$$

Parameter $\Delta T = \dfrac{\gamma_1}{\lambda_1\chi_0^2\xi^2}$ determines the temperature region of stability of the paraelectric improper ferroelastic (antiferrodistorsive) phase ($\eta \neq 0$, $\mathbf{P} = 0$). The dimensionless parameter $a = \dfrac{2\beta_2\gamma_1}{\chi_0\xi^3} < 0$ defines the region of stability of the polar phase ($\eta \neq 0$, $\mathbf{P} \neq 0$) and the of the ferroelectric phase transition.

For $a \leq -1$, the ferroelectric phase transformation is a continuous phase transition at the temperature $T_{c2} = T_{c1} - \Delta T$. For the values of this parameter in the range $-1 < a < -0.5$, the temperature T_{c2} will define the temperature of first-order transition from the improper ferroelastic to the ferroelectric phase (the case $-0.5 < a < 0$, see [17]). The proximity of the ferroelectric phase transition to the tricritical point on the sides of both the first- and second-order phase transitions (temperature hysteresis) is determined by parameter $[(a + 1)/a]^2\Delta T$ and depends on the value of a at a fixed value of ΔT. The magnitude of parameter a can be derived from temperature dependences of the permittivity variation under an external bias field [17].

In the absence of an external bias field, the temperature dependences of reciprocal dielectric permittivity in the high-temperature symmetric (I) and the improper ferroelastic (II) phases and their regions of stability can be presented in the form

(I) $\eta = P = 0$,

$$1/\chi = 1/\chi_0, \quad T > T_{c1}, \tag{3}$$

(II) $P = 0$, $\eta \neq 0$,

$$1/\chi = \{1 - [(T_{c1} - T)/\Delta T]^{1/2}\}/\chi_0, \quad T_{c2} < T < T_{c1}, \tag{4}$$

where $\Delta T = \dfrac{\gamma_1}{\lambda_1\chi_0^2\xi^2} = T_{c1} - T_{c2}$ defines, as already mentioned, the stability region of the improper ferroelastic (paraelectric) phase.

Equation (4) was used to approximate the temperature dependence of reciprocal dielectric permittivity in the improper ferroelastic phase of the crystals studied. For the BPI crystal, the phase transition temperatures T_{c1} and T_{c2} are specified by arrows in Fig. 2. In the $BPI_{0.97}BP_{0.03}$ crystals, acoustic and dielectric measurements yield $T_{c2} \cong 180$ K for the ferroelectric phase transition temperature [20, 21]. In $BPI_{0.9}BP_{0.1}$ crystals, the literature data give approximately 50 K for the ferroelectric phase transition point, a figure outside the temperature interval studied. The external field–induced change in the dielectric permittivity of the paraelectric phase of this crystal is small compared to that for BPI (see Fig. 3), which implies that the ferroelectric phase transition in it occurs at a temperature substantially below 150 K, the lower limit of the temperature interval covered in the present study. Figure 2 compares the experimental and theoretical relations for the reciprocal dielectric permittivity in BPI and $BPI_{0.9}BP_{0.1}$ obtained with the use of Eq. (4). We readily see good agreement between the experimental data and theoretical curves. The best-fit values of the parameters, namely, of the background dielectric permittivity $\varepsilon_P = 1 + 4\pi\chi_0$ and ΔT, are listed in the table for the three crystals investigated.

Temperatures of the improper ferroelastic (T_{c1}) and ferroelectric (T_{c2}) phase transitions and calculated temperature regions of stability of the improper ferroelastic phase ΔT, background dielectric permittivy ε_P, and coupling coefficient ξ in BPI_xBP_{1-x} crystals

Crystal	T_{c1}, K	T_{c2}, K ($T_{c1} - \Delta T$)	ΔT, K	ε_P	ξ
BPI	355	204	151	63	−0.094
$BPI_{0.97}BP_{0.03}$	355	178	177	66	−0.082
$BPI_{0.9}BP_{0.1}$	360	39	321	56	−0.074

An analysis shows that the phenomenological model with two coupled order parameters is capable of describing with sufficient accuracy the temperature behavior of the reciprocal dielectric permittivity in the improper ferroelastic phase of both BPI and the $BPI_{0.97}BP_{0.03}$ and $BPI_{0.9}BP_{0.1}$ solid solutions within the temperature interval studied. An important result is the determination of the parameter $\Delta T = T_{c1} - T_{c2}$, which permits one to calculate the temperature of the loss of stability of the improper ferroelastic phase (or the ferroelectric phase transition point) based on the parameters of the dielectric anomaly at T_{c1} in the high-temperature region of the improper ferroelastic phase. It should be pointed out that the background dielectric permittivities obtained in analyzing the temperature dependences in the improper ferroelastic phase turn out to be slightly lower (by no more than 10%) than the dielectric permittivity in the high-temperature symmetric phase. This suggests an additional contribution to dielectric permittivity entailing a considerable increase in $\tan\delta$ (see Fig. 1b) whose mechanism may not be directly connected with the phase transition at T_{c1}.

The quantity ΔT is a generalized characteristic of the effect of the nonpolar order parameter for the high-temperature phase transition at T_{c1} on the polar instability in the crystal. This quantity includes the properties of the nonpolar mode, namely, the ratio λ_1/γ_1, the back-

ground dielectric susceptibility χ_0, and the coupling coefficient ξ connecting the polar mode with the nonpolar mode. Let us consider the factors affecting the quantity ΔT in more detail. As seen from the table, the values of the background dielectric permittivity are practically the same for the BPI and $BPI_{0.97}BP_{0.03}$ crystals and are slightly smaller for $BPI_{0.9}BP_{0.1}$. Calculations show that this small decrease in the background dielectric permittivity in $BPI_{0.9}BP_{0.1}$ cannot give rise to a substantial decrease in the ferroelectric phase transition temperature compared to that in BPI. The calculated temperature of the loss of stability of the improper ferroelastic phase in $BPI_{0.9}BP_{0.1}$ (or of the ferroelectric phase transition temperature, if the phase transition is continuous, which corresponds to $a \le -1$), as is evident from the table, is $T_{c2} \cong 40$ K. This value of T_{c2}, while being slightly lower, is nevertheless close to the ferroelectric phase transition point, $T_{c2} \cong 50$ K, measured in [11, 13] for this solid solution. This reduction of T_{c2} is the consequence of a substantial weakening of the dielectric anomaly observed at T_{c1} in this crystal. The ratio $\gamma_1/\lambda_1 = (33 \pm 1)$ K was determined for BP [22]. Because the temperatures of the improper ferroelastic phase transition in the BPI and BP crystals differ by only 10 K, the phase transition at T_{c1} remains close to the tricritical point in all the crystals studied, and the order parameter in both crystals is determined by the extent to which the betaine molecules are ordered (order in the organic subsystem of the crystal), one may safely assume that the λ_1/γ_1 ratio does not vary noticeably in the BPI–BP mixed crystals under partial substitution in the inorganic subsystem of the crystal. This suggestion is corroborated by acoustic studies [16, 20, 23], which suggest that the elastic modulus c_{22} in the improper ferroelastic phase has a fairly large contribution that is proportional to the squared order parameter and approximately the same for the BP and BPI crystals. The magnitude of this contribution near the phase transition at the tricritical point depends on the λ_1/γ_1 ratio. Since this ratio varies only weakly with the component concentration x, the main factor responsible for the reduction of the ferroelectric phase transition temperature in the BPI_xBP_{1-x} solid solutions ($0.9 \le x \le 1$) can only be a decrease in magnitude of the coupling coefficient $|\xi|$ connecting the nonpolar order parameter η for the high-temperature phase transition with the polar instability in the crystal. The calculated values of the coupling coefficient ξ are listed in the table. One readily sees that, in the BPI_xBP_{1-x} solid solutions ($0.9 \le x \le 1$), an increase in BP concentration in BPI brings about a decrease in the absolute magnitude of the coupling coefficient ξ relating the polar order parameter to the nonpolar order parameter.

ACKNOWLEDGMENTS

The authors are indebted to J. Albers and A. Klöpperpieper for providing the crystals and to V.A. Yankovskaya for preparing the samples.

This study was supported by the Russian Foundation for Basic Research (project no. 01-02-17873) and the program for support of leading scientific schools (grant no. 00-15-96754).

REFERENCES

1. J. Albers, Ferroelectrics **78**, 3 (1988).
2. M. Dörffel, Th. Narz, and S. Haussühl, Z. Kristallogr. **186**, 71 (1989).
3. P. Freude and D. Michel, Phys. Status Solidi B **195**, 297 (1996).
4. W. Schildkamp, G. Schäfer, and J. Spilker, Z. Kristallogr. **168**, 187 (1984).
5. W. Schildkamp and J. Spilker, Z. Kristallogr. **168**, 159 (1984).
6. J. Albers, A. Klöpperpieper, H. J. Rother, and S. Haussühl, Ferroelectrics **81**, 27 (1988).
7. J. Albers, A. Klöpperpieper, H. J. Rother, and K. H. Ehses, Phys. Status Solidi A **74**, 533 (1982).
8. I. Fehst, M. Paasch, S. L. Hutton, *et al.*, Ferroelectrics **138**, 1 (1993).
9. R. Sobiestianskas, J. Grigas, Z. Czapla, and S. Dacko, Phys. Status Solidi A **136**, 223 (1993).
10. H. Bauch, J. Banys, R. Böttcher, *et al.*, Phys. Status Solidi B **187**, K81 (1995).
11. M. L. Santos, M. R. Chaves, A. Almeida, *et al.*, Ferroelectr. Lett. Sect. **15**, 17 (1993).
12. H. Ries, R. Böhmer, I. Fehst, and A. Loidl, Z. Phys. B **99**, 401 (1996).
13. R. Böttcher, A. Pöppl, G. Völkel, *et al.*, Ferroelectrics **208–209**, 105 (1998).
14. H. Bauch, G. Völkel, R. Böttcher, *et al.*, Phys. Rev. B **54**, 9162 (1996).
15. J. Banys, S. Lapinskas, A. Kajokas, *et al.*, Phys. Rev. B **66**, 144113 (2002).
16. E. V. Balashova and V. V. Lemanov, Ferroelectrics **247** (4), 269 (2000).
17. E. V. Balashova, V. V. Lemanov, and A. Klöpperpieper, Fiz. Tverd. Tela (St. Petersburg) **44**, 1522 (2002) [Phys. Solid State **44**, 1597 (2002)].
18. M. Iwata and Y. Ishibashi, J. Phys. Soc. Jpn. **65**, 2900 (1996).
19. J. V. Samulionis, J. Banys, and G. Völkel, J. Alloys Compd. **310**, 176 (2000).
20. E. V. Balashova, V. V. Lemanov, J. Albers, and A. Klöpperpieper, Fiz. Tverd. Tela (St. Petersburg) **40**, 1090 (1998) [Phys. Solid State **40**, 995 (1998)].
21. E. V. Balashova, V. V. Lemanov, J. Albers, and A. Klöpperpieper, Ferroelectrics **208–209**, 63 (1998).
22. P. Freude, D. Michel, J. Totz, and A. Klöpperpieper, Ferroelectrics **208–209**, 93 (1998).
23. M. Maeda, J. Phys. Soc. Jpn. **57**, 3059 (1988).

Translated by G. Skrebtsov

Physics of the Solid State, Vol. 45, No. 7, 2003, pp. 1315–1321. Translated from Fizika Tverdogo Tela, Vol. 45, No. 7, 2003, pp. 1256–1262.

LATTICE DYNAMICS AND PHASE TRANSITIONS

Anisotropy of the Phonon–Phason Dynamics and the Pinning Effect in Icosahedral AlPdMn Quasicrystals

Y. A. Kozinkina*, V. L. Lorman, and S. B. Rochal***

**Rostov State University, pr. Stachki 194, Rostov-on-Don, 344090 Russia*

e-mail: y_kozinkina@mail.ru

***Laboratoire de Physique Mathématique et Théorique, Centre National de la Recherche Scientifique–Université Montpellier 2, 34095 Montpellier, France*

Received November 1, 2002

Abstract—A minimal model of the phonon–phason dynamics in icosahedral quasicrystals with inclusion of the pinning effect is suggested. Resonant attenuation of low-frequency acoustic waves in the temperature range corresponding to thermal activation of phasons is considered. In the long-wave length limit, the velocity of acoustic phonons is isotropic; however, the phonon–phason coupling causes anisotropy of the velocity and of the attenuation of acoustic waves with small wave vectors. These effects manifest themselves most strongly at an acoustic wave frequency close to the inverse relaxation time of phasons with the same wave vector. The pinning effect can cause a significant decrease in the anisotropy of the velocity and of attenuation of acoustic waves. © *2003 MAIK "Nauka/Interperiodica".*

1. INTRODUCTION

Quasicrystals, discovered in 1984 [1], feature a long-range quasiperiodic order combined with noncrystallographic rotational symmetry. The quasicrystalline density function can be expanded into a Fourier series. In this case, the number N of basis vectors spanning the reciprocal space exceeds the dimensionality of the physical space in which the real quasicrystal (QC) exists. Therefore, the QC is characterized by additional Goldstone phason degrees of freedom (vector $\mathbf{w}$) that are absent in the crystalline state [2]. A uniform variation of $\mathbf{w}$ corresponds to a relative shift of the incommensurate density waves forming the QC [2]. A nonuniform variation of $\mathbf{w}$ contributes to the QC elastic energy [3], which causes specific elastic properties of the QC.

A set of elastodynamic equations for describing the viscoelastic behavior of the icosahedral QC was first suggested in [4, 5]:

$$\begin{aligned}
\partial_t \rho + \nabla \mathbf{g} &= 0,\\
\partial_t g_i - \nabla_j(\eta_{ijkl}\nabla_k g_l) &= -\frac{\delta F}{\delta u_i} - \rho\nabla_i\frac{\delta F}{\delta \rho},\\
\partial_t u_i + \Gamma_u\frac{\delta F}{\delta u_i} - v_i &= 0,\\
\partial_t w_i + \Gamma_w\frac{\delta F}{\delta w_i} &= 0,
\end{aligned} \tag{1}$$

where ρ is the density, $\mathbf{g}$ is the mass density flux, η_{ijkl} is the ordinary viscosity tensor, F is the ratio of the total energy of the QC to its volume, Γ_u and Γ_w are the dissipative kinetic coefficients, and v_i is the velocity of a given volume element. The first equation in set (1) is the ordinary continuity equation. The second equation is a version of the Navier–Stokes equation [6] whose right-hand side is the elastic force acting on a unit volume. Within the model, this force is caused by a displacement of the volume under consideration and by a change in its density. The left-hand side of the second equation in set (1) is equivalent to the statement that a fraction of the applied elastic force imparts acceleration to the unit volume and the rest balances the viscous force. The third and fourth equations describe the phonon and phason relaxation.

Recent experimental studies [7–10] have shown that the elastic behavior of quasicrystalline systems is similar to that of ordinary metal alloys up to temperatures close to the QC melting point. A small deformation is always elastic, while a plastic deformation (mass transfer) arises beginning from a certain critical load. However, the third equation in set (1) is, in fact, inconsistent with the concept of the QC as an elastic solid. In this equation, the volume element velocity v_i (obviously understood as the momentum of a volume corresponding to a unit mass) differs form the time derivative of the displacement field. This difference between v_i and $\partial_t u_i$ is well known and is caused by material flow with respect to an inhomogeneous spatial structure. For example, in the case of liquid crystals (smectics and cholesterics), the flow is initiated at indefinitely small deformation of a considered volume [11]. In the case of elastic (crystalline or, as the experimental results cited above show, quasicrystalline) materials subjected to deformation, the values of v_i and $\partial_t u_i$ can also differ. However, this difference takes place only if the defor-

mation is appreciable and becomes plastic. When solving the problem of sound propagation, the medium deformation should be considered small and Γ_u may be set equal to zero. Thus, the third of Eqs. (1) is, in fact, excluded from consideration. In the absence of plastic deformation, the continuity equation and the second term in the right-hand side of the second equation can also be excluded from set (1).

Hereafter, we refer to this model of the elastodynamics of the icosahedral QC as the minimal one. This paper is aimed at the study and subsequent generalization of the minimal model. In Section 2, we consider exact solutions of the minimum model for symmetry directions of the wave vector. The terms allowing for the pinning of phason modes are also included in the equations of the model. In the final section, the resonant phonon–phason coupling is considered taking into account the pinning effect (PE).

2. DIAGONALIZATION OF THE MINIMAL MODEL FOR SYMMETRY DIRECTIONS OF THE WAVE VECTOR

With the phonon–phason elastic energy [3], the above-formulated set of linear differential equations can be written in the explicit form and solved using the conventional Fourier method. A solution to the set is sought in the form of damping phonon–phason plane waves characterized by six-dimensional polarization vector **U** and ordinary three-dimensional wave vector **q** [12]. If the phonon–phason coupling is small, waves can have predominantly phonon or phason polarization.

After expansion into a Fourier series, the differential equations of the phonon–phason elastodynamics are reduced to the following set of six algebraic linear equations for the components of the six-dimensional polarization vector **U**:

$$\sum_{j=1}^{6} [C_{kj}(\mathbf{q}) + G_{kj}(\mathbf{q})]U_j = \lambda(k)U_k, \qquad (2)$$

where $k, j = 1, \ldots, 6$; $G_{kj}(\mathbf{q})$ is the matrix corresponding to the Fourier transform of the viscosity tensor η_{ijkl} and having nonzero components if $k, j \le 3$; $C_{kj}(\mathbf{q})$ is the phonon–phason dynamic matrix (DM) [13]; U_j is the six-component polarization, consisting of two three-dimensional vectors, namely, ordinary polarization **u** and phason polarization **w**; and $\lambda(k) = \rho\omega^2$ if $k = 1, 2, 3$ and $\lambda(k) = iD\omega$ if $k = 4, 5, 6$ ($i = \sqrt{-1}$). Instead of the coefficient Γ_w, we introduced $D = -1/\Gamma_w$ to make set (2) simpler. Solutions to set (2) are the dispersion relations $\omega(q)$ and the corresponding polarizations. The homogeneous system admits a nonzero solution if its determinant is zero. However, the determinant of set (2) is represented by a very cumbersome analytical expression. Therefore, we analytically consider only three special cases, corresponding to the wave vectors parallel to the fivefold [1, τ, 0], threefold [τ_2, 1, 0], and twofold [1, 0, 0] axes, respectively. The orientation of the icosahedral QC is identical to that chosen in [13]. For these directions, the determinant becomes the product of three second-order determinants of the type

$$\begin{vmatrix} \nu q^2 - \rho\omega^2 - i\eta_{\text{eff}}\omega q^2 & Iq^2 \\ Iq^2 & Kq^2 - iD\omega \end{vmatrix}, \qquad (3)$$

where ν, I, and K are the effective constants of the phonon elasticity, phonon–phason coupling, and phason elasticity, respectively, and η_{eff} is the effective viscosity constant. In all three special cases, there are longitudinal and transverse waves. A wave is longitudinal (transverse) if the phonon component of its polarization vector is parallel (perpendicular) to the wave vector.

In the case of longitudinal and transverse waves, we have $\nu = \lambda + 2\mu$ and $\nu = \mu$, respectively. The viscosity in the minimal model is defined by the tensor η_{ijkl} that is isotropic in the case of icosahedral symmetry. After the corresponding diagonalization of this tensor, we have $\eta_{\text{eff}} = \eta^{\parallel}$ for longitudinal waves and $\eta_{\text{eff}} = \eta^{\perp}$ for transverse waves, where $\eta^{\perp}$ and $\eta^{\parallel}$ are two independent coefficients of viscosity. It is noteworthy that a similar phason viscosity making a contribution of the same type to the element lying in the second row and the second column is anisotropic [12]. The table lists the coefficients necessary for calculating determinant (3). The constant of phason internal friction D and the density ρ are not affected by the diagonalization. The minimal model suggests several important physical consequences.

(i) The effective phonon–phason coupling and the effective constant of phason elasticity, in contrast to the effective phonon elastic constant, are anisotropic and characterized by icosahedral symmetry.

(ii) The doubly degenerate transverse mode propagating along the fivefold axis does not interact with the corresponding phason mode.

(iii) The account of the phonon–phason coupling lifts the degeneracy of a transverse wave propagating along the diad axis.

Now, we briefly discuss some restrictions to the applicability of the minimal model and consider some of its generalizations.

First, quasicrystals have a discrete atomic structure. In the case of crystals and continuous isotropic media, normal modes are classified by their frequencies and wave vectors.

In the case of quasicrystals, such a classification is possible only for the acoustic branches near the center of the Brillouin zone. In the case of modes with rather high frequencies, it is impossible to determine an accurate value of the wave vector. Atomic motion in this case is represented as a superposition of waves with slightly different wave vectors. Hence, the finite width

Effective elastic constants K and I of the icosahedral quasicrystal depending on the direction of vector **q** and polarization **u** of an acoustic wave

q, m^{-1}	**u**, m	**w**, m	K, N/m^2	I, N/m^2	N
$q\langle 1, \tau, 0\rangle/N$	$u\langle 1, \tau, 0\rangle/N$	$w\langle \tau, -1, 0\rangle/N$	$K_1 - (4/3)K_2$	$-2K_3$	$\sqrt{\tau + 2}$
	$u\langle 0, 0, 1\rangle$	$w\langle 0, 0, 1\rangle$	$K_1 + (2/3)K_2$	0	1
	$u\langle -\tau, 1, 0\rangle/N$	$w\langle 1, \tau, 0\rangle/N$	$K_1 + (2/3)K_2$	0	$\sqrt{\tau + 2}$
$a\langle \tau^2, 1, 0\rangle/N$	$u\langle \tau^2, 1, 0\rangle/N$	$w\langle 1, \tau^2, 0\rangle/N$	$K_1 + (4/3)K_2$	$(2/3)K_3$	$\sqrt{3\tau + 3}$
	$u\langle 0, 0, -1\rangle$	$w\langle 0, 0, 1\rangle$	$K_1 - (2/3)K_2$	$(4/3)K_3$	1
	$u\langle -1, \tau^2, 0\rangle/N$	$w\langle -\tau^2, 1, 0\rangle/N$	$K_1 - (2/3)K_2$	$(4/3)K_3$	$\sqrt{3\tau + 3}$
$q\langle 1, 0, 0\rangle$	$u\langle 1, 0, 0\rangle$	$w\langle 1, 0, 0\rangle$	$K_1 - (1/3)K_2$	K_3	1
	$u\langle 0, 1, 0\rangle$	$w\langle 0, 1, 0\rangle$	$K_1 + (\tau - 1/3)K_2$	K_3/τ	1
	$u\langle 0, 0, 1\rangle$	$w\langle 0, 0, 1\rangle$	$K_1 + (2/3 - \tau)K_2$	$-\tau K_3$	1

of the acoustic dispersion curves is caused not only by the finite lifetime of phonons, calculated from the imaginary part of the $\omega_{phn}(q)$ dependence, but also by the discrete atomic structure of quasicrystals. It is impossible to consider this effect within the model developed in the continuum approximation. Therefore, the minimal model is applicable only to the propagation of acoustic waves with wavelengths sufficiently long in comparison with the interatomic spacings.

Second, the acoustic-wave propagation causes the local density to vary [11]; therefore, the local temperature differs from the average QC temperature and, in order to analyze the acoustic wave propagation, one must consider, in addition to elastic stresses, the stresses caused by temperature variations. The above-mentioned mechanism results in additional damping of an acoustic wave due to the elastic-to-thermal energy conversion. In the case of icosahedral symmetry and an isotropic medium, such damping manifests itself only for longitudinal waves and contributes to the phonon elastic constant λ [12].

A third interesting extension of the minimal model is the inclusion of the nonlinear spatial dispersion of acoustic modes. Even in the simplest model of a linear chain of atoms of the same species, the acoustic dispersion branch is linear only near reciprocal-lattice sites. As was shown in [14], the quartic and higher order terms in the wave vector in the DM make the icosahedral QC different from an isotropic medium. In the case of QCs, the phonon block in the DM has one additional independent coefficient in comparison to the isotropic case. This means that even in the low-temperature region, where phasons are frozen, the dispersion of acoustic phonons in the icosahedral QC is isotropic only in the long-wavelength limit. With the quartic terms retained in the DM, the total number of independent coefficients is equal to nine, more specifically, three phonon–phonon, three phason–phonon, and three phason–phason coefficients. The DM of the icosahedral QC with quartic terms included was calculated in [14].

Finally, the simplest modification of the minimal model makes it possible to take into account the pinning of phason modes and to consider the influence of the pinning on the dynamics of acoustic phonons in the QC. The pinning of phason modes is well known for incommensurate structures other than quasicrystalline ones. For example, in incommensurate structures consisting of mutually incommensurable periodic sublattices, the PE manifests itself provided the relative displacement of the sublattices as a whole gives rise to restoring elastic forces. The resulting elastic energy of this system depends not only on spatial derivatives of the vector **w** but also on the magnitude of this vector [15]. The phason mode in such structures is often similar to an acoustic mode; however, as the wave vector tends to zero, the phason mode frequency tends not to zero but to a finite value defined by the pinning strength. After a phase transition during which the incommensurate sublattices become commensurate, the phason mode transforms into an ordinary optical mode and the PE elastic constant f_s defines its frequency at the center of the first Brillouin zone. The quasicrystalline structure cannot be represented as several incommensurate periodic sublattices. However, in the phenomenological dynamic model of the QC, the PE can be taken into account in much the same way; it is sufficient to add the term $f_s\mathbf{w}^2/2$ to the QC elastic energy. In this case, the phason block of the DM will change only slightly; namely, the term f_s will be added to each of its three diagonal elements. Hence, determinant (3) will be somewhat changed: the term f_s will also be added to the element lying in the second row and the second column. The dynamics of acoustic modes in the icosahedral QC will be considered in the next section with allowance for the pinning.

3. INFLUENCE OF PHASONS ON THE DYNAMICS OF ACOUSTIC MODES

The minimal model allows quantitative estimation of the features of the acoustic-phonon dispersion near the long-wavelength limit. For simplicity, we consider transverse modes, since longitudinal acoustic waves in the case of icosahedral symmetry undergo the above-

mentioned additional weak damping caused by the temperature spatial nonuniformity arising in the course of sound propagation. Thus, we study the properties of the solution $\omega_{phn}(q)$ to the equation

$$\begin{Vmatrix} \mu q^2 - \rho\omega^2 - i\eta^\perp \omega q^2 & Iq^2 \\ Iq^2 & Kq^2 - iD\omega + f_s \end{Vmatrix} = 0, \quad (4)$$

where the coefficients K and I depend on the vector $\mathbf{q}$ direction and the polarization (see table). The coefficient of phason internal friction D is considered as a decreasing function of temperature, which corresponds to the assumption that D is large at low temperatures and, hence, phasons are frozen, whereas at high temperatures D is small and phasons can relax. The mobility of phasons is controlled by their lifetime τ_{phs}, which, using Eq. (4) and neglecting the phonon–phason interaction, can be estimated as $\tau_{phs} \approx D/(Kq^2 + f_s)$. All the other coefficients of the equation are ordinary constants.

First, let us analyze the extreme cases. If the phason friction coefficient D tends to infinity (i.e., the temperature tends to absolute zero), we have

$$\omega_{phn} = \frac{-i\eta^\perp q^2 + \sqrt{4\rho\mu q^2 - (\eta^\perp)^2 q^4}}{2\rho}. \quad (5)$$

It is evident that the real and imaginary parts of the $\omega_{phn}(q)$ dependence are isotropic and the pinning is of no importance.

In the opposite extreme case, the phason relaxation time is small and $D = 0$. In this case, we have

$$\omega_{phn} = \frac{-i\eta^\perp q^2 + \sqrt{4\rho q^2\left(\mu - \frac{I^2 q^2}{Kq^2 + f_s}\right) - (\eta^\perp)^2 q^4}}{2\rho}. \quad (6)$$

We can see from Eq. (6) that $\mathrm{Im}\,\omega_{phn}(q)$ is isotropic and, if $f_s = 0$ or $Kq^2 \gg f_s$, the velocity of sound, provided that the coefficient $\eta^\perp$ is small, is written as

$$V = \sqrt{\frac{\mu - \frac{I^2}{K}}{\rho}}. \quad (7)$$

In the case of transverse waves propagating along various symmetry axes, the quantity $\mu - I^2/K$ is the effective shear modulus. If the PE is taken into account, the dispersion relation (6) becomes less anisotropic. The velocity of sound in the long-wavelength limit is isotropic, $V = \sqrt{\mu/\rho}$.

To make estimates in the case of intermediate values of D, it is necessary to employ material constants of icosahedral QCs. For an $Al_{70.3}Pd_{21.5}Mn_{8.2}$ alloy, these constants are as follows: $\rho = 5100$ kg/m^3 [16], $\mu = 0.65 \times 10^{11}$ N/m^2, and $\lambda = 0.75 \times 10^{11}$ N/m^2 [17]. According to various estimates [18, 19], $K_1 = 0.81 \times 10^{11}$ and $K_2 = -0.42 \times 10^{11}$ N/m^2. Reliable (even order-of-magnitude) estimates of the phonon–phason coupling constant K_3 seem to be unavailable to date. According to theoretical estimations [20], the phonon–phason coupling constant K_3 is ten times smaller than other constants. According to the results of an analysis of the profile of diffuse scattering near Bragg reflections [19], K_3 exceeds the phason elastic constant K_1 in magnitude. In publications [21, 22], also devoted to an analysis of the profile of diffuse scattering near Bragg reflections, the constant K_3 is disregarded. As far as we know, the influence of the PE on the dynamics of phonon–phason modes in QCs has not yet been studied and no estimate of f_s has been made in the literature. The pinning decreases the anisotropy of the acoustic-phonon dispersion. Below, we present dispersion curves for the cases $f_s = 0$ and $f_s = 3 \times 10^{12}$ kg/m^3 s^2. In the latter case, the anisotropy is approximately three times smaller.

Finally, we estimate the isotropic viscosity $\eta^\perp$. The internal friction Q^{-1} is equal to ν/π, where ν is the logarithmic damping decrement; therefore, $Q^{-1} = 2|\mathrm{Im}(\omega_{phn})/\mathrm{Re}(\omega_{phn})|$. The internal friction Q^{-1} was measured outside the resonance range (at a frequency of 2000 Hz and a temperature of 550 K) [23] to be 1.3×10^{-4}. The form of the imaginary part in expressions (5) and (6) suggests that the ratio $\eta^\perp q^2/(\rho\omega/\pi) \approx \pi\omega\eta^\perp/\mu$ may be considered within the model at hand as the contribution of the viscosity η_{ijkl} to the logarithmic damping decrement ν. Hence, $\eta^\perp = 670$ N s/m^2. We can see from expression (5) that $q^2 \ll 4\rho\mu/(\eta^\perp)^2$. Hence, these estimates of $\eta^\perp$ are valid only at $q \ll 10^{-4}$ nm^{-1}. In the case of shorter wavelengths, the dependence of the coefficient $\eta^\perp$ on the wavelength should be taken into account.

The data on internal friction in a sample are conventionally presented as a $Q^{-1}(T)$ dependence. In the suggested model, the quantity most heavily dependent on temperature is D and this parameter varies in a very wide range. Therefore, it is reasonable to consider the $Q^{-1}(\ln(D))$ dependence (see Fig. 1). In this and subsequent figures, cases *a* and *b* correspond to $f_s = 0$ and $f_s = 3 \times 10^{12}$ kg/m^3 s^2, respectively, and we set $K_3 = 0.1K_1$. The internal friction is often measured at a fixed frequency. Since the dependence of the vibration frequency on the wave vector is almost linear, $\mathrm{Re}\,\omega_{phn} \approx q\sqrt{\mu/\rho}$, the differences between the curves constructed at a constant vibration frequency and at a constant wave vector are very small in comparison with the scale of Fig. 1. The same is also true for Fig. 2. Therefore, Figs. 1 and 2 are constructed at a fixed wave vector approximately corresponding to a vibration frequency of 2000 Hz.

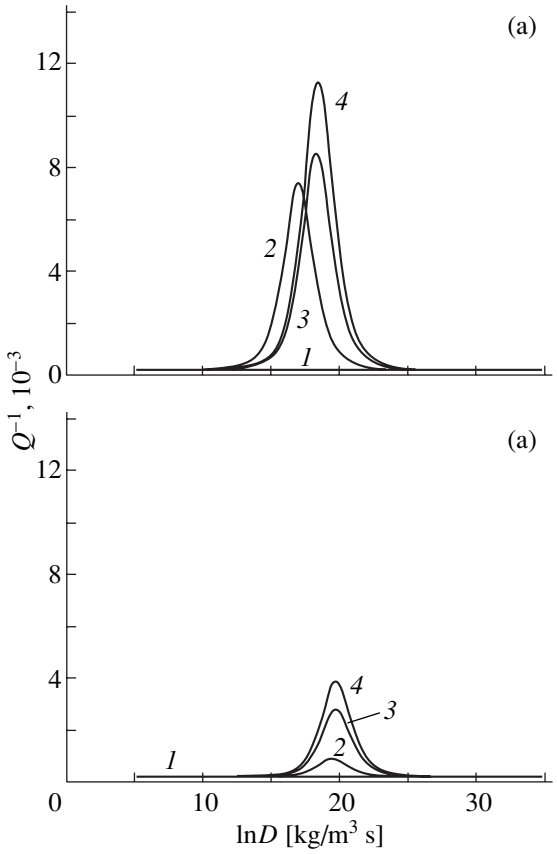

Fig. 1. (a) Dependence of the internal friction Q^{-1} for various transverse modes in the icosahedral QC on the logarithm of the phason friction coefficient D without regard for pinning. The vibration frequency is 2000 Hz. Straight line *1* corresponds to the transverse mode propagating along the fivefold axis; (*2*) the first transverse mode propagating along the diad axis [100] and polarized along [010], (*3*) the transverse mode propagating along the triad axis, and (*4*) the second transverse mode propagating along the diad axis and polarized along [001]. (b) The same with inclusion of pinning.

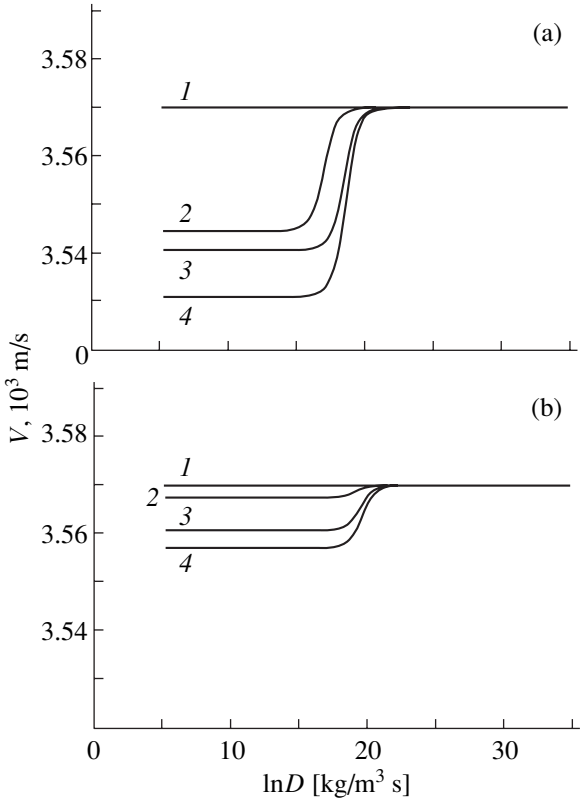

Fig. 2. (a) Dependence of the velocities of various transverse modes in the icosahedral QC on the logarithm of the phason friction coefficient D without regard for pinning. The vibration frequency is 2000 Hz. Here and in the other figures, the mode designations are the same as in Fig. 1. (b) The same with inclusion of pinning.

The experimental $Q^{-1}(T)$ dependence for the system *i*-AlPbMn exhibits two absorption peaks. The authors of [23] relate the high-temperature peak B to excitation of collective atomic vibrations. Therefore, the theoretical maximum of internal friction corresponding to activation of collective phason modes (Fig. 1) can correspond to this peak. As the temperature increases, absorption peak B shifts to higher frequencies. In the temperature range 770–920 K, the experimental position of the absorption maximum ω_{max} satisfies the Arrhenius relation

$$\frac{1}{\omega_{max}} = \tau_{max} = \tau_\infty \exp\left(\frac{H}{k_B T}\right), \qquad (8)$$

where τ_∞ is the characteristic time constant, H is the activation enthalpy, and k_B is the Boltzmann constant. In the model under consideration, the positions of resonant absorption maxima for acoustic modes are defined to a good accuracy by the resonance condition $\tau_{phs}\,\mathrm{Re}\,\omega_{phn} \approx 1$, where ω_{phn} is the phonon frequency and τ_{phs} is the phason relaxation time with the same wave vector. Therefore, the acoustic-wave attenuation maximum corresponds to the value of D for which the relation

$$D \approx \left(Kq + \frac{f_s}{q}\right)\sqrt{\frac{\rho}{\mu}} \approx \frac{K\rho\,\mathrm{Re}\,\omega_{phn}}{\mu} + \frac{f_s}{\mathrm{Re}\,\omega_{phn}} \qquad (9)$$

is valid and the temperature dependence of D in the above-mentioned temperature range can be obtained by substituting ω_{max} from Eq. (8) into Eq. (9). From the latter equation, as well as from a direct comparison of Figs. 1a and 1b, one readily sees that the resonant absorption peaks corresponding to different polarizations of acoustic modes come much closer together (in temperature) after inclusion of the pinning. Furthermore, the peaks are shifted to larger values of D, i.e., to lower temperatures. The pinning causes a decrease in the absorption peak heights above the isotropic-background level. Using relation (9), the absorption peak

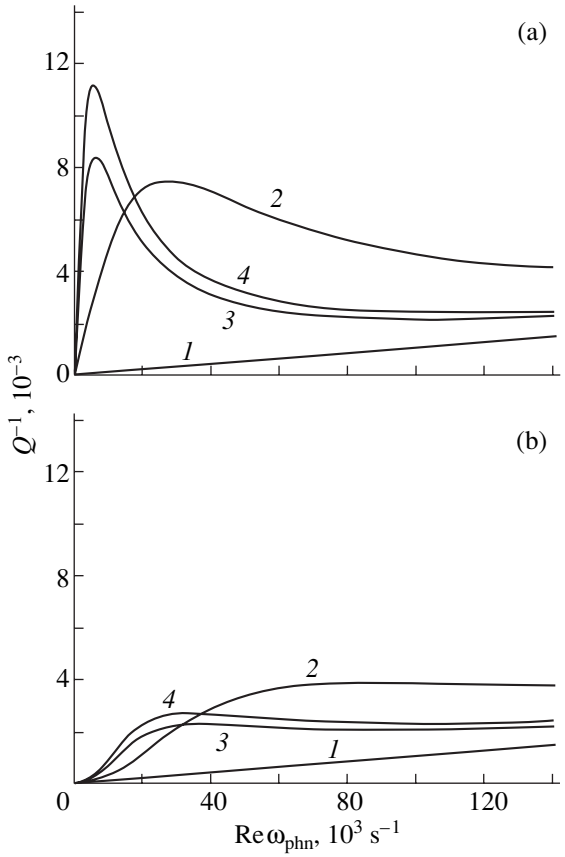

Fig. 3. (a) Dependence of the internal friction Q^{-1} for various transverse modes in the icosahedral QC on the real part of the phonon-mode frequency without regard for pinning. The phason friction coefficient is $D = \exp(17.85)$ kg/m^3 s. (b) The same with inclusion of pinning.

height may be analytically estimated with respect to the level of the "background" internal friction as

$$Q^{-1}_{\max} \approx \frac{I^2 q^2}{2\mu(Kq^2 + f_s)} \approx \frac{I^2(\mathrm{Re}\,\omega_{phn})^2\rho}{2\mu(K\rho(\mathrm{Re}\,\omega_{phn})^2 + f_s\mu)}. \quad (10)$$

In Fig. 1, the phonon internal friction associated with the coefficient $\eta^\perp$ (line *1*) is given by the expression $\mathrm{Re}\,\omega_{phn}\eta^\perp/\mu$, as follows from Eqs. (5) and (6) and the approximate relation between $\mathrm{Re}\,\omega_{phn}$ and q. Form the table, it can be see that, in the simplest model under consideration, the minimum internal friction corresponds to transverse vibrations of a sample cut out along the fivefold axis. The transverse mode propagating along this axis does not interact with the corresponding phason mode in the harmonic approximation (in the case of small-amplitude vibrations), and the resonant absorption peak is absent for such vibrations in the model under discussion. (This peak can arise in the model taking into account anharmonic phonon–phason coupling.) However, the data from [23] are insufficient for understanding whether or not the absorption peak *B* height varies for samples cut out along different symmetry directions.

Internal-friction measurements in the same alloy at a frequency of 2.8 Hz and a temperature of 1000 K [24] show that the high-temperature wing of the absorption peak *B* for a sample cut out along the fivefold axis corresponds to smaller values of Q^{-1} than for a sample cut out along the diad axis. Moreover, it was shown that, in the high-temperature range, the effective shear modulus measured for transverse vibrations of the former sample exceeds that of the latter sample by approximately 2 GPa. This result qualitatively conforms to the conclusion (see above) that the interaction between the transverse mode propagating along the fivefold axis and phason excitations is absent in the harmonic approximation.

If we set $K_3 \cong 0.1K_1$, then at sufficiently high frequencies (in the range where estimate (7) is applicable) the velocity of transverse waves propagating along the fivefold axis ($I^2/K = 0$) will exceed that along the triad axis by approximately one percent: $I^2/K = 16K_3^2/9[K_1 - (2/3)K_2]$ (see table). We note that the velocity estimate (7) is applicable only to the dependences shown in Fig. 2a in the range where $D \le \exp(15)$ kg/m^3 s. At the f_s value we selected, the velocity split in Fig. 2b is smaller and reaches estimate (7) at a frequency close to 80×10^3 s^{-1} (cf. Fig. 4b). If K_3 becomes two orders-of-magnitude smaller than the other constants, i.e., $K_3 \cong 0.01K_1$, Fig. 2 will change such that the maximum difference between velocities 1 and 4 will decrease by 100 times and will be as low as 0.4 m/s. Probably, it would be impossible to detect such anisotropy of the velocity of sound experimentally. The absorption peak height above the background level (Fig. 1) will also decrease by 100 times. However, the Q^{-1} background level can be decreased by going to lower frequencies and the anisotropy of resonant attenuation of low-frequency acoustic waves due to the phonon–phason coupling seems to be still detectable. We note that the dependences in Figs. 1 and 2 conform to the extreme cases $D = 0$ and $D = \infty$.

To test the model suggested, it is of interest to measure the frequency dependence of the internal friction and of the velocity of sound (Figs. 3, 4) at a fixed temperature of 800–900 K (fixed *D*). At low frequencies, the relative contribution of the isotropic term $iD\omega + f_s$ to element (2, 2) of the determinant in Eq. (4) is the most significant. Hence, the anisotropy of the velocity of sound disappears and the internal friction tends to zero. In the limit $q \longrightarrow 0$, the phason components of the six-dimensional polarization of acoustic-type waves tend to zero. Indeed, an acoustic wave with a given amplitude and wave vector **q** causes local deformation proportional to q in the vicinity of any fixed point of the medium. Hence, the induced phason deformation in the vicinity of the same point, being proportional to the ordinary deformation, tends to zero in the long-wavelength limit. Therefore, the influence of phasons on the phonon dispersion is negligible. Nevertheless, the slope

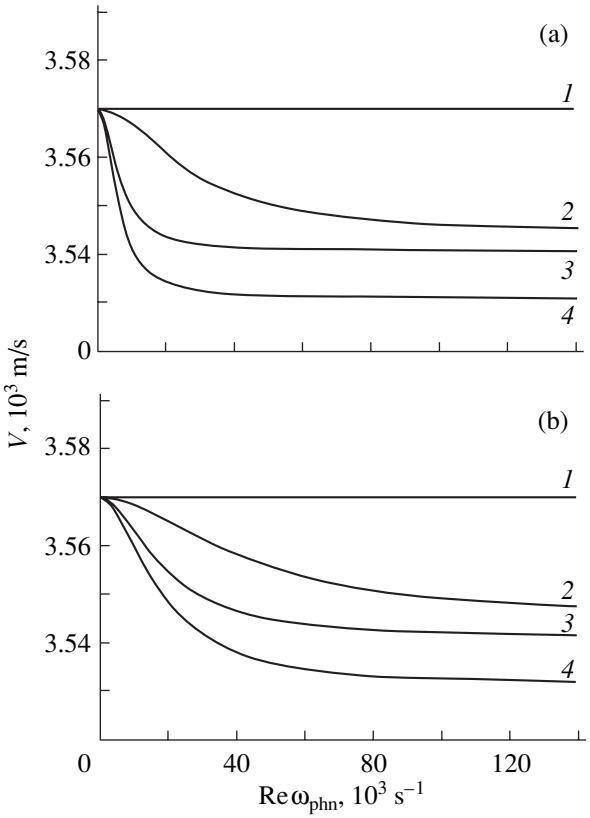

Fig. 4. (a) Dependence of the velocities of various transverse modes in the icosahedral QC on the real part of the phonon-mode frequency without regard for pinning. The phason friction coefficient is $D = \exp(17.85)$ kg/m^3 s. (b) The same with inclusion of pinning.

of the $Q^{-1}(\mathrm{Re}\,\omega_{phn})$ curve in the case of $f_s = 0$ remains anisotropic (Fig. 3a).

If $\mathrm{Re}\,\omega_{phn} \gg D\mu/K\rho$ (for instance, 60×10^3 s^{-1}, i.e., 60 kHz, for Figs. 3a, 4a and 90×10^3 s^{-1} for Figs. 3b, 4b), the acoustic-wave dispersion conforms to expression (6) (similar to the case $D = 0$). In this limit, $\mathrm{Im}\,\omega_{phn}$ is isotropic. Therefore, the anisotropy of Q^{-1} is associated with the anisotropy of the real part of the frequency and the phason effect mainly manifests itself in a weak anisotropic decrease in the velocities of sound. This decrease takes place in the range where the resonant phonon–phason coupling is observed. In the case $f_s = 0$ (Fig. 3a), the resonance corresponds to the maximum $Q^{-1}(\mathrm{Re}\,\omega_{phn})$ dependence. The estimated internal friction maximum with respect to the isotropic background level is $Q^{-1}_{max} \approx I^2/2K\mu$. If the pinning is taken into account, the maximum in the frequency dependence of Q^{-1} can disappear. For example, the absorption maximum almost disappeared in curve 2 in Fig. 3b.

ACKNOWLEDGMENTS

S.B. Rochal is grateful for the support of the Russian Foundation for Basic Research (project no. 02-02-17871).

REFERENCES

1. D. Shechtman, I. Blech, D. Gratias, and J. W. Cahn, Phys. Rev. Lett. **53** (20), 1951 (1984).
2. P. Bak, Phys. Rev. Lett. **54** (14), 1517 (1985).
3. D. Levine, T. C. Lubensky, S. Ostlund, *et al.*, Phys. Rev. Lett. **54** (14), 1520 (1985).
4. T. C. Lubensky, S. Ramaswamy, and J. Toner, Phys. Rev. B **32** (11), 7444 (1985).
5. T. C. Lubensky, in *Quasiperiodic Structures*, Ed. by M. V. Jaric (Academic, Boston, 1988), p. 200.
6. L. D. Landau and E. M. Lifshitz, *Course of Theoretical Physics*, Vol. 6: *Fluid Mechanics*, 4th ed. (Nauka, Moscow, 1988; Pergamon, New York, 1987).
7. M. Feuerbacher, M. Weller, J. Diehl, and K. Urban, Philos. Mag. Lett. **74**, 81 (1996).
8. M. Feuerbacher, M. Metzmacher, M. Wollgarten, *et al.*, Mater. Sci. Eng. A **233**, 103 (1997).
9. K. Urban, M. Feuerbacher, M. Wollgarten, M. Bartsch, and U. Messerschmidt, in *Physical Properties of Quasicrystals*, Ed. by Z. M. Stadnik (Springer, Berlin, 1999).
10. S. Takeuchi, Mater. Res. Soc. Symp. Proc. **553**, 283 (1999).
11. L. D. Landau and E. M. Lifshitz, *Course of Theoretical Physics*, Vol. 7: *Theory of Elasticity*, 4th ed. (Nauka, Moscow, 1987; Pergamon, New York, 1986).
12. S. B. Rochal and V. L. Lorman, Phys. Rev. B **62** (2), 874 (2000).
13. M. V. Jaric and D. R. Nelson, Phys. Rev. B **37** (9), 4458 (1988).
14. S. B. Rochal, Phys. Rev. B **64**, 144204 (2001).
15. D. Schmicker, S. van Smaalen, J. L. de Boer, and C. Haas, Phys. Rev. Lett. **74** (5), 734 (1995).
16. M. A. Chernikov, A. Bianchi, and H. R. Ott, Phys. Rev. B **51** (1), 153 (1995).
17. Y. Amazit, M. de Boissieu, and A. Zarembowitch, Europhys. Lett. **20**, 703 (1992).
18. M. E. Newman and C. L. Henley, Phys. Rev. B **52** (9), 6386 (1995).
19. M. J. Capitan, Y. Calvayrac, A. Quivy, *et al.*, Phys. Rev. B **60** (9), 6398 (1999).
20. W. J. Zhu and C. L. Henley, Europhys. Lett. **46**, 748 (1999).
21. M. de Boissieu, M. Boudard, B. Hennion, *et al.*, Phys. Rev. Lett. **75** (1), 89 (1995).
22. M. Boudard, M. de Boissieu, A. Letoublon, *et al.*, Europhys. Lett. **33**, 199 (1999).
23. B. Damson, M. Weller, M. Feuerbacher, *et al.*, Mater. Sci. Eng. **206**, 294 (2000).
24. M. Feuerbacher, M. Weller, and K. Urban, in *Proceedings of 6th International Conference on Quasicrystals*, Ed. by S. F. Takeuchi (World Sci., Singapore, 1998), p. 521.

Translated by A. Kazantsev

Physics of the Solid State, Vol. 45, No. 7, 2003, pp. 1322–1326. Translated from Fizika Tverdogo Tela, Vol. 45, No. 7, 2003, pp. 1263–1266.

LATTICE DYNAMICS AND PHASE TRANSITIONS

Structural Transformations and Phase Transitions in Aqueous Solutions of Gadolinium Nitrate in the Course of Freezing

G. P. Vishnevskaya*, E. N. Frolova*, A. M. Gataullin, F. M. Gumerov**, and A. R. Fakhrutdinov***

** Zavoĭskiĭ Physicotechnical Institute, Kazan Scientific Center, Russian Academy of Sciences, Sibirskiĭ trakt 10/7, Kazan, 420029 Tatarstan, Russia*

*** Kazan State University of Power Engineering, Kazan, Tatarstan, Russia*

Received November 11, 2002

Abstract—The microstructure of $Gd(NO_3)_3$ aqueous solutions in the course of cooling at different rates is investigated using electron paramagnetic resonance. The local concentrations of Gd^{3+} ions in microregions are estimated, the concentration boundary at which the solution is completely vitrified throughout its volume is revealed, and the temperature of vitrification of liquid microregions (eutectic temperature) and the eutectic composition are determined. It is found that the adsorption of Gd^{3+} aqua ions on the capillary surface affects the crystallization of water and the process of concentration of the solute. It is demonstrated that the anomalous experimental dependence $\delta H(C_0)$, which is observed for vitrified water–glycerol solutions with a uniform distribution of paramagnetic centers over the sample, agrees well with the theoretical curve in the case when allowances are made not only for the dipole–dipole interactions but also for the inhomogeneous broadening of the EPR lines in the spectra with an incompletely resolved fine structure. © *2003 MAIK "Nauka/Interperiodica".*

1. INTRODUCTION

Our interest in the processes observed during freezing of $Gd(NO_3)_3$ aqueous solutions is motivated, among other factors, by the lack of reliable information on the phase diagrams of eutectic temperatures, crystallization, and eutectic compositions. The main objective of the present work was to investigate the transformation of the microstructure of the studied solutions during freezing of free water and to determine the eutectic compositions and eutectic temperatures. For this purpose, we used electron paramagnetic resonance (EPR) spectroscopy. Electron paramagnetic resonance studies can provide valuable information on the behavior of both individual and interacting paramagnetic complexes. It should be noted that the EPR method has already been used for analyzing the specific features observed in the processes of freezing and vitrifying aqueous solutions of different ions, such as VO^{2+} [1, 2], Mn^{2+} [3–5], and Cr^{3+} [6–9]. To the best of our knowledge, similar investigations of Gd^{3+} aqueous solutions have never been performed before. The sole exception is the work carried out by Ross [3], who measured the EPR spectrum of Mn^{2+} ions and the spectrum of a $Gd(ClO_4)_2$ aqueous solution. However, the large width of the EPR line made it impossible at that time to analyze the Gd^{3+} aqueous solutions in greater detail. The vitrification temperatures for aqueous solutions of lanthanides were determined using differential thermal analysis [10].

The results obtained in our investigations are also of considerable interest both from the standpoint of cryochemistry and cryobiology, which concern the problems of low-temperature conservation of biological objects, and from the point of view of catalytic reactions whose efficiency can be increased by concentrating a solute in liquid microregions in the course of cooling.

2. SAMPLE PREPARATION AND EXPERIMENTAL TECHNIQUE

The aqueous solutions used in the experiments were prepared from a salt of gadolinium nitrate (analytical grade). The concentration of Gd^{3+} ions in the aqueous solutions prepared varied in the range from 0.02 to 3.6 *M*. The samples obtained were cooled using two methods: (i) slow stepwise cooling in liquid-nitrogen vapors, where the sample was allowed to stand at each temperature for approximately 20–30 min and the overall process of cooling from 293 to 100 K proceeded for 8–10 h; and (ii) rapid freezing through immersion of the sample in liquid nitrogen. In order to exclude crystallization of water at low temperatures and to obtain samples completely vitrified throughout the bulk, we used solutions containing glycerol (10–20 vol %), because, as is known, glycerol is one of the best cryoprotectors capable of preventing biological objects from degrading in the course of low-temperature conservation. The EPR spectra were recorded on a JEOL production-type spectrometer operating in the *X* band. The samples to

1063-7834/03/4507-1322$24.00 © 2003 MAIK "Nauka/Interperiodica"

be studied were placed in thin capillaries ~1 mm in diameter. The electron spin–lattice relaxation times T_1 were estimated using the technique of nonresonance paramagnetic absorption in parallel fields [11].

3. EXPERIMENTAL RESULTS AND DISCUSSION

Let us now consider the results of investigations into the concentration dependences of the EPR linewidth for vitrified solutions of gadolinium nitrate. Since vitrified solutions can be treated as momentarily frozen liquid solutions in which rotational and translational motions of liquid particles are absent, we assume that dissolved particles are uniformly distributed over the volume of the studied solutions ($C_0 = C_{loc}$).

The theoretically calculated dependence of the EPR linewidth on the initial concentration C_0 of paramagnetic centers for a Lorentzian line shape can be described by the following relationship [12–14]:

$$\delta H = \delta H_0 + AC_0, \quad (1)$$

where δH_0 is the concentration-independent contribution to the linewidth due to both the relaxation broadening associated with intramolecular mechanisms and the possible contribution from the unresolved fine structure, C_0 is the initial concentration expressed in M, and A is the coefficient accounting for the line broadening attributed to dipole–dipole interactions. For equivalent spins, the coefficient A can be determined from the expression

$$A = 30.4 \times 10^{20} g\beta\sqrt{S(S+1)}. \quad (2)$$

In the case when the paramagnetic centers with spin $S = 7/2$ are uniformly distributed over the volume of the sample, we have $A = 223.7$ G/M.

At high concentrations of paramagnetic centers, the Lorentzian line can transform into a Gaussian line. In order to determine the shape of the resonance line, we used two simple techniques described in [15]: (i) the method of normalized graphs and (ii) the method of the slope of differential absorption curves. It was found that the resonance line has a Lorentzian shape over a wide range of concentrations and takes a shape intermediate between the Lorentzian and Gaussian line shapes at concentrations $C_0 > 3$ M. Since the dipole–dipole interactions are very strong ($S = 7/2$), the difference between the linewidths for the Lorentzian and intermediate shapes is of little significance. Moreover, we note that the concentrated vitrified solutions can be considered a system in which the distribution of paramagnetic centers is intermediate between irregular and regular. In this case, the resonance line has a Lorentzian shape in the central portion and a Gaussian shape at the edges [14]. For this reason, the experimental linewidths were theoretically treated by assuming a Lorentzian line shape over the entire range of concentrations.

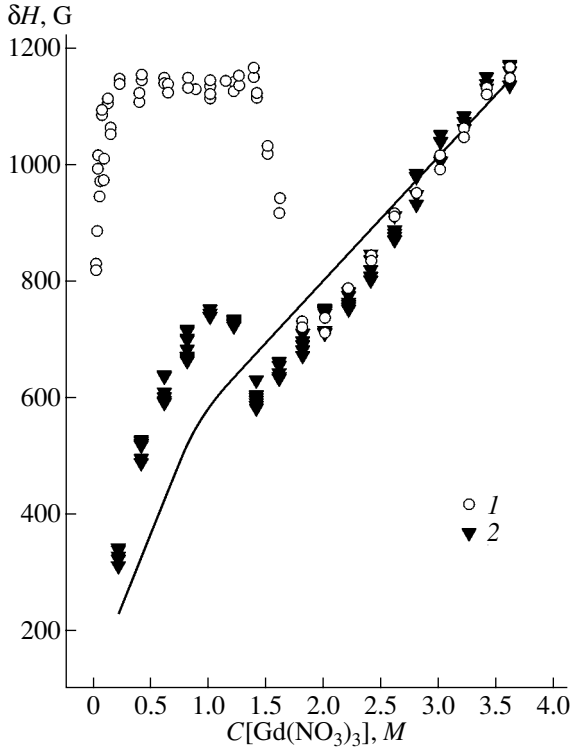

Fig. 1. Dependences of the total EPR linewidth on the $Gd(NO_3)_3$ concentration in (*1*) aqueous solutions rapidly frozen at a temperature of 77 K and (*2*) vitrified water–glycerol solutions at 77 K. The solid line represents the concentration dependence of the linewidth in the EPR spectra simulated in the framework of the theory of dipole–dipole interactions at fine structure parameters $\delta H_0 = 100$ G and $D = 180$ G.

Figure 1 shows the concentration dependence of the total EPR linewidth δH for vitrified water–glycerol solutions of $Gd(NO_3)_3$ at a temperature of 77 K. It is seen from Fig. 1 that the dependence $\delta H(C_0)$ is not strictly linear with the same slope over the entire range of concentrations, as might be expected from relationship (1) at a constant value of δH_0. In actual fact, the dependence $\delta H(C_0)$ exhibits a kink at a concentration $C_0 \sim 1.5$ M.

First, we verified the assumption (even though highly improbable) that dilute aqueous solutions of gadolinium nitrate with ~15 vol % glycerol undergo an incomplete vitrification. It turned out that an increase in the concentration of a glass-forming agent (in our case, glycerol) from 10 to 30 vol % does not affect the experimental dependence $\delta H(C_0)$. Then, we assumed that the similar behavior of the EPR linewidth can be associated with the overlap of a number of fine components in the EPR spectrum due to an enhancement of dipole–dipole interactions, which is usually observed at small values of the fine structure parameter D. Indeed, the linewidths in the EPR spectra simulated within the framework of

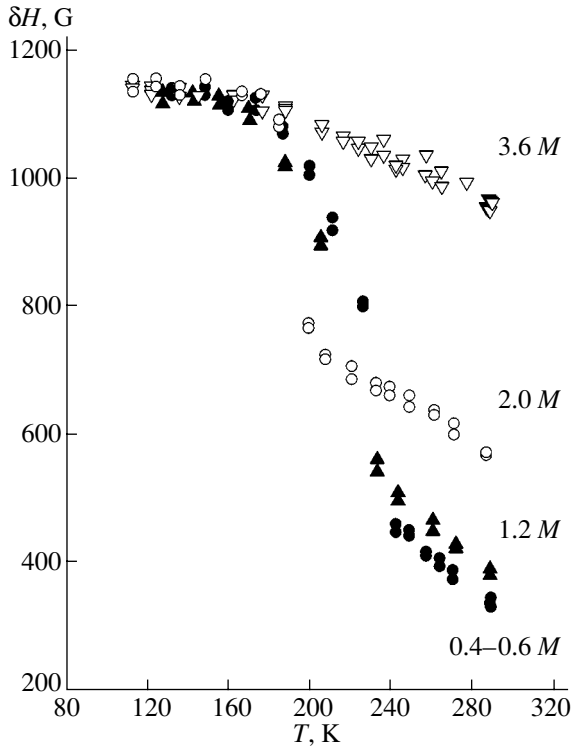

Fig. 2. Temperature dependences of the EPR linewidth measured for $Gd(NO_3)_3$ aqueous solutions with different initial concentrations during slow cooling.

the theory of dipole–dipole interactions in the concentration range 0.2–3.6 *M* for a Lorentzian line shape at the fine structure parameter $D = (185 \pm 5)$ G, which was determined from the relaxation data and is characteristic of the majority of Gd^{3+} aqua ions in solutions [16], and the concentration-independent contribution (δH_0 = 100 G) to the linewidth at $C_0 \longrightarrow 0$ are in good agreement with the experimental results (Fig. 1).

The concentration dependence of the total EPR linewidth δH for $Gd(NO_3)_3$ aqueous solutions subjected to rapid freezing at a temperature of 77 K is also depicted in Fig. 1. At low initial concentrations ($C_0 < 0.2$ *M*), the linewidth δH increases rapidly with an increase in the concentration C_0. In the concentration range $0.2 \le C_0 \le 1.5$ *M*, there appears a plateau at $\delta H = (1150 \pm 20)$ G. Judging from the constancy of the linewidth $\delta H(C_0)$ in this range, we can assert that, whatever the initial salt concentration, the crystallization of water is accompanied by the displacement of solute molecules into microregions of constant composition. The number of microregions in the volume of the solution depends on the initial salt concentration. With the aim of determining the degree of concentration of the dissolved salt in the microregions, we compared the EPR linewidths for Gd^{3+} ions in frozen aqueous solutions with those for Gd^{3+} ions in water–glycerol solutions completely vitrified over the volume. For microregions of constant composition, we obtained the local concentration $C_{loc} = 3.6$ *M*. In this case, the minimum local concentration was estimated to be $C_{loc} = 2.1$ *M*. The impossibility of forming microregions of constant composition with low concentrations of Gd^{3+} ions even at a temperature of 77 K is most likely associated with intensive adsorption of Gd^{3+} aqua ions on the capillary surface [17]. The degree of concentration of the dissolved salt C_{loc}/C_0 in the microregions changes from 18 at $C_0 = 0.2$ *M* to 2.4 at $C_0 = 1.5$ *M*, depending on the initial concentration of $Gd(NO_3)_3$.

A further increase in the initial concentration from 1.5 to 1.8 *M* leads to a considerable decrease in the EPR linewidth. At $C_0 > 1.8$ *M*, the dependence $\delta H(C_0)$ measured for rapidly frozen aqueous solutions is similar to that obtained for vitrified water-glycerol solutions; i.e., at concentrations above 1.8 *M*, the aqueous solution is vitrified over the entire volume. The vitrification becomes possible in the case when all water molecules are in the bound state and no freezing responsible for the segregation of dissolved substances occurs. Now, we should take into account that, for each $Gd(NO_3)_3$ molecule at $C_0 = 1.8$ *M*, there are 26 water molecules and that each nitrate anion is capable of binding three water molecules [18]. On this basis, we found that, in addition to the first hydration shell, each Gd^{3+} ion at $C_0 = 1.8$ *M* forms the second hydration shell composed of eight or nine water molecules. It is worth noting that the second hydration shell is sufficiently stable to be revealed by EPR spectroscopy. The shortest distance between the complexes was estimated from the formula $d = \frac{1}{\sqrt[3]{(C_0)}}$ [14]. As a result, the radius of the aqua complex was determined to be $r = 4.87$ Å. For the initial concentration $C_0 = 3.6$ *M*, at which there are 11 water molecules for each $Gd(NO_3)_3$ molecule and only one hydration shell can be formed, we obtained the radius $r = 3.87$ Å, which is in good agreement with the x-ray diffraction data ($r = 3.81$ Å[19]). It seems likely that the narrow concentration range from 1.5 to 1.8 *M* corresponds to a crossover from vitrification in microregions to vitrification over the entire volume of the solution.

The temperature dependences of the EPR linewidth measured for $Gd(NO_3)_3$ aqueous solutions with different initial concentrations of Gd^{3+} ions in the course of slow cooling are shown in Fig. 2. It is seen from Fig. 2 that, at initial concentrations ranging from 0.4 to 2.0 *M*, the dependence $\delta H(T)$ can be divided into three portions. As the temperature decreases, a slow increase in the linewidth δH gives way to a more rapid increase. At a temperature of (186 ± 2) K, the EPR linewidths for $Gd(NO_3)_3$ aqueous solutions with different initial concentrations of Gd^{3+} ions coincide to within the limits of experimental error and become independent of the temperature: $\delta H = (1150 \pm 25)$ G. It should be noted that,

upon slow and fast cooling, the linewidths δH corresponding to the plateau coincide with each other. Consequently, the solutions in both cases have similar structures. For a $Gd(NO_3)_3$ aqueous solution with an initial concentration of 3.6 *M*, which is close to the solubility limit of the $Gd(NO_3)_3$ salt in water, the linewidth δH changes insignificantly with a decrease in the temperature.

The behavior of the dependence $\delta H(T)$ upon slow cooling agrees with the phase diagram of the solutions under investigation. A decrease in the temperature beginning from 273 K leads to a gradual freezing of free water, whereas the dissolved salt is displaced to nonfreezing regions and, hence, the local concentrations increase. As a consequence, the intermolecular dipole–dipole interactions in microregions are enhanced and the EPR linewidth increases. Moreover, an increase in the EPR linewidth δH is due to a weakening of the averaging effect of the molecular motion with a decrease in the temperature. At the eutectic temperature, the liquid regions containing the dissolved salt solidify and the EPR linewidth becomes independent of the temperature, as was predicted from the theory of intermolecular interactions in solids. The results of measurements of the spin–lattice relaxation times demonstrate that the microregions remain liquid at temperatures above $T = (185 \pm 5)$ K (the electron spin–lattice relaxation times were estimated as $T_1 \sim 10^{-9}$ s) and undergo solidification below this temperature ($T_1 \sim 10^{-7}$ s).

Therefore, the temperature $T = (185 \pm 5)$ K can be considered the eutectic temperature and the composition with $C_{loc} = 3.6$ *M*, which corresponds to the linewidth $\delta H = (1150 \pm 25)$ G, can be treated as the eutectic composition. Unfortunately, we failed to compare our results of the EPR measurements with data on the phase diagrams because of the lack of reliable information on aqueous solutions of gadolinium nitrate. Such a comparison performed in our earlier work [5] for aqueous solutions of manganese nitrate demonstrated excellent agreement between the results obtained using electron paramagnetic resonance and dynamic calorimetry.

It should be noted that, at the initial stage of cooling, the weaker concentration of the solute in relatively diluted solutions of $Gd(NO_3)_3$ can be due to a manifestation of the aforementioned adsorption on the capillary surface [16, 17]. We believe that, as the temperature decreases to some value, the Gd^{3+} aqua complexes directly interacting with the capillary surface are either not involved or involved only partly in the segregation of the solute in microregions. A further decrease in the temperature brings about the activation of the above process; as a result, the local concentrations of gadolinium ions in microregions increase drastically. It is worth noting that, in Mn^{2+} and Cr^{3+} aqueous solutions (where no adsorption effect is observed), the solutes are concentrated at the same rate during freezing of free water [4–7]. In highly concentrated solutions, free water is either contained in insignificant amounts or absent [recall that, at $C_0 = 3.6$ *M*, there are 11 water molecules for each $Gd(NO_3)_3$ molecule]. Consequently, no appreciable concentration of the solute is observed in the course of cooling. A slight increase in the EPR linewidth δH with a decrease in the temperature to the eutectic point is most likely associated with the change in the rate of molecular motion in the solution.

In conclusion, we note that, upon slow cooling at the rates used in this work, the solidified microregions should be considered to be vitrified, because the EPR spectra of Gd^{3+} ions in these microregions are similar to the spectra of Gd^{3+} ions in solutions vitrified over the entire volume, provided the local concentrations C_{loc} correspond to the initial concentrations C_0. As was shown in our previous studies of the frozen solutions of Cr^{3+} and Mn^{2+} salts [4–9], the crystallization of vitrified microregions requires a slower variation in the temperature. In this case, the EPR spectrum has a shape typical of polycrystalline hydrates. For gadolinium nitrate, similar investigations will be performed in the immediate future.

ACKNOWLEDGMENTS

This work was supported by the Russian Foundation for Basic Research, project no. 00-03-32915a.

REFERENCES

1. O. Ya. Grinberg, A. T. Nikitaev, K. I. Zamaraev, and Ya. S. Lebedev, Zh. Strukt. Khim. **10**, 230 (1969).
2. R. F. Khaĭrutdinov and K. I. Zamaraev, Izv. Akad. Nauk SSSR, Ser. Khim., 1524 (1970).
3. T. Ross, J. Chem. Phys. **42**, 3919 (1965).
4. G. P. Vishnevskaya and F. M. Gumerov, Zh. Fiz. Khim. **52** (8), 1884 (1978).
5. G. P. Vishnevskaya, F. M. Gumerov, and M. Zh. Yagfarov, Zh. Fiz. Khim. **53** (3), 609 (1979).
6. G. P. Vishnevskaya, F. M. Gumerov, and B. M. Kozyrev, Dokl. Akad. Nauk SSSR **239** (5), 1124 (1978).
7. G. P. Vishnevskaya and F. M. Gumerov, Zh. Fiz. Khim. **55** (4), 955 (1981).
8. G. P. Vishnevskaya and A. R. Fakhrutdinov, Fiz. Tverd. Tela (St. Petersburg) **35** (7), 1825 (1993) [Phys. Solid State **35**, 912 (1993)].
9. G. P. Vishnevskaya and A. R. Fakhrutdinov, Zh. Fiz. Khim. **68** (1), 71 (1994).
10. H. Kanno and Y. Akama, J. Phys. Chem. **91**, 1263 (1987).
11. B. A. Volkov, G. P. Vishnevskaya, V. A. Gorozhanin, and R. G. Ramazanov, Prib. Tekh. Éksp., No. 4, 167 (1973).

12. S. A. Al'tshuler and B. M. Kozyrev, *Electron Paramagnetic Resonance in Compounds of Transition Elements*, 2nd ed. (Nauka, Moscow, 1972; Halsted, New York, 1975).
13. K. I. Zamaraev, Yu. N. Molin, and K. M. Salikhov, *Spin Exchange* (Nauka, Novosibirsk, 1977).
14. Ya. S. Lebedev and V. I. Muromtsev, *EPR and Relaxation of Stabilized Radicals* (Khimiya, Moscow, 1972).
15. R. S. Alger, *Electron Paramagnetic Resonance: Techniques and Application* (Interscience, New York, 1968).
16. G. P. Vishnevskaya, E. N. Frolova, and A. R. Fakhrutdinov, Zh. Fiz. Khim. **76** (5), 874 (2002).
17. G. P. Vishnevskaya, E. N. Frolova, and A. M. Gataullin, Fiz. Tverd. Tela (St. Petersburg) **45** (5), 818 (2003) [Phys. Solid State **45** (5), 859 (2003)].
18. V. I. Elfimov, V. D. Dzhuraev, and M. F. Vuke, *Molecular Physics and Biophysics of Aqueous Systems* (Leningr. Gos. Univ., Leningrad, 1973), p. 70.
19. T. Yamaguchi, M. Nomura, H. Wakita, and H. Ohtaki, J. Chem. Phys. **89** (8), 5153 (1988).

Translated by O. Borovik-Romanova

Physics of the Solid State, Vol. 45, No. 7, 2003, pp. 1327–1331. Translated from Fizika Tverdogo Tela, Vol. 45, No. 7, 2003, pp. 1267–1271.

LOW-DIMENSIONAL SYSTEMS AND SURFACE PHYSICS

Plasma Optics of Nanostructures

A. V. Klyuchnik, S. Yu. Kurganov, and Yu. E. Lozovik

Institute of Spectroscopy, Russian Academy of Sciences, Troitsk, Moscow oblast, 142190 Russia

Received July 4, 2002

Abstract—Analytical expressions for dispersion curves of plasmons in a metal cylinder and a cylindrical cavity in metal are derived at small radii of the cylinder. The plasmon path length and the plasmon energy transfer in such structures are estimated. © *2003 MAIK "Nauka/Interperiodica".*

1. INTRODUCTION

Recently, considerable attention has been paid to the effects of the interaction of optical radiation with conducting nanostructures. In particular, experiments have been carried out on efficient light transmission through small holes in a metal, with the hole diameters being much smaller than the wavelength [1]. A conceivable physical mechanism responsible for this effect can be a plasma mode excitation at one end of the channel, propagation of the plasmon through the channel, and its de-excitation at the other end of the channel. The efficiency of this light transmission is controlled by the efficiency of the conversion of the incident electromagnetic wave energy into the energy of a plasma wave (and vice versa), as well as by plasmon damping as it propagates in the channel.

In the context of the development of surface probe microscopy, the possible plasma wave excitation and propagation over a metal probe of a near-field microscope is of great interest. This method would increase the efficiency of radiation energy transport to the microscope tip and improve microscope resolution [2–4].

Plasma modes in resonant nanostructures, e.g., in narrow slits and gaps, are also of considerable interest. Plasma modes whose field is localized in the spacing between the tip of a probe microscope and the surface under examination can cause amplification of the electromagnetic field in the spacing and light emission. We note that plasma waves can transport excitation energy in such structures where other types of electromagnetic eigenwaves are absent. This energy may then be output and de-excited as ordinary photons [5–14].

The evolution of nanotechnology has made it possible to produce metal structures that are a few nanometers in diameter. In this context, it also seems of interest to study the mechanisms of resonant excitation of plasma waves in such structures and to analyze the conditions for the propagation of plasma waves, including the conditions of their minimum damping.

All the effects listed above relate to the currently fast developing field of plasma optics. In this study, we consider the effects of resonant excitation and propagation of plasma waves in conducting nanostructures. As a simple model, we consider a thin cylindrical conductor and a cylindrical hole. The types of eigenwaves in an insulating rod are well known. However, they were analyzed in detail for the case of waveguide modes whose wavelengths are comparable to the diameter [15, 16]. In Section 2, we analyze the eigenmodes in the limit $\lambda \ll a$, where a is the waveguide radius. Based on the dispersion relations obtained, we analyze the possible types of plasma oscillations in finite structures. To this end, we use a simple model in which the appearance of boundaries does not change the spatial field structure and the boundary itself is characterized by the plasma wave reflectance.

We describe the metal permittivity within the Drude model as $\varepsilon = I - \omega_P^2/\omega(\omega + i\gamma)$. In the case of metals, the characteristic frequency of electron collisions with impurities $\gamma = 1/\tau$ is much lower than the plasma frequency, $\tau\omega_P \gg 1$. In the nanostructures under consideration, scattering at wall roughnesses (diffuse scattering) should be taken into account in addition to collisions with impurities, $\tau = l/v_F + a/v_F$, where l is the average distance between impurities, v_F is the Fermi velocity, and a is the characteristic size of roughnesses. Along with collisions, there is another mechanism of energy dissipation of electromagnetic waves, namely Landau damping, corresponding to energy transfer from the plasma collective degree of freedom of electrons into single-particle degrees of freedom of electrons. In the structures under study, we are concerned with a wave propagating along the cylinder axis and a standing wave in the cross section. Therefore, we can distinguish between Landau damping, arising when the phase velocity of the plasma wave along the axis becomes equal to the Fermi velocity, and transverse Landau damping. The latter is caused by the fact that the cross-sectional distribution of the field, when expanded into a Fourier series, contains Fourier components with any wave vectors, including those with phase velocities equal to the Fermi velocity. The Landau damping caused by mirror reflection of particles at the bound-

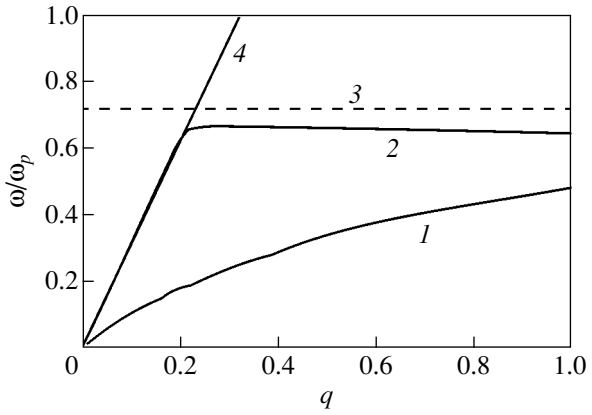

Fig. 1. Dispersion curves for (*1*) the symmetric *E* mode in the cylinder, (*2*) the first asymmetric ($m = 1$) mode in the cylinder, (*3*) the surface plasmon ($\omega/\omega_p = 1/\sqrt{2}$), and (*4*) the light ($\omega = ck_z$); $q = k_z a$.

aries is weaker than the damping due to collisions in the systems under consideration.

2. EIGENMODES IN A THIN CYLINDER

Let us consider an infinite metal cylinder with permittivity $\varepsilon(\omega)$ placed in a medium with permittivity ε_1. We study eigenwaves under the assumption that $a \ll \lambda$, where a is the cylinder radius and λ is the wavelength. The z axis of the cylindrical coordinate system is directed along the cylinder axis.

From the boundary conditions, we obtain the dispersion relation for the wavenumbers χ_1 and χ_2:

$$\left[\chi_2 a\frac{J_m'(\chi_1 a)}{J_m(\chi_1 a)} - \chi_1 a\frac{H_m^{(2)'}(\chi_2 a)}{H_m^{(2)}(\chi_2 a)}\right]\left[\frac{\varepsilon}{\varepsilon_1}\chi_2 a\frac{J_m'(\chi_1 a)}{J_m(\chi_1 a)} - \chi_1 a\frac{H_m^{(2)'}(\chi_2 a)}{H_m^{(2)}(\chi_2 a)}\right] - m^2\left(\frac{k_z k}{\chi_1\chi_2}\right)^2\left(\frac{\varepsilon}{\varepsilon_1} - 1\right)^2 = 0, \quad (1)$$

where $\chi_1 = \sqrt{\varepsilon k^2 - k_z^2}$ and $\chi_2 = \sqrt{\varepsilon_1 k^2 - k_z^2}$.

First, we consider the symmetric mode. As follows from Eq. (1), the dispersion relation for the symmetric mode ($m = 0$) splits into two equations for *E* and *H* waves. This split does not take place in the case of asymmetric (in angle) eigenwaves, which means that E_z and H_z are simultaneously nonzero. The dispersion curve for the symmetric *E* wave in the cylinder is shown in Fig. 1.

The plasmon spectrum is defined by two dimensionless parameters: $q = k_z a$ and $b = \omega_p a/c$. In the case of metals such as Ag and Cu type ($\omega_p \sim 10^{16}$ s^{-1}), we have $b^2 \approx 0.1$ at the conductor diameter $2a = 20$ nm. In extreme cases, the dispersion relation takes on a simple form:

$$\text{for } 1 > q \gg \exp(-2/b^2),\ \omega/\omega_p \cong k_z a \ln^{1/2}(1/k_z a); \quad (2)$$

$$\text{for } q \ll b\exp(-4/b^2),\quad \omega \approx k_z c[1 - 4/b^2\ln(b^2/4q^2)]^{1/2}. \quad (3)$$

In the limit $q \gg 1$ ($q \gg b\omega$), the dispersion relation asymptotically approaches the surface plasmon frequency $\omega_p/\sqrt{2}$. The dispersion relation (3) suggests that, as the wave vector decreases, the dispersion curve approaches that for light but does not cross it at any q and does not leave the radiation stability region.

Let us find the plasmon group velocity v_G in a thin metal fiber. At $q \gg \exp(-2/b^2)$, we have $v_G/c \approx b\ln^{1/2}(1/k_z a)$, while at $q \ll b\exp(-4/b^2)$ the group velocity tends to the speed of light in vacuum. Thus, the symmetric *E* mode in the cylinder is a slow wave over a wide range of wave vectors.

The dispersion relation for the symmetric *H* wave has no real roots. Hence, no radiation-stable *H* wave exists in the metal cylinder.

Figure 1 also shows the dispersion curve for the first asymmetric *E* mode.

3. POLARITONS IN A NARROW ROUND HOLE (CHANNEL)

Let us consider a narrow cylindrical hole in a metal and study polariton propagation in such a channel. A solution for plasma waves in the hole can be obtained from solution (1) for the cylinder by interchanging ε and ε_1.

The dispersion relation for the symmetric mode in the hole, as well as in the cylinder, splits into two equations for *E* and *H* waves.

3.1. E Wave in the Channel

In the case of the symmetric *E* mode in the hole at $q \gg \exp(-2/b^2)$ we have

$$\omega = \sqrt{1 - q^2/2\ln(1/q)}. \quad (4)$$

In the region $q \ll \exp(-2/b^2)$, we have $\omega = 1 - z_0^2(1 + q^2/z_0^2 b^4)/2$ where $z_0 = \exp(-2/b^2)/b$. We can see from Eq. (4) that the surface plasmon frequency in the cylindrical channel at $q = 0$ is not equal to the plasma frequency, but is displaced downward from the latter by $z_0^2/2$. The dispersion curves for the zero mode and for the first asymmetric *E* mode in the cylindrical hole are shown in Fig. 2.

An analysis shows that there are no radiation-stable *H* waves in thin channels.

4. ENERGY TRANSFER BY PLASMONS

When estimating the energy transfer by plasma modes, we come up against a curious paradox. Indeed, the magnetic field in the electrostatic approximation is assumed to be zero. In this case, the energy flux, which is proportional, as is known, to the Poynting vector ~($\mathbf{E} \times \mathbf{H}$), should also vanish. On the other hand, the energy transport is related to the group velocity of the eigenmodes under study. If the group velocity of plasmons is nonzero, the energy flux should also be nonzero.

To analyze this paradox in more detail, we consider the energy transport by an ordinary surface plasmon and a plasmon in a thin film. These simple cases allow an exact solution (taking into retardation). In the case of the surface plasmon polariton (the field components E_z, E_x, and H_y are nonzero; the x axis is perpendicular to the surface, the z axis is along the wave propagation direction), the dispersion relation is written as $\omega = (\omega_p/\sqrt{2})[1 + 2k_z^2/k_p^2 - (1 + 4k_z^4/k_p^4)^{1/2}]^{1/2}$, where q is the polariton wave vector along the z axis and $k_p = \omega_p/c$. The group velocity of the surface plasmon and, hence, the energy flux vanish when the retardation effects are disregarded. This result is confirmed by a direct calculation of the Poynting vector: $S_z = A^2\omega^3(1-\varepsilon)\kappa/8\pi c^2\kappa_1^2$, where $\kappa = [k_z^2 - (\omega/c)^2]^{1/2}$, $\kappa_1 = [k_z^2 - \varepsilon(\omega/c)^2]^{1/2}$, and A is the amplitude of the surface electric field.

However, as is well known, the frequency dispersion and the nonzero group velocity of the surface plasmon arise in the electrostatic approximation if the spatial dispersion is taken into account. Moreover, in the case of plasma modes in films, narrow slits, and thin channels, the group velocity differs from zero in the electrostatic limit even if the spatial dispersion and retardation are disregarded. As shown above, the dispersion relation for the plasmon in a thin fiber is $\omega \sim k_z \ln^{1/2}(1/k_z a)$ and the group velocity is not small. Therefore energy transport by plasmons should also take place in the electrostatic limit.

This paradox is resolved if we take into account the fact that the Poynting vector is equal to the vector product $\mathbf{E} \times \mathbf{H}$ multiplied by the speed of light c. In the electrostatic limit, we have $\mathbf{H} \longrightarrow 0$ and $c \longrightarrow \infty$; therefore, an accurate calculation of the energy flux requires evaluation of the indeterminate form obtained. To calculate the energy transport rate, we need to determine the ratio of the energy flux density to the total energy per unit volume. A calculation shows that the energy transport with the group velocity of the eigenwaves under study takes place in the electrostatic limit. The energy flux in a thin plane gap of width $2d$ ($k_z d \ll 1$) in the electrostatic limit is equal to $S_z = A^2 k_z^2 \omega\varepsilon/4\pi$ for the symmetric plasma mode with the dispersion relation $\omega = \omega_p(qd)^{1/2}$. The energy flux is $S_z = \omega/2k_z^3 \ln(1/k_z R)$ in a thin cylindrical fiber and $S_z = \omega\varepsilon/2k_z^3 \ln(1/k_z R)$ and in the cylindrical channel. The maximum energy flux for a cylindrical channel of radius $R = 100$ nm at the frequency $\omega = 0.95\omega_p$ (equal to 1.57×10^{16} s^{-1} for copper) is $S_z = 6$ mW/cm^2 at the breakdown voltage $E = 30$ kV/cm^2.

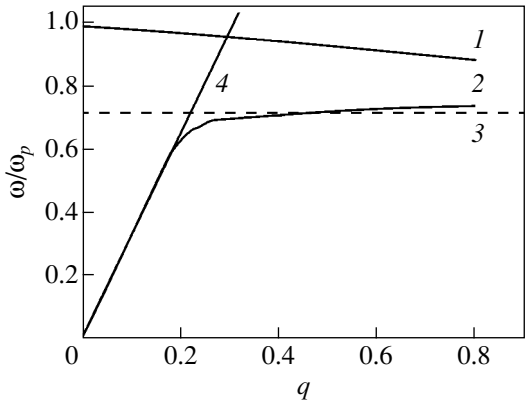

Fig. 2. Dispersion curves of polaritons in a cylindrical cavity for (*1*) the symmetric mode, (*2*) the first asymmetric ($m = 1$) mode, (*3*) the surface plasmon ($\omega/\omega_p = 1/\sqrt{2}$), and (*4*) light; $q = k_z a$.

5. PLASMA MODES IN FINITE SYSTEMS

Examples of plasma modes in finite systems are plasmons in thin aciculae, narrow channels, gaps, small metal particles, and holes. Such modes can be resonantly excited by various external sources, e.g., light or charged particles. Nanostructures are cavities for plasma modes. The spectrum and Q factor of such nanocavities are controlled by their size and boundaries.

The propagation of plasmons in narrow plane slits was considered in [17]. It was shown that plasmons could be localized at smooth inhomogeneities. In this paper, we analyze the opposite case of sharp boundaries, when the inhomogeneity sizes are smaller than the plasmon wavelength.

As an example, we consider a narrow cylindrical channel of length L. A plasma mode can propagate in a channel of finite length. At the channel end, reflection takes place with the reflectance $R = r\exp(i\varphi)$. The resonance condition is written as $kL + \varphi = \pi n$. This condition yields a set of wave vectors k_n. The spectrum of resonant frequencies is determined from the equation $\omega_n = \omega(k_n)$. In the case of the asymmetric mode with $m = 1$, the eigenfrequencies are $\omega_n = c(\pi n - \varphi)/L$ at $L > 5a$. At high frequencies, the spectrum is condensed to the surface plasmon frequency.

To estimate the reflectance R, we calculate the radiation power of the plasma mode, assuming that the oscillating charge source at the point where the channel

Table 1. Path lengths L_p of surface plasmon polaritons for the symmetric and first asymmetric modes in a silver cylinder at various values of the cylinder radius a and various optical frequencies ω at 273 K

Cylinder radius a, nm	Plasmon frequency ω, 10^{15} s^{-1} (ω/ω_p is given in parentheses)	Path length L_p, μm; zero mode in cylinder	Path length L_p, μm; first mode in cylinder
4	2.5 (0.18)	1.6	8.5
4	4.8 (0.35)	0.9	8.5
40	2.5 (0.18)	28	8.5
40	4.8 (0.35)	12	8.5

Table 2. Path lengths L_p of surface plasmon polaritons for the symmetric and first asymmetric modes in a cylindrical cavity in silver at various values of the cylinder radius a and various optical frequencies ω at 273 K

Hole radius a, nm	Plasmon frequency ω, 10^{16} s^{-1} (ω/ω_p is given in parentheses)	Path length L_p, μm; zero mode in the hole	Path length L_p, μm; first mode in hole
4	1.2 (0.9)	0.3	8.5
4	1.1 (0.8)	0.1	8.5
40	1.1 (0.8)	1.0	8.5
40	1.0 (0.73)	0.1	8.5

emerges to the surface is the radiation. We take the charge distribution to be equal to that found for an infinite channel. In the case of the modes with $m = 1$, we have an oscillating dipole moment at the "cutoff." For the symmetric mode with $m = 0$, we have an oscillating electric field at the cutoff, and radiation can be estimated as that of a magnetic dipole with the magnetic moment $\mathbf{m} = (E_s S_r/\omega)\mathbf{e}_t$. We estimate the Q factor of the cavity formed by the cylindrical channel of length L from the ratio of the radiation energy flux density for the symmetric mode [which is $\sim E^2(\omega/c)^2/k_z^4$] to the plasmon electrostatic energy inside the cavity ($\sim E^2 L/k_z^2$). An order-of-magnitude estimation of the radiation Q factor gives $Q_{\text{rad}} \sim L\omega/ck_z$.

6. PLASMON DAMPING

There are three sources of plasma wave damping: dissipative damping related to electron scattering at impurities and at boundary, radiative damping associated with photon emission, and the Landau damping. In the optical frequency range under consideration, dissipative damping, as a rule, dominates; this damping can become weak for noble metals or at low temperatures.

To estimate the damping, we proceed from the general expression for the imaginary part $\omega'' = P/2W$ of the eigenfrequency $\omega = \omega' + i\omega''$, where P is the electromagnetic energy loss power and W is the stored energy. We write the loss power and the stored energy in terms of the electric field and permittivity as

$$W = \frac{1}{8\pi}\int \frac{\partial(\omega\varepsilon(\omega))}{\partial\omega}|\mathbf{E}(\mathbf{r})|^2 d\mathbf{r}, \qquad P = i\omega\int \mathbf{E}\mathbf{P}^* - \text{c.c.}, \tag{5}$$

where $\mathbf{P}$ is the polarization vector. We determine the power and the stored energy, using the perturbation theory, under the assumption that the field has the form obtained above in the absence of damping.

The dissipative damping is given by $\omega'' = \gamma/2$.

To estimate the Landau damping, we invoke the kinetic equation. In the case of a weak field, we seek the electron distribution function in the form $f = f_0 + f_1$, where f_0 is the electron distribution function unperturbed by the field and f_1 is its field-induced change, which meets the mirror reflection condition $f_1(d, v_n) = f_1(d, -v_n)$ at the boundary d, where v_n is the electron velocity component normal to the boundary. We calculate a correction to the distribution function using the method suggested in [18]. Let us expand the field and the distribution function into a Fourier (for a narrow plane slit or a plate) or Fourier–Bessel (for a cylinder) series. For example, in the case of the symmetric (in potential) plasma mode in the plate, f_1 is given by

$$f_1 = -e(\partial f_0/\partial\varepsilon)\varphi_n \mathbf{k}\mathbf{v}/[\omega - \mathbf{k}\mathbf{v}], \qquad \mathbf{k} = (k_n, k_z), \quad k_n = (\pi n/d),$$

where φ_n is the Fourier component of the electric field potential. The contribution to the power given by Eq. (5) comes only from the imaginary part, which is derived from the pole in the distribution function, i.e., from the condition $\omega - k_z v_z - \pi n/d = 0$. It is important that, even at $k_z = 0$, the resonance condition can be met at a sufficiently large $n \sim \omega/v_F$. Such large n values can correspond to sufficiently small values of the Fourier components of the electric field. This is the cause of the Landau damping in such systems being weaker than the collisional damping. In particular, for the symmetric mode in the plate, we obtain

$$\omega''/\omega' = (3/4)(k_z d)^3 v_F/(d\omega_p).$$

7. PLASMON PATH LENGTH IN A CYLINDER

It is of interest to estimate the characteristic path length of the plasmon, which can be defined as the product of the packet group velocity and the characteristic damping time $\tau \approx 1/2\omega''$, i.e., $L_p \approx v_G/2\omega''$. The surface plasmon path lengths in a cylinder and a cylindrical cavity are listed in Tables 1 and 2.

The dissipative damping appreciably weakens as the temperature decreases. This causes an increase in the polariton path length. Tables 1 and 2 list the path lengths at a temperature of 273 K. At 77 K, the path length increases approximately by an order of magnitude.

ACKNOWLEDGMENTS

This study was supported by the Russian Foundation for Basic Research, project nos. 02-02-17852 and 02-02-17937.

REFERENCES

1. T. W. Ebbesen, H. J. Lezec, H. F. Ghaemi, *et al.*, Nature **391**, 667 (1998).
2. M. Volcker, W. Krieger, and H. Walther, Phys. Rev. Lett. **66** (13), 1717 (1991).
3. M. Specht, J. D. Pedarnig, W. M. Heckt, and T. W. Hansch, Phys. Rev. Lett. **68** (4), 476 (1992).
4. R. Berndt, R. Gaisch, W. D. Schneider, *et al.*, Phys. Rev. Lett. **74** (1), 102 (1995).
5. M. Moskovits, Rev. Mod. Phys. **57** (3), 783 (1985).
6. A. Nitzan, J. Chem. Phys. **74** (9), 5321 (1981).
7. R. Fuchs, K. L. Kliewer, and W. J. Pardee, Phys. Rev. **150** (2), 589 (1966).
8. A. V. Klyuchnik, Yu. E. Lozovik, and A. V. Solodov, Zh. Tekh. Fiz. **65** (6), 203 (1995) [Tech. Phys. **40**, 633 (1995)].
9. H. Morawitz and M. R. Philpott, Phys. Rev. B **10** (12), 4863 (1974).
10. S. Efrima and H. Metiu, J. Chem. Phys. **70** (4), 1602 (1979).
11. U. Fano, Phys. Rev. **103** (5), 1202 (1956).
12. J. J. Hopfield, Phys. Rev. **112** (5), 1555 (1958).
13. R. R. Chance, A. Prock, and R. Silbery, Adv. Chem. Phys. **37**, 1 (1978).
14. H. Kuhn, J. Chem. Phys. **53** (1), 101 (1970).
15. G. G. Aers, A. D. Bcardman, and B. V. Paranjape, J. Phys. F **10** (1), 53 (1980).
16. S. S. Martinos and E. N. Economou, Phys. Rev. B **28** (6), 3173 (1983).
17. V. N. Agranovich, V. E. Kravtchov, and T. A. Leskova, Solid State Commun. **47** (11), 925 (1983).
18. A. N. Kondratenko, *Surface and Volume Waves in Limited Plasma* (Énergoatomizdat, Moscow, 1985).

Translated by A. Kazantsev

Physics of the Solid State, Vol. 45, No. 7, 2003, pp. 1332–1341. Translated from Fizika Tverdogo Tela, Vol. 45, No. 7, 2003, pp. 1272–1279.

LOW-DIMENSIONAL SYSTEMS AND SURFACE PHYSICS

Drag Effect of One-Dimensional Electrons upon Photoionization of $D^{(-)}$ Centers in a Longitudinal Magnetic Field

V. D. Krevchik and A. B. Grunin

Penza State University, Penza, 440017 Russia

e-mail: physics@diamond.stup.ac.ru

Received September 10, 2002

Abstract—A theory is elaborated for the impurity photon drag effect in a semiconductor quantum wire exposed to a longitudinal magnetic field **B** directed along the axis of the quantum wire. The phonon drag effect is associated with the transfer of the longitudinal photon momentum to localized electrons in optical transitions from $D^{(-)}$ states to hybrid-quantized states of the quantum wire, which is described by a confinement parabolic potential. An analytical expression for the drag current density is derived within the model of a zero-range potential in the effective mass approximation, and the spectral dependence of the drag current density is examined at different magnitudes of **B** and parameters of the quantum wire upon electron scattering by a system of impurities with short-range potentials. It is established that the spectral dependence of the drag current density exhibits a Zeeman doublet with a clear beak-shaped peak due to optical transitions of electrons from $D^{(-)}$ states to states with the magnetic quantum number $m = 1$. The possibility of using the photon drag effect in a longitudinal magnetic field for the development of laser radiation detectors is analyzed. © *2003 MAIK "Nauka/Interperiodica".*

1. INTRODUCTION

The photon drag effect is caused by the transfer of photon momentum to an electron (hole) subsystem during absorption. The inclusion of the photon momentum leads to asymmetry in the distribution of charge carriers in the quasi-momentum space, i.e., to the generation of drag current. The photon drag effect of two-dimensional electrons upon optical transitions between quantum-confined states of a heterostructure was investigated theoretically by Vas'ko [1], who demonstrated that, under certain conditions, this effect can be sufficiently strong. Rasulov *et al.* [2] considered the contributions from intersubband and interband optical transitions to the photon drag effect of holes in an infinitely deep quantum well of a semiconductor. A reduction in the dimension upon the $2D \longrightarrow 1D$ transition should result in significant variations in the physical properties of quantum-confined structures. In particular, the reduction in the dimension should be accompanied by a more radical change in local electron states and the appearance of specific features in the spectrum of impurity optical absorption due to the characteristic properties of one-dimensional electron states. The problem of controlled modulation of the binding energy of impurity centers [3] and, correspondingly, control of the energies of optical transitions [4] have given impetus to the investigation of the magneto-optical properties of structures with quantum wires. As was shown by Jain and Kivelson [5] and Azbel [6], the magnetic field **B** applied along the axis of the quantum wire can noticeably affect the lateral geometric confinement. Therefore, by varying the magnetic field **B**, it is possible to change the effective geometric size of the system and, consequently, to control the optical properties.

The purpose of this work was to investigate the photon drag effect of electrons upon photoionization of $D^{(-)}$ centers of a quantum wire in a longitudinal magnetic field. In this case, the photon drag effect of one-dimensional electrons is induced by absorption of light with the transverse polarization $\mathbf{e}_{\lambda\perp}$ with respect to the axis of the quantum wire; in other words, the photon drag effect is caused by absorption of photons with the momentum $\hbar\mathbf{q}_{\|}$ directed along the axis of the quantum wire.

Single-electron states in a quantum wire are described in terms of the confinement parabolic potential $V(x, y) = m^*\omega_0^2(x^2 + y^2)/2$, where m^* is the effective electron mass and ω_0 is the characteristic frequency of the confinement potential. The vector potential of the homogeneous static magnetic field $\mathbf{A}(\mathbf{r})$ is chosen in a symmetric gauge: $\mathbf{A} = (-By/2, Bx/2, 0)$. Hence, the effective Hamiltonian of the interaction with the field of a light wave in the cylindrical coordinate system can be written in the form

$$\hat{H}_{\text{int}} = -\lambda_0\sqrt{\frac{2\pi\hbar^2\alpha^* I_0}{m^{*2}\omega}} \times \exp(iq_z z)\left[i\hbar\left(\cos(\Theta-\varphi)\frac{\partial}{\partial\rho} + \frac{1}{\rho}\sin(\Theta-\varphi)\frac{\partial}{\partial\varphi}\right) + \frac{|e|B}{2}\rho\sin(\varphi-\Theta)\right], \quad (1)$$

1063-7834/03/4507-1332$24.00 © 2003 MAIK "Nauka/Interperiodica"

where ρ, φ, and z are the cylindrical coordinates; q_z is the projection of the photon wave vector $\mathbf{q}_\parallel = (0, 0, q_z)$ onto the axis of the quantum wire; Θ is the polar angle of the polarization vector of light $\mathbf{e}_{\lambda\perp}$; λ_0 is the coefficient of the local field; α* is the fine structure constant with allowance made for the permittivity ε; I_0 is the light intensity; ω is the frequency of the light wave; $|e|$ is the magnitude of the elementary charge; and B is the magnitude of the magnetic induction.

The potential $V_\delta(\mathbf{r}, \mathbf{R}_a)$ of an impurity center is described within the model of a zero-range potential [7]:

$$V_\delta(\boldsymbol{\rho}, z, \boldsymbol{\rho}_a, z_a) = \gamma\delta(\boldsymbol{\rho} - \boldsymbol{\rho}_a)\delta(z - z_a) \times\left[1 + (\boldsymbol{\rho} - \boldsymbol{\rho}_a)\frac{\partial}{\partial\boldsymbol{\rho}} + (z - z_a)\frac{\partial}{\partial z}\right], \quad (2)$$

where $\gamma = 2\pi\hbar^2/(\alpha m^*)$ and α is determined by the binding energy E_i of the localized electron state at the same impurity center in the bulk semiconductor. Within this model, the impurity center is located at the point $\mathbf{R}_a = (\boldsymbol{\rho}_a, z_a)$. According to Pakhomov *et al.* [8], this model is applicable to the description of $D^{(-)}$ states corresponding to the attachment of an excess electron to a shallow-level donor. As will be shown below, the method of a zero-range potential makes it possible to obtain an analytical solution for the wave function of a localized carrier in an external longitudinal magnetic field. This is of particular importance in analyzing the positional disorder in a quantum wire with a parabolic potential distribution and also in deriving an explicit formula for the drag current of one-dimensional electrons. The energy spectrum of the Hamiltonian in our model can be written in the form [9]

$$E_{n, m, k_z} = \frac{\hbar\omega_B m}{2} + \hbar\omega_0\sqrt{1 + \frac{\omega_B^2}{4\omega_0^2}}(2n + |m| + 1) + \frac{\hbar^2 k_z^2}{2m^*}, \quad (3)$$

where $n = 0, 1, 2, \ldots$ is the quantum number corresponding to the Landau levels; $m = 0, \pm1, \pm2, \ldots$ is the magnetic quantum number; $\omega_B = |e|B/m^*$ is the cyclotron frequency; and $\hbar k_z$ is the projection of the electron quasi-momentum onto the Oz axis.

The impurity-unperturbed single-electron states $\Psi_{n, m, k_z}(\rho, \varphi, z)$ in the longitudinal magnetic field can be represented in the following form[1] [9]:

$$\Psi_{n, m, k_z}(\rho, \varphi, z) = \frac{1}{2^{\frac{|m|+1}{2}}\sqrt{\pi L_{QW}}a_1^{|m|+1}}\left[\frac{n!}{(n + |m|)!}\right]^{1/2}\rho^{|m|} \times \exp\left(-\frac{\rho^2}{4a_1^2}\right)L_n^{|m|}\left(\frac{\rho^2}{2a_1^2}\right)\exp(im\varphi)\exp(ik_z z), \quad (4)$$

where $a_1^2 = a^2/(2\sqrt{1 + a^4/(4a_B^4)})$, $a^2 = \hbar/(m^*\omega_0)$, $a_B^2 = \hbar/(m^*\omega_B)$, $L_n^\alpha(x)$ are the Laguerre polynomials [10], and L_{QW} is the length of the quantum wire.

In this paper, the drag current of one-dimensional electrons upon photoionization of impurity centers is calculated in the case of strong magnetic quantization when the characteristic length of the oscillator is considerably longer than the magnetic length. The calculation is performed with due regard for elastic electron scattering by a system of impurities with short-range potentials, which is simulated by the sum of zero-range potentials [11–13].

2. CALCULATION OF THE BINDING ENERGY OF A $D^{(-)}$ CENTER IN A LONGITUDINAL MAGNETIC FIELD

Let us consider the effect of positional disorder in a semiconductor quantum wire with a confinement parabolic potential in a longitudinal magnetic field. It is assumed that an impurity center is located at the point $\mathbf{R}_a = (\rho_a, \varphi_a, z_a)$. The wave function $\Psi_{\lambda_B}(\rho, \varphi, z; \rho_a, \varphi_a, z_a)$ of an electron localized at a $D^{(-)}$ center satisfies the Lippmann–Schwinger equation for a bound state, which, in the cylindrical coordinate system, can be represented in the form

$$\Psi_{\lambda_B}(\rho, \varphi, z; \rho_a, \varphi_a, z_a) = \int_0^\infty\int_0^{2\pi}\int_{-\infty}^{+\infty}\rho_1 d\rho_1 d\varphi_1 dz_1 G(\rho, \varphi, z, \rho_1, \varphi_1, z_1; E_{\lambda_B}^{(0)}) \times V_\delta(\rho_1, \varphi_1, z_1; \rho_a, \varphi_a, z_a)\Psi_{\lambda_B}(\rho_1, \varphi_1, z_1; \rho_a, \varphi_a, z_a). \quad (5)$$

Here, $G(\rho, \varphi, z, \rho_1, \varphi_1, z_1; E_{\lambda_B}^{(0)})$ is the single-electron Green's function corresponding to the source at the point (ρ_1, φ_1, z_1) and to the energy $E_{\lambda_B}^{(0)} = -\hbar^2\lambda_B^2/(2m^*)$, [$E_{\lambda_B}^{(0)}$ are the eigenvalues of the Hamiltonian $\hat{H}_B$ =

[1] In what follows, we will consider the case of strong localization of an impurity electron when $\lambda_B a_1 \gg 1$, where λ_B^{-1} is the radius of the localized state in the magnetic field. This suggests that the single-electron states in the longitudinal magnetic field are not perturbed by the impurity potential.

$(\hat{\mathbf{p}} + |e|\mathbf{A})^2/(2m^*) + V(x, y) + V_\delta(\rho, \varphi, z; \rho_a, \varphi_a, z_a)$, where $\hat{\mathbf{p}}$ is the operator of the electron momentum]:

$$G(\rho, \varphi, z, \rho_1, \varphi_1, z_1; E^{(0)}_{\lambda_B}) = \int_{-\infty}^{+\infty} d\left(\frac{k_z L_{QW}}{2\pi}\right) \sum_{n, m} \frac{\Psi^*_{n, m, k_z}(\rho_1, \varphi_1, z_1)\Psi_{n, m, k_z}(\rho, \varphi, z)}{E^{(0)}_{\lambda_B} - E_{n, m, k_z}}. \quad (6)$$

Upon substituting expression (2) into relationship (5), we obtain

$$\Psi_{\lambda_B}(\rho, \varphi, z; \rho_a, \varphi_a, z_a) = \gamma G(\rho, \varphi, z, \rho_a, \varphi_a, z_a; E^{(0)}_{\lambda_B}) \times (\hat{T}\Psi_{\lambda_B})(\rho_a, \varphi_a, z_a; \rho_a, \varphi_a, z_a), \quad (7)$$

where

$$(\hat{T}\Psi_{\lambda_B})(\rho_a, \varphi_a, z_a; \rho_a, \varphi_a, z_a) \equiv \lim_{\rho \to \rho_a, \varphi \to \varphi_a, z \to z_a} \left[1 + (\boldsymbol{\rho} - \boldsymbol{\rho}_a)\frac{\partial}{\partial \boldsymbol{\rho}} + (z - z_a)\frac{\partial}{\partial z}\right] \times \Psi_{\lambda_B}(\rho, \varphi, z; \rho_a, \varphi_a, z_a). \quad (8)$$

By applying operation (8) to both sides of relationship (7), we derive an expression describing the dependence of the binding energy of the impurity center on the parameters of the quantum wire, the coordinates of the impurity center, and the magnitude of the magnetic induction B:

$$1 = \gamma(\hat{T}G)(\rho_a, \varphi_a, z_a, \rho_a, \varphi_a, z_a; E^{(0)}_{\lambda_B}). \quad (9)$$

In accordance with formula (9), the energy of the bound state of the electron in the total field is the pole of the Green's function, which, taking into account expressions (3), (4), and (6), can be written as

$$G(\rho, \varphi, z, \rho_a, \varphi_a, z_a; E^{(0)}_{\lambda_B}) = -\frac{\hbar^2}{4\pi^2 m^* E_d a_1^2} \times \int_{-\infty}^{+\infty} dk_z \exp[ik_z(z - z_a)] \sum_{n, m} C^2_{n, m}(\rho_a \rho)^{|m|} \times \exp\left(-\frac{\rho_a^2 + \rho^2}{4a_1^2}\right) L_n^{|m|}\left(\frac{\rho_a^2}{2a_1^2}\right) L_n^{|m|}\left(\frac{\rho^2}{2a_1^2}\right) \times \exp[im(\varphi - \varphi_a)](\eta_B^2 + ma^{*-2} + \beta^{-1}\sqrt{1 + \beta^2 a^{*-4}} \times (2n + |m| + 1) + k_z^2 a_d^2)^{-1}, \quad (10)$$

where $C_{n, m} = 2^{-|m|/2} a_1^{-|m|} \sqrt{n!/(n + |m|)!}$, $a^* = a_B/a_d$, a_d is the effective Bohr radius, $\eta_B^2 = \left|E^{(0)}_{\lambda_B}\right|/E_d$, E_d is the effective Bohr energy, $\beta = L^*/(4\sqrt{U_0^*})$, $L^* = 2L/a_d$, $2L$ is the diameter of the quantum wire, $U_0^* = U_0/E_d$, and U_0 is the amplitude of the potential of the quantum wire.

The summation in expression (10) over n can be performed using a trivial relationship,

$$(\eta_B^2 + ma^{*-2} + \beta^{-1}\sqrt{1 + \beta^2 a^{*-4}}(2n + |m| + 1) + k_z^2 a_d^2)^{-1} = \int_0^{+\infty} \exp[-(\eta_B^2 + ma^{*-2} + \beta^{-1} \times \sqrt{1 + \beta^2 a^{*-4}}(2n + |m| + 1) + k_z^2 a_d^2)t]dt, \quad (11)$$

and the Hille–Hardy formula for the bilinear generating function [10],

$$\sum_{n=0}^{\infty} \frac{n!}{\Gamma(n + \alpha + 1)} L_n^\alpha(x) L_n^\alpha(y) z^n = (1 - z)^{-1} \times \exp\left(-z\frac{x + y}{1 - z}\right)(xyz)^{-\alpha/2} I_\alpha\left(2\frac{\sqrt{xyz}}{1 - z}\right). \quad (12)$$

Here, $|z| < 1$ and $I_\alpha(u)$ is the modified Bessel function of the first kind [10]. In expression (10), the series can be summed over m with the use of the formula for the generating function of the Bessel functions of the first kind $J_k(z)$; that is,

$$\sum_{k=-\infty}^{+\infty} J_k(z) t^k = \exp\left[\frac{1}{2}\left(t - \frac{1}{t}\right)z\right]. \quad (13)$$

Finally, taking into account that the integration with respect to k_z in expression (10) results in

$$\int_{-\infty}^{+\infty} \exp[ik_z(z - z_a) - k_z^2 a_d^2 t]dk_z = \frac{1}{a_d}\sqrt{\frac{\pi}{t}} \exp\left[-\frac{(z - z_a)^2}{4a_d^2 t}\right] \quad (14)$$

and using the Weber integral [10] (in our designations)

$$\int_0^{+\infty}\frac{1}{t\sqrt{t}}\exp\left[-\frac{(\rho-\rho_a)^2}{4a_1^2t}-\frac{(z-z_a)^2}{2a^2t}\right]\exp[-(\beta\eta_B^2+\sqrt{1+\beta^2a^{*-4}})t]dt$$

$$=\sqrt{2\pi}a\frac{\exp\left[-\sqrt{2(\beta\eta_B^2+\sqrt{1+\beta^2a^{*-4}})}\sqrt{\frac{(\rho-\rho_a)^2\sqrt{1+\beta^2a^{*-4}}(z-z_a)^2}{a^2}}\right]}{\sqrt{(\rho-\rho_a)^2\sqrt{1+\beta^2a^{*-4}}+(z-z_a)^2}}, \quad (15)$$

the single-electron Green's function in expression (10) can be represented in the form

$$G(\rho,\varphi,z,\rho_a,\varphi_a,z_a;E_{\lambda_B}^{(0)})=-\frac{\hbar^2}{2^3\pi^{\frac{3}{2}}E_da_d^3m^*\sqrt{\beta}}$$

$$\times\left\{\int_0^{+\infty}\frac{1}{\sqrt{t}}\exp\left[-\left((\beta\eta_B^2+w)t+\frac{(z-z_a)^2}{4\beta a_d^2t}\right)\right]\right.$$

$$\times\left[2w(1-\exp(-2wt))^{-1}\exp\left[-\frac{(\rho_a^2+\rho^2)w}{4\beta a_d^2}\right.\right.$$

$$\times\frac{(1+\exp(-2wt))}{(1-\exp(-2wt))}\left.\left.\right]\exp\left[\frac{1}{2}\left(\exp\left(i(\varphi-\varphi_a)-\frac{\beta}{a^{*2}}t\right)\right.\right.\right. \quad (16)$$

$$\left.\left.+\exp\left(-i(\varphi-\varphi_a)+\frac{\beta}{a^{*2}}t\right)\right)\frac{\rho_a\rho w\exp(-wt)}{\beta a_d^2(1-\exp(-2wt))}\right]$$

$$\left.-\frac{1}{t}\exp\left[-\frac{(\rho-\rho_a)^2w}{4\beta a_d^2t}\right]\right]dt+2\sqrt{\pi\beta}a_d$$

$$\left.\times\frac{\exp\left[-\frac{1}{a_d}\sqrt{\frac{\beta\eta_B^2+w}{\beta}}\sqrt{(\rho-\rho_a)^2w+(z-z_a)^2}\right]}{\sqrt{(\rho-\rho_a)^2w+(z-z_a)^2}}\right\},$$

where $w=\sqrt{1+\beta^2a^{*-4}}$.

Upon substituting relationship (16) into expression (9) and carrying out necessary passages to the limits, we obtain the following equation (in Bohr units) for the binding energy of the $D^{(-)}$ center in the longitudinal magnetic field:

$$\sqrt{\eta_B^2+\beta^{-1}w}=\eta_i-\frac{1}{\sqrt{\pi\beta}}\int_0^{+\infty}\frac{1}{\sqrt{t}}\exp[-(\beta\eta_B^2+w)t]$$

$$\times\left(\frac{1}{2t}-w(1-\exp(-2wt))^{-1}\right.$$

$$\times\exp\left[-\frac{\rho_a^{*2}w}{2\beta(1-\exp(-2wt))}(1+\exp(-2wt)\right. \quad (17)$$

$$\left.\left.-(\exp(-\beta a^{*-2}t)+\exp(\beta a^{*-2}t))\exp(-wt))\right]\right)dt,$$

where $\rho_a^*=\rho_a/a_d$.

Equation (17) can be numerically analyzed using a computer. However, in this case, the following two circumstances must be taken into account. First, the localized states can also exist at energy levels between the quantum-well bottom and the first quantum-well level $\varepsilon_{0,0}$ [8]. In this situation, the condition $E_{\lambda_B}^{(0)}>0$ is satisfied for the impurity levels lying above the quantum-well bottom and the parameter λ_B becomes imaginary. Second, by virtue of the quantum-well effect, the binding energy E_{λ_B} of the $D^{(-)}$ center in the quantum wire in the longitudinal magnetic field must be determined as follows [14]:

$$E_{\lambda_B}=\begin{cases}\varepsilon_{0,0}+\left|E_{\lambda_B}^{(0)}\right|, & E_{\lambda_B}^{(0)}<0\\ \varepsilon_{0,0}-E_{\lambda_B}^{(0)}, & E_{\lambda_B}^{(0)}>0\end{cases}$$

or, in Bohr units,

$$E_{\lambda_B}/E_d=\begin{cases}\beta^{-1}w+\eta_B^2, & E_{\lambda_B}^{(0)}<0\\ \beta^{-1}w-\eta_B'^2, & E_{\lambda_B}^{(0)}>0,\end{cases} \quad (18)$$

where $\varepsilon_{0,0}=\hbar\omega_0\sqrt{1+\omega_B^2/(4\omega_0^2)}$ and $\eta_B'^2=-\eta_B^2$.

Figure 1 presents the results of the numerical analysis of expression (17) with due regard for relationship (18) for $D^{(-)}$ states in InSb-based semiconductor quantum wires. In these calculations, the effective electron mass in InSb is determined as $m^*=0.0133m_0$ (where m_0 is the rest mass of the electron), the permittivity is esti-

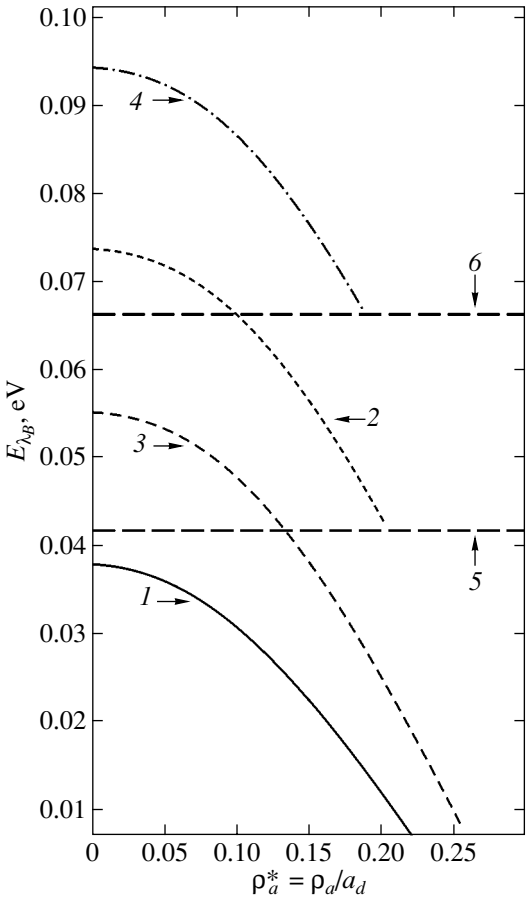

Fig. 1. Dependences of the binding energy E_{λ_B} of the $D^{(-)}$ center at $2L = 71.6$ nm and $U_0 = 0.2$ eV on the polar radius $\rho_a^* = \rho_a/a_d$ of the impurity (in Bohr units) for different magnetic inductions B: (*1*) $E_{\lambda_B}^{(0)} > 0$, $|E_i| = 5 \times 10^{-3}$ eV, and $B = 0$; (*2*) $E_{\lambda_B}^{(0)} < 0$, $|E_i| = 3.5 \times 10^{-2}$ eV, and $B = 0$; (*3*) $E_{\lambda_B}^{(0)} > 0$, $|E_i| = 5 \times 10^{-3}$ eV, and $B = 12$ T; and (*4*) $E_{\lambda_B}^{(0)} < 0$, $|E_i| = 3.5 \times 10^{-2}$ eV, and $B = 12$ T. Dashed lines *5* and *6* indicate the locations of the energy levels in the ground state in a quantum wire at $B = 0$ and 12 T, respectively.

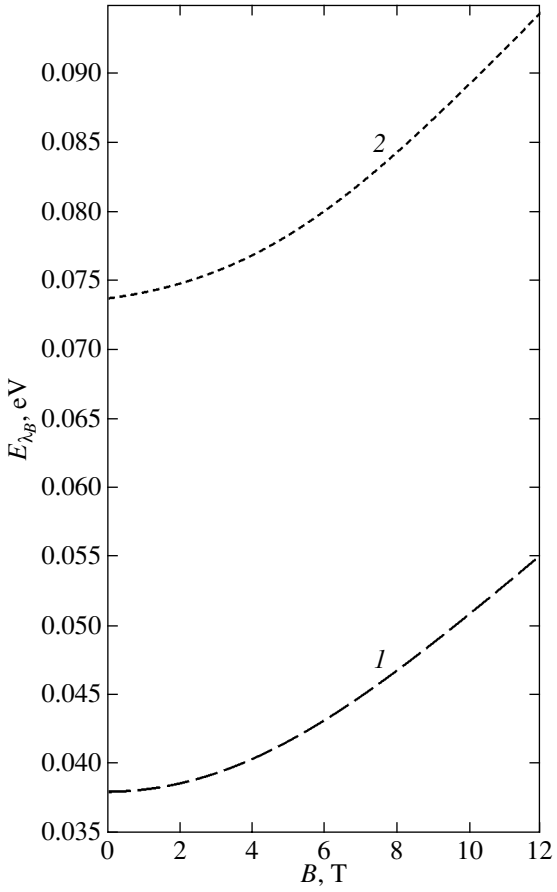

Fig. 2. Dependences of the binding energy $E_{\lambda_B}^{(0)}$ of the $D^{(-)}$ center located at the point $\mathbf{R}_a = (0, 0, z_a)$ for $2L = 71.6$ nm and $U_0 = 0.2$ eV on the magnetic induction B: (*1*) $E_{\lambda_B}^{(0)} > 0$, $|E_i| = 5 \times 10^{-3}$ eV and (*2*) $E_{\lambda_B}^{(0)} < 0$, $|E_i| = 3.5 \times 10^{-2}$ eV.

mated to be $\varepsilon \approx 18$, and the effective Bohr energy is $E_d \approx 5.5 \times 10^{-4}$ eV. It can be seen from Fig. 1 that, in both cases, i.e., when $E_{\lambda_B}^{(0)} > 0$ and $E_{\lambda_B}^{(0)} < 0$ (curves *1* and *2*, respectively), the binding energy E_{λ_B} of the $D^{(-)}$ center is a decreasing function of the radial coordinate ρ_a. This behavior is associated with the radical change in the local electron states near the boundaries of the quantum wire. In the magnetic field, the binding energy of the $D^{(-)}$ center increases significantly. As can be seen from Fig. 2 (for example, curve *2*; $E_{\lambda_B}^{(0)} < 0$), the gain in the binding energy is more than 0.02 eV for the $D^{(-)}$ center located at the origin of coordinates. Note that, in the longitudinal magnetic field, the existence conditions of the bound state become less stringent, which can be judged from the comparison of curves *1*, *3* and *2*, *4* in Fig. 1. Thus, the magnetic field stabilizes the $D^{(-)}$ states in the quantum wire. It should also be noted that the gain in the binding energy of $D^{(-)}$ centers with an increase in the magnetic field **B** has been observed experimentally in systems with multiple quantum wells, for example, GaAs–$Ga_{0.75}Al_{0.25}As$ [15]. The problem concerning efficient control of the energies of optical transitions in a magnetic field is of fundamental importance in view of the prospects for creating photodetectors with a controlled operating frequency and sensitivity in the range of impurity optical absorption.

3. CALCULATION OF THE DRAG CURRENT OF ONE-DIMENSIONAL ELECTRONS IN A LONGITUDINAL MAGNETIC FIELD

It follows from relationship (7) that the wave function $\Psi_{\lambda_B}(\rho, \varphi, z; \rho_a, \varphi_a, z_a)$ of the localized electron with the short-range potential differs from the single-electron Green's function $G(\rho, \varphi, z, \rho_a, \varphi_a, z_a; E^{(0)}_{\lambda_B})$ by only a factor:

$$\Psi_{\lambda_B}(\rho, \varphi, z; \rho_a, \varphi_a, z_a) = -C\tilde{G}(\rho, \varphi, z, \rho_a, \varphi_a, z_a; E^{(0)}_{\lambda_B}), \quad (19)$$

where

$$\tilde{G}(\rho, \varphi, z, \rho_a, \varphi_a, z_a; E^{(0)}_{\lambda_B}) = 2^{3/2}\beta^{1/2}E_d a_d^3 G(\rho, \varphi, z, \rho_a, \varphi_a, z_a; E^{(0)}_{\lambda_B})$$

and

$$C = \left[2^{3/2}\beta^{1/2}a_d^3\frac{\partial\tilde{G}}{\partial(\eta_B^2)}(\rho_a, \varphi_a, z_a, \rho_a, \varphi_a, z_a; E^{(0)}_{\lambda_B})\right]^{-1/2}$$

is the normalizing factor. In the case when the $D^{(-)}$ center is located at the point $\mathbf{R}_a = (0, 0, z_a)$, from relationship (10), we obtain

$$\Psi_{\lambda_B}(\rho, \varphi, z, 0, 0, z_a) \equiv \Psi_{\lambda_B}(\rho, \varphi, z; z_a) = 2^{1/4}\pi^{-1/4}\beta^{-3/4}a_d^{-3/2}w^{5/4}\left[\zeta\left(\frac{3}{2}, \frac{\beta\eta_B^2}{2w} + \frac{1}{2}\right)\right]^{-1/2} \times \int_0^{+\infty}\frac{1}{\sqrt{t}}\exp\left[-\left((\beta\eta_B^2 + w)t + \frac{(z - z_a)^2}{4\beta a_d^2 t}\right)\right] \times [1 - \exp(-2wt)]^{-1}\exp\left[-\frac{\rho^2 w(1 + \exp(-2wt))}{4\beta a_d^2(1 - \exp(-2wt))}\right]dt, \quad (20)$$

where $\zeta(s, u)$ is the generalized Riemann zeta function [10].

The problem of the impurity photon drag effect in a quantum wire can be solved in terms of the Boltzmann kinetic equation written in the relaxation-time approximation. The source term of this equation is determined by the photon-induced quantum transitions of carriers from the $D^{(-)}$ center to the hybrid-quantized band, which are calculated in the approximation linear with respect to the photon momentum. For a short circuit, the density $j(\omega)$ of drag current of electrons in a quantum wire placed in a longitudinal magnetic field can be represented in the form

$$j(\omega) = -\frac{|e|N_0}{2\pi^2\hbar^2}\int_0^{L_{QW}}dz_a n_\lambda \times \sum_{n, m}\theta\left[\hbar\omega - \left|E^{(0)}_{\lambda_B}\right| - \frac{\hbar\omega_B m}{2} - \frac{\hbar\Omega}{2}(2n + |m| + 1)\right] \times \int_{-\infty}^{+\infty}\frac{\partial E_{n, m, k_z}}{\partial k_z}\tau(E_{n, m, k_z})|M_{f, \lambda}|^2[f_0(E^{(0)}_{\lambda_B}) - f_0(E_{n, m, k_z})] \times \delta\left[\hbar\omega - \left|E^{(0)}_{\lambda_B}\right| - \frac{\hbar\omega_B m}{2} - \frac{\hbar\Omega}{2}(2n + |m| + 1) - \frac{\hbar^2 k_z^2}{2m^*}\right]dk_z, \quad (21)$$

where N_0 is the concentration of $D^{(-)}$ centers in the quantum wire, η_λ is the linear concentration of $D^{(-)}$ centers located at points $\mathbf{R}_a = (0, 0, z_a)$ along the axis of the quantum wire, $\hbar\omega$ is the photon energy, $\tau(E_{n, m, k_z})$ is the relaxation time of electrons in the quantum wire, $f_0(E)$ is the quasi-equilibrium distribution function of electrons in the quantum wire, $\delta(x)$ is the delta function, $M_{f, \lambda}$ are the matrix elements determining the optical transitions of an electron from the ground state of the $D^{(-)}$ center to the hybrid-quantized states of the quantum wire, $\theta(s)$ is the Heaviside unit function ($\theta(s) = 1$ at $s \geq 0$ and $\theta(s) = 0$ at $s < 0$) [16], and $\Omega = \sqrt{4\omega_0^2 + \omega_B^2}$ is the hybrid frequency.

By using relationship (1), the expression for the matrix elements $M_{f, \lambda}$ can be written as the sum of two terms: $M_{f, \lambda} = I_1 + I_2$, where

$$I_1 = -\lambda_0\sqrt{\frac{2\pi\hbar^2\alpha^*}{m^{*2}\omega}I_0}\left\langle\Psi^*_{n, m, k_z}(\rho, \varphi, z) \times \left|e^{iq_z z}i\hbar\left(\cos(\Theta - \varphi)\frac{\partial}{\partial\rho} + \frac{1}{\rho}\sin(\Theta - \varphi)\frac{\partial}{\partial\varphi}\right)\right| \times \Psi_{\lambda_B}(\rho, \varphi, z; z_a)\right\rangle, \quad (22)$$

$$I_2 = -\lambda_0\sqrt{\frac{2\pi\hbar^2\alpha^*}{m^{*2}\omega}I_0} \times \left\langle\Psi^*_{n, m, k_z}(\rho, \varphi, z)\left|e^{iq_z z}\frac{|e|B}{2}\rho\sin(\varphi - \Theta)\right|\Psi_{\lambda_B}(\rho, \varphi, z; z_a)\right\rangle. \quad (23)$$

When calculating the component I_1, we obtain the integrals

$$\int_0^{2\pi}\exp(-im\varphi)\cos(\varphi - \Theta)d\varphi = \begin{cases}\pi\exp(\mp i\Theta), & m = \pm 1\\ 0, & m \neq \pm 1,\end{cases} \quad (24)$$

$$\int_{-\infty}^{+\infty} \exp\left[i(q_z - k_z)z - \frac{(z - z_a)^2}{4\beta a_d^2 t}\right] dz = 2a_d\sqrt{\pi\beta}\sqrt{t} \times \exp[-\beta a_d^2 (q_z - k_z)^2 t + i(q_z - k_z)z_a]. \quad (25)$$

Upon integrating in formula (22) with respect to ρ and using the standard relationship [10]

$$\int_0^{+\infty} \rho^3 \exp\left[-\frac{\rho^2 w}{2\beta a_d^2 (1 - \exp(-2wt))}\right] L_n^1\left(\frac{\rho^2 w}{2\beta a_d^2}\right) d\rho = \frac{2\beta^2 a_d^4}{w^2}(n+1)(1 - \exp(-2wt))^2 \exp(-2nwt), \quad (26)$$

we derive the following expression:

$$I_1 = 2^{11/4} i\pi^{1/2} L_{QW}^{-1/2} \exp(\mp i\Theta) \times \lambda_0 \sqrt{\frac{\alpha^* I_0}{\omega}} \beta^{-1/4} E_d a_d^{3/2} w^{5/4} (n+1)^{1/2} \times \exp[i(q_z - k_z)z_a] \left[\zeta\left(\frac{3}{2}, \frac{\beta\eta_B^2}{2w} + \frac{1}{2}\right)\right]^{-1/2} \times [\beta\eta_B^2 + (2n+2)w + \beta a_d^2 (q_z - k_z)^2] \times [\beta\eta_B^2 + (2n+1)w + \beta a_d^2 (q_z - k_z)^2]^{-1} \times [\beta\eta_B^2 + (2n+3)w + \beta a_d^2 (q_z - k_z)^2]^{-1}. \quad (27)$$

In the case of I_2, the integrals with respect to the coordinates z and ρ coincide with integrals (25) and (26), respectively, and the integration with respect to φ is reduced to calculating the integral

$$\int_0^{2\pi} \exp(-im\varphi)\sin(\varphi - \Theta) d\varphi = \begin{cases} \mp\pi i \exp(\mp i\Theta), & m = \pm 1 \\ 0, & m \neq \pm 1. \end{cases} \quad (28)$$

It follows from formulas (24) and (28) that the optical transitions from the impurity level become possible only in the state with the quantum number $m = \pm 1$. Taking into account formulas (25), (26), and (28), we obtain the following relationship:

$$I_2 = \pm 2^{11/4} i\pi^{1/2} L_{QW}^{-1/2} \exp(\mp i\Theta) \times \lambda_0 \sqrt{\frac{\alpha^* I_0}{\omega}} \beta^{3/4} a^{*-2} E_d a_d^{3/2} w^{5/4} (n+1)^{1/2} \times \exp[i(q_z - k_z)z_a] \left[\zeta\left(\frac{3}{2}, \frac{\beta\eta_B^2}{2w} + \frac{1}{2}\right)\right]^{-1/2} \times [\beta\eta_B^2 + (2n+1)w + \beta a_d^2 (q_z - k_z)^2]^{-1} \times [\beta\eta_B^2 + (2n+3)w + \beta a_d^2 (q_z - k_z)^2]^{-1}. \quad (29)$$

In the approximation linear with respect to q_z, the matrix elements $|M_{f,\lambda}|^2$ in formula (21) can be written as

$$|M_{f,\lambda}|^2 = |I_1 + I_2|^2 = \frac{2^{15/2}\pi}{L_{QW}} \lambda_0^2 \frac{\alpha^* I_0}{\omega} a_d^5 E_d^2 \beta^{1/2} w^{5/2} q_z \left[\zeta\left(\frac{3}{2}, \frac{\beta\eta_B^2}{2w} + \frac{1}{2}\right)\right]^{-1} (n+1)k_z \times \left[\frac{2(\beta\eta_B^2 + (2n+2)w + \beta a_d^2 k_z^2)}{(\beta\eta_B^2 + (2n+1)w + \beta a_d^2 k_z^2)(\beta\eta_B^2 + (2n+3)w + \beta a_d^2 k_z^2)} - (\beta\eta_B^2 + (2n+2)w \pm \beta a^{*-2} + \beta a_d^2 k_z^2)^{-1}\right] \times \frac{(\beta\eta_B^2 + (2n+2)w \pm \beta a^{*-2} + \beta a_d^2 k_z^2)^2}{(\beta\eta_B^2 + (2n+1)w + \beta a_d^2 k_z^2)^2 (\beta\eta_B^2 + (2n+3)w + \beta a_d^2 k_z^2)^2}. \quad (30)$$

After substituting expression (30) into formula (21), the drag current density takes the form

$$j(\omega) = -\frac{|e| q_z N_0}{\pi\hbar L_{QW}} 2^{15/2} \lambda_0^2 \alpha^* I_0 n_\lambda a_d^4 E_d \beta^{5/2} w^{5/2} X \int_0^{L_{QW}} dz_a \left[\zeta\left(\frac{3}{2}, \frac{\beta\eta_B^2}{2w} + \frac{1}{2}\right)\right]^{-1} \tau(E_d(X - \eta_B^2))$$

$$\times [f_0(-E_d\eta_B^2) - f_0(E_d(X-\eta_B^2))]\sum_{n=0}^{N}(n+1)\sum_{m=-1}^{1}\delta_{|m|,1}\theta(X-\eta_B^2 - m/a^{*2} - w/\beta(2n+|m|+1))$$
$$\times \frac{\sqrt{X-\eta_B^2 - m/a^{*2} - w/\beta(2n+|m|+1)}}{(\beta(X-ma^{*-2}) - |m|w)^2(\beta(X-ma^{*-2}) + (2-|m|)w)^2}$$
$$\times\left[\frac{2\beta(X-ma^{*-2})}{(\beta(X-ma^{*-2}) - |m|w)(\beta(X-ma^{*-2}) + (2-|m|w))} - \beta^{-1}X^{-1}\right], \quad (31)$$

where $X = \hbar\omega/E_d$ is the photon energy expressed in terms of the effective Bohr energy E_d; $N = [A_0]$ is the integer part of the number $A_0 = \beta(X - \eta_B^2 + a^{*-2})/(2w) - 1$; and $\delta_{|m|,1}$ is the Kronecker delta, which accounts for the selection rules for the magnetic quantum number m.

When deriving relationship (31) for the drag current density, we took into account that, upon integration with respect to k_z in formula (21), it is necessary to calculate the roots of the argument of the δ function $(k_z)_{1,2}$ that satisfy the equation

$$X - \eta_B^2 - m/a^{*2} - w/\beta(2n+|m|+1) - k_z^2 a_d^2 = 0. \quad (32)$$

Before proceeding to an analysis of the spectral dependence of the drag current density, we consider the mechanism of charge carrier scattering in a quantum wire and, correspondingly, determine the relaxation time in relationship (31). Let us assume that electrons in the hybrid-quantized conduction band of the quantum wire undergo elastic scattering by a system of impurities with short-range potentials [17]. In the approximation of strong magnetic quantization, when $a_1 \ll a$ ($\omega_0 \ll \Omega$), the expression for the relaxation time $\tau(E_d(X-\eta_B^2))$ can be written as [17]

$$\tau(E_d(X-\eta_B^2))$$
$$= 2^{-9/2}\pi^{-1}\hbar E_d^{-1}L^{*2}(n_i a_d^3)^{-1}\left(\frac{\lambda_s}{a_d}\right)^{-2}\sqrt{\frac{w}{\beta}}$$
$$\times\left|1 + \frac{1}{\sqrt{2}a^*}\left(\frac{\lambda_s}{a_d}\right)\zeta\left(\frac{1}{2}, \frac{1}{2} - \frac{\beta(X-\eta_B^2)}{2w}\right)\right|^2 \quad (33)$$
$$\times\left[\sum_{n=0}^{N_1}\left(\frac{\beta(X-\eta_B^2)}{2w} - n - \frac{1}{2}\right)^{-1/2}\right]^{-1},$$

where λ_s is the scattering length; n_i is the concentration of impurity scattering centers in the quantum wire; and $N_1 = [A_1]$ is the integer part of the number A_1, where $A_1 = \beta(X-\eta_B^2)/(2w) - 1/2$ for $[A_1] \neq A_1$ and $N_1 = [A_1] - 1$ for $[A_1] = A_1$.

According to Geĭler *et al.* [17], the distribution function $f_0(E_{n,m,k_z})$ of electrons in the quantum wire in the case under consideration can be represented in the form

$$f_0(E_{n,m,k_z}) = 8\sqrt{\pi}(n_e a_d^3)\sqrt{\delta_T}\beta w^{-1}\sinh(\delta_T w\beta^{-1})$$
$$\times\exp\left(-\delta_T\frac{E_{n,m,k_z}}{E_d}\right), \quad (34)$$

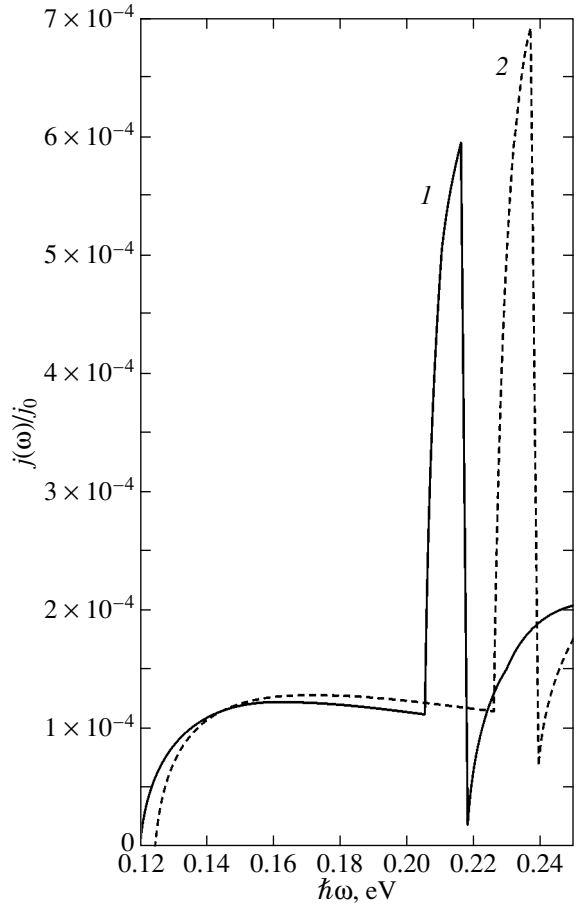

Fig. 3. Spectral dependences of the drag current density $j(\omega)/j_0$ (in relative units) at the parameters $|E_i| = 5.5 \times 10^{-2}$ eV, $n_\lambda = 1.4 \times 10^5$ cm^{-1}, $2L = 71.6$ nm, $U_0 = 0.2$ eV, $n_e = 1.36 \times 10^{16}$ cm^{-3}, $n_i = 2.7 \times 10^{15}$ cm^{-3}, $\lambda_s = 28.6$ nm, and $T \approx 7$ K. Magnetic induction B: (*1*) 10 and (*2*) 12 T.

where n_e is the electron concentration, $\delta_T = E_d/(kT)$, and T is the temperature.

Let us consider the situation where $\delta_T = 1$. For an InSb quantum wire, this case corresponds to $T \approx 7$ K and the impurity states can be considered completely filled; i.e., in relationship (31), we have $f_0(-E_d\eta_B^2) = 1$. Hence, with allowance made for expressions (33) and (34), relationship (31) for the drag current density takes the form

$$
\begin{aligned}
j(\omega) &= j_0 L^{*2} n_\lambda a_d (n_i a_d^3)^{-1}\left(\frac{\lambda_s}{a_d}\right)^{-2} \\
&\times \beta^2 w^3 X\left[\zeta\left(\frac{3}{2}, \frac{\beta\eta_B^2}{2w} + \frac{1}{2}\right)\right]^{-1} \\
&\times \left|1 + \frac{1}{\sqrt{2}a^*}\left(\frac{\lambda_s}{a_d}\right)\zeta\left(\frac{1}{2}, \frac{1}{2} - \frac{\beta(X-\eta_B^2)}{2w}\right)\right|^2 \\
&\times \left[\sum_{n=0}^{N_1}\left(\frac{\beta(X-\eta_B^2)}{2w} - n - \frac{1}{2}\right)^{-1/2}\right]^{-1} \\
&\times [1 - 8\sqrt{\pi}(n_e a_d^3)\sqrt{\delta_T}\beta w^{-1}\sinh(\delta_T w\beta^{-1}) \\
&\times \exp[-\delta_T(X-\eta_B^2)]]\sum_{n=0}^{N}(n+1) \\
&\times \sum_{m=-1}^{1}\delta_{|m|,1}\theta\left(X - \eta_B^2 - \frac{m}{a^{*2}} - \frac{w}{\beta}(2n + |m| + 1)\right) \\
&\times \frac{\sqrt{X - \eta_B^2 - \frac{m}{a^{*2}} - \frac{w}{\beta}(2n + |m| + 1)}}{(\beta(X - ma^{*-2}) - |m|w)^2(\beta(X - ma^{*-2}) + (2 - |m|)w)^2} \\
&\times \left[\frac{2\beta(X - ma^{*-2})}{(\beta(X - ma^{*-2}) - |m|w)(\beta(X - ma^{*-2}) + (2 - |m|w))}\right. \\
&\left. - \beta^{-1}X^{-1}\right],
\end{aligned}
\tag{35}
$$

where $j_0 = -4\pi^{-3}\lambda_0^2\alpha^* N_0|e|a_d^4 I_0 q_z$.

Now, we estimate the drag current density for an InSb quantum wire. For this purpose, we use the following numerical parameters in relationship (35): $E_i = 0.06$ eV, $L \approx 43$ nm, $n_\lambda = 1.4 \times 10^5$ cm^{-1}, $n_i = 2.7 \times 10^{15}$ cm^{-3}, $n_e = 1.4 \times 10^{16}$ cm^{-3}, $U_0 = 0.2$ eV, $\lambda_s \approx 29$ nm, $h\nu = 0.21$ eV, and $B = 10$ T. As a result, we obtain $j(\omega) \approx (1.7 \times 10^{-18} N_0)$ A/m^2. In the case when $N_0 = 10^{15}$ cm^{-3}, we have $j(\omega) \approx 1.7 \times 10^{-1}$ A/cm^2, which is one order of magnitude greater than the drag current density in a semiconductor single quantum well in the absence of a magnetic field [18]. Figure 3 shows the spectral dependences of the drag current density j/j_0 of one-dimensional electrons (in relative units) upon photoionization of $D^{(-)}$ centers in a longitudinal magnetic field. As can be seen from Fig. 3, the spectral dependence of the drag current density is characterized by a Zeeman doublet with a clear beak-shaped peak associated with the optical transitions of electrons from the $D^{(-)}$ states to the states with the magnetic quantum number $m = 1$. As the magnitude of the magnetic field increases, the beak shifts to the short-wavelength range of the spectrum and the beak height increases (curves *1*, *2*). The distance between the band and the peak in the doublet is equal to $\hbar\omega_B$, and the mean period of the occurrence of the doublet is $\hbar\Omega$; i.e., it is determined by the hybrid frequency. It can also be seen from Fig. 3 that, as the magnetic field changes by 2 T, when one goes from curve *1* to curve *2*, the wavelength corresponding to the beak decreases by approximately 10^4 Å. This shows promise for the creation of photodetectors on the basis of the photon drag effect in one-dimensional semiconductor structures with sensitivity controlled in a magnetic field.

The proposed theory of the impurity photon drag effect in a longitudinal magnetic field can form a basis for the design of laser radiation detectors. Since the drag current density j is proportional to I_0 [see formula (35)], these detectors can possibly determine the energy characteristics of laser pulses, in particular, the pulse power.

Unfortunately, as far as we know, there has been no experimental work dealing with the photon drag effect of charge carriers in semiconductor low-dimensional systems, in particular, involving impurity centers. However, it seems likely that the level of δ-doping technology (see review in [9]) can provide a means for setting up the above problem. It should also be noted that the high sensitivity of the photon drag effect to the energy spectrum, the relaxation mechanism of charge carrier momenta, and the type of optical transitions is of interest from the standpoint of the theoretical physics of semiconductor quantum-confined structures.

Let us now estimate the sensitivity G of a photodetector operating on the basis of the photon drag effect of one-dimensional electrons in a longitudinal magnetic field. According to Agafonov *et al.* [20], the sensitivity can be represented by the formula $G = V/W$, where V is the photovoltage, $W = I_0 h\nu S$ is the power of radiation incident on the photodetector, ν is the frequency of the light wave, and S is the cross-sectional area of the light beam. In the free-running mode, the photovoltage V can be found from the condition that the drag current in the given direction is equal to the corre-

sponding conduction current. As a result, the expression for G takes the form

$$G = \frac{V}{W} = \frac{S\rho_0}{S_0 W}\int_0^{L_{QW}} j\,dz \approx \frac{\rho_0 L_{QW} j}{I_0 S_0 \hbar\nu}, \qquad (36)$$

where S_0 is the cross-sectional area of the quantum wire and ρ_0 is the resistivity of the quantum wire material.

For a semiconductor structure consisting of an InSb quantum wire, we use the following parameters in relationship (36): $S_0 \sim L^2 \approx 1.8 \times 10^{-11}$ cm^2, $I_0 h\nu = 10^{10}$ W/m^2, $L_{QW} \approx 7.2 \times 10^3$ nm, $B = 10$ T, and $\rho_0 \sim 10^{-4}\ \Omega$ m. For $\lambda \approx 6 \times 10^4$ Å, we obtain $G \approx 6.8 \times 10^{-2}$ V/W.

Thus, the photon drag effect of one-dimensional electrons in a longitudinal magnetic field is quite accessible for experimental observation.

REFERENCES

1. F. T. Vas'ko, Fiz. Tekh. Poluprovodn. (Leningrad) **19** (7), 1319 (1985) [Sov. Phys. Semicond. **19**, 808 (1985)].
2. R. Ya. Rasulov, Yu. E. Salenko, T. Éski, and A. Tukhtamatov, Fiz. Tverd. Tela (St. Petersburg) **40** (9), 1710 (1998) [Phys. Solid State **40**, 1555 (1998)].
3. V. I. Belyavskiĭ, Yu. V. Kopaev, and N. V. Kornyakov, Usp. Fiz. Nauk **166** (4), 447 (1996) [Phys. Usp. **39**, 415 (1996)].
4. V. D. Kulakovskiĭ and L. V. Butov, Usp. Fiz. Nauk **165** (2), 229 (1995) [Phys. Usp. **38**, 219 (1995)].
5. J. K. Jain and S. A. Kivelson, Phys. Rev. Lett. **60** (15), 1542 (1988).
6. M. Y. Azbel, Phys. Rev. B **43** (3), 2435 (1991).
7. V. D. Krevchik and R. V. Zaĭtsev, Fiz. Tverd. Tela (St. Petersburg) **43** (3), 504 (2001) [Phys. Solid State **43**, 522 (2001)].
8. A. A. Pakhomov, K. V. Khalipov, and I. N. Yassievich, Fiz. Tekh. Poluprovodn. (St. Petersburg) **30** (8), 1387 (1996) [Semiconductors **30**, 730 (1996)].
9. L. D. Landau and E. M. Lifshitz, *Course of Theoretical Physics*, Vol. 3: *Quantum Mechanics: Non-Relativistic Theory*, 3rd ed. (Nauka, Moscow, 1974; Pergamon, New York, 1977).
10. I. S. Gradshteyn and I. M. Ryzhik, *Table of Integrals, Series, and Products*, 4th ed. (Fizmatgiz, Moscow, 1962; Academic, New York, 1980).
11. A. I. Baz', Ya. B. Zel'dovich, and A. M. Perelomov, *Scattering, Reactions, and Decays in Nonrelativistic Quantum Mechanics*, 2nd ed. (Nauka, Moscow, 1971; Israel Program for Scientific Translations, Jerusalem, 1966).
12. Yu. N. Demkov and G. F. Drukarev, Zh. Éksp. Teor. Fiz. **49**, 257 (1965) [Sov. Phys. JETP **22**, 182 (1965)].
13. Yu. N. Demkov and V. N. Ostrovskiĭ, *Zero-Range Potentials and Their Applications in Atomic Physics* (Leningr. Gos. Univ., Leningrad, 1975; Plenum, New York, 1988).
14. G. Bastard, Phys. Rev. B **24** (8), 4714 (1981).
15. S. Huant, S. P. Najda, and B. Etienne, Phys. Rev. Lett. **65** (12), 1486 (1999).
16. P. Antosik, J. Mikusinski, and R. Sikorski, *Theory of Distributions: Sequential Approach* (PWN, Warsaw, 1973; Mir, Moscow, 1976).
17. V. A. Geĭler, V. A. Margulis, and L. I. Filina, Zh. Éksp. Teor. Fiz. **113** (4), 1376 (1998) [JETP **86**, 751 (1998)].
18. V. D. Krevchik and É. Z. Imamov, Fiz. Tekh. Poluprovodn. (Leningrad) **17** (7), 1235 (1983) [Sov. Phys. Semicond. **17**, 780 (1983)].
19. A. Ya. Shik, Fiz. Tekh. Poluprovodn. (St. Petersburg) **26** (7), 1161 (1992) [Sov. Phys. Semicond. **26**, 649 (1992)].
20. V. G. Agafonov, P. M. Valov, B. S. Ryvkin, and I. D. Yaroshetskiĭ, Fiz. Tekh. Poluprovodn. (Leningrad) **7** (12), 2316 (1973) [Sov. Phys. Semicond. **7**, 1540 (1973)].

Translated by O. Moskalev

Physics of the Solid State, Vol. 45, No. 7, 2003, pp. 1342–1346. Translated from Fizika Tverdogo Tela, Vol. 45, No. 7, 2003, pp. 1280–1283.

LOW-DIMENSIONAL SYSTEMS AND SURFACE PHYSICS

Quantum-Confined Stark Effect and Intraband Transitions in a Semiconductor Spherical Layer

V. A. Arutyunyan

Gyumri Educational Center, State Engineering University of Armeniya, Gyumri, 377503 Armeniya

Received August 6, 2002; in final form, November 26, 2002

Abstract—The effect of an external homogeneous electric field on the states of charge carriers in a size-quantized spherical layer is considered. An explicit dependence of the energy shift on the external field strength and the geometric sizes of the sample is obtained, and the electro-optical absorption coefficient for intraband dipole transitions is calculated. © *2003 MAIK "Nauka/Interperiodica".*

1. INTRODUCTION

At present, the optical and electro-optical properties of quasi-zero-dimensional structures with spherical symmetry, such as quantum dots (see the review by Gaponenko [1]) and multilayer spherical nanoheterostructures [2–6], have been studied intensively. This stems from the fact that heterophase systems are very promising for use in designing new elements and devices in optoelectronics. It is clear that a necessary stage of the comprehensive study of these structures is investigation of the physical properties of a single nanocrystalline spherical layer. From the physical and practical points of view, such a nanocrystal is interesting, first and foremost, because it exhibits a unique combination of properties inherent in size-quantized films and spherical quantum dots and, consequently, can be used both in a pure form and as a constituent of multilayer spherical nanoheterostructures with required characteristics. In this connection, it is of particular interest to investigate the effect of an external electric field on the states of charge carriers in a nanocrystalline spherical layer. There are many experimental and theoretical works concerned with the Stark splitting of levels and electro-optical phenomena in size-quantized films. A number of papers [8–10] deal also with the quantum-confined Stark effect in quantum spherical dots. In particular, Ekimov *et al.* [8] and Nomura and Kobayashi [9] experimentally revealed a dependence of the Stark shift in the energy levels on the geometric sizes of the sample due to quantizing of the motion of electrons and holes. Pokutniĭ [10] developed a theory of the Stark effect in quantum dots under conditions where a separate quantization of the motion of each of the charge carriers can be accompanied by the creation of a bulk exciton from an electron–hole pair. Moreover, Pokutniĭ [10] proposed a new electro-optical method for determining the critical sphere size above which the generation of a three-dimensional exciton in this sphere becomes possible. Among the wide variety of optoelectronic phenomena in low-dimensional semiconductors, intraband optical transitions between quantum-confined states in different quantum wells are of the greatest interest owing to their possible use in the design of infrared detectors, high-speed modulators, emitters, and cascade lasers [11].

The goal of this work was to analyze theoretically the evolution of the energy spectrum of charge carriers in a size-quantized spherical layer under the action of a homogeneous electric field and to investigate how the external field affects the band of intraband optical absorption.

2. ELECTRONIC STATES IN A LAYER

Let us consider the situation where a layer is sufficiently thin and the quantum confinement is very pronounced, i.e., when the thickness L of the layer is substantially less than the Bohr radius a_0 of a three-dimensional exciton. However, from the practical standpoint, it is more appropriate to use a spherical layer of large radius when the thickness L of the layer is also appreciably less than the radii of the core R_1 and the external shell R_2; that is,

$$\frac{L^2}{R_1^2} \ll 1 \quad (L = R_2 - R_1). \tag{1}$$

In this case, the layer under consideration can be adequately described in the framework of the model of a quantum well rolled into a sphere [12]:

$$U(r) = \begin{cases} 0, & R_1 \le r \le R_2 \\ \infty, & r \ge R_2, \quad r \le R_1. \end{cases} \tag{2}$$

Within this model (see Appendix) in the approximation of the isotropic effective mass μ, for the energy and the

1063-7834/03/4507-1342$24.00

envelopes of the wave functions for unperturbed single-electron states in the layer, we obtain the relationships

$$E_{n,l}^{(0)} = \frac{\pi^2\hbar^2 n^2}{2\mu L^2} + \frac{\hbar^2 l(l+1)}{2\mu R_0^2} \equiv E_{1,0}^{(0)} n^2 + E_l(R_0) \equiv E_{\text{conf}} + E_{\text{rot}}, \tag{3}$$

$$\psi_{n,l,m}^{(0)}(r,\vartheta,\varphi) = \phi_n^{(0)}(r) Y_{l,m}(\vartheta,\varphi) \equiv \sqrt{\frac{2}{L}}\frac{1}{r}\sin\pi n/L(r-R_1) Y_{l,m}(\vartheta,\varphi), \tag{4}$$

where n, l, and m are the radial, orbital, and azimuthal quantum numbers, respectively; $Y_{l,m}(\vartheta,\varphi)$ are the normalized spherical functions in the spherical coordinate system; r, ϑ, and φ are the spherical coordinates; and R_0 is the effective rotational radius, which is determined from the condition

$$U_l(R_0) = \frac{1}{2}[U_l(R_1) + U_l(R_2)]. \tag{5}$$

Now, we assume that an external homogeneous electric field with the strength $\mathbf{F}$ is directed along the z axis: $\mathbf{F} = \mathbf{F}(0, 0, F)$. In the general case, when the permittivities of the core ε_1, the layer ε_2, and the external shell ε_3 differ from one another, we derive the following expression for the perturbation $\hat{V}$ related to the electrostatic potential in the layer [13]:

$$\hat{V} = qF\left(\text{Br} + \frac{C}{r^2}\right)\cos\vartheta,$$
$$B = \frac{C}{R_1^3}\frac{\varepsilon_3 + 2\varepsilon_2}{\varepsilon_2 - \varepsilon_1}; \tag{6}$$
$$C = \frac{3\varepsilon_1(\varepsilon_2 - \varepsilon_1)R_1^3 R_2^3}{(\varepsilon_2 + 2\varepsilon_1)(\varepsilon_3 + 2\varepsilon_2)R_2^3 + 2(\varepsilon_1 - \varepsilon_2)(\varepsilon_2 - \varepsilon_3)R_1^3}.$$

The external field can be considered a perturbation under the condition

$$\frac{qFL}{\varepsilon} \ll E_{1,0}^{(0)}, \tag{7}$$

where q is the particle charge, $\varepsilon = (2\varepsilon_{2,3} + \varepsilon_{2,1})/3$, $\varepsilon_{2,3} = \varepsilon_2/\varepsilon_3$, $\varepsilon_{2,1} = \varepsilon_2/\varepsilon_1$, and $E_{1,0}^{(0)}$ is the ground-state energy of the particle in the layer in the absence of the external electric field, i.e., in the case when the energy imparted to the particle by the field is considerably less than the quantum-confinement energy.

It follows from expressions (6) that the linear Stark effect in the system is absent. For the second-order correction $\Delta E_{n,l}^{(2)}$ to the energy of an arbitrary state $|n, l, m\rangle$, we can write in the general form,

$$\Delta E_{n,l}^{(2)} = |V_{l,l-1}|^2 \sum_{n \neq n'} \frac{|V_{n,n'}|^2}{E_{n,l}^{(0)} - E_{n',l-1}^{(0)}} + |V_{l,l+1}|^2 \sum_{n \neq n'} \frac{|V_{n,n'}|^2}{E_{n,l}^{(0)} - E_{n',l+1}^{(0)}}, \tag{8}$$

where $V_{n,n'}$ is the matrix element of the operator determined by expression (6), which is constructed using the radial wave functions $\Phi_n^{(0)}(r)$ described by formula (4); that is,

$$V_{n,n'} = q\frac{FL}{\pi^2}\frac{8nn'}{(n^2 - n'^2)^2}\left[-B + C\frac{R_1^3 + R_2^3}{R_1^3 R_2^3}\right] \equiv V(R_1, R_2)\frac{nn'}{(n^2 - n'^2)^2}qFL. \tag{9}$$

For the matrix elements $V_{l,l\pm1}$, we have

$$V_{l,l\pm1} = \begin{cases} i\sqrt{\dfrac{(l+m)(l-m)}{(2l+1)(2l-1)}}, & l \longrightarrow l-1 \quad (l = 1, 2, \ldots) \\ -i\sqrt{\dfrac{(l+m+1)(l-m+1)}{(2l+3)(2l+1)}}, & \\ l \longrightarrow l+1 \quad (l = 0, 1, 2, \ldots). & \end{cases} \tag{10}$$

Upon substituting expressions (9) and (10) into formula (8) and summing over n' [14], the second-order correction $\Delta E_{n,l}^{(2)}$ can be represented as

$$\Delta E_{n,l}^{(2)} = \frac{q^2F^2L^2}{48n^2E_{n,0}^{(0)}}|V(R_1, R_2)|^2(f_{n,l} + g_{n,l}), \tag{11}$$

where $f_{n,l}$ and $g_{n,l}$ have the form

$$f_{n,l} = \left(1 - \frac{15}{\pi^2 n^2}\right)(|V_{l,l-1}|^2 + |V_{l,l+1}|^2), \tag{12}$$

$$g_{n,l} = \left(\frac{1}{5} + \frac{1}{2\pi^2 n^2} - \frac{21}{\pi^4 n^4}\right)\left(\frac{L}{R_0}\right)^2 \times [(l+1)|V_{l,l+1}|^2 - l|V_{l,l-1}|^2]. \tag{13}$$

In the general form, the expression for the perturbed part of the wave function $\psi^{(1)}_{n,l,m}(r, \vartheta, \varphi)$ can be written as

$$\psi^{(1)}_{n,l,m}(r, \vartheta, \varphi) \cong Y_{l,m}(\vartheta, \varphi)\cos\vartheta \times \frac{1}{E^{(0)}_{1,0}} \sum_{n \neq n'} \frac{V_{n,n'}\Phi^{(0)}_{n'}(r)}{n^2 - n'^2}. \quad (14)$$

3. INTRABAND TRANSITIONS IN A HOMOGENEOUS ELECTRIC FIELD

According to Ansel'm [15], for a perturbation associated with the action of a light wave, we can write the relationship

$$\hat{A} = \frac{eA_0}{m_0 c}(\mathbf{e}\hat{\mathbf{p}}), \quad (15)$$

where A_0 is the amplitude of the light wave, m_0 is the mass of the free electron, e is the charge of the free electron, c is the velocity of light in free space, and $\hat{\mathbf{p}}$ is the three-dimensional operator of the momentum. It is assumed that the incident wave with the frequency ω is linearly polarized and the polarization vector $\mathbf{e}$ is directed along the Z axis. Now, we calculate the dipole matrix elements of operator (15) for the intraband transitions $i \longrightarrow f$. Upon integrating over the azimuthal angle, we obtain the selection rule for the azimuthal quantum number: $\Delta m = 0$. This rule is common to all the transitions $|n_i, l_i, m_i\rangle \longrightarrow |n_f, l_f, m_f\rangle$. The selection rules for the orbital quantum number are as follows: $\Delta l = \pm 1$ for the matrix elements of the zeroth order of smallness $M^{(0)}_{f,i}$ and $\Delta l = 0, \pm 2$ for the matrix elements of the first order of smallness $M^{(1)}_{f,i}$. For these matrix elements, we obtain the following expressions:

$$M^{(0)}_{f,i} \cong \hbar \frac{|e|A_0}{m_0 cL} A_{l,l\pm 1} \times \begin{cases} \left(l + \frac{1}{2} \pm \frac{1}{2}\right)\ln\frac{R_2}{R_1}, & n_f = n_i;\ (l \equiv l_i) \\ \frac{4n_f n_i}{n_f^2 - n_i^2}, & n_f \pm n_i = \pm(2k+1) \\ 0, & n_f \pm n_i = \pm 2k, \end{cases} \quad (16)$$

$$M^{(1)}_{f,i} \cong \frac{4\hbar e^2 A_0}{m_0 cL}\frac{FL}{E^{(0)}_{1,0}} V(R_1, R_2)\frac{n_f n_i}{n_f^2 - n_i^2}\left(\frac{1}{n_f^2} + \frac{1}{n_i^2}\right) \times \begin{cases} |V_{l,l+1}|^2 + |V_{l,l-1}|^2, & l_f = l_i = l;\ n_f \neq n_i \\ V_{l,l\pm 1}V_{l,l\pm 2}, & l_f = l \pm 2;\ n_f \neq n_i \\ 0, & n_f = n_i, \end{cases} \quad (17)$$

where $k = 0, 1, 2, \ldots$. Hereafter, $A_{l_i,l_f} \equiv V_{l_i,l_f}$, which follows from relationships (4), (6), and (15). The form of the matrix elements $V_{l,l\pm 2}$ is well known from [16], and we will not present them explicitly. According to the selection rules, the final expression for the absorption coefficient $\alpha(\omega)$ does not involve interference terms of the $M^{(0)}_{f,i}M^{(1)}_{f,i}$ type and the coefficient $\alpha(\omega)$ can be represented as the sum of two components, for which the explicit form is given incompletely; that is,

$$\alpha(\omega) = \alpha^{(0)}(\omega) + \alpha^{(1)}(\omega),$$

$$\alpha^{(0)}(\omega) \sim \sum_{f,i} \left|M^{(0)}_{f,i}\right|^2 \delta(E_f - E_i \mp \hbar\omega), \quad (18)$$

$$\alpha^{(1)}(\omega) \sim \sum_{f,i} \left|M^{(1)}_{f,i}\right|^2 \delta(E_f - E_i \mp \hbar\omega),$$

where ω is the frequency of the light wave, $\delta(x)$ is the delta function, and

$$E_{f,i} = E^{(0)}_{f,i} + \Delta E^{(2)}_{f,i}. \quad (19)$$

In relationships (18), the upper sign corresponds to absorption and the lower sign, to photon emission in the course of intraband dipole transitions.

4. RESULTS AND DISCUSSION

The following inferences can be made in the framework of the proposed model.

(1) The band of intraband optical absorption consists of two series, namely, the main series $\alpha^{(0)}(\omega)$ and the field satellite $\alpha^{(1)}(\omega)$ with different threshold frequencies and different selection rules, which excludes superposition of these two series.

(2) For diagonal transitions with respect to the radial quantum number, the frequencies of absorption (emission) for a given orbital quantum number l differ from one another by the same value of $\Delta\omega$:

$$\Delta\omega = \frac{1}{\hbar}\left\{\frac{\hbar^2}{\mu R_0^2} + \Delta E^{(2)}_{n,l+1} + \Delta E^{(2)}_{n,l-1}\right\}.$$

In the absence of the external electric field, when $n_f = n_i \equiv n$, the resultant absorption for a given orbital quantum number l would be observed at equidistant frequencies

$$\omega_l = \frac{\hbar l}{\mu R_0^2}.$$

(3) The diagonal transitions with respect to the radial quantum number are also associated with the finiteness of the sample size. It follows from formulas (11), (16), and (18) that, when $R_1, R_2 \longrightarrow \infty$, not only the transitions between the states with $n_f = n_i$ are absent but the

Table

Material	a, nm	ε_0	E_g, eV	μ_c/m_0	μ_v/m_0	U^c, eV	U^v, eV	ΔU^c, eV	ΔU^v, eV	a_{ex}
CdS	0.5818	9.1	2.5	0.2	0.7	−3.8	−6.3	–	–	≈3
HgS	0.5851	18.2	0.5	0.036	0.044	−5	−5.5	1.2	−0.8	≈50

Note: μ_c and μ_v are the effective masses of the charge carriers; a is the lattice constant; E_g is the band gap of the bulk sample; U_c is the conduction band bottom measured from the vacuum level; U^v is the valence band top; ΔU^c and ΔU^v are the energy discontinuities for the conduction and valence bands, respectively; a_{ex} is the Bohr radius of a three-dimensional exciton in the given material; and ε is the static permittivity.

complete series $\alpha^{(0)}(\omega)$ transforms into a band characteristic of intraband absorption in a plane-parallel film in an external homogeneous electric field [7].

(4) Compared to the series $\alpha^{(0)}(\omega)$, the series $\alpha^{(1)}(\omega)$ is characterized by an additional modulation due to the field factor:

$$\frac{FL}{E^{(0)}_{1,0}} V(R_1, R_2)\left(\frac{1}{n_f^2} + \frac{1}{n_i^2}\right).$$

Moreover, the intensity of the transitions in this series depends on the effective mass of the charge carriers in the band, which is also associated with the external electric field.

Thus, the intraband absorption under the given conditions substantially depends on the external field. The frequency and the magnitude of the intraband absorption can be controlled by varying the field strength and the geometric sizes of the sample.

APPENDIX

Let us apply the model approach developed in this work to the heterostructure CdS/HgS/CdS. The table presents selected characteristics for the β modifications of CdS and HgS semiconductor crystals (data are taken from [2–4, 17, 18]).

A.1. APPLICABILITY OF THE PROPOSED MODEL

We consider an HgS layer of thickness $L \sim 5$–10 nm. In this case, the Coulomb interaction can be disregarded ($L^2/a_{ex}^2 \sim 0.01$–0.04) and the quantum confinement of charge carriers in the layer is very pronounced. If the radius of the core is taken as $R_1 \sim 15$–30 nm, size effects for charge carriers are absent in the core (and in the external shell) ($R_1/a_{ex} \sim 5$–10). At the same time, conditions (1) are satisfied ($L^2/R_1^2 \sim 0.1$) and the separation of the particle motion into radial and rotational components is justified. For the chosen sizes of the system, the energies E_{conf} and E_{rot} for electrons c and holes v are estimated as follows:

(a) $L = 5$, $R_1 = 15$, $R_2 = 20$ nm;

$$E^c_{conf} \approx 42.4 \times 10^{-3}, \quad E^v_{conf} \approx 34.7 \times 10^{-3} \text{ eV}; \quad \text{(A.1.1)}$$
$$E^c_{rot} \approx 3.7 \times 10^{-3}, \quad E^v_{rot} \approx 3 \times 10^{-3} \text{ eV};$$

(b) $L = 10$, $R_1 = 30$, $R_2 = 40$ nm;

$$E^c_{conf} \approx 10.6 \times 10^{-3}, \quad E^v_{conf} \approx 8.7 \times 10^{-3} \text{ eV}; \quad \text{(A.1.2)}$$
$$E^c_{rot} \approx 1 \times 10^{-3}, \quad E^v_{rot} \approx 0.82 \times 10^{-3} \text{ eV}.$$

A comparison of the quantum-confinement energies of the charge carriers $E^{c,v}_{conf}$ [see formulas (A.1.1) and (A.1.2)] with the band discontinuities $\Delta U^{c,v}$ presented in the table clearly demonstrates that, in the case when the states are not strongly excited, the model of a quantum well specified by expression (2) is also valid, to sufficient accuracy, for the chosen composition.

A.2. THE EXTERNAL FIELD AS A PERTURBATION

For the chosen composition, we have $\varepsilon = (2\varepsilon_{2,3} + \varepsilon_{2,1})/3 = 2$; hence, condition (7) takes the form

$$qFL \ll 2E_{conf}. \quad \text{(A.2.1)}$$

For the strength F, we obtain the following limitations: (a) at $L = 5$ nm, $F \ll 1.7 \times 10^5$ V/cm, and (b) at $L = 10$ nm, $F \ll 4.2 \times 10^4$ V/cm. In other words, when the layer thickness L falls in the range 5–10 nm, the upper limits for the external field as a perturbation can be taken as $F \sim 10^4$ and $F \sim 10^3$ V/cm, respectively.

A.3. ESTIMATION OF THE STARK SHIFT

By virtue of the relationships $\varepsilon_2 = 2\varepsilon_1 = 2\varepsilon_3$ for the permittivities of the core, the layer, and the external shell, the dependence of the perturbation $V(R_1, R_2)$ on the radii R_1 and R_2 in formula (9) turns out to be very weak. As a result, the second-order correction to the ground state ($n = 1$, $l = 0$), which is of principal interest,

can be represented by the following rather exact working formula:

$$\Delta E_{1,0}^{(2)} \approx 0.2\mu/\hbar^2 (qFL^2)^2. \quad \text{(A.3.1)}$$

For $L = 5$ nm and $F = 2 \times 10^4$ V/cm, the second-order correction $\Delta E_{1,0}^{(2)}$ is estimated as

$$\Delta E_{1,0}^{(2)} \approx 2.5 \times 10^{-4} \text{ eV}.$$

The same result can be obtained by direct calculations according to formula (11).

In the case when the field strength F and the thickness L vary in the ranges allowed by the approximation used, the key parameter in experiments is the quantity FL^2. The quantitative results of the experiment substantially depend on this parameter and, hence, are very sensitive to variations in both the strength of the external field and the geometric sizes of the system.

REFERENCES

1. S. V. Gaponenko, Fiz. Tekh. Poluprovodn. (St. Petersburg) **30**, 577 (1996) [Semiconductors **30**, 315 (1996)].
2. J. W. Haus, H. S. Zhou, I. Honma, and H. Komiyama, Phys. Rev. B **47** (3), 1359 (1993).
3. D. Schooss, A. Mews, A. Eychmuller, and H. Weller, Phys. Rev. B **49** (24), 17072 (1994).
4. A. Mews, A. V. Kadavanich, U. Banin, and A. P. Alivasatos, Phys. Rev. B **53** (20), 13242 (1996).
5. N. V. Tkach, Fiz. Tverd. Tela (St. Petersburg) **39**, 1109 (1997) [Phys. Solid State **39**, 995 (1997)].
6. N. V. Tkach, V. A. Holovatsky, and O. N. Voĭtsekhovskaya, Fiz. Tekh. Poluprovodn. (St. Petersburg) **34**, 602 (2000) [Semiconductors **34**, 583 (2000)].
7. S. Schmitt-Rink, D. S. Chemia, and D. A. B. Miller, Adv. Phys. **38**, 89 (1989).
8. A. I. Ekimov, P. A. Skvortsov, and T. V. Shubina, Zh. Tekh. Fiz. **59** (3), 202 (1989) [Sov. Phys. Tech. Phys. **34**, 371 (1989)].
9. S. Nomura and T. Kobayashi, Solid State Commun. **74** (10), 1153 (1990).
10. S. I. Pokutniĭ, Fiz. Tekh. Poluprovodn. (St. Petersburg) **34**, 1120 (2000) [Semiconductors **34**, 1079 (2000)].
11. É. P. Sinyavskiĭ and S. M. Sokovnich, Fiz. Tekh. Poluprovodn. (St. Petersburg) **33**, 828 (1999) [Semiconductors **33**, 761 (1999)]; B. F. Levine, K. K. Choi, C. C. Bethea, *et al.*, Appl. Phys. Lett. **50**, 1092 (1987); J. Faist, F. Capasso, and D. L. Sinco, Science **264**, 553 (1994).
12. V. V. Rotkin and R. A. Suris, Fiz. Tverd. Tela (St. Petersburg) **36** (12), 3569 (1994) [Phys. Solid State **36**, 1899 (1994)].
13. W. R. Smythe, *Static and Dynamic Electricity*, 2nd ed. (McGraw-Hill, New York, 1950; Inostrannaya Literatura, Moscow, 1954).
14. A. P. Prudnikov, Yu. A. Brychkov, and O. I. Marichev, *Integrals and Series* (Nauka, Moscow, 1981; Gordon and Breach, New York, 1986).
15. A. I. Ansel'm, *Introduction to the Theory of Semiconductors* (Nauka, Moscow, 1978).
16. L. D. Landau and E. M. Lifshitz, *Course of Theoretical Physics*, Vol. 3: *Quantum Mechanics: Non-Relativistic Theory*, 3rd ed. (Nauka, Moscow, 1974; Pergamon, New York, 1977).
17. N. V. Tkach, A. M. Makhanets, and G. G. Zegrya, Fiz. Tekh. Poluprovodn. (St. Petersburg) **36**, 543 (2002) [Semiconductors **36**, 511 (2002)].
18. *Tables of Physical Data: A Reference Book*, Ed. by I. K. Kikoin (Atomizdat, Moscow, 1976).

Translated by O. Moskalev

Physics of the Solid State, Vol. 45, No. 7, 2003, pp. 1347–1354. Translated from Fizika Tverdogo Tela, Vol. 45, No. 7, 2003, pp. 1284–1291.

LOW-DIMENSIONAL SYSTEMS AND SURFACE PHYSICS

Influence of Phonons on the Electronic Energy Spectrum of Small Semiconductor Quantum Dots in a Dielectric Matrix

N. V. Tkach and R. B. Fartushinskiĭ

Chernivtsi National University, Chernivtsi, 58012 Ukraine
e-mail: theormyk@chnu.cv.ua

Received November 27, 2002

Abstract—A diagrammatic technique developed for Green's functions with inclusion of multiphonon processes is used to investigate the electronic energy levels and the phonon replicas corresponding to them in a semiconductor quantum dot (QD) embedded in a dielectric matrix. It is shown, with reference to GaAs, CdSe, and CuCl quantum dots embedded in glass, that in the case of QD potential wells of a finite depth the shifts of the electronic energy levels decrease with decreasing QD size, irrespective of the strength of electron–phonon coupling in the nanoheterostructure. Theoretically calculated positions of the phonon replicas for CdSe in glass agree with the experimental data on Raman scattering. © *2003 MAIK "Nauka/Interperiodica"*.

1. INTRODUCTION

In developing the theory of electron–phonon interaction in low-dimensional systems [1–3], including quantum dots (QDs) [3–8], considerable attention has been given to the study of the effect of the nanosystem size on the lowest energy bands or ground levels renormalized by interaction with phonons.

Quantum dots with weak electron–phonon interaction have been studied using perturbation theory [3–5]. In this case, different mechanisms make virtually additive contributions to the shift of the ground level, which made it possible to investigate the effect of confined (L) and interface (I) phonons, as well as of intra- and interlevel interaction, on the electronic energy levels within different models of nanosystems. Emphasis was placed on the analysis of the influence of the QD size on the relative contributions from different mechanisms to the ground-level shift.

In nanosystems with intermediate and strong electron–phonon interactions, the contributions from different mechanisms to the electronic-level shifts are not additive and can be separated rather arbitrarily. In this case, different methods, models, and approximations have been used [8] to investigate the dependence of the phonon-induced shift of the electronic ground level on the QD size and the results obtained have been compared.

However, it should be noted that even if different methods give similar results for any QD size, this does not necessarily mean that the results are adequate for QDs of small radii. For example, it was shown in [5, 8] that, as the radius of a spherical semiconducting QD embedded in a dielectric medium is decreased, the shift of the electronic ground level in the nanosystem sharply increases irrespective of the strength of electron–phonon coupling. This result, being formally correct, is not adequate, because it was obtained in [5, 8] under the assumption that the potential well is infinitely deep, which is not the case for QDs of small sizes. On physical grounds, it is clear that, as the radius of a QD with an infinitely deep potential well is decreased, a quasiparticle in the well becomes localized to a greater extent and, hence, its interaction with phonons strengthens, causing the energy level shift to increase. However, in a real QD, the potential-well depth is finite; therefore, as the QD radius is decreased, the quasiparticle will become less localized and, hence, its interaction with phonons will be weaker, which will cause the electronic energy level shift to decrease. The objective of this paper is to substantiate this conclusion.

It should be noted that up to now, there has been no method enabling one to theoretically study the phonon replicas arising in the spectrum of a nanosystem as the result of the electron–phonon interaction, although such replicas have already been studied experimentally [3] (using, in particular, Raman scattering).

In this paper, we modify the diagrammatic technique for Green's functions in such a way as to effectively include both the electronic energy spectrum and virtual multiphonon processes. With this technique, we investigate the renormalization of no-phonon electronic energy levels and their phonon replicas in nanosystems consisting of spherical semiconducting QDs embedded in a dielectric medium in the case of arbitrarily strong electron–phonon interaction. Calculation of the electronic spectrum renormalized by interaction with L and I phonons at $T = 0$ is illustrated through the examples of semiconducting GaAs, CdSe, and CuCl quantum dots

1063-7834/03/4507-1347$24.00

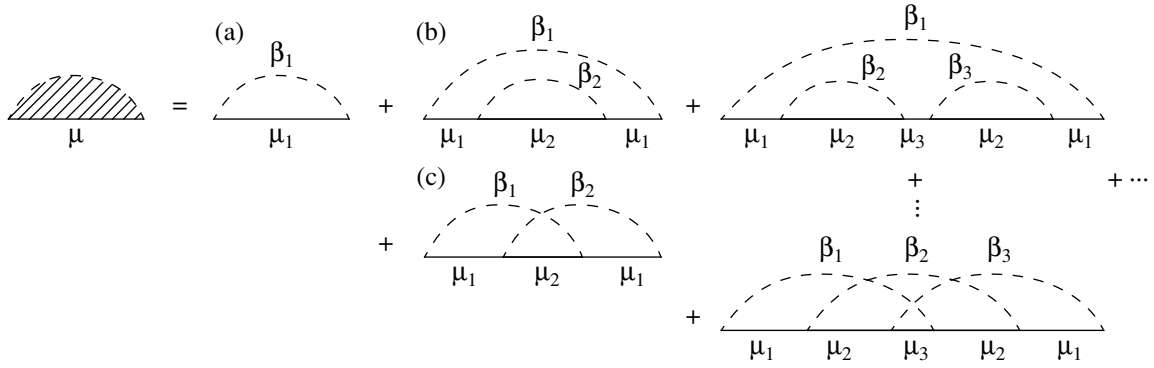

Fig. 1. Diagrammatic expansion of the self-energy.

in glass with weak, intermediate, and strong electron–phonon interactions, respectively.

The reasonable agreement, shown in this paper to be between the theoretically and experimentally determined electronic levels and their phonon replicas on the frequency scale, shows promise for extending our theory to the case of arbitrary temperatures in studying the excitonic QD spectrum. By applying the Kubo method to an exciton–phonon system interacting with an electromagnetic field, one will be able to calculate the Raman spectrum of a QD without considering the excitonic line width Γ as an adjustable parameter [9].

2. THE HAMILTONIAN, GREEN'S FUNCTIONS, AND THE SELF-ENERGY

The Hamiltonian of the electron–phonon system of a spherical semiconducting QD embedded in a dielectric matrix is a particular case of the Hamiltonian of a multilayered QD considered in [6, 7]. In those papers, electrons were treated in the effective-mass approximation and confined and interface phonons were described in terms of the dielectric-continuum model. Within these approximations, the second-quantized Hamiltonian of the electron–phonon system was found to be

$$H = \sum_{\mu} E_{\mu} a_{\mu}^{+} a_{\mu} + \sum_{\beta} \Omega_{\beta} (b_{\beta}^{+} b_{\beta} + 1/2) + \sum_{\mu_1 \mu_2 \beta} \varphi_{\mu_1 \mu_2}(\beta) a_{\mu_1}^{+} a_{\mu_2} (b_{\beta} + b_{\beta}^{+}). \quad (1)$$

Here, E_{μ} is the energy of an electron in a state characterized by quantum numbers $\mu\{p, l, m\}$, where $p = \{n, k\}$; n is the radial quantum number, which characterizes the discrete energy spectrum; $k\sqrt{2m_1 E}/\hbar$ $(E > 0)$ characterizes the continuous spectrum; m_1 is the electronic mass in the dielectric medium; and l and m are the orbital and magnetic quantum numbers, respectively. Ω_{β} is the phonon energy, with $\beta = \{\sigma, l, m\}$, where $\sigma = \{L, I^{\pm}\}$ characterizes confined and interface phonons. Comprehensive information on the energy spectrum and wave functions of quasiparticles, as well as on the polarization potentials and phonon spectrum, can be found in [6, 7]. It will be recalled that the energy spectrum of bare electrons was calculated for a potential well of a finite width using the effective-mass approximation and boundary conditions for which the wave functions and the probability flux densities are continuous at the boundary of the nanoheterostructure. The phonon spectrum and polarization potentials were calculated within the dielectric-continuum model with electrodynamic boundary conditions. In this approach, the energies of electrons and phonons, as well as their coupling constants

$$\varphi_{\mu_1, \mu_2}(\beta) = \Phi^{p_2 l_2 m_2}_{p_1 l_1 m_1}(\sigma l m) \quad (2)$$

are determined unambiguously from first principles; that is, fitting parameters are absent and only experimentally measurable quantities are involved: the effective masses and potential energies of electrons and the energies of optical phonons in the different media of the system and the dielectric constants of these media.

In order to investigate the electronic spectrum renormalized by interaction with phonons at low temperatures (strictly speaking, at $T = 0$), it is convenient to use Fourier transforms of the electron Green's functions that satisfy the Dyson equation:

$$G_{\mu}(\omega) = G_{\mu\mu}(\omega) = \{\omega - E_{\mu} - M_{\mu}(\omega)\}^{-1}, \quad (3)$$

where $M_{\mu}(\omega) \equiv M_{\mu\mu}(\omega)$ are the diagonal self-energy operators. In terms of the Pines diagrammatic technique [10], these operators are represented by an infinite series of diagrams, as presented in Fig. 1. According to this technique, the first three diagrams in Fig. 1 correspond to the expressions

$$\text{(a)} \longrightarrow \sum_{\mu_1 \beta_1} \frac{\varphi_{\mu\mu_1}(\beta_1)\varphi_{\mu_1\mu}(\beta_1)}{\omega - E_{\mu_1} - \Omega_{\beta_1}}, \quad (4)$$

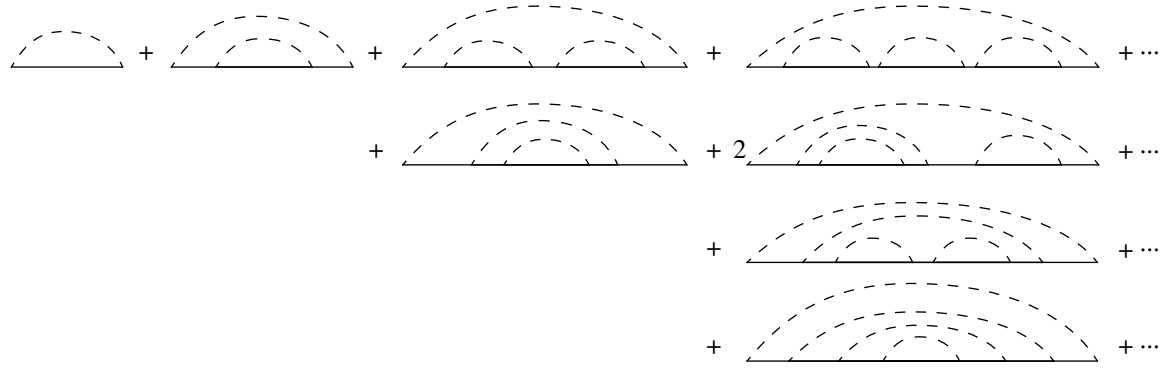

Fig. 2. Series of diagrams without phonon line crossings.

$$(b) \longrightarrow \sum_{\mu_1\mu_2\beta_1\beta_2} \frac{\varphi_{\mu\mu_1}(\beta_1)\varphi_{\mu_1\mu_2}(\beta_2)}{(\omega - E_{\mu_1} - \Omega_{\beta_1})} \times \frac{\varphi_{\mu_2\mu_1}(\beta_2)\varphi_{\mu_1\mu}(\beta_1)}{(\omega - E_{\mu_2} - \Omega_{\beta_1} - \Omega_{\beta_2})(\omega - E_{\mu_1} - \Omega_{\beta_1})}, \quad (5)$$

$$(c) \longrightarrow \sum_{\mu_1\mu_2\beta_1\beta_2} \frac{\varphi_{\mu\mu_1}(\beta_1)\varphi_{\mu_1\mu_2}(\beta_2)}{(\omega - E_{\mu_1} - \Omega_{\beta_1})} \times \frac{\varphi_{\mu_2\mu_1}(\beta_1)\varphi_{\mu_1\mu}(\beta_2)}{(\omega - E_{\mu_2} - \Omega_{\beta_1} - \Omega_{\beta_2})(\omega - E_{\mu_1} - \Omega_{\beta_2})}. \quad (6)$$

The Pines diagrammatic technique allows one to write out an analytical expression corresponding to an arbitrary diagram of the series presented in Fig. 1. However, the series itself cannot be described by a simple analytical expression. It is known [6, 7] that the series consisting of all diagrams without phonon line crossings (Fig. 2) can be summed analytically and is described by the integral equation

$$M_\mu^l(\omega) = \sum_{\mu_1\beta_1} \frac{|\varphi_{\mu\mu_1}(\beta_1)|^2}{\omega - E_{\mu_1} - \Omega_{\beta_1} - M_{\mu_1}^l(\omega - \Omega_{\beta_1})}, \quad (7)$$

which is equivalent to the nonterminating continued fraction (with sums or integrals)

$$M_\mu^l(\omega) = \sum_{\mu_1\beta_1} \frac{|\varphi_{\mu\mu_1}(\beta_1)|^2}{\omega - E_{\mu_1} - \Omega_{\beta_1} - \sum_{\mu_2\beta_2} \frac{|\varphi_{\mu_1\mu_2}(\beta_2)|^2}{\omega - E_{\mu_2} - \Omega_{\beta_1} - \Omega_{\beta_2} - \ldots} - \sum_{\mu_n\beta_n} \frac{|\varphi_{\mu_{n-1}\mu_n}(\beta_n)|^2}{\omega - E_{\mu_n} - \sum_{i=1}^{n} \Omega_{\beta_i} - \ldots}}. \quad (8)$$

While $M_\mu^l(\omega)$ includes virtual multiphonon processes, this quantity is only a lower estimate of the full self-energy, because in each order in perturbation theory the diagrammatic series in Fig. 2 contains only part of the diagrams of the exact series in Fig. 1. An upper estimate $M_\mu^u(\omega)$ can be found as follows. On physical grounds, it is clear that, at $T = 0$, the system contains only virtual phonons, which interact with an electron when they are emitted. Since real phonons are absent at $T = 0$ (the average occupation numbers for them are zero), there is no mechanism causing the electron lifetime in the discrete states to be finite in the electron–phonon system. Mathematically, this is due to the fact that the signs of the energies of the electron and phonons in the energy denominators of the expressions corresponding to diagrams of any order are always negative and there are no integrals which, according to Dirac's rule, have both real and imaginary parts. Thus, the contribution from any diagram to the full self-energy is real. A calculation of low-order terms of the self-energy for the Hamiltonian of the system under study shows that diagrams with the same maximum number of phonon lines above the electron line in each order make comparable contributions, although the contributions from crossed diagrams are smaller than those from uncrossed diagrams (Fig. 3).

Therefore, we will obtain an upper estimate of the full self-energy if the contributions from the diagrams with the same maximum number of phonon lines over the electron line are taken to be equal. The sum of these diagrams (Fig. 4) can be shown to correspond to the nonterminating continued fraction (with sums or integrals):

Fig. 3. Crossed diagrams.

$$M_\mu^u(\omega) = \sum_{\mu_1\beta_1} \frac{|\varphi_{\mu\mu_1}(\beta_1)|^2}{\omega - E_{\mu_1} - \Omega_{\beta_1} - 2\sum_{\mu_2\beta_2} \frac{|\varphi_{\mu_1\mu_2}(\beta_2)|^2}{\omega - E_{\mu_2} - \Omega_{\beta_1} - \Omega_{\beta_2} - \ldots - N\sum_{\mu_N\beta_N} \frac{|\varphi_{\mu_{N-1}\mu_N}(\beta_N)|^2}{N}}{\omega - E_{\mu_N} - \sum_{i=1} \Omega_{\beta_i} - \ldots}}. \quad (9)$$

We note, by the way, that, for a single-level (E) electron–phonon system (or for a system without interlevel configuration interaction), expression (9) for the self-energy is exact. As shown in [6], the self-energy in this case can be written as the nonterminating continued fraction:

$$M(\omega) = \frac{|\varphi|^2}{\omega - E - \Omega - \frac{2|\varphi|^2}{\omega - E - 2\Omega - \ldots - \frac{N|\varphi|^2}{\omega - E - N\Omega - \ldots}}}. \quad (10)$$

This self-energy includes multiphonon processes for any value of the coupling constant φ, and the results based on this self-energy coincide with those following from the exact solution found by using the unitary-transformation method.

The summed continued fractions (8) and (9) have the same structure and are a lower and an upper estimate of the full self-energy, respectively. An approximate self-energy can be obtained by replacing the coefficients of the Nth sums in the expressions M_μ^u and M_μ^l (N and 1, respectively) by their arithmetic average $(N + 1)/2$. Therefore, the approximate expression ($M_\mu^a(\omega)$) of the self-energy is

$$M_\mu^a(\omega) = \sum_{\mu_1\beta_1} \frac{|\varphi_{\mu\mu_1}(\beta_1)|^2}{\omega - E_{\mu_1} - \Omega_{\beta_1} - \frac{3}{2}\sum_{\mu_2\beta_2} \frac{|\varphi_{\mu_1\mu_2}(\beta_2)|^2}{\omega - E_{\mu_2} - \Omega_{\beta_1} - \Omega_{\beta_2} - \ldots - \frac{N+1}{2}\sum_{\mu_N\beta_N} \frac{|\varphi_{\mu_{N-1}\mu_N}(\beta_N)|^2}{N}}{\omega - E_{\mu_N} - \sum_{i=1} \Omega_{\beta_i} - \ldots}}. \quad (11)$$

This approximate self-energy includes both virtual multiphonon processes and the interlevel configuration interaction, and, therefore, it can be used to investigate the renormalized electronic energy levels and their phonon replicas in systems differing in the magnitude of the electron–phonon interaction strength.

The sums in expression (11) for the self-energy are of the same type, and the calculation procedure can be

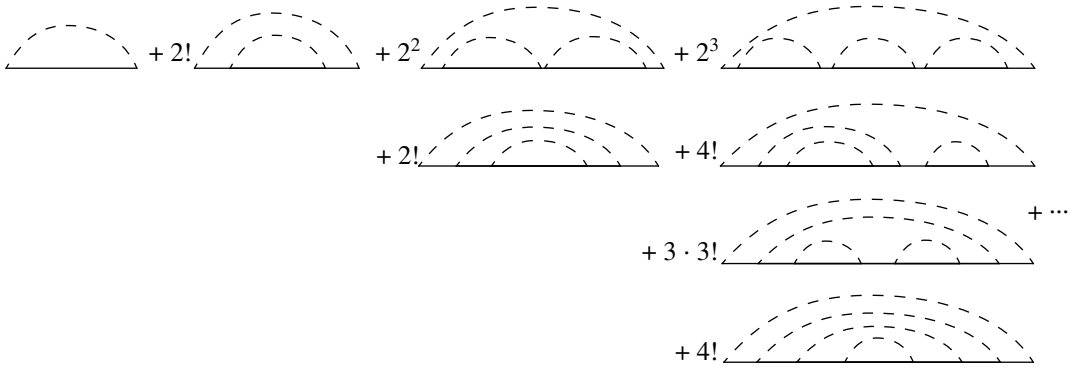

Fig. 4. Series approximating the self-energy.

easily programmed for a computer. First, we put the $(N + 1)$th sum equal to zero and, using a recurrent formula, compute $M^a_\mu(\omega)$ to the Nth approximation. Next, the energy levels and their phonon replicas computed in the Nth and $(N + 1)$th approximations to the self-energy are compared. By making computations for progressively increasing values of N, the electronic energy spectrum of the system can be determined with the required accuracy. If we retain only the first sum in Eq. (11), we will have the so-called one-phonon approximation (corresponding to diagram (a) in Fig. 1); this approximation is valid in the weak-coupling case and contains information on the renormalized energy of the no-phonon electronic state and on the bare one-phonon replicas (for a multiphonon system).

By successively including the other sums in the self-energy, we can refine the renormalized electronic energy levels and phonon replicas calculated in the preceding cycles and obtain new phonon replicas. As the coupling constants are increased, we should retain a progressively larger numbers of terms (sums) in the continued fraction (11) in order to compute the energy spectrum with the required accuracy. The convergence of the calculations of M^a_μ must be investigated separately in each specific case. However, it is well known that the convergence of expressions like the nonterminating continued fraction in Eq. (11) is more rapid than that of usual power series.

3. ELECTRONIC ENERGY LEVELS AND PHONON REPLICAS IN GaAs, CdSe, AND CuCl QUANTUM DOTS EMBEDDED IN GLASS

The theory developed in the previous section allows one to find the quasiparticle energy spectra in arbitrary nanoheterostructures. Here, we present the results of calculations performed for GaAs, CdSe, and CuCl quantum dots embedded in glass. These QDs cover a fairly wide range of electron–phonon interactions (from a weak one in GaAs to a strong one in CuCl). The calculated renormalized energies of the electronic ground states are compared with the results obtained using other methods [4, 5]. The calculated phonon replicas in the energy spectrum are compared for the first time with the experimental data on Raman scattering in CdSe quantum dots incorporated into glass [3].

Crystal parameters

Medium	U, meV	m_e/m_0	ε_0	ε_∞	Ω_L, meV	Ω_T, meV
CdSe	1820	0.13	9.3	6.1	26.54	21.49
GaAs	2028	0.067	12.9	10.9	36.2	33.3
CuCl	1100	0.504	7.9	3.61	35.54	17.33
Glass	0	1	6.0	–	–	–

The physical parameters of the nanosystems used in the calculations (electronic mass m_e, dielectric constants ε_0 and ε_∞, the bulk values of optical-phonon energies Ω_L and Ω_T for the QD materials, potential-well depth U) are listed in the table (the electronic mass in glass was taken to be equal to its value m_0 in vacuum). The potential-well depths for electrons in QDs are taken from [11], and the values of the other parameters are the same as in [8].

For a spherical QD embedded in a dielectric medium, the electronic energy spectrum renormalized by the interaction with confined and interface phonons is characterized by an energy density, which can be expressed, in terms of the Green's function [12], as

$$\begin{aligned}\rho^a_{nlm}(\omega) &= -2\mathrm{Im}\,G_{nlm}(\omega)\\ &= -2\mathrm{Im}\{\omega - E_{nl} - M^a_{nlm}(\omega)\}^{-1}.\end{aligned} \tag{12}$$

Here, the approximate self-energy includes the electronic energy spectrum of the system and multiphonon processes. This self-energy was found in Section 2 to be

$$M^a_{nlm}(\omega) = \sum_{\substack{p_1 l_1 m_1\\ \lambda_1' l_1' m_1'}} \frac{\left|\Phi^{p_1 l_1 m_1}_{nlm}(\lambda_1' l_1' m_1')\right|^2}{\omega - E_{p_1 l_1} - \Omega_{\lambda_1' l_1'} - \ldots - \dfrac{N+1}{2}\displaystyle\sum_{\substack{p_N l_N m_N\\ \lambda_N' l_N' m_N'}} \dfrac{\left|\Phi^{p_N l_N m_N}_{n_{N-1} l_{N-1} m_{N-1}}(\lambda_N' l_N' m_N')\right|^2}{N}}{\omega - E_{p_N l_N} - \displaystyle\sum_{i=1} \Omega_{\lambda_i' l_i'} - \ldots}. \tag{13}$$

In Eq. (13), we explicitly indicated the dependence of the coupling constants on the quantum numbers (n, l, m), in accordance with Eq. (2). Analytical expressions for the coupling constants were derived and used in [6, 7]. Those expressions, as well as the expressions for the energy density $M^a_{nlm}(\omega)$ and the self-energy $\Phi^{n_2 l_2 m_2}_{n_1 l_1 m_1}(\lambda lm)$, allow the following general conclusions to be drawn.

Since the electron–phonon interaction at $T = 0$ takes place only in the process of emission of L and I phonons, expression (13) for the self-energy has no finite imaginary part for any energy; therefore, the

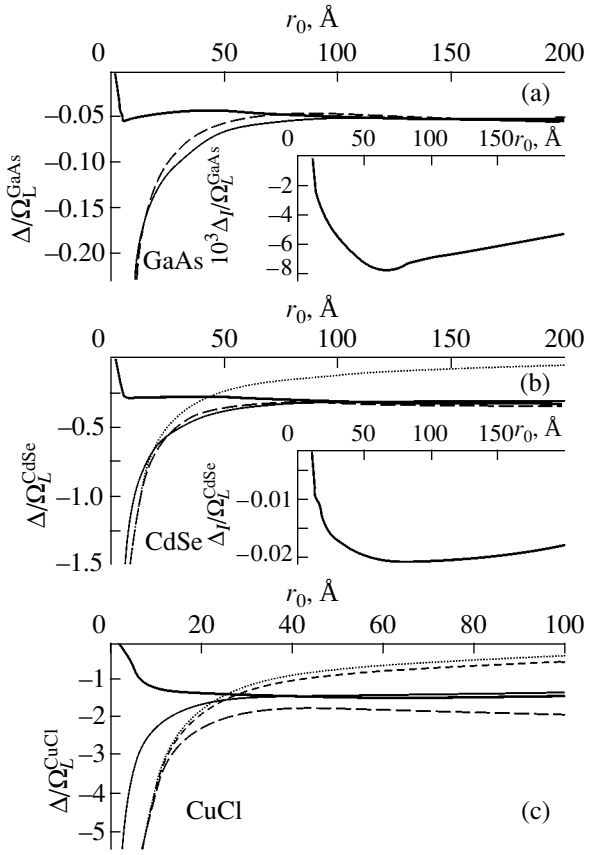

Fig. 5. Dependences of Δ on the radius of (a) GaAs, (b) CdSe, and (c) CuCl quantum dots in glass as calculated in [5] (short-dashed line), in [8] (dotted and long-dashed lines), and in this paper (solid lines). Thin lines correspond to $U \longrightarrow \infty$, and thick lines, to $U \neq \infty$.

spectral lines described by Eq. (12) are δ-function peaks, whose positions (in energy units) are given by the dispersion relation

$$\omega - E_{nl} - M^a_{nlm}(\omega) = 0. \tag{14}$$

Solution of Eq. (14) gives the renormalized energy spectrum of the system, i.e., the electronic energy levels $\tilde{E}_{nlm}$ and their N_Lth L-phonon, N_Ith I-phonon, and combined (N_L, N_I) phonon replicas ($\tilde{E}^{N_L}_{nlm}$), ($\tilde{E}^{N_I}_{nlm}$), and ($\tilde{E}^{N_L, N_I}_{nlm}$), respectively.

Due to the electron–phonon interaction, the electronic energy levels shift by Δ_{nlm} and their phonon replicas Δ^{N_L, N_I}_{nlm} arise, defined by

$$\begin{aligned} \Delta_{nlm} &= \tilde{E}_{nlm} - E_{nl}, \\ \Delta^{N_L, N_I}_{nlm} &= \tilde{E}^{N_L, N_I}_{nlm} - (E_{nl} + N_{L,I}\Omega_{l,I}). \end{aligned} \tag{15}$$

As seen from expression (13) for the self-energy, the electron–phonon interaction removes the degeneracy with respect to the magnetic quantum number m; therefore, the lth purely electronic energy level splits into $l + 1$ levels for each value of l.

Another general conclusion is drawn from the fact that there are no interface phonons in spherically symmetric states ($l = m = 0$) [6, 7, 13] and electrons in such states do not interact with I phonons in other states (due to the symmetry of the coupling constants); therefore, only L-phonon replicas will arise for the electronic energy levels corresponding to the spherically symmetric states.

Before discussing the renormalized spectra of specific nanoheterostructures, we note that, in a real QD, the potential-well depth is finite and, therefore, summation over the quantum number p in calculating the electronic self-energy covers not only the discrete energy spectrum ($n = 1, 2, \ldots$) but also the continuum ($0 \le k < \infty$), i.e.,

$$\sum_k \longrightarrow \int_0^\infty dk \quad \left(k = \frac{\sqrt{2m_1 E}}{\hbar}, E > 0\right). \tag{16}$$

The presence of a continuous spectrum makes the inclusion of electron–phonon interaction and numerical computations much more complicated. However, the continuum should be taken into account, because, as computations show, its contribution to the renormalized characteristics of the energy spectrum is larger than 10%, irrespective of the electron–phonon interaction strength.

Now, we discuss the results of computing the electronic energy spectra renormalized by interaction with phonons performed on the basis of self-energy (13) for GaAs, CdSe, and CuCl quantum dots embedded in glass. The calculated ground-state energy shifts ($\Delta = \Delta_{100}$) as a function of the radius r_0 of QDs of these three types are shown in Fig. 5 by thick and thin solid lines for finite and infinite potential-well depths, respectively. For the sake of comparison, Fig. 5 also shows the dependences of Δ on r_0 calculated using the Lee–Low–Pines unitary-transformation method [8] (long-dashed lines), adiabatic approximation [8] (short-dashed lines), and perturbation theory [5] (dotted lines).

It can be seen from Fig. 5 that, in the case of a potential well of an infinite depth, our method and the Lee–Low–Pines method give similar results for the energy shift for any QD size. In the more realistic case of QD potential wells of a finite width, the dependence of the energy shift on the QD radius is radically different; our calculations (Fig. 5) show that, in this case, a decrease in the QD size causes the energy shift to decrease (as one might expect on physical grounds) rather than increase. Indeed, as the QD size is decreased, the electronic energy level in the potential well shifts upward and the electron becomes less localized. As a result, the electron–phonon interaction becomes weaker (irrespective of the strength of the polarization field, which is confined to the QD boundary) and the energy shift decreases in absolute value. Therefore, the dependence

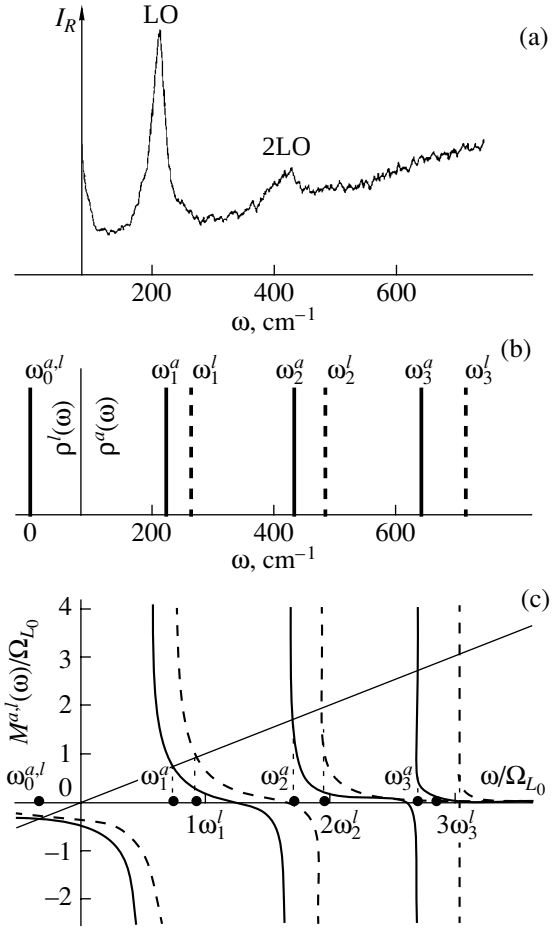

Fig. 6. (a) Raman scattering intensity I_R, (b) ρ^a and ρ^l, and (c) M^a and M^l as a function of frequency ω for r_0 = 19 Å.

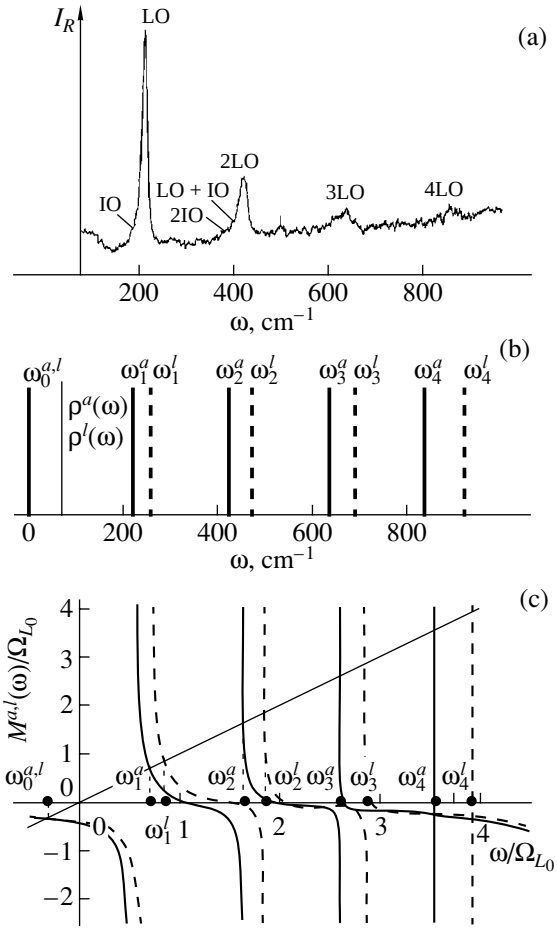

Fig. 7. (a) Raman scattering intensity I_R, (b) ρ^a and ρ^l, and (c) M^a and M^l as a function of frequency ω for r_0 = 40 Å.

of Δ on r_0 found in [5, 8] for small values of the QD radius ($r_0 \le 50$ Å) is inadequate; this is not due to the inadequacy of the methods applied but is rather due to the infinitely deep potential-well model inadequately describing real nanosystems with small semiconducting QDs incorporated into a dielectric medium.

In GaAs and CdSe quantum dots, the electron–phonon coupling is fairly weak; therefore, the contributions from *I* and *L* phonons to the shift Δ are additive, $\Delta = \Delta_L + \Delta_I$. The relative values of these contributions are seen from the insets to Figs. 5a and 5b, where the contribution from interface phonons to the energy shift (Δ_I) is shown as a function of r_0. It is seen that the contribution from *I* phonons is an order of magnitude smaller than that from *L* phonons. In CuCl quantum dots, the electron–phonon coupling is fairly strong; therefore, the contributions from *I* and *L* phonons are not additive and cannot be separated.

Expression (13) for the self-energy includes virtual multiphonon processes and, hence, allows one to calculate not only the renormalized energy level of the no-phonon ground state but also its phonon replicas.

Figures 6 and 7 show the frequency dependences of the calculated self-energies $M^a(\omega)$ and $M^l(\omega)$ (Figs. 6c, 7c), the calculated energy densities $\rho^a(\omega)$ and $\rho^l(\omega)$ (Figs. 6b, 7b), and the experimental Raman scattering intensity $I_R(\omega)$ (Figs. 6a, 7a) [3] for a nanosystem consisting of CdSe quantum dots incorporated into glass for two values of the QD radius, r_0 = 19 and 40 Å. It can be seen from these figures that the *L*-phonon replicas (ω_n^l) calculated from the self-energy $M^l(\omega)$ given by Eq. (8) are in rather poor agreement with the experimental data and the disagreement becomes progressively worse as the phonon replica energy increases. The calculations based on the approximate self-energy $M^a(\omega)$ agree with the experimental data for any phonon replica energy.

According to the theory developed above, an electron in the *S* state ($l = 0$) does not interact with interface phonons in $l \ne 0$ states (interface phonons cannot be in the *S* state). Therefore, *I* phonons contribute only to the energy shifts of the renormalized ground state and of its *L*-phonon replicas (as seen from Figs. 6, 7), but the

I-phonon replicas are absent because there is no direct interaction between an electron in the *S* state and *I* phonons. An electron in an $l \neq 0$ state can interact with an *I* phonon in the same state. Therefore, such electronic states must be accompanied by *I*-phonon replicas.

The results presented above are valid for a QD of ideal spherical shape. In actual systems, the shape of QDs can differ from spherical to a greater or lesser extent and, hence, the electronic ground state can be a superposition of the *S* and $l \neq 0$ states. In this case, an electron in the ground state directly interacts with *I* phonons ($l \neq 0$) and *I*-phonon replicas of the ground level can arise. It is clear that the larger the deviation of the QD shape from spherical, the larger the contribution from the $l \neq 0$ states to the wave function of the electron in the ground state and the stronger the interaction of the electron with *I* phonons, which should be manifested experimentally by an increase in the intensity of *I*-phonon replicas at $T \neq 0$.

The arguments presented above can qualitatively explain the experimental Raman scattering spectra [3]. Indeed, the absence of *I*-phonon replicas in the experimental spectrum presented in Fig. 6a for CdSe quantum dots embedded in glass indicates that the shape of the QDs under study is close to spherical. The spectrum presented in Fig. 7a exhibits the first *I*-phonon replica, faintly visible against the background, which may indicate that the QD shape in this case is different from spherical. A consistent theory of the electron–phonon and electron–exciton interactions and of the electronic Raman scattering spectrum in nonspherical QDs embedded in a dielectric medium will be presented in our future publications.

REFERENCES

1. N. Mori and T. Ando, Phys. Rev. B **40** (9), 6175 (1989).
2. G. Q. Hai, F. M. Peeters, J. T. Devreese, and L. Wendler, Phys. Rev. B **48** (16), 12016 (1993).
3. M. Klein, F. Hache, D. Richard, and C. Flytzanis, Phys. Rev. B **42** (17), 11123 (1990).
4. R. M. Crus, S. W. Teitsworch, and M. A. Strocia, Phys. Rev. B **52** (12), 1489 (1995).
5. J. S. Marini, B. Stebe, and E. Kartheuser, Phys. Rev. B **50** (19), 14302 (1994).
6. N. V. Tkach, Fiz. Tverd. Tela (St. Petersburg) **39** (6), 1109 (1997) [Phys. Solid State **39**, 995 (1997)].
7. M. Tkach, V. Holovatsky, O. Voitsekhivska, and M. Min'kova, Phys. Status Solidi B **203** (2), 373 (1997).
8. K. Oshiro, K. Akai, and M. Matsuura, Phys. Rev. B **58** (12), 7986 (1998).
9. M. Tkach, V. Holovatsky, O. Voitsehivska, *et al.*, Phys. Status Solidi B **225** (2), 331 (2001).
10. Yu. A. Firsov, *Polarons* (Nauka, Moscow, 1975).
11. O. Madelung, *Semiconductors. Basic Data*, 2nd ed. (Springer, Berlin, 1996), p. 247.
12. A. A. Abrikosov, L. P. Gor'kov, and I. E. Dzyaloshinskiĭ, *Methods of Quantum Field Theory in Statistical Physics* (Fizmatgiz, Moscow, 1962; Prentice Hall, Englewood Cliffs, N.J., 1963).
13. E. P. Pokatilov, S. N. Klimin, V. M. Fomin, *et al.*, Phys. Rev. B **65** (7), 075316 (2002).

Translated by Yu. Epifanov

Physics of the Solid State, Vol. 45, No. 7, 2003, pp. 1355–1359. Translated from Fizika Tverdogo Tela, Vol. 45, No. 7, 2003, pp. 1292–1296.

LOW-DIMENSIONAL SYSTEMS AND SURFACE PHYSICS

Nonlinear Absorption in Dielectric Layers Containing Copper Nanoparticles

R. A. Ganeev[1], A. I. Ryasnyanskiĭ[2], A. L. Stepanov[3, 4], and T. Usmanov[1]

[1]*Akadempribor Research and Production Association, Academy of Sciences of Uzbekistan, Tashkent, 700143 Uzbekistan*

[2]*Samarkand State University, Samarkand, 703004 Uzbekistan*

e-mail: ryasn2000@yahoo.com

[3]*I Physikalisches Institut, Aachen Technical University RWTH, Aachen, D-52056 Germany*

[4]*Kazan Physicotechnical Institute, Russian Academy of Sciences, Sibirskiĭ trakt 10/7, Kazan, 420029 Tatarstan, Russia*

Received December 15, 2002

Abstract—The nonlinear absorption in copper nanoparticles contained in glass matrices is investigated using the *Z*-scan technique at the wavelength of a picosecond Nd : YAG laser (λ = 1064 nm). The experimental data obtained for copper nanoparticle–containing composites synthesized through ion implantation are analyzed. It is demonstrated for the first time that, upon exposure to laser radiation at frequencies outside the range of surface plasma resonance, the nonlinear absorption in metallic particles can be caused by the two-photon effect. The optical limiting due to two-photon absorption is discussed for composites containing copper particles.

1. INTRODUCTION

Over the last twenty years, composite materials based on dielectrics containing metallic nanoparticles have been the subject of extensive investigations in the field of nonlinear optics [1–5]. Moreover, research in this direction continues to attract considerable attention of many physicists [6–10], because these materials hold promise for application both in optical switches with an ultrashort response [9] and in optical limiters embodying the specific features of nonlinear absorption in their operation [7, 10]. The dielectric composites containing metallic nanoparticles possess high third-order nonlinear susceptibilities $\chi^{(3)}$, which are responsible for the optical Kerr effect, especially in the case when the frequency of laser radiation lies in the spectral range of linear selective absorption due to surface plasma resonance in metallic nanoparticles. This stems from the fact that the nonlinear response of nanoparticles is most pronounced under resonance excitation of free electrons involved in these particles, which is observed at surface plasma resonance frequencies. It is known that the frequencies of surface plasma resonance in nanoparticles of different metals embrace a fairly wide spectral region (from UV to near-IR), depending on many factors (such as the metal type; the shape, structure, and size of particles; and the properties of the surrounding dielectric matrix). For example, in the case of spherical particles, the location of the surface plasma resonance peak within the quasi-static approximation can be determined by the relationship [11]

$$\varepsilon_1(\omega_p) + 2\varepsilon_m(\omega_p) = 0, \quad (1)$$

where ε_1 is the real part of the permittivity of the metallic particle (the imaginary part of the permittivity satisfies the inequality $\varepsilon_2 \ll 1$), ε_m is the permittivity of the surrounding matrix, and ω_p is the frequency of surface plasma resonance in the particle. It follows from relationship (1) that the surface plasma resonance peak of copper nanoparticles lies in the visible spectral range (at approximately 600 nm).

A large number of studies concerned with the nonlinear optical characteristics of the composite materials under consideration have been performed with lasers operating at frequencies that correspond to the spectral range of the surface plasma resonance in metallic particles [3, 4, 8]. In particular, Serna *et al.* [9] studied composite layers based on copper clusters incorporated into Al_2O_3. The nonlinear absorption coefficient β was examined using the Z-scan technique at a wavelength of 596 nm (the surface plasma resonance in copper clusters is observed at 590 ± 5 nm). The nonlinear absorption coefficient β was measured as a function of the pumping intensity of a dye laser (τ = 6 ps). It was established that the value of β varies from 0.8×10^{-4} to 0.2×10^{-4} cm W^{-1} with an increase in the intensity from 2×10^7 to 2×10^8 cm W^{-2}. In [12], the spectral dependence of the third-order nonlinear susceptibility $\chi^{(3)}$ in composites formed by silver nanocrystals in the BaO–B_2O_3–P_2O_3 glass was investigated by the degenerate four-photon mixing and Z-scan techniques with the use of femtosecond laser radiation in the visible range. The maximum value of the imaginary part of $\chi^{(3)}$ was experimentally found to be equal to -1.5×10^{-10} CGSE in the vicinity of the peak of the surface plasma resonance in

silver nanocrystals (420 nm). It was demonstrated that the imaginary part of $\chi^{(3)}$ is positive in the wavelength range 441–576 nm and negative in the range 385–437 nm.

The manifestation of surface plasma resonance in nanoparticles provides a means for examining composites with these particles at frequencies of laser radiation such that nonlinear responses reach maximum values. However, from the viewpoint of actual applications of such materials in practice, it should be remembered that currently available and practically used Nd : YAG (λ = 1064 nm), Ti : Al_2O_3 (λ = 800 nm), and other lasers operate at strictly fixed frequencies. Therefore, when designing and searching for new optimum materials suitable for complex use in existing laser systems, it is necessary to investigate the nonlinear optical properties of composite materials not only in the spectral range of the surface plasma resonance in metallic particles but also at specific frequencies of commercial lasers.

In this work, the nonlinear absorption in composites based on glasses with copper nanoparticles synthesized through ion implantation were investigated by the Z-scan technique at the wavelength of a picosecond Nd : YAG laser (λ = 1064 nm). The experimental results obtained were used to estimate the optical limiting in the samples. The possible fields of application of the studied materials were discussed.

2. SAMPLES AND EXPERIMENTAL TECHNIQUE

Silicate glass SiO_2 (SG, Heraeus) and soda–lime–silica glass (SLSG, Societa Italiana Vetro) with a homogeneous composition of the chemical components (70 at. % SiO_2, 20 at. % Na_2O, 10 at. % CaO) were used as substrates for preparing composite materials. The refractive indices n_0 of silicate and soda–lime–silica glasses were 1.5 and 1.54, respectively. The glasses were prepared in the form of plates 2×2 cm in size. The thicknesses of the plates were equal to 1.05 mm for silicate glass and 3.1 mm for soda–lime–silica glass. The implantation was performed with Cu^+ ions at an energy of 60 keV, a dose of 8.0×10^{16} ions/cm^2, and an ion current density of 10 μA/cm^2. The glasses were cemented to a massive metal plate with a heat-conducting paint. The temperature of the metal plate was controlled and carefully regulated using a system composed of a resistance heater and a gas cooler. The plate temperature during the implantation was approximately equal to 40°C. The mean size of the metallic particles synthesized was estimated with the use of x-ray reflectometry in an angular dispersive mode [13]. The composite samples were analyzed by grazing-incidence small-angle x-ray scattering (GISAXS). The optical transmittance was measured on a Perkin-Elmer Lambda 19 double-beam spectrophotometer in the wavelength range 300–1100 nm.

The nonlinear optical characteristics of the samples were investigated on λ a Z-scan setup with an open aperture. The experimental scheme was similar to that described in our previous work [14] and made it possible to examine the nonlinear absorption in the samples. The output parameters of Nd : YAG laser radiation were as follows: pulse duration, 35 ps; pulse energy, 1 mJ; and λ = 1064 nm. The laser radiation was focused on a sample through a lens with a focal distance of 25 cm. The beam diameter in the focal waist was equal to 150 μm. The studied samples were transferred in steps of 2 mm along the *Z* optical axis when scanning the focal region. The fluctuations of the laser energy from pulse to pulse did not exceed 10%. The radiation energy of single laser pulses was recorded with a calibrated FD-24K photodiode and measured on a V4-17 digital voltmeter. Calibrated neutral filters were used for measuring the laser radiation energy. The signal from the second FD-24K photodiode, which was positioned at a distance of 50 cm from the focal region, was sent to the V4-17 digital voltmeter. This distance was chosen such that the detector accumulated the total radiation passed through the sample. In order to eliminate the effect of instability of the output energy laser parameters on the results of measurements, the signal detected by the second photodiode was normalized to the signal detected by the first photodiode. The scheme with an open aperture enabled us to determine the nonlinear absorption coefficient.

3. RESULTS AND DISCUSSION

In the course of implantation, metallic nanoparticles nucleate and grow in the glass when the concentration of metal atoms exceeds the solubility limit, which, in turn, is determined by an ion dose of the order of 10^{16} ions/cm^2 at an ion energy of 60 keV [15, 16]. In the present work, the formation of metallic nanoparticles was revealed by x-ray diffraction and optical spectroscopy. The GISAXS measurements made it possible to estimate the mean size of spherical nanoparticles at 3.4–4.5 nm and showed that nanoparticles are characterized by a sufficiently narrow size distribution [8]. At the given implantation energy, metallic particles in the glasses are located at a depth of no more than 60 nm [17].

The formation of nanoparticles is confirmed by the appearance of selective absorption bands with minima at wavelengths of 550–600 nm in the optical transmittance spectra of the implanted glasses (Fig. 1). These bands are associated with the surface plasma resonance in copper particles [11]. Depending on the ion implantation conditions, the incorporation of accelerated ions into silicate glasses leads to the generation of radiation-induced defects, which can initiate reversible and irreversible transformations in the glass structure [16]. This can result in structural imperfections of different types, such as the generation of extended and point defects, local crystallization and amorphization, the formation of a new phase either from atoms involved

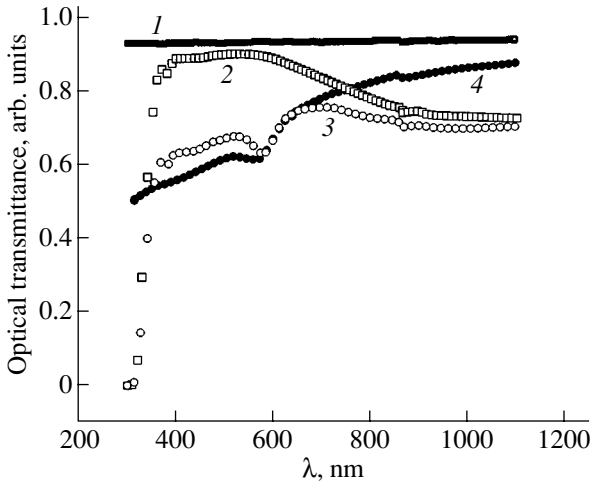

Fig. 1. Optical transmittance spectra of (*1*) SG, (*2*) SLSG, (*3*) SG : Cu, and (*4*) SLSG : Cu samples.

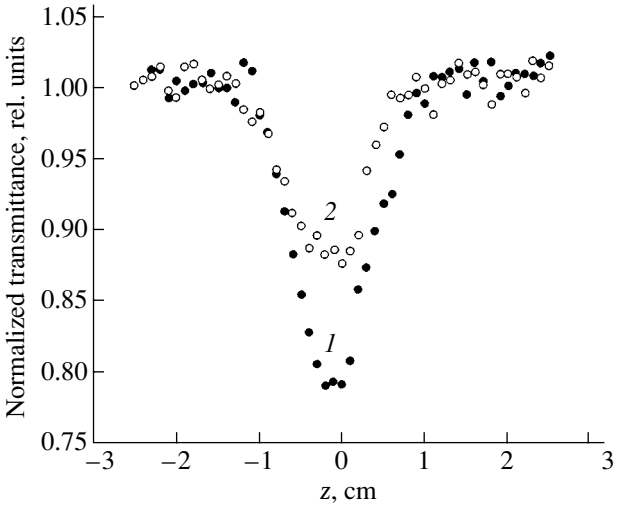

Fig. 2. Normalized transmittance as a function of the position of (*1*) SG : Cu and (*2*) SLSG : Cu composites in the scheme with an open aperture.

the glass structure or from implanted ions, etc. In particular, the formation of metallic particles in the glass brings about an increase in its volume and the generation of internal stresses within an implanted layer. The radiation-induced defects are responsible for an increase in the absorption in the range of the UV fundamental absorption edge in the spectrum of the glass. In our case, this effect can be observed in the short-wavelength range of the optical transmittance spectra displayed in Fig. 1. It should be noted that, in this work, all nonlinear optical investigations were performed upon exposure of the samples to laser radiation at a wavelength of 1064 nm, which lies far from the UV spectral range of the linear absorption attributed to the surface plasma resonance and interband transitions in metallic particles and glasses. For this reason, in what follows, the contributions associated with interband transitions and radiation-induced defects will be eliminated from the analysis of the experimental results.

Figure 2 shows the experimental dependences of the normalized transmittance measured for both glasses containing copper nanoparticles in the scheme with an open aperture. Recall that the measurements carried out in this scheme make it possible to determine the nonlinear absorption coefficient β. It can be seen from Fig. 2 that the experimental dependences exhibit specific features inherent in nonlinear absorption: the normalized transmittance decreases as the focal point is approached and reaches a minimum at $z = 0$. Each point in the graphs was obtained by averaging over the values measured for 40 pulses. The scatter of the experimental points in the graphs is caused, to some extent, by the energy instabilities and, for the most part, by the time instabilities of laser radiation.

The nonlinear absorption coefficient β of composite materials can be determined from the relationship for the normalized transmittance, which, in the case of the scheme with an open aperture, can be written in the form [18]

$$T(z) = q(z)^{-1}\ln(1 + q(z)). \quad (2)$$

Here, $q(z) = \beta I(z) L_{\text{eff}}$ is the laser beam parameter, $L_{\text{eff}} = (1 - e^{-\alpha L})/\alpha$ is the effective optical path in the sample, L is the sample thickness, α is the linear absorption coefficient at the laser radiation wavelength, and $I(z)$ is the intensity of the light passed through the sample as a function of its position along the z axis. The parameter $q(z)$ describes the propagation of the laser beam in the material, because the following relationship holds:

$$1/q(z) = 1/P(z) - 2\lambda\Delta\phi/\pi w^2 - i\lambda/\pi w^2, \quad (3)$$

where $P(z) = z[1 + (z_0^2/z^2)]$ is the radius of the wave front curvature in the z direction, $z_0 = kw^2/2$ is the diffraction length of the beam, $k = 2\pi/\lambda$ is the wave vector, $\Delta\phi = \Delta\Phi_0/(1 + z^2/z_0^2)$, $w(z) = w_0(1 + z^2/z_0^2)^2$ is the beam radius at the point z, and w_0 is the beam radius at the focal point (at a level of e^{-2}).

At $z = 0$ (focal plane), the parameter $q(0) = q_0$ is defined by the expression

$$q_0 = \beta I_0 L_{\text{eff}}, \quad (4)$$

where $I_0 = I(0)$.

From formulas (2) and (4), we obtain

$$T_0 = q_0^{-1}\ln(1 + q_0), \quad (5)$$

where T_0 is the minimum normalized transmittance in the focal plane in the scheme with an open aperture. Expression (5) permits us to determine the nonlinear absorption coefficient β. The values of β calculated in

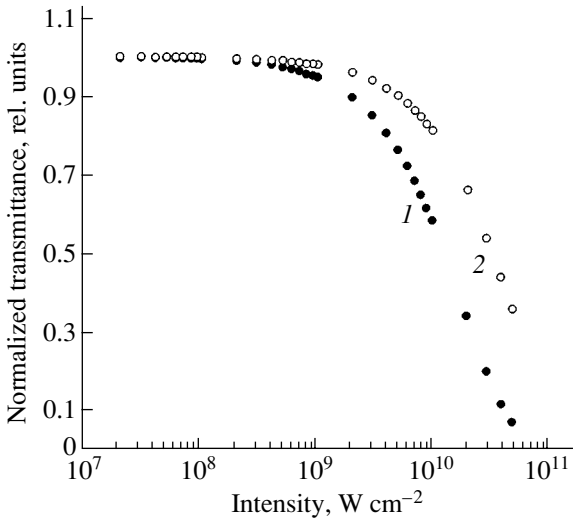

Fig. 3. Calculated normalized transmittance as a function of the incident radiation intensity for (*1*) SG : Cu ($\beta = 9 \times 10^{-6}$ cm W^{-1}) and (*2*) SLSG : Cu ($\beta = 3.42 \times 10^{-6}$ cm W^{-1}) composites.

this way from the experimental data for the SLSG : Cu and SG : Cu composites are equal to 3.42×10^{-6} and 9×10^{-6} cm W^{-1}, respectively. As can be seen, the nonlinear absorption coefficients for these composites differ by a factor of 2.63.

Let us now consider the possible mechanisms of nonlinear absorption in the studied media with metallic nanoparticles. In order to compare correctly the nonlinear absorption coefficients β for the SLSG : Cu and SG : Cu composites, it is necessary to take into account the linear absorption coefficients α for layers with copper nanoparticles in different matrices ($\alpha^{SG:Cu} = 9340$ cm^{-1} and $\alpha^{SLSG:Cu} = 5800$ cm^{-1}). By assuming that the thicknesses of the layers with nanoparticles in the studied glasses are virtually identical (~60 nm) [17], we normalize the nonlinear absorption coefficient β to the linear absorption coefficient α for the relevant composite ($G = \beta/\alpha$). As a result, we obtain the parameters $G^{SG:Cu} = 9.64 \times 10^{-10}$ cm^2 W^{-1} and $G^{SLSG:Cu} = 6.73 \times 10^{-10}$ cm^2 W^{-1}, which differ by a factor of 1.432. To account for this discrepancy between the parameters G for different samples, proper allowance must be made not only for the difference in the linear absorption coefficients α but also for the specific features in the location of the surface plasma resonance peaks attributed to copper nanoparticles. As can be seen from Fig. 1, the surface plasma resonance peak assigned to metallic particles is observed at 565 nm ($\omega_p = 17699.1$ cm^{-1}) for the SG : Cu composite and at 580 nm ($\omega_p = 17241.4$ cm^{-1}) for the SLSG : Cu composite. Now, we assume that, in our systems, there can occur a two-photon resonance related to the surface plasma resonance. It is known that, in the range of excitations and their associated transitions in nonlinear systems, the optical nonlinearities become more pronounced with a decrease in the detuning of the frequency from the resonance (in our case, two-photon) excitation [19]. In our experiment, the frequency detuning should be treated as the difference between the frequency of the surface plasma resonance and the frequency of two photons of the laser radiation used ($\omega_{20} = 18\,797$ cm^{-1}). The difference in the location of the surface plasma resonance peaks for copper nanoparticles in the SG and SLSG composites can be estimated from the following ratio:

$$M = (\omega_{20} - \omega_p^{SG:Cu})^{-1}/(\omega_{20} - \omega_p^{SLSG:Cu})^{-1} = 1.42. \quad (6)$$

This value is in qualitative agreement with a ratio of 1.432 between the nonlinear absorption coefficients β normalized to the linear absorption coefficients α.

Therefore, we can draw the following inferences:

(1) In the near-IR range, the large nonlinear absorption coefficients determined experimentally for glasses containing copper nanoparticles are explained by the surface plasma resonance in metallic particles.

(2) The locations of the surface plasma resonance peaks attributed to copper nanoparticles determine the intensity of two-photon absorption in the studied composites at a wavelength of 1064 nm.

Note that the possibilities of using two-photon absorption associated with the surface plasma resonance in silver colloidal particles in solutions were demonstrated earlier in [14, 20].

When analyzing the results obtained in the present work, it is expedient to dwell on the possible fields of practical application of the studied composites. As is known, media with nonlinear (in particular, two-photon) absorption are very promising as materials for optical limiters, which can serve, for example, for the protection of eyes and highly sensitive detectors against intense optical radiation. The majority of studies in this field have been performed using nanosecond laser pulses. In this case, the main mechanisms responsible for nonlinear effects are associated with the reverse saturable nonlinear absorption (fullerenes and organic and metalloorganic compounds) and nonlinear scattering (solutions of colloidal metal aggregates). Picosecond and subpicosecond laser pulses have been used only to examine the optical limiting in media belonging primarily to semiconductor materials (two-photon absorption and strong nonlinear refraction).

Since two-photon absorption at a wavelength of 1064 nm is observed in the SG : Cu and SLSG : Cu samples, it is of interest to investigate the optical limiting in these composites in the scheme with an open aperture. In the theoretical analysis, it was assumed that the sample is located in the region corresponding to a minimum transmittance, i.e., in the focal plane of a beam ($z = 0$). The nonlinear absorption was studied experimentally at an operating intensity of 10^{10} W cm^{-2}. The breakdown intensity for samples containing copper nanoparticle is equal to 6×10^{10} W cm^{-2}. On this basis,

the upper limit of the intensity for theoretical estimates was taken equal to 5×10^{10} W cm^{-2}. With the use of the linear and nonlinear (two-photon) absorption coefficients, we obtained the dependences of the normalized transmittance on the laser radiation intensity (Fig. 3). It can be seen from Fig. 3 that, at the maximum intensity, the SG : Cu composite is characterized by an approximately fifteenfold limiting, whereas the SLSG : Cu composite exhibits an approximately threefold limiting. Consequently, these composites can serve as nonlinear materials for optical limiting. It is clear that the SG : Cu composite is more preferable from the practical standpoint.

4. CONCLUSIONS

Thus, we experimentally investigated the nonlinear optical characteristics of silicate glasses with copper nanoparticles incorporated through ion implantation. The nonlinear absorption coefficients for glasses containing copper nanoparticles were measured using the *Z*-scan technique. It was demonstrated that the nonlinear absorption can be associated with two-photon absorption at a wavelength of 1064 nm. The optical limiting was analyzed for the composite materials studied. It was predicted that the SG : Cu composite is characterized by a 15-fold limiting.

ACKNOWLEDGMENTS

R.A. Ganeev and T. Usmanov acknowledge the support of the Uzbek Research and Technical Center (project no. Uzb-29). A.I. Ryasnyanskiĭ acknowledges the support of the Uzbek State Committee of Science and Engineering (project no. 7/01). A.L. Stepanov acknowledges the support of Alexander von Humboldt-Stiftung (Germany) and the Russian Foundation for Basic Research (project no. 00-15-96615).

REFERENCES

1. D. Ricard, P. Raussignol, and C. Flytzanis, Opt. Lett. **10**, 511 (1985).
2. F. Hache, D. Ricard, and C. Flytzanis, J. Opt. Soc. Am. B **3**, 1647 (1986).
3. F. Hache, D. Ricard, C. Flytzanis, and U. Kreibig, J. Appl. Phys. A **47**, 354 (1988).
4. K. Ushida, S. Kaneko, S. Omi, *et al.*, J. Opt. Soc. Am. B **11**, 1236 (1994).
5. L. Yang, K. Becker, F. M. Smith, *et al.*, J. Opt. Soc. Am. B **11**, 457 (1994).
6. M. Kyoung and M. Lee, Opt. Commun. **171**, 145 (1999).
7. Y.-P. Sun, J. E. Riggs, H. W. Rollins, and R. Guduru, J. Phys. Chem. **103**, 77 (1999).
8. J. Olivares, J. Requejo-Isidro, R. Del Coso, *et al.*, J. Appl. Phys. **90**, 1064 (2001).
9. R. Serna, J. M. Ballesteros, J. Solis, *et al.*, Thin Solid Films **318**, 96 (1998).
10. J. Staromlynska, T. J. McKay, and P. Wilson, J. Appl. Phys. **88**, 1726 (2000).
11. U. Kreibig and M. Vollmer, *Optical Properties of Metal Clusters* (Springer-Verlag, Berlin, 1995).
12. Y. Hamanaka, N. Hayashi, A. Nakamura, and S. Omi, J. Lumin. **87–89**, 859 (2000).
13. A. Nadon and D. Thaiaudiere, J. Appl. Crystallogr. **30**, 822 (1997).
14. R. A. Ganeev, A. I. Ryasnyansky, Sh. R. Kamalov, *et al.*, J. Phys. D: Appl. Phys. **34**, 1602 (2001).
15. A. L. Stepanov, D. E. Hole, and P. D. Townsend, J. Non-Cryst. Solids **260**, 56 (1999).
16. P. D. Townsend, P. J. Chandler, and L. Zhang, *Optical Effects of Ion Implantation* (Cambridge Univ. Press, Cambridge, 1994).
17. A. L. Stepanov, V. A. Zhikharev, and I. B. Khaĭbullin, Fiz. Tverd. Tela (St. Petersburg) **43**, 733 (2001) [Phys. Solid State **43**, 766 (2001)].
18. Ch. H. Kwak, Y. L. Lee, and S. G. Kim, J. Opt. Soc. Am. B **16**, 600 (1999).
19. J. F. Reintjes, *Nonlinear-Optical Parametrical Processes in Liquids and Gases* (Academic, Orlando, 1984).
20. S. V. Karpov, A. K. Popov, and V. V. Slabko, Pis'ma Zh. Éksp. Teor. Fiz. **66**, 97 (1997) [JETP Lett. **66**, 106 (1997)].

Translated by O. Borovik-Romanova

Physics of the Solid State, Vol. 45, No. 7, 2003, pp. 1360–1373. Translated from Fizika Tverdogo Tela, Vol. 45, No. 7, 2003, pp. 1297–1310.

LOW-DIMENSIONAL SYSTEMS AND SURFACE PHYSICS

The Anomalous Hanle Effect in Semimagnetic Semiconductor Quantum Wells

A. V. Kudinov, Yu. G. Kusraev, I. A. Merkulov, K. V. Kavokin, I. G. Aksyanov, and B. P. Zakharchenya

Ioffe Physicotechnical Institute, Russian Academy of Sciences, Politekhnicheskaya ul. 26, St. Petersburg, 194021 Russia

Received December 18, 2002

Abstract—The behavior of the optical-orientation signal under resonant optical excitation of localized excitons in quantum wells with semimagnetic layers was studied both experimentally and theoretically. The most remarkable experimental observation made in this study is the increase in the degree of polarization of the quantum well radiation in the conditions in which the Hanle effect is observed. The behavior of magnetically induced circular luminescence polarization in a slightly tilted field (quasi-Voigt geometry) also appears unusual. Possible specific contributions to the optical exciton orientation in semimagnetic nanostructures are discussed. A theoretical model is proposed which, while being based on the well-known concepts of collective spin dynamics of magnetic ions in the exchange field of a photoexcited hole, takes into account fluctuations of the local magnetization. The calculations agree quantitatively with experiment for reasonable values of the parameters. © *2003 MAIK "Nauka/Interperiodica".*

1. INTRODUCTION

In the 1920s, at the dawn of optical spectroscopy, Wood and Hanle discovered that a magnetic field can act on the polarization of resonance fluorescence of mercury and sodium vapors. A systematic investigation of the relevant phenomena was initiated by the studies of Kastler, which laid the foundation for the method of optical pumping (optical orientation) [1]. In optical-pumping experiments, the circular polarization of secondary luminescence disappears if the emitting medium is placed in a transverse magnetic field. The depolarization of radiation in a transverse magnetic field was called the Hanle effect.

Progress reached in the methods of optical pumping in solids made the Hanle effect a major tool for probing the optical orientation of spins, and this effect has been, for a long time, nearly the only possible way to study fast spin evolution in crystals [2]. In the classical version of the Hanle effect applied to semiconductors, the degree of photoluminescence polarization in zero magnetic field and the halfwidth of the depolarization curve make it possible, given the g factor of conduction band electrons, to derive their lifetime and spin relaxation time. In other cases, the shape of the Hanle depolarization curve may contain information on carrier and nonequilibrium spin transport, diffusion, photon reemission, and surface recombination [3, 4]. Hanle curves do not always exhibit a monotonic decay of the degree of polarization; indeed, there have been observations of oscillating depolarization in cascade processes [2, 5] and even of a temporary recovery of the original polarization in the conditions where the external field cancels the nuclear exchange field [2, 6].

The present communication deals with Hanle curves of a specific type which are frequently observed in CdTe/(Cd,Mn)Te or (Cd,Mn)Te/(Cd,Mg,Mn)Te quantum wells (QWs) containing Mn magnetic ions. The strongly anisotropic g factor of heavy holes in such QWs favors unusual collective dynamics of the exciton and manganese spins in a magnetic field applied parallel to the QW plane. Starting from the mid-1990s, various manifestations of these dynamics were revealed in experiments on multiple spin-flip scattering of light by manganese ions [7], ultrafast magnetization oscillations detected using a pump probe with an ultrahigh time resolution [8–11], and energy transfer from the Zeeman to magnetic-polaron reservoir [12]. A theoretical consideration of the spin dynamics in this system can be found in [13].

That such systems could exhibit, under the Hanle effect conditions, an increase in the degree of polarization in place of depolarization, i.e., a "negative" or anomalous Hanle effect (AHE), was first reported in [14]. This effect was qualitatively explained as being due to the fact that the manganese ion magnetization induced by an external magnetic field leaves the QW plane as a result of precession in the net effective magnetic field (external field + the exchange field of a photoexcited hole) [14, 15]. We are still following, in general terms, this interpretation.

It has been established in recent years that the AHE, rather than being a specific property of one sample, is frequently observed (under resonance photoexcitation) in QWs with semimagnetic layers and that the magnetic ions may reside both in the QW and barrier layers, with the manganese concentration varying over a broad

1063-7834/03/4507-1360$24.00

range. On the other hand, development of a model capable of quantitatively describing the observed curves required that a proper understanding of the important part played by thermal fluctuations of the local magnetization in the photohole spin dynamics in semimagnetic QWs be attained [16] and was spurred by an experimental observation of the enhancement of hole spin relaxation in a transverse magnetic field [9].

The present communication reports on experimental data obtained on the AHE and related effects in multiple quantum-well structures. A fluctuation-dynamic AHE model that provides a satisfactory description of the experiment is also proposed. The theory takes into account the effect of fluctuations in the local magnetization on the collective spin dynamics of the hole interacting with magnetic ions. While the physical mechanisms underlying the model are not novel, the AHE as a whole is a new and interesting phenomenon, which demonstrates, in particular, that the "Voigt configuration" (more specifically, the "Hanle effect conditions") and the "luminescence depolarization" are in no way synonymous.

2. EXPERIMENT

We studied QW heterostructures CdTe/$Cd_{1-x}Mn_xTe$ (x = 0.18) and $Cd_{1-x}Mn_xTe/Cd_{1-x-y}Mn_xMg_yTe$ (x = 0.07, y = 0.29) grown by molecular-beam epitaxy on (001)InSb and (001)CdTe substrates, respectively. The CdTe/$Cd_{1-x}Mn_xTe$ structures had two QWs each, which were 40 and 80 Å wide and separated by $Cd_{1-x}Mn_xTe$ barriers 60 Å (sample 1) and 150 Å (sample 2) wide. The $Cd_{1-x}Mn_xTe/Cd_{1-x-y}Mn_xMg_yTe$ structure contained five quantum wells 9, 16, 45, 80, and 300 Å wide (sample 3). The structures were optically pumped by a tunable Al_2O_3 : Ti laser. The exciting light was propagated along the growth axis of the structure, and the radiation was detected at a small angle to this axis. The circular polarization of the radiation was measured with a photoelastic polarization modulator and a double-channel photon-counting system. The magnetic field was generated by a superconducting coil or electromagnet and was applied either parallel to the growth axis (Faraday geometry) or perpendicular to it (Voigt geometry).

Because of the existence of an efficient channel of spin relaxation through exchange scattering from magnetic ions in semimagnetic semiconductors and QWs with semimagnetic layers, their electrons and holes usually exhibit short spin relaxation times. This makes observation of the optical spin orientation effect in such systems under continuous excitation a difficult problem. Nevertheless, the optical orientation signal can be detected by properly varying the relative magnitude of the lifetime and spin relaxation time. This can be attained either by choosing sufficiently wide QWs with manganese ions in the barriers to reduce the carrier wave function penetration depth into the magnetic layers [17, 18] or by reducing the lifetime efficiently by providing carrier escape by tunneling through a semitransparent barrier [14, 19]. Even so, the degree of luminescence polarization is usually small (on the order of a few percent).

It should be pointed out that semiconductors containing magnetic ions can exhibit a specific pseudodynamic effect of optical exciton orientation, which was discovered and explained by Warnock and coworkers [20]. The existence of this effect in size-quantized structures was reported in [21]. The Warnock orientation effect is due to the splitting of excitonic states by the exchange fields of magnetic fluctuations; it differs from the "traditional" optical orientation in that the exciton spin polarization produced by light practically does not change during the exciton lifetime [20, 22]. Optical orientation through the Warnock mechanism requires resonant excitation of localized excitonic states; therefore, in the absence of a strong magnetic-polaron shift, this effect is observed at pump frequencies close to the luminescence light frequency. Resonant excitation of localized excitons can be efficiently achieved through both the traditional dynamic and the Warnock mechanism; in these conditions, the question of the nature of the optical-orientation signal (in a zero field) should be answered taking into account both these possibilities. We stress this point, because it is the resonant excitation that is required to make AHE observation possible (see below).

Hanle effect experiments made under optical-orientation conditions on QWs with magnetic ions exhibit, in many cases, the expected monotonic radiation depolarization caused by precession of the average spin of carriers (or excitons) in a transverse magnetic field. The Hanle curve usually has a Lorentzian shape [19], sometimes with the addition of a field-independent part, which was interpreted in [18] as a hole contribution to the optical-orientation signal. At the same time, in other cases, application of a magnetic field in Voigt geometry brings about, in place of depolarization, enhancement of the luminescence polarization. The first curve of this kind was obtained by us in a study of optical orientation in a 40-Å wide CdTe/CdMnTe QW that was tunneling-coupled with a 80-Å wide QW (sample 1) [14]. Because of the high tunneling transparency of the inner barrier, excitons transfer from the 40-Å wide QW to the neighboring well in a time shorter than that required for their recombination; therefore, the luminescence emitted from this QW is two orders of magnitude weaker than that from the 80-Å wide QW. However, when excited in resonance with localized excitonic states in the 40-Å wide QW, a secondary luminescence is observed in the form of a long-wavelength wing near the laser line (Fig. 1a) and a separate peak spaced from the latter by the optical phonon energy. The long-wavelength wing exhibits a structure when excited in a certain energy region. What we have is actually resonant scattering of light by excitons. The excitation profile of the wing nearly coincides with that of the luminescence

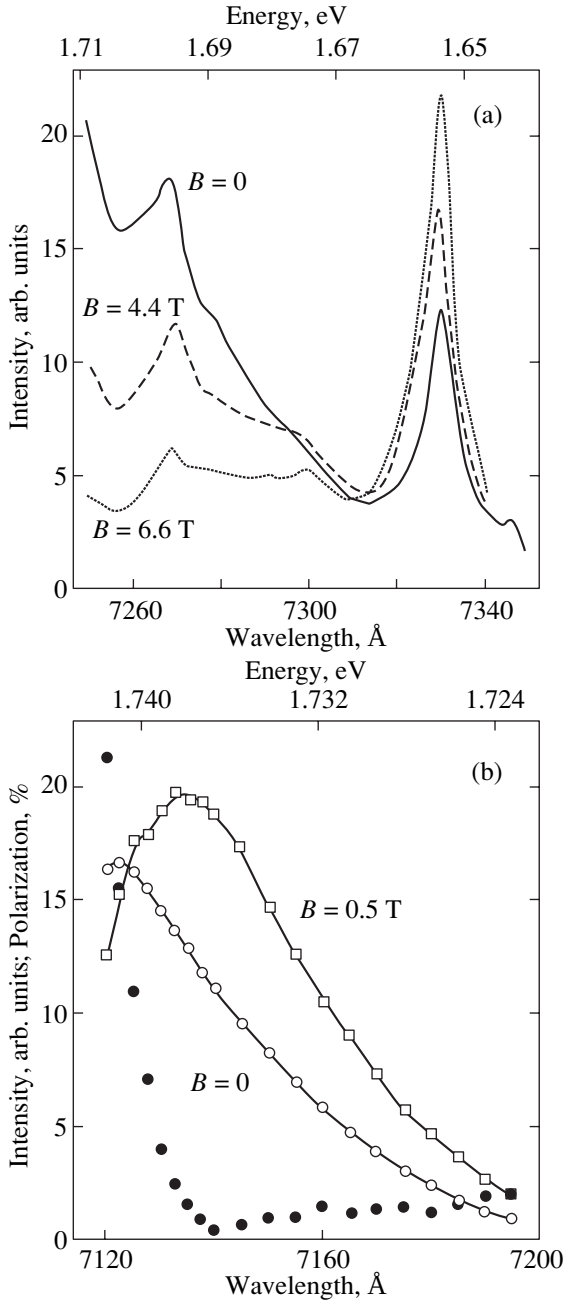

Fig. 1. Quantum-well emission spectra under excitation in the region of localized exciton states (T = 2 K) for (a) a 40-Å-wide QW in sample 1 measured in different longitudinal magnetic fields (pump photons $\hbar\omega_{ex}$ = 1.712 eV) and (b) a 80-Å-wide QW in sample 3 measured at B = 0 and in a transverse magnetic field B = 0.5 T (pump photons $\hbar\omega_{ex}$ = 1.743 eV). Panel (b) also displays an optical-orientation spectrum obtained in a zero field.

spectrum (i.e., it lies in the region of localized excitonic states), whereas the *LO*-line excitation profile is shifted shortward by 18 meV. This result apparently means that the observed features in the secondary-luminescence spectrum are accounted for by various intermediate states; more specifically, in the case of the wing, such intermediate states are the localized excitons and, in the case of the *LO* line, most probably quasi-free excitons. Both features can be observed simultaneously in the same spectrum (at the same excitation energy) due to the strong inhomogeneous broadening in the sample. Application of a magnetic field (both in the Voigt and Faraday geometry) affects the radiation intensity substantially (Fig. 1a), which indicates variation of the density of states (and, hence, of the absorption coefficient) at the pump frequency because of the giant Zeeman splitting. The variation in radiation intensity depends on the exciting photon energy ($\hbar\omega_{ex}$), so that, for the energy $\hbar\omega_{ex}$ = 1.712 eV chosen in Fig. 1a, the intensity of the wing decreases and that of the *LO* line increases with increasing magnetic field. When excited by photons of energy $\hbar\omega_{ex}$ = 1.721 eV (it is at this energy that the AHE curves were measured) in a longitudinal magnetic field, the radiation intensity decays both in the wing and in the *LO* line. That different features of the emission spectrum vary differently in a magnetic field lends support to the above hypothesis on the nature of the intermediate states. We shall see that polarization measurements are likewise in accord with this conjecture.

If circularly polarized light is used for the pumping, the radiation also turns out partially polarized. The optical-orientation signal at the wing decays, as usual [18], with increasing distance from the laser line, to increase again near the *LO* line. The detected signal was not related to penetration of diffusely scattered laser light into the monochromator slit. Measurement of the Hanle effect in the *LO* line reveals the expected monotonic depolarization of the radiation (Fig. 2a) approximated by a Lorentzian. By contrast, a similar measurement performed in the wing shows a substantial growth in the degree of circular polarization of the radiation, to be replaced by polarization decay only in stronger fields (Fig. 2b). We call the phenomenon of the latter kind the anomalous Hanle effect. The effect is an odd function of the field, as should be expected from the experiment symmetry. The different behavior of polarization in the wing and in the *LO* line under a magnetic field lends support to the hypothesis of these spectral features being of different natures. A decrease in circular polarization of the exciting light proportionally reduces both the polarization of radiation in zero magnetic field and the amplitude of the polarization rise in a magnetic field. Studies of the spectral response of AHE revealed that the amplitude of the polarization increase also decays as one moves away from the laser line. It should be pointed out, however, that, as follows from the dependence of the amplitude of the effect on excitation density (see below), the magnitude of AHE does not show a distinct correlation with polarization in a zero field. Note also that the effect does not depend on the exciton lifetime; indeed, in sample 2, in which the lifetime in the 40 Å wide QW is a few orders of magnitude longer (the luminescence from both QWs has the same efficiency), we observed the same magnetic field

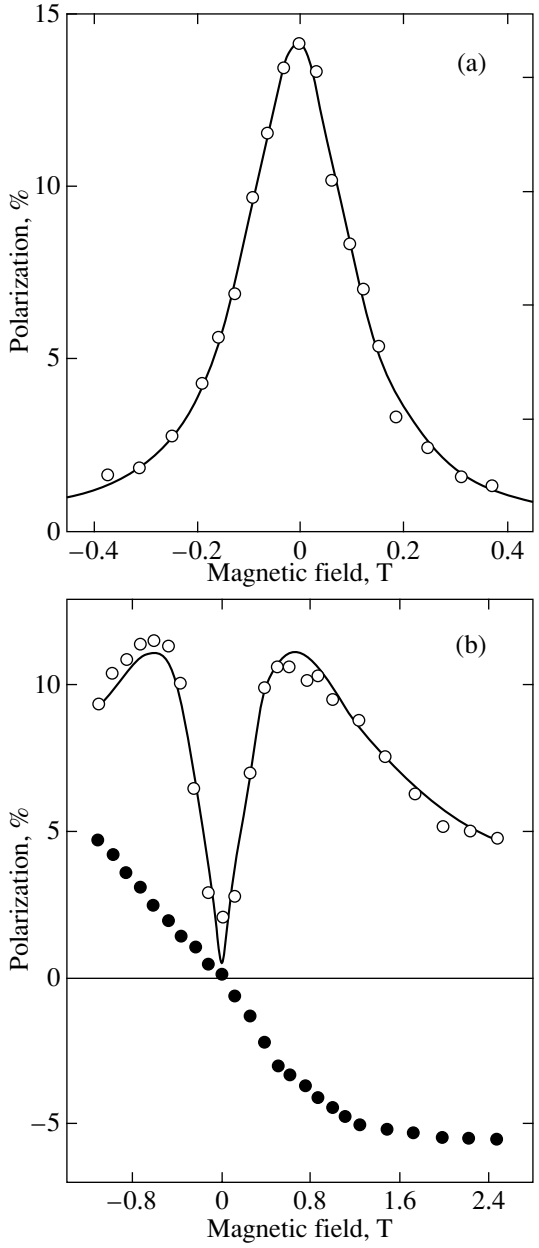

Fig. 2. (a) Normal and (b) anomalous Hanle effect in a 40-Å-wide QW (sample 1). Emission measurement: (a) in the *LO* line and (b) in the wing near the laser line (Fig. 1a). Panel (b) also plots (filled circles) the magnetic field dependence of radiation polarization obtained under unpolarized pumping (thermal polarization generated in quasi-Voigt geometry). Solid curves a Lorentzian profile with halfwidth $\Delta H = 0.24$ T (panel (a)) and theoretical relation, Eq. (15), with $\tau_{s0} = 1.6$ ps and $\Omega_0 = 0.11$ ps^{-1} ($B_0 = 0.63$ T) (panel (b)).

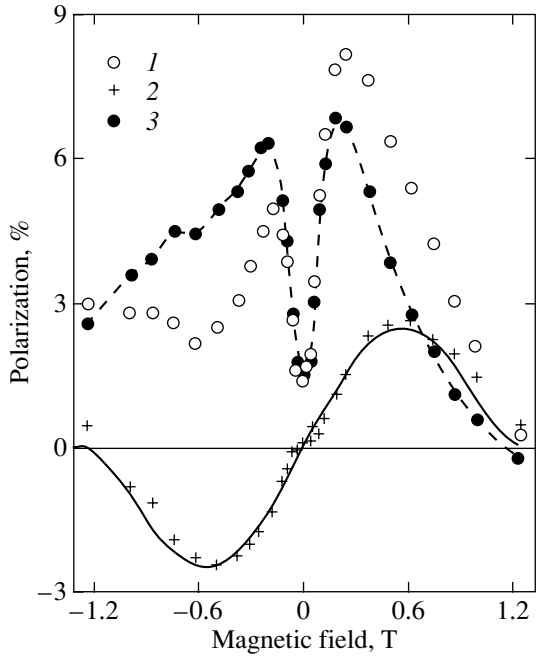

Fig. 3. Magnetic field dependence of circular radiation polarization measured in a QW with $L = 80$ Å (sample 3) in quasi-Voigt geometry: (*1*) experimental data for circularly polarized excitation, (*2*) same for linearly polarized pumping (thermal polarization), and (*3*) difference between data *1* and *2* (an attempt to compensate for the misalignment in geometry).

dependences of the polarization. One might think that polarization in zero magnetic field and the anomalous behavior of the magnetic field dependence are not related in any way with each other and have different sources. (In the normal Hanle effect, the effect of the magnetic field on the spin evolution of the carriers responsible for zero-field polarization accounts for the monotonic decrease in the polarization.)

The AHE in sample 3 is observed in similar conditions, i.e., under excitation into the band of localized exciton states (Fig. 3). Note that the zero-field radiation spectrum also has the shape of a wing on the laser line, with a peak seen to split off in a magnetic field, which indicates dynamic formation of a hole magnetic polaron through the mechanism proposed in [12] (see Fig. 1b). Measurements of the AHE in this sample, performed in various conditions, showed that the degree of optical orientation in a zero field varies strongly with the pumping power (Fig. 4a), from zero under strong pumping (>12 mW) to 10% under weak pumping (~0.5 mW). At the same time, the AHE is affected by power variation more weakly (Fig. 4a). Figure 4b illustrates more comprehensive measurements of circular polarization as a function of the magnetic field carried out at a high excitation power in sample 3. It is known that, in semimagnetic QWs, high-power optical pumping may give rise to heating of the manganese spin system, with absorption in the substrate having been identified in sample 3 as the main heating channel [23]. Therefore, the inessential changes in the AHE occurring as the pumping is increased can be assigned to a heating-induced decrease in the magnetic susceptibility of the manganese system. The nature of the strong

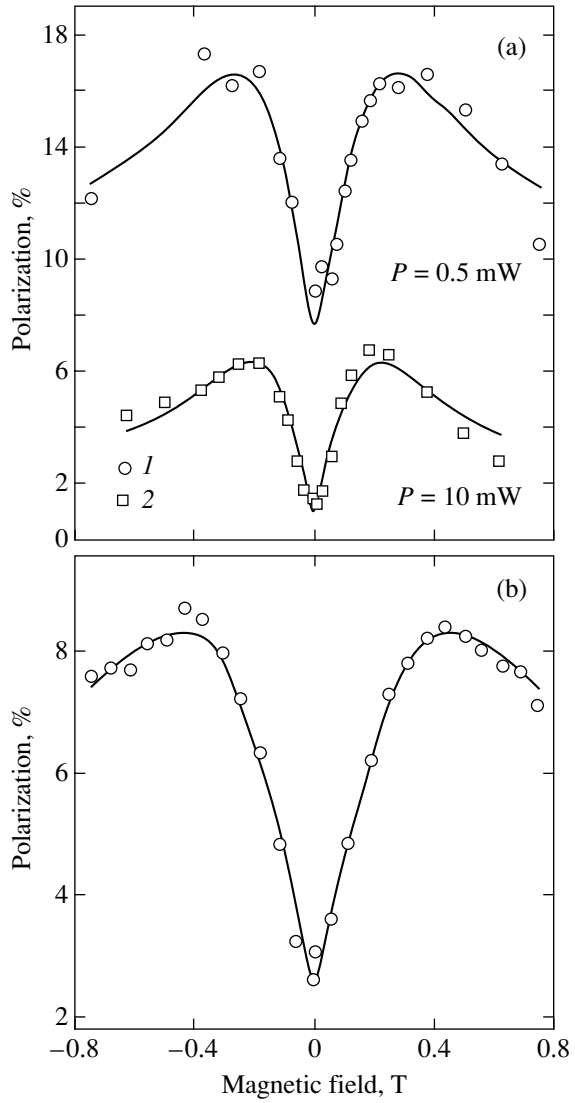

Fig. 4. Anomalous Hanle effect in a 80-Å-wide QW (sample 3) measured under different optical-excitation densities: (a) (*1*) P = 0.5 and (*2*) 10 mW; (b) expanded plot for P = 8 mW. Solid curves are theoretical dependences based on the plots in Eq. (15). For the curve in panel (b), τ_{s0} = 3.1 ps and $\Omega_0 = 0.04$ ps^{-1} (B_0 = 0.2 T).

dependence of the magnitude of zero-field polarization on excitation power is more difficult to comprehend. Because the power dependences, as well as the spectral response, do not exhibit a distinct correlation between zero-field polarization and the behavior of the AHE, we assume in what follows that the AHE is an independent phenomenon which occurs in magnetic QWs under experimental conditions favoring the Hanle effect and which can be accompanied (but not necessarily) by radiation polarization in a zero field.

Note one more specific feature of AHE experiments. Such experiments require precise alignment of the magnetic field with respect to the QW layer plane; otherwise, a small magnetic-field component along the growth axis z may induce a z component of the magnetization, which will give rise to an explosive growth of "thermal" circular polarization of the radiation. Thermal polarization is observed to exist under both circular polarized and unpolarized pumping and is enhanced in QWs with magnetic layers because of the giant spin splittings of the electrons and holes. Therefore, if the angle between the field and the QW plane is only a few degrees, the signal produced by thermal polarization may turn out comparable to that due to optical polarization and the AHE.

To combat thermal polarization, we employed a system designed to rotate a sample about its surface normal in the Voigt geometry. At room temperature, the parallelism of sample fixing on the holder stage can be monitored by directing the laser beam on the holder surface, rotating the stage, and following the movement of the reflected spot on a distant screen. The rotation system can also be conveniently used for fine positional adjustment of a sample already immersed in helium. Experience points to the following typical error in sample positioning: while the system rotation axis and the magnetic field direction are perpendicular to each other with a satisfactory accuracy, the sample axis z is not parallel to the rotation axis. In these conditions, one can adjust the magnetic field parallel to the sample surface (and the QW layer) by rotating the stage properly. The Voigt geometry precision can be conveniently controlled by exciting the sample with unpolarized light and trying to zero the thermal polarization signal at an applied magnetic field. As we shall see, however, the field applied must not be too strong.

It might seem that the above measures are unnecessary because the Hanle effect (including the AHE) and thermal polarization have different symmetry with respect to magnetic field inversion: the expected magnetic field dependences are even and odd in the field, respectively. True, the AHE is even in precise Voigt geometry, and thermal polarization is odd in a slightly tilted field but only in the case of unpolarized excitation (Figs. 2b, 3)! If pumping in a tilted field is done with circularly polarized light, the field dependence of the polarization cannot be represented as the sum of an even- and an odd-in-field contribution at all; this is particularly true for strong fields (Fig. 3). In other words, the contributions due to the AHE and to the thermal polarization are not additive. This result is not at odds with common sense, because the situations with positive and negative longitudinal field components are not physically equivalent without simultaneous switching of pumping from the right- to left-hand polarization [a manifestation of the (σ, H) invariance]. It appears clear, however, that AHE measurements should be performed in as close to the Voigt geometry as possible and, at any rate, not in fields so high that the AHE curve can no longer be symmetrized by subtracting the odd-in-field contribution.

Interestingly, while pure thermal polarization (produced by unpolarized pumping) in an inclined field is odd in field, it exhibits an unexpected behavior in strong magnetic fields (Fig. 3). As the magnetic field increases, the longitudinal component of the field also increases. If only the longitudinal field component acted on the thermal polarization, the latter would continue to grow and saturate close to 100%, as occurs in the Faraday geometry (see, e.g., [24]). Instead, the polarization increases to a few percent only (the actual magnitude depends on the field tilt), after which the growth of the polarization is replaced by its decay. This behavior of thermal polarization should be assigned to the presence of a transverse (Voigt) magnetic-field component. That the growth of polarization with increasing field transfers to its decay permits the conclusion that the Voigt component begins to dominate over the Faraday component starting at certain fields. Because the action of the Faraday field component, that induces thermal polarization is linear in field, the Voigt component destroying this polarization cannot involve the transverse *g* factor of electrons or heavy holes [25] (because the energies associated with them are also linear in field). Therefore, it appears probable that the mechanism of action of the Voigt component is based on the field-induced mixing of the hole subbands, in which the hole doublet splitting in weak fields is cubic in field [26] and which, hence, is capable of overcoming the linearly growing contribution.

Note that it is in the fields in which the state mixing occurs and thermal polarization decays (Fig. 3) that the possibility of symmetrizing the AHE curves in a tilted field (i.e., the additivity of the even and odd contributions to polarization) breaks down. On the other hand, judging from the position of the maximum in thermal polarization in Fig. 3, state mixing occurs in fields of the same order (slightly higher) as the transition of the AHE curve from the polarization growth to decay. This gave us grounds to use the concept of magnetic-field-induced subband mixing in explaining the polarization decay in the AHE conditions theoretically.

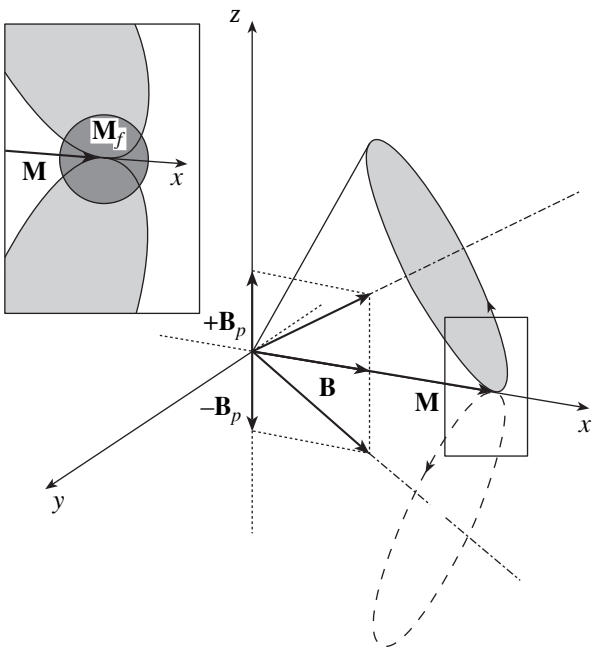

Fig. 5. Local magnetic moment **M** induced by an external magnetic field **B** in the quantum-well plane (*xy*) precessing around an effective field representing the sum of field **B** and the hole exchange field $\mathbf{B}_p$ (polaron field). Also shown are trajectories of the magnetic-moment precession about the upper and (dashed line) lower polaron state. Inset: expanded fragment of the figure showing the region of **M** fluctuations.

3. CALCULATION AND DISCUSSION

The main universal features observed in anomalous Hanle curves are (a) a fast growth of polarization in a weak field; (b) the passage of polarization through a maximum, with this maximum value being $\rho_{max} \sim 0.1 \ll 1$; and (c) a slower decay of polarization with a further increase in the field. We take, as a starting point, the chief qualitative cause for the growth of polarization, which was pointed out as far back as in [14], namely, the formation of a longitudinal component (along the QW normal) of local magnetization as a result of its precession in the effective magnetic field.

It appears appropriate to recall here the scenario proposed in [14]of the phenomena bringing about sign reversal of the Hanle effect, because that interpretation is pertinent to the present consideration. Circularly polarized light resonantly excites localized excitons with the angular momentum projection $|+1\rangle$ (heavy hole $|+3/2\rangle$ and electron $|-1/2\rangle$) in the QW. In a zero magnetic field, the nonequilibrium spin of the electrons and holes interacts with magnetic ions to relax on a picosecond scale [9, 10, 27] and, thus, does not live up to recombination, which occurs on a time scale of hundreds of picoseconds [28, 29]. As a result, the recombination radiation ends up weakly polarized or entirely unpolarized. If, however, a magnetic field $\mathbf{B} = (B, 0, 0)$ is applied in the QW plane, a field-induced local magnetic moment (LMM) $\mathbf{M} = (M_B, 0, 0)$ builds up; i.e., the manganese ion spins undergo an alignment with the field (along the *x* axis) to a certain extent in the region where a localized hole is generated by light. Because the effective hole exchange field $\mathbf{B}_p$ (the polaron field), directed along the *z* axis, is added to the external field **B**, generation of a hole with a strongly anisotropic *g* factor changes the magnitude and direction of the field acting on **M** [12, 13]. Due to Larmor precession of vector **M** in the net field, the component of this vector along the *z* axis becomes nonzero (Fig. 5). Because the hole *g* factor has only one large component, g_{zz}, it is the appearance of the *z* component in the local magnetization that brings about splitting of the $|+3/2\rangle$ and $|-3/2\rangle$ hole states. As a result, starting from a certain moment in this evolution, the polarization of holes will be deter-

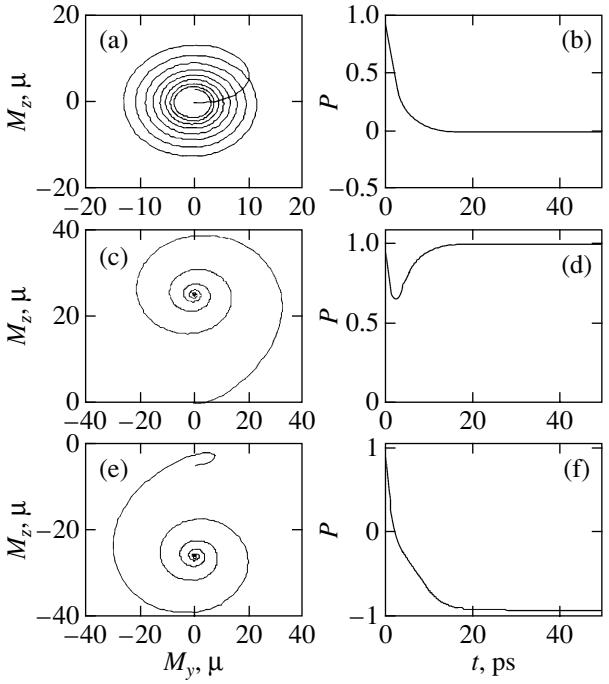

Fig. 6. (a, c, e) LMM phase trajectories plotted using Eqs. (1) and (2) and (b, d, f) the corresponding hole spin dynamics. Parameters for panels (a, b): $kT = 0.5$ meV, $\tau_s = 3$ ps, $T_2 = 200$ ps, $B = 1$ T, $B_p = 0.6$ mT, $\chi = 50\,000$ μ/T, and $\chi^{-1}(d\Delta/dB_\parallel) = 10^{-4}$ meV/μ (reconstruction of the conditions chosen in [10]). Parameters for panels (c–f): $kT = 0.16$ meV, $\tau_s = 3$ ps, $T_2 = 45$ ps, $B = 1$ T, $B_p = 0.8$ T, $\chi = 100$ μ/T, and $\chi^{-1}(d\Delta/dB_\parallel) = 0.1$ meV/μ (reconstruction of our experimental conditions). In the cases (c) and (d), the original LMM orientation is $\mathbf{M}_0 = (\chi B, 0, 0)$, and for the (e) and (f) cases, $\mathbf{M}_0 = (\chi B, 0, -0.1\chi B)$.

mined not by their short intrinsic "spin memory" but rather by the fact that the average hole polarization in the quasi-static exchange field of magnetic ions is nonzero.

The process outlined above is actually nothing other than energy transfer from the Zeeman reservoir (energy of the magnetic ion interaction with the field) to the exchange reservoir (energy of the magnetic ion interaction with the hole) or, in other words, dynamic formation of a hole magnetic polaron [12]. It goes without saying that the hole acts with its exchange field on the spins of magnetic ions to reach the magnetic polaron state in the absence of a magnetic-field as well. In this case, however, the characteristic polaron formation time is not the period of manganese magnetic moment precession in a field of the order of B_p (tens of picoseconds) but rather the longitudinal-magnetization relaxation time T_1, which, in such structures, while being longer than or on the order of the exciton lifetime [28, 29], is certainly in excess of the precession period. Therefore, although the final emitting state in a given QW is a polaron even in a zero field, this state forms slower than in the same QW in a transverse magnetic field and the original orientation of the hole spin exerts a weaker effect on the radiation polarization.

While being certainly attractive in its simplicity, the above purely dynamic scenario is difficult to fit to a quantitative description of the experimental data.

3.1. Difficult Points in the Dynamic Approach

The collective spin dynamics of a localized hole and magnetic ions in a transverse field was studied in [10, 13]. We write the dynamic equations in the form

$$\frac{d\mathbf{M}}{dt} = \mathbf{\Omega}\times\mathbf{M} - \frac{1}{T_2}\left(\mathbf{M} - \mathbf{\Omega}\frac{\mathbf{\Omega}\mathbf{M}}{\Omega^2}\right),$$
$$\frac{dP}{dt} = -\frac{1}{\tau_s}\left[P - \tanh\left(\frac{\Delta(M_z)}{2kT}\right)\right], \quad (1)$$

where T_2 and τ_s are the transverse magnetization relaxation and hole spin relaxation times, respectively; $\Delta(M_z)$ is the spin (exchange) splitting of the $|+3/2\rangle$ and $|-3/2\rangle$ hole states caused by the z component of the local magnetic moment; kT is thermal energy; and

$$\mathbf{\Omega} = \mathbf{\Omega}_B + P\mathbf{\Omega}_p \quad (2)$$

is the "vector" Larmor frequency ($\mathbf{\Omega}_B = \mu g\mathbf{B}/\hbar$, $\mathbf{\Omega}_p = \mu g\mathbf{B}_p/\hbar$, μ and g are the Bohr magneton and the manganese g factor ($g = 2$), and $\mathbf{B}_p$ is the z-oriented exchange field exerted on the LMM by the fully spin-aligned hole).

In the first of Eqs. (1), we neglected the longitudinal relaxation. Equation (2) for the field acting on the LMM is represented in the short correlation time approximation; since τ_s the shortest of the various times, it is assumed that the exchange field of a hole is proportional to its average polarization. Neglecting LMM fluctuations, the initial conditions for coupled equations (1) are as follows: $P = 1$ and $\mathbf{M} = (\chi B, 0, 0)$, where χ has the meaning of the magnetic susceptibility normalized to the hole localization volume.

The equations describing the dynamics of the spin system considered have solutions of two types. Depending on the values of the parameters, the phase trajectories wind either on the external field direction or on one of the two low-symmetry magnetic polaron states. The first version corresponds to the weak exchange field of the hole. In particular, Eqs. (1) closely approximate the solutions for **M** presented in [10]. The solutions of this type (Fig. 6a) apparently satisfy the conditions of most experiments on ultrafast spin dynamics measured by the time-resolved Faraday or

Kerr rotation method [9–11].[1] Note that, in these conditions, the average hole spin relaxes to zero (Fig. 6b) in a time much shorter than the exciton lifetime, so that in a steady state one may expect the radiation to be practically entirely unpolarized.

The approach proposed in [16] permitted us to estimate the magnetic polaron parameters of interest from the experimental data on Zeeman splitting Δ and the degree of magnetically induced circular polarization of the luminescence ρ_{MCPL} in a longitudinal field. Estimation made for the original values $d\Delta/dB_\parallel = 10$ meV/T [31] and $d\rho_{MCPL}/dB_\parallel = 5\ T^{-1}$ (40-Å-wide QW, sample 1) yields the following values:

$$E_p \sim \frac{1}{2\pi kT}\left[\frac{(d\Delta/dB_\parallel)^2}{(d\rho_{MCPL}/dB_\parallel)^2}\right] \approx 4 \text{ meV},$$

$$B_p \sim \frac{d\Delta/dB_\parallel}{\pi kT(d\rho_{MCPL}/dB_\parallel)^2} \approx 0.8 \text{ T},$$

$$M_p \sim \frac{E_p}{B_p} \approx 5 \text{ meV/T} \approx 80\ \mu, \qquad (3)$$

$$M_f = \sqrt{\langle M^2\rangle} \sim \frac{\sqrt{\pi}}{2} kT \frac{d\rho_{MCPL}}{dB_\parallel}$$

$$\approx 0.75 \text{ meV/T} \approx 13\ \mu.$$

The situation realized in the 80-Å-wide QW in sample 3 is qualitatively similar: for the original values $d\Delta/dB_\parallel = 20$ meV/T [12] and $d\rho_{MCPL}/dB_\parallel = 10\ T^{-1}$, estimation yields $E_p \approx 4$ meV, $B_p \approx 0.4$ T, $M_p \approx 160\ \mu$, and $M_f \approx 26\ \mu$. These figures can be commented on as follows. First, the equilibrium polaron energy E_p has a sizable magnitude (4 meV), whereas the photoluminescence line obtained in a zero-field experiment does not exhibit the polaron shift [32]. This argues for slow magnetic-polaron formation T_1 (on the exciton lifetime scale) [29], i.e., for the possibility of neglecting the longitudinal relaxation in Eq. (1). Second, the equilibrium polaron moment M_p substantially exceeds (by a factor of 6.5) the fluctuation moment M_f, whose existence is associated with the smallness of the hole localization radius [16]. This relation will be employed subsequently. Third, the figures presented in Eq. (3) permit direct estimation of the parameters of the dynamic model, because the susceptibility is $\chi = M_p/B_p \approx 100\ \mu$/T and the splitting is $\Delta(M_z) = (d\Delta/dB_\parallel)(M_z/\chi)$.

By substituting the values thus obtained in to Eqs. (1) and solving it numerically, one can readily verify that, in the case of interest to us here, the system evolves in the polaron regime (Figs. 6c, 6d). The field-induced magnetic moment relaxes to the direction of the equilibrium polaron moment (Fig. 6c). The average hole polarization relaxes very rapidly to a nonzero value, which is close to unity already in comparatively low fields (Fig. 6d). Thus, the hole in the final polaron state is fully polarized, which should correspond to 100% luminescence polarization. The variation in τ_s by one or two orders of magnitude does not change the situation. There is also no factor which could bring about polarization decay within this model. Because the maximum luminescence polarization in our experiments is ten percent at most, we have to admit that the dynamic model is invalid for description of the available experimental data.

Note two more points. First, our choice of the values of T_2 was based on the reasoning that the nonuniformity of the exchange field should be of the order of the exchange field itself because of the nonuniform density of the hole wave function in the polaron, so that the time T_2 should be on the order of the LMM precession period. As the external field increases, the total field becomes increasingly more uniform, so that transverse relaxation can slow down somewhat. However, Eqs. (1) include an additional transverse-relaxation mechanism that is disregarded in T_2. It is related to retardation of the hole exchange field (because of the nonzero τ_s). Therefore, transverse relaxation occurs efficiently enough even for an infinitely long T_2.

The second point provides, in our opinion, the key to understanding the experimental results. Although the general pattern of the solutions to Eqs. (1) of interest to us here and, in particular, the complete average hole polarization during all of its lifetime are fairly stable with respect to variation of the parameters of Eqs. (1), even a slight change in the initial conditions for **M** may suffice to transfer the system to another final state (Figs. 6e, 6f). While this will be again a polaron state, it will have a negative z component of the local magnetic moment, with the oppositely directed hole spin and, accordingly, negative radiation polarization. One would have only to take into account fluctuations of the initial conditions for **M**, and then part of the polarons

[1] The question of why (for similar samples) Kerr rotation experiments allow their interpretation with a hole exchange field of the order of 1 mT [10], whereas experiments on cw-excited luminescence and Raman scattering require fields three orders of magnitude higher (about 1 T) for their explanation, ([12, 16, 30], see also below), certainly deserves discussion. This discrepancy was also pointed out in [10]. We believe that its origin lies in the difference between the experimental conditions accepted in the two types of experiments. Estimates based on the data from [10] suggest that the peak power of optical excitation when pumped by subpicosecond laser pulses is six to seven orders of magnitude higher and the hole concentration (10^{10} cm^{-2}) is two to three orders of magnitude higher than the respective values measured in stationary experiments. It may be conjectured that, at such high concentrations, the holes are primarily delocalized and the average exchange (molecular) field exerted on the manganese ions by them (which is proportional to the hole concentration) is exactly three orders of magnitude lower than the polaron field of a localized hole. Considered along these lines, millitesla-scale exchange fields involved in Kerr rotation experiments have meaning not only on the average [10] but on the local scale as well. Otherwise, it would be difficult to explain the linear dependence of the magnetization precession frequency on magnetic field in the range of weak fields (see [10, Fig. 3a]).

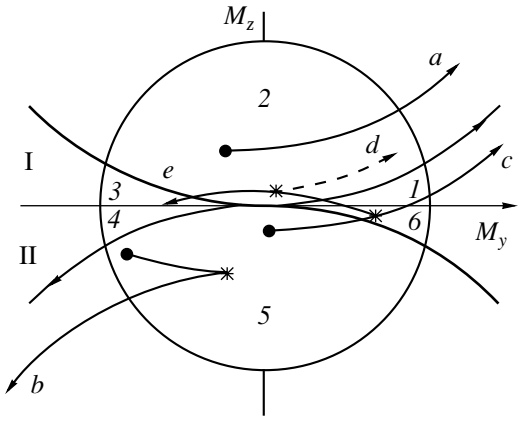

Fig. 7. Section of the LMM phase space by the plane $M_x = \chi B$ (see text and inset to Fig. 5). The critical line (thick solid) separates the "trapping zones" of the upper and lower polaron states. Several versions of trajectories are shown: hole (*a*) is created in the upper zone and attracted to the upper polaron state; (*b*) is created in the lower zone and attracted to the lower polaron state; (*c*, *d*) is created in the lower zone, crosses the critical surface, and is attracted to the upper polaron state; or (*e*) is created in the lower zone and returns there after two crossings of the critical surface (reentrant trajectory). The points of hole creation are specified by circles, and those of spin flip, by stars.

would be in the spin-up final state and the other part in the spin-down final state. The polarization of the radiation will now be determined by the balance between the concentrations (or formation probabilities) of such polarons.

A direct way to realize this idea could be by averaging the solutions to Eqs. (1) over the initial conditions. The efficiency of such an approach is, however, questionable, and its computational complexity only too obvious, because the equations are not integrable. In the next section, we formulate a model that permits the inclusion of LMM fluctuations in a physically more revealing way.

3.2. Fluctuation-Dynamic Model

To understand the way in which holes created in states with nonzero LMM fluctuations become distributed between the final polaron states of two types (spin-up and spin-down), consider first the case of a sufficiently strong external field ($B \sim B_p$). Based on the results obtained in the preceding section, we assume the holes to separate within the first few picoseconds after their creation and that, if the LMM starts to precess in a large circle around one of the polaron states (Fig. 5), it is finally attracted to this state because of efficient transverse relaxation and the hole no longer relaxes in spin.

Figure 7 presents the section of the LMM space by the $M_x = \chi B$ plane. The circle conventionally defines the bounds of scatter of the LMM components transverse to the M_x axis. Thus, the circle confines the possible positions of the end point of the LMM vector at the instant of hole creation. Also shown are two critical trajectories (I, II), namely, the trajectories of rotation of the LMM vector end point around the upper and lower polaron states which touch the M_y axis. The critical trajectories are actually circles of large radius centered on the upper and lower polaron states.[2]

The two critical trajectories and the M_y axis divide the fluctuation circle into six regions (*1–6*). Consider first the case of zero temperature and an infinitely fast spin relaxation of holes with a highly anisotropic *g* factor. In these conditions, immediately after the hole creation, its spin aligns with the LMM *z* component in the region where the hole was borne. As for the LMM, it may occupy any position at the point of hole creation within the fluctuation circle. When speaking subsequently about "hole creation at a point within the circle", we assume that the hole was created in the region where the LMM is directed exactly as it is at this point in the circle.

Thus, in the case of instantaneous hole spin relaxation, the hole exchange field in the upper half-plane is always directed upward and the LMMs move along trajectories with a positive curvature (such as trajectory I). The holes created in regions *1* and *2* drive the LMMs up from the fluctuation region to eventually form spin-up polarons. The trajectories of the holes borne in region *3* cross the M_y axis with a spin flip; the LMMs transfer to trajectories with a negative curvature (as trajectory II) and leave the fluctuation region downward. Similarly, the final state of the holes created in the lower semicircle in region *6* is the spin-up polaron state and of those borne in regions *4* and *5*, the spin-down state. Thus, in the case of instantaneous hole relaxation, half of the fluctuation realizations (regions *1*, *2*, *6*) result in the formation of spin-up polarons and the other half (regions *3–5*) evolve to the lower polaron state. The net radiation polarization is zero. The "upper" zone (*1*, *2*, *6*) and the "lower" zone (*3–5*) are separated from each other by a critical line (a critical surface in space) made up of parts of critical trajectories I and II.

Let us now take into account the finiteness of the hole relaxation time. Viewed from a qualitative standpoint, this means that, if holes are created with spin up, their spin do not flip for a time on the order of τ_s even if the holes are created on the lower half-plane. Within this time interval, therefore, the LMMs move along type-I trajectories on the lower half-plane. As a result, the LMMs from regions *3–5* have a certain chance of reaching region *6* before the hole relaxation, i.e., to transfer from the lower to the upper zone, which corresponds to a change of the final state. It is easy to verify that the radiation polarization in such a scenario will be

[2] The critical trajectories do not lie in the $M_x = \chi B$ plane; therefore, parts of these trajectories are given in Fig. 7 as projected onto the plane in the form of arcs of ellipses with the semimajor axis directed along M_y.

twice the fraction of the LMMs that passed into the upper zone.

This reasoning permits us to reduce the AHE problem to a calculation of the probability flux through the critical surface separating regions *5* and *6*. Assuming the LMM fluctuations to obey a Gaussian distribution

$$\Phi(M_{x0}, M_{y0}, M_{z0}) = \left(\frac{1}{\sqrt{2\pi}M_f}\right)^3 \times \exp\left[-\frac{(M_{x0} - \kappa\Omega_B)^2 + M_{y0}^2 + M_{z0}^2}{2M_f^2}\right] \quad (4)$$

($\kappa = \chi\hbar/\mu g$), one can calculate the probability flux from regions *3–5* through the boundary as

$$F = \int_{3-5} d\mathbf{M}_0 \Phi(\mathbf{M}_0) \exp\left(-\frac{t_{\text{rel}}(\mathbf{M}_0)}{\tau_s}\right), \quad (5)$$

where t_{rel} is the time accepted for the hole spin relaxation. A few words on the meaning of this parameter would be appropriate at this point. In our theory, t_{rel}, the time taken to cross the fluctuation region, plays an important part similar to that of lifetime in the traditional theory of optical orientation [2]. The quantity t_{rel}^{-1} characterizes the rate of trapping of an optically oriented photohole to a polaron state. After the trapping, spin relaxation stops, i.e., the hole preserves its spin. Thus, the spin relaxation of holes competes with trapping into a polaron state, whereas in optical orientation it competes with recombination. As already mentioned, the spin relaxation rate τ_s^{-1} in semimagnetic systems is very high. The optical-orientation signal in the AHE conditions increases because the hole trapping through the fluctuation-dynamic mechanism turns out to be a sufficiently fast process.

The time t_{rel} for holes created in regions *4* and *5* is the total time of LMM motion from the point of creation $\mathbf{M}_0$ to that of crossing the critical surface (by a type-I trajectory). In this communication, we invariably neglect the possibility of hole spin flip from the state "along" the LMM to that in the opposite direction. In view of the typically large values of hole spin splitting in semimagnetic semiconductors (substantially higher than the temperature), this conjecture should probably be considered reasonable. However, it is along the LMMs that the holes created in region *3* are spin aligned from the instant of their creation until they cross the $M_z = 0$ plane. Therefore, to be consistent in our reasoning, we have to exclude the possibility of spin relaxation for $M_z > 0$ for these holes, so that the time t_{rel} for them will be the time in which they move (by a type-I trajectory) from the boundary between regions *3* and *4* to the critical surface.

Note that the holes that have crossed the critical surface retain the potential to spin flip on the way to the upper half-space (in region *6*). These holes will eventually enter the region $M_z > 0$, because both types of trajectories leaving region *6* end there. A spin-down hole, however, may continue moving by a type-II trajectory in the upper half-space as well, to return finally to the lower half-space. We disregard such reentrant trajectories, because it can be shown that the corresponding correction to F is small.

In conclusion to the above qualitative analysis of the model, let us discuss the decay of polarization which replaces its growth with increasing magnetic field (Figs. 2b, 3, 4). We have to recall here experimental studies [8, 9], which revealed, in direct measurements, a considerable reduction of the hole spin relaxation time in semimagnetic QWs placed in a transverse magnetic field. If the acceleration of the hole spin relaxation is associated with the light- and heavy-hole subband mixing, then the dependence of τ_s on Ω_B (i.e., on magnetic field) will have a Lorentzian shape [33]:

$$\tau_s(\Omega_B) = \frac{\tau_{s0}}{1 + \Omega_B^2/\Omega_0^2}, \quad (6)$$

where Ω_0 is a parameter dependent on the subband splitting. True, this interpretation of the $\tau_s(\Omega_B)$ relation is questioned in [9], but even if the doubts expressed in [9] are justified this should affect only the meaning of the parameter Ω_0. One way or the other, acceleration of the hole spin relaxation is observed to occur experimentally and the relation follows a close-to-Lorentzian pattern. As applied to our model, the reduction of τ_s implies a decrease in the flux through the critical surface, i.e., a tendency of the radiation polarization to decrease with increasing field.

3.3. Calculation of the Flux through the Critical Surface

The LMM dynamics equations become simplified on short time scales of the order of τ_s and t_{rel} because one may neglect transverse relaxation ($T_2 \longrightarrow \infty$). On the other hand, the concept of average hole polarization and, accordingly, the second of Eqs. (1) lose their meaning to a considerable extent in this time domain, because the time t_{rel} featuring now in the problem is not short compared to τ_s. Therefore, the hole exchange field must now be considered constant and the hole spin relaxation, a probabilistic (Poisson) process. We assume, for the sake of simplicity, that the probability for the hole spin to flip from the state counter to $\mathbf{M}$ to that along $\mathbf{M}$ does not depend on the magnitude of $\mathbf{M}$ and is characterized by the time τ_s and we also disregard the possibility of reverse spin flips altogether.

With such an approach, the first of Eqs. (1) transforms to an equation of precession with a frequency

$\mathbf{\Omega} = \mathbf{\Omega}_B + \mathbf{\Omega}_p$. This equation, subject to arbitrary initial conditions, is readily solved to give

$$\begin{aligned} M_x(\mathbf{M}_0, t) &= a - b\frac{\Omega_p}{\Omega}\sin\Omega t + c\frac{\Omega_p}{\Omega}\cos\Omega t, \\ M_y(\mathbf{M}_0, t) &= c\sin\Omega t + b\cos\Omega t, \\ M_z(\mathbf{M}_0, t) &= a\frac{\Omega_p}{\Omega_B} + b\frac{\Omega_B}{\Omega}\sin\Omega t - c\frac{\Omega_B}{\Omega}\cos\Omega t, \end{aligned} \tag{7}$$

where

$$\begin{aligned} a &= \frac{\Omega_B^2}{\Omega^2}M_{x0} + \frac{\Omega_p\Omega_B}{\Omega^2}M_{z0}, \\ b &= M_{y0}, \\ c &= \frac{\Omega_p}{\Omega}M_{x0} - \frac{\Omega_B}{\Omega}M_{z0}. \end{aligned} \tag{8}$$

We bear in mind subsequently that M_{y0}, $M_{z0} \sim M_f$, whereas the external field is assumed to be sufficiently strong (so that $M_{x0} \sim \kappa\Omega_B \gg M_f$). Recalling that for times $t \sim \tau_s$ the arc $\Omega t \ll 1$, we expand Eq. (7) into a power series:

$$\begin{aligned} M_x(\mathbf{M}_0, t) &\approx M_{x0} - M_{y0}\Omega_p t - \frac{1}{2}M_{x0}\Omega_p^2 t^2, \\ M_y(\mathbf{M}_0, t) &\approx M_{y0} + M_{x0}\Omega_p t, \\ M_z(\mathbf{M}_0, t) &\approx M_{z0} + M_{y0}\Omega_B t + \frac{1}{2}M_{x0}\Omega_p\Omega_B t^2, \end{aligned} \tag{9}$$

where we have retained terms quadratical in time (in addition to linear ones) but only in the cases where they enter combinations with a large field-induced magnetization M_{x0}.

The critical trajectories I and II each have a single common point with the $M_z = 0$ plane. Therefore, the easiest way to find these trajectories is to equate $M_z(\mathbf{M}_0, t)$ in Eq. (9) to zero and consider this equality as a quadratic equation with respect to t:

$$t_{1,2} = \frac{-M_{y0} \pm \sqrt{(M_{y0})^2 - 2(\Omega_p/\Omega_B)M_{x0}M_{z0}}}{\Omega_p M_{x0}}. \tag{10}$$

Equating to zero its determinant yields an equation for the critical surfaces:

$$M_y^2 = 2(\Omega_p/\Omega_B)M_x M_z, \tag{11}$$

with one of the surfaces corresponding to positive values of Ω_p and M_z and the other, to negative values of these parameters.

Let us now find the time t_k the LMM takes to reach the critical surface. Because $M_{x0} \sim \kappa\Omega_B \gg M_f$, the projection M_x changes very little in crossing the fluctuation region, a process entailing a change in the LMM vector coordinates of the order of M_f. Combining Eqs. (11) and (9) and retaining terms of the same order of smallness as before, we obtain

$$\begin{aligned} (M_{y0} + M_{x0}\Omega_p t_k)^2 &= -2(\Omega_p/\Omega_B)M_{x0} \\ &\times\left(M_{z0} + M_{y0}\Omega_B t_k + \frac{1}{2}M_{x0}\Omega_p\Omega_B t_k^2\right). \end{aligned} \tag{12}$$

The minus sign on the right in Eq. (12), compared to Eq. (11), arises from the fact that the LMMs move along a trajectory with a positive curvature ($\Omega_p > 0$, expressions in parentheses), whereas the curvature of the critical surface is negative ($\Omega_p < 0$). Therefore, one may conveniently take into account the difference in the signs explicitly and understand under Ω_p the same (positive) quantity in what follows. Solving Eq. (12) yields, for holes created in regions *4* and *5*,

$$\begin{aligned} t_{\text{rel}-} &= t_k \\ &= \frac{-M_{y0} + \sqrt{(M_{y0}/\sqrt{2})^2 - (\Omega_p/\Omega_B)M_{x0}M_{z0}}}{\Omega_p M_{x0}} \end{aligned} \tag{13}$$

(for the chosen direction of motion along the orbit, we should choose the plus before the root sign). As already pointed out in the preceding section, for holes from region *3*, the initial part of motion (before crossing the $M_z = 0$ plane) does not involve spin relaxation. Therefore, the easiest way to find t_{rel} for these holes lies in subtracting the time (10) from time (13); in this case, the root in Eq. (10) should be taken with the minus sign. As a result, we obtain for region *3*

$$t_{\text{rel}+} = (1 + \sqrt{2})\frac{\sqrt{(M_{y0}/\sqrt{2})^2 - (\Omega_p/\Omega_B)M_{x0}M_{z0}}}{\Omega_p M_{x0}}. \tag{14}$$

Equations (13) and (14), combined with distribution (4) and boundaries of the regions (11), suffice to find the probability flux (5). A calculation of the integral is presented in detail in the appendix.

Retaining only the first two terms in (A12), changing back to the previous variables, and including the $\tau_s(B)$ relation given by Eq. (6), we obtain finally for the polarization

$$\begin{aligned} \rho(\Omega_B) &= 2F \approx 0.64\frac{\Omega_B\tau_{s0}}{1 + \Omega_B^2/\Omega_0^2} \\ &+ 0.94\frac{M_p}{M_f}\left(\frac{\Omega_B\tau_{s0}}{1 + \Omega_B^2/\Omega_0^2}\right)^2. \end{aligned} \tag{15}$$

The solid lines in Figs. 2b and 4 show the fits of Eq. (15) to the experimental data. The fitting parameters were τ_{s0} and Ω_0, and the ratio M_p/M_f for each sample was estimated from Eq. (3). The experimental and calculated relations are seen to be in good qualitative agreement. The best-fit values of τ_{s0} are of a few picoseconds, which is in accord with direct measurements [8–10] and validates the expansions in $\Omega\tau_s$.

4. CONCLUSIONS

To sum up, we have studied the anomalous behavior of the optical-orientation signal in QWs with semimagnetic layers under a magnetic field applied parallel to the QW plane. In place of a decrease in the degree of circular photoluminescence polarization (the Hanle effect) observed under resonant excitation in the region of localized excitonic states, many samples exhibit an increase in the polarization, replaced subsequently by its decay [14]. We have called relations of this kind the anomalous Hanle effect [15].

In this communication, we have presented new experimental results, analyzed various versions of collective spin dynamics of a localized hole and magnetic ions, and proposed a theoretical model for the AHE. Considered on a qualitative basis, the model is as follows. The luminescence originates from magnetic polaron states, with the polaron itself forming in a dynamic manner through the mechanism put forward in [12]. The polarization of the radiation is determined by the balance between the probabilities of formation of spin-up and spin-down polaron states. Excitons are distributed over these two types of states within the first few picoseconds following the exciton creation, and this distribution depends on the local magnetization fluctuation which has been realized by the instant of the photogeneration event in the given region. When unoriented holes are excited, one half of the fluctuation realizations relaxes to the spin-up state and the other half, to the spin-down state. The excitation of spin-polarized holes with their exchange field imparts the starting impulse to the magnetic-fluctuation distribution, and this biased distribution produces spin-up and spin-down polaron states already with unequal probabilities.

In the theoretical treatment, we abandoned numerical averaging of the dynamic equations over the initial conditions, one of the reasons for this being that the applicability of equations of type (1) to short time scales is questionable. Instead, we calculated the fluctuation flux through a critical surface separating the "trapping zones" of the upper and lower polaron states. The price paid for the simplicity of the analytical result represented by Eq. (15) was a number of approximations, in particular, the assumption of $M_p \gg M_f$ and $\Omega_{B,p}\tau_s \ll 1$. Estimates show, however, that for typical experimental conditions these approximations are more or less justified.

In conclusion, we should like to focus attention on a recent study [34], in which *M*-shaped Hanle curves, qualitatively similar to the ones considered by us, were observed in GaAs/(Ga,Al)As nonmagnetic QWs (see [34, Fig. 2d]). These *M*-shaped relations apparently find a radically different interpretation involving spin-dependent formation of "trions" (three-particle electronic excitations X^-) consisting of optically oriented excitons and electrons [34].

ACKNOWLEDGMENTS

The authors are indebted to D.R. Yakovlev and A. Waag for providing sample 3, in which an increase in magnetic polaron energy in a transverse magnetic field was revealed earlier [12].

This study was supported by the Russian Foundation for Basic Research (project nos. 00-02-16941, 01-02-17906) and grants of the Ministry of Industry, Sciences, and Technologies of the Russian Federation.

APPENDIX

The flux through a boundary is given by the integral

$$F = \int_{-\infty}^{+\infty} dM_x \int_{-\infty}^{0} dM_z \int_{-\infty}^{\sqrt{-2\frac{\Omega_p}{\Omega_B}M_xM_z}} dM_y \Phi(\mathbf{M}) \times \exp\left(-\frac{t_{\text{rel}-}(\mathbf{M})}{\tau_s}\right) + \int_{-\infty}^{+\infty} dM_x \int_{0}^{+\infty} dM_z \times \int_{-\infty}^{-\sqrt{2\frac{\Omega_p}{\Omega_B}M_xM_z}} dM_y \Phi(\mathbf{M}) \exp\left(-\frac{t_{\text{rel}+}(\mathbf{M})}{\tau_s}\right). \quad \text{(A1)}$$

Here and subsequently, we drop the subscript "0" of the vector **M** and of its components, while nevertheless assuming integration over the initial LMM orientations. One can conveniently transfer in Eq. (A1) from integration over M_z to that over time. Using Eqs. (13) and (14) for the first and second integrals, respectively, we obtain

$$F = \int_{-\infty}^{+\infty} dM_x \int_{0}^{\infty} dt \int_{-\frac{\sqrt{2}M_x\Omega_p t}{1+\sqrt{2}}}^{+\infty} dM_y 2\Omega_B(M_x\Omega_p t + M_y) \times \Phi(M_x, M_y, M_{z-}) \exp(-t/\tau_s) + \int_{-\infty}^{+\infty} dM_x \int_{0}^{\infty} dt \int_{-\infty}^{-\frac{\sqrt{2}M_x\Omega_p t}{1+\sqrt{2}}} dM_y \frac{2\Omega_B M_x \Omega_p t}{(1+\sqrt{2})^2} \times \Phi(M_x, M_y, M_{z+}) \exp(-t/\tau_s), \quad \text{(A2)}$$

where

$$M_{z-} = \frac{\Omega_B}{\Omega_p}\left[\frac{M_y^2}{2M_x} - \frac{(M_x\Omega_p t + M_y)^2}{M_x}\right], \quad \text{(A3)}$$

$$M_{z+} = \frac{\Omega_B}{\Omega_p}\left[\frac{M_y^2}{2M_x} - \frac{M_x(\Omega_p t)^2}{(1+\sqrt{2})^2}\right]. \quad \text{(A4)}$$

We transfer now in Eq. (A2) to dimensionless variables $m_\alpha = M_\alpha/\sqrt{2}M_f$, $\tau = t/\tau_s$, and $\omega_{B,p} = \Omega_{B,p}\tau_s$, to come to

$$F = \frac{2\omega_B}{\pi^{3/2}}\left\{\int_{-\infty}^{+\infty} dm_x \int_0^{+\infty} e^{-\tau} d\tau \int_{-\frac{\sqrt{2}}{1+\sqrt{2}}m_x\omega_p\tau}^{+\infty} dm_y (m_x\omega_p\tau + m_y)\right.$$
$$\times e^{-((m_x-\tilde{\kappa}\omega_B)^2 + m_y^2 + m_{z-}^2)} + \int_{-\infty}^{+\infty} dm_x \int_0^{+\infty} e^{-\tau} d\tau \qquad \text{(A5)}$$
$$\left.\times \int_{-\infty}^{-\frac{\sqrt{2}}{1+\sqrt{2}}m_x\omega_p\tau} dm_y \frac{m_x\omega_p\tau}{(1+\sqrt{2})^2} e^{-((m_x-\tilde{\kappa}\omega_B)^2 + m_y^2 + m_{z+}^2)}\right\}.$$

We do not write out here expressions for renormalized $\tilde{\kappa}$, m_{z-}, and m_{z+}, because they are very simple to derive. Rearranging Eq. (A5) and replacing $m_x - \tilde{\kappa}\omega_B \longrightarrow m_x$, which corresponds to translating the reference frame to the point of equilibrium magnetization, we obtain

$$F = \frac{2\omega_B}{\pi^{3/2}}\left\{\int_0^{+\infty} d\tau e^{-\tau} \int_{-\infty}^{+\infty} dm_x \int_{-\frac{\sqrt{2}}{1+\sqrt{2}}m_p\omega_B\tau}^{+\infty} dm_y m_y\right.$$
$$\times e^{-(m_x^2 + m_y^2 + m_{z-}^2)} + m_p\omega_B \int_0^{+\infty} d\tau\tau e^{-\tau} \int_{-\infty}^{+\infty} dm_x \int_{-\infty}^{+\infty} dm_y$$
$$\times e^{-(m_x^2 + m_y^2 + m_{z-}^2)} + m_p\omega_B \int_0^{+\infty} d\tau\tau e^{-\tau} \int_{-\infty}^{+\infty} dm_x \qquad \text{(A6)}$$
$$\left.\times \int_{-\infty}^{-\frac{\sqrt{2}}{1+\sqrt{2}}m_p\omega_B\tau} dm_y \left[\frac{e^{-m_{z+}^2}}{(1+\sqrt{2})^2} - e^{-m_{z-}^2}\right] e^{-(m_x^2 + m_y^2)}\right\}.$$

The change of the variable also affects the expressions for m_{z-} and m_{z+}, which now take on the form

$$m_{z-} = -\frac{m_y^2}{2m_p} - 2\omega_B\tau m_y - m_p\omega_B^2\tau^2, \qquad \text{(A7)}$$

$$m_{z+} = \frac{m_y^2}{2m_p} - \frac{m_p\omega_B^2\tau^2}{(1+\sqrt{2})^2}. \qquad \text{(A8)}$$

In Eqs. (A6)–(A8), we neglected the fluctuation magnetization m_x compared to $\tilde{\kappa}\omega_B$ and took into account that $\tilde{\kappa}\omega_p = m_p$, which is the (dimensionless) equilibrium moment of the magnetic polaron (see Eq. (3)).

To follow the logic underlying the theory, after factoring out ω_B in the solution, we should retain terms either of order unity or of order $\omega_B m_p$. An analysis of Eqs. (A7) and (A8) reveals that each of the terms in the right-hand parts of these expressions is small in a certain parameter (for instance, the first term in Eq. (A7) is small in parameter m_p^{-1}; the second, in ω_B; and the third, in $m_p\omega_B^2$), so that the corresponding exponentials in Eq. (A6) can be replaced by unity.

The last simplification makes the expressions readily integrable. Integration over m_x yields everywhere the factor $\sqrt{\pi}$. The second triple integral in Eq. (A6) can be taken without any difficulty. In calculating the first and the third integrals, we change the order of integration, and in the case of the first integral, we have also to take into account that when integrating an odd function of m_y the integral taken in the limits symmetric with respect to $m_y = 0$ vanishes. We come finally to

$$F = \frac{\omega_B}{\pi}\left\{\int_0^{+\infty} dm_y m_y e^{-m_y^2} \int_0^{\lambda m_y} d\tau e^{-\tau}\right.$$
$$\left. + \sqrt{\pi}m_p\omega_B - \frac{\sqrt{2}}{\lambda}\int_0^{+\infty} dm_y e^{-m_y^2} \int_0^{\lambda m_y} d\tau\tau e^{-\tau}\right\} \qquad \text{(A9)}$$
$$= \frac{\omega_B}{\pi}\left\{\lambda Q(\lambda) + \frac{\sqrt{2}}{\pi}[2Q(\lambda) + \lambda + \sqrt{2\pi} - \lambda^2 Q(\lambda)]\right\},$$

where

$$\lambda = \frac{1+\sqrt{2}}{\sqrt{2}m_p\omega_B},$$
$$Q(\lambda) = \frac{\sqrt{\pi}}{2}e^{\lambda^2/4}\left(1 - \mathrm{erf}\frac{\lambda}{2}\right) \qquad \text{(A10)}$$

and erf(x) is an error integral. If $m_p\omega_B \le 1$, we can use the asymptotic expression [35]

$$\sqrt{\pi}ze^{z^2}(1 - \mathrm{erf}(z)) \approx 1, \qquad \text{(A11)}$$

to obtain a simpler functional relation,

$$F \approx \frac{\omega_B}{\pi}\left(1 + \frac{2\sqrt{2\pi}}{1+\sqrt{2}}m_p\omega_B + \frac{4\sqrt{2}}{(1+\sqrt{2})^2}(m_p\omega_B)^2\right) \qquad \text{(A12)}$$
$$\approx 0.32\omega_B + 0.66m_p\omega_B^2 + 0.31m_p^2\omega_B^3,$$

which clearly demonstrates how the flux under study depends on the parameters of the model.

Figure 8 plots the function $F(\omega_B)$ for $m_p = 4.5$; one can find here the exact result (A9), (A10) and relation (A12), with the contributions from the first term and from the sum of first and second terms in (A12) shown separately.

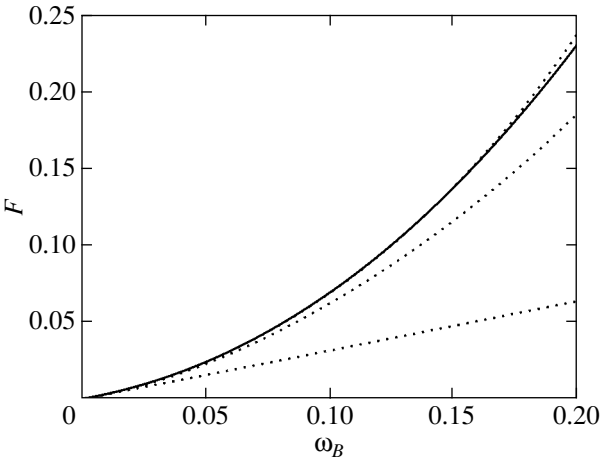

Fig. 8. Plot of function $F(\omega_B)$ for $m_p = 4.5$. The solid line is a plot of Eq. (A9) calculated using (A10). The three dashed lines (the top one practically coincides with the solid curve) show calculations made using Eq. (A12) with inclusion of the first term, of the first two terms, and of all three terms in Eq. (A12), respectively.

One readily sees that, in the range of interest to us, namely, $\omega_B \ll 1$ and $F \leq 0.1$, the simple result (A12) is quite satisfactory; moreover, it is sufficient to restrict oneself to the sum of the first two terms in (A12).

REFERENCES

1. J. Brossel and A. Kastler, C. R. Acad. Sci. **229**, 1213 (1949).
2. *Optical Orientation*, Ed. by F. Meier and B. P. Zakharchenya (North-Holland, Amsterdam, 1984; Nauka, Leningrad, 1989).
3. R. I. Dzhioev, B. P. Zakharchenya, R. R. Ichkitidze, *et al.*, Fiz. Tverd. Tela (St. Petersburg) **35**, 2821 (1993) [Phys. Solid State **35**, 1396 (1993)].
4. R. I. Dzhioev, B. P. Zakharchenya, K. V. Kavokin, and P. E. Pak, Fiz. Tverd. Tela (St. Petersburg) **36**, 2752 (1994) [Phys. Solid State **36**, 1501 (1994)].
5. A. S. Volkov, A. I. Ekimov, S. A. Nikishin, *et al.*, Pis'ma Zh. Éksp. Teor. Fiz. **25**, 560 (1977) [JETP Lett. **25**, 526 (1977)].
6. V. A. Novikov and V. G. Fleĭsher, Zh. Éksp. Teor. Fiz. **71**, 776 (1976) [Sov. Phys. JETP **44**, 410 (1976)].
7. J. Stühler, G. Schaack, M. Dahl, *et al.*, Phys. Rev. Lett. **74**, 2567 (1995).
8. S. A. Crooker, J. J. Baumberg, F. Flack, *et al.*, Phys. Rev. Lett. **77**, 2814 (1996).
9. S. A. Crooker, D. D. Awschalom, J. J. Baumberg, *et al.*, Phys. Rev. B **56**, 7574 (1997).
10. R. Akimoto, K. Ando, F. Sasaki, *et al.*, Phys. Rev. B **57**, 7208 (1998).
11. C. Camilleri, D. Scalbert, J. Allègre, *et al.*, in *Proceedings of 7th International Symposium on Nanostructures: Physics and Technology, St. Petersburg* (1999).
12. D. R. Yakovlev, K. V. Kavokin, I. A. Merkulov, *et al.*, Phys. Rev. B **56**, 9782 (1997).
13. K. V. Kavokin and I. A. Merkulov, Phys. Rev. B **55**, R7371 (1997).
14. Yu. G. Kusrayev, A. V. Koudinov, K. V. Kavokin, *et al.*, in *Proceedings of 23rd International Conference on the Physics of Semiconductors, Berlin, 1996*, Ed. by M. Sheffler and R. Zimmermann (World Sci., Singapore, 1996), p. 2459.
15. K. V. Kavokin, in *Optical Properties of Semiconductor Nanostructures*, Ed. by M. Sadowski, M. Potemski, and M. Grynberg (Kluwer Academic, Dordrecht, 2000), p. 255, NATO Science Series–High Technology, Vol. 81; e-print cond-mat/9912084.
16. I. A. Merkulov, G. R. Pozina, D. Coquillat, *et al.*, Phys. Rev. B **54**, 5727 (1996).
17. Yu. G. Kusrayev, A. V. Koudinov, and B. P. Zakharchenya, in *Proceedings of 22nd International Conference on the Physics of Semicondiconductors, Vancouver, Canada, 1994*, Ed. by D. J. Lockwood (World Sci., Singapore, 1994), p. 2501.
18. Yu. G. Kusrayev, A. V. Koudinov, B. P. Zakharchenya, *et al.*, Solid State Commun. **95**, 149 (1995).
19. B. P. Zakharchenya, A. V. Kudinov, and Yu. G. Kusraev, Pis'ma Zh. Éksp. Teor. Fiz. **63**, 241 (1996) [JETP Lett. **63**, 256 (1996)].
20. J. Warnock, R. N. Kershaw, D. Ridgley, *et al.*, J. Lumin. **34**, 25 (1985).
21. V. P. Kochereshko, I. A. Merkulov, K. V. Kavokin, *et al.*, in *Proceedings of International Conference on Semiconductor Heteroepitaxy, Montpellier, France, 1995*, Ed. by B. Gil and R.-L. Aulombard (World Sci., Singapore, 1995), p. 218.
22. B. P. Zakharchenya, A. V. Kudinov, and Yu. G. Kusraev, Zh. Éksp. Teor. Fiz. **110**, 177 (1996) [JETP **83**, 95 (1996)].
23. A. V. Koudinov, Yu. G. Kusrayev, and I. G. Aksyanov, Phys. Rev. B (in press).
24. D. Heiman, P. Becla, R. Kershaw, *et al.*, Phys. Rev. B **34**, 3961 (1986).
25. Yu. G. Kusrayev, A. V. Koudinov, I. G. Aksyanov, *et al.*, Phys. Rev. Lett. **82**, 3176 (1999).
26. S. I. Gubarev, Phys. Status Solidi B **134**, 211 (1986).
27. M. R. Freeman, D. D. Awschalom, J. M. Hong, and L. L. Chang, Phys. Rev. Lett. **64**, 2430 (1990).
28. E. O. Göbel, R. Hellmann, G. Mackh, *et al.*, Mater. Sci. Forum. **182–184**, 519 (1995).
29. D. R. Yakovlev and K. V. Kavokin, Comments Condens. Matter Phys. **18**, 51 (1996).
30. I. A. Merkulov, D. R. Yakovlev, K. V. Kavokin, *et al.*, Fiz. Tverd. Tela (St. Petersburg) **39**, 2079 (1997) [Phys. Solid State **39**, 1859 (1997)].
31. W. Heimbrodt, O. Goede, Th. Köpp, *et al.*, J. Cryst. Growth **117**, 859 (1992).
32. B. P. Zakharchenya and Yu. G. Kusraev, Pis'ma Zh. Éksp. Teor. Fiz. **50**, 199 (1989) [JETP Lett. **50**, 225 (1989)].
33. I. A. Merkulov (unpublished).
34. R. I. Dzhioev, V. L. Korenev, B. P. Zakharchenya, *et al.*, Phys. Rev. B **66**, 153409 (2002).
35. *Handbook of Mathematical Functions*, 2nd ed., Ed. by M. Abramowitz and I. A. Stegun (Dover, New York, 1971; Nauka, Moscow, 1979).

Translated by G. Skrebtsov

Physics of the Solid State, Vol. 45, No. 7, 2003, pp. 1374–1378. Translated from Fizika Tverdogo Tela, Vol. 45, No. 7, 2003, pp. 1311–1315.

LOW-DIMENSIONAL SYSTEMS AND SURFACE PHYSICS

Resonant Raman Scattering Spectra in a ZnCdSe/ZnSe Structure with a Quantum Well and Open Nanowires

V. Kh. Kaĭbyshev, V. V. Travnikov, and V. Yu. Davydov

Ioffe Physicotechnical Institute, Russian Academy of Sciences, Politekhnicheskaya ul. 26, St. Petersburg, 194021 Russia
e-mail: travn@spectr.ioffe.rssi.ru

Received July 1, 2002; in final form, December 23, 2002

Abstract—Resonance Raman scattering (RS) spectra of a ZnCdSe/ZnSe sample containing a single quantum well and quantum well–based open nanowires were studied at T = 300 K. The longitudinal optical (LO) phonons involved in the formation of the observed spectra of the quantum-well and nanowire regions differ noticeably in energy. The LO phonon energies in the structures under study were calculated taking into account the compositional effect (doping of Cd into ZnSe) and biaxial strain. When excited in the exciton resonance region, RS is shown to occur via free (extended) excitonic states with the involvement of LO phonons of the ZnCdSe strained layer with final wave vectors near the Brillouin zone center. When excited below the excitonic resonance in the ZnCdSe layer, resonance scattering via localized exciton states provides a noticeable contribution to the observed RS lines. Because of the finite size of a localized state, phonons with large wave vectors are involved in these scattering processes. The RS lines produced under excitation in the excitonic region of the thick barrier layers are due to scattering from the ZnSe barrier phonons. © *2003 MAIK "Nauka/Interperiodica".*

1. INTRODUCTION

Raman scattering (RS) is a widely used method for probing the lattice vibration spectra of quantum-well (QW) structures. One of the components in most of such structures (either the well or the barrier) is formed by a binary compound, and the second is realized by adding a third component to the binary substance. Adding a third component changes the phonon frequencies in the ternary compound (compositional effect) as compared to the starting binary substance. The characteristic phonon energies can also vary as a result of a lattice misfit both between the constituents of the QW structures and between these constituents and the substrate. For low concentrations of the third component in ternary solid solutions, the phonon frequencies in the barrier and the well materials are similar, a factor that considerably complicates analysis of the observed RS spectra. Assignment of the phonon states involved in the formation of RS spectra is also made difficult by the fact that the compositional effect and strains can partially cancel each other and bring the characteristic phonon energies of the binary-compound layers and of the ternary solid solution closer.

This communication reports on a study of resonance RS spectra in a ZnCdSe/ZnSe QW structure. RS in these structures has been dealt with in many publications (see, e.g., [1–4]). Interpretation of the observed spectra was, however, fairly controversial in view of the above factors. Some authors assigned the RS lines to scattering from the QW-material (ZnCdSe) phonons, while others attributed such lines to scattering from phonons of the barrier (ZnSe). This was partially due, apparently, to the lack of a quantitative analysis of the phonon spectra, which could have taken into account the compositional effect and the strains simultaneously. The present study deals with RS spectra measured under excitation both in the region of the ZnSe barrier excitonic transitions and in the excitonic region of the ZnCdSe quantum wells and wires. The experimental data obtained are compared with theoretical estimates of the characteristic phonon energies made with due account of both the compositional effect and strains.

2. EXPERIMENT

The starting ZnCdSe/ZnSe structures with a single quantum well were grown by molecular-beam epitaxy (MBE) on a GaAs(100) substrate. The 5-nm-thick QW with an ~13% Cd content is sandwiched between the buffer (25 nm) and cap (20 nm) ZnSe barrier layers. One-dimensional structures (nanowires) were fabricated on part of the surface of the original samples by using interference lithography followed by reactive ion etching [5]. Etching was performed practically down to the GaAs substrate. The period in the one-dimensional structure studied was ~260 nm, and the wire width was $L \sim 70$ nm. The effect of one-dimensional confinement on exciton spectra for these wire widths is insignificant [1], and we call the one-dimensional structures thus obtained nanowires. The wire axis was aligned with the [011] direction. The presence of both etched regions with nanowires (NWs) and the original unetched areas with QWs on the sample surface made it possible to compare the properties of NWs and QWs.

1063-7834/03/4507-1374$24.00

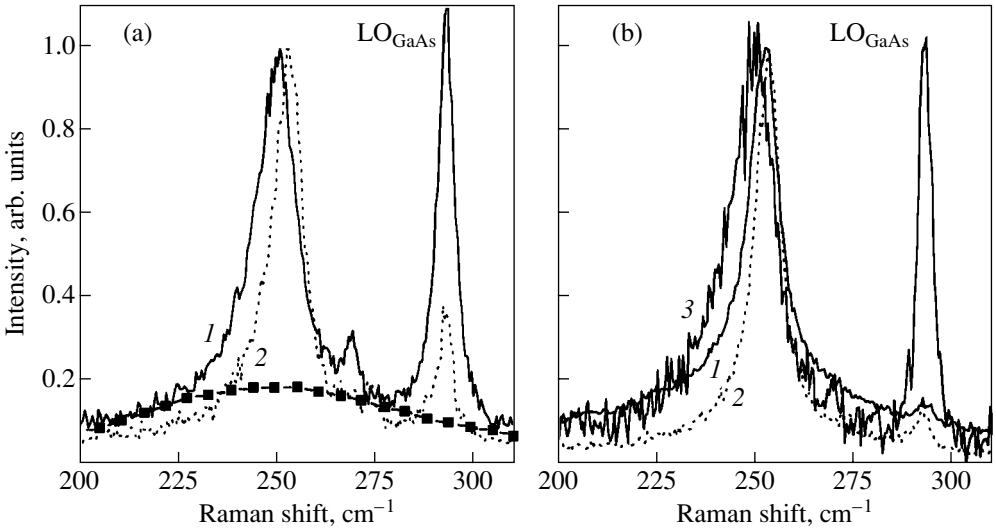

Fig. 1. Raman spectra obtained in (a) the nanowire and (b) quantum-well regions of the sample under excitation with (*1*) the 476.5-, (*2*) 457.9-, and (*3*) 488.0-nm laser lines. T = 300 K.

RS was excited by the 457.9-, 476.5-, and 488.0-nm Ar^+ laser lines. The studies were conducted at room temperature. The scattering was measured in the $z(yy)\bar{z}$ geometry (with the z axis coinciding with the growth direction perpendicular to the QW plane and the y axis aligned with the wire axis). The spectral resolution was ~0.5 cm^{-1}.

3. EXPERIMENTAL RESULTS

The RS spectra of our structures, produced by any of the laser lines used and under excitation in both the QW and the NW regions (Figs. 1, 2), feature two main lines. The line at 290 cm^{-1} maintains a fixed position in all the spectra studied. Varying the excitation energy or changing the sample area being probed brought about only a change in the intensity of this line. Based on its energy position, this line can be assigned to RS by longitudinal optical (LO) phonons of the GaAs substrate [6].

The position of the second line, at ~250 cm^{-1}, depends on both the excitation energy and the sample area probed (QW or NW region). This line is close in position to the energy of LO phonons in materials of the barrier (ZnSe) and of the well (ZnCdSe) [1–4, 7]. While the component of the ZnCdSe/ZnSe structure to which this line belongs cannot be identified *a priori*, this line is certainly due to LO phonons in the structures under investigation; subsequently, we call it the LO line.

Figure 1a displays RS spectra of the NW part of the sample obtained with two laser excitation lines, 457.9 and 476.5 nm. When excited by the 476.5-nm line (spectrum *1*), the scattering lines are superposed on a broad luminescence band denoted by squares. This band corresponds to emission of the ground-state E_{1H} exciton (heavy exciton) in the ZnCdSe NW. Estimation of the E_{1H} resonance energy in NWs from the position of the luminescence maximum (when excited above the ZnSe band edge) made with due account of the position of the maximum in the reflection spectrum yielded 2.570 eV (the E_{1H} resonance energy in the well is less than this energy by ~4 meV [8]). The 457.9-nm line excitation (2.707 eV) corresponds to the energy region of the ZnSe barrier exciton ground state, whose position at T = 300 K was estimated by us to be ~2.70 eV. As seen from Fig. 1a, the LO line excited in the region of the ZnSe excitonic resonance (spectrum *2*) shifts toward higher energies as compared to the case of excitation into the region of ZnCdSe resonance. Excitation in the QW region of the sample by the same laser lines

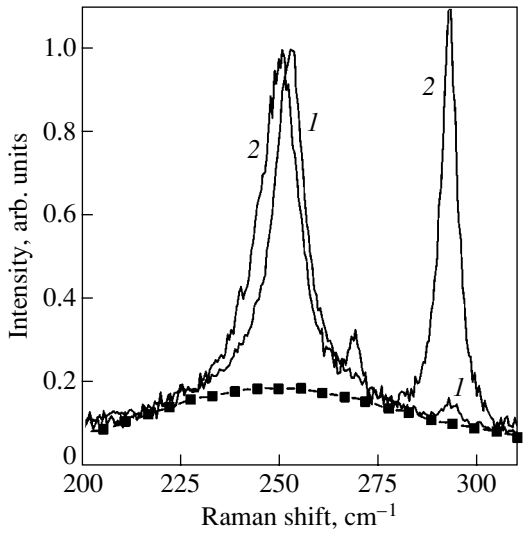

Fig. 2. Raman spectra obtained under excitation with the 476.5-nm line of (*1*) the quantum-well and (*2*) nanowire regions. T = 300 K.

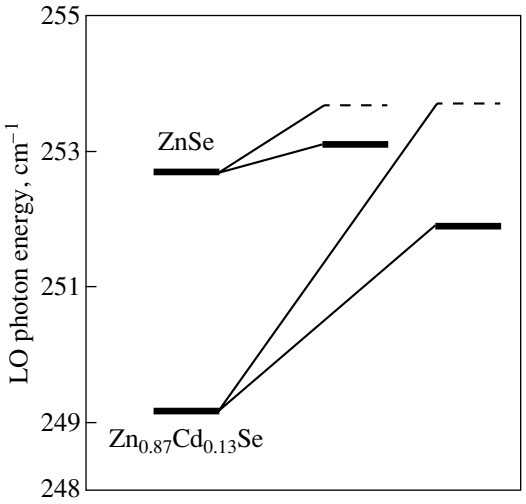

Fig. 3. LO phonon energy in unstrained (left) and biaxially strained (right) ZnSe and $Zn_{0.87}Cd_{0.13}Se$ crystals. $T = 300$ K. Dashed lines identify the energy levels corresponding to phonons with wave vectors along the *z* axis.

(457.9 and 476.5 nm) brings about a similar shift of the LO line, but the magnitude of the shift is noticeably smaller (spectra *1*, *2* in Fig. 1b). Excitation by the 488.0-nm line below the exciton ground state of ZnCdSe shifts the LO line maximum still further toward lower energies (spectrum *3* in Fig. 1b). This also brings about a noticeable broadening of the LO line; interestingly, this broadening is asymmetric, with the low-frequency wing of the line increasing in intensity.

Figure 2 compares the RS spectra obtained under excitation by the 476.5-nm line from the QW sample region (spectrum *1*) and the NW region (spectrum *2*). We readily see that the LO line produced under this excitation in the NW region is shifted noticeably toward low frequencies relative to its position in the QW region.

4. ESTIMATION OF LONGITUDINAL OPTICAL PHONON ENERGIES IN THE STRUCTURES STUDIED

The phonon spectrum of the structures studied may differ from that of the bulk ZnSe material because of more than one factor, namely, the compositional effect, strains in the material, and, finally, size quantization.

An analysis shows that the effect of size quantization on the phonon spectrum in our structures with quantum wells 5-nm-thick QWs may be neglected [1].

We conducted a quantitative analysis of the influence of the compositional effect and strains on the optical phonon energy in these structures in [8, 9]. Figure 3 displays estimates of the room-temperature energy levels of the fundamental LO mode for unstrained and biaxially strained ZnSe and $Zn_{0.87}Cd_{0.13}Se$ crystals. The LO phonon energy of the starting ZnSe material presented in Fig. 3 corresponds to the energy of the LO mode derived from our room-temperature measurements of RS spectra in a bulk ZnSe sample. The LO mode energy for the free $Zn_{0.87}Cd_{0.13}Se$ solid solution was calculated using the equations given in [10]. The data required for the calculation were taken from [7].

The total thickness of the ZnCdSe and ZnSe layers in our structure is 50 nm. This value is substantially less than the thickness of coherent growth in the ZnSe/GaAs system (~1000 nm [11]). As a result, the ZnCdSe and ZnSe layers are biaxially compressed in the *xy* plane, because the lattice constant of the thick GaAs substrate (0.5653 nm) is substantially smaller than that of $Zn_{0.87}Cd_{0.13}Se$ (0.5721 nm) and ZnSe (0.5668 nm). Using equations from [12], we estimated the LO phonon energy in a biaxially strained $Zn_{0.87}Cd_{0.13}Se$ solid solution. As seen from the right-hand part of Fig. 3, biaxial strain brings about an increase in energy for the LO phonon and its doublet splitting. The levels with the highest energy in such doublets are due to LO phonons with wave vectors aligned with the *z* axis (dashed lines in Fig. 3). While the ZnSe and ZnCdSe layers are similar in terms of the pattern of the phonon energy level shift and splitting, the corresponding values for the former layers are substantially smaller (Fig. 3), because the lattice misfit between ZnSe and GaAs is smaller than that between GaAs and ZnCdSe.

The results displayed in Fig. 3 show that the redshift of the phonon energy levels (relative to those in the starting material ZnSe) caused by the compositional effect in the ZnCdSe layers is compensated to a large extent by the blueshift originating from the influence of biaxial strains. As a result, the phonon energies in ZnCdSe layers turn out fairly close to those of the bulk ZnSe material. This proximity apparently accounts for the observation that the scattering processes occurring in the QW material have been assigned in some publications to interaction with the barrier-material phonons (see, e.g., [4]).

5. DISCUSSION

Scattering in the barrier and the well materials may both contribute to the observed RS spectra. The scattering intensity is proportional to the scattering volume. In our structures, the ZnSe barrier material substantially exceeds the well material in volume. When excitation is far from the QW-material resonances, this factor may cause the dominant contribution from scattering in the barrier material to the observed RS spectra to be and, as a consequence, give rise to the emergence of barrier phonons in the RS spectra. However, the Ar^+ laser lines used most frequently in RS studies lie close to the excitonic resonances of the ZnCdSe/ZnSe structure. When analyzing the observed variability of RS spectra, it is crucial to take into account the position of the exciting lines relative to the excitonic resonances.

The 457.9-nm-line excitation is close to the energy of the excitonic resonance of the ZnSe barrier material (see above). In this case, both because of the resonance excitation conditions being met and as a result of the larger volume of the barrier material, the observed RS spectra should undoubtedly originate from scattering in ZnSe. The excitation photon energy (2.602 eV) for the 476.5-nm line is separated from E_{1H} (2.570 eV) by approximately the LO phonon energy and meets the resonance condition for scattered light where the scattered photon energy coincides with the exciton resonance energy E_{1H} in ZnCdSe. In this case, as shown by us in low-temperature studies of RS profiles [8, 9], the observed LO line is due to scattering of light in the ZnCdSe layer by its phonons. It is because of the excitation being resonant that scattering in a thin well layer dominates over that in substantially thicker barrier layers. Thus, the small long-wavelength shift of the LO line observed to occur in RS studies of the QW region in going from excitation by the 457.9-nm line to that with the 476.5-nm line (Fig. 1b) should obviously be assigned to a transition from scattering in the barrier to that in the well material by LO phonons of the ZnCdSe layers. This leads us to the conclusion that the energy of the ZnCdSe LO phonons involved in the formation of the observed LO lines is smaller than that of ZnSe LO phonons.

The estimates presented in Fig. 3 show that LO phonons in the strained ZnCdSe layer with wave vectors in the well plane fit this conclusion. This is in accord with the formation of the LO line of resonant RS in QWs via intermediate states of free (extended) excitons; this mechanism was proposed in [8, 13]. Elastic scattering was demonstrated in [8, 13] to provide an important contribution, in addition to the direct inelastic scattering by LO phonons, to the observed scattering lines. Elastic scattering occurring under excitation above the resonance involves additional intermediate states (real excitonic states with large wave vectors) in the scattering. This accounts for the strong enhancement of the RS intensity [14]. The additional elastic processes in QW structures are associated to a considerable extent with scattering from interface roughness [8, 13]. Roughness can be approximated by a set of "roughness wave vectors" in the well plane (k_{xy}) [15]. As a result, the wave vector conservation law in RS brings about the involvement of excitons and phonons with k_{xy} wave vectors in the scattering. LO phonons with k_{xy} wave vectors correspond to the low-energy component of the phonon doublet in strained ZnCdSe (Fig. 3). The energy of this component is less than the LO phonon energy of the strained ZnSe layer, which is in agreement with experiment (Fig. 1).

Note that because of the LO phonons involved in the RS under study have finite wave vectors, their energies should be redshifted relative to their values at $k_{xy} = 0$ [16]. The magnitude of this shift is, however, small. As follows from our estimates based on the energy and momentum conservation laws for scattering via states of the E_{1H} exciton band, the wave vectors of the LO phonons under consideration are not large (less than 10% of their values at the Brillouin zone edge), which yields ~1 cm^{-1} for the above 1LO-line redshift. Because the exciton ground states in ZnCdSe and ZnSe differ only very slightly in effective mass, this shift is practically the same for the two materials; therefore, its inclusion does not affect the above conclusions bearing on the relative energies of the LO components which contribute to the RS lines produced in scattering in the well and barrier materials.

The LO line shift observed in the NW region under excitation with the 457.9- and 476.5-nm lines (Fig. 1a) greatly exceeds that in the QW region (Fig. 1b). The wires used in this study are open (not buried). Strain relaxation at the open wire edges may affect the structure of the observed RS lines [1, 2]. Our estimates (Fig. 3) show that the difference between the phonon energies in ZnCdSe and ZnSe for free materials is noticeably larger than that for strained ones. The increase in this LO line shift should obviously be assigned to a manifestation of strain relaxation. The effect of strain relaxation on the phonon states of a wire becomes obvious when comparing the spectra obtained from the QW region with those associated with the NW region under laser excitation at 476.5 nm (Fig. 2).

The 488.0-nm line produces excitation below the excitonic ground state of the well. We believe the emergence of the low-energy wing on the LO line to be related to an enhanced contribution from resonant scattering via localized exciton states. When excited in the region of the exciton ground state, RS occurs via free exciton states [8, 13]. In this process, phonons with small wave vectors close to the Brillouin zone center are involved. As one moves away from resonance, the probability of such scattering naturally decreases. At the same time, moving toward lower energies may enhance the probability of resonant scattering via localized exciton states, whose density-of-states tail may extend down energywise to large distances. This scattering is similar in nature to the RS via bound exciton states observed earlier in [17, 18]. In this case, because of the finite size of the localized states phonons with larger wave vectors and, accordingly, with lower energies can be involved in scattering. This is apparently what accounts for the intensity enhancement of the low-energy wing on the RS line under excitation below the exciton ground state in the well (Fig. 1b).

6. CONCLUSIONS

Thus, we have analyzed the influence of the compositional effect and strains on the LO phonon spectrum in biaxially strained ZnCdSe/ZnSe structures. It was shown that, for low Cd concentrations, these two effects compensate each other to a considerable extent, thus bringing the LO phonon energy levels in the

ZnCdSe layers closer to those in unstrained bulk ZnSe crystals. Studies were made of RS under excitation in the neighborhood of excitonic resonances in both the ZnCdSe and ZnSe layers. When excited into the excitonic region of thick barrier layers, the observed RS lines are due to scattering by phonons of the ZnSe layer. RS originating from excitation into the excitonic resonance region of a thin ZnCdSe layer occurs via free (extended) exciton states. In this case, LO phonons of this strained layer with small in-plane wave vectors participate in the scattering. When excited below the excitonic resonance in the ZnCdSe layer, resonant scattering via localized exciton states provides a noticeable contribution to the observed RS lines. Because of the small size of the localized state, the scattering in this case involves phonons with large wave vectors far from the Brillouin zone center.

ACKNOWLEDGMENTS

The authors are indebted to S.I. Nesterov, V.I. Skopina†, and E.M. Tanklevskaya for preparing the samples with nanowires and to I.N. Goncharuk for his assistance in the spectral measurements.

REFERENCES

1. G. Lermann, T. Bischof, A. Materny, *et al.*, J. Appl. Phys. **81** (3), 1446 (1997).
2. T. Kummell, G. Bacher, A. Forchel, *et al.*, Phys. Rev. B **57** (24), 15439 (1998).
3. I. Reshina, A. Toropov, S. Ivanov, *et al.*, Solid State Commun. **112** (6), 351 (1999).
4. N. N. Melnik, Yu. G. Sadofyev, T. N. Zavaritskaya, and L. K. Vodop'yanov, Nanotechnology **11** (4), 252 (2000).
5. S. A. Gurevich, O. A. Lavrova, N. V. Lomasov, *et al.*, Semicond. Sci. Technol. **13** (1), 139 (1998).
6. *Landolt–Bornstein. Numerical Data and Functional Relationships in Science and Technology* (Springer, New York, 1984), Group III, Vol. 17a, p. 243.
7. R. G. Alonso, E.-K. Suh, A. K. Ramdas, *et al.*, Phys. Rev. B **40** (6), 3720 (1989).
8. V. V. Travnikov and V. Kh. Kaĭbyshev, Fiz. Tverd. Tela (St. Petersburg) **45** (7), 1316 (2003) [Phys. Solid State **45**, 1379 (2003)].
9. V. V. Travnikov, V. H. Kaibyshev, N. V. Lomasov, *et al.*, Nanotechnology **12**, 602 (2001).
10. D. L. Peterson, A. Petrou, W. Giriat, *et al.*, Phys. Rev. B **33** (2), 1160 (1986).
11. C. D. Lee, B. K. Kim, J. W. Kim, *et al.*, J. Cryst. Growth **138** (1–4), 136 (1994).
12. F. Cerdeira, C. Buchenauer, F. Pollak, and M. Cardona, Phys. Rev. B **5** (2), 580 (1972).
13. A. J. Shields, C. Trallero-Giner, M. Cardona, *et al.*, Phys. Rev. B **46** (11), 6990 (1992).
14. A. A. Gogolin and E. I. Rashba, Solid State Commun. **19** (12), 1177 (1976).
15. *Surface Polaritons*, Ed. by V. M. Agranovich and D. L. Mills (North-Holland, Amsterdam, 1982; Nauka, Moscow, 1985).
16. B. Hennion, F. Moussa, G. Pepy, and K. Kunc, Phys. Lett. A **36A** (5), 376 (1971).
17. P. J. Colwell and M. Klein, Solid State Commun. **8** (24), 2095 (1970).
18. T. C. Damen and J. Shah, Phys. Rev. Lett. **27** (22), 1506 (1971).

† Deceased.

Translated by G. Skrebtsov

Physics of the Solid State, Vol. 45, No. 7, 2003, pp. 1379–1387. Translated from Fizika Tverdogo Tela, Vol. 45, No. 7, 2003, pp. 1316–1324.

LOW-DIMENSIONAL SYSTEMS AND SURFACE PHYSICS

Resonance Exciton–Phonon Spectra in Open ZnCdSe/ZnSe Nanowires: Raman Scattering and Hot Luminescence, Extended and Localized Exciton States

V. V. Travnikov and V. Kh. Kaĭbyshev

Ioffe Physicotechnical Institute, Russian Academy of Sciences, Politekhnicheskaya ul. 26, St. Petersburg, 194021 Russia
e-mail: travn@spectr.ioffe.rssi.ru

Received July 1, 2002; in final form, December 23, 2002

Abstract—Low-temperature ($T \sim 8$ K) secondary emission spectra of open $Zn_{0.87}Cd_{0.13}Se/ZnSe$ nanowires were studied comprehensively in the region of the ground excitonic state under tunable laser excitation. The spectra revealed a fine structure produced in the interaction of excitons with optical phonons. The observed resonance exciton–phonon (REP) lines are shown to be formed through two different mechanisms. The strongest component is due to Raman scattering via free excitonic states. The other REP lines are generated in the hot luminescence of localized excitons. The spectrum of the optical phonons involved in the formation of the REP lines in the biaxially strained $Zn_{0.87}Cd_{0.13}Se/ZnSe$ structures was analyzed. *© 2003 MAIK "Nauka/Interperiodica".*

1. INTRODUCTION

The secondary emission spectra obtained at helium temperatures under laser excitation in the region of excitonic resonances of ZnCdSe layers reveal a number of narrow lines formed in the interaction of excitons with various optical phonons (see, e.g., [1–10]). Such resonance exciton–phonon (REP) lines were found earlier to exist in the spectra of both thick ZnCdSe layers [1, 6] and of various ZnCdSe/ZnSe quantum-well structures [2–5]. The interpretation of these lines was fairly controversial. In some communications, these lines were considered as being due to Raman scattering, while in others, they were assigned to hot luminescence. The nature of the excitonic and phonon states involved in the observed REP lines was also regarded from different standpoints.

This communication reports on a comprehensive investigation of the dependence of the fine structure and intensity of REP lines produced at $T \sim 8$ K in open ZnCdSe/ZnSe nanowires as a function of laser excitation energy. The observed spectra were found to exhibit REP lines of two types simultaneously. The strongest REP component is due to Raman scattering via extended exciton states. The other, weaker components are produced in the hot luminescence of localized excitons. The spectrum of the optical phonons involved in REP-line formation in the strained $Zn_{0.87}Cd_{0.13}Se/ZnSe$ structures studied is analyzed. The preliminary results of this study were published in [7].

2. EXPERIMENTAL TECHNIQUE

The original ZnCdSe/ZnSe single quantum-well (QW) structures were grown through molecular-beam epitaxy on a GaAs(100) substrate. A 5-nm-thick QW with 13% Cd fabricated in these structures was sandwiched between a buffer (25 nm) and a cap (20 nm) ZnSe barrier layer. Nanowire (NW) structures were fabricated on part of the surface of the original samples by interference lithography followed by reactive ion etching down to the GaAs substrate [8]. The wires were $L \sim 70$ nm wide and separated by ~180 nm. The wire axis was aligned with [011]. The presence of both etched regions with NWs and the original unetched regions on the sample surface permitted comparison of the properties of NWs and QWs.

Excitation was provided by a tunable dye laser (Stilbene 3) pumped by an Ar^+ laser UV line. The studies were conducted at $T \sim 8$ K in the backscattering geometry. Both emission and excitation spectra (dependence of the intensity in a selected spectral interval on exciting energy) were measured. The pump and detected light beams were polarized parallel to the wire axis.

3. EXPERIMENTAL RESULTS

Figure 1 presents excitation spectra (ESs) of the secondary emission from the NW (solid line) and QW region (dashed line) of the sample. The ESs displayed were measured at the detection energy (E_{det}) in the low-energy region of the photoluminescence (PL) bands of the ground exciton state E_{1H} (heavy exciton) of ZnCdSe. Shown on the left in Fig. 1 are the QW and NW PL bands obtained under excitation in the ZnSe

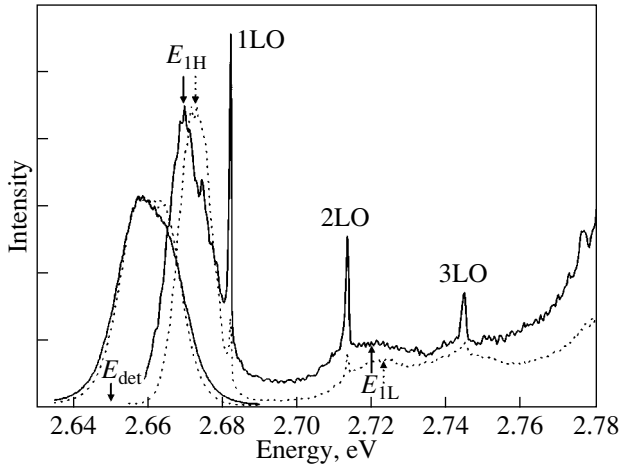

Fig. 1. Excitation spectra of the emission from nanowires (solid line) and the quantum well (dashed curve). The excitation spectra were measured at the detection energy E_{det} = 2.650 eV at $T \sim 8$ K. Shown on the left are the corresponding photoluminescence spectra obtained at an excitation energy (2.83 eV) considerably in excess of the ZnSe absorption edge.

barrier absorption region. The exciton state energy E_{1H} can be derived from the position of the main maximum in the ES. As seen from Fig. 1, the E_{1H} excitonic state in the NW (2.667 eV) is shifted to lower energies compared to its position in the QW spectrum. This redshift results from a partial strain relaxation in the structure due to the presence of free side ZnCdSe walls in open NWs [11]. The absence of a blueshift implies that one-dimensional quantization insignificantly affects the position of excitonic levels in our NWs (L = 70 nm); it is this that accounts for our calling these structures nanowires rather than quantum wires. The weaker broad E_{1L} maxima in ESs at about 2.72 eV should evidently be assigned to the light-exciton ground state.

The ES contains, besides broad bands corresponding to absorption maxima, narrow 1LO, 2LO, and 3LO lines due to exciton scattering by longitudinal optical (LO) phonons [12]. As is evident from Fig. 1, at the same detection energy, the relative intensity of these LO lines in the NW ES is substantially higher than that in the well emission ES. The relative intensity of the LO lines in the ES increases strongly for E_{det} in the E_{1H} resonance region. This is seen clearly from Fig. 2, which presents the ES of NW emission obtained for E_{det} = 2.667 eV. In this case, one can observe up to five LO lines. Figure 2 also shows that the LO lines in the periodic structure are not strictly equidistant. The interval between the detection energy and position of the 1LO line (~31.7 meV) is noticeably larger than the energy separations between the 1LO and 2LO (~31.3 meV) and between the 2LO and 3LO (~31.4 meV) lines.

Three weaker but still discernible lines *a*, *b*, and *c* are seen on the low-energy side of the 1LO line (see inset to Fig. 2). Similar lines are also present near the 2LO and 3LO lines. The energy position of the *a*, *b*, and *c* lines and of their replicas is given by the relation $E = E_{det} + (\omega_i + n\omega_{LO})$, where $i = a, b, c$; $n = 0, 1, 2$; and the energies ω_a, ω_b, and ω_c are 24.8, 26.4, and 28.4 meV, respectively. These energies lie in the region of longitudinal–transverse splitting for ZnSe optical phonons [13] and correspond apparently to some optical phonons in the structures under study.

In addition to the ES, we thoroughly studied emission spectra as a function of excitation energy E_{ex} (Fig. 3). A characteristic feature of these spectra is the presence of REP lines with maxima at the emission energies $E_{em} = E_{ex} - \omega_i$, where ω_i are the above-mentioned optical phonon energies (i = LO, *a*, *b*, *c*). The

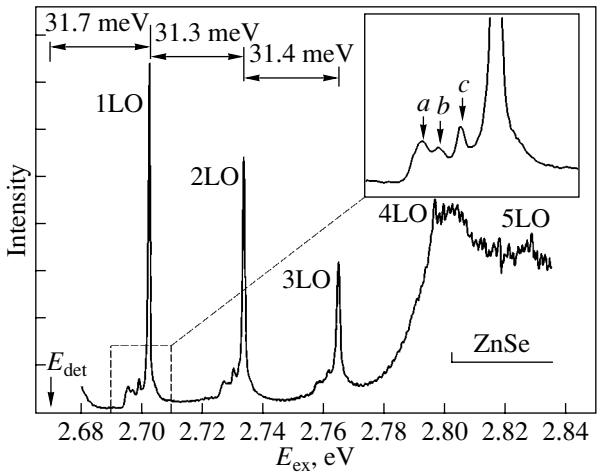

Fig. 2. Excitation spectra of the emission from nanowires measured at the detection energy E_{det} = 2.671 eV ($T \sim 8$ K). Inset shows part of the spectrum in expanded scale.

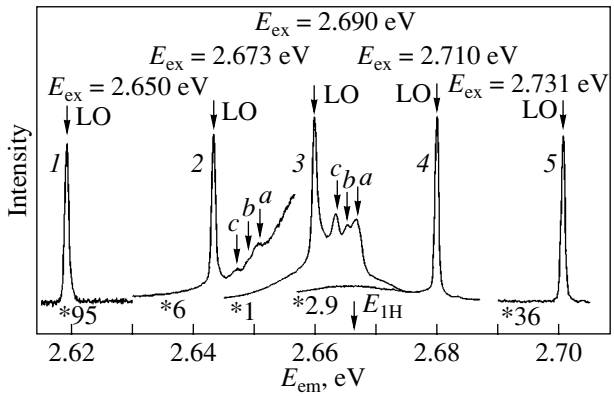

Fig. 3. Nanowire emission spectra obtained at various excitation energies E_{ex} ($T \sim 8$ K).

broad PL background band is also seen in the emission spectra at the corresponding E_{ex} (spectrum *3* in Fig. 3). While the original QW structures emit similar REP lines, the relative intensity of the PL bands in this case is substantially larger.

We obtained spectra corresponding to "pure" exciton–phonon optical transitions by subtracting the PL band background. After this, we decomposed these spectra into phonon constituents. This decomposition is exemplified in Fig. 4, in which the horizontal axis plots the phonon shift energy relative to the excitation energy, $\omega_i = E_{ex} - E_{em}$. The strongest component of this deconvolution corresponds naturally to the 1LO maximum (~31.7 meV). The slightly asymmetric shape chosen by us for this component is characteristic of excitation far from the resonance. The other components were fitted by Gaussian profiles with energies ω_a, ω_b, and ω_c. It was found to be impossible to fit the shape of the REP spectra without introducing a fourth component *d* (~31.1 meV).

We measured resonance profiles (RPs), i.e., the dependence of the component intensity on excitation energy, for all the phonon components obtained. The RP maxima of different phonon components are shifted in energy with respect to one another. To facilitate comparison of the RP pattern for different components, the normalized component intensities are plotted in Fig. 5 as a function of energy: $E = E_{em} - E_{1H} = E_{ex} - (\omega_i + E_{1H})$, where $E_{1H} = 2.667$ eV. Figure 5 shows clearly that the RPs for the *a*, *b*, *c*, and *d* components (open symbols) coincide to within experimental error while being at the same time substantially different from the RP of the LO component (filled circles).

The horizontal axis in Fig. 5 shows the energy shift of the final (emitting) states plotted vs. energy E_{1H}. The luminescence spectra can likewise be represented as functions of energy $E = E_{em} - E_{1H}$. This offers the possibility of comparing the efficiency of REP processes with that of luminescence for states with the same final energy. The solid line in Fig. 5 depicts a luminescence spectrum obtained at an excitation energy 2.712 eV [the narrow 1LO and 2LO lines in this spectrum are Raman lines (see below)].

The *a*, *b*, and *c* lines are observed in emission spectra only in the energy regions with a noticeable PL background intensity (spectra *2–4* in Fig. 3). When excited far from the resonance, where there is no PL background, the emission spectrum contains LO lines only (spectra *1*, *5* in Fig. 3). When the temperature is raised, the relative intensities of lines *a*, *b*, and *c* fall off gradually to a negligible level. At room temperature, only the LO lines persist in emission spectra as seen from Fig. 6, which displays the emission spectrum obtained when pumping with the 476.5-nm argon laser line (2.602 eV). The position of the E_{1H} resonance (2.57 eV) at $T = 300$ K, identified by an arrow, was estimated from those of the maxima in the reflectance and luminescence spectra (when excited far from the resonance). In addition to the LO line corresponding to Raman scattering in the ZnCdSe/ZnSe structure (see below), the spectrum contains an LO_{GaAs} line associated with Raman scattering in the GaAs substrate. The broad emission band under the lines corresponds to the

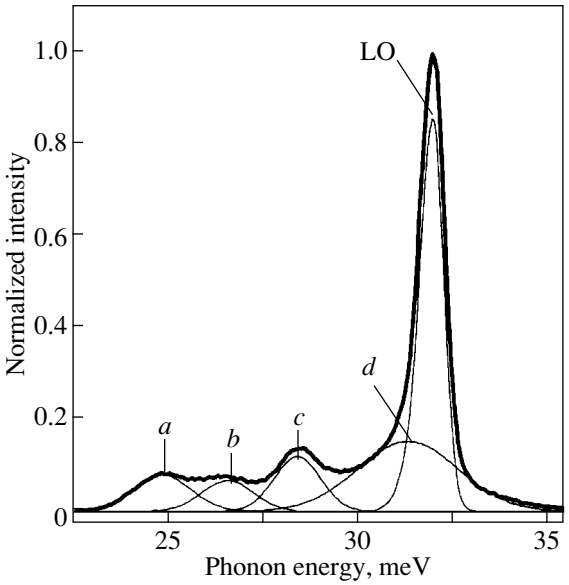

Fig. 4. Decomposition of a "pure" (see text) resonance exciton–phonon emission spectrum ($E_{ex} = 2.698$ eV).

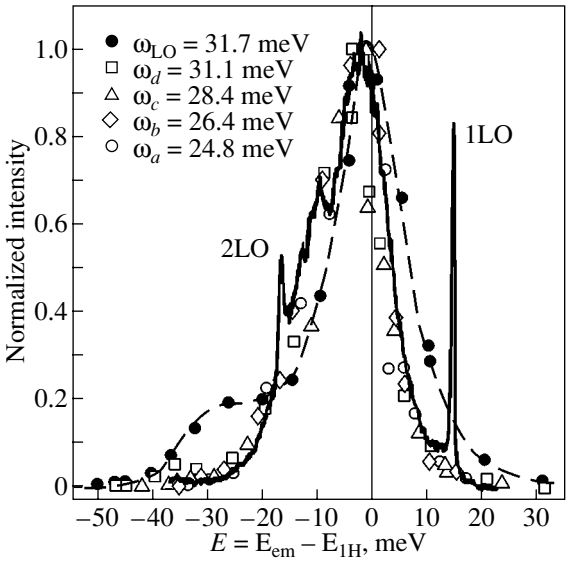

Fig. 5. Resonance profiles (filled and open symbols) of REP components. The dashed line was drawn to isolate the experimental values corresponding to the 1LO component (filled circles). The solid line is the emission spectrum of the nanowires measured at an excitation energy $E_{ex} = 2.712$ eV (1LO and 2LO are Raman scattering lines).

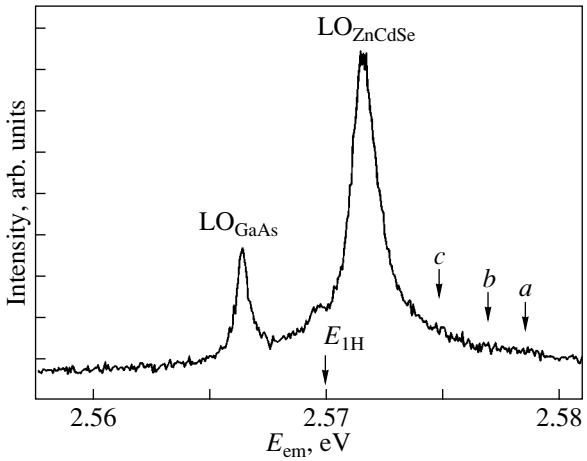

Fig. 6. Room temperature emission spectrum obtained under excitation by the 476.5-nm (2.602 eV) Ar^+ laser line. Arrows *a*, *b*, and *c* specify expected energy positions of the corresponding resonance exciton–phonon components. The E_{1H} arrow shows the energy (~2.57 eV) of the exciton ground state of the nanowire at $T \sim 300$ K.

PL of the exciton ground state in the ZnCdSe quantum well.

4. DISCUSSION AND ANALYSIS OF THE EXPERIMENTAL DATA

4.1. Lines a, b, and c (Hot Luminescence of Localized Excitons)

It is well known (see, e.g., [14]) that, at low temperatures, the PL in QW structures is actually the emission of localized excitons. That the RPs of the *a–d* components coincide in shape with the PL band indicates that these components form apparently through a mechanism similar to that responsible for localized-exciton luminescence. In view of this, and taking into account that the intensity of the *a–d* components is noticeable only in the region where the PL background exists, we assume the *a–d* components to originate from the hot luminescence (HL) of localized excitons.

The luminescence intensity for emission from a state with energy E can, in general, be written as

$$I_{PL}(E) \sim N(E)W_r(E),$$

where $W_r(E)$ and $N(E)$ are the probability of radiative recombination and the population of states with energy E, respectively. The population function is determined by the distribution function $F(E)$ and the density of states $\rho(E)$:

$$N(E) = \rho(E)F(E).$$

At low temperatures, the equilibrium distribution of excitons over localized states cannot be attained. As a result, the distribution function should be derived from the kinetic equation

$$dF(E)/dt = G(E) - F(E)[W_r(E) + W_{nr}(E)],$$

where $G(E)$ is the generation rate of localized excitons with energy E and $W_{nr}(E)$ is the probability of nonradiative decay of the localized excitons.

Under stationary excitation, the population of localized exciton states of energy E is given by the expression

$$N(E) \sim G(E)\rho(E)/[W_r(E) + W_{nr}(E)].$$

Excitation in the neighborhood of the resonance offers the possibility of isolating two main channels of population of a localized exciton state with energy E. One channel involves direct generation of a localized exciton in a light absorption event accompanied by the generation of phonons of the corresponding frequency ω_i (phonon-assisted absorption). The population produced under monochromatic excitation (δ-function generation) exhibits a strongly nonequilibrium (quasi-δ-function, "hot" [15]) character. It is the emission from such states, populated in a nonequilibrium manner, that apparently accounts for the appearance of the *a–d* components in the spectrum. The other channel is the population of emitting states through transitions from other (previously excited) states. In this case, in the first stage, absorption of light in the region above the resonance gives rise to the formation of free or localized excitons. Subsequent energy relaxation and localization processes populate localized states with different energies in the vicinity of the E_{1H} resonance. It is the emission from these states that apparently forms the observed luminescence band background. Thus, in the case of monochromatic excitation near the resonance, the luminescence spectrum can be represented by the sum of two contributions, namely, the HL lines (I_{HL}) and the PL band background (I_{PL}):

$$I(E) = I_{HL}(E) + I_{PL}(E),$$

where

$$I_{HL}(E) = G_{HL}(E)\rho(E)W_r(E)/[W_r(E) + W_{nr}(E)], \quad (1)$$

$$I_{PL}(E) = G_{PL}(E)\rho(E)W_r(E)/[W_r(E) + W_{nr}(E)]. \quad (2)$$

The energy positions of the HL lines are connected rigidly with the excitation energy $E_{em} = E_{ex} - \omega_i$. This offers the possibility of presenting the resonance profiles of the HL lines as functions not of excitation energy but rather of the energy of emitted photons. Such functions are given by Eq. (1). The PL band spectrum is determined by Eq. (2). It follows form Eqs. (1) and (2) that all the factors determining the shape of the HL RPs and of the PL bands (as functions of the emitted photon energy E) are identical, with the exception of the $G(E)$ functions.

As already mentioned, the shape of the RPs of the *a–d* components is close to that of the PL bands. This

suggests the conclusion that the shape in both cases is dominated by the density of states and the energy dependence of the probabilities $W_r(E)$ and $W_{nr}(E)$. The possible differences are obviously associated with differences in the energy dependence of the generation functions for the HL lines and the PL band; these functions, however, are apparently fairly smooth and do not affect the shape of the spectra under consideration substantially. It should be pointed out that the shape of the PL band itself depends noticeably on the excitation energy. This dependence, however, is determined by the difference between the $G(E)$ functions for different E_{ex} and is not very significant; the difference in shape between the PL bands obtained at different E_{ex} does not exceed the error in the REP line profile measurement.

The observed temperature quenching of the HL lines (Fig. 6) is obviously caused by the depopulation of localized states through their delocalization. These processes affect the magnitude of W_{nr}, and their probability is proportional to ~exp($-E_b/kT$), where E_b is the exciton localization energy. The localization energies are fairly small in our case (the averaged localization energies in the ZnCdSe/ZnSe QW structures are estimated as ~2–5 meV [16]), so that, at room temperature, all localized states should be depleted. As a result, the HL lines are no longer seen in the emission spectra (Fig. 6). The temperature quenching of the *a*, *b*, and *c* lines can be considered direct proof of their luminescence nature.

4.2. LO Lines (Raman Scattering)

In view of the fact that the LO lines do not suffer temperature quenching (Fig. 6) and that they are also observed, unlike the HL lines, under excitation below the excitonic ground state (no luminescence occurs under such excitation), one can maintain with confidence that the LO lines are produced in Raman scattering (RS).

The RP of an LO line has a characteristic shape with a clearly pronounced outgoing resonance at the scattered light frequency ($E_{ex} = E_{1H} + \omega_{LO}$) and with an incoming resonance at the excitation frequency ($E_{ex} = E_{1H}$) which manifests itself as a shoulder. Such a shape is typical of resonant Raman scattering (RRS) via intermediate free-exciton states and was observed earlier in studies of RRS in bulk semiconductors [17, 18] and QW structures [19, 20]. In view of the RP shape of LO lines, we may conjecture that the LO lines correspond to optical-phonon RRS occurring via free exciton states.

The motion of free excitons in real QW structures is limited by localization processes, so that only exciton states with energies in excess of the amplitude of potential fluctuations are extended and can be considered free particles with a "good" wave vector in the QW plane. Obviously enough, it is such extended exciton states that are responsible for the observed LO lines.

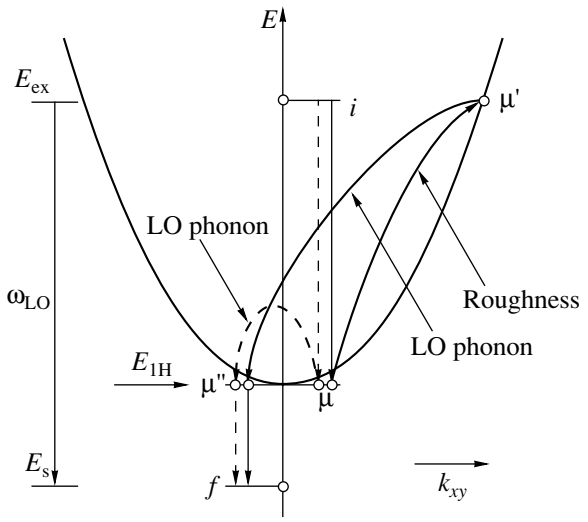

Fig. 7. Schematic diagram of the Raman scattering.

In contrast to the HL, which originates from a sequence of two one-photon processes (absorption followed by emission [21, 22]), RS is a direct two-photon process [21]. In RS, the disappearance of the exciting photon of energy E_{ex} is accompanied simultaneously by the creation of a phonon and the appearance of a scattered photon of energy E_s. Figure 7 presents a sketch to illustrate the formation of RRS lines (it represents a perturbation-theoretical approach). Let the *z* direction be perpendicular to the QW plane. Extended excitons are characterized in this case by k_{xy} wave vectors. The exciting and the scattered photons have very small wave vectors ($k_{xy} \longrightarrow 0$) and, therefore, are shown as dots on the vertical axis of Fig. 7. Due to the wave-vector conservation law, the first and last steps in the process (interaction with photons) involve virtual excitonic states (μ and μ") with $k_{xy} \sim 0$.

If only phonons participated in RS, only the excitonic states μ and μ" with $k_{xy} \sim 0$ would be intermediate states. In Fig. 7, this process is shown by dashed lines (*i*–μ–μ"–*f* sequence). In this case, the maxima in the RP that correspond to the incoming and outgoing resonances should both have approximately the same intensity [19, 20].

The presence of additional, elastic scattering processes under excitation above the exciton resonance results in scattering via real excitonic states (μ') with large wave vectors k_{xy} (the solid lines and sequence *i*–μ–μ'–μ"–*f* in Fig. 7). The involvement of real excitonic states, on the one hand, increases the RRS intensity substantially [23] but on the other, makes the outgoing resonance dominant [17–20]. In QW structures, elastic processes are related, to a considerable extent, to scattering from QW interface roughness [20]. We believe that, in our case, the elastic processes are also connected with roughness at the ZnSe/ZnCdSe interface.

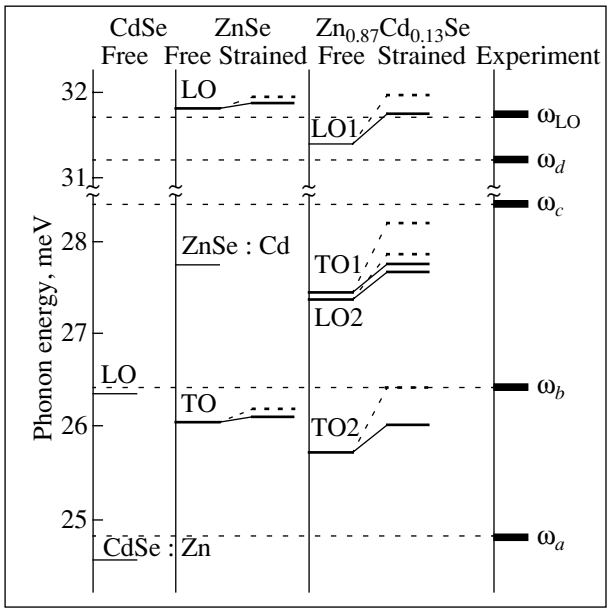

Fig. 8. Optical phonon energies in free and biaxially strained ZnSe and $Zn_{0.87}Cd_{0.13}Se$ crystals ($T \sim 8$ K). The energies for bulk, free CdSe and ZnSe materials were taken from [1]. The energies for the strained materials were estimated in accordance with [27]. Dotted lines refer to phonon energies corresponding to lattice vibrations along the *z* axis.

4.3. Spectral Analysis of Optical Phonons Involved in the Formation of the Observed Resonance Exciton–Phonon Lines

The fine structure associated with the emergence of various phonon components of ZnCdSe layers in optical spectra was also observed earlier (see, e.g., [1–6]), but its interpretation proposed at the time was fairly controversial. The appearance of four observed phonon components in the RS spectra of thick (>300 nm) $Zn_{1-x}Cd_xSe$ ($x \sim 15\%$) epitaxial layers was assigned to RS from the phonon modes corresponding to those of the ZnCdSe solid solution, i.e., they were attributed to a compositional effect (introduction of Cd into ZnSe) [1]. The three phonon components seen in the PL spectra of $Zn_{1-x}Cd_xSe/ZnSe$ ($x > 30\%$) [3] QW structures were assigned to the ZnSe LO phonon, the impurity phonon mode of Cd in ZnSe, and the LO mode of CdSe. The structure observed in the PL spectra of ZnCdSe/ZnSe systems was related [2] to exciton interaction with phonons at Brillouin zone points with a high density of states. It was assumed that interaction with phonons having large wave vectors is made possible through the breaking of the wave-vector conservation law by the localization effect [2].

Figure 8 shows the characteristic phonon energies required to analyze the observed spectra. The phonon energies corresponding to bulk ZnSe and CdSe crystals were taken from [1] and are specified in the left-hand part of Fig. 8. The LO and TO energy levels refer to the energies of longitudinal and transverse optical phonons at the Γ point of the Brillouin zone (for $T < 10$ K). The phonon levels of ZnSe : Cd and CdSe : Zn correspond to Cd impurity local lattice vibrations in ZnSe and to Zn vibrations in CdSe, respectively [1].

The phonon mode spectrum in our ZnCdSe/ZnSe structures can differ from those of the base bulk material ZnSe because of the following factors: size quantization, strains, and compositional effects.

The possibility of phonon quantum-confinement effects becoming manifest in RS scattering in ZnCdSe quantum wells was considered in [24]. The corresponding analysis permitted neglect of the effect of size quantization on the phonon mode spectrum in 4-nm-thick QWs. Since the thickness of the ZnCdSe layers was noticeably larger (5 nm) in our case, we also considered disregarding this effect justifiable.

Rather than being described by a one- or two-mode behavior, the phonon spectra of $Zn_{1-x}Cd_xSe$ solid solutions belong to an intermediate case [1]. The main components (LO_1, TO_2) of optical phonon modes at the Γ point of the Brillouin zone follow the one-mode behavior; namely, their energies displace continuously from one extreme point of the solid solution ($x = 1$) to the other extreme ($x = 0$). The two remaining phonon modes (LO_2, TO_1) become local impurity modes at $x = 1$ or 0, with their energies being equal within the longitudinal–transverse splitting region [1]. We estimated, in accordance with [25], the energies of the above phonon modes for a free $Zn_{1-x}Cd_xSe$ solid solution with $x = 13\%$ (right-hand part of Fig. 8).

The total thickness of our ZnCdSe/ZnSe structure is 50 nm, which is substantially smaller than the thickness of coherent growth in the ZnSe/GaAs system (~1000 nm [26]). Therefore, the lattice constants of thin ZnCdSe and ZnSe layers (for free layers, these values are $a_{ZnCdSe} = 0.5721$ nm and $a_{ZnSe} = 0.5668$ nm, respectively) should become equal to that of a thick GaAs substrate ($a_{GaAs} = 0.5653$ nm). As a result, the ZnCdSe and ZnSe layers are biaxially strained (compressed in the *xy* plane), which should affect the optical phonon energy [27]. We used the relations derived in [27] to estimate the energies of all optical phonon modes for a biaxially strained ZnCdSe solid solution with $x = 13\%$ (the ZnSe and CdSe crystal parameters were taken from [27]). Biaxial strain brings about an increase in the energy of all phonon levels and their splitting. The highest energy levels in such doublets correspond to lattice vibrations along the *z* axis (in Fig. 8, these components are identified by dashed lines). The shift and splitting of the phonon energy levels in ZnSe layers are smaller than those in ZnCdSe, because the lattice misfit between ZnSe and GaAs is smaller than that between GaAs and ZnCdSe. It should be stressed that the phonon energies shown in Fig. 8 correspond to the Brillouin zone center, i.e., to zero values of the wave vectors ($q = 0$).

Since the thickness of the ZnSe barriers in our structures is much larger than that of the ZnCdSe layer, scattering in the ZnSe regions can, in principle, provide a certain contribution to the observed spectra. The LO series observed in multiphonon RRS in the energy region of the ZnCdSe well (and below the ZnSe barrier) were assigned in [28] to scattering by ZnSe barrier LO phonons. Our experiments show, however, that when excited in the energy region of ZnCdSe, the observed LO lines are due to scattering in the ZnCdSe layer and are related to lattice vibrations of this layer. This conclusion draws from the following two observations.

(1) The 1LO line intensity grows resonantly by two orders of magnitude in the region of the ZnCdSe ground state. This resonant increase implies that it is in the ZnCdSe layer that the scattering occurs.

(2) The measured energy of the 1LO component is noticeably closer to the estimated values of the LO_1 (q_{xy}) mode of the ZnCdSe layer than to those of the ZnSe layers (Fig. 8). Moreover, room-temperature measurements conducted with a better spectral resolution [29] showed that the energy of the 1LO component in the QW region, when excited at the ZnCdSe excitonic resonance, was redshifted by $\Delta \sim 0.1$ meV with respect to its position under excitation at the ZnSe resonance. This observation corroborates our estimates. The energy of the LO_1 (q_{xy}) mode at the zone center estimated for a strained $Zn_{0.87}Cd_{0.13}Se$ layer is redshifted by ~0.15 meV relative to the corresponding values calculated for a strained ZnSe layer (Fig. 8).

Thus, a comparison of the measured energies of phonons involved in the formation of the LO line with their estimates suggests that the phonons participating in the line formation have small wave vectors q_{xy} near the Γ point of the Brillouin zone. This correlates with the above diagram of the Raman scattering process (Fig. 7). Indeed, the smallness of the wave vectors argues for the RS under study being close to the process in which the wave vector is conserved and, hence, for the involvement of free excitons in this process. The closeness of the LO component energy to the values estimated for LO_1 phonons with wave vectors q_{xy} lends support to the conjecture that additional elastic scattering from roughness contributes to the Raman process, because the roughness profile both at the ZnCdSe/ZnSe interface and at the sidewalls of open wires can be represented by a set of "roughness wave vectors" lying in the *xy* plane [30].

As is evident from Fig. 8, the energy position of the *a–d* components differs noticeably from the energies estimated for all optical modes at the zone center. This is in accord with the proposed assignment of the corresponding lines as being due to HL. Indeed, the HL lines are produced in emission of localized excitons, which form in the absorption of light with simultaneous creation of the corresponding phonon states. The wave-vector conservation law is not valid for this absorption process, and this process can involve phonons from different points of the Brillouin zone. The resulting population of localized states, which determines the fine structure of HL spectra, should be a complex function depending both on the density of states of phonons created in the process of absorption and on the dependence of the probability of localized-exciton formation on the wave vector of the phonons involved in the process. In view of the above, it appears difficult to associate the observed components with specific features in the phonon spectra, all the more so since the phonon dispersion and, hence, the phonon density of states for the ZnCdSe solid solution are not known. Figure 8 shows that the *b–d* components lie in the range between the estimated energies for the main optical modes (LO_1, TO_2) into which the LO_2 and TO_1 modes originating from the compositional effect also fall. Because the phonon density of states is concentrated usually in the region between the main longitudinal and transverse optical phonons [13], we can only maintain, in view of the above difficulties, that the *b–d* components form with the involvement of various optical phonons with large wave vectors far from the zone center. One also readily sees from Fig. 8 that, while the energy of phonons corresponding to the *a* line is noticeably less than all the estimated energies, this energy is fairly close to that of the Zn impurity mode in CdSe [1]. In this connection, it may be conjectured that the *a* line is related to lattice vibrations of CdSe clusters, whose formation in ZnCdSe layers is very likely [31]. An alternative explanation could lie in the existence of a singularity in phonon mode dispersion, which would create a noticeable density of phonon states in the corresponding energy region.

4.4. Multi-LO-Phonon Scattering

The presence of strong *n*LO lines in excitation spectra is a characteristic feature of most polar semiconductors [32]. The formation of these lines is usually treated as multi-LO-phonon RRS via real excitonic states with large wave vectors or as the HL emerging in cascade scattering by LO phonons via the same exciton states [12]. Because the type and number of the phonons, as well as the character of the intermediate states involved in RRS and HL, are the same, these processes are difficult to separate [12]. In any case, in bulk semiconductors, the RS involving LO phonons obeys the wave-vector conservation law. The *n*LO lines in our structures (Fig. 2) are apparently identical in nature to the analogous lines in bulk semiconductors. In this case, the LO phonon–mediated scattering involving extended excitonic states should obey the wave-vector conservation law in the *xy* plane. As a result, the LO phonons involved in the process under consideration should have finite values of the k_{xy} wave vectors and their energies should be redshifted relative to their values for $k_{xy} = 0$ [13]. As shown by our estimates (based on the energy and momentum conservation laws for scattering via the states of the E_{1H} band), the wave vectors of

phonons involved in RS are not large (less than 10% of their values at the zone edge). The corresponding redshift for the 1LO line in the excitation energy region used should be in the range ~0–0.17 meV, and that for the 2LO line, within the interval 0.17–0.9 meV. Such estimates are in accord with the fact that the energy of the LO phonons involved in the formation of the 1LO line is noticeably larger than the corresponding energies for the 2LO and 3LO lines (Fig. 2). Thus, the observed properties of the LO lines indicate the applicability of the wave-vector conservation law to the exciton–phonon interaction and, thus, support the conjecture that the exciton states involved in the formation of an RS line may indeed be considered free extended states.

The LO lines are the strongest ES components in our structures (Fig. 2). Their presence in the observed spectra indicates the operation of an efficient channel of LO phonon–mediated energy relaxation [12, 32]. In view of the fact that the LO phonon energy also agrees with the period of the weaker replicas associated with the *a–d* components, we come to the conclusion that free-exciton scattering by LO phonons is responsible for the initial relaxation stages in the formation of localized excitons. The *a–d* phonon components participate in the final stage of energy relaxation. This stage consists obviously in trapping the free exciton into the region of the fluctuating-potential minimum. In this stage, the wave-vector conservation law is no longer valid and, as a result, exciton trapping into a localized state is mediated by phonons from the whole Brillouin zone.

5. CONCLUSIONS

To sum up, exciton–phonon interaction in ZnCdSe/ZnSe structures maintained under resonance excitation and at low temperatures has been shown to give rise to the simultaneous appearance of RS and HL lines in resonance secondary luminescence spectra. The RS proceeds via intermediate states of free, extended excitons. The HL is associated with the emission of localized excitons. The elastic scattering from roughness and inelastic scattering from LO phonons in the ZnCdSe layer near the Brillouin zone center are responsible for the observed RRS lines. The HL lines involve phonons with large wave vectors. Lattice vibrations in CdSe clusters also possibly take part in HL. The HL lines disappear with increasing temperature, to leave only RS lines in room-temperature spectra.

ACKNOWLEDGMENTS

The authors are indebted to Professor S.A. Permogorov for valuable discussions. Special thanks are due to Professor F. Henneberger and the NATO Science Program for giving us the opportunity to work with a tunable laser at the Humboldt University (Berlin). We express our warm gratitude to S.I. Nesterov, V.I. Skopina†, and E.M. Tanklevskaya for preparing the samples with nanowires and to V.Yu. Davydov and I.N. Goncharuk for their assistance in room-temperature measurements.

REFERENCES

1. R. G. Alonso, E.-K. Suh, A. K. Ramdas, *et al.*, Phys. Rev. B **40** (6), 3720 (1989).
2. S. Permogorov, A. Reznitsky, L. Tenishev, *et al.*, in *Proceedings of the 23rd International Conference on the Physics of Semiconductors, Berlin, 1996*, Ed. by M. Scheffler and R. Zimmermann (World Sci., Singapore, 1996), p. 2015.
3. M. Lowish, M. Rabe, B. Stegemann, *et al.*, Phys. Rev. B **54** (16), R11074 (1996).
4. I. Reshina, A. Toropov, S. Ivanov, *et al.*, Solid State Commun. **112** (6), 351 (1999).
5. A. A. Toropov, T. V. Shubina, S. V. Sorokin, and A. V. Lebedev, Phys. Rev. B **59** (4), R2510 (1999).
6. J. Avendano-Lopez, F. L. Castillo-Alvarado, A. Escamilla-Esquivel, *et al.*, Solid State Commun. **100** (1), 33 (1996).
7. V. V. Travnikov, V. H. Kaibyshev, N. V. Lomasov, *et al.*, Nanotechnology **12** (4), 602 (2001).
8. S. A. Gurevich, O. A. Lavrova, N. V. Lomasov, *et al.*, Semicond. Sci. Technol. **13** (1), 139 (1998).
9. P. Ils, Ch. Greus, A. Forchel, *et al.*, Phys. Rev. B **51** (7), 4272 (1995).
10. N. V. Lomasov, V. V. Travnikov, S. O. Kognovitskiĭ, *et al.*, Fiz. Tverd. Tela (St. Petersburg) **40** (8), 1559 (1998) [Phys. Solid State **40**, 1413 (1998)].
11. T. Kummell, G. Bacher, A. Forchel, *et al.*, Phys. Rev. B **57** (24), 15439 (1998).
12. S. A. Permogorov, in *Excitons*, Ed. by E. I. Rashba and M. D. Sturge (North-Holland, Amsterdam, 1982), p. 177.
13. B. Hennion, F. Moussa, G. Pepy, and K. Kunc, Phys. Lett. A **36A** (5), 376 (1971).
14. E. Runger, A. Schülzgen, F. Henneberger, and R. Zimmermann, Phys. Status Solidi B **188**, 547 (1995).
15. S. Permogorov and V. Travnikov, Solid State Commun. **29** (8), 615 (1979).
16. M. Godlewski, J. P. Bergman, B. Monemar, *et al.*, Appl. Phys. Lett. **69** (19), 2843 (1996).
17. A. A. Klochikhin and A. G. Plyukhin, Pis'ma Zh. Éksp. Teor. Fiz. **21** (5), 267 (1975) [JETP Lett. **21**, 122 (1975)].
18. S. Permogorov and V. Travnikov, Phys. Status Solidi B **78** (1), 389 (1976).
19. W. Kauschke, A. K. Sood, M. Cardona, and K. Ploog, Phys. Rev. B **36** (3), 1612 (1987).
20. A. J. Shields, C. Trallero-Giner, M. Cardona, *et al.*, Phys. Rev. B **46** (11), 6990 (1992).
21. Y. R. Shen, Phys. Rev. B **9** (2), 622 (1974).
22. M. V. Klein, Phys. Rev. B **8** (2), 919 (1973).
23. A. A. Gogolin and E. I. Rashba, Solid State Commun. **19** (12), 1177 (1976).

† Deceased.

24. G. Lermann, T. Bischof, A. Materny, *et al.*, J. Appl. Phys. **81** (3), 1446 (1997).

25. D. L. Peterson, A. Petrou, W. Giriat, *et al.*, Phys. Rev. B **33** (2), 1160 (1986).

26. C. D. Lee, B. K. Kim, J. W. Kim, *et al.*, J. Cryst. Growth **138** (1–4), 136 (1994).

27. F. Cerdeira, C. Buchenauer, F. Pollak, and M. Cardona, Phys. Rev. B **5** (2), 580 (1972).

28. N. N. Melnik, Yu. G. Sadofyev, T. N. Zavaritskaya, and L. K. Vodop'yanov, Nanotechnology **11** (4), 252 (2000).

29. V. Kh. Kaĭbyshev, V. V. Travnikov, and V. Yu. Davydov, Fiz. Tverd. Tela (St. Petersburg) **45** (7), 1311 (2003) [Phys. Solid State **45**, 1374 (2003)].

30. *Surface Polaritons*, Ed. by V. M. Agranovich and D. L. Mills (North-Holland, Amsterdam, 1982; Nauka, Moscow, 1985).

31. N. Peranio, A. Rosenauer, D. Gerthsen, *et al.*, Phys. Rev. B **61** (23), 16015 (2000).

32. S. Permogorov, Phys. Status Solidi B **68** (1), 9 (1975).

Translated by G. Skrebtsov

Physics of the Solid State, Vol. 45, No. 7, 2003, pp. 1388–1391. Translated from Fizika Tverdogo Tela, Vol. 45, No. 7, 2003, pp. 00–00.

LOW-DIMENSIONAL SYSTEMS AND SURFACE PHYSICS

Rare-Earth Metal Adsorption on Silicon: Variation of the Work Function

S. Yu. Davydov[1, 2] and A. V. Pavlyk[2]

[1]*Ioffe Physicotechnical Institute, Russian Academy of Sciences, Politekhnicheskaya ul. 26, St. Petersburg, 194021 Russia*
e-mail: sergei.davydov@mail.ioffe.ru
[2]*St. Petersburg State Electrotechnical University, ul. Prof. Popova 5, St. Petersburg, 197376 Russia*
Received November 22, 2002

Abstract—The variation of the work function of the (111)Si surface under deposition of submonolayer Sm, Eu, and Yb films was calculated with inclusion of the dipole–dipole adatom repulsion and the metallization effects. The results of the calculations agree satisfactorily with experiment. © *2003 MAIK "Nauka/Interperiodica".*

1. Interaction of the rare-earth metals (REMs) Sm, Eu, and Yb with the (111)Si surface was studied experimentally in [1–3]. Those studies involved measurement of the variation of the work function $\Delta\varphi$ of an adsorption system as a function of surface coverage $\Theta = N/N_{ML}$ by adatoms (N is the adatom concentration and N_{ML} is their concentration in a monolayer). We recently proposed a simple model capable of satisfactorily describing $\Delta\varphi(\Theta)$ for the case of alkali metal adsorption on (100)Si [4] and (110)TiO_2 [5]. It is this model that we employ in this study to interpret the results of [1–3].

Strictly speaking, the model proposed in [4, 5] is inapplicable to REMs. Indeed, while alkali metals contain only one electron in the outer *s* shell, the 6*s* shell in REMs is completely filled. However, as follows from experiments [1–3], the maximum reduction of the work function $\Delta\varphi_{max}$ caused by REM adsorption is on the order of 1.6–1.7 eV, whereas in the case of adsorption of alkali metals on silicon we have $\Delta\varphi_{max} \sim -3$ eV. Hence, the number of electrons donated by REM atoms interacting with silicon to the substrate is smaller than that transferred from alkali metals. For this reason alone, one may formally assume that only one 6*s* electron is involved in adsorption,[1] which validates the use of the model from [4, 5]. We present, however, an additional substantiation of the above statement.

2. Consider a single adatom in terms of the Anderson Hamiltonian (see, e.g., [6, 7]). The *s*-shell occupation numbers $n_{0\pm}$ for the spin-up and spin-down electrons, respectively, are given by the self-consistent coupled equations

$$n_{0+} = \frac{1}{\pi}\operatorname{arccot}\frac{\varepsilon + Un_{0-} - \varepsilon_F}{\Gamma_0},$$
$$n_{0-} = \frac{1}{\pi}\operatorname{arccot}\frac{\varepsilon + Un_{0+} - \varepsilon_F}{\Gamma_0}. \quad (1)$$

Here, ε is the unperturbed single-particle energy of the *s* state, ε_F is the Fermi energy for the substrate, U is the energy of electron Coulomb repulsion in the *s* shell, and Γ_0 is the quasi-level halfwidth of a single adatom.

We look for a nonmagnetic solution to the problem by setting $n_+ = n_- = n_0/2$ and assuming the total adatom occupation number to be n_0. In this case, Eqs. (1) reduce to one self-consistent equation,

$$n_0 = \frac{2}{\pi}\operatorname{arccot}\frac{\varepsilon + Un_0/2 - \varepsilon_F}{\Gamma_0}. \quad (2)$$

We next assume that only one electron per adatom can tunnel into the substrate. By introducing the adatom charge $Z_0 = 1 - n_0$, Eq. (2) can be recast in the form

$$Z_0 = \frac{2}{\pi}\arctan\frac{\tilde{\varepsilon}}{\Gamma_0}, \quad \tilde{\varepsilon} = \left(\varepsilon - \varepsilon_F + \frac{1}{2}U\right) - \frac{1}{2}UZ_0. \quad (3)$$

The charge of a single adatom in the model at hand [4, 5] is defined as

$$Z_0 = \frac{2}{\pi}\arctan\frac{\Omega}{\Gamma_0}, \quad \Omega = I - \varphi + \Delta, \quad \Delta = \frac{e^2}{4\lambda}, \quad (4)$$

where I is the *s*-shell ionization energy; φ is the substrate work function; e is the positron charge; 2λ is the double adsorption bond length, which is equal, within the chosen model, to the thickness of the double electric layer [8, 9]; and $\Delta$is the Coulomb shift of the adatom energy level caused by interaction of the adatom elec-

[1] We assume here that only one electron can tunnel from an REM adatom to the substrate, a process accounting for the formation of a double layer, which brings about the reduction of the work function of an adsystem. As for the adsorption bonding, *f* electrons also take part in its formation, which makes the desorption energy of REMs two to three times higher than that for the alkali metals.

tron with the substrate electrons. Note that the last term in the second of expressions (3) relates to the Coulomb interaction of the adatom electron with the electrons of the substrate, which is disregarded in the standard Anderson model [6]. A comparison of Eqs. (3) and (4) shows that the two-electron model from [6] differs from the single-electron model only in the renormalization of the quasi-level position.[2]

3. In accordance with the model from [4, 5], the adatom occupation number $Z(\Theta)$ for a finite coverage can be written as

$$Z(\Theta) = \frac{2}{\pi}\arctan\frac{\Omega - \xi\Theta^{3/2}Z(\Theta)}{\Gamma(\Theta)},$$
$$\xi = 2e^2\lambda^2 N_{ML}^{3/2}A, \quad \Gamma = \Gamma_0(1+\gamma\Theta). \tag{5}$$

Here, ξ is the adatom dipole–dipole repulsion constant, $A = 10$ is a dimensionless coefficient weakly dependent on the adatom lattice geometry, and γ is a dimensionless parameter accounting for the band broadening, i.e., the metallization effects [4, 5]. The adsorption-induced variation of the work function $\Delta\varphi$ is given by

$$\Delta\varphi(\Theta) = -\Phi\Theta Z,$$
$$\Phi = 4\pi e^2 N_{ML}\lambda. \tag{6}$$

To determine the model parameters, we use the scheme proposed in [4, 5]. The monolayer adatom concentration is estimated from the nearest neighbor separation in bulk REM samples [10] (we believe the N_{ML} values quoted in [1–3] to be exaggerated). The adsorption bond length is derived from the magnitude of the REM atomic radii r_a [11] assuming $\lambda \sim 0.7r_a$.[3] Taking $\varphi = 4.6$ eV for the (111)Si surface [1–3, 11], we obtain the values of the energy parameters listed in the table.

Figures 1–3 compare the results of a numerical calculation of $\Delta\varphi(\Theta)$ with experimental data. For europium and ytterbium (Figs. 2, 3) the agreement is quite satisfactory. For samarium (Fig. 1), there is a clearly pronounced minimum in the work function at $\Theta \approx 0.7$, which is not explained in the theory. Because the calculated value of $\Delta\varphi(\Theta)$ is less in magnitude than the observed value, this means that the theory overestimates the depolarization effects. The same conclusion can be drawn from the table; indeed, the values of parameters Γ_0 and γ for Sm are considerably larger than those for Eu and Yb. It appears appropriate to stress here once more (see also [4, 5]) that our model of the adlayer does not have a structure and that the coverage affects only the adatom density in the layer. Experiment reveals, however, structural phase transitions.

Model parameters

	Ω	Γ_0	Φ	ξ	γ	N_{ML}	λ	Z_0	Z_{ML}
Sm	1.725	2.55	17.6	10.0	1.87	7.5	1.3	0.38	0.08
Eu	1.50	1.87	15.5	8.6	0.45	6.0	1.4	0.43	0.12
Yb	1.12	1.37	15.3	8.1	0.10	6.5	1.3	0.44	0.11

Note: Parameters Ω, Γ_0, Φ, and ξ are in electrovolts, λ in angstroms, and N_{ML}, in units of 10^{14} atom/cm^2.

It is of interest to analyze why the present model is applicable to the case of adsorption on semiconductors even though it draws on studies dealing with adsorption on metals. The answer to this question is not so difficult to find as it might seem at first glance. Because the position of the center of gravity for an adatom quasi-level Ω (reckoned from the Fermi level) exceeds the silicon band gap width $E_g = 1.11$ eV, the quasi-level at zero coverage is certain to overlap the conduction band, which is typical metallic behavior. The positions of the quasi-level under monolayer coverage, $\tilde{\Omega} = \Omega - \xi Z_{ML}$, for Sm, Eu, and Yb are 0.95, 0.47, and 0.23 eV, respectively. Because the Si samples used in [1–3] were *n* type, the center of the quasi-level in those samples also lies above the conduction band bottom.

4. A model describing the effect of temperature T on the work function of metal substrates bearing submonolayer metal films was proposed in [12]. It was assumed that the temperature coefficient of the work

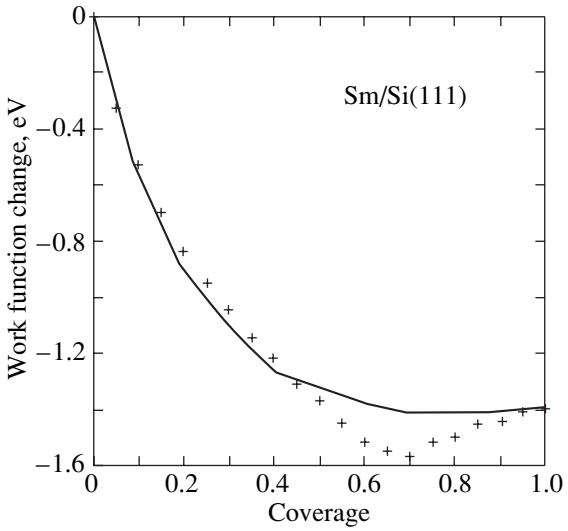

Fig. 1. Work function change plotted vs. coverage for adsorption of samarium on silicon. Crosses are experimental points.

[2] It should be stressed that the self-consistency is lost in going from Eq. (3) to Eq. (4). Moreover, finite coverages give rise, in accordance with Eq. (3), to a shift of the quasi-level center of gravity caused by the intratomic Coulomb repulsion U (in addition to the shift due to dipole–dipole interaction; see below). It is essential, however, that screening by the substrate electrons substantially reduces the value of the parameter U, which is ~10 eV for an REM atom, and this parameter can apparently be neglected compared to the dipole–dipole interaction constant.

[3] Generally speaking, the choice of the parameters is not unique. This ambiguity stems, however, from objective factors. Indeed, even the monolayer concentration of adatoms is a poorly determined parameter; as a result, many experimental studies quote only the exposure time.

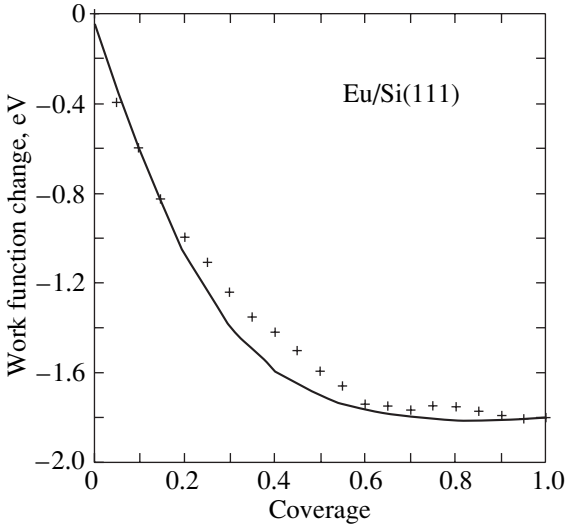

Fig. 2. Same as in Fig. 1, but for adsorption of europium on silicon.

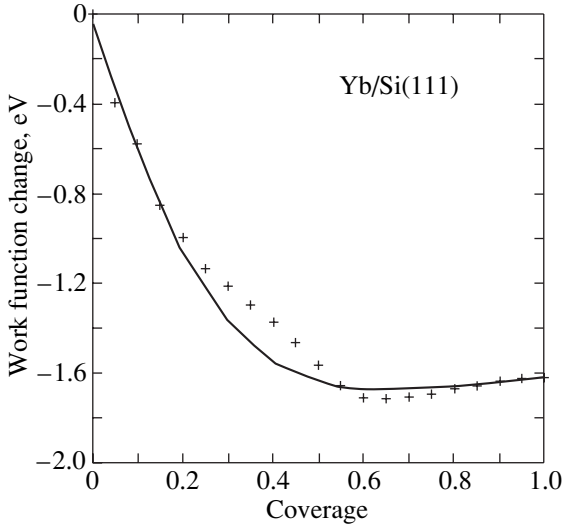

Fig. 3. Same as in Fig. 1, but for adsorption of ytterbium on silicon.

function of the adsystem κ is presentable in the form of a sum:

$$\kappa = \kappa_s + \kappa_a,$$
$$\kappa_s = d\varphi/dT, \quad \kappa_a = d\Delta\varphi/dT, \tag{7}$$

where κ_s is the temperature coefficient of the substrate work function and κ_a is that of the adsorption-induced variation of the work function. The model proposed in [12] provided a satisfactory explanation for the effect of temperature on the work function of the Eu/W(100) adsystem studied in [13], which also dealt with adsorption of Eu on Si(111). Unfortunately, the approach developed in [12] for metal substrates is not directly applicable to semiconductor substrates. We use, however, the observation that the work function of a clean (111)Si surface φ is practically temperature-independent [13]. The only thing left now is to estimate the temperature coefficient κ_a, which is defined, as shown in [12], by the expressions

$$\kappa_a = \kappa_a^{st} + \kappa_a^{dyn}, \tag{8}$$

where the static contribution to the temperature coefficient is

$$\kappa_a^{st} = -\Theta\Phi\alpha_a(Z_0 + 2\rho_0\Omega\tilde{\gamma}\lambda), \tag{9}$$

and the dynamic contribution is

$$\kappa_a^{dyn} = -\Theta\Phi\alpha_a\rho_0\Omega(2\tilde{\gamma}\lambda)^2\frac{\Gamma_0^2 - \Omega^2}{\Gamma_0^2 + \Omega^2}. \tag{10}$$

Here, $\alpha_a = \frac{3}{4}(k_B/E_{ads})$ and $\rho_0 = \Gamma_0/\lambda(\Omega^2 + \Gamma_0^2)$, where k_B is the Boltzmann constant, E_{ads} is the adsorption energy, and $\tilde{\gamma} = 1$ Å^{-1} is the characteristic reciprocal length of decay of the adatom–substrate-atom interatomic matrix element. Despite the fact that the Coulomb shift Δ and the metallization effects γ were disregarded in [12], we use Eqs. (8)–(10) for rough estimation of κ_a. Substituting the values of the parameters from the table into Eqs. (8)–(10) and recalling that $E_{ads} = 4.8$ eV [3], we obtain $\kappa_a^{st} \approx -2.72\Theta \times 10^{-4}$, $\kappa_a^{dyn} \approx -1.10\Theta \times 10^{-4}$, and $\kappa_a \approx -3.82\Theta \times 10^{-4}$ eV K^{-1}. Thus, for $\Theta = 0.1$, the temperature coefficient is $\kappa_a \approx -0.4 \times 10^{-4}$ eV K^{-1}. In the temperature range $T = 300$–1000 K and for $\Theta = 0.1$ [13, curve *2* in Fig. 2], experiment yields $\kappa_a \approx -1.4 \times 10^{-4}$ eV K^{-1}, which is larger (in magnitude) than the theoretical value by a factor of 3.5. Generally speaking, there is nothing strange in this discrepancy and the fact that the experimental and calculated values of κ_a are of the same sign and the coefficients are of the same order of magnitude is in itself an argument for the validity of our model for analyzing (although only semiquantitative) the temperature effects. At the same time, it should be pointed out that a semiconductor substrate is much more sensitive to metal adsorption (compared to a high-melting *d* substrate, where the coefficient κ is, by the way, an order of magnitude smaller [13]), which becomes manifest, in particular, in complex structural rearrangements of the surface of both the substrate and the adlayer. It is, therefore, not inconceivable that representing the work function φ as $\tilde{\varphi} = \varphi + \Delta\varphi$ is fully appropriate for calculation of the coverage dependence of the work function (i.e., essentially, of the first derivative $\partial\varphi/\partial\Theta$) while being too simplified to analyze temperature effects. Indeed, to calculate the coefficient κ in the zero coverage limit would now require determination of the second derivative of the type $\partial^2\varphi/\partial T\partial\Theta$, and we know only too well

from theory that calculation of each successive derivative entails an increase in the error [14].

REFERENCES

1. T. V. Krachino, M. V. Kuz'min, M. V. Loginov, and M. A. Mittsev, Fiz. Tverd. Tela (St. Petersburg) **39** (9), 1672 (1997) [Phys. Solid State **39**, 1493 (1997)].
2. T. V. Krachino, M. V. Kuz'min, M. V. Loginov, and M. A. Mittsev, Fiz. Tverd. Tela (Leningrad) **40** (10), 1937 (1998) [Phys. Solid State **40**, 1758 (1998)].
3. T. V. Krachino, M. V. Kuz'min, M. V. Loginov, and M. A. Mittsev, Fiz. Tverd. Tela (St. Petersburg) **42** (3), 553 (2000) [Phys. Solid State **42**, 566 (2000)].
4. S. Yu. Davydov and A. V. Pavlyk, Fiz. Tekh. Poluprovodn. (St. Petersburg) **35** (7), 831 (2001) [Semiconductors **35**, 796 (2001)].
5. S. Yu. Davydov and I. V. Noskov, Pis'ma Zh. Tekh. Fiz. **27** (20), 1 (2001) [Tech. Phys. Lett. **27**, 844 (2001)].
6. C. Kittel, *Quantum Theory of Solids* (Wiley, New York, 1963; Nauka, Moscow, 1967), Chap. 18.
7. O. M. Braun and V. K. Medvedev, Usp. Fiz. Nauk **157** (4), 631 (1989) [Sov. Phys. Usp. **32**, 328 (1989)].
8. J. P. Muscat and D. M. Newns, J. Phys. C: Solid State **7** (15), 2630 (1974).
9. S. Yu. Davydov, Fiz. Tverd. Tela (Leningrad) **19** (11), 3376 (1977) [Sov. Phys. Solid State **19**, 1971 (1977)].
10. C. Kittel, *Introduction to Solid State Physics*, 5th ed. (Wiley, New York, 1976; Nauka, Moscow, 1978).
11. *Physical Quantities. Handbook*, Ed. by I. S. Grigor'ev and E. Z. Meĭlikhov (Énergoatomizdat, Moscow, 1991).
12. S. Yu. Davydov, Fiz. Tverd. Tela (St. Petersburg) **45** (5), 926 (2003) [Phys. Solid State **45**, 972 (2003)].
13. M. V. Kuz'min and M. A. Mittsev, Pis'ma Zh. Tekh. Fiz. **27** (10), 86 (2001) [Tech. Phys. Lett. **27**, 437 (2001)].
14. A. B. Migdal, *Qualitative Methods in Quantum Theory* (Nauka, Moscow, 1975; Benjamin, Reading, Mass., 1977).

Translated by G. Skrebtsov

Physics of the Solid State, Vol. 45, No. 7, 2003, pp. 1392–1395. Translated from Fizika Tverdogo Tela, Vol. 45, No. 7, 2003, pp. 1329–1332.

LOW-DIMENSIONAL SYSTEMS AND SURFACE PHYSICS

Study of the Initial Stage of Yttrium Oxidation Using Characteristic Electron-Energy-Loss Spectroscopy

M. N. Mikheeva, V. G. Nazin, and A. S. Kiparoidze

Russian Research Centre Kurchatov Institute, pl. Kurchatova 1, Moscow, 123182 Russia

Received December 3, 2002

Abstract—The characteristic electron-energy-loss (EEL) spectra of the pure surface of metallic yttrium and of this surface in the initial stages of oxidation are recorded. The energy of the primary electron beam E_p is 200–1000 eV. The spectra exhibit high- and low-frequency peaks. During oxidation, the positions of the basic peaks in the EEL spectra are significantly shifted. The peaks corresponding to the bulk energy loss shift toward higher energies upon oxidation. The peak corresponding to the low-frequency surface oscillations also shifts, but toward lower energies, and its intensity monotonically decreases with increasing oxygen dose. The differences between the spectra recorded at different E_p are explained as resulting from an increase in the electron escape depth with E_p. *© 2003 MAIK "Nauka/Interperiodica".*

The discovery of high-temperature superconductivity in complex nonstoichiometric oxides [1] has evoked great interest in the study of oxides of various metals. Moreover, investigation of the surface of a pure metal and its interaction with oxygen is extremely important for solving problems in surfaces physics and physical metallurgy and enhances the understanding of the properties of metals and, in particular, the interaction of metals with their environment. Earlier, we studied the oxidation of metallic lanthanum and revealed interesting features in its electronic structure [2]. Therefore, it is interesting to compare those data with analogous results on yttrium, whose electronic configuration is close to that of lanthanum. Interest in yttrium is also stimulated by the fact that its oxide is used as insulating dielectric layers in modern microcircuit production technologies.

The purpose of this work is to study the electronic structure of metallic yttrium and its variation with oxidation of yttrium by using characteristic electron-energy-loss spectroscopy (EELS).

We performed investigations using a synchrotron radiation source at the photoelectron spectroscopy station located at the Kurchatov Institute. We used a high-purity (99.9%) polycrystalline yttrium sample $10 \times 15 \times 4$ mm in size. Its surface was cleaned using a unique method with a tungsten brush consisting of 1200 wires 0.037 mm in diameter. A layer ~2–5 μm thick was removed from the sample surface in one cycle of cleaning. It should be noted that, after the oxidized surface had been cleaned, no photoelectron emission was observed from oxide states characteristic of insufficiently clean sample surfaces. Hence, the method of cleaning the sample surface provided a clean, though not ideally smooth, surface. The residual pressure in the chamber during measurements was $\sim 10^{-10}$ Torr. These vacuum conditions allow measurements on a clean yttrium surface for 1.0–1.5 h, after which the emission caused by oxide forming due to interaction with residual gases becomes considerable.

Samples were oxidized by bleeding pure oxygen into a chamber over 14–400 s. Oxygen was prepared by heating copper oxide CuO, which decomposes to yield copper and oxygen at temperatures above 500°C. The oxygen content in the chamber was determined *in situ* during oxidation by using mass spectrometric analysis. Oxidation was carried out in one leak-in of oxygen by both small and large (up to 45 L, where $1L = 10^{-6}$ Torr s) doses. A dose of 1L (langmuir) means that approximately one monolayer grows onto a material under study in a time t at a pressure p ($pt = 1L$), provided the accommodation coefficient is equal to unity. If this coefficient is smaller than unity, the actual amount of oxygen adsorbed on the surface can be significantly smaller than that calculated in langmuirs. To record EEL spectra from samples with various degrees of oxidation, we cleaned their surfaces before each leak-in of oxygen.

All manipulations with samples and measurements were performed at room temperature. To record electron energy spectra, we used a Perkin-Elmer 15-255GAR energy analyzer equipped with an electron gun. The energy resolution of the energy analyzer is less than 0.1 eV at energies from 0 to 1500 eV. The electron gun built in the first stage of the analyzer allows one to record EEL spectra (in the reflection mode) at an electron energy E_p in the range 5–5000 eV. To measure the optical absorption, we used synchrotron radiation monochromatized in the same way as in [3]. Spectra were recorded in the electron-counting mode depending on the electron kinetic energy at each spec-

1063-7834/03/4507-1392$24.00

trum point; the energy analyzer and recording of spectra were controlled using a microcomputer.

EEL spectra of the yttrium sample are shown in Figs. 1 and 2. They were recorded at a primary electron beam energy of E_p = 200 (Fig. 1) and 1000 eV (Fig. 2) at room temperature. The abscissa is the energy of secondary electrons, and the ordinate is I/I_{max} for each spectrum (the signal in each spectrum is normalized to its maximum intensity). A complete EEL spectrum is shown in Fig. 1 (curve *7*). The full width at half-maximum of elastically reflected electrons (Fig. 1, curve *7*) does not exceed 0.65 eV, which means that the spectra are recorded with an energy resolution of about 0.65 eV. The spectra were recorded in the electron-counting mode at each point in the spectrum. The energy step was 0.05 eV. The zero in the energy axis was taken to be the energy of an elastically reflected peak. Figures 1 and 2 (curve *1*) show EEL spectra for the yttrium sample with a cleaned surface; high- and low-frequency peaks are clearly visible in them. The high-frequency peak at ~12.4 eV corresponds to the excitation of a bulk plasmon, and the low-frequency peak near ~3.9 eV is due to the superimposition of a surface plasmon on the *d–d* interband transition [4]. The fraction of the low-frequency plasmon excitations in the spectrum taken at E_p = 1000 eV is low. The low-frequency plasmon is weakly pronounced in the left slope of the bulk plasmon in this spectrum, because the surface energy loss length at this energy is shorter. At the primary electron energy E_p = 200 eV, the surface plasmon interferes with the *d–d* interband transition to form a total peak. The shape of the spectrum agrees well with the EEL calculation results [4] and the experimental results [5, 6]. Although the calculation was performed for the bulk electronic states of yttrium, many specific features agree well with the data for the surface of pure yttrium. Based on optical measurements, Weaver and Olson [7] calculated EEL spectra for both the bulk and surface states. Those calculated spectra [7] correspond to our data obtained at various energies of the primary electron beam. The spectrum at E_p = 200 eV contains peaks at 3.3 and 12.4 eV, and that at E_p = 1000 eV, peaks at 3.9 and 12.3 eV.

We also measured light absorption in pure metallic yttrium by using the CFS (quantum-yield) method at photon energies of 10–20 eV. The absorption spectra usually agree well with the corresponding EEL spectra. The spectrum in Fig. 3 contains one peak corresponding to an increase in the light absorption due to excitation of a bulk plasmon. The position (12.5 eV) of the absorption maximum agrees well with the EELS data for pure yttrium (Figs. 1, 2). At photon energies below 10 and above 22 eV, the desired signal was extremely low, which led to large errors at the edges of the spectrum. It should be noted that the light penetration depth is much greater than the photoelectron escape depth and is equal to 40–80 nm in this range of photon energies.

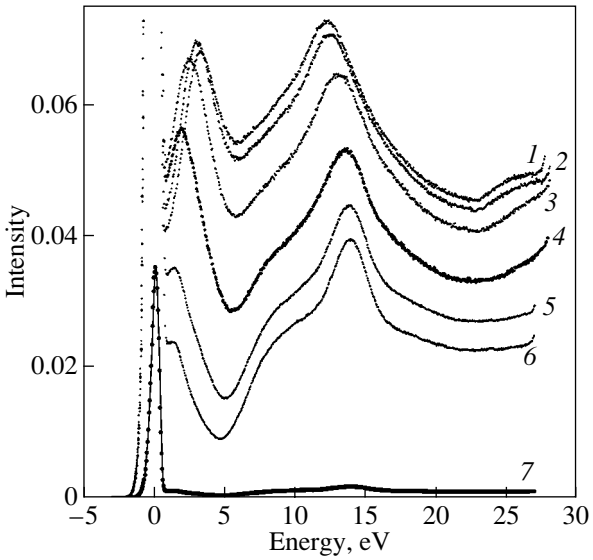

Fig. 1. EEL spectra of the yttrium surface at various oxygen doses (L): (*1*) 0, (*2*) 5.5, (*3*) 9.3, (*4*) 15.2, (*5*) 22.7, and (*6*) 45. Curve *7* is curve *6* drawn on a scale such that the peak of elastically reflected electrons is visible. The energy of the primary electron beam is E_p = 200 eV.

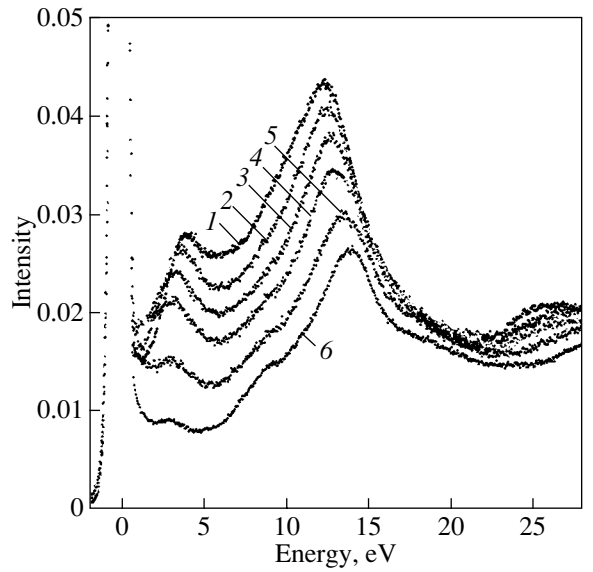

Fig. 2. EEL spectra of the yttrium surface at various oxygen doses (L): (*1*) 0, (*2*) 6.7, (*3*) 18.4, (*4*) 34.6, (*5*) 55.1, and (*6*) 145.5. E_p = 1000 eV.

Figures 1 and 2 also show the EEL spectra recorded at the incident electron energies E_p = 200 and 1000 eV for yttrium with various degrees of oxidation of the preliminarily cleaned surface. As the dose of bleeding-in oxygen increases, the spectrum structure changes (see curves *2–6*).

The positions of both (low- and high-frequency) peaks significantly shift in this set of curves. The peak

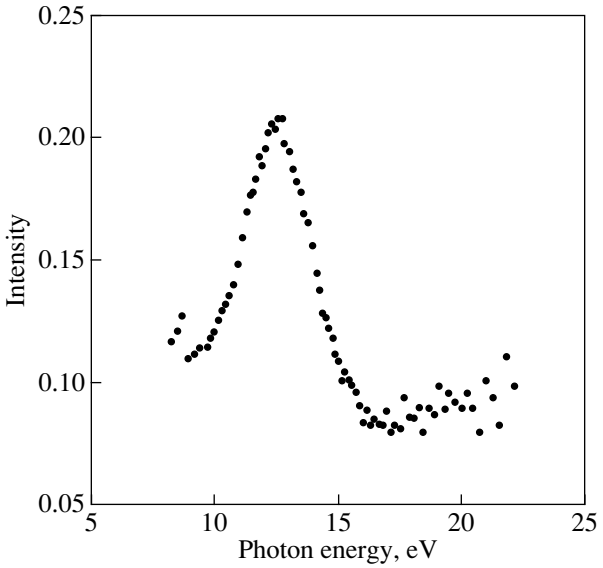

Fig. 3. Optical absorption spectrum of metallic yttrium.

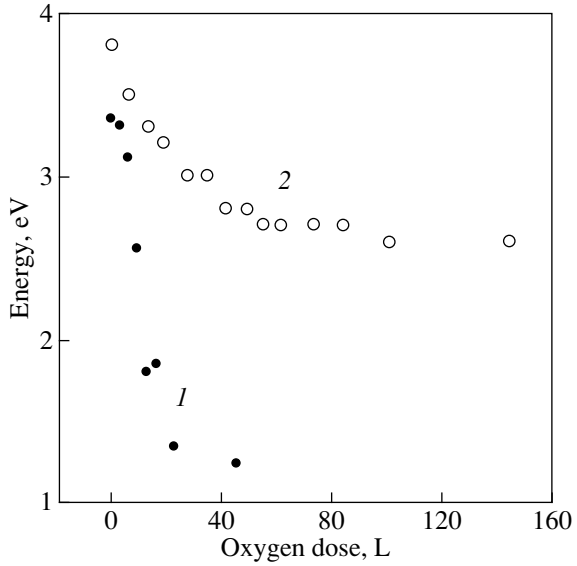

Fig. 4. The energy of the low-frequency peak in the EEL spectrum of the yttrium surface as function of the oxygen dose at (*1*) E_p = 200 and (*2*) 1000 eV.

corresponding to the bulk energy loss shifts toward higher energies due to oxidation. At large oxygen doses, the shift is more pronounced and an additional peak appears on the left slope of the bulk plasmon at ~6–8 eV. This phenomenon is explained by an interband transition from the oxide energy band to electronic states above the Fermi level. The peak corresponding to low-frequency surface excitations also shifts, but toward lower energies, and its intensity monotonically decreases with increasing oxygen dose. Figure 4 shows the variation of the energy of the low-frequency peak from the spectra given in Figs. 1 and 2 with the oxygen dose. At low oxygen doses, the energy of the low-frequency peak varies with E_p only insignificantly. However, as the dose increases further, the low-frequency peak "splits" into two branches with different energies at the saturating oxygen doses. It should be noted, however, that these branches were measured at different energies of the primary electron beam. To interpret this behavior, it should be taken into account that the electron penetration depth in solids depends significantly on the electron energy. For electrons with E_p = 200 eV, the penetration depth is typically 0.5–1.0 nm, whereas for electrons with E_p = 1000 eV it can bears large as 3–4 nm. Then, all the data in Fig. 4 can be explained if we suppose that, as the oxygen dose is increased above 40L, the thickness of the oxide layer changes only insignificantly and is larger than the penetration depth for electrons with E_p = 200 eV but is smaller than the penetration depth for electrons with E_p = 1000 eV. In this case, the low-frequency peak for E_p = 200 eV corresponds to the excitation of a surface plasmon at the oxide–vacuum interface, whereas that for E_p = 1000 eV is due to the excitation of a plasmon at the metal–oxide interface. It should be noted that the energy of the low-frequency peak is lower than the band gap of the oxide (about 4.5 eV).

It can be seen from Fig. 2 that the EEL spectra recorded at the primary electron beam energy E_p = 1000 eV change even at oxygen doses higher than 100L. This behavior is due to the fact that the electron penetration depth in solids significantly increases at E_p = 1000 eV and, hence, the effective thickness of the layer analyzed by this method increases by several times as compared to the case with E_p = 200 eV. Therefore, the spectra become saturated at substantially larger oxygen doses, for which a thicker metal layer is oxidized. Curves *6* in Figs. 1 and 2 are the EEL spectra of the heavily oxidized sample surface. These spectra, like the others, contain two pronounced peaks; however, their intensities are lower than those in spectrum *1*, which is caused by the appearance of a thicker oxide film on the sample surface. The shapes of the spectra agree well with the data from [6] on bulk plasmons in yttrium oxide. Unfortunately, a poor energy resolution (>1 eV) did not allow Lynch and Swan [5] to reveal the specific feature that was clearly visible in our case in the EEL spectrum near the elastic peak. The spectrum recorded at E_p = 200 eV for the yttrium surface subjected to the maximum oxidation exhibits peaks at 1.3 and 13.7 eV, and that recorded at E_p = 1000 eV, peaks at 2.8 and 14 eV. It is probable that the oxide can penetrate further into the bulk of the sample, but the data obtained do not allow us to confirm this. The oxide formed on the surface is likely close to the stoichiometric composition, Y_2O_3; however, small deviations are possible, which is indicated by the 1.3-eV surface plasmon observed in the spectrum taken at E_p = 200 eV. This plasmon is not usually detected when studying

bulk oxide samples. The whole process of oxidation is basically close to the oxidation of lanthanum [2]; the only difference is that the yttrium surface is less active than the lanthanum surface and, hence, the oxide signal is saturated at by an order-of-magnitude higher oxygen dose.

ACKNOWLEDGMENTS

This work was supported by the Russian Foundation for Basic Research, project no. 01-02-17307.

REFERENCES

1. J. G. Bednorz and K. A. Muller, Z. Phys. B **64**, 189 (1986).
2. V. G. Nazin, M. B. Tsetlin, M. N. Mikheeva, *et al.*, Poverkhnost, No. 9, 102 (1996).
3. S. N. Ivanov, V. V. Mikhaĭlin, M. N. Mikheeva, *et al.*, Prib. Tekh. Éksp., No. 4, 231 (1988).
4. I. I. Mazin, E. G. Maksimov, S. N. Rashkeeva, and Yu. A. Uspenskiĭ, Metalloopt. Sverkhprovodimost **190**, 30 (1988).
5. M. S. Lynch and J. B. Swan, Aust. J. Phys. **21**, 811 (1968).
6. B. Brousseau-Lahave, C. Collex, J. Frandon, *et al.*, Phys. Status Solidi B **69**, 257 (1975).
7. J. W. Weaver and C. G. Olson, Phys. Rev. B **15**, 590 (1977).

Translated by K. Shakhlevich

Physics of the Solid State, Vol. 45, No. 7, 2003, pp. 1396–1402. Translated from Fizika Tverdogo Tela, Vol. 45, No. 7, 2003, pp. 1333–1338.

FULLERENES AND ATOMIC CLUSTERS

Classification of Two-Shell Nanotubes with Commensurate Structures of Shells

Yu. E. Lozovik, A. M. Popov, and A. V. Belikov

Institute of Spectroscopy, Russian Academy of Sciences, Troitsk, Moscow oblast, 142092 Russia

e-mail: lozovik@isan.troitsk.ru

Received September 26, 2002; in final form, November 21, 2002

Abstract—A classification of two-shell carbon nanotubes with commensurate structures of shells is proposed. The classification is based on the concept of equivalence classes as a set of shells with chiral indices of the (*kf*, *kg*) type, where *f* and *g* are the chiral indices of the equivalence class and *k* is the index of the shell diameter. All two-shell nanotubes with commensurate shells that are characterized by the chiral indices (k_1f_1, k_1g_1) and (k_2f_2, k_2g_2), where k_1 and k_2 are integral numbers, make up a family of nanotubes of different radii but with equal geometric parameters (such as the intershell distance, the unit cell length of the nanotube, and the difference between the chiral angles of the shells). The geometric parameters of nanotubes are calculated for a number of families, the distribution of different types of two-shell nanotubes with commensurate shells over the outer-shell radii is determined, and the threshold forces required to induce relative motion of nanotube shells are evaluated. The possible use of two-shell nanotubes with commensurate shells in nanostructures is discussed.

1. INTRODUCTION

A unique combination of electronic and mechanical properties [1, 2] renders carbon nanotubes very attractive for practical applications in nanoelectronics and nanomechanics. In particular, carbon nanotubes can be used in nanometer-size devices, for example, diodes [3], transistors [4], memory unit cells [5], nanopincers [6, 7], and atomic-force microscope tips [8–10]. The above examples of the possible areas of nanotube usage are based on the electronic and mechanical properties of single-shell nanotubes or individual shells of multishell nanotubes. However, recent experimental investigations revealed that individual shells of multishell nanotubes can readily move relative to each other due to weak van der Waals interactions; furthermore, it was demonstrated that the relative motion of nanotube shells can be arbitrary [11, 12] or controlled using a special manipulator [13]. The theoretical principles of the operation of nanometer-size devices embodying the concept of the relative motion of nanotube shells have been described for a nanobearing [14], a nanogear [15], a nanospring [13], a mechanical nanoswitch [16], and an electric nanoswitch and a nanodrill [17].

From the aforesaid, it is evident that an analysis of the geometric relationships for the structures [18] and the parameters of interaction [19–23] between two neighboring shells of a nanotube is an important problem in nanomechanics. It should be noted that two-shell nanotubes have already been produced through arc-discharge synthesis [2], heating [24], and electron irradiation [25] of single-shell nanotubes containing fullerenes. At present, there exists a classification of nonhelicoidal two-shell nanotubes [18]. Moreover, the energy barriers to relative motion and rotation of shells in several two-shell nanotubes [19–23] and the barriers to relative rotation of shells of two-shell nanoparticles [26, 27] are calculated theoretically.

Since the nanotube shell is considered a one-dimensional crystal [28, 29], the structures of the neighboring shells can be either commensurate or incommensurate [22]. As will be shown below, the threshold force **F** required to induce motion of one nanotube shell relative to the neighboring shell in the case of commensurate structures of the shells is several orders of magnitude greater than the threshold force needed to induce relative motion of shells with incommensurate structures. In addition, the threshold force **F** for shells with incommensurate structures is determined by the shell length. Consequently, nanotubes with commensurate and incommensurate structures of shells can be used in radically different mechanical nanometer-size devices. In this respect, the purpose of the present work was to elaborate a classification of two-shell nanotubes with commensurate structures of shells and to calculate the relevant geometric parameters. The proposed classification of two-shell nanotubes can also be considered a classification of pairs of neighboring shells with commensurate structures in multishell nanotubes.

2. STRUCTURE AND RELATIVE MOTION OF SHELLS IN TWO-SHELL NANOTUBES

The structure of a nanotube shell is specified by a pair of integral numbers, namely, the chiral indices (*n*, *m*), which correspond to the components of the vector of the graphite lattice $\mathbf{c} = n\mathbf{a}_1 + m\mathbf{a}_2$ (where $\mathbf{a}_1$ and $\mathbf{a}_2$ are

the unit vectors of the graphite plane). Upon rolling a fragment of the graphite plane into a nanotube shell, the segment corresponding to the vector **c** transforms into a circumference (Fig. 1) [28, 29]. The radius R of the nanotube shell can be represented by the formula

$$R = \frac{|\mathbf{c}|}{2\pi} = \frac{a_0\sqrt{n^2 + mn + m^2}}{2\pi}, \quad (1)$$

where a_0 is the magnitude of the unit vector of the graphite plane. The unit cell length of the nanotube shell can be written as

$$b = \frac{\sqrt{3}a_0\sqrt{n^2 + mn + m^2}}{GCD(2m + n, 2n + m)}, \quad (2)$$

where $GCD(2m + n, 2n + m)$ is the greatest common divisor of the numbers $2m + n$ and $2n + m$. The chiral angle defined as the angle between the vectors $\mathbf{a}_1$ and **c** is represented by the relationship

$$\theta = \arccos\frac{2n + m}{\sqrt{n^2 + m^2 + mn}}. \quad (3)$$

Since the graphite plane has a sixfold symmetry axis, only the shells determined by the vectors **c** lying within an angle of 60° (i.e., when $m > 0$ and $n > 0$) are inequivalent. Nanotube shells with chiral indices of the (n, n) and (n, 0) types are nonhelicoidal, and the remaining shells are helicoidal. The nanotube shells specified by the chiral indices (n, m) and (m, n) exhibit mirror symmetry; i.e., they have a left-handed helicoidal structure for $n > m$ and a right-handed helicoidal structure for $m > n$.

The structures of the nanotube shells are commensurate to each other if the ratio of their unit cell lengths b_1/b_2 is a rational fraction. For commensurate shells, the two-shell nanotube can be treated as a one-dimensional crystal with a unit cell length equal to the least common multiple of the unit cell length of the shells.

In the case when the contribution from atoms located at the edges of the nanotube shells to the intershell interaction energy is ignored, the energy barrier ΔU_c for relative motion of shells with commensurate structures can be determined from the expression $\Delta U_c = \Delta U_1 N_c$, where ΔU_1 is the energy barrier per unit cell of the nanotube and N_c is the number of unit cells in the nanotube. In other words, if the nanotube is sufficiently long, the energy barrier ΔU_c is proportional to the nanotube length.[1] This implies that, in the case of nanotube shells with commensurate structures, the possibility exists of synthesizing a nanotube with a specified energy barrier ΔU_c. The energy barrier ΔU_i for relative motion of nanotube shells with incommensurate structures does not increase with an increase in the nanotube length but fluctuates about a mean value, as is the case with the sum of the terms in the expansion of cos$j$ [22, 23]. The energy barriers to relative motion of commensurate and incommensurate shells along the nanotube axis (see [19, 22, 23]) are given in Table 1. It follows from the above consideration and the results presented in Table 1 that, for nanotubes approximately 10 μm long, the energy barrier to relative motion along the nanotube axis for commensurate shells is three or four orders of magnitude higher than the barrier for incommensurate shells. The mean threshold force, which is required to induce relative motion of shells along the nanotube axis, can be estimated as $F \approx 2\Delta U/l$, where ΔU is the barrier to relative motion of the nanotube shells and l is the displacement of the nanotube shells between their relative positions corresponding to the minima of the intershell interaction energy. Since there is only one equivalent minimum for each atom of the shell, according to Damnjanovic *et al.* [23], the displacement l cannot be less than $a_0/2$. In our case, this value of displacement l was used to estimate the threshold forces needed to induce relative motion of commensurate and incommensurate shells along the nanotube axis. The estimates obtained are also presented in Table 1. It can be seen from Table 1 that, for nanotubes approximately 10 μm long, the threshold forces exerted to induce relative motion along the nanotube axis for commensurate shells is three or four orders of magnitude greater than those for incommensurate shells. An examination of the relative motion of nanotube shells with the use of an atomic-force microscope revealed two types of relative shell motion, for which the threshold forces required to induce relative motion of the shells differed from each other by several orders of magnitude [12]. For relative shell motion of the first type, the threshold forces were found to be of the order of 100 nN/μm, which is in agreement with our estimates made for relative motion of shells with commensurate structures (Table 1). For relative shell motion of the sec-

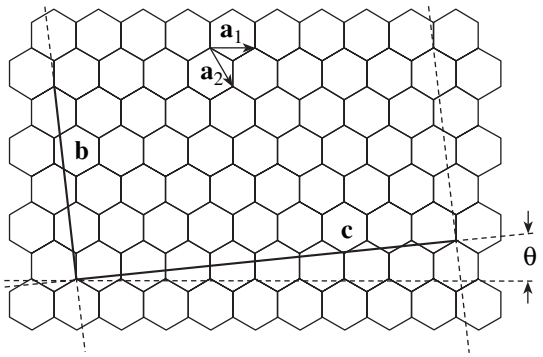

Fig. 1. A fragment of the graphite plane rolled into a nanotube shell. Designations: $\mathbf{a}_1$ and $\mathbf{a}_2$ are the unit vectors of the graphite plane, **b** is the unit vector, and θ the chiral angle. The nanotube shell is uniquely determined by the vector **c**.

[1] In recent years, it has become possible to synthesize nanotubes with a length ranging from 200 nm (nanotubes prepared through evaporation of carbon on a substrate [30]) to 30 μm (nanotubes produced through thermal decomposition of acetylene with a catalyst [31].

Table 1. Energy barriers and threshold forces required to induce relative motion of nanotube shells along the nanotube axis

Nanotube	Commensurability of shell structures	ΔU_m, meV	ΔU, eV/μm	F_m, nN	F, nN/μm
(14,0)@(16,10)	Incommensurate	300 [22]		0.8	
(12,12)@(18,6)	"	400 [23]		1.0	
(12,12)@(29,1)	"	400 [23]		1.0	
(12,12)@(24,9)	"	600 [23]		1.6	
(7,7)@(12,12)	Commensurate		200 [22]		500
(7,7)@(12,12)	"		1000 [23]		2600
(12,12)@(17,17)	"		500 [23]		1300
(5,5)@(10,10)	"		37 [19]		100

Note: ΔU_m is the maximum barrier to relative motion of nanotube shells with incommensurate structures, ΔU is the energy barrier to relative motion of nanotube shells with commensurate structures (per unit length of the nanotube), F_m is the threshold force required to induce relative motion of nanotube shells with incommensurate structures, and F is the threshold force required to induce relative motion of nanotube shells with commensurate structures (per unit length of the nanotube).

ond type, the threshold forces proved to be less than the force sensitivity of the microscope. It can be assumed that these two types of relative shell motion correspond to commensurate and incommensurate shells, respectively. Therefore, the threshold forces required to induce relative motion of nanotube shells with commensurate structures are more accessible for exact control of this motion in mechanical nanodevices, for example, with the use of a special manipulator [13].

Moreover, according to the calculations of the energy barrier to relative motion of nanotube shells with incommensurate structures as a function of the nanotube length [22, 23], a change in the length of one of the nanotube shells by only 1 nm causes the energy barrier ΔU_i to change by one order of magnitude. In this case, the synthesis of nanotubes with a specified barrier ΔU_i and, hence, with a specified force controlling the relative motion of the nanotube shells involves considerable difficulties.

Thus, we believe that relative motions of nanotube shells with commensurate and incommensurate structures can be used in radically different mechanical nanodevices. In particular, fast relative motions of nanotube shells with incommensurate structures that occur under the action of forces considerably stronger than the threshold force hold promise for use in nanodevices for which one of the important performance characteristics is the rate of relative motion of the nanotube shell. As an example, we refer to a nanobearing [14], a nanogear [15], a nanospring [13], and a nanodrill [17]. Slow relative motions of nanotube shells with commensurate structures that proceed under the action of forces with magnitudes of the order of the threshold force can be applied in nanodevices for which one of the important performance characteristics is the accuracy in determining the relative position of the nanotube shell. Examples of such nanodevices are provided by mechanical [16] and electric [17] nanoswitches.

3. CLASSIFICATION AND GEOMETRIC PARAMETERS OF NANOTUBES WITH TWO COMMENSURATE SHELLS

It follows from relationship (2) that all nanotube shells with chiral indices of the (kf, kg) type, where k is an integral number, have equal lengths of the unit cells,

$$b = \frac{\sqrt{3}a_0\sqrt{f^2 + fg + g^2}}{GCD(2f + g, f + 2g)} \quad (4)$$

and, hence, commensurate structures. For these shells, the chiral angles are also equal to each other. In what follows, a set of nanotube shells will be referred to as the equivalence class, provided f and g are relatively prime numbers; a pair of numbers (f, g) will be termed the chiral indices of the equivalence class; and k will stand for the index of the shell diameter. The equivalence classes with chiral indices (f, g) and (g, f) are assumed to be different, because, in the general case, the relevant shells of mirror symmetry with chiral indices (n, m) and (m, n) should be characterized by different energy barriers to motion relative to the neighboring shells. For the same equivalence class, the distance between nanotube shells with chiral indices ($k_1 f$, $k_1 g$) and ($k_2 f$, $k_2 g$), where $k_2 > k_1$, can be determined from the expression

$$\Delta R = \frac{a_0 \Delta k}{2\pi}\sqrt{f^2 + fg + g^2} \quad (5)$$

and depends only on the difference between the indices of the shell diameters $\Delta k = k_2 - k_1$. Consequently, for each equivalence class, there are families of two-shell nanotubes with an identical intershell distance determined by the difference Δk. In the case when the nanotube shells are formed simultaneously [32], the intershell distance corresponds to a minimum intershell interaction energy [33]. According to the calculations, this energy is close to the minimum energy for nano-

tubes with an intershell distance ΔR ranging from 3.3 to 3.5 Å. When the inner shell is formed after the outer shell (for example, under electron irradiation of fullerene-containing nanotubes), the intershell distance ΔR reaches 3.7 Å [25]. By virtue of the relationship $\Delta R \le 3.7$ Å, the shells belonging to the same equivalence class can be adjacent to each other in a particular nanotube only under the following condition:

$$f^2 + fg + g^2 \le \frac{(3.7 \times 2\pi\Delta k)^2}{a_0^2} < 91. \qquad (6)$$

The bond length $a_0/\sqrt{3}$ (the distance between the nearest neighbor carbon atoms in the nanotube shell) is taken to be equal to 1.41 Å, which is in agreement with both the calculations carried out in [34] and the experiments performed in [33]. Condition (6) is satisfied only for the equivalence classes with small chiral indices (f, g). All these equivalence classes and the corresponding geometric parameters of two-shell nanotubes with left-handed helicoidal shells of the same equivalence class are presented in Table 2. The upper part of this table contains all equivalence classes for which the distance ΔR between nanotube shells of the same class falls in the experimentally found range $I \equiv [3.3; 3.7]$ Å. The surprising thing is that the number of aforementioned equivalence classes is equal to only six. It should also be noted that two-shell nanotubes composed of shells belonging to the equivalence classes with chiral indices (f, g) and (g, f) exhibit mirror symmetry and, consequently, are characterized by equal geometric parameters.

Let us now consider a nanotube composed of shells belonging to different equivalence classes. For this nanotube with chiral indices $((k_1f_1, k_1g_1)@(k_2f_2, k_2g_2)$, the difference between the shells is determined by the formula

$$\Delta R = \frac{a_0}{2\pi}\sqrt{f_2^2 + f_2g_2 + g_2^2} \times\left(k_2 - k_1\frac{b_1 GCD(2f_1 + g_1, f_1 + 2g_1)}{b_2 GCD(2f_2 + g_2, f_2 + 2g_2)}\right). \qquad (7)$$

In the case when nanotube shells belonging to different equivalence classes have commensurate structures, i.e., when $b_1/b_2 = p/q$ (where p and q are relatively prime numbers corresponding to the ratio of the unit cell lengths of the shells), there are families of two-shell nanotubes with identical intershell distances for each pair of equivalence classes. It can easily be demonstrated that nanotube shells with commensurate structures always satisfy the relationship

$$\frac{GCD(2f_1 + g_1, f_1 + 2g_1)}{GCD(2f_2 + g_2, f_2 + 2g_2)} = 1. \qquad (8)$$

Table 2. Families of two-shell nanotubes with left-handed helicoidal shells of the same equivalence class with intershell distances $\Delta R < 3.7$ Å

(f, g)	Δk	ΔR, Å	b, Å	θ, deg
(1,0)	9	$3.50 \in I$	4.23	0.00
(1,1)	5	$3.37 \in I$	2.44	−30.00
(3,2)	2	$3.39 \in I$	18.44	−23.41
(4,1)	2	$3.56 \in I$	6.46	−10.89
(7,3)	1	$3.45 \in I$	37.60	−17.00
(8,1)	1	$3.32 \in I$	36.14	−5.82
(2,1)	4	3.09	11.19	−19.11
(3,1)	3	2.80	15.25	−13.90
(4,3)	1	2.36	25.73	−25.28
(5,1)	1	2.17	23.55	−8.95
(5,2)	1	2.43	8.81	−16.10
(5,3)	1	2.72	29.61	−21.79
(5,4)	1	3.04	33.04	−26.33
(6,1)	1	2.55	27.74	−7.59
(7,1)	1	2.93	10.65	−6.59
(7,2)	1	3.18	34.62	−12.22

Note: f and g are the chiral indices of the equivalence class; ΔR is the intershell distance; $\Delta k = k_2 - k_1$ is the difference between the indices of the shell diameters, which corresponds to the intershell distance ΔR; and b and θ are the unit cell length and the chiral angle of the shells, respectively. The characteristics of the nanotubes with intershell distances $\Delta R \in I \equiv [3.3; 3.7]$ Å are given in the upper part of the table.

For each family, the indices of the shell diameters can be written as

$$k_1^{(i)} = k_1^{(0)} + lq, \quad k_2^{(i)} = k_2^{(0)} + lp, \qquad (9)$$

where $k_1^{(0)}$ and $k_2^{(0)}$ are the indices of the shell diameters for any of the nanotubes of the family and l is an integral number. For each pair of equivalence classes, there is only one family with a specified intershell distance ΔR. Note that the indices of the shell diameters $k_1^{(i)}$ and $k_2^{(i)}$ are positive for nanotubes with chiral indices $(k_1^{(i)}f_1, k_1^{(i)}g_1)@(k_2^{(i)}f_2, k_2^{(i)}g_2)$ and negative for nanotubes with chiral indices $(-k_2^{(i)}f_2, -k_2^{(i)}g_2)@(-k_1^{(i)}f_1, -k_1^{(i)}g_1)$, in which the equivalence classes corresponding to the inner and outer shells change places.

Multishell nanotubes with an outside diameter up to 30 nm were obtained experimentally by Iijima [2]. For different equivalence classes, pairs of nanotube shells with commensurate structures in a multishell nanotube with an outside diameter up to 30 nm can belong to one of several hundreds of families. Since the number of these families is very large, they are not presented in this paper. The geometric parameters of two-shell nan-

Table 3. Families of two-shell nanotubes with left-handed helicoidal shells of different equivalence classes with intershell distances $\Delta R \in I = [3.3; 3.7]$ Å

(f_1, g_1)	(f_2, g_2)	$k_1^{(0)}$	$k_2^{(0)}$	p	q	ΔR, Å	$R_2^{\min}$, Å	H, Å	$\Delta\theta$, deg
(1,0)	(5,3)	5	2	1	7	3.50	5.44	29.61	21.79
(1,0)	(8,7)	4	1	1	13	3.50	5.05	54.99	27.80
(8,7)	(5,3)	2	5	13	7	3.50	13.60	384.93	6.01
(1,1)	(11,2)	2	1	1	7	3.37	4.71	17.10	21.79
(1,0)	(16,5)	10	1	1	19	3.50	7.39	80.37	13.17
(16,5)	(5,3)	1	4	19	7	3.50	10.88	562.59	8.61
(16,5)	(8,7)	5	8	19	13	3.50	40.42	1044.81	14.62
(4,1)	(20,17)	5	1	1	7	3.56	12.47	45.23	16.43
(1,1)	(22,1)	8	1	1	13	3.37	8.75	31.75	27.80
(11,2)	(22,1)	3	2	7	13	3.37	17.50	222.24	6.01
(1,0)	(24,11)	22	1	1	31	3.50	12.05	131.13	17.90
(5,3)	(24,11)	12	3	7	31	3.50	36.15	917.91	13.89
(24,11)	(8,7)	6	15	31	13	3.50	75.79	1704.69	9.90
(3,2)	(25,9)	5	1	1	7	3.39	11.86	129.07	8.61
(1,1)	(26,11)	14	1	1	19	3.37	12.79	46.40	13.17
(11,2)	(26,11)	2	1	7	19	3.37	12.79	324.81	8.61
(3,2)	(30,1)	5	1	1	7	3.39	11.86	129.07	21.79
(1,0)	(33,7)	28	1	1	37	3.50	14.38	156.51	9.43
(5,3)	(33,7)	4	1	7	37	3.50	14.38	1095.57	12.36
(1,0)	(35,13)	34	1	1	43	3.50	16,71	181.89	15.18
(5,3)	(35,13)	11	2	7	43	3.50	33.43	1273.23	6.61
(8,1)	(37,32)	6	1	1	7	3.32	23.25	252.99	21.79
(1,0)	(39,16)	40	1	1	49	3.50	19.05	207.27	16.43
(4,1)	(43,25)	11	1	1	13	3.56	23.16	84.00	10.42
(7,3)	(45,26)	6	1	1	7	3.45	24.18	263.18	4.22
(1,0)	(45,32)	58	1	1	67	3.50	26.04	283.41	24.43
(1,1)	(46,13)	26	1	1	31	3.37	20.87	75.71	17.90
(46,13)	(11,2)	3	14	31	7	3.37	65.98	529.96	3.89
(4,1)	(47,20)	11	1	1	13	3.56	23.16	84.00	6.01
(1,1)	(47,26)	32	1	1	37	3.37	24.91	90.36	9.43
(8,1)	(48,19)	6	1	1	7	3.32	23.25	252.99	10.15

Note: (f_1, g_1) and (f_2, g_2) are the chiral indices of the equivalence classes for the inner and outer shells of the nanotube, respectively; $k_1^{(0)}$ and $k_2^{(0)}$ are the indices of the diameters of the inner and outer shells in the nanotube with the smallest radius of the outer shell $R_2^{\min}$ in the family with the specified indices (f_1, g_1) and (f_2, g_2), respectively; p and q are relatively prime numbers corresponding to the ratio of the unit cell lengths of the shells; H is the unit cell length of the nanotube; and $\Delta\theta$ is the difference between the chiral angles of the shells. The families included in the table are characterized by chiral indices of the equivalence classes $f_1, f_2 < 50$ and radius $R_2 < 100$ Å for at least one of the nanotubes of the family.

otubes with commensurate structures of the shells for a number of families are given in Table 3. All nanotubes of the same family are characterized by equal geometric parameters: the intershell distance ΔR, the unit cell length of the nanotube H, and the difference between the chiral angles of the shells $\Delta\theta$.

Thus, we constructed a complete classification of two-shell carbon nanotubes with commensurate structures of the shells. The nanotube shells can be helicoidal and nonhelicoidal. In this respect, the two-shell nanotubes can be separated into three types: (1) nanotubes with two nonhelicoidal shells, (2) nanotubes with

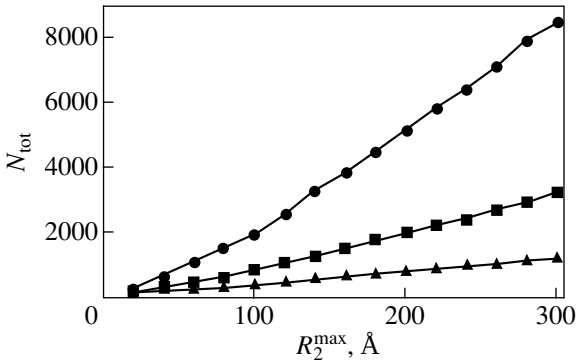

Fig. 2. The total number N_{tot} (with allowance made for the difference between the left-handed and right-handed helicoidal shells) of different-type two-shell nanotubes with commensurate structures of shells with an outer-shell radius less than R_2^{max} as a function of the largest outer-shell radius R_2^{max}.

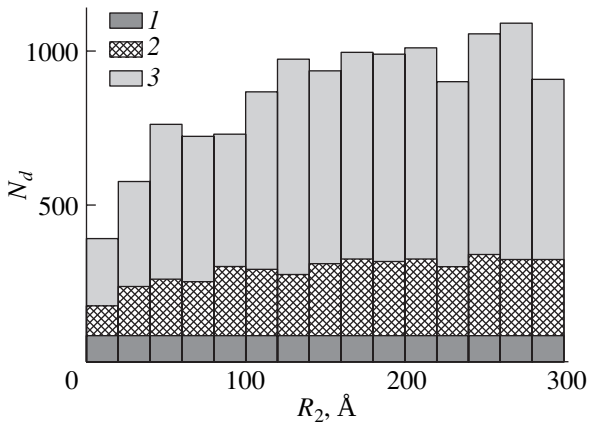

Fig. 3. Distribution of the numbers N_d of different-type two-shell nanotubes with commensurate shells over the outer-shell radii R_2: (*1*) nanotubes with two nonhelicoidal shells, (*2*) nanotubes with a helicoidal shell and a nonhelicoidal shell, and (*3*) nanotubes with two helicoidal shells.

a helicoidal shell and a nonhelicoidal shell, and (3) nanotubes with two helicoidal shells. Figure 2 presents the total number N_{tot} (with allowance made for the difference between the left-handed and right-handed helicoidal shells) of different-type two-shell nanotubes with commensurate structures of shells with an outer-shell radius less than R_2^{max} as a function of the largest outer-shell radius R_2^{max}. The distribution of the numbers N_d of different-type two-shell nanotubes with commensurate shells over the outer-shell radii is shown in Fig. 3. Since all nanotubes with two nonhelicoidal shells belong to only two families [(1, 0), (1, 0) and (1, 1) (1, 1)], the total number of nanotubes of this type increases linearly with an increase in the largest outer-shell radius. The total number of nanotubes of the other two types increases more rapidly, because the number of different families contributing to the total number of nanotubes also increases with an increase in the largest outer-shell radius.

The classification proposed in this work is applicable not only to carbon nanotubes but also to nanotubes whose shells are formed by rolling up a two-dimensional crystal with a unit cell similar to the unit cell of the graphite plane (a rhomb with a 60-degree angle between the elementary vectors of the lattice). Since the initial two-dimensional crystal has an n_c-fold symmetry axis, the nanotube shells determined by the crystal lattice vectors with an angle of $360°/n_c$ are indistinguishable. As a result, the number of different equivalence classes of the nanotube shells decreases by a factor of n_c as compared to the crystal without symmetry axes. In the case where the initial two-dimensional crystal, like the graphite plane, has a sixfold symmetry axis (for example, the crystal with a triangular lattice), the number of different equivalence classes of nanotube shells rolled up from these crystals coincides with the number of equivalence classes of the shells forming carbon nanotubes. If the initial two-dimensional crystal is characterized by a threefold (or twofold) symmetry axis or has no symmetry axes, the number of different equivalence classes of nanotube shells rolled up from these crystals is two (three) or six times greater than that of the shells forming carbon nanotubes. An interesting example of such nanotubes is provided by WS_2 nanotubes [35], whose shells are rolled up from a two-dimensional crystal with a threefold symmetry axis. In these nanotubes, the chemical interaction between atoms inside a shell is considerably stronger than the van der Waals interaction between atoms of neighboring shells, as is the case in carbon nanotubes. For this reason, we assume that, in WS_2 nanotubes, the shells can also readily move relative to each other.

Furthermore, the proposed classification can easily be extended to nanotubes whose shells are considered one-dimensional crystals. It can be demonstrated that a nanotube shell rolled up from a two-dimensional crystal with the elementary vectors $\mathbf{d}_1$ and $\mathbf{d}_2$ of the lattice represents a one-dimensional crystal only in the situation where α^2 and $\alpha\cos\phi$ are rational numbers. Here, $\alpha = |\mathbf{d}_2|/|\mathbf{d}_1|$ and ϕ is the angle between the vectors $\mathbf{d}_1$ and $\mathbf{d}_2$. (Examples of such two-dimensional crystals are crystals with a square lattice or crystals with a rectangular lattice for which the ratio between the elementary vectors is a rational fraction.) For these nanotubes, like carbon nanotubes, the shell is uniquely determined by the vector $\mathbf{h} = n\mathbf{d}_1 + m\mathbf{d}_2$. It is worth noting that nanotube shells with the chiral indices (n, m) and (m, n) have an identical structure but different helicities. As in the case of carbon nanotubes [see relationship (4)], all shells of the nanotubes with chiral indices of the (kf, kg) type, where k is an integral number, belong to the same equivalence class and are characterized by equal lengths of the unit cells:

$$b = \frac{s_1(f, g)}{s_2(f, g)} d_2(1 - \cos^2\varphi)\sqrt{f^2 + 2\alpha fg\cos\varphi + \alpha^2 g^2}, \quad (10)$$

where s_1 and s_2 are natural numbers.

Since the number of possible two-shell nanotubes with commensurate structures of the shells is relatively large, there arise considerable difficulties in examining the correlations between the geometric parameters and the characteristics of the relative shell motion. We believe that the proposed classification can be useful in analyzing these correlations and determining the pairs of nanotube shells promising for applications in nanomechanics. For example, this classification can be used in searching for pairs of neighboring shells with maximum and minimum energy barriers to relative rotation and motion of the shells along the nanotube axis. Moreover, Saito *et al.* [21] made a prediction regarding two-shell nanotubes with incommensurate shells for which the potential relief of the intershell interaction energy would be similar to a male–female screw thread. However, as was already noted in the present work, nanotubes with commensurate and incommensurate structures of shells can be used in radically different nanodevices. In our opinion, the proposed classification can also be applied in searching for pairs of neighboring nanotube shells with commensurate structures for which the potential relief of the intershell interaction energy is similar to a thread.

ACKNOWLEDGMENTS

This work was supported by the Russian Foundation for Basic Research and the research program of the Ministry of Science of the Russian Federation.

REFERENCES

1. S. Iijima, J. Cryst. Growth **50**, 675 (1980).
2. S. Iijima, Nature **345** (6348), 56 (1991).
3. R. Tamura, Phys. Rev. B **64** (20), 201404(R) (2001).
4. S. J. Tans, A. R. M. Verschueren, and C. Dekker, Nature **393** (6680), 49 (1998).
5. T. Rueches, P. Kim, E. Joselevich, *et al.*, Science **289** (5476), 94 (2000).
6. P. Kim and C. M. Lieber, Science **286** (5449), 2148 (1999).
7. S. Akita, Y. Nakayama, S. Mizooka, *et al.*, Appl. Phys. Lett. **79** (11), 1691 (2001).
8. S. S. Wong, E. Joselevich, A. T. Wolley, *et al.*, Nature **394** (6688), 52 (1998).
9. J. H. Haflier, C. L. Cheung, and C. M. Lieber, Nature **398** (6730), 761 (1999).
10. S. P. Jarvis, T. Uchihashi, T. Ishida, *et al.*, J. Phys. Chem. B **104** (26), 6091 (2000).
11. M. F. Yu, O. Lourie, M. J. Dyer, *et al.*, Science **287** (5453), 637 (2000).
12. M. F. Yu, B. I. Yakobson, and R. S. Ruoff, J. Phys. Chem. B **104** (37), 8764 (2000).
13. J. Cumings and A. Zettl, Science **289**, 602 (2000).
14. R. E. Tuzun, D. W. Noid, and B. G. Sumpter, Nanotechnology **6** (2), 52 (1995).
15. D. W. Srivastava, Nanotechnology **8** (4), 186 (1997).
16. L. Forro, Science **289** (5479), 560 (2000).
17. Yu. E. Lozovik, A. V. Minogin, and A. M. Popov, Microelectron. Eng. (in press).
18. A. Charlier, E. McRae, R. Heyd, *et al.*, Carbon **37** (11), 1779 (2000).
19. J.-C. Charlier and J. P. Michenaud, Phys. Rev. Lett. **70** (12), 1858 (1993).
20. Y. K. Kwon and D. Tomanek, Phys. Rev. B **58** (24), R16001 (1998).
21. R. Saito, R. Matsuo, T. Kimura, *et al.*, Chem. Phys. Lett. **348** (3–4), 187 (2001).
22. A. N. Kolmogorov and V. H. Crespi, Phys. Rev. Lett. **85** (22), 4727 (2000).
23. M. Damnjanovic, T. Vukovic, and I. Milosevic, Eur. Phys. J. B **25** (2), 131 (2002).
24. J. Sloan, R. E. Dunin-Borkowski, J. L. Hutchison, *et al.*, Chem. Phys. Lett. **316** (3–4), 191 (2000).
25. S. Bandow, M. Takizawa, K. Hirahara, *et al.*, Chem. Phys. Lett. **337** (1–3), 48 (2001).
26. M. Yoshida and E. Osawa, Fullerene Sci. Technol. **1** (1), 54 (1993).
27. Yu. E. Lozovik and A. M. Popov, Fiz. Tverd. Tela (St. Petersburg) **44** (1), 180 (2002) [Phys. Solid State **44** (1), 186 (2002)].
28. R. Saito, M. Fujita, G. Dresselhaus, and M. S. Dresselhaus, Appl. Phys. Lett. **60** (18), 2204 (1992).
29. R. A. Jishi, M. S. Dresselhaus, and G. Dresselhaus, Phys. Rev. B **47** (24), 16671 (1993).
30. M. Ge and K. Sattler, Science **260** (5107), 515 (1993).
31. X. B. Zhang, X. F. Zhang, D. Bernaerts, *et al.*, Europhys. Lett. **27** (2), 141 (1994).
32. Yu. E. Lozovik and A. M. Popov, Usp. Fiz. Nauk **167** (7), 751 (1997) [Phys. Usp. **40**, 717 (1997)].
33. A. Burian, J. C. Dore, H. E. Fisher, and J. Sloan, Phys. Rev. B **59** (3), 1665 (1999).
34. O. Gulseren, T. Yildirim, and S. Liraci, Phys. Rev. B **65** (15), 153405 (2002).
35. R. Tenne, L. Margulis, M. Genut, and G. Hodes, Nature **360** (445), 6403 (1992).

Translated by O. Borovik-Romanova

Physics of the Solid State, Vol. 45, No. 7, 2003, pp. 1403–1407. Translated from Fizika Tverdogo Tela, Vol. 45, No. 7, 2003, pp. 1339–1342.

FULLERENES AND ATOMIC CLUSTERS

Unwinding Algorithm for Numerical Generation and Writing of Fullerenes

A. M. Livshits and Yu. E. Lozovik

Institute of Spectroscopy, Russian Academy of Sciences, Troitsk, Moscow oblast, 142092 Russia

e-mail: lozovik@isan.troitsk.ru

Received July 11, 2002; in final form, December 10, 2002

Abstract—An efficient algorithm is proposed for the numerical generation of fullerenes of an arbitrary structure. The algorithm is a combination of the method for unwinding fullerenes into a triangular network and the topological-invariants method for describing quasi-two-dimensional closed clusters. Graphs of possible structures of C_n fullerenes are found satisfying the isolated-pentagon rule for numbers of atoms in the range $100 < n \le 150$. © *2003 MAIK "Nauka/Interperiodica".*

1. INTRODUCTION

Considerable recent attention has been focused on fullerenes and other cluster structures based on quasi-two-dimensional carbon atomic networks [1, 2]. Such structures are candidates for nanoelectronic technologies; in particular, podlike carbon structures (a nanotube with a fullerene which can move within it) [3] may serve as a basis for nanoswitches and the system consisting of two nanotubes and a fullerene placed between them can be used as a nanovariometer, with its resistance varying by several orders of magnitude when one of the nanotubes is rotated through a small angle relative to the fullerene. Fullerenes find application as high-quality masks against photochemical etching used for preparing nanostructures. Since the first excited triplet level of a fullerene molecule is close to resonance with the metastable singlet level of an oxygen molecule, fullerenes can be employed as a sensitizer in photochemical reactions with the release of singlet oxygen and are candidates for photodynamic therapy. Fullerenes are used as initial elements for the molecular design and fabrication of new materials with unique properties, such as ultrahard materials (obtained through polymerization of fullerenes) and new superconducting materials [4]. Therefore, the task of finding possible isomers of the C_n fullerene is of considerable importance from both a theoretical and technological standpoint.

Various algorithms have been developed for numerical generation of fullerene structures [1, 5–7]. The most popular generating scheme is the ring-spiral algorithm, based on the assumption that the surface of any fullerene can be unwound into a spiral of touching pentagons and hexagons [8]. Although it was found later that there are fullerenes which cannot be unwound into a spiral (e.g., the fullerene with tetrahedral symmetry with $n = 380$ [9]), the ring-spiral algorithm remained a convenient and reliable method for describing small and medium-sized fullerenes. In various studies, it has been confirmed that this algorithm generates all possible fullerene structures for $n \le 100$. However, in the case of large values of n, other methods should be applied for investigating all possible fullerene structures.

There are several methods of fullerene generation [1, 10, 11] based on fullerene unwinding into a planar hexagonal or triangular network. In this paper, one of those methods [1] is used and developed further. Any C_n fullerene can be cut so that, when it is unwound into a triangular network, the sites corresponding to the pentagonal faces of the fullerene will be at the corners of a closed, 22-sided polygon. This polygon can be uniquely determined by 11 vectors of the triangular network, and the area $S(n)$ of the polygon is equal to $(\sqrt{3}/4)n$, where n is the number of carbon atoms in the fullerene molecule. The face-dual network (FDN) can be inverted to obtain the original fullerene. By constructing all possible FDNs of area $S(n)$, we will find all isomers of the C_n fullerene. Given a triangular FDN of a fullerene, we can construct the fullerene graph and, using quantum-chemical calculations, find all required characteristics.

However, a fullerene can be cut in a variety of ways; therefore, one isomer can be associated with a large number of FDNs (the upper estimate is 12, which corresponds to the number of permutations of 12 pentamers). In the method developed in [1], one calculates the atomic coordinates for the fullerenes corresponding to all FDNs to be tested and then the structures found are compared using the HMO full energies and the HOMO and LUMO eigenvalues. The number of isomers tends to increase with increasing n. Indeed, for $n = 80$, we have seven fullerenes with isolated pentagons (IPRs); for $n = 90$, this number is 46; and for $n = 100$, we have

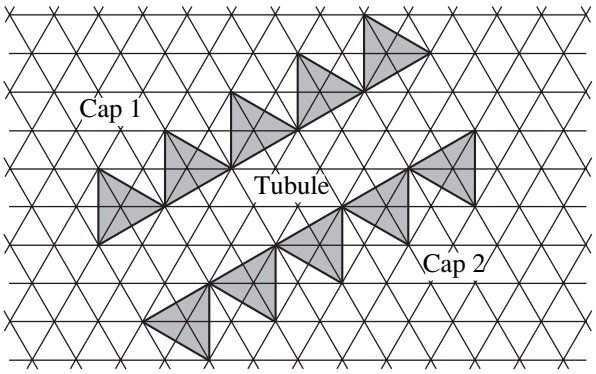

Fig. 1. Triangular face-dual network of the fullerene C_{70} (D_{5h}).

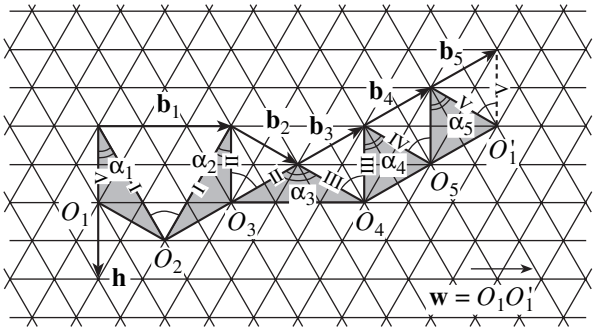

Fig. 2. Structure of a cap segment.

450 IPR isomers [1]. Therefore, for $n > 100$, a more efficient method for eliminating equivalent FDNs is called for instead of quantum-chemical calculations, as the latter are very time consuming.

The distance matrix **D** of the fullerene-dual graph uniquely determines the structure of the fullerene graph. One can calculate the invariants of the distance matrix that are independent of the order of numbering the graph vertices. Based on a triangular FDN of a fullerene, we can find the distance matrix **D** and calculate its invariants. If the invariants for different FDNs are identical, these FDNs correspond to the same fullerene. This algorithm is very efficient, because calculations are performed, for the most part, for an integer-numbered network.

2. METHOD

We consider fullerenes of an arbitrary structure, i.e., closed clusters of sp^2-hybridized carbon consisting of five- and six-membered rings only. An idealized model is used (unless otherwise specified) in which a fullerene is treated as a convex polyhedron, with its vertices corresponding to carbon atoms and its edges, to σ bonds. In accordance with Euler's theorem, we have

$$f + v - e = 2, \tag{1}$$

where f, v, and e are the numbers of faces, vertices, and edges of the polyhedron, respectively. It follows that an arbitrary fullerene always has 12 five-membered rings (pentagonal faces).

There is a one-to-one correspondence between a triangular and a hexagonal network: the centers of the faces of the hexagonal network correspond to the sites of the triangular network, and the centers of the faces of the triangular network, to the sites of the hexagonal network. A fullerene can be cut and unwound into both a planar hexagonal and a planar triangular network. In the latter case, the centers of hexagonal and pentagonal fullerene faces will be at the network sites. According to the method proposed in [1], an arbitrary fullerene can be cut and unwound into a planar triangular network so that the network is a plane 22-sided polygon consisting of two cap segments and of one tubular segment (Fig. 1).

Let us consider the structure of a cap segment in more detail (Fig. 2). The cap consists of five nonoverlapping triangles whose bases form a continuous broken line $O_1O_2O_3O_4O_5O_1'$ and whose vertices opposite to the bases lie on one side of this line. The adjacent lateral sides of neighboring triangles are equal, and the angle between them is $\pi/3$. Thus, there is a sequence of five equilateral triangles which complements the cap segment. The angles α_k ($k = 1, \ldots, 5$) are not fixed, but their values satisfy the equality

$$\sum_{k=1}^{5} \alpha_k = 5\pi/3. \tag{2}$$

The cap segment is unambiguously determined by the five triangular-network vectors $\mathbf{b}_k$. The vector **w** (Fig. 2) also characterizes the cap segment and is related to the vectors $\mathbf{b}_k$ through the relation $\mathbf{w} = \sum_1^5 \mathbf{b}_k$.

Thus, the FDN consists of two cap segments (the other cap segment is rotated through an angle of $\pi/2$) and one tubular segment. A necessary condition for fullerene unwinding to be possible is the equality of the vectors **w** of the two cap segments. The tubular segment lies between the cap segments and is a closed dodecagon without self-crossings. The "lateral" sides of the tubular segment are equal and parallel and are determined by the vector **h** (Fig. 2). The area of the FDN is $\sqrt{3}n/4$, where n is the number of fullerene atoms.

The scheme we employed to search for isomers of the C_n fullerene is as follows. Iterations are performed with respect to the vectors **w** and **h**. For each value of **w**, all possible pairs of cap segments with a given vector **w** are tested. Enantiomorphous structures are considered to be identical; therefore, it will suffice to deal with

only cap segments characterized by a vector $\mathbf{w} = \overline{(i, j)}$ with $i \geq j \geq 0$. Only FDNs having area $\sqrt{3}n/4$ and satisfying the isolated-pentagon rule are chosen.

Since a fullerene can be cut in various ways, the generation algorithm described above gives a great quantity of isomorphic configurations (Fig. 3). The number of different FDNs corresponding to the same fullerene depends on the structure of the specific fullerene. An upper estimate is given by the number of ways in which the pentamer vertices can be enumerated and is equal to 12 (the number of permutations of 12 pentamers). In order to eliminate isomorphic configurations, we perform the following procedure. One or a few invariants I_{G^*} are calculated for each FDN (see below). Next, FDNs are checked, one by one, for whether or not a configuration with the given invariant or the given set of invariants has already been dealt with. If this is the case, the configuration at hand is ignored and we pass to the next FDN; otherwise, the configuration at hand and its invariant I_{G^*} are stored.

Let G^* be a graph that is dual to the fullerene graph G; that is, the vertices of the graph G^* correspond to the faces of the fullerene graph G and the vertices of the graph G correspond to the faces of the graph G^*. There is a single way in which the fullerene graph can be arranged on a sphere; therefore, there is a one-to-one correspondence $G \rightleftharpoons G^*$. We define the distance between two vertices of a graph as the length of the shortest simple path connecting these vertices. A triangular FDN of a C_n fullerene carries complete information on the incidence of the N vertices ($N = n/2 - 2$) of graph G^* dual to the fullerene graph. For each FDN, we calculate the $N \times N$ distance matrix of graph G^*. The distance matrix of a graph determines the incidence matrix of the graph and, hence, the graph itself.

There are invariants that are independent of the order of numbering of the graph vertices. For example, as such an invariant for a given vertex i of graph G^*, one can take a function (symmetric under any permutation of its arguments) of the distances between the given vertex and all other vertices of the graph:

$$V_i(f) = \sum_j{}' f(d_{ij}), \tag{3}$$

where d_{ij} is the distance between the vertices i and j and the prime on the sum indicates that the summation is carried out over all vertices except the vertex i. The function f can be taken to be a power-law function:

$$V_i(p) = \sum_j{}' d_{ij}^p, \tag{4}$$

where p is an arbitrary integer, rational, or real number.

Each vertex i of graph G^* is characterized by the distribution $n_k^i(d_k)$ of its distances from the other vertices of the graph, where n_k^i is the number of vertices whose distances from the vertex i are equal to d_k (belonging to the set of distances $\{d_{ij}\}$). The function f should be chosen such that, for any two vertices a and b of graph G^* characterized by different distributions $n_k^a(d_k)$ and $n_k^b(d_k)$, the respective invariants $V_a(f)$ and $V_b(f)$ are also different.

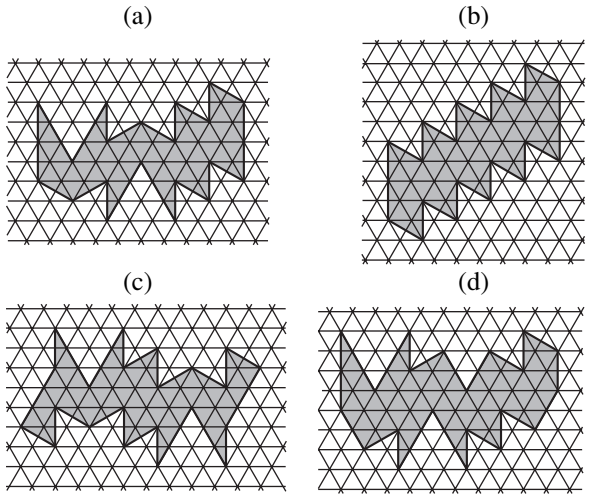

Fig. 3. Fullerene C_{60} (I_h), cut and unwound into a triangular network in four different ways: a, b, c, and d.

We calculated the invariant $V_i(h)$ of a vertex i using the values of the so-called hash function, which gives a hash value (integer) corresponding to an entered key (set of integers). The key was the distance distribution $n_k^i(d_k)$ for the vertex i. The hash function was defined using the XOR operation and bit-by-bit shift as is done for the standard hash function in the STL library [12].

Invariants of the full graph G^* are the expressions

$$I_{G^*}(f, g_1, g_2) = \sum_{i>j} g_1(V_i(f), V_j(f))g_2(d_{ij}), \tag{5}$$

where g_1 is an arbitrary function symmetric under permutation of its two arguments and g_2 is an arbitrary function. In our calculations, we used the invariant

$$I_{G^*} = \sum_{i>j} [V_i(h)V_j(h)]^{1/2}\delta(d_{ij} - 1), \tag{6}$$

where $V_i(h)$ and $V_j(h)$ are values of the hash function. The function $\delta(d_{ij} - 1)$ is equal to unity when the vertices i and j are incident; otherwise, it is zero.

We also performed calculations using different combinations of several invariants (5). The results obtained in this case are identical to those obtained with

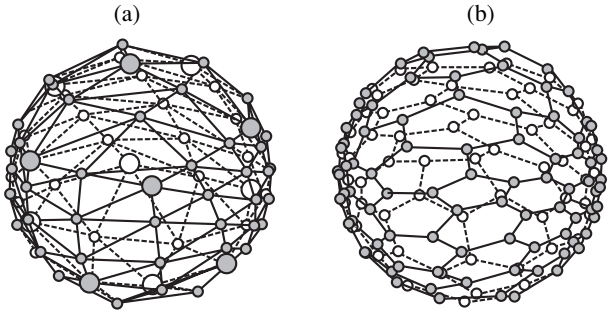

Fig. 4. Dual graphs G^* and G of the fullerene C_{150} arranged on a sphere. The vertices on the back side of the sphere are represented by open circles. (a) Fullerene graph G^*; the pentamer vertices are represented by larger circles. (b) Graph G of the same fullerene with the same orientation in space; the vertices of graph G correspond to the centers of the faces of graph G^*, and *vice versa*.

invariant (6). Therefore, invariant (6) uniquely determines the graph of the C_n fullerene in the range $20 \le n \le 150$ considered in this paper.

Numbers of isomers of isolated-pentagon fullerenes C_n for different values of n ($100 < n \le 150$)

n	k
102	616
104	823
106	1233
108	1799
110	2355
112	3342
114	4468
116	6063
118	8148
120	10 774
122	13 977
124	18 769
126	23 589
128	30 683
130	39 393
132	49 878
134	62 372
136	79 362
138	98 541
140	121 354
142	151 201
144	186 611
146	225 245
148	277 930
150	335 569

3. RESULTS

Using the scheme described above, we found possible configurations of C_n fullerenes with isolated pentagons for $100 < n \le 150$. The results obtained for fullerenes satisfying the isolated-pentagon rule in the case of $60 \le n \le 100$ and for arbitrary fullerenes in the case of $20 \le n \le 60$ agree with the results obtained earlier [1]. Figure 4 shows the graphs G^* and G arranged on a sphere for one of the isomers found for the C_{150} fullerene. The numbers of isomers of IPR fullerenes C_n for different values of n ($100 < n \le 150$) are listed in the table.[1]

The number of isomers of C_n fullerenes increases sharply (by three orders of magnitude) as n increases from 100 to 150. Fullerenes of high symmetry (T, T_d, T_h, I, I_h) have been found earlier [5]. A comparison with the data from [5] shows that fullerenes with $n > 100$ are predominantly of low symmetry. For instance, according to our calculations for $n = 120$, there are 10 774 isomers of isolated-pentagon fullerenes and only one of them has tetrahedral symmetry. It should be noted that here we deal with the highest possible symmetry of fullerenes; in actuality, the symmetry of a fullerene may be lower due to Jahn–Teller distortions.

4. CONCLUSIONS

Thus, a scheme for the numerical generation of fullerenes has been proposed in which a modified method for unwinding a fullerene into a planar triangular network is used. In order to find possible configurations, topological invariants of the fullerene graph have been calculated. Such calculations are much less time consuming than quantum-chemical calculations. Using the method proposed, we have found face-dual networks of all possible isomers of isolated-pentagon fullerenes C_n with $n \le 150$.

A face-dual network of a fullerene carries information on all σ bonds of the fullerene; therefore, it can be taken as a starting point for quantum-chemical calculations.

REFERENCES

1. M. Yoshida and E. Osawa, Bull. Chem. Soc. Jpn. **68**, 2073 (1995).
2. V. Georgakilas, F. Pellarini, M. Prato, *et al.*, Proc. Natl. Acad. Sci. USA **99**, 5075 (2002).
3. S. Berber, Y. Kwon, and D. Tomanek, Phys. Rev. Lett. **88**, 185502 (2002).
4. M. Capone, M. Fabrizio, C. Castellani, and E. Tosatti, Science **296**, 2364 (2002).

[1] Electronic files containing the calculated FDNs and distance matrices for other configurations can be made available by the authors.

5. P. W. Fowler, J. E. Cremona, and J. I. Steer, Theor. Chim. Acta **73**, 1 (1998).
6. B. L. Zhang, C. Z. Wang, K. M. Ho, *et al.*, J. Chem. Phys. **98** (4), 3095 (1993).
7. A. T. Balaban, D. Babic, and D. J. Klein, J. Chem. Educ. **72**, 693 (1995).
8. D. E. Manolopoulos and P. W. Fowler, J. Chem. Phys. **96**, 7603 (1992).
9. D. E. Manolopoulos and P. W. Fowler, Chem. Phys. Lett. **204**, 1 (1993).
10. M. Fujita, R. Saito, G. Dresselhaus, and M. S. Dresselhaus, Phys. Rev. B **45**, 13834 (1992).
11. D. L. D. Caspar, Philos. Trans. R. Soc. London, Ser. A **343**, 133 (1993).
12. B. Stroustrup, *The C++ Programming Language*, 3rd ed. (Addison-Wesley, Reading, Mass., 1997; Binom, Moscow, 1999).

Translated by Yu. Epifanov